La mise en forme de métaux et d'alliages métalliques par fusion laser sur lit de poudre pour applications à haute température

par

Aurore LECLERCQ

THÈSE PAR ARTICLES PRÉSENTÉE À L'ÉCOLE DE TECHNOLOGIE SUPÉRIEURE COMME EXIGENCE PARTIELLE À L'OBTENTION DU DOCTORAT EN GÉNIE
Ph. D.

MONTRÉAL, LE 12 DÉCEMBRE 2025

ÉCOLE DE TECHNOLOGIE SUPÉRIEURE
UNIVERSITÉ DU QUÉBEC

Aurore Leclercq 2025

Cette licence Creative Commons signifie qu'il est permis de diffuser, d'imprimer ou de sauvegarder sur un autre support une partie ou la totalité de cette œuvre à condition de mentionner l'auteur, que ces utilisations soient faites à des fins non commerciales et que le contenu de l'œuvre n'ait pas été modifié.

PRÉSENTATION DU JURY

CETTE THÈSE A ÉTÉ ÉVALUÉE

PAR UN JURY COMPOSÉ DE :

M. Vladimir Brailovski, directeur de thèse
Département de génie mécanique à l'École de technologie supérieure

M. François Blanchard, président du jury
Département de génie électrique à l'École de technologie supérieure

M. Mohammad Jahazi, membre du jury
Département de génie mécanique à l'École de technologie supérieure

M. Souheil-Antoine Tahan, membre du jury
Département de génie mécanique à l'École de technologie supérieure

M. Sylvain Turenne, membre du jury
Professeur retraité du Département de génie mécanique à Polytechnique Montréal

M. Manuel Martin, examinateur externe
Centre national de recherches Canada

ELLE A FAIT L'OBJET D'UNE SOUTENANCE DEVANT JURY ET PUBLIC

LE 3 DÉCEMBRE 2025

À L'ÉCOLE DE TECHNOLOGIE SUPÉRIEURE

REMERCIEMENTS

Pour commencer, je voudrais remercier mon directeur de recherche, le professeur Vladimir Brailovski, sans qui ce travail n'aurait pu aboutir. Je vous suis particulièrement reconnaissante pour votre investissement, vos conseils, mais plus que tout votre grande disponibilité. Vous m'avez poussée à me dépasser et m'avez guidée jusqu'au bout de ce projet avec une grande rigueur.

Je tiens également à remercier le professeur François Blanchard d'avoir accepté de présider ce jury ainsi que les professeurs Mohammad Jahazi, Souheil-Antoine Tahan et messieurs Manuel Martin et Sylvain Turenne d'avoir accepté d'évaluer ce travail.

Je voudrais également remercier nos partenaires outre-Atlantique sur ce projet, Adriana Wrona, Anna Czech, Marcin Lis et Witold Kurylak, qui nous ont offert une superbe visite de l'IMN et un très bel accueil en Pologne, ainsi que nos partenaires régionaux Mathieu Picard et Patrick Dubois avec qui les échanges étaient toujours très intéressants et conviviaux.

Un grand merci à Thibault Mouret, Ph. D., qui, plus qu'un coauteur sur la majorité des articles, aura été mon partenaire de travail pendant la moitié du projet. Merci infiniment d'avoir partagé la charge de travail avec moi, d'avoir sacrifié quelques fins de semaine et beaucoup trop d'heures de ton temps libre, mais surtout de m'avoir épaulée tout au long de ces travaux. Cette thèse n'aurait définitivement pas la même allure sans ton soutien, tes conseils et ton savoir-faire !

Merci également à tous mes collègues de l'équipe du LAMSI, Alena, Anatolie, Atefeh, Donatien, Emma, Erika, Etienne, Julien, Matheus, Morgan, Mykhailo, Neda, Quentin, Salah, William et Xavier, ainsi qu'aux stagiaires Clara, Lola, Rafaël et Simon. Vous m'avez, pour certains, pris sous votre aile, conseillée, accueillie et intégrée à ce laboratoire et plus largement à ce pays, et, pour d'autres, partagé mon labeur, mes inquiétudes et de très bons moments, mais vous avez surtout tous contribué à faire de ma thèse une expérience inoubliable.

Je tiens à adresser mon plus grand respect à l'équipe de professionnels et techniciens de l'école, Anthony Remington, Joël Grignon, Michel Drouin, Mohammad Saadati, Radu Romanica, Serge Plamondon, Stephane Kodia et Xavier Rimpault. Je n'aurais pas pu mener à bien ce projet sans votre aide, votre disponibilité, votre grande adaptabilité et vos nombreux conseils.

Je tiens à remercier chaleureusement ma famille et mes amis, vous qui m'avez soutenu depuis les coulisses et avez fait preuve d'une infinie patience face à mes récits très détaillés à chaque étape. Et à toi, Léo, mon mari, qui m'aura accompagné dans cette folle aventure à l'autre bout du monde et m'aura épaulée en toutes circonstances.

Enfin, une dernière pensée à chaque lecteur qui sera suffisamment brave pour se rendre jusqu'au bout de ce document.

La mise en forme de métaux et d'alliages métalliques par fusion laser sur lit de poudre pour applications à haute température

Aurore LECLERCQ

RÉSUMÉ

Pour de nombreux dispositifs travaillant à haute et très haute température, l'augmentation des performances vient avec l'élévation de la température d'opération. Bien que les procédés de fabrication additive permettent d'élargir la plage d'utilisation des matériaux traditionnels, de nouveaux matériaux sont nécessaires pour dépasser leurs limites. Ce projet se concentre sur la recherche d'une alternative plus performante aux matériaux communément utilisés dans la chambre de combustion et l'assemblage du rotor d'une microturbine à architecture renversée. Ce projet vise des métaux réfractaires, un alliage de titane de nouvelle génération et un intermétallique à base d'aluminures de titane, mis en forme par fusion laser sur lit de poudre.

L'objectif est de réduire les contraintes d'intégration des nouveaux matériaux sur des machines à puissance limitée, sans contrôle de température dans la chambre d'impression. Le projet commence par collecter des informations sur le bain de fusion par des approches numériques et expérimentales, puis continue avec un plan d'expériences réduit pour produire des échantillons pour analyses structurales et tests mécaniques et obtenir des jeux de paramètres optimisés spécifiques à chaque matériau. Enfin, des pièces de précision, d'autres à géométries complexes, voire de premiers prototypes, sont fabriqués pour tester l'imprimabilité et la robustesse des paramètres retenus.

Le projet débute avec le tungstène et le molybdène. Un modèle numérique a permis de définir rapidement un plan d'expériences et d'obtenir des échantillons sans fissures, avec des propriétés compétitives par rapport à la métallurgie des poudres conventionnelle. L'ajout de rhénium au molybdène et le recours à des post-traitements ont amélioré les propriétés mécaniques, bien que des problèmes d'oxydation aient limité les performances à haute température. Les limites d'imprimabilité ont été déterminées, et un prototype d'injecteur micro-

prémélangé en molybdène pur a été produit, bien qu'il n'ait pas pu être testé en conditions réelles.

Ensuite, ne pouvant recourir au modèle numérique pour l'alliage de titane nouvelle génération Ti-6Al-2Sn-4Zr-6Mo, la démarche a été adaptée de manière expérimentale. Cette approche a permis de définir des plages réduites de paramètres de fabrication pour enfin obtenir des échantillons de qualité, avec des jeux de paramètres optimisés offrant le choix entre productivité et précision. Cependant, les tests mécaniques ont révélé un manque de ductilité critique dans le cadre de cette application, que des post-traitements ont su améliorer au détriment de la résistance mécanique. Enfin, le passage vers un équipement de capacité équivalente a mis en avant que la différence d'architecture seule d'un tel équipement suffît à compromettre les propriétés obtenues, justifiant la nécessité d'ajustement des paramètres de fabrication pour chaque équipement de fabrication.

Enfin, pour l'intermétallique à base d'aluminures de titane Ti-22Al-25Nb, les modifications des paramètres de fabrication n'ont pas suffi à éviter les fissures dans les pièces. Un post-traitement en sortie d'impression a permis d'obtenir des échantillons sains, mais le passage à des géométries plus complexes et plus larges a révélé les limites de cette solution. Les données recueillies ont cependant permis de définir des critères d'imprimabilité pour cet alliage, tout en soulignant les contraintes de sa mise en forme sur des machines à puissance limitée sans contrôle de température dans la chambre d'impression.

Ce projet montre que, bien que prometteuse, l'implémentation de nouveaux métaux pour application à haute température par le procédé de fusion laser sur lit de poudre reste soumise à des défis techniques liés à l'optimisation des paramètres de fabrication et de post-traitements avant d'envisager leur intégration dans des dispositifs fonctionnels.

Mots clefs : Fabrication additive, métaux réfractaires, alliages de titane, intermétalliques à base d'aluminures de titane, tests haute température, post-traitements, géométries complexes

Processing of metals and alloys via laser powder bed fusion for high-temperature applications

Aurore LECLERCQ

ABSTRACT

For many systems operating at high and very high temperatures, performance improvements come with an increase in operating temperature. Although additive manufacturing processes allow for an expanded range of use for traditional materials, new classes of materials are needed to surpass their inherent limitations. This project focuses on offering an alternative for metals actually used in the combustor and the rotor assembly of an inside-out microturbine. To this end, refractory metals, a next-generation titanium alloy, and a titanium aluminide-based intermetallic have been selected to be processed using the laser powder bed fusion (LPBF) additive manufacturing process.

The objective is to reduce the integration constraints of new materials on low-power machines without temperature control in the printing chamber. The project begins by collecting information about the melt pool through both numerical and experimental approaches, then developing a reduced plan of experiments to produce samples for structural analysis and mechanical testing in order to obtain optimized parameter sets specific to each material. Finally, precision parts, others with complex geometries, and initial prototypes are manufactured to test the printability and robustness of the selected parameters.

The project starts with tungsten and molybdenum. A numerical model allowed for the quick definition of a reduced plan of experiments and the production of crack-free samples with properties competitive with conventional powder metallurgy. The addition of rhenium to molybdenum and the use of post-processing improved the mechanical properties, although oxidation problems limited high-temperature performance. Printability limits were determined, and a pure molybdenum micro-premixed injector prototype was produced, though it could not be tested in real conditions.

Next, due to the complexity of the fusion and solidification phenomena in the next-generation titanium alloy Ti-6Al-2Sn-4Zr-6Mo, the approach was adapted experimentally. This method enabled the definition of reduced ranges of process parameters, ultimately producing high-quality samples with optimized parameter sets offering a choice between productivity and precision. However, mechanical testing revealed a critical lack of ductility for this application, which was improved through post-processing at the expense of mechanical strength. Finally, moving to an equivalent capacity equipment highlighted that the architectural difference between the two equipment alone was enough to compromise the obtained properties, justifying the need to adjust the process parameters for each new piece of equipment.

Finally, for the titanium aluminide-based intermetallic Ti-22Al-25Nb, modifications to the process parameters were not sufficient to prevent cracking in the parts. A post-processing step after printing allowed for the production of sound samples, but moving to more complex and larger geometries revealed the limits of this solution. However, the data collected allowed for the definition of printability criteria for this alloy, while emphasizing the constraints of printing on machines with limited power and no temperature control in the printing chamber.

This project demonstrates that, although promising, the implementation of new metals for high-temperature applications using laser powder bed fusion still faces technical challenges related to the optimization of process and post-process parameters before their integration into functional devices.

Keywords: Additive manufacturing, refractory metals, titanium alloys, titanium aluminide-based intermetallics, high-temperature testing, post-processing, complex geometries

TABLE DES MATIÈRES

Page

INTRODUCTION 1

CHAPITRE 1 REVUE DE LITTÉRATURE 3
1.1 Contexte 3
1.2 Amélioration des composants à haute température 5
1.3 Nouvelle génération de matériaux 13
1.4 La fusion laser sur lit de poudre 28
1.5 Résumé et définition des objectifs du projet 46

CHAPITRE 2 IMPROVING LASER POWDER BED FUSION PRINTABILITY OF TUNGSTEN POWDERS USING SIMULATION DRIVENPROCESS OPTIMIZATION ALGORITHMS 51
2.1 Avant-propos 51
2.2 Résumé 51
2.3 Abstract 52
2.4 Introduction 53
2.5 Materials and Methods 57
2.6 Results 74
2.7 Discussion 87
2.8 Conclusions 92
2.9 Future Work 93
2.10 Author Contributions 94
2.11 Funding 94
2.12 Institutional Review Board Statement 94
2.13 Informed Consent Statement 94
2.14 Data Availability Statement 94
2.15 Acknowledgments 95
2.16 Conflicts of Interest 95

CHAPITRE 3 LASER POWDER BED FUSION OF MOLYBDENUM: DENSITY, STRUCTURE AND MECHANICAL PROPERTIES AT ROOM AND ELEVATED TEMPERATURE 97
3.1 Avant-propos 97
3.2 Résumé 97
3.3 Abstract 98
3.4 Introduction 99
3.5 Materials and methods 103
3.6 Results 117
3.7 Discussion 132
3.8 Conclusions 139

3.9 CRediT authorship contribution statement 140
3.10 Declaration of competing interest 140
3.11 Acknowledgments 141
3.12 Data availability 141

CHAPITRE 4 MOLYBDENUM 8WT% RHENIUM ALLOY PROCESSED BY LASER POWDER BED FUSION: FROM POWDER PRODUCTION TO MECHANICAL TESTING AT ELEVATED TEMPERATURES 143
4.1 Avant-propos 143
4.2 Résumé 143
4.3 Abstract 144
4.4 Introduction 145
4.5 Materials and methods 151
4.6 Results 160
4.7 Discussions 173
4.8 Conclusions 177
4.9 CRediT authorship contribution statement 178
4.10 Declaration of competing interest 178
4.11 Acknowledgments 178
4.12 Data availability 178

CHAPITRE 5 LPBF PRINTABILITY AND AS-PRINTED MECHANICAL PROPERTIES OF A TI6246 ALLOY AS FUNCTIONS OF PRINTING PARAMETERS AND MICROSTRUCTURE 179
5.1 Avant-propos 179
5.2 Résumé 180
5.3 Abstract 180
5.4 Introduction 181
5.5 Material and methods 186
5.6 Results 193
5.7 Discussion 205
5.8 Conclusion 214
5.9 CRediT authorship contribution statement 215
5.10 Declaration of competing interest 215
5.11 Acknowledgments 215
5.12 Data availability 215

CHAPITRE 6 IMPRIMABILITÉ DE L'ALLIAGE DE TITANE TI-6AL-2SN-4ZR-6MO ET EFFETS DE POST-TRAITEMENTS EN VUE DE SON INTEGRATION POUR APPLICATION STRUCTURALE 217
6.1 Effect of layer thickness on the as-built density, microstructure, mechanical properties, surface roughness and printability of LPBF Ti6246 components 218
6.2 Effect of heat treatments on the structure and mechanical properties of a laser powder fused Ti-6Al-2Sn-4Zr-6Mo alloy at room and elevated temperatures 247

CHAPITRE 7 ÉTUDE PRÉLIMINAIRE SUR L'EFFET DES PARAMÈTRES D'IMPRESSION SUR L'IMPRIMABILITÉ DE L'INTERMÉTALLIQUE À BASE D'ALUMINURES DE TITANE TI-22AL-25NB PRODUIT PAR FUSION LASER SUR LIT DE POUDRE....267
7.1 Traces de passe unique de laser....268
7.2 Phénomène de fissuration....271
7.3 Conclusion....277

CHAPITRE 8 DISCUSSION GÉNÉRALE....279
8.1 Fabrication d'un prototype d'injecteur micro-mélangé en molybdène pur par fusion laser sur lit de poudre et effets des post-traitements....279
8.2 Transfert de connaissances au sujet de l'impression de l'alliage Ti-6Al-2Sn-4Zr-6Mo....282
8.3 Poursuite du développement de l'alliage de Ti-22Al-25Nb....291
8.4 Limitations du modèle numérique lors de la prédiction de bains de fusion d'alliages de titane....300

CONCLUSION....305

APPENDICE A....307

APPENDICE B....311

APPENDICE C....313

ANNEXE I MICRO-MIXING INJECTOR MANUFACTURING IN REFRACTORY METAL USING LASER POWDER BED FUSION PROCESS....317

ANNEXE II LASER POWDER BED FUSION AND HOT ISOSTATIC PRESSING OF PURE MOLYBDENUM: PHYSICAL AND MECHANICAL PROPERTIES AT ELEVATED TEMPERATURES....339

ANNEXE III LASER POWDER BED FUSION AND HOT ISOSTATIC PRESSING OF MO AND MO8WT%RE PARTS: STRUCTURE AND MECHANICAL PROPERTIES AT ELEVATED TEMPERATURES....353

LISTE DE RÉFÉRENCES BIBLIOGRAPHIQUES....367

LISTE DES TABLEAUX

Page

Tableau 1-1 Sommaire d'exigences pour les trois composants 13

Tableau 1-2 Quelques propriétés physiques du tungstène et du molybdène pur Tiré de J. R. Davis & ASM International (1998, p. 115, 629) 15

Tableau 1-3 Température maximale de service, résistance ultime à la température de service et résistance à l'oxydation pour différents alliages de titane et intermétalliques à base d'aluminures de titane Adapté de J. Dai et al. (2016); Feng et al. (2017); Hucek (1979); Kim & Kim (2018, p. 201); Peters et al. (2003); Smallman & Ngan (2014); « Timetal 21S » (2000); Z. Zheng et al. (2017) 28

Tableau 2-1 Rheological properties of the −41 + 20 μm tungsten powder (indexes adopted from Brika et al. (2020)): BD (bulk density), CI (compressibility Index), PD (pressure drop), SE (specific energy), $AE10$ (aeration energy at 10 mm/s air velocity), BFE (basic flow energy), CC (Cohesion coefficient) 59

Tableau 2-2 Property variation ranges considered as model inputs; material density is taken from J. R. Davis & ASM International (1998, p. 115), and bulk density is extracted from the rheometer test (BD, Tableau 2-1); calculated properties are obtained using equations (in brackets); remaining properties are taken from Tolias (2017) 63

Tableau 2-3 Coefficients of the polynomial function linking dimensionless melt pool metrics to printed density 66

Tableau 2-4 DOE: Parameters sets definition 69

Tableau 2-5 Optimized sets of printing parameters and corresponding printed densities for 200 and 400 W LPBF printers (numerical predictions) 91

Tableau 3-1 Rheological properties of molybdenum powder (indexes adopted from Brika et al. (2020)): BD (Bulk Density), CI (Compressibility Index), PD (Pressure Drop), SE (Specific Energy), $AE10$ (Aeration Energy at 10 mm/s air velocity) BFE (Basic Flow Energy), CC (Cohesion Coefficient) 105

Tableau 3-2 Properties variation ranges considered as model inputs: Material density is taken from Baker (1998); powder bed density is extracted from the rheometer test (BD, Tableau 3-1); Dense material: Specific heat capacity, thermal conductivity and electrical resistivity extrapolated from Plansee (2023) and absorptivity calculated using equation (3.8); Powder bed: Thermal conductivity and absorptivity are calculated using equations (3.7)-(3.10) 108

Tableau 3-3 Parameter sets definition 111

Tableau 3-4 Mechanical properties in compression at room and elevated temperatures 130

Tableau 4-1 Plasma spheroidization process parameters 152

Tableau 4-2 List of metrics extracted from the rheometer FT4 analysis and their subsequent influence on the powder flowability 154

Tableau 4-3 Variations of the two parameters sets (I and II) printed with a layer thickness of 30 µm 156

Tableau 4-4 Chemical composition (Mo and Re: EDS, O: IR), morphology and physical properties of the pure and alloyed molybdenum powders 162

Tableau 4-5 Powder rheological characteristics (Hall flow and FT4 rheometer) 165

Tableau 4-6 Boundary densities, grain density, size and circularity of the two Mo8Re samples retained and the pure molybdenum from the reference work Tiré de Leclercq, Mouret, et al. (2025) 170

Tableau 4-7 Mechanical properties in compression at room and elevated temperatures 172

Tableau 5-1 Plan of experiments in terms of the laser power (P), scanning speed (v) and hatching space (h) values used for each of the nine parameter sets 188

Tableau 5-2 Laser power (P), scanning speed (v) and single-track width (W) for each of the nine parameter sets 194

Tableau 5-3 Evolution of the calculated overlap value (N) as a function of the VED and h variations 207

Tableau 6-1 Printing parameter sets used to process the Ti6246 alloy with the two layer thicknesses (t) considered 225

Tableau 6-2 Physical and mechanical properties of the as-built samples printed using two different layer thicknesses t.....235

Tableau 6-3 Elemental concentration (wt% normalized according to the certified reference material) obtained by the EDS points measurements in dark and light areas on samples after P875 and P950.....260

Tableau 6-4 Mechanical properties of the as-built and post-treated samples at room and elevated temperatures 263

Tableau 7-1 Plan d'expériences en termes de puissance laser (P), vitesse de balayage (v) et écart vecteur (h) retenus pour chacun des 9 ensembles de paramètres 270

Tableau 7-2 Largeur des traces de passe unique de laser pour chaque ensemble de paramètres en fonction de l'écart vecteur h 271

Tableau 7-3 Taux de recouvrement en fonction de l'écart vecteur pour chaque ensemble de paramètres; NP signifie échantillon Non Produit et les données en gras représentent les échantillons sélectionnés pour analyses structurales.....275

Tableau 8-1 Récapitulatif de la densité et des propriétés mécaniques à température ambiante obtenues avec les ensembles de paramètres optimisés pour chaque matériau réfractaire étudié 280

Tableau 8-2 D10, D50 et D90 extrait des distributions du volume et sphéricité des porosités observées par µCT dans les échantillons UDS et ETS.....283

Tableau 8-3 Largeur mesurée des aiguilles de α'' et de lamelles de α pour les échantillons UDS et ETS 287

Tableau 8-4 Mesures de dureté pour les échantillons brut et après post-traitements de UDS et ETS.....288

Tableau 8-5 Propriétés mécaniques extraites des tests de traction pour les échantillons brut et après post-traitements de UDS et ETS.....290

Tableau 8-6 Groupes d'auteurs étudiés, leur modèle d'équipement et le rayon du faisceau laser associé 301

Tableau 8-7 Propriétés du Ti-6Al-4V à 0.8Tm retenues comme données d'entrée du modèle numérique.....301

LISTE DES FIGURES

Page

Figure 1-1 Courbes de Pareto montrant l'énergie de conversion atteignable en fonction de la densité de puissance des turbogénérateurs pour les systèmes à cycle récupéré et à cycle simple, à différents niveaux de température d'entrée des gaz (TIT)
Adapté de Picard et al. (2020).....4

Figure 1-2 a) Schéma de l'architecture en cycle récupéré à un seul arbre; b) architecture conceptuelle de la turbine ICT
Adapté de Picard et al. (2020).....5

Figure 1-3 a) Photo de l'injecteur micro-mélangé actuel et b) zoom sur les trous d'injection du carburant
Tiré de Landry-Blais et al. (2022).....7

Figure 1-4 a) Schéma en vue éclatée et photo de l'assemblage du rotor, résultats de simulations numérique par méthode aux éléments finis mettant en avant les champs b) de température et c) de contraintes de Von Mises présents dans l'assemblage du rotor
Tiré de a) Dubois, Landry-Blais, et al. (2022) et b) et c) de Dubois, Landry, et al. (2022) 8

Figure 1-5 Résistance spécifique en fonction de la température pour différents groupes de métaux
Adapté de Thomas (2020, p. 3).....10

Figure 1-6 Schéma a) en coupe de l'injecteur, b) de l'anneau de refroidissement et (c,d,e,f) des deux architectures de moyeu
Tiré de a) Landry-Blais et al. (2022), b) Dubois, Landry-Blais, et al. (2022) et (cdef) Dubois, Landry, et al. (2022).....11

Figure 1-7 Changements de masse mesurés pour des échantillons de molybdène pur exposé à de l'air à différentes températures
Tiré de Nelson et al. (2014) 18

Figure 1-8 Représentation schématique des effets de différents d'alliages sur les diagrammes de phases des alliages de titane
Tiré de Lütjering & Williams (2007, p. 24).....20

Figure 1-9 Diagramme de phase des alliages de titane et des intermétalliques à base d'aluminure de titane en fonction de la concentration atomique en aluminium
Tiré de Schuster & Palm (2006, p. 256) 21

Figure 1-10 a) Contrainte d'écoulement en fonction de la température pour différents alliages de titane; b) comparaison qualitative des principales caractéristiques des différentes familles d'alliage de titane
a) Données extraites de diverses sources Joseph R. Davis & ASM International (2010, p. 587); Feng, Zhang, Cui, Chen, & Yu (2017); Froes (2015, p. 117); Peters, Kumpfert, Ward, & Leyens (2003); Smallman & Ngan (2014); « Timetal 21S » (2000); Veeck, Lee, Boyer, & Briggs (2004); Z. Zheng, Balint, & Dunne (2017) et b) adapté de Bhat (2018, p. 33) 22

Figure 1-11 Contrainte d'écoulement en fonction de la température pour différents intermétalliques à base d'aluminures de titane
Données extraites de Kim & Kim (2018, p. 201); Lütjering & Williams (2007, p. 352) 24

Figure 1-12 Représentation schématique des couches d'oxides et de la diffusion de l'oxygène dans les alliages de titane et intermétalliques à base d'aluminures de titane
Tiré de Peters et al. (2003).....26

Figure 1-13 Gain de masse en fonction du temps pour différents alliages de titane et intermétallique à base d'aluminures de titane exposé à l'air sous différentes températures
Données extraites de diverses sources Guleryuz & Cimenoglu (2009); Lavisse et al. (2020); Leyens & Peters (2004); Vincent et al. (2021) 27

Figure 1-14 Schéma représentant a) la chambre d'impression et b) le lit de poudre avec la nomenclature et les différents paramètres
Adapté de Centre technique des industries mécaniques (2019, p. 16, 20).....30

Figure 1-15 Porosités et microfissures dans un échantillon de tungstène pur fabriqué par LPBF
Tiré de D. Gu et al. (2020).....32

Figure 1-16 a) Observations au microscope électronique à balayage (MEB) et b) cartographie par diffraction d'électrons rétrodiffusés (EBSD) d'un échantillon de tungstène pur mettant en avant une microstructure colonnaire orientée selon la direction de fabrication; c) et d) observations optiques d'un échantillon de Ti-6Al-2Sn-4Zr-6Mo tel que fabriqué mettant en avant une microstructure colonnaire et martensitique; La flèche noire représente la direction de fabrication Tiré de (a, b) Braun et al. (2019) et (c, d) Alessandro Carrozza, Aversa, Fino, & Lombardi (2021) 33

Figure 1-17 Surface de rupture d'un échantillon de a) molybdène pur et b) tungstène pur Tiré de Braun et al. (2019).....35

Figure 1-18 Contrainte ultime en fonction de la déformation obtenue pour différents matériaux bruts produits par LPBF; Les cercles représentent les métaux réfractaires, les triangles les alliages de titane de type $\alpha + \beta$ et les étoiles les intermétalliques à base d'aluminures de titane de type orthorhombique Données extraites de diverses sources Bartolomeu et al. (2022); Alessandro Carrozza et al. (2021); Alessandro Carrozza, Aversa, Fino, & Lombardi (2022); Q. Chen, Xu, Zhao, Hao, & Han (2023); Chlebus et al. (2015); M. Guo et al. (2019); Illarionov et al. (2023); Jamhari et al., (2023); Y. Liu, Shan, Yang, Jiao, & Huang (2023); Oehlerking et al. (2022); Polozov et al. (2021); Rebesan, Ballan, et al. (2021); Shi et al. (2023); Tan et al. (2018); Vrancken et al. (2022); Wen et al. (2019); C. Xu et al. (2020); X.-Q. Zhang et al. (2025); Zhou et al. (2021).....43

Figure 1-19 Organigramme résumant la structure du document.....49

Figure 2-1 Summary diagram of the methodology followed in this study.....58

Figure 2-2 Geometric characteristics of the tungsten powder: a) particle size distribution and b) particle morphology 58

Figure 2-3 Temperature evolutions of the pure tungsten properties adapted from Tolias (2017): a) specific heat capacity and thermal conductivity; b) electrical resistivity.....62

Figure 2-4 a) Schematic representation of the melt pool, melt pool dimensions (depth D, width W and length L) and process variables (layer thickness t and hatching space h); b) calculated (0.8TM) melt pool for pure tungsten (P = 300 W, v = 400 mm/s et rf= 50 µm) and c) photo of a single laser track for the same process parameters from Xiong et al. (2020); d) comparison between the measured Rebesan, Ballan, et al. (2021); S. Sharma et al. 2023; Vrancken et al. (2022); Xiong et al. (2020) and calculated (0.8TM) melt pool widths for pure tungsten with 95% confidence margins. 64

Figure 2-5 Response surface of the polynomial function relating printed density to dimensionless melt pool metrics (experimental points in purple dots): a) 3-dimensional view and b) $D/t - W/h$ plane view highlighting a maximum density area defined from the experiment 66

Figure 2-6 Example of the tungsten density processing map for a TruPrint 1000 (t = 30 µm, h = 80 µm); insert contains the region with the highest predicted density 68

Figure 2-7 Density maps for tungsten powders with a) h = 20 µm and b) h = 80 µm and selected $VED - BR$ sets for a TruPrint 1000; c) schematic representation of the printed specimens with different cuts; d) photo of a baseplate with printed specimens 69

Figure 2-8 a) LEXT and b) binarized images, c) pore size diagram and d) pore shape diagram for Specimen E-80.....71

Figure 2-9 a) Compression stress–strain diagram with the obtained metrics and b) photo of Specimen E-80 during the compression test at a total compression strain of 0.1 73

Figure 2-10 Nominal structure of the printed specimens: a) 50% and 60% porosity gyroid lattice structures, b) minimum wall artifact and c) minimum gap artifact. Dimensions are given in mm.....74

Figure 2-11 a) Printed densities measured using the Archimedes' and image analysis techniques, where dotted lines correspond to the 95% confidence interval margins; b) SEM micrograph of Specimen D-20 containing unfused particles inside pores; c) microcracks in Specimen A-40.....76

Figure 2-12 Comparison between the measured and predicted printed densities with the confidence interval margins.....77

Figure 2-13 a) Predicted and b) measured printed densities as functions of the h/t ratio for five $VED - BR$ sets (arrows indicate maxima, trend lines are added for visualization purposes) 78

Figure 2-14 Microscopic observations of a) Specimen E-60 and b) Specimen E-100 having the same printed density of 92% but different pore sizes and pore densities 79

Figure 2-15 a) Pore density, b) pore size and c) pore circularity as functions of the h/t ratio for five $VED - BR$ sets (arrows indicate extrema, trend lines are added for visualization purposes) 80

Figure 2-16 EBSD maps (IPF Y) for specimens a) C-40 and b) A-60 with the same printed density of 92% but different pore and grain structures, and c) example of the pole figures corresponding to Specimen E-80 81

Figure 2-17 a) UCS and b) compression strain under maximum load as functions of the h/t ratio for five $VED - BR$ sets (arrows indicate maxima, trend lines are added for visualization purposes) 82

Figure 2-18 a) UCS versus strain under maximum load (printed density is presented in color) showing a brittle-to-ductile failure separation line at 6%; photo and schematic representation of the b) ductile and c) brittle rupture modes 83

Figure 2-19 a) XRD analyses of the selected specimens (A-80, B-80, C-80, D-80 and E-80), with four detected crystallographic orientations indicated by a diamond sign; b) XPS analysis of the specimen E-80; c) EDS observation of the fracture surface of Specimen E-80; d) EDS observation with a closer look at some traces of oxides 85

Figure 2-20 Printed design artifacts: a) gyroids (numbers correspond to nominal printed densities), b) wall and c) gap artifacts 86

Figure 2-21 Linear regression between the nominal and the microscope-measured thicknesses of a) walls and b) gaps 87

Figure 2-22 a) Comparison of the mechanical properties of pure tungsten LPBF specimens (our study and Tan et al. (2018)) and tungsten parts formed by other processes Tan et al. (2018); b) UCS vs printed density of LPBF tungsten specimens for different layer thicknesses(data from M. Guo et al. (2019); Shi et al. (2023); Tan et al. (2018)) 88

Figure 2-23 Predicted density for two layer thicknesses (20 and 30 µm) as a function of the h/t ratio: a) using the $VED - BR$ set E (417 J/mm^3; 1.62 cm^3/h) optimized for the 200 W laser and b) using the $VED - BR$ set (444 J/mm^3; 3.24 cm^3/h) specifically optimized for the 400 W laser 90

Figure 3-1 Geometry characteristics of molybdenum powder: a) particle size distribution and b) particle morphology 104

Figure 3-2 a) Comparison between the measured Gan et al. (2024); Rebesan, Ballan, et al. (2021) and calculated melt pool widths for pure molybdenum with 95 % confidence margins; b) photo of a single laser track extracted from Rebesan, Ballan, et al. (2021) ($P = 130$ W, $v = 500$ mm/s, $rf = 20$ µm) and c) calculated temperature field of the melt pool with properties taken at 0.8TM (Tableau 3-2).....109

Figure 3-3 a) Schematic representation of the melt pool, melt pool dimensions (depth D, width W and length L) and process variables (layer thickness t and hatching space h); b) example of the calculated (0.8TM) melt pool for pure molybdenum, c) response surface of the polynomial function relating printed density to dimensionless melt pool metrics (experimental points in purple dots) Leclercq & Brailovski (2024) and d) example of the density map for molybdenum ($t = 30$ µm, $h = 80$ µm) with the selected five $VED - BR$ experimental sets for a TruPrint 1000.....110

Figure 3-4 a) Photo of a baseplate with printed specimens; b) schematic representation of a printed specimen with samples for structural analyses and mechanical testing 112

Figure 3-5 C-60 specimen (z-y cross-section): a) microscopic image; b) binarized image (density d = 97%, pore population 40 p/mm^2, $DE50p = 82$ µm and $C50p = 0.55$; C-40 specimen: c) microscopic image (z-y cross-section, cracks are shown by red arrows); d) binarized images (density d = 89%, pore population 100 p/mm^2, $DE50p = 100$ µm and $C50p = 0.30$ 114

Figure 3-6 Drawings of the printed geometric artifacts: a) walls, b) gaps, c) 50 and 60% porosity gyroid lattice structures; d) printed artifacts. Dimensions are given in mm. 117

Figure 3-7 a) Predicted and b) measured printed densities for different process parameters sets (arrows point to the C-60 and E-120 sets leading to the highest measured printed densities). 119

Figure 3-8 Binarized surfaces of the samples a) C-60 and b) E-120 with segmented pores and their pore distributions: c) C-60 and d) E-120 120

Figure 3-9 C-60 parameter set: (a and b) SEM images of oxidation traces observed on the compressive fracture surface; (c) SEM image on the polished cross-section and (d) corresponding EDS map. 121

Figure 3-10 Band contrast (BC) diagrams of samples a) C-60 and b) E-120; c) BC cumulative histograms and d) MacKenzie plots of samples C-60 and E-120; e) pole figures of sample C-60 123

Figure 3-11 LAGB, HAGB densities and grain size (DE90g) as functions of the h/t ratio for the $VED - BR$ set C a) and E b); phase maps highlighting LAGB (yellow) and HAGB (red) for the specimens C-60 c) and E-120 d); orientation maps (IPF Y) for the specimens C-60 e) and E-120 (f).....125

Figure 3-12 a) Stress-strain diagrams of the C-60 and B-60 samples highlighting two distinct behaviors observed during the compression tests; SEM images of the fracture surfaces of samples b) C-60 and c) B-60 127

Figure 3-13 YS and UCS for C and E process parameter sets; arrows point to the C-60 and E-120 specimens with the highest printed densities 128

Figure 3-14 Thermocouple-instrumented sample: a) Photo with the oxide layer; b) XRD before and after the temperature cycling (without load).....129

Figure 3-15 Representative stress-strain compression diagrams (C-60) at 20, 600, 800 and 1000 °C 130

Figure 3-16 a) Optical microscopy observations of walls; b) measurement of its top thickness using the height profile line represented in red; c) linear regressions between the nominal and the microscope-measured thickness of (c) walls and (d) gaps, with the confidence interval at 95% margins 132

Figure 3-17 a) Image-measured printed density in the $VED - BR$ plan for this study ($h/t = 2$) and the current literature Bajaj et al. (2019); Faidel et al. (2015); Guan et al. (2023); Higashi et Ozaki (2020); red ellipse indicates zone corresponding to microcracks. Dashed lines delimit the frontier of 100, 200 and 400W printers' boundaries 134

Figure 3-18 Evolution of the Ultimate Strength depending on the mechanical testing temperature. Comparison is made to the standard B387-18 B10 Committee (2018) and the literature Carreker & Guard (1956); « Climax Molybdenum » (1950); Fernandez-Zelaia et al. (2022); Rebesan, Ballan, et al. (2021) 137

Figure 4-1 a) Schematic representation of a printed specimen with samples for structural analyses and mechanical testing; b) Pineapple artifact with design features 157

Figure 4-2 Scanning electron microscope images: a) Mo8Re powder after mechanical blending, b) Mo8Re after plasma spheroidization, c) Pure Mo used as reference, d) Particle size distributions of both spheroidized powders (Mo8Re and pure Mo) 161

Figure 4-3 XRD diffractograms of the alloyed powder at different steps of the process and of pure molybdenum used for the reference study Tiré de Leclercq, Mouret, et al. (2025) 163

Figure 4-4 a) Stability test plots and b) Additive Manufacturing Suitability (AMS) radar chart for pure Mo and alloyed Mo8Re powders 166

Figure 4-5 a) Measured printed densities as functions of the h/t ratio for the two $VED - BR$ sets; Examples of the binarized surfaces of the samples b) II-80 and c) II-100 167

Figure 4-6 WDS mapping of the II-100 (98%) sample: a) polished surface, b) molybdenum and c) rhenium distributions; d) Superposition of the Band Contrast (BC) and bcc molybdenum phase maps of the II-100 (98%) sample; e) BC cumulative histograms of the two retained samples (II-80 (97%) and II-100 (98%)) 168

Figure 4-7 a) MacKenzie plots of Mo8Re (97%) and Mo8Re (98%) samples; b) orientation map (IPF Y) and c) pole figures of a Mo8Re (98%) sample 169

Figure 4-8 a) Evolution of the Ultimate Compression Strength as a function of the testing temperature; b) Typical stress-strain curves at all tested temperatures for b) Mo8Re (98%) and c) Mo (97%) samples.....171

Figure 4-9 a) Side view and b) inclined view of the pineapple artifacts printed using Mo8Re powder.....173

Figure 4-10 a) Powder bed of Mo8Re during printing. b) Agglomerates of Mo8Re powders observed during the printer unloading. c) Unsealed containers for storing samplings of pure Mo and alloyed.....174

Figure 5-1 Ti6246 powder: a) Particle size distribution and b) SEM observations....186

Figure 5-2 Representation of the nine $VED - BR$ experimentally printed parameter sets; the dashed line represents the $VED - BR$ limit corresponding to a maximal laser power of 200 W....188

Figure 5-3 a) Drawing of one of the cubic samples with 18 single tracks; b) photo of three cubic samples with single tracks; c) photo of a baseplate with printed cylindrical specimens; d) schematic representation of the cylindrical specimen with samples used for various analyses....189

Figure 5-4 Optical observations of the a) continuous, b) irregular and c) partially fused single tracks; d) single track widths according to the scanning speed v and the linear energy density P/v....193

Figure 5-5 CT-scan measured density in the $VED - BR - h$ space, with different types of porosities encircled....195

Figure 5-6 Examples of the porosity distributions inside the 15 mm-high cylindrical specimens printed at different VED: a) 135 J/mm^3 A-50; b) 100 J/mm^3 B-150; c) 50 J/mm^3 E-100; 3D segmented process-induced flaws: d) a keyhole pore (A-50) and e) a lack-of-fusion (E-50); Pore distributions for different VED: f) volume; g) sphericity....197

Figure 5-7 Optical images of the a) keyhole porosities (A-75) and b) lack-of-fusion porosities (E-100)....198

Figure 5-8 Microstructural evolution observed through XRD diffractograms depending on a) the parameter sets ($VED - BR$) with constant h value (h = 50 µm) and b) the h value at a constant $VED - BR$ parameter set (set A)....199

Figure 5-9 Observations with confocal microscope (a, b, c, d) and SEM (e, f) of (a, c, e) sample with the as-built α'' martensite microstructure (B-150) and (b, d, f) heterogeneous sample with α' and β phases (A-50)....200

Figure 5-10 a) Thickness of the α'' layer on the top surface of heterogeneous samples (set A) depending on the h ratio. b) Needle widths of α' and α'' martensite as functions of the h value (set A)....201

Figure 5-11 Evolution of the microhardness measured for the parameter sets A, B, C and E in the $VED - BR - h$ space....202

Figure 5-12 a) The representative compression stress-strain diagrams (A-50, B-50, E-50, D-50, H-50). The dashed lines correspond to data obtained after detecting an acoustic signal that indicates the onset of cracking identified by an arrow; Photo of the sample at the onset of cracking b) A-50, c) H-50, SEM fractographies: d) A-50 with "brittle" fracture, e) F-50 with "ductile" fracture 204

Figure 5-13 a) YS at 0.2% offset versus strain at failure. The relative printed density of the samples is presented in color; b) YS at 0.2% offset in function of the hatching space 205

Figure 5-14 a) Schematic drawing of the melt pool and different associated metrics. Representation of the $h < W$ case with overlaps and of the $h > W$ case without overlaps, b) optical observations of the melt pools overlapping in sample A-125. The hatched zone is remelted two times (N = 1.8) 207

Figure 5-15 Cross-section of printed samples with partial transformation toward stable phase: a) A- 50 and b) B-50. c) Position of the samples printed using these two printing parameters on the baseplate.....209

Figure 5-16 Evolution of the microhardness values reported in literature Alessandro Carrozza et al. (2021); Cobbinah et al. (2024); Hassanin et al. (2021); Peng et al. (2023) depending on a) the VED and b) the width of the α"/α' martensite needles or the α grains 213

Figure 6-1 a) SEM observations of the Ti6246 powder; b) Photo of the printing chamber describing the different compartments.....224

Figure 6-2 Schematic representation of the a) cubic specimen with single tracks printed on its upper surface; b) cylindrical specimen with samples used for various analyses. Drawings of the printed geometric artefacts: c) walls and d) gaps. Printed artefacts using 25 and 50 µm layer thicknesses: e) walls and f) gaps. All dimensions are in millimeters (mm) 226

Figure 6-3 Schematic representation of the pressure drop artefacts: a) full view, b) cut view to observe the channels and c) zoomed view at the channels extremity; d) printed pressure drop artefacts. Green dotted lines on full view highlights the surfaces for roughness measurement 227

Figure 6-4 Optical observations of the continuous single tracks printed using a) Set I and b) Set II. Equivalent pore diameter distributions corresponding to a volume of 1 cm3: c) Set I – 50 µm, d) Set II – 25 µm; (cylindrical specimens) 233

Figure 6-5 a) XRD diffractograms of the Ti6246 powder and of the as-built samples printed with both parameter sets; SEM images with the α'' martensite needles in samples printed with b) Set I and c) Set II 234

Figure 6-6 Surface roughness (Ra) measured on the pressure drop artefact as a function of the build angle for both parameter sets. 0° and 90° were obtained on the top and lateral surfaces of the artefact.....236

Figure 6-7 Average a) wall thickness and b) gap width for Sets I and II artefacts printing after segmentation of the µCT 2D XY sections; error bars are smaller than the markers 237

Figure 6-8 Evolution of the segmented 3D volume compared to the nominal volume for both parameter sets for a) walls and b) gaps. In each figure, black dashed lines correspond to the nominal thickness of features.....239

Figure 6-9 3D visualization of the deviation map compared to the CAD for walls printed with: a) Set I (t = 50 µm), b) Set II (t = 25 µm) 240

Figure 6-10 3D Deviation distribution for the geometric artefacts: a) walls Set I (t = 50 µm), b) walls Set II (t = 25 µm), c) gaps Set I (t = 50 µm), d) gaps Set II (t = 25 µm) 241

Figure 6-11 a) Overlapping of the µCT scan (Set I) and the CAD mesh (orange line) after registration in the 2D XZ section to highlight the down-skin effect on the upper surface of the channels. b) Segmented 2D XZ slice with the cross-sectional areas measured after segmentation.....242

Figure 6-12 Evolution of the cross-section areas along the XZ direction of: a) channels 1 to 7, b) channel 8. Deviation distribution obtained for the pressure drop specimen printed with parameter sets: c) Set I, d) Set II 243

Figure 6-13 2D slice of the reduced section of the widest channel (n°8) printed with a) Set I (t = 50 µm) and b) Set II (t = 25 µm). The section is partially clogged using the parameter with the higher layer thickness. c) 3D view of one extremity of the deviation map computed for the height channels: c) Set I (t = 50 µm), d) Set II (t = 25 µm).....244

Figure 6-14 Ti6246 powder a) Particle size distribution and b) SEM observations.....251

Figure 6-15 Two post-treatment sequences involving low-temperature annealing at 600 °C (S600) followed by two annealing conditions: subtransus 875 °C (P-875) and supertansus 950 °C (P-950); all heat treatments lasted 2h, with heating and cooling rates of 5 and 2 °C/min, respectively....253

Figure 6-16 DSC graph of the as-built sample; the dashed lines highlight the endothermic peaks....254

Figure 6-17 Schematic representation of the a) cylindrical specimen divided into samples used for various analyses and b) tensile testing sample; all dimensions are in mm....254

Figure 6-18 XRD diffractograms for different Ti6226 states including powder, as-built and heat-treated samples (S600, P875 and P950): a) 35-90° 2θ range and b) zoom in the 42-50° 2θ range....257

Figure 6-19 Observations with confocal microscope (a-d) and SEM (e-l) of: (a, e, i) as-built sample with orthorhombic α'' martensite; (b, f, j) samples after 600 °C annealing showing the beginning of $\alpha'' \rightarrow \alpha + \beta$ decomposition; (c, g, k) and (d, h, l) P875 and P950 annealed samples, respectively, with duplex $\alpha + \beta$ phase....258

Figure 6-20 SEM observations and EDS maps: (a,b,c,d) P875 sample and (e,f,g,h) P950 sample....259

Figure 6-21 Superposition of the SEM observations and the EDS Sn map showing Sn precipitates in the a) P875 and b) P950 samples....260

Figure 6-22 Representative tension stress-strain diagrams of the as-built and post-treated samples at: a) 20 °C and b) 480 °C; mechanical properties of the as-built and post-treated samples at c) room temperature and d) elevated temperature. The UTS values obtained for wrought Ti6246 and Ti64 alloys J. R. Davis & ASM International (1998, p. 587) are given as target values....262

Figure 7-1 Poudre de Ti2225 : a) Distribution de taille des particules et b) Observation au MEB....268

Figure 7-2 a) schéma d'un échantillon cubique avec les traces de passe unique de laser; b) photo de trois échantillons cubiques avec les traces de passe unique de laser; c) représentation 3D dans le volume $VED - BR - h$ des 63 paramétries testées pour les traces de passe unique de laser....269

Figure 7-3 Observations au microscope optique d'une trace de passe unique de laser a) continue, b) irrégulière et c) discontinue; d) largeur mesurée des traces de passe unique de laser en fonction de la vitesse de balayage v et de la densité d'énergie linéique P/v 271

Figure 7-4 Échantillons présentant des fissures visibles à l'œil nu a) attachés à la plaque de fabrication et b) une fois retiré de la plaque; c) radiographie au rayons X d'un échantillon fissuré mettant en avant la présence de fissures internes et d) échantillon retiré de la plaque d'impression possédant une forte coloration de surface 273

Figure 7-5 a) Taux de recouvrement et b) continuité des traces de passe unique de laser en fonction de la densité d'énergie volumique VED, du taux de construction BR et de l'écart vecteur h pour chaque ensemble de paramètres 275

Figure 7-6 Spectres de diffractions à rayon X de la poudre et des échantillons B-175 ($R\%$ = 2%), I-100 ($R\%$ = 21%), A-50 ($R\%$ = 57%) et C-50 ($R\%$ = 65%) 277

Figure 8-1 a) Pièce de test d'impression de trous de différents diamètres; photo du b) demi-prototype et c) prototype complet d'injecteur micro-mélangé en molybdène pur 281

Figure 8-2 Distributions a) du volume et b) de la sphéricité des porosités observées par µCT dans les échantillons UDS et ETS 283

Figure 8-3 Résultats d'analyses par diffraction à rayons X de la poudre de Ti6246, d'échantillon UDS brut et post-traités selon les protocoles P875 et P950 284

Figure 8-4 Observations au microscope confocal des échantillons bruts (a,d) et post-traités selon les protocoles P875 (b,e) et P950 (c,f) de (a-c) UDS et (d-f) ETS.....285

Figure 8-5 Observation au MEB de : a) l'échantillon brut avec les aiguilles de α'', b) l'échantillon après protocole P875 avec la phase $\alpha + \beta$ et c) et d) l'échantillon après le protocole P950 montrant la microstructure bi-lamellaire composée de lamelles de α primaire et d'aiguilles de α secondaire contenues dans des grains β 286

Figure 8-6 Observations MEB et cartographies EDS des échantillons UDS après (a,b,c,d) protocole P875 et (e,f,g,h) protocole P950 287

Figure 8-7 Courbes contrainte-déformation obtenues pour a) les trois échantillons bruts UDS et b) représentatives des échantillons ayant subi les protocoles P875 et P950 289

Figure 8-8 Photo d'une plaque de fabrication après post-traitements montrant une coloration bleutée des échantillons signifiant le phénomène d'oxydation.....292

Figure 8-9 Résultats d'analyses par radiographie à rayons X mettant en avant les phénomènes de fissuration pour chacun des ensembles de paramètres en fonction a) de la densité d'énergie volumique VED, du taux de production BR et de l'écart vecteur h et b) de la densité d'énergie linéique P/v et de la vitesse v 293

Figure 8-10 Vue d'une tranche dans le plan XY normal à la direction de fabrication mettant en avant le phénomène de *beam hardening* et b) extraction de la porosité de l'échantillon E-175 295

Figure 8-11 a) Densité mesurée par µCT des échantillons imprimés sans fissures en fonction de la densité volumique d'énergie VED, du taux de production BR et de l'écart vecteur h et b) distributions du volume et de la sphéricité des pores contenus dans l'échantillon E-175 296

Figure 8-12 a) Résultats d'analyse par diffraction à rayons X des échantillons E-100, I-125 et F-150; observations b) confocal et c) MEB de l'échantillon E-100 mettant en avant des grains colonnaires de β primaire et des aiguilles de O et de $\alpha 2$ et de la phase $\alpha 2$ concentrée aux joints de grains 297

Figure 8-13 Histogrammes des mesures de microdureté sur les échantillons sans fissures des ensemble E, F et I en fonction de l'écart vecteur h.....298

Figure 8-14 a) Photo d'une plaque de fabrication d'éprouvettes prismatiques fissurées et photos des géométries de test d'épaisseur de b) parois et c) interstices mettant en avant le phénomène de distorsions 299

Figure 8-15 Prédictions numériques face aux mesures expérimentales (vert pour trace continue, orange pour irrégulière, rouge pour discontinue et bleu pour non-indiquée); largeurs a) toutes les traces et b) traces continues ou non-indiquées uniquement; profondeurs : c) toutes les traces; d) traces régulières uniquement. 302

LISTE DES ABRÉVIATIONS, SIGLES ET ACRONYMES

AB	As-built
AM	Additive manufacturing
ASTM	American Society for Testing and Materials
BC	Band contrast
BR	Taux de construction (build rate)
CAD	Computer assisted design
CAO	Conception assistée par ordinateur
CFD	Computational fluid dynamics
CTE	Coefficient of thermal expansion
CIT	Combustion inlet temperature
CVD	Chemical vapor deposition
DBTT	Ductile brittle transition temperature
DED	Directed energy deposition
DEM	Discrete elements model
DOE	Design of experiments
DSC	Differential scanning calorimetry
EB-PBF	Electron beam powder bed fusion
EBSD	Diffraction d'électrons rétrodiffusés (electron backscatter diffraction)
EDS/EDX	Energy-dispersive X-ray spectroscopy
ET	Elevated temperature
ETS	École de Technologie Supérieure de Montréal
FA	Fabrication additive

FEM	Méthode aux éléments finis (finite element method)
GB	Grain boundaries
HAGB	High angle grain boundary
HAPC	Halide activated pack cementation
HDS	Hot dip silicon-plating
HIP	Compression isostatique à chaud (hot isostatique pressing)
ICT	Inside-out ceramic turbine
IR	Infrared
LAR	Least absolute residuals
LAGB	Low angle grain boundary
LED	Linear energy density
LPBF	Laser powder bed fusion
MANOVA	Multivariate analysis of variance
MEB	Microscope électronique à balayage
NASP	National aviation security plan
NERVA	Nuclear engine for rocket vehicle application
NOx	Oxides d’azote
OAZ	Oxygen affected zone
PM	Métallurgie des poudres (powder mettalurgy)
PREP	Plasma rotating electrode process
PSD	Particle size distribution
RT	Température ambiante (room temperature)

SEM	Scanning electron microscope
SPS	Spark plasma sintering
TBC	Thermal barrier coating
Ti6246	Alliage de titane Ti-6Al-2Sn-4Zr-6Mo
Ti64	Alliage de titane Ti-6Al-4V
Ti2225	Intermétallique à base d'aluminure de titane Ti-22Al-25Nb
TIT	Turbine inlet temperature
TM	Melting temperature
TZM	Titanium-Zirconium-Molybdenum
UDS	Université de Sherbrooke
VED	Volumetric energy density
VTOL	Avions à décollage et atterrissage verticaux
XPS	X-ray photoelectron spectroscopy
XRD	X-Ray diffraction
WDS	Wavelength-dispersive X-ray spectroscopy
µ-CT	Micro-tomographie à rayons X (micro-computed X-Ray tomography)

LISTE DES SYMBOLES ET UNITÉS DE MESURE

A	Absorptivity
A	Area (mm^2)
AE	Aeration energy (mJ/g)
AMS	Additive manufacturing suitability
AR	Aeration ratio
BD	Bulk density (kg/m^3)
BFE	Basic flow energy (mJ)
BR	Taux de construction (build rate, cm^3/h)
C	Circuarity
CBD	Coefficient of bulk density
CC	Cohesion coefficient (kPa)
CI	Compression index (%)
DE	Equivalent diameter (µm)
cp	Mass heat capacity (J/(kg.K))
D	Melt pool depth (m)
d	Distance interréticulaire (m)
dt	Time (s)
FF	Flow function
FRI	Flow rate index
h	Écart-vecteur (hatching space, µm)
HV	Dureté Vickers (microhardness, HV)
k	Thermal conductivity (W/(m/K))

L	Melt pool length (m)
LED	Densité d'énergie linéique (linear energy density, J/mm)
N	Number of overlapping times
n	Ordre de diffraction
P	Puissance du laser (laser power, W)
PD	Pressure drop
Pe	Peclet number
rf	Laser beam radius (m)
Rs	Electric resisitivity (Ω.m)
$R\%$	Taux de recouvrement (remelting fraction, %)
S	Sphericity
Sh	Surface fraction
SE	Specific energy (mBar)
t	Épaisseur de couche (layer thickness, µm)
T	Température (K)
UCS	Ultimate compression strength (MPa)
UTS	Ultimate tension strength (MPa)
v	Vitesse de balayage (scanning speed, mm/s)
V	Volume (mm^3)
VED	Densité d'énergie volumique (volumetric energy density, J/mm^3)
W	Melt pool width (m)
YS	Yield strength (MPa)

α	Thermal diffusivity (m^2/s)
δ	Strain under maximum load (%)
ε	Emissivity
θ	Angle de Bragg (°)
ϕ	Fractional porosity
λ	Laser wavelength (m)
ρ	Density (kg/m^3)
σ	Contrainte mécanique (MPa)

INTRODUCTION

Afin d'améliorer les performances de dispositifs à haute température, une solution est de recourir à de nouvelles gammes de métaux et alliages plus prometteurs de par leurs propriétés physiques et mécaniques. Cependant, pour ne pas compromettre l'architecture ni altérer la conception déjà établie, ces nouveaux matériaux doivent être compatibles avec la technologie de fabrication déjà en place dans les dispositifs. Pour des systèmes complexes, la technologie de fabrication additive est souvent retenue, car elle offre une plus grande liberté de conception, permet de réduire le nombre de pièces dans un assemblage ou encore d'alléger la structure. Parmi les procédés disponibles compatibles avec de nombreux métaux, la fusion laser sur lit de poudre (LPBF) est la plus largement répandue, car moins coûteuse et plus précise que ces compétiteurs directs. Néanmoins, l'implémentation de nouveaux métaux et alliages par ce procédé n'est pas chose aisée en raison de la multitude de phénomènes physiques mis en jeu, contrôlés par plusieurs centaines de paramètres pouvant agir de manière couplée. Différentes approches sont alors envisagées pour réduire la formation de défauts caractéristiques de ce procédé, tels que la porosité ou la fissuration, et parvenir à la création de pièces complexes prêtes à être intégrées dans un dispositif.

Le dispositif-pilote pour cette étude est une microturbine disposant d'une nouvelle génération d'injecteurs micro-prémélangés dans la chambre de combustion et d'un assemblage de rotor avec une architecture particulière, imposée par le recours à des aubes en céramique devant être maintenues en compression par un anneau en matériau composite. Il s'agit ici de remplacer le superalliage à base nickel employé pour l'injecteur par un métal réfractaire pour tenter d'atteindre les 1000 °C d'opération et de remplacer les alliages de titane et de nickel retenus dans l'assemblage du rotor par des matériaux plus légers et plus résistants à haute température, comme les nouvelles générations d'alliages de titane et les intermétalliques à base d'aluminures de titane. Pour cela, une démarche commune d'implémentation est employée pour déterminer des paramètres de fabrication optimisés pour chaque matériau, permettant d'obtenir à la fois des pièces aux propriétés mécaniques compétitives et des structures complexes atteignant les requis de conception de l'architecture actuelle.

D’abord, les détails du dispositif et le cahier des charges associé sont présentés, amenant à la problématique et aux choix des différents matériaux d’étude. Leurs caractéristiques ainsi que les difficultés liées à leur implémentation sont ensuite énoncées avant que les objectifs de recherche, la méthodologie employée et l’organisation de la thèse ne soient décrits. Les résultats de ces travaux ont été transcrits dans six articles de revue, constituant les premiers chapitres du document. Les travaux sur le dernier matériau, encore au stade préliminaire, sont ensuite présentés avant un dernier chapitre abordant les notions de fabrication de prototype et de transfert de connaissances. Des précisions sur le prototypage en métaux réfractaires sont données en annexe sous la forme de trois articles de conférence.

CHAPITRE 1

REVUE DE LITTÉRATURE

1.1 Contexte

Dans un contexte de changement climatique et avec une croissance estimée de 5 à 7% par année dans les prochaines décennies, l'industrie aéronautique s'est fixée comme objectif ambitieux de réduire de moitié ses émissions. Cependant, les technologies actuelles à zéro émission, telles que les moteurs à batterie et à hydrogène, sont loin d'atteindre la densité énergétique requise pour voler, nécessitant alors l'amélioration de la technologie turboélectrique. Pour que la propulsion turboélectrique succède aux turbocompresseurs actuels, des avancées majeures doivent être réalisées pour les moteurs électriques à grande vitesse en parallèle du développement de turbines à gaz à haute densité et à puissance élevée. De telles améliorations dans les turbines à gaz pourraient profiter aux actuels avions régionaux et d'affaires à turbines et à moteurs à piston, mais également au développement des avions à décollage et atterrissage verticaux (VTOL) (Dubois, Landry, et al., 2022; Picard, Picard, Plante, & Rancourt, 2020).

Les microturbines, délivrant une puissance de l'ordre du mégawatt et moins, sont principalement conçues sur le principe du cycle de Brayton avec récupérateur de chaleur afin d'atteindre de plus hautes efficacités. Dans un tel cycle, l'augmentation du rendement vient de l'augmentation de la température d'entrée des gaz (TIT pour *Turbine Inlet Temperature*) tout en conservant des ratios de pression relativement faibles (généralement 5 :1 et 10 :1). Dans l'état de l'art actuel, la TIT pour des turbines à pales métalliques sans refroidissement se situe proche des 1000 °C et la limite d'efficacité pour des cycles récupérés à cette TIT est d'environ 38%. Un objectif à court terme serait de dépasser les 1275 °C, permettant de surpasser la limite d'efficacité imposée par une TIT de 1000 °C et, sur le plus long terme, dépasser 1527 °C, afin d'atteindre la barre des 45% d'efficacité et de se rendre ainsi compétitif avec les moteurs diesel actuellement utilisés (Figure 1-1). Néanmoins, de telles températures excèdent les limites du fonctionnement de pales métalliques sans système de refroidissement. Il est à noter que les

techniques de refroidissement avancées, telles qu'actuellement utilisées dans les turbines à gaz à haute production, ne peuvent pas être considérées ici, car elles réduiraient la température des gaz d'échappement en diluant l'air de refroidissement dans le flux principal, ce qui pénaliserait l'efficacité du cycle. De fait, afin d'élever la TIT, il devient nécessaire de se tourner vers des matériaux plus avancés (McDonald & Rodgers, 2009; Picard et al., 2020).

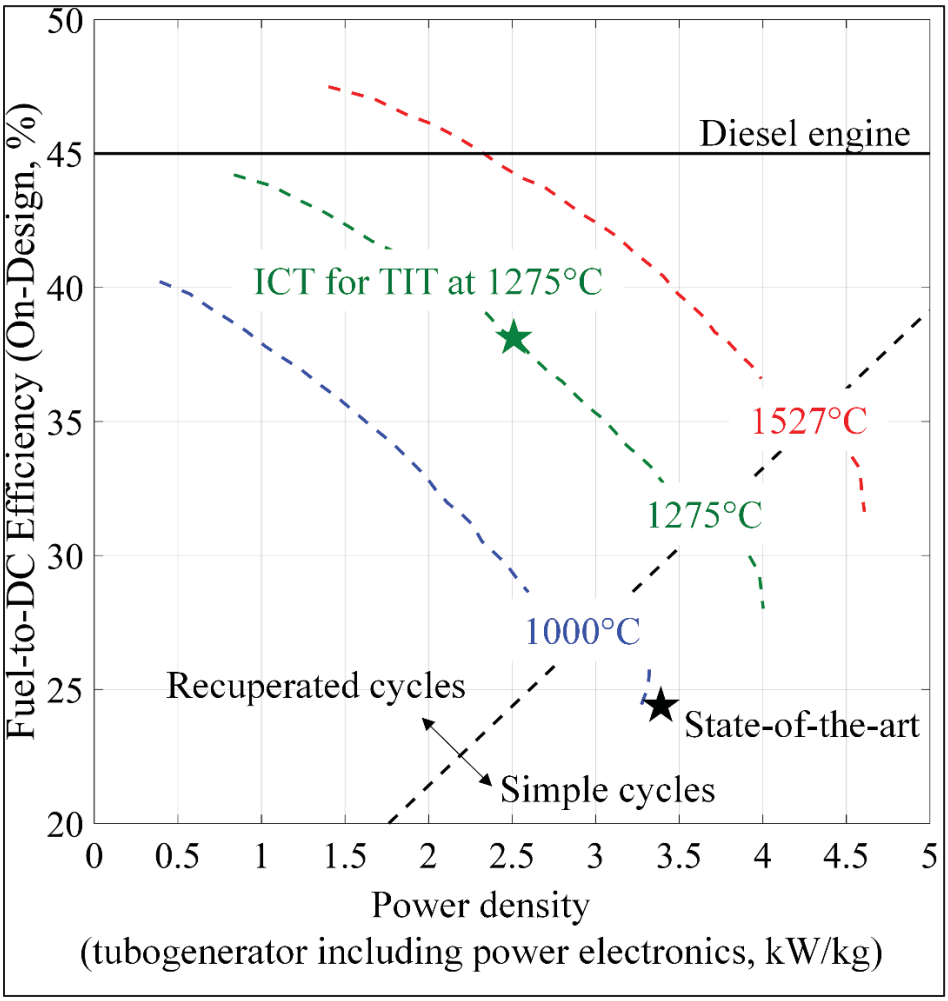

Figure 1-1 : Courbes de Pareto montrant l'énergie de conversion atteignable en fonction de la densité de puissance des turbogénérateurs pour les systèmes à cycle récupéré et à cycle simple, à différents niveaux de température d'entrée des gaz (TIT)
Adapté de Picard et al. (2020)

Dans cette optique, une nouvelle architecture de turbine a été proposée par la compagnie Exonetik (Sherbrooke, Canada) basée sur l'incorporation d'aubes en céramiques dans l'assemblage du rotor. Cette configuration appelée ICT pour *Inside-out Ceramic Turbine* est basée sur un cycle récupéré à un seul arbre avec contrôle de vitesse (Figure 1-2a) et se décompose en deux principales zones à haute température à savoir, la chambre de combustion et l'assemblage du rotor (Figure 1-2b). Par définition, la chambre de combustion correspond au lieu de création de la flamme et son principal composant est l'injecteur (Figure 1-3). L'assemblage du rotor est, quant à lui, constitué d'un moyeu métallique sur lequel sont installées des pales en céramiques maintenues en compression au moyen d'un anneau de composite à fibre de carbone (Figure 1-4). Les pales et l'anneau de composite sont séparés par un anneau de refroidissement métallique, permettant ainsi de limiter la surchauffe de l'anneau de composite.

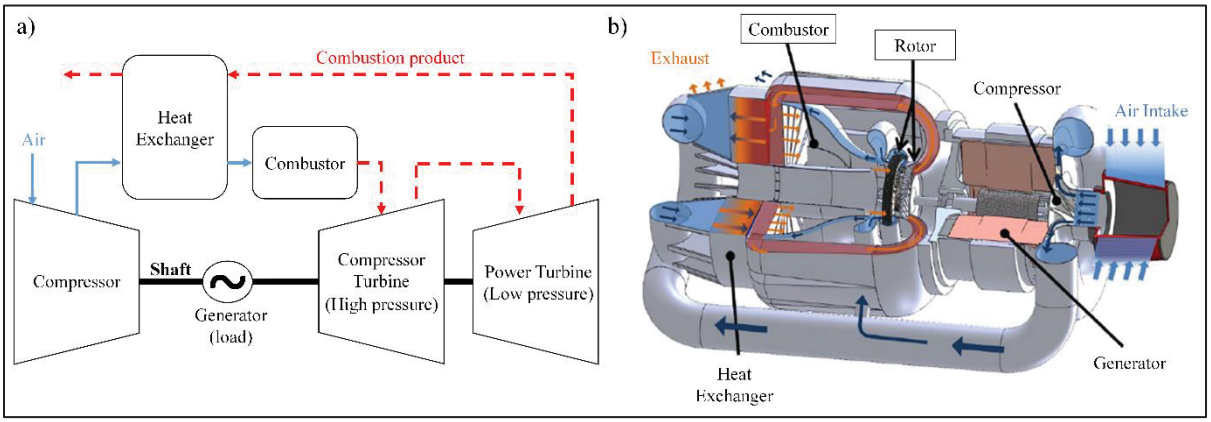

Figure 1-2 : a) Schéma de l'architecture en cycle récupéré à un seul arbre; b) architecture conceptuelle de la turbine ICT
Adapté de Picard et al. (2020)

1.2 Amélioration des composants à haute température

1.2.1 Chambre de combustion

La température dans la chambre de combustion est directement liée à la température de flamme (CIT pour *Combustion Inlet Temperature*) produite en sortie d'injecteur, qui définit également

la TIT. Ainsi, afin d'augmenter la TIT et donc l'efficacité de la turbine, il est primordial d'augmenter la CIT. Dans une architecture à cycle récupéré, les risques d'auto-allumages et de retour de flammes dans les injecteurs prémélangés sont importants, et ce d'autant plus avec des carburants réactifs tels que l'hydrogène. Comme ce carburant est très prometteur dans un contexte de décarbonisation, ce type d'injecteur est donc à proscrire. D'un autre côté, les injecteurs non prémélangés génèrent énormément d'oxydes d'azote (NOx), des polluants atmosphériques, et sont donc également à éviter. Ainsi, les recherches actuelles visent au développement d'injecteurs micro-mélangés, alliant à la fois la sécurité des injecteurs non prémélangés et la réduction des émissions de Nox (Harald H.-W. Funke, Beckmann, Keinz, & Horikawa, 2021; Landry-Blais, Sivić, & Picard, 2022; Leonard & Stegmaier, 1994, p. 30).

Ce type d'injecteurs se base sur le principe de création d'une multitude de flammes non prémélangées au moyen de l'injection d'une grande quantité de jets de carburants au travers de trous d'injection (Figure 1-3). C'est la rapidité de mélange qui permet de limiter le temps de résidence à haute température de flamme et de fait, la production de NOx (Blouch, Li, Mueller, & Hook, 2012). Bien qu'ayant démontré des performances satisfaisantes, la stabilité de ces injecteurs doit encore être améliorée afin de pouvoir opérer sécuritairement dans une large plage de température. La stabilité de la combustion s'obtient en diminuant le temps de réaction chimique, qui dépend de la pression, de la composition chimique et de la température du mélange. Ainsi, élever la température du carburant permet de stabiliser la réaction. Cependant, si la température des produits de la combustion peut dépasser les 1500 °C, les superalliages de nickel actuellement utilisés pour la fabrication des injecteurs ne permettent pas d'opérer à plus de 1000 °C (Z. Dai et al., 2022). Des stratégies doivent donc être déployées pour, soit protéger les matériaux actuels en recourant à des doublures refroidies, par exemple, soit faire évoluer les matériaux de fabrication des injecteurs. L'incorporation de systèmes de protection étant contraignante pour la conception de l'injecteur et de la chambre de combustion, l'implémentation de matériaux permettant de supporter de plus hautes températures semble plus prometteuse.

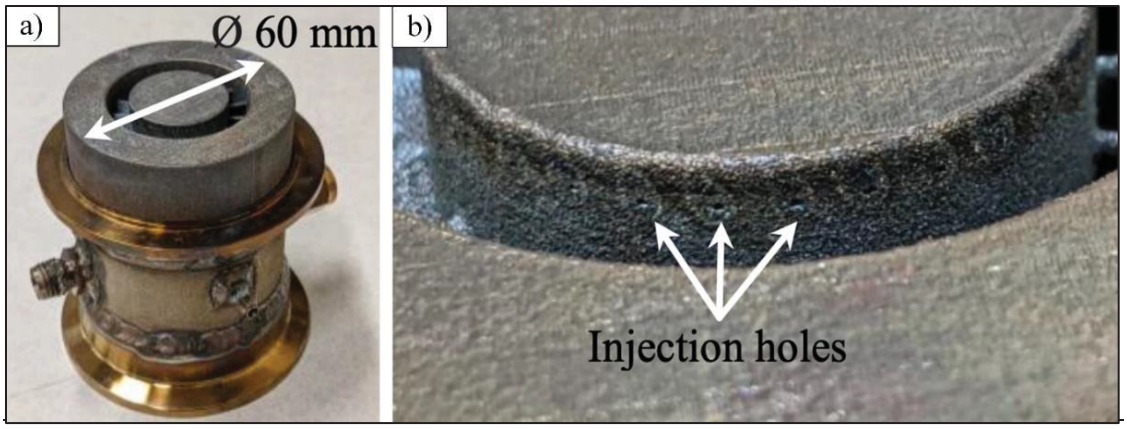

Figure 1-3 : a) Photo de l'injecteur micro-mélangé actuel et b) zoom sur les trous d'injection du carburant
Tiré de Landry-Blais et al. (2022)

L'injecteur demeurant statique, aucune exigence particulière en termes de résistance mécanique ou de masse ne lui est associée, si ce n'est que le gain en performances doit pouvoir surpasser une éventuelle masse ajoutée. En revanche, compte tenu de la sévérité de l'environnement dans la chambre de combustion, le matériau retenu doit disposer d'une haute résistance face à l'oxydation ou doit être compatible avec un revêtement de protection viable sur toute la plage de température considérée.

1.2.2 Assemblage du rotor

Grâce à l'incorporation de pales en céramique dans l'assemblage du rotor, la configuration ICT de la turbine permettrait d'atteindre une plus haute TIT, tout en conservant un volume et une masse réduits. Le principal avantage de cette architecture est qu'elle ne nécessite aucun système de refroidissement des pales et, pour augmenter la fiabilité de l'assemblage du rotor, elles sont entourées d'un anneau en composite carbone-polymère qui permet de convertir la force centrifuge en contraintes de compression. En revanche, cet anneau en composite ne pouvant pas supporter de températures supérieures à 300 °C, un anneau de refroidissement, actuellement en un alliage de titane, Ti-6Al-4V) est incorporé, servant d'intermédiaire entre les pales et l'anneau de compression (Figure 1-4) (Dubois, Landry-Blais, et al., 2022; Dubois, Landry, et al., 2022).

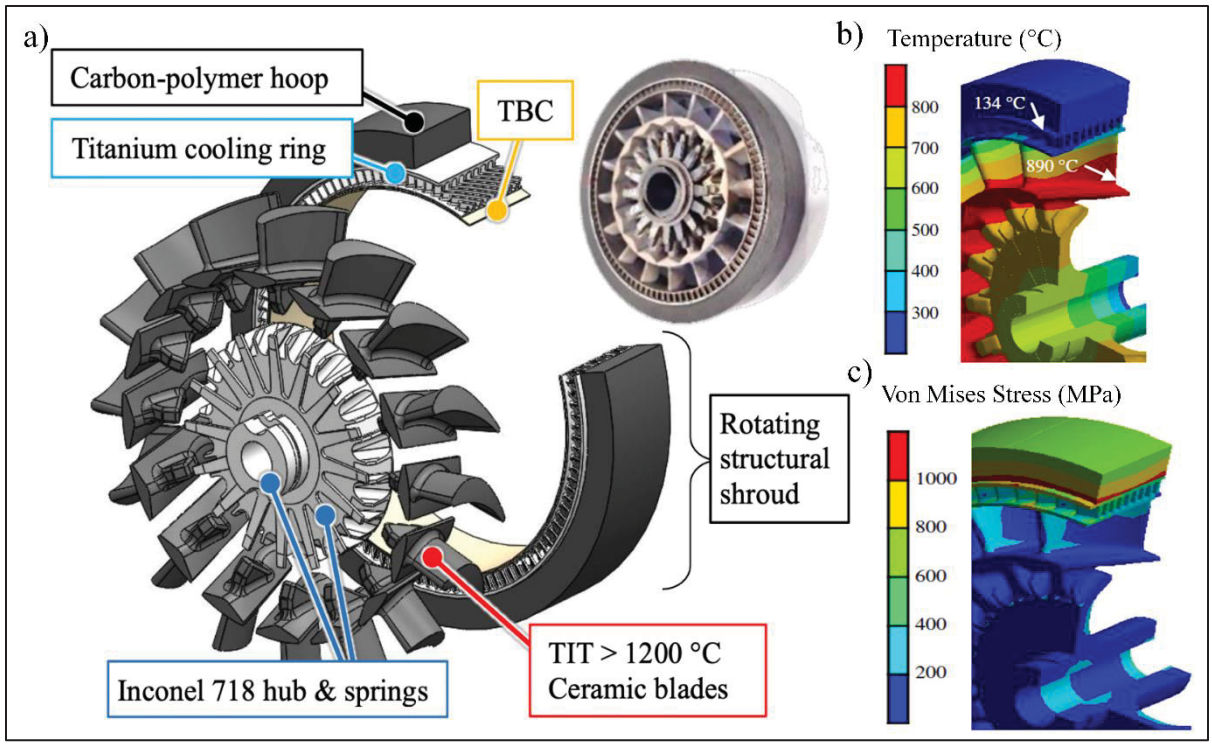

Figure 1-4 : a) Schéma en vue éclatée et photo de l'assemblage du rotor, résultats de simulations numérique par méthode aux éléments finis mettant en avant les champs b) de température et c) de contraintes de Von Mises présents dans l'assemblage du rotor
Tiré de a) Dubois, Landry-Blais, et al. (2022) et b) et c) de Dubois, Landry, et al. (2022)

Cet anneau de refroidissement doit à la fois générer un gradient de température radial important pour protéger l'anneau en composite des gaz chauds dans l'écoulement principal, tout en transmettant la charge structurale radiale afin de maintenir les pales en compression (Figure 1-4). En outre, la charge centrifuge extrême de l'anneau de refroidissement rend difficile le maintien de son propre poids et limite l'enveloppe de conception à des échangeurs de chaleur ayant une résistance spécifique suffisante. À ce sujet, des géométries complexes, contenant des ailettes et des canaux de refroidissement internes, sont proposées pour trouver le meilleur compromis entre le transfert de chaleur et la résistance spécifique (Dubois, Landry-Blais, et al., 2022). Aussi, en plus d'excellentes propriétés mécaniques (limite d'écoulement à température ambiante > 1000 MPa et > 500 MPa à 480 °C), le matériau qui compose l'anneau de refroidissement doit disposer de propriétés physiques et chimiques permettant son assemblage avec les composants voisins et son bon fonctionnement dans l'environnement de la turbine. En effet, afin de pouvoir être assemblé au mieux avec l'anneau de composites, la

conductivité thermique du matériau candidat doit être la plus faible possible et son coefficient d'expansion thermique (CTE pour Coefficient of Thermal Expansion) doit s'apparenter à celui de la barrière de protection environnementale (TBC pour *Thermal Barrier Coating*) en zircone stabilisée à l'oxyde d'yttrium 8YSZ (CTE = 10 – 11 µm/m/K) qui recouvre l'anneau de composite. Enfin, compte tenu de l'atmosphère de travail, l'anneau de refroidissement doit être résistant face à l'oxydation pour les plages de températures considérées.

De manière plus exploratoire, le moyeu du rotor, actuellement en superalliage de nickel Inconel 718, pourrait lui aussi bénéficier d'un changement de matériau au profit d'un alliage plus léger disposant cependant toujours d'excellentes propriétés mécaniques à des températures de 600 °C à 850 °C dépendamment de la conception (Dubois, Landry, et al., 2022). Les problématiques associées aux propriétés physiques et chimiques sont les mêmes que pour celles de l'anneau de refroidissement, puisqu'évoluant dans le même environnement et faisant partie du même assemblage.

1.2.3 Contraintes de fabrication

Qu'il s'agisse de l'injecteur dans la chambre de combustion ou bien de l'anneau de refroidissement et du moyeu dans l'assemblage du rotor, se tourner vers de nouveaux métaux ou alliages permettrait d'améliorer les performances de la turbine ICT sans en compromettre l'architecture. Concernant l'injecteur pour lequel la température doit être la plus élevée possible et la masse n'est pas critique, les matériaux réfractaires pourraient être de bons remplacements à un superalliage de nickel actuellement utilisé (IN625) tandis que dans l'assemblage du rotor, les alliages de titane de nouvelle génération pour l'anneau de refroidissement (actuellement en Ti64) et les intermétalliques à base d'aluminures de titane pour le moyeu du rotor (actuellement en IN718) semblent être des choix plus pertinents, compte tenu de leur résistance spécifique à haute température avantageuse en comparaison avec les matériaux actuellement utilisés(Figure 1-5).

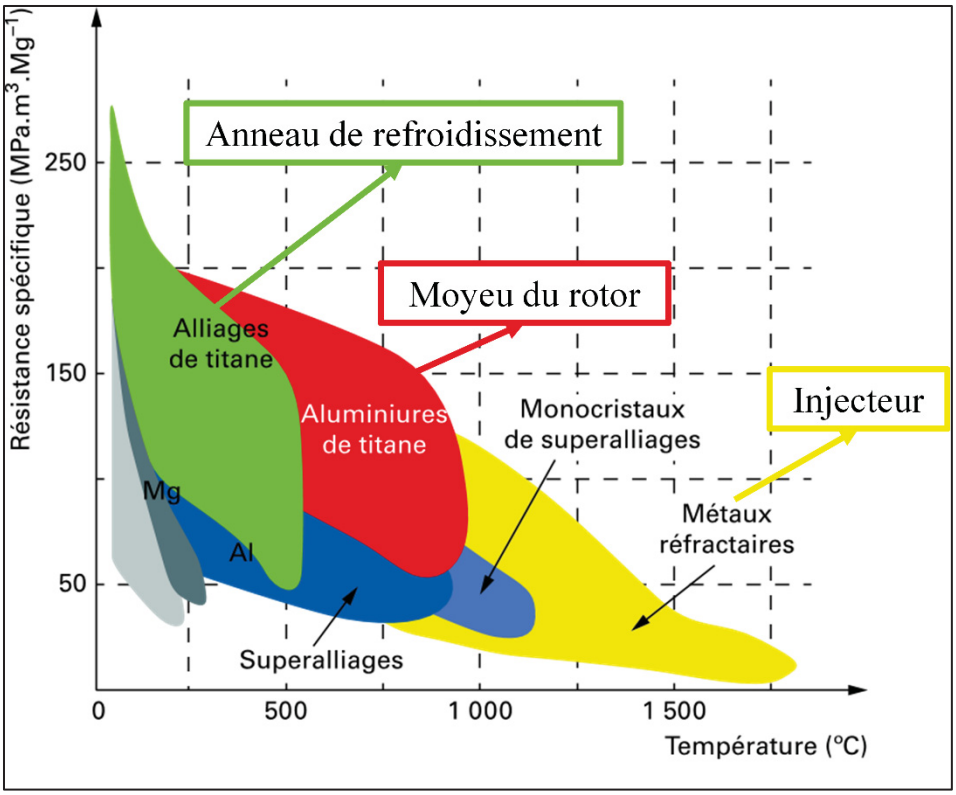

Figure 1-5 : Résistance spécifique en fonction de la température pour différents groupes de métaux
Adapté de Thomas (2020, p. 3)

Cependant, les requis géométriques de ces pièces imposent des défis supplémentaires pour la fabrication, impactant de fait le choix des nouveaux matériaux. L'injecteur a une structure interne complexe (Figure 1-6a) et intègre de petits trous permettant d'injecter le carburant et dont les dimensions sont critiques compte tenu de leur influence sur les émissions de gaz polluants : plus les trous seront de petites dimensions et plus faible sera l'émission de NOx. Pour égaler les performances actuelles, des trous plus petits que 0,5 mm de diamètre dans une paroi de 0,35 mm d'épaisseur doivent alors pouvoir être produits. L'anneau de refroidissement, quant à lui, mesure environ 200 mm de diamètre pour une faible épaisseur et dispose d'une centaine de petits canaux séparés les uns des autres par des parois minces (Figure 1-6b). Pour être efficace, le diamètre des canaux doit être le plus petit possible avec, comme référence, 0,25 mm de diamètre, de même que l'épaisseur des parois ne doit pas excéder 0,40 mm. Enfin, il existe deux architectures pour le moyeu du rotor, l'une rigide avec des plans inclinés sur

lesquels les pales en céramique glissent vers l'extérieur ou l'intérieur selon l'intensité de la force centrifuge (Figure 1-6c,d), et l'autre, utilisant un moyeu à ressort en lames flexibles pour serrer les pales en céramique contre l'enveloppe structurelle et suivre le déplacement radial des pales (Figure 1-6e,f). Si la première n'impose pas de contrainte particulière de conception, la deuxième est, quant à elle plus complexe.

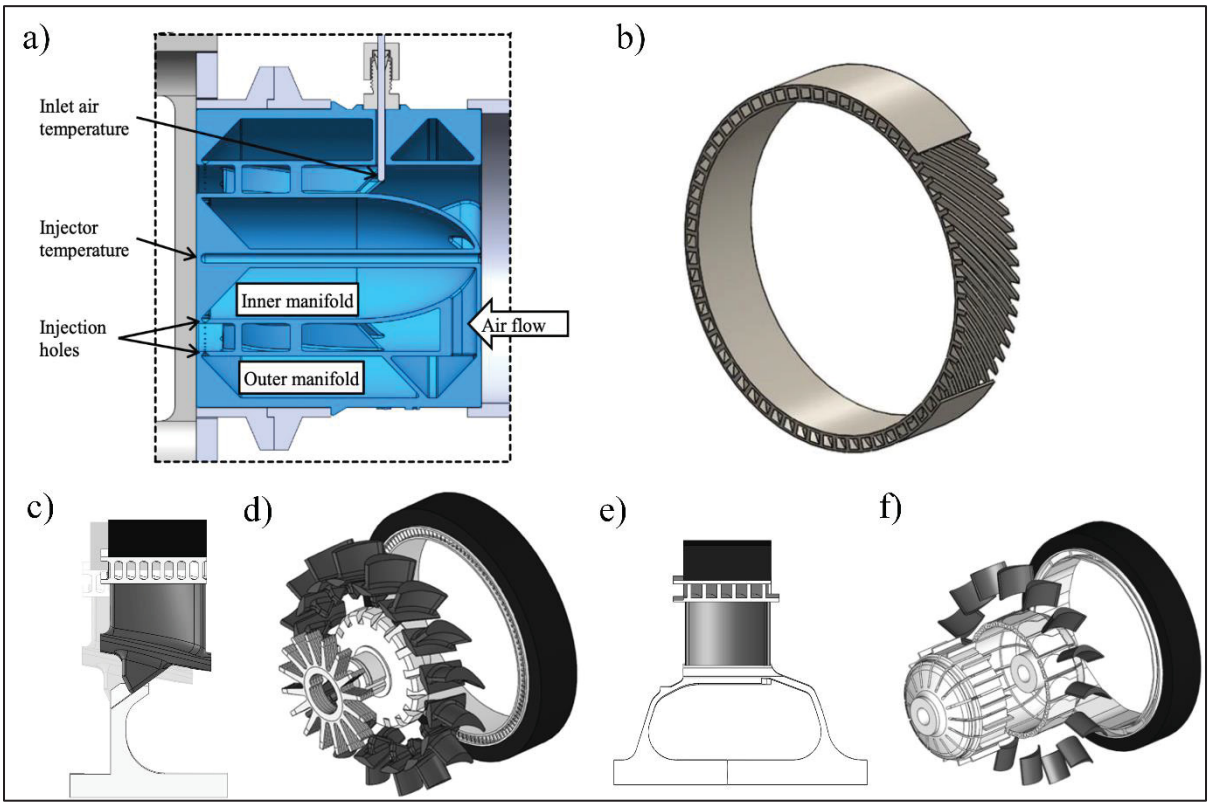

Figure 1-6 : Schéma a) en coupe de l'injecteur, b) de l'anneau de refroidissement et (c,d,e,f) des deux architectures de moyeu
Tiré de a) Landry-Blais et al. (2022), b) Dubois, Landry-Blais, et al. (2022) et (cdef) Dubois, Landry, et al. (2022)

Compte tenu de la complexité géométrique des trois composants d'étude, le procédé de fabrication additive par fusion laser sur lit de poudres a été retenu. Ce procédé de fabrication impose des contraintes supplémentaires pour la sélection des matériaux, avec, comme premier critère, la disponibilité des métaux retenus sous forme de poudres (matière première utilisée

pour ce procédé) dans des gammes de prix raisonnables. D'autres considérations propres à ce procédé seront détaillées dans une section dédiée.

1.2.4 Sommaire des exigences

Le Tableau 1-1 fournit un récapitulatif des exigences pour chacune des trois pièces d'étude, ainsi que les matériaux actuels et les familles de matériaux envisagées pour améliorer leurs performances.

Tableau 1-1 : Sommaire d'exigences pour les trois composants

	Température de service	Propriétés physiques	Propriétés mécaniques	Propriétés géométriques	Matériau actuel	Matériau envisagé
Injecteur micro-melangé	>1000°C	Faible coefficient de dilatation thermique Haute résistance à l'oxydation	N\A	Trous de diamètre < 0,5 mm sur paroi de 0,35 mm d'épaisseur	Super-alliage à base nickel Inconel 625	Métal réfractaire
Anneau de refroidissement	Jusqu'à 500°C	Faible conductivité thermique Coefficient d'expansion thermique ~10 µm/m/K Haute résistance face à l'oxydation Bonne usinabilité	>1000 MPa à température ambiante >500 MPa à 480°C	Canaux de diamètre < 0.25 mm; Parois épaisseur < 0,40 mm	Alliage de titane Ti-6Al-4V	Alliage de titane nouvelle génération
Moyeu du rotor	Jusqu'à 600 ou 850°C		>145 MPa/g/cm^3 à température ambiante > 130 MPa/g/cm^3 à 600°C <35 MPa/g/cm^3 À 850°C	N\A	Super-alliage à base nickel Inconel 718	Intermétallique à base d'aluminure de titane

1.3 Nouvelle génération de matériaux

1.3.1 Les métaux réfractaires

1.3.1.1 Propriétés physiques et mécaniques

Parmi les matériaux disponibles, les métaux réfractaires se présentent comme de candidats intéressants pour l'injecteur dans la chambre de combustion. En effet, les métaux regroupés

sous cette appellation possèdent les plus hauts points de fusion parmi tous les métaux, avec une température d'entrée dans le groupe définie à 1800 °C et un maximum de 3410 °C avec le tungstène, ce dernier représentant un matériau de choix dans le contexte d'amélioration de la turbine. Un deuxième matériau candidat est le molybdène, avec une température de fusion de 2600 °C et le meilleur rapport résistance mécanique haute température/densité de tous les métaux réfractaires (Tableau 1-2). Compte tenu de leur proximité dans le tableau périodique, ces deux métaux possèdent tous les deux une structure cristallographique de type cubique centré (bcc) et des propriétés similaires, comme de bonnes conductivités thermique et électrique, un faible coefficient de dilatation thermique, mais une densité élevée (Tableau 1-2). Ces propriétés couplées à une dureté élevée, une bonne imperméabilité aux radiations et leur capacité à maintenir des propriétés mécaniques élevées à haute température ont suscité l'engouement pour ces métaux entre les années 1950s et les années 1990s, quand la tendance était aux programmes nucléaires (par exemple, le programme américain NERVA (*Nuclear Engine for Rocket Vehicle Application*) ou russe NASP (*National Aviation Security Plan*) (Philips, Carl, & Cunningham, 2020).

Tableau 1-2 : Quelques propriétés physiques du tungstène et du molybdène pur
Tiré de J. R. Davis & ASM International (1998, p. 115, 629)

	Tungstène (W)	Molybdène (Mo)
Propriétés atomiques et nucléaires		
Numéro atomique	74	42
Masse atomique relative (u)	183,85 ± 0.02	95,95 ± 0.02
Configuration électronique	$5d^4 6s^2$	$4d^5 s^1$
Degré de valence	-2 à +6	+2 à +6
Propriétés structurales		
Structure cristalline	Cubique centré	Cubique centré
Paramètre de maille (nm)	0,316	0,315
Densité théorique (g/cm^3)	19,25	10,22
Rayon atomique (pm)	139	145
Volume molaire (m^3/mol)	$9{,}55*10^{-6}$	$9{,}38*10^{-6}$
Propriétés thermiques et électriques		
Température de fusion (°C)	3410	2610
Capacité thermique massique (kJ/kg.K)	0,128	0,276
Conductivité thermique (W/m.K)	160	142
Coefficient d'expansion linéaire thermique (µm/m.K)	3,01 à 8,87	5
Résistivité électrique (nΩ.m)	52	53

Outre leurs propriétés intéressantes pour applications, le tungstène et le molybdène possèdent un point de transition ductile-fragile (*Ductile Brittle Transition Temperature*, DBTT) très haut (300 °C pour le tungstène (J. R. Davis & ASM International, 1998)), ce qui limite leur déformabilité à température ambiante. Deux principales solutions se dégagent alors pour leur mise en forme : créer des alliages (notamment avec du rhénium (Okamoto, 1998)) pour abaisser leur DBTT ou bien les travailler à température élevée, au-delà de leur DBTT. Si cette dernière solution semble attrayante, puisqu'elle permet de conserver des métaux purs, elle n'en demeure pas moins complexe compte tenu de la forte tendance à l'oxydation à haute température (à partir de 500 °C) de ces deux métaux. Là encore, le recours à des éléments d'alliages, tels que l'aluminium ou le chrome par exemple, permet de limiter ce phénomène mais rendent leur température d'utilisation limitée par la température de fusion de ces éléments d'addition. Pour conserver des métaux purs, le travail sous atmosphère contrôlée devient la meilleure solution pour pallier ce problème.

En dépit des difficultés précédemment énoncées, des techniques de fabrication et de mise en forme des métaux réfractaires ont tout de même été développées. Des procédés traditionnels de mise en forme à chaud peuvent être retenus, comme les techniques de forgeage, de laminage à chaud ou encore de soudage et brasage. Mais les procédés les plus fréquemment rencontrés pour ces métaux sont des procédés basés sur la métallurgie des poudres, comme le frittage ou la compression isostatique à chaud (J. R. Davis & ASM International, 1998). Ces procédés ont pour avantage de pouvoir outrepasser le DBTT tout en limitant l'oxydation et d'être relativement bon marché. Cependant, il existe un paradoxe entre les propriétés mécaniques attendues à haute température et les procédés conventionnels de métallurgie des poudres : les matériaux doivent posséder une faible résistance mécanique et une grande ductilité dans une gamme de température allant de 1200 °C à 1400 °C (suffisamment loin du DBTT) pour parvenir à leur mise en forme par ces procédés, alors même que ces matériaux sont appréciés pour leur grande résistance mécanique dans cette même plage de température et au-delà (Philips et al., 2020). Du fait de ces contraintes de mise en forme, le tungstène et le molybdène sont principalement utilisés comme revêtements de protection thermique (dans les fours de compression isostatique travaillant sous atmosphère inerte par exemple), de protection aux radiations (pour des applications nucléaires principalement, comme par exemple dans le cadre du projet ITER) ou de protection aux frottements (dans le secteur automobile comme revêtement de segments de piston ou de bagues de synchronisation par exemple). Ces métaux sont également rencontrés sous des formes géométriques simples : filament de lampe, anodes d'équipement par radiographie à rayons X, composants électroniques ou encore creusets à saphir.

Compte tenu de la complexité géométrique des injecteurs micro-mélangés et des limites de mise en forme de ces métaux par des procédés conventionnels, il apparaît primordial le développement de nouvelles techniques de mise en forme de ces métaux. Pour le concept actuel, le procédé de fusion laser sur lit de poudre est retenu et les considérations nécessaires à l'implémentation de ces métaux par celui-ci seront développées ultérieurement.

1.3.1.2 Comportement en environnement sévère

Au-delà de la résistance à haute température et de la complexité géométrique, le matériau retenu doit pouvoir survivre dans un environnement sévère. En effet, en condition de travail, le matériau est exposé à une large gamme de températures, de pressions et aussi à plusieurs espèces gazeuses oxydantes et corrosives. En revanche, sans revêtement protecteur, le tungstène et le molybdène subissent une forte oxydation pour des températures supérieures à 500 °C (Figure 1-7) formant ainsi les espèces volatiles MoO_3 et WO_3, qui s'évaporent à partir de 795 °C (MoO_3) et 1000 °C (WO_3), les rendant inaptes pour un emploi à haute température. Pour pallier ce problème, il est possible soit de recourir à des éléments d'alliages au matériau de base afin de modifier les phases d'oxydation et de former des films d'oxydes denses et plus adhérents, soit d'appliquer un revêtement protecteur pour empêcher l'entrée en contact du matériau avec l'oxygène. Cette dernière solution est la plus répandue, notamment, car elle permet de ne pas altérer les propriétés du matériau de base, ce qui est d'autant plus pertinent dans le cadre des applications hautes températures (J. R. Davis & ASM International, 1998; Gatzen, Smokovych, Scheffler, & Krüger, 2021; Nelson, Sooby, Kim, Cheng, & Maloy, 2014).

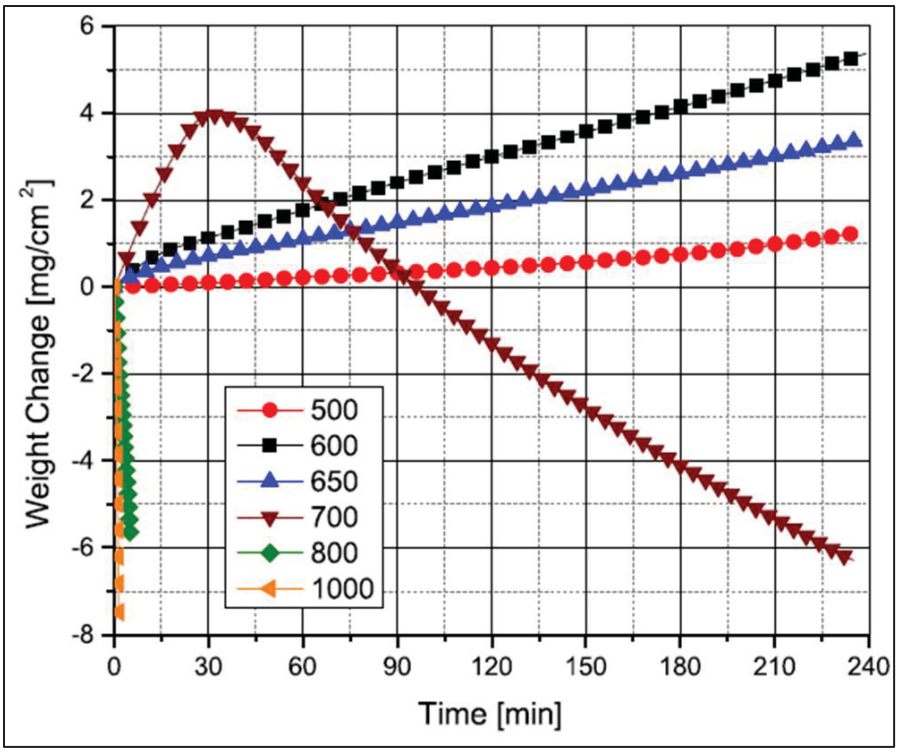

Figure 1-7 : Changements de masse mesurés pour des échantillons de molybdène pur exposé à de l'air à différentes températures
Tiré de Nelson et al. (2014)

Parmi les revêtements les plus courants, les intermétalliques à base d'aluminides ou de silicides sont généralement retenus pour protéger le tungstène et le molybdène. Des revêtements de type Al_4W, WSi_2 et $MoSi_2$ sont généralement rencontrés, permettant de former à la surface une couche dense de passivation de type Al_2O_3 ou SiO_2, pouvant résister à une exposition prolongée à des températures allant jusqu'à 1600 – 1700 °C dans des atmosphères sèches, conjointement aux oxydes WO_3 et MoO_3 qui se volatilisent à ces températures (Das, Rao, Pabi, Sankaranarayana, & Nandy, 2014; Gatzen et al., 2021; Gorr et al., 2021; Martinz et al., 2006; Mitra, 2019). Les revêtements en silicides sont également parfois enrichis en Bore ou en YSZ pour améliorer leurs performances. Cependant, deux inconvénients majeurs sont rencontrés pour ces revêtements : i) pour des températures comprises entre 400 et 600 °C, les oxydes WO_3 et MoO_3 demeurent solides et causes des fissures dans le revêtement, phénomène appelé « *pesting* » dans la littérature et ii) ces revêtements sont inutilisables dans des atmosphères humides, en raison de la formation d'hydroxydes de silicium ($Si(OH)_4$, SiOOH, etc...), qui se

volatilisent et causent une récession de la couche protectrice. Une solution envisagée pour contourner ce dernier obstacle consiste à envisager des revêtements étagés (Gatzen et al., 2021; Perepezko, 2018).

Au-delà de la composition du revêtement, sa méthode d'application impose également des restrictions et aura une incidence sur la qualité du revêtement en termes d'épaisseur ou d'homogénéité (Fu et al., 2021), et de fait sur sa durée de vie. La rugosité de la surface et la complexité géométrique de la pièce (canaux internes, changement d'épaisseur de section, etc..) sont également des défis pouvant limiter l'emploi de certaines méthodes d'applications. Pour les substrats en métaux réfractaires, les méthodes d'applications les plus rencontrées sont le dépôt chimique en phase vapeur (CVD pour *Chemical Vapor Deposition*), la cémentation par halogénures activés (HAPC pour *Halide Activated Pack Cementation*), le placage au silicium trempé à chaud (HDS pour *Hot Dip Silicon-plating*) ou les méthodes de suspension (Fu et al., 2022; Y. Zhang et al., 2022).

1.3.2 Les alliages de titane nouvelle génération et les intermétalliques à base d'aluminures de titane (structure et propriétés)

Afin d'améliorer les performances et d'offrir une plus grande latitude de conception, le matériau qui compose l'anneau de refroidissement doit également évoluer vers des matériaux capables de supporter d'importants gradients thermiques jusqu'à de hautes températures tout en conservant la meilleure résistance spécifique que possible sur cette même gamme de températures. Parmi les métaux disponibles, les alliages de titane nouvelle génération et les intermétalliques à base d'aluminure de titane sont d'excellents candidats, en raison notamment de leur résistance spécifique jusqu'à haute température (Figure 1-5). Pour cette même raison, ils pourraient succéder aux alliages de nickel actuellement contenu dans le moyeu du rotor.

1.3.2.1 Alliages de titane et intermétalliques à base d'aluminures de titane (structure)

Le titane appartient à la classe des matériaux légers (4,5 g/cm^3 (J. R. Davis & ASM International, 1998) et possède deux formes allotropiques à l'état solide : la phase α-Ti (HCP)

à basse température qui se transforme en β-Ti (BCC) à haute température à partir de 882,5 °C. Il peut être allié avec soit des éléments pouvant stabiliser la phase α et donc augmenter la température de β-transus (Al, O, N et C), soit des éléments permettant de stabiliser la phase β (Mo, V, Nb et Ta) ou constitutifs d'eutectoïdes (Fe, Cr, Mn, Ni et Si), qui réduisent le β-transus, soit finalement avec des éléments neutres (Zr, Sn et Hf) n'ayant pas d'effet sur le β-transus (Figure 1-8) (Lütjering & Williams, 2007).

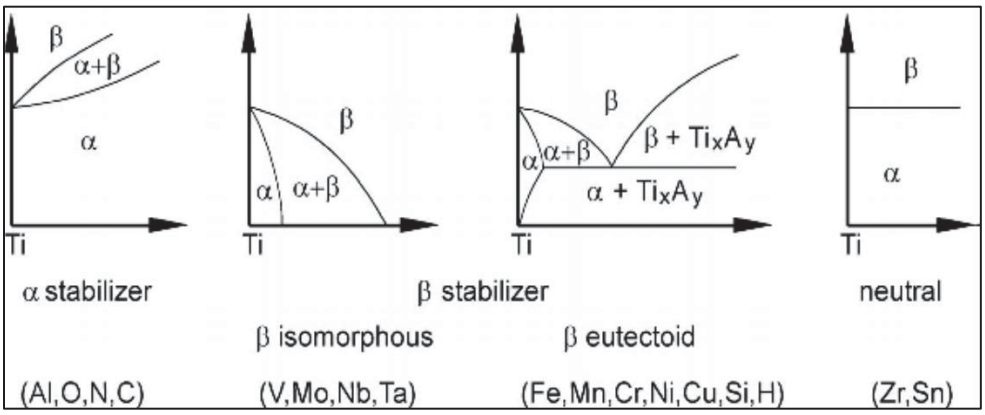

Figure 1-8 : Représentation schématique des effets
de différents d'alliages sur les diagrammes de phases des alliages de titane
Tiré de Lütjering & Williams (2007, p. 24)

En fonction de la teneur des éléments d'alliage et de la composition de phase formée, les alliages de titane sont classés en α- et pseudo-α-, ($\alpha + \beta$), pseudo-β- et β-alliages, dont la teneur en aluminium n'excède pas les 10%. Les intermétalliques à base d'aluminure de titane quant à eux se décomposent en trois catégories dépendamment de s'ils possèdent une base en Ti_3Al, Ti_2AlNb ou TiAl. Les intermétalliques Ti_3Al sont appelés intermétalliques α_2 en raison de la phase qu'ils forment et se composent d'environ 23 à 25 at% d'aluminium et 11 à 18% de niobium. Ceux à base Ti_2AlNb, aussi appelés orthorhombiques du fait de la formation de la phase O, contiennent 21 à 25 at% d'aluminium et 25 à 30% de niobium. Enfin, les intermétalliques appelés γ à base de TiAl contiennent 48 à 54 at% d'aluminium et 1 à 10 at% d'autres éléments d'alliages, à savoir vanadium, chrome, manganèse, niobium, tantale, tungstène ou molybdène. La Figure 1-9 présente le diagramme de phase des alliages titane-aluminium (Bhat, 2018; J. R. Davis & ASM International, 1998; Froes, 2015).

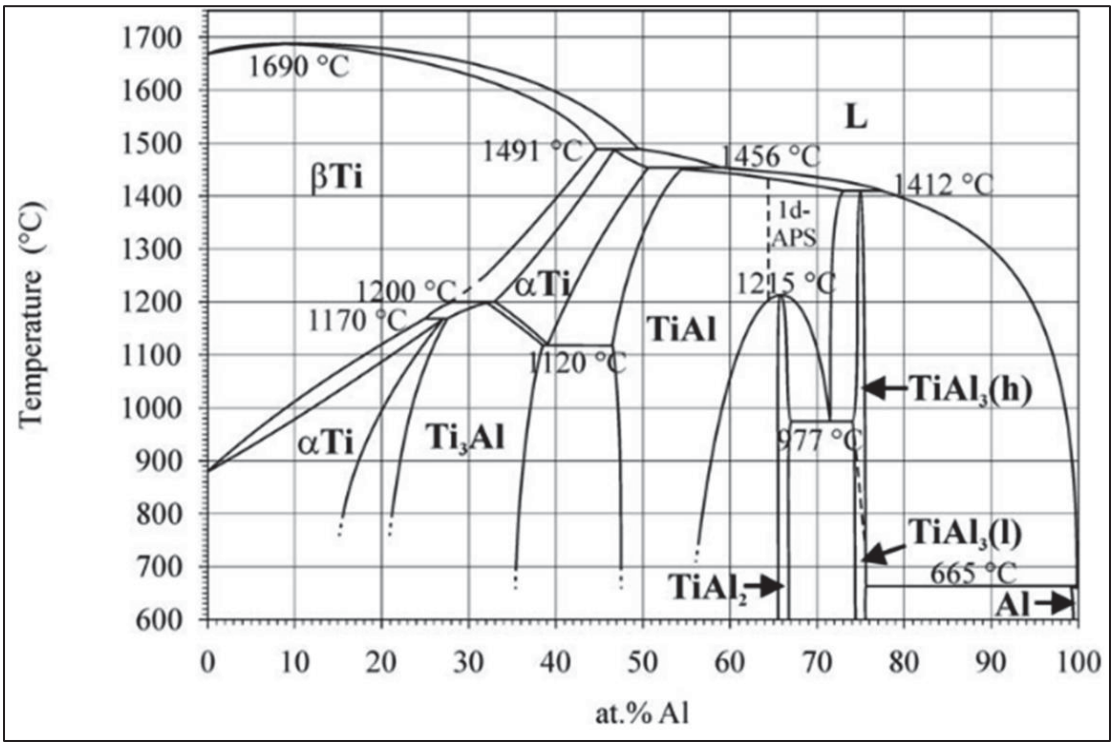

Figure 1-9 : Diagramme de phase des alliages de titane et des intermétalliques à base d'aluminure de titane en fonction de la concentration atomique en aluminium
Tiré de Schuster & Palm (2006, p. 256)

1.3.2.2 Alliages de titane (propriétés)

En ce qui a trait aux alliages de titane alliés avec moins de 10% d'aluminium, chaque groupe a un ensemble distinct de propriétés, pour lesquelles certaines tendances peuvent être distinguées : i) les alliages à plus forte teneur en β peuvent être traités thermiquement de manière à obtenir une haute résistance, surtout à température ambiante (Figure 1-10a) et ii) ont une meilleure formabilité à des niveaux de résistance équivalents, cependant, iii) cela se traduit par une baisse de la résistance en fluage à haute température (Figure 1-10a), iv) et un déficit en soudabilité (Bhat, 2018; J. R. Davis & ASM International, 1998). Le schéma de la Figure 1-10b illustre qualitativement ces tendances en prenant comme référence le Ti-6Al-4V, l'alliage $\alpha + \beta$ le plus communément répandu dans l'industrie actuelle. Il est également

important de noter que les alliages de type pseudo-β et β sont métastable du fait de la variation de composition chimique qui subvient en fonction de la température.

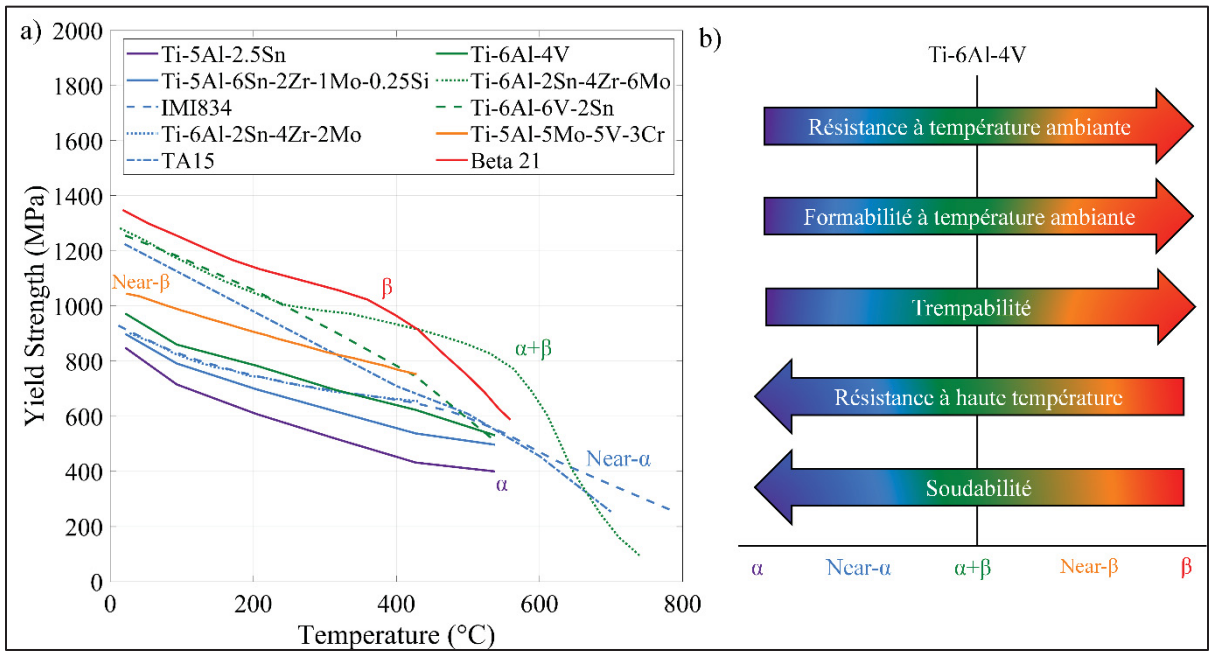

Figure 1-10 : a) Contrainte d'écoulement en fonction de la température pour différents alliages de titane; b) comparaison qualitative des principales caractéristiques des différentes familles d'alliage de titane
a) Données extraites de diverses sources Joseph R. Davis & ASM International (2010, p. 587); Feng, Zhang, Cui, Chen, & Yu (2017); Froes (2015, p. 117); Peters, Kumpfert, Ward, & Leyens (2003); Smallman & Ngan (2014); « Timetal 21S » (2000); Veeck, Lee, Boyer, & Briggs (2004); Z. Zheng, Balint, & Dunne (2017) et b) adapté de Bhat (2018, p. 33)

Tous les procédés de mise en forme conventionnels sont disponibles pour les alliages de titane, mais tous les alliages de titane ne sont pas nécessairement compatibles avec chacun des procédés. À titre d'exemple, les alliages de type β sont les plus difficiles à usiner, mais peuvent être mis en forme à froid sous forme de feuilles plus aisément que les alliages de type α. Ils sont souvent considérés pour des applications où le ratio résistance/poids est une donnée critique et où la plage de températures excède celle des alliages d'aluminium, notamment dans les composants de turbine à gaz par exemple. Leur excellente résistance à la corrosion les rend également très présents dans les secteurs de l'aéronautique, de l'automobile de haute performance, des engins marins ou encore dans le secteur médical pour différentes prothèses.

Finalement, ils sont rencontrés en tant que structure de support d'appareils optiques pour les systèmes de surveillance et de guidage des missiles, applications pour lesquelles la variation de température est très importante et nécessite des matériaux possédant un coefficient de dilatation thermique proche de celui des optiques (J. R. Davis & ASM International, 1998).

1.3.2.3 Intermétalliques à base d'aluminures de titane (propriétés)

Les intermétalliques à base d'aluminures de titane possèdent généralement une relativement bonne raideur associée à de hauts module d'Young et ont des propriétés mécaniques intéressantes à haute température, notamment en termes de résistance en tension et à la fatigue (Figure 1-10) (Bhat, 2018; J. R. Davis & ASM International, 1998; Djanarthany, Viala, & Bouix, 2001; Rowe, 1992). Compte tenu de la haute teneur en aluminium, les intermétalliques γ-TiAl possèdent la plus faible densité des alliages titane-aluminium ($\rho \approx 3{,}9 - 4{,}2$ g/cm³). Ils disposent également d'une conductivité thermique élevée (~17 - 25 W/(m.K) dans la plage de 25 à 900 °C) et d'une bonne résistance à l'oxydation à haute température (Clemens & Mayer, 2013). Ils possèdent également une bonne résistance au fluage à des températures élevées (750 °C (Bhat, 2018)) et une stabilité de surface adéquate à ces températures et, de fait, conservent leur résistance pendant des périodes de service prolongées sans fragilisation. Les intermétalliques α_2-Ti_3Al sont également caractérisés par une faible densité ($\rho \approx 4{,}3$-$5{,}1$ g/cm³) et possèdent une résistance au fluage à haute température supérieure à celles des alliages de titane conventionnels, qui s'explique notamment par le fait que la phase α_2 soit ordonnée (« Titanium alloys for aerospace structures and engines », 2012). En revanche, ces intermétalliques disposent d'une faible résistance à la propagation de fissures en fatigue et souffrent d'une forte fragilisation due à l'oxydation active à des températures supérieures à 550 °C (Djanarthany et al., 2001). Enfin, les intermétalliques orthorhombiques Ti_2AlNb possèdent quant à eux la densité la plus élevée ($\rho \approx 5{,}3$ g/cm³) des alliages titane-aluminium en raison de leur haute teneur en niobium. La présence de niobium permet également une conductivité thermique élevée (K = 25 à 40 W/(m.K)) et contribue à l'amélioration de la résistance à l'oxydation à haute température (jusqu'à 700 °C) notamment grâce à la formation d'une couche mixte $TiO_2/AlNbO_4$. Ils possèdent également une résistance spécifique plus

élevée ($\sigma_{0.2}/g_\rho$) à des températures élevées par rapport aux alliages pseudo-α et ($\alpha + \beta$) (Kim & Kim, 2018; Lütjering & Williams, 2007).

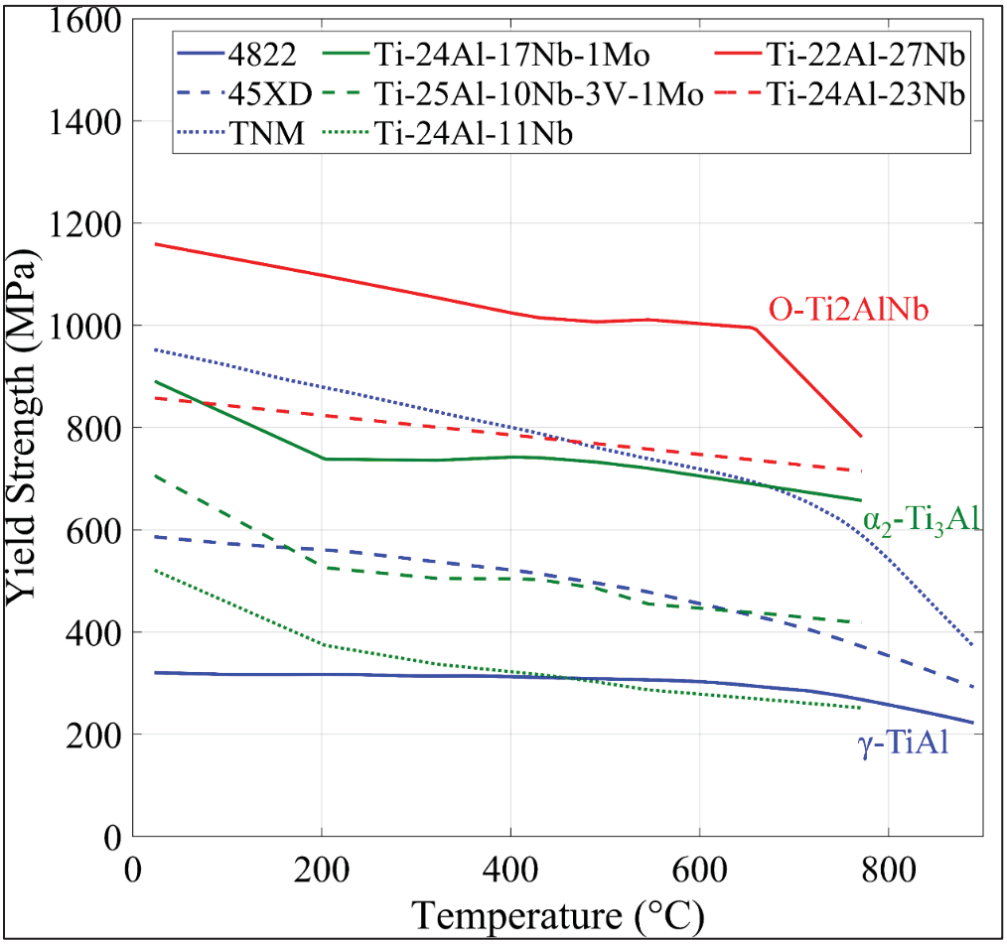

Figure 1-11 : Contrainte d'écoulement en fonction de la température pour différents intermétalliques à base d'aluminures de titane
Données extraites de Kim & Kim (2018, p. 201);
Lütjering & Williams (2007, p. 352)

En dépit des nombreux avantages des intermétalliques à base d'aluminures de titane, leur faible ductilité et ténacité à la rupture ont historiquement limité leur développement. En effet, ils sont fragiles à température ambiante et nécessitent une mise en forme à haute température en raison de leur DBTT élevé (700 à 750 °C). Bien que le procédé de moulage soit le plus répandu pour les intermétalliques γ, la différence significative dans les propriétés physiques du matériau de base et des éléments d'alliage, en particulier la densité et les températures de fusion de Al

(660 °C) et Nb (2468 °C) aboutit à un risque non négligeable de conserver des infondus ou de vaporiser une partie de l'aluminium, ce qui entraîne une inhomogénéité chimique et de phase et une texture de cristallisation défavorable. De fait, ce procédé n'est actuellement pas développé pour les orthorhombiques. Pour produire des pièces en aluminures de titane, les procédés de métallurgie des poudres sont généralement retenus. Malgré les efforts d'introduction de cette classe d'alliages, les intermétalliques à base d'aluminures de titane sont encore considérés comme des matériaux en développement et les coûts associés à leur production et les rendements réalisables limitent fortement leur utilisation à l'heure actuelle. Ils demeurent cependant des matériaux de choix pour remplacer les superalliages de nickel à des températures de service jusqu'à 700 °C, afin d'alléger les structures tout en maintenant des niveaux constants de contrainte de fonctionnement et serait donc fortement attrayant pour l'industrie des moteurs d'avion à poids critique ou l'aérospatial (Bhat, 2018; Djanarthany et al., 2001).

1.3.2.4 Comportement face à l'oxydation des alliages de titane et intermétalliques à base d'aluminures de titane

La limite de température d'utilisation des alliages de titane est principalement causée par une forte tendance à l'oxydation plus qu'à une baisse des propriétés mécaniques. En contact avec une atmosphère oxydante à haute température, trois réactions chimiques peuvent avoir lieu :

$$\frac{1}{2}Ti(s) + O_2(g) = TiO(s) \quad (1.1)$$

$$TiO(s) + \frac{1}{2}O_2(g) = TiO_2(s) \quad (1.2)$$

$$2Al(s) + \frac{3}{2}O_2(g) = Al_2O_3(s) \quad (1.3)$$

L'énergie d'activation du TiO (-28.27 eV) est très similaire de celle de l'Al_2O_3 (-30.00 eV) tandis que celle du TiO_2 (-54.99 eV) est bien inférieure à ces derniers. Par ailleurs, le TiO est un oxyde extrêmement instable, et par conséquent, en pratique, le monoxyde TiO est rapidement oxydé en dioxyde TiO_2. Si dans l'état initial d'oxydation, Al_2O_3 et TiO_2 se forment en même temps et croissent le long de leur direction optimale de croissance, la vitesse de

croissance du TiO_2 étant plus élevée et son énergie d'activation beaucoup plus faible que celle du Al_2O_3, c'est le dioxyde de titane qui est rencontré en surface. À basse température, la couche d'oxyde TiO_2 peut complètement recouvrir la surface et protéger le substrat de l'environnement en empêchant la diffusion de l'oxygène. En revanche, à haute température, cette couche devient poreuse, permettant la diffusivité de l'oxygène dans le substrat. Sous cette couche d'oxyde de TiO_2, une zone enrichie en aluminium se forme alors à la suite de l'appauvrissement en titane et permet alors la formation de l'oxyde Al_2O_3 majoritairement. La couche inférieure est alors encore appauvrie en aluminium et le phénomène inverse se produit et ainsi de suite, créant alors une structure multicouche qui se compose généralement d'un mélange de couches enrichies en TiO_2, couches enrichies en Al_2O_3, dans des proportions variables, et une zone très mince affectée par l'oxygène de l'extérieur à l'intérieur (Figure 1-12). Cela entraîne alors une augmentation de l'épaisseur de la couche d'oxyde et une diminution de la cohésion entre la couche et le substrat (J. Dai, Zhu, Chen, & Weng, 2016; Leyens & Peters, 2004).

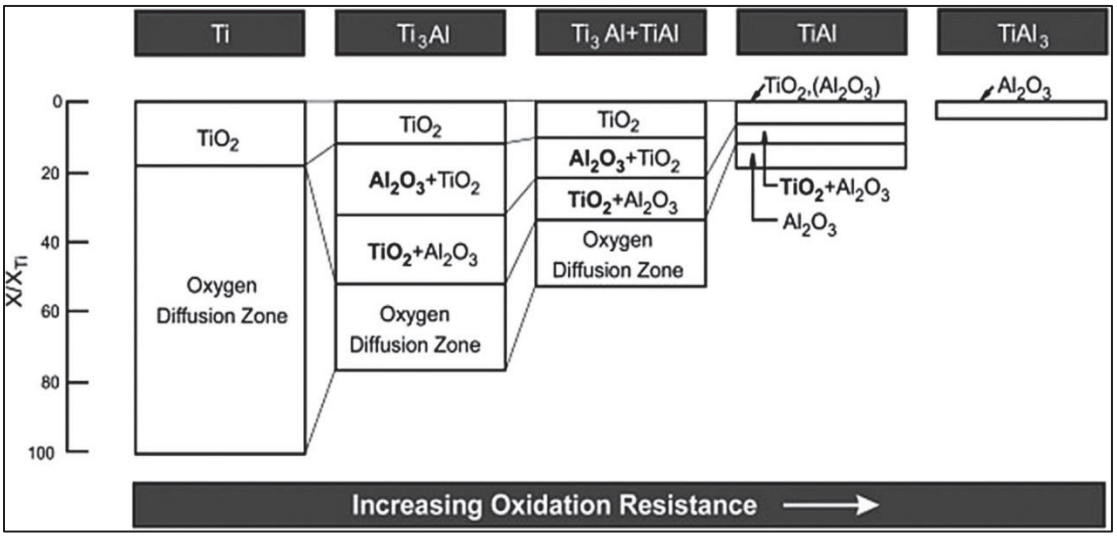

Figure 1-12 : Représentation schématique des couches d'oxides et de la diffusion de l'oxygène dans les alliages de titane et intermétalliques à base d'aluminures de titane
Tiré de Peters et al. (2003)

L'épaisseur de la zone affectée par l'oxygène (OAZ pour O*xygen Affected Zone*) ainsi que les cinétiques d'oxydation varient en fonction de la composition de l'alliage et des phases en

présence (Figure 1-13), ce qui impose des températures limites d'utilisation propre à chacun (Tableau 1-3). Les intermétalliques à base d'aluminures de titane ont généralement une meilleure résistance à l'oxydation que les alliages de titane en raison de la forte teneur en aluminium.

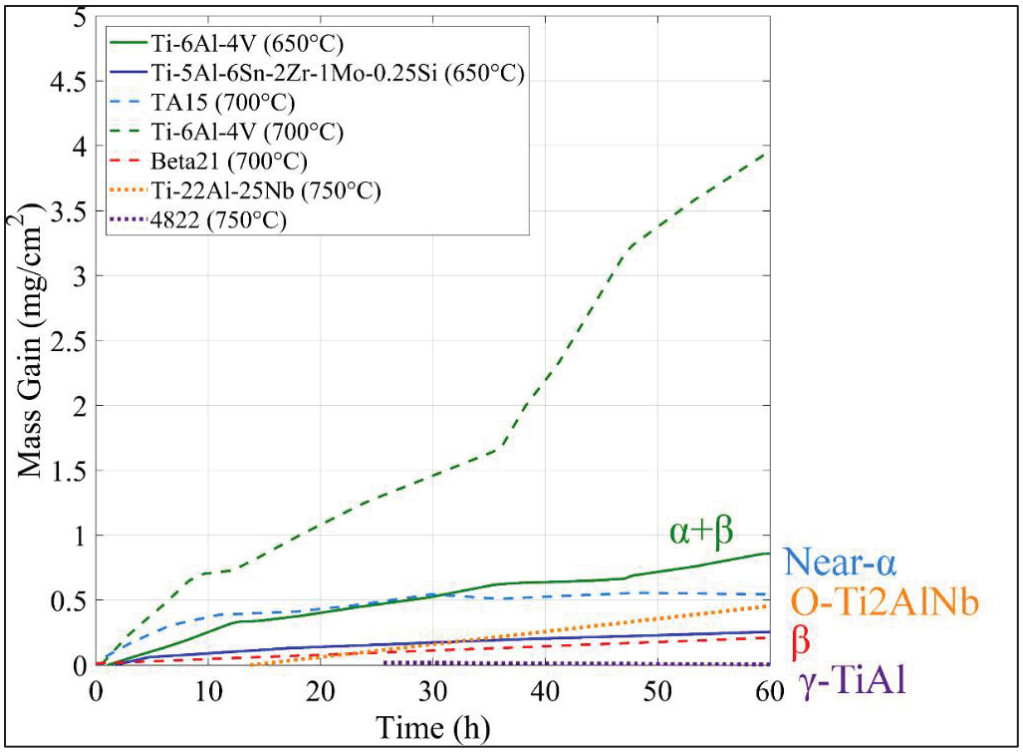

Figure 1-13 : Gain de masse en fonction du temps pour différents alliages de titane et intermétallique à base d'aluminures de titane exposé à l'air sous différentes températures
Données extraites de diverses sources Guleryuz & Cimenoglu (2009); Lavisse et al. (2020); Leyens & Peters (2004); Vincent et al. (2021)

1.3.2.5 Sommaire sur les alliages de titane et intermétalliques à base d'aluminures de titane

Le choix des matériaux pour l'anneau de refroidissement et le moyeu du rotor est dicté par une multitude de raisons. Tout d'abord, il s'agit de s'assurer que les propriétés physiques et mécaniques permettent améliorer les performances par rapport aux matériaux déjà en place. Ensuite, les coûts d'acquisition et de développement de ces matériaux doivent être rentabilisés

par le gain en performances. Enfin, comme la complexité géométrique des composants exige l'utilisation du procédé de fusion laser sur lit de poudre, les matériaux choisis doivent à la fois être compatibles avec ce procédé de fabrication et disponibles sous forme de poudres (matière première nécessaire pour ce procédé de fabrication). Pour ces différentes raisons, les alliages de titane $\alpha + \beta$, en l'occurrence Ti-6Al-2Sn-4Zr-6Mo (Ti6246), semblent se distinguer pour l'anneau de refroidissement tandis que les aluminures de titane de type orthorhombique (Ti-22Al-27Nb) représentent des candidats potentiels pour le moyeu du rotor (Tableau 1-3).

Tableau 1-3 : Température maximale de service, résistance ultime à la température de service et résistance à l'oxydation pour différents alliages de titane et intermétalliques à base d'aluminures de titane
Adapté de J. Dai et al. (2016); Feng et al. (2017); Hucek (1979); Kim & Kim (2018, p. 201); Peters et al. (2003); Smallman & Ngan (2014); « Timetal 21S » (2000); Z. Zheng et al. (2017)

Type	Alliage	Température maximale de service (°C)	Limite d'écoulement à température maximale de service (MPa)	Résistance à l'oxydation
α + β	Ti-6Al4V	300 - 400	620	+
α + β	Ti-6Al-2Sn-4Zr-6Mo	400 - 450	900	+
Proche-α	Ti-6Al-2Sn-4Zr-2Mo	400 - 450	660	+
Proche-α	IMI834	550 - 600	450	++
Proche-α	TA15	500	600	++
β	Beta21	550	580	++
Orthorhombique	Ti-22Al-27Nb	700	800	+++
γ-TiAl	4822	830	245	+++

1.4 La fusion laser sur lit de poudre

1.4.1 Définition et paramètres

Qu'il s'agisse de l'injecteur, de l'anneau de refroidissement ou du moyeu du rotor, la complexité géométrique des pièces implique le recours à de nouveaux types de procédés permettant plus de liberté de conception, ce qu'offre notamment la fabrication additive (FA).

Il s'agit d'une technologie regroupant plusieurs procédés permettant de construire des pièces par ajout de matière à partir d'un modèle numérique 3D (norme NF EN ISO/ASTM 52900). Cette technologie, développée dans les années 1960, était à l'origine considérée uniquement pour le prototypage. Cependant, le rapide développement de la technologie d'impression, du domaine informatique ainsi que du domaine de conception assistée par ordinateur a permis à cette technologie de s'installer dans les lignes de production directe de pièces fonctionnelles, permettant ainsi de répondre à certaines limites des procédés conventionnels, sans pour autant s'y substituer. En effet, la FA permet d'envisager des pièces aux géométries plus complexes, répondant particulièrement à la demande de pièces sur mesure, et aux petites séries de pièces à haute valeur ajoutée. De nos jours, cette technologie se retrouve sous plusieurs déclinaisons de procédés pour une multitude de matériaux disponibles (Blum Guillaume, De Blois, & Tadjine, 2017; Centre technique des industries mécaniques, 2019; Chowdhury et al., 2022; Wohlers Associates, 2016).

Parmi les procédés métalliques, la fusion laser sur lit de poudre (LPBF pour *Laser Powder Bed Fusion* en anglais) est le plus vieux procédé de fabrication additive métallique et est particulièrement répandue de par sa précision (rugosité de surface entre 10 et 20 µm) et ses coûts très compétitifs par rapport à ses concurrents directs que sont la fusion laser par faisceau d'électrons (EB-PBF pour *Electron Beam Powder Bed Fusion*) ou encore le dépôt d'énergie dirigée (DED pour *Directed Energy Deposition*) (Pragana, Sampaio, Bragança, Silva, & Martins, 2021). Ce procédé à étape unique, c'est-à-dire que les pièces brutes sont obtenues en une seule étape, repose sur la fusion par un laser (diamètre du faisceau variant généralement de 40 à 200 µm pour une puissance allant de 200 à 1000 W) d'une couche de poudre métallique (souvent de 20 à 60 µm d'épaisseur) déposée à l'aide d'un racleur sur une plateforme de fabrication pouvant parfois être préchauffée. Une fois la couche fondue, la plateforme descend de la hauteur d'une couche et l'opération est alors répétée jusqu'à l'obtention de la pièce finale (Figure 1-14). Ce processus se déroule sous atmosphère pressurisée et inerte (souvent de l'argon avec une teneur résiduelle typique en oxygène autour de 800 ppmv) afin de limiter les risques d'oxydation. Il s'agit d'un procédé complexe, dont plus d'une centaine de paramètres peuvent influer de façon directe ou indirecte sur la qualité des pièces. Ces paramètres peuvent

être regroupés par catégorie, selon qu'ils soient liés au laser, à la stratégie de balayage laser, à la poudre ou à l'enceinte. Généralement, seuls quelques-uns d'entre eux sont étudiés pour maîtriser le procédé et optimiser les propriétés des pièces fabriquées, et ce, de manière plus ou moins indépendante. De fait, de nombreuses études sont menées afin de comprendre et maîtriser l'influence des paramètres de fabrication sur la qualité (l'amélioration de la densité et également des propriétés mécaniques) des pièces produites afin de trouver des techniques visant à optimiser l'implémentation de nouveaux alliages (Bartolomeu, Gasik, Silva, & Miranda, 2022; Enneti, Trasorras, & Kestler, 2020; Funch & Proust, 2024; Illarionov et al., 2023; Jamhari et al., 2023; Ma et al., 2025; Talignani et al., 2022).

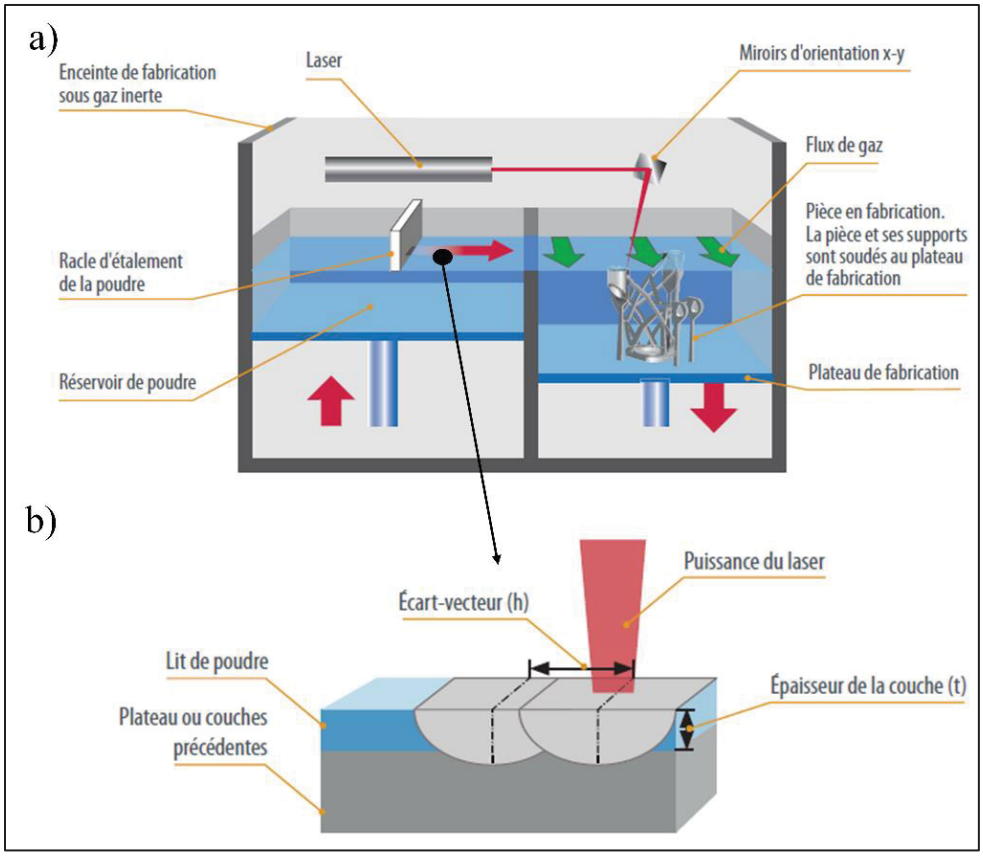

Figure 1-14 : Schéma représentant a) la chambre d'impression et b) le lit de poudre avec la nomenclature et les différents paramètres
Adapté de Centre technique des industries mécaniques (2019, p. 16, 20)

1.4.2 Difficultés d'impression des matériaux d'étude

S'agissant d'un procédé complexe et encore relativement récent, peu de métaux sont disponibles auprès des commerçants de machine de fusion laser sur lit de poudres. À titre d'exemple, la compagnie EOS Gmbh (Hambourg, Allemagne), un des leaders mondiaux du secteur, ne propose dans son catalogue de matériaux qu'une dizaine d'aciers et d'alliages de nickel, une poignée d'alliages d'aluminium et de cuivre, deux alliages de titane et un seul alliage de cobalt chrome. Aussi, bien que proposés au catalogue, ils ne sont pas disponibles pour toutes leurs imprimantes. Ce maigre éventail de matériaux disponibles s'explique par la complexité à implémenter de nouveaux alliages, en raison notamment de défauts typiques générés par ce procédé.

Le premier défi est d'obtenir des pièces denses. Or, un des défauts caractéristiques de ce procédé est la porosité (Figure 1-15), ces vides créés à l'intérieur de la matière variant généralement entre 5 à 500 µm et pouvant adopter des formes aussi bien sphériques qu'aciculaires. Ils résultent principalement d'un manque de fusion ou, au contraire, d'une instabilité dans le bain de fusion (effet « *keyhole* »). La porosité peut également être liée au phénomène de « *balling* », qui se traduit par la formation de boules de matières solides ayant un diamètre supérieur à l'épaisseur d'une couche, créant des irrégularités sur la couche suivante propices à la formation de pores.

Un autre défaut typique de ce procédé est la propension à la fissuration. En effet, les contraintes thermiques élevées causées par les gradients thermiques (pouvant atteindre les 3000°C/mm) et les vitesses de refroidissement (pouvant atteindre les 10^6 °C/s) caractéristiques de ce procédé mènent à la formation de fissures, à la fois longitudinales et transversales, pouvant aller de 30 à 100 µm (Figure 1-15) (Bartolomeu et al., 2022; Funch & Proust, 2024; Hooper, 2018; Illarionov et al., 2023; D.-Z. Wang et al., 2019).

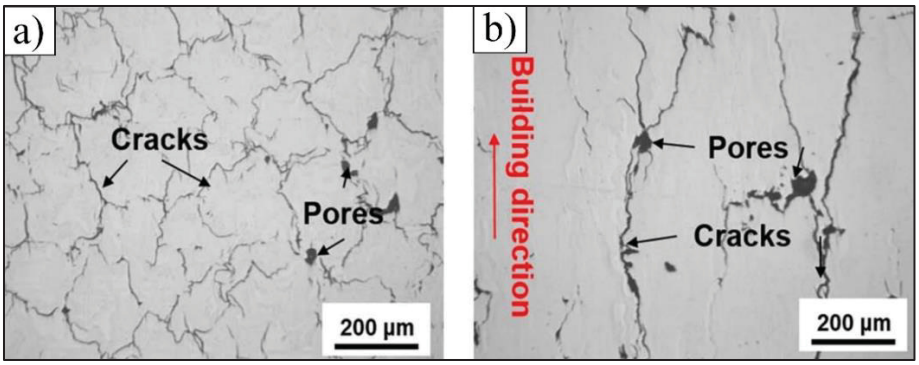

Figure 1-15 : Porosités et microfissures dans un échantillon
de tungstène pur fabriqué par LPBF
Tiré de D. Gu et al. (2020)

En plus des contraintes internes, les gradients thermiques ont un effet sur les microstructures obtenues. En effet, la morphologie de la microstructure peut varier d'équiaxe à colonnaire suivant la direction de fabrication (Figure 1-16). Les réfractaires ne pouvant former qu'une phase, la microstructure obtenue est stable, ce qui n'est en revanche pas le cas pour les alliages de titane. Pour ces derniers, la phase obtenue est souvent une phase métastable dite martensitique et composée de fines aiguilles (d'une centaine de nanomètres à quelques dizaines de micromètres) à l'intérieur des grains, qui varie selon la composition.

Pour les alliages à moins de 10% d'aluminium, la martensite hexagonale α' est majoritairement rencontrée pour les alliages de type α et $\alpha + \beta$ et la martensite orthorhombique α'' subvient lorsque la proportion d'éléments d'alliage permettant de stabiliser la phase β augmente ((Bartolomeu et al., 2022), Figure 1-16c,d). Pour les intermétalliques à base d'aluminures de titane, des microstructures plus complexes sont observées. Dans les intermétalliques orthorhombiques par exemple, il est possible de rencontrer simultanément les phases ordonnées O, α_2 et B2 et la phase désordonnée β (Illarionov et al., 2023; Liao, Fan, Luo, & Du, 2025).

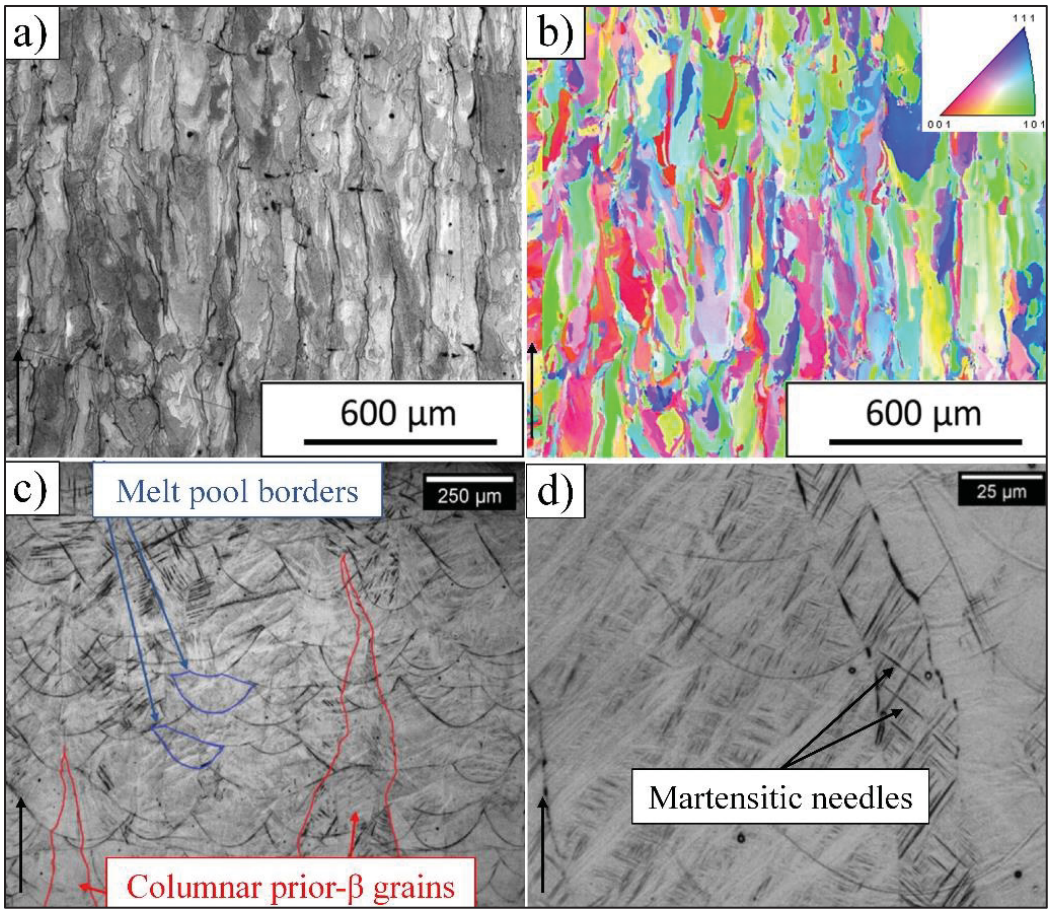

Figure 1-16 : a) Observations au microscope électronique à balayage (MEB)
et b) cartographie par diffraction d'électrons rétrodiffusés (EBSD)
d'un échantillon de tungstène pur mettant en avant une microstructure
colonnaire orientée selon la direction de fabrication;
c) et d) observations optiques d'un échantillon de Ti-6Al-2Sn-4Zr-6Mo
tel que fabriqué mettant en avant une microstructure colonnaire et martensitique;
La flèche noire représente la direction de fabrication
Tiré de (a, b) Braun et al. (2019) et
(c, d) Alessandro Carrozza, Aversa, Fino, & Lombardi (2021)

Aussi, au sujet des alliages de titane et des intermétalliques à base d'aluminures de titane toujours, la composition peut varier en fonction des paramètres en raison des différences de température de fusion des différents éléments d'alliage. Les auteurs rapportent à ce sujet une évaporation de l'aluminium lorsque l'énergie volumique fournie par le laser est trop élevée et la formation de précipités due à une absence de fusion de certains éléments, comme par exemple le niobium, lorsque l'énergie est trop faible. Ces variations de compositions peuvent

amener à des changements au niveau des digrammes de phases et de fait impacter les propriétés mécaniques et les effets des post-traitements (Illarionov et al., 2023; Liao et al., 2025).

La matière première est également un enjeu, et ce, particulièrement lorsqu'il s'agit d'alliages. En effet, des études (Brika, Letenneur, Dion, & Brailovski, 2020; Illarionov et al., 2023; Philips et al., 2020) ont mis en avant que la sphéricité et la granulométrie de la poudre ont un impact non négligeable sur les propriétés des pièces produites. Aussi, le choix d'une poudre préalliée ou d'un mélange de poudres élémentaires pour obtenir un alliage a un effet sur les propriétés mécaniques d'une part, mais également sur le coût d'acquisition et la disponibilité (seules peu de poudres préalliées sont disponibles avec des sphéricités et des granulométries adéquates pour la fabrication additive) ou bien sur le temps et la complexité d'obtention d'un mélange de poudres adapté. À titre d'exemple, pour les intermétalliques à base d'aluminures de titane de type orthorhombique, seul le Ti-22Al-25Nb a été produit sous forme de poudre préalliée jusqu'en 2018 où quelques nouvelles compositions ont fait leur entrée sur le marché (Illarionov et al., 2023).

Concernant le tungstène et le molybdène, malgré le contrôle de l'atmosphère, l'oxygène résiduel contenu dans celle-ci peut entraîner la formation d'oxydes, souvent situés aux joints de grains ou à l'intérieur des pores (Figure 1-17) et pouvant limiter les propriétés mécaniques des pièces imprimées (Braun et al., 2019).

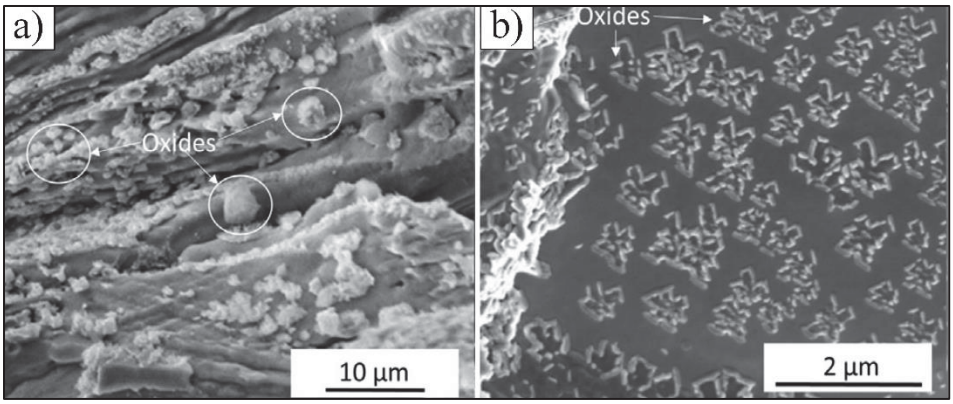

Figure 1-17 : Surface de rupture d'un échantillon de a) molybdène pur et b) tungstène pur
Tiré de Braun et al. (2019)

Pour limiter l'apparition de ces défauts, des stratégies peuvent être mises en place pendant l'impression, comme notamment le recours à des machines haute puissance (jusqu'à 1000 W (Bartolomeu et al., 2022; Polozov, Sufiiarov, Kantyukov, & Popovich, 2019)), à des plateformes d'impression préchauffées (jusqu'à 1000 °C (Braun et al., 2019; Illarionov et al., 2023; Müller et al., 2019; Xiuxuan Yang, Zhang, Bai, & Xie, 2021)) ou encore à des stratégies de lasage double exposition (Alinejadian, Wang, Kollo, & Prashanth, 2023). Si en recourant à ses stratégies, un grand nombre d'auteurs sont parvenus à obtenir des pièces saines et denses (densité > 99.9%) sur une large variété d'alliages de titane (Bartolomeu et al., 2022; Illarionov et al., 2023), les métaux réfractaires imposent plus de difficultés, si bien qu'aucune pièce n'a été produite en tungstène ou en molybdène purs avec une densité supérieure à 99% et dépourvue de fissures. La stratégie souvent alors retenue pour ces métaux est d'envisager des éléments d'alliages pour améliorer leur ductilité et limiter leur propension à la fissuration (Funch & Proust, 2024).

L'intégration de nouveaux métaux par le procédé LPBF est une démarche complexe et souvent fastidieuse, qui nécessite de comprendre puis de contrôler les paramètres du procédé afin de limiter l'apparition de défauts caractéristiques tels que la porosité ou les microfissures et d'obtenir les microstructures désirées. Comme discutées dans la section suivante, différentes approches peuvent être envisagées pour simplifier cette démarche.

1.4.3 Méthode d'implémentation de nouveaux matériaux pour le procédé LPBF

La première étape à l'implémentation de nouveaux alliages dans le procédé LPBF est la fusion complète de la poudre afin de former une pièce finale la plus saine possible, c'est-à-dire dans un premier temps la plus dense et sans défauts. Plusieurs recherches ont mis en avant les effets de la puissance (P, en W) et de la vitesse (v, en mm/s) du laser sur la qualité de la fusion, déterminant ainsi les plages opérationnelles d'impression. S'apercevant que les effets de ces deux paramètres devaient être considérés de manière couplée, une métrique de densité d'énergie (LED pour *Linear Energy Density* en J/mm, (1.4)) fournie au lit de poudre a émergée par analogie au procédé de soudure (Hanzl, Zetek, Bakša, & Kroupa, 2015). Aussi, en intégrant les effets de l'épaisseur de couche (t, en mm) et de l'écart vecteur (h, en mm appelé plus communément *hatching space*), cette métrique est devenue volumique (VED pour *Volumetric Energy Density*, en J/mm^3, (1.5)). Il a ainsi été supposé que la qualité de la consolidation du matériau dépende des dimensions des bains de fusion et de leur capacité à correctement se superposer lors de la fabrication (Gong, Rafi, Starr, & Stucker, 2013).

$$LED = \frac{P}{v} \tag{1.4}$$

$$VED = \frac{P}{vht} \tag{1.5}$$

La densité des pièces n'est cependant pas l'unique critère témoignant de la bonne qualité d'une pièce imprimée. En effet, les propriétés mécaniques, le fini de surface et les distorsions sont également à considérer. Les propriétés mécaniques sont déterminées d'une part par la microstructure, et d'autre part, par les éventuelles contraintes résiduelles. À ce sujet, les gradients thermiques et les vitesses de refroidissement sont principalement influents et se manifestent à travers les choix de vitesse et de stratégie de balayage laser, le préchauffage éventuel de la plateforme ou encore l'orientation de la pièce dans le plateau de fabrication (D. Gu et al., 2020; Letenneur, Kreitcberg, & Brailovski, 2019; D.-Z. Wang et al., 2019).

Pour faciliter la maîtrise des effets du procédé sur la qualité des pièces produites, trois types d'approches sont principalement rencontrées : les approches expérimentales, numériques ou bien analytiques.

1.4.3.1 Approches expérimentales

Les approches expérimentales consistent en l'observation d'un phénomène ou la validation d'une hypothèse à travers une succession de tests contrôlés et répétés. Ces approches sont particulièrement employées pour optimiser le procédé LPBF puisqu'il s'agit d'un procédé relativement récent et encore peu maîtrisé. À titre d'exemple (D.-Z. Wang et al., 2019) utilisent les approches expérimentales pour discuter des effets de la morphologie de la poudre sur les caractéristiques de pièces fabriquées en tungstène pur, en fixant tous les autres paramètres du procédé. (D. Gu et al., 2020), quant à eux décrivent les effets de différentes stratégies de balayage sur ce même matériau.

Cependant, il est possible que les effets de certains paramètres soient couplés, notamment au travers de la densité d'énergie. À ce sujet, certains auteurs (M. Guo et al., 2019; Kaserer et al., 2019; Tan et al., 2018; Xiong et al., 2020) étudient les effets de la densité d'énergie fournie par le laser en faisant varier successivement la vitesse et la puissance, tout en maintenant l'épaisseur de couche et l'écart vecteur fixes, tandis que d'autres (J. Chen et al., 2020; Enneti et al., 2020; Faidel, Jonas, Natour, & Behr, 2015; Rebesan, Ballan, et al., 2021; Sidambe, Tian, Prangnell, & Fox, 2019) s'attachent à faire varier la vitesse de balayage et l'écart vecteur en maintenant la puissance et l'épaisseur de couche fixes. Ainsi, pour décrire l'effet d'une seule métrique, ici la densité d'énergie, différentes approches peuvent être envisagées.

L'avantage des méthodes expérimentales est qu'elles fournissent la base pour comprendre les phénomènes du procédé tout en étant relativement simples à mettre en œuvre et peuvent être fondées sur des analyses post mortem ou in situ, (à condition que l'équipement approprié soit mis en place). Aussi, elles ne requièrent aucune information préalable sur le matériau et sont donc particulièrement compatibles avec de nouveaux alliages créés à partir de mélange de

poudres ou dont les propriétés physiques ne sont pas encore connues. Cependant, les modèles expérimentaux demeurent conséquents, ce qui rend la caractérisation coûteuse en temps, en matière première et en personnel qualifié. De plus, pour le procédé LPBF, les résultats sont difficiles à transférer d'un équipement à un autre et d'un matériau d'entrée à un autre, tant il y a beaucoup de paramètres influents. Les paramètres optimaux sont donc différents à chaque fois, ce qui nécessite de reproduire les expériences pour tout nouvel équipement ou matière première. En outre, les analyses post mortem n'offrent pas la possibilité de comprendre en temps réel les effets des paramètres, mais seulement d'en observer les conséquences, tandis que les analyses in situ sont souvent limitées à une seule couche d'observation et peuvent parfois nécessiter la création de bancs d'essai personnalisés, encore une fois très coûteux en termes de ressources humaines et matérielles.

1.4.3.2 Approches numériques

Un modèle numérique représente la résolution par ordinateur d'un système d'équations dans le but de formuler une réponse approchée à un problème physique. Plusieurs phénomènes physiques peuvent être décrits à différentes échelles par ce type d'approches, dépendamment des hypothèses formulées (H. Chen et al., 2022; Chowdhury et al., 2022; Letenneur et al., 2019; Todo, Ishimoto, Gokcekaya, Oh, & Nakano, 2022; Vrancken, Ganeriwala, & Matthews, 2022).

Dans le cadre de l'optimisation des paramètres de fabrication du procédé de fusion laser sur lit de poudre métallique, ces approches peuvent être utilisées pour simuler différents aspects du procédé, comme l'étalement de la poudre par le racleur (H. Chen et al., 2022) ou, plus généralement, l'interaction entre le laser et le lit de poudre (H. Chen et al., 2022; Fernandez-Zelaia et al., 2022; Todo et al., 2022; Vrancken et al., 2022). Il existe principalement deux méthodes de résolution numérique : la méthode aux éléments finis et la méthode aux éléments discrets. L'une ou l'autre de ces méthodes sera privilégiée par un auteur en fonction de ses hypothèses de travail.

Comparativement aux approches expérimentales, les approches numériques permettent de réduire considérablement les coûts liés aux plans d'expérience à répétition. Les effets du procédé peuvent être caractérisés sans l'ajout de capteurs ou la modification de l'enceinte de fabrication, voire même sans avoir recours à aucune ressource matérielle. De ce fait, un plus large éventail de paramètres peut être étudié, et ce, sur divers équipements et matériaux. Ces simulations permettent notamment de formuler des prédictions sur le comportement du procédé et, une fois le modèle calibré, d'optimiser le procédé de fabrication de nouveaux alliages.

En revanche, ces modèles numériques sont extrêmement dépendants des hypothèses formulées par les auteurs et ne peuvent s'affranchir d'une connaissance de certaines propriétés physiques du matériau et d'une vérification expérimentale. Aussi, la précision du modèle est étroitement liée au temps de calcul : plus le modèle se voudra proche du procédé, plus nombreux et complexes seront les phénomènes à considérer et, ce faisant, plus longs seront les temps de calcul. Aussi, des problèmes de convergence peuvent être rencontrés, de même que des problèmes de calibration du modèle si trop de phénomènes sont considérés.

1.4.3.3 Approches analytiques

Contrairement aux approches numériques, les approches analytiques consistent en la résolution exacte d'une équation mathématique connue. Cette équation mathématique traduit le ou les phénomènes observés et peut être plus ou moins complexe, mais possèdera toujours une seule et unique solution (Khaimovich, Balyakin, Oleynik, Meshkov, & Smelov, 2022; Letenneur et al., 2019; Promoppatum, Yao, Pistorius, & Rollett, 2017; Y. Wang, Ji, & Liang, 2023). Dans la plupart des études (Bajaj, Wright, Todd, & Jägle, 2019; Letenneur et al., 2019; Wolfer et al., 2019), cette approche est utilisée pour décrire l'effet des paramètres de fabrication sur la fusion en elle-même, et se focalise donc principalement sur l'interaction entre le laser et la matière.

Comme les approches numériques, les approches analytiques ont l'avantage d'être moins coûteuses en ressources que les approches expérimentales, puisqu'elles aussi ne demandent

des expériences qu'à des fins de validation. Elles sont également sujettes à l'interprétation des phénomènes physiques et leurs résultats dépendent fortement des hypothèses et des phénomènes considérés. Elles peuvent donc, tout comme les approches numériques, se montrer moins représentatives que les approches expérimentales du procédé réel.

En comparaison avec les approches numériques, les approches analytiques sont beaucoup plus simples à mettre en place, rapides dans les temps de calcul et ne posent pas de problème de convergence. En revanche, elles sont plus limitées en termes de considérations physiques, car lorsque la complexité de l'équation augmente, elle perd de sa linéarité et ne peut alors plus être résolue analytiquement.

1.4.4 Propriétés des pièces imprimées et effets des post-traitements

Peu importe l'approche envisagée pour l'implémentation de nouveaux alliages, et même une fois les paramètres optimisés au mieux, des défauts et des microstructures anisotropes ou instables peuvent subsister dans les pièces. Mais en dépit de cela, les propriétés des pièces telles que fabriquées sont comparables, voire compétitives, devant celles de pièces issues de procédés de mise en forme conventionnels et peuvent être modifiées par le biais de post-traitements.

1.4.4.1 Propriétés mécaniques à température ambiante

Au sujet des métaux réfractaires, des études ont su démontrer le potentiel du procédé LPBF pour la production de pièces en tungstène pur. À titre d'exemple (Tan et al., 2018) sont parvenus à obtenir une contrainte ultime en compression (UCS pour *Ultimate Compression Strength*) de 1015 MPa pour des pièces d'une densité de 98,5 % et (Wen et al., 2019) de 1523 MPa pour une densité de pièce de 98,71%. Sans aucun post-traitement, ces derniers sont parvenus à surpasser la barre des 1200 MPa fixée par les procédés conventionnels de métallurgie des poudres (J. R. Davis & ASM International, 1998; Tan et al., 2018) et ce, en dépit de la présence de fissures (Figure 1-18). En revanche, s'ils sont parvenus à atteindre une contrainte ultime en compression de 1030 MPa pour une densité de 98,5%, les auteurs (X.-Q.

Zhang, Liu, Zhu, & Wu, 2025) ont mis en avant la nécessité de recourir à des post-traitements pour refermer les fissures en n'atteignant que 290 MPa de contrainte ultime en tension avec les mêmes paramètres de fabrication optimisés.

Le molybdène est quant à lui bien moins étudié que son compère et les résultats sont encore loin d'égaler ceux des procédés conventionnels. Seuls (Oehlerking, Stawovy, Ohm, & Imandoust, 2022) ont essayé des tests en compression sur des pièces imprimées à 98.5% de densité et ont obtenu une UCS d'environ 375 MPa. De leur part, (Rebesan, Ballan, et al., 2021) sont parvenus à atteindre une contrainte ultime en tension (UTS pour *Ultimate Tension Strength*) de 350 MPa pour des pièces à 99,5% denses (Figure 1-18), contre un UTS = 470 MPa pour la métallurgie des poudres ou encore UTS = 620 MPa selon la norme B387-18 (B10 Committee, 2018).

Les alliages de titane et les aluminures à base de titane sont une famille plus vaste et plus étudiée que les métaux réfractaires. Au sujet des alliages de titane de type $\alpha + \beta$, le plus communément étudié est le Ti-6Al-4V pour lequel les études révèlent que les pièces telles que fabriquées possèdent une contrainte à rupture élevée en comparaison avec celles obtenues par des procédés conventionnels ($\sigma_{LPBF} \geq$ 1000 MPa contre $\sigma_{conv} \leq$ 900 MPa) mais peu ou pas de ductilité (≤ 10%) (Bartolomeu et al., 2022; Jamhari et al., 2023; Ni et al., 2025). Cela s'explique par la présence de la phase martensitique et impose le recours à des post-traitements pour atteindre les requis pour les implants chirurgicaux ou les pièces aéronautiques par exemple (ASTM F136–13, ASTM F1108–14, AMS4930, AMS6932). Des observations similaires ont été faites sur d'autres alliages de titane de type α+β comme, notamment, le Ti-6Al-2Sn-4Zr-6Mo (Alessandro Carrozza et al., 2021; Pirro, Martucci, Morri, Lombardi, & Ceschini, 2025) ou le Ti-6Al-17Nb (Chlebus, Kuźnicka, Dziedzic, & Kurzynowski, 2015; C. Xu et al., 2020) (Figure 1-18).

En ce qui concerne les intermétalliques à base d'aluminures de titane de type orthorhombique, les propriétés obtenues sur des échantillons tels que fabriqués en Ti-22Al-25Nb s'étendent d'une contrainte ultime en traction de 286 MPa et 0% d'élongation (Polozov, Starikov,

Popovich, & Sufiiarov, 2021) à 1140 MPa pour 24% d'élongation (Zhou et al., 2021) (Figure 1-18). Cette variation assez significative dans les propriétés mesurées s'explique par des différences majeures dans les microstructures obtenues (phases en présence, taille et formes de grains, présence de précipités, etc.) et requiert là encore l'application de post-traitements (Illarionov et al., 2023; Liao et al., 2025).

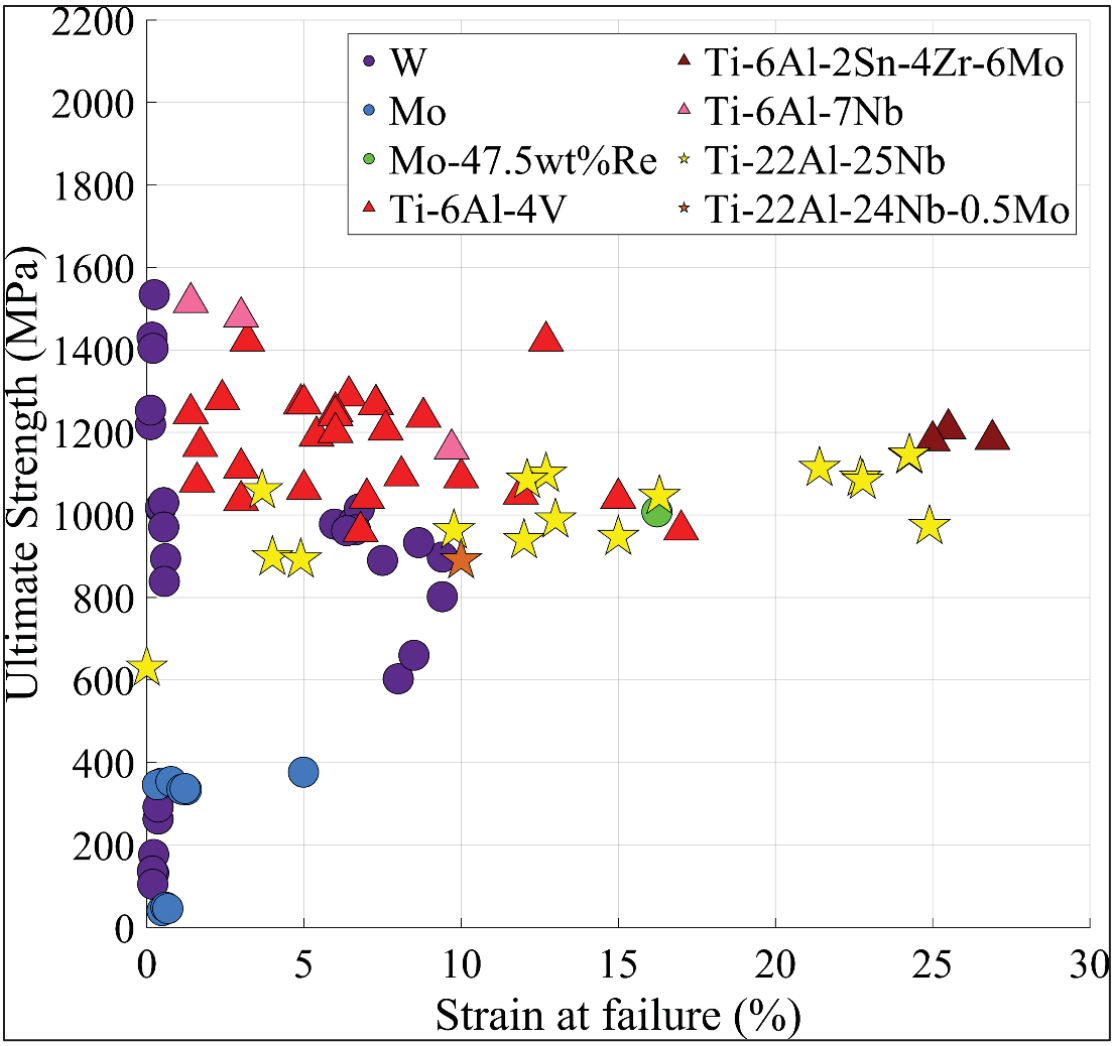

Figure 1-18 : Contrainte ultime en fonction de la déformation obtenue pour différents matériaux bruts produits par LPBF; Les cercles représentent les métaux réfractaires, les triangles les alliages de titane de type $\alpha + \beta$ et les étoiles les intermétalliques à base d'aluminures de titane de type orthorhombique
Données extraites de diverses sources Bartolomeu et al. (2022); Alessandro Carrozza et al. (2021); Alessandro Carrozza, Aversa, Fino, & Lombardi (2022); Q. Chen, Xu, Zhao, Hao, & Han (2023); Chlebus et al. (2015); M. Guo et al. (2019); Illarionov et al. (2023); Jamhari et al., (2023); Y. Liu, Shan, Yang, Jiao, & Huang (2023); Oehlerking et al. (2022); Polozov et al. (2021); Rebesan, Ballan, et al. (2021); Shi et al. (2023); Tan et al. (2018); Vrancken et al. (2022); Wen et al. (2019); C. Xu et al. (2020); X.-Q. Zhang et al. (2025); Zhou et al. (2021)

1.4.4.2 Propriétés mécaniques à haute température

Néanmoins, compte tenu des difficultés d'impression du tungstène et du molybdène pur et de l'instabilité des phases formées lors de l'impression des alliages de titane et des intermétalliques à base d'aluminures de titane, seuls peu d'auteurs caractérisent leurs propriétés mécaniques à haute température, ce qui constitue un paradoxe avec le choix même de ces métaux. Parmi elles, une seule étude a été réalisée sur des pièces imprimées en molybdène pur (Rebesan, Ballan, et al., 2021). Avec une densité supérieure à 99% et malgré la présence de microfissures, les auteurs sont parvenus à obtenir une contrainte ultime en tension de 250 MPa à 600 °C, ce qui égale quasiment les 260 MPa obtenus via métallurgie des poudres à cette même température (Carreker & Guard, 1956; J. R. Davis & ASM International, 1998). Pour le tungstène en revanche, aucune étude n'a été menée à ce jour à la connaissance de l'auteur.

Du côté des alliages de titane de type α+β, même le très répandu Ti-6Al-4V n'est que peu étudié à haute température et seuls (Y. He, Ma, Zhang, & Wang, 2022) ont réalisé des tests de traction à des températures de 350 à 550 °C. Ils sont parvenus à atteindre des contraintes ultimes de 927 et 573 MPa à 350 et 550 °C, respectivement, sans aucun traitement thermique, mais ne font pas mention de la ductilité (qui ne semblent pas excéder 0.8% au regard des courbes qu'ils fournissent).

Enfin, du côté des intermétalliques à base d'aluminures de titane de type orthorhombique, un peu plus d'études sont rencontrées sur des essais mécaniques à 650 °C (Xiuxuan Yang et al., 2021; K. Zhang, Lei, Chen, Yang, & Bao, 2019; K. Zhang, Lei, Ni, Zhou, & Chen, 2021; Y. Z. Zhang, Liu, Zhao, & Tang, 2016; Zhou et al., 2021). Ces études mettent en avant les contraintes ultimes variant entre 400 et 750 MPa (élongations entre 0 et 10%) pour des pièces en Ti-22Al-25Nb et ≤820 MPa (élongation 3%), pour des pièces en Ti–22Al–24Nb-0.5Mo.

1.4.4.3 Effets des post-traitements

Enfin, pour réduire la présence des différents défauts, pour relâcher les contraintes internes et pour contrôler la microstructure (et donc de fait les propriétés mécaniques), des post-traitements sont souvent considérés. En ce qui concerne les métaux réfractaires, très peu d'investigation sont menées à ce sujet et seuls quelques auteurs (J. Chen et al., 2020; Mao et al., 2025; Shi et al., 2023; Singh et al., 2020) ont déjà envisagé des traitements thermiques ou thermomécaniques tels que la compression isostatique à chaud (HIP pour *Hot Isostatic Pressing*) sur des pièces de tungstène pur fabriquées par LPBF. Ces auteurs sont parvenus à augmenter la densité finale des pièces, leur conductivité thermique et modifier leurs propriétés mécaniques sans pour autant parvenir à éliminer complètement les microfissures initialement présentes. En revanche, aucune étude sur les effets des post-traitements sur des pièces en molybdène pur fabriquées par LPBF n'est à ce jour proposée dans la littérature, à la connaissance de l'auteur.

Pour les alliages de titane et les intermétalliques à base d'aluminures de titane, les effets des post-traitements sont beaucoup plus abordés dans la littérature et ont pour objectif d'apporter des changements significatifs sur les microstructures, notamment la décomposition des phases instables au profit de phases stables (martensite α' et α'' en la phase stable $\alpha + \beta$ pour les alliages de type $\alpha + \beta$ par exemple). Cependant, les paramètres de ces post-traitements sont nombreux (température, durée du palier, vitesses de montée et de descente, type de refroidissement, etc.) et leurs effets sont difficiles à anticiper, ce qui requiert donc des études spécifiquement dédiées (Bartolomeu et al., 2022; Illarionov et al., 2023; Jamhari et al., 2023; Liao et al., 2025; Man, Huang, He, Yang, & Lin, 2024; Ni et al., 2025). Étant donné que leurs effets dépendent également de la microstructure de départ et que celle-ci est très variable, il n'existe pas encore de consensus dans la communauté scientifique au sujet de post-traitements recommandés et les recherches à ce sujet doivent encore être approfondies.

1.5 Résumé et définition des objectifs du projet

Afin d'améliorer les performances des microturbines, et particulièrement de la Turbine ICT, une solution est de se tourner vers des matériaux plus performants pour remplacer les alliages de certaines pièces, notamment dans les chambres à haute et très haute température. Dans la chambre d'injection, les métaux réfractaires, notamment le tungstène et le molybdène semblent être des candidats prometteurs pour remplacer l'actuel alliage de nickel de l'injecteur, tandis que de nouvelles générations d'alliages de titane et les intermétalliques à base d'aluminures de titane se distinguent pour remplacer l'actuel alliage de l'anneau de refroidissement situé dans l'assemblage du rotor, ainsi que le moyeu de celui-ci. Cependant, ces changements de matériaux doivent être réalisés sans compromettre la géométrie des pièces, qui, en l'occurrence, nécessite le recours à des procédés de fabrication additive compte tenu de leur complexité. Parmi les procédés de fabrication additive disponibles pour les métaux, la fusion laser sur lit de poudre est actuellement employée, car elle permet d'obtenir une excellente précision à des coûts compétitifs. En revanche, l'implémentation de nouveaux métaux et alliages pour ce procédé n'est pas chose aisée compte tenu des différents phénomènes multiphysiques mis en jeu et du nombre de paramètres pouvant les influencer.

Ce survol de la littérature a notamment permis de mettre en avant les difficultés d'impression du tungstène, du molybdène, des alliages de titane et des intermétalliques à base d'aluminures de titane, ainsi que le manque d'études sur des propriétés mécaniques à haute température de ces métaux imprimés par fusion laser sur lit de poudre. La présente étude vise à partiellement combler ce manque au travers d'une démarche complète d'implémentation de nouveaux métaux et alliages, du contrôle de la matière première jusqu'à l'obtention de pièces à géométries complexes. Pour ce faire, différents objectifs spécifiques ont été définis, à savoir :

- Caractériser les poudres métalliques et définir les propriétés optimales de celles-ci d'un point de vue de leur utilisation dans le procédé de fusion laser sur lit de poudre;
- Développer une démarche d'implémentation et de caractérisation des effets de certains paramètres du procédé basée sur d'abord, l'étude numérique et expérimentale des bains

de fusion générés, puis sur l'analyse des propriétés physiques et mécaniques d'échantillons de test;

- Optimiser les paramètres du procédé pour maximiser la densité et les propriétés mécaniques de pièces imprimées et de minimiser l'occurrence de défauts de fabrication (pores et fissures) dans celles-ci;
- Optimiser les conditions de post-traitements (traitement thermique et pression isostatique à chaud) pour améliorer la microstructure et les propriétés mécaniques de pièces imprimées;
- Concevoir, fabriquer et valider différents artefacts à géométrie complexe en vue de la production des pièces fonctionnelles adaptées à des utilisations spécifiques.

Les travaux effectués dans le cadre de cette thèse sont séparés en deux parties, la première se concentrant sur les métaux réfractaires pour le remplacement de l'injecteur, et la deuxième tournée vers l'assemblage du rotor, pour l'amélioration de l'anneau de refroidissement et du moyeu à l'aide d'un alliage de titane nouvelle génération et d'un intermétallique à base d'aluminures de titane. Il s'agit pour chaque famille de métaux de considérer un choix très prometteur en termes de performances, mais plus risqué d'un point de vue de l'implémentation (le tungstène pur pour les réfractaires et l'intermétallique à base d'aluminures de titane de type orthorhombique Ti-22Al-25Nb) et un choix plus sûr, mais moins performant (le molybdène pur d'une part et l'alliage de titane de type $\alpha + \beta$ Ti-6Al-2Sn-4Zr-6Mo d'autre part).

D'abord, le chapitre 2 traite du développement et de la validation expérimentale d'un modèle numérique permettant de faciliter l'implémentation de nouveaux alliages pour le procédé LPBF par le biais d'expériences menées sur du tungstène pur. En se basant sur la même méthodologie, le chapitre 3 se concentre sur les propriétés physiques et mécaniques jusqu'à haute température d'échantillons en molybdène pur, puis sur les limites d'imprimabilité de ce matériau au travers de différentes géométries spécifiques. Le chapitre 4 discute de l'élaboration d'une poudre d'alliage molybdène-rhénium pour le procédé LPBF et des effets de l'ajout de cet élément sur les propriétés physiques et mécaniques jusqu'à haute température, et aborde

l'imprimabilité de cet alliage au travers d'une nouvelle géométrie complexe spécialement conçue.

Ensuite, la section sur l'implémentation d'un nouvel alliage de titane débute au chapitre 5, avec le développement d'une méthode expérimentale pour l'intégration du Ti-6Al-2Sn-4Zr-6Mo, un alliage de titane nouvelle génération de type $\alpha + \beta$, par le procédé LPBF sur une machine à puissance limitée sans contrôle de la température dans la chambre d'impression, et des effets des paramètres du procédé sur les propriétés physiques et mécaniques de spécimens imprimés. Une fois les paramètres d'impression définis, des travaux permettant d'améliorer la précision géométrique de pièces imprimées par le biais de la réduction de l'épaisseur de couche d'impression sont présentés au chapitre 7. Aussi, cet alliage de titane ne pouvant pas être utilisé tel qu'imprimé, des études sur différents post-traitements ont été réalisées afin de contrôler la microstructure et d'améliorer les propriétés mécaniques jusqu'à haute température et sont détaillées dans ce même chapitre.

En reprenant les grandes étapes ayant permis l'intégration du Ti-6Al-2Sn-4Zr-6Mo, le chapitre 8 aborde les premiers résultats obtenus sur le développement par LPBF du Ti-22Al-25Nb, un intermétallique à base d'aluminures de titane retenu pour remplacer les superalliages à base de nickel pour le moyeu du rotor et des défis à relever avant de pouvoir envisager la production de pièces complexes.

Enfin, le chapitre 9 aborde les notions d'application et de transfert de connaissances, en s'intéressant d'abord à la fabrication et aux tests préliminaires sur un injecteur micro-mélangé à échelle réduite en molybdène pur, puis aux défis que représente la reproductibilité des résultats sur l'alliage de Ti-6Al-2Sn-4Zr-6Mo lors du passage à une machine de même gabarit, mais à l'architecture différente. Les essais de post-traitement sur l'intermétallique Ti-22Al-25Al et les tentatives de changement de géométrie closent ce chapitre. Les articles de conférences associés sont présentés en annexes I, II et III.

L'organigramme Figure 1-19 résume le plan du document.

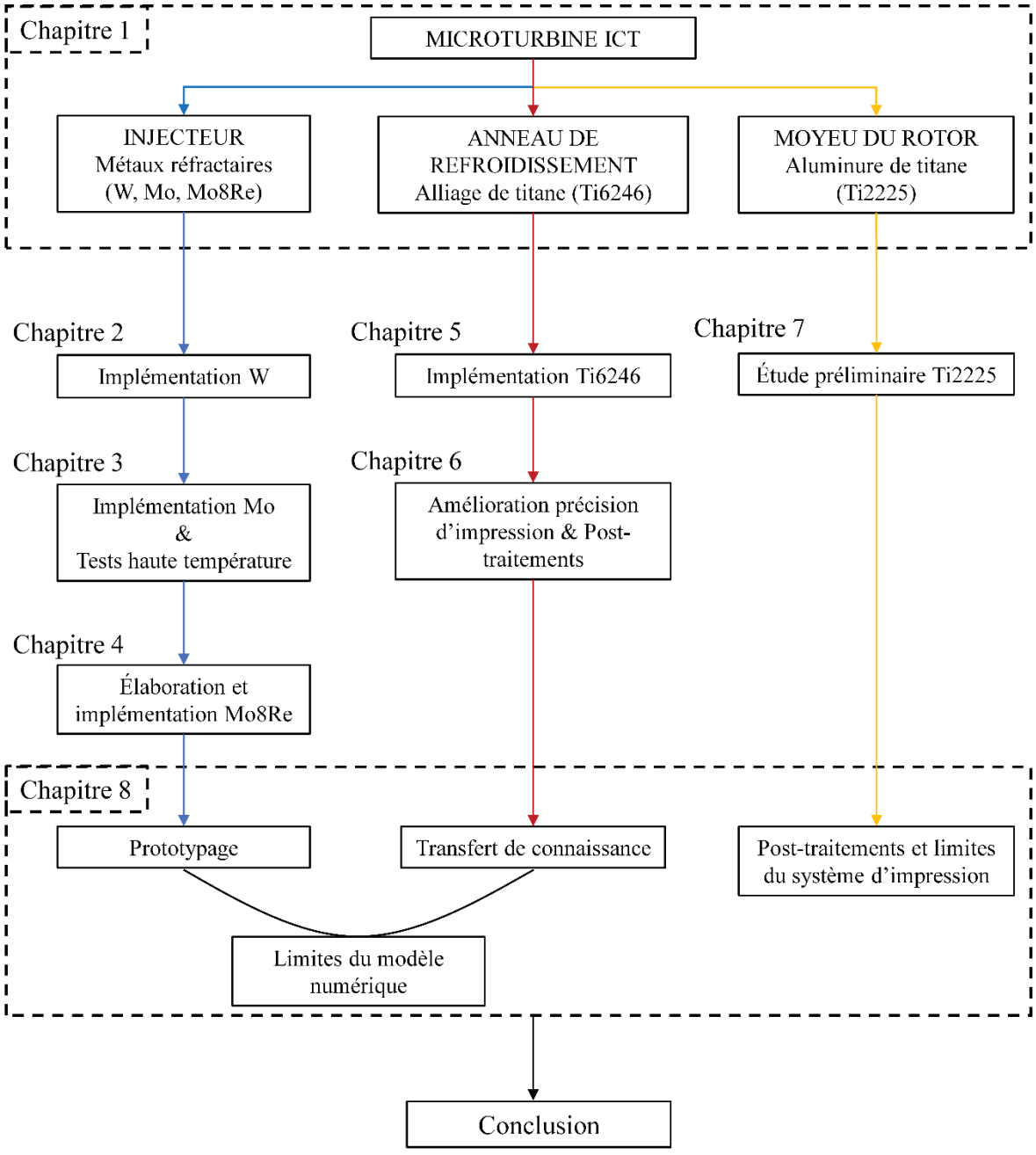

Figure 1-19 : Organigramme résumant la structure du document

Les retombées de ce projet sont d'abord l'accès à un nouveau procédé de fabrication additive pour les métaux réfractaires et les alliages de titane et intermétalliques à base d'aluminures de titane, permettant d'élargir l'éventail de géométries et applications disponibles pour ceux-ci au

travers d'un procédé de fabrication possédant de réels avantages économiques et écologiques comparativement à des procédés de fabrication conventionnels.

Ensuite, le recours à un modèle numérique a pour objectif de réduire les coûts associés à l'implémentation des métaux réfractaires par le procédé de fusion laser sur lit de poudre. Pour les alliages de titane et intermétalliques à base d'aluminures de titane pour lesquels cette approche numérique n'est pas adaptée, une alternative expérimentale rationalisée permet de mettre en avant des effets complexes sur les propriétés physiques des pièces en un nombre restreint d'analyses, permettant ainsi le développement d'une méthode sûre et à coûts réduits. Enfin, l'optimisation des paramètres du procédé sur une machine d'impression à faible puissance et sans contrôle de température dans la chambre permet d'augmenter l'accessibilité des métaux étudiés. Par ailleurs, les études sur les effets de différents post-traitements pour chaque famille de métaux et alliage permettent d'augmenter la compréhension des mécanismes mis en jeu et de proposer des pistes de solutions pour l'amélioration des propriétés physiques et mécaniques en fonction de l'application visée.

L'intérêt de ces différents métaux et alliages est démontré au travers d'une application spécifique.

CHAPITRE 2

IMPROVING LASER POWDER BED FUSION PRINTABILITY OF TUNGSTEN POWDERS USING SIMULATION DRIVEN PROCESS OPTIMIZATION ALGORITHMS

Aurore Leclercq[a], Vladimir Brailovski[b]

[a,b]Département de Génie mécanique, École de Technologie Supérieure,
1100 Notre-Dame Ouest, Montréal, Québec, Canada H3C 1K3

Article publié dans « Materials », avril 2024

2.1 Avant-propos

Afin d'améliorer les performances de la turbine ICT au travers d'un changement de matériau pour l'injecteur, le tungstène a d'abord été envisagé compte tenu de sa température de fusion la plus élevée de tous les métaux. Dans cette première publication, une méthodologie basée sur une modélisation numérique simplifiée des champs thermiques lors de l'interaction entre le laser et la matière et la validation expérimentale, a été employée pour introduire ce matériau par le procédé de fusion laser sur lit de poudre. Des analyses physiques et des essais mécaniques ont ensuite été réalisés afin de déterminer un jeu de paramètres optimisés, menant à l'obtention d'échantillons sans fissures, aux propriétés mécaniques compétitives avec les procédés conventionnels de métallurgie des poudres et permettant la production de pièces à géométries variables. Une fois validé, le modèle numérique peut servir au développement de nouveaux jeux de paramètres pour des machines de différents calibres ou bien aider à l'implémentation de nouveaux alliages.

2.2 Résumé

Cette étude applique des techniques numériques et expérimentales pour étudier l'effet des paramètres du procédé sur la densité, la structure et les propriétés mécaniques des échantillons

de tungstène pur fabriqués par fusion laser à lit de poudre. Un modèle numérique basé sur l'analyse simplifiée d'un champ thermique généré dans le lit de poudre par une source de chaleur mobile a été utilisé pour calculer les dimensions des bains de fusion, prédire la densité des pièces imprimées et construire un plan d'expériences réduit. Les échantillons imprimés à partir d'une puissance laser de 188 W, d'une vitesse de balayage de 188 mm/s, d'un écart vecteur de 80 µm et d'une épaisseur de couche de 30 µm ont montré une densité imprimée maximale de 93,2 %, une contrainte ultime en compression de 867 MPa et une déformation maximale à défaillance de ~7,0 %; qui sont conformes aux exigences standard pour les pièces en tungstène obtenues par des techniques conventionnelles de métallurgie des poudres. En utilisant les paramètres d'impression optimisés, des artefacts géométriques sélectionnés ont été fabriqués pour caractériser les limites d'imprimabilité. Une étude numérique complémentaire a suggéré que la diminution de l'épaisseur de la couche, l'augmentation de la puissance du laser, l'application d'un post-traitement de compression isostatique à chaud et l'ajout de rhénium comme élément d'alliage sont les directions les plus prometteuses pour améliorer davantage les propriétés physiques et mécaniques des pièces en tungstène imprimées.

2.3 Abstract

This study applies numerical and experimental techniques to investigate the effect of process parameters on the density, structure and mechanical properties of pure tungsten specimens fabricated by laser powder bed fusion. A numerical model based on the simplified analysis of a thermal field generated in the powder bed by a moving laser source was used to calculate the melt pool dimensions, predict the density of printed parts and build a cost-effective plan of experiments. Specimens printed using a laser power of 188 W, a scanning speed of 188 mm/s, a hatching space of 80 µm and a layer thickness of 30 µm showed a maximum printed density of 93.2%, an ultimate compression strength of 867 MPa and a maximum strain to failure of ~7.0%, which are in keeping with the standard requirements for tungsten parts obtained using conventional powder metallurgy techniques. Using the optimized printing parameters, selected geometric artifacts were manufactured to characterize the printability limits. A complementary numerical study suggested that decreasing the layer thickness, increasing the laser power,

applying hot isostatic pressing and alloying with rhenium are the most promising directions to further improve the physical and mechanical properties of printed tungsten parts.

Keywords: laser powder bed fusion; tungsten; modeling; numerical predictions; mechanical testing; crack-free specimens; geometric analysis

2.4 Introduction

Tungsten (W) belongs to the group of refractory metals. Among its characteristics are the highest melting point of all metallic materials (3683 K), the lowest coefficient of thermal expansion of all pure metals (~4.6×10^{-6} m/(m.K)), excellent mechanical properties at elevated temperatures (tensile strength of ~620 MPa at 1000 ◦C (J. R. Davis & ASM International, 1998)) and a low evaporation propensity (Karhu, Kivikytö-Reponen, & Mroueh, 2015). These unique properties, coupled with radiation impermeability, have significantly increased interest in tungsten, especially in areas of high-temperature applications, such as space, aeronautics and energy (especially nuclear). However, forming tungsten parts by conventional deformation-based technological processes is complicated because of the high ductile–brittle transition temperature range (200–700 °C) and significant sensitivity to oxidation at elevated temperatures (>350 °C).

Due to the above-mentioned difficulties, tungsten parts are mainly shaped in simple geometric forms such as sheets, rods, wires or tubes using powder metallurgy processes such as sintering and hot isostatic pressing (J. R. Davis & ASM International, 1998; Karhu et al., 2015). To address the challenges that this metal poses in terms of producing parts with complex geometry, new solutions are offered by additive manufacturing (AM) processes, which rely on the use of numerical 3D models to manufacture parts by adding materials in successive layers. Among the AM processes suitable for tungsten parts, laser directed energy deposition (L-DED) and laser and electron beam powder bed fusion (L(EB)-PBF) are the most commonly encountered (Enneti et al., 2020; Talignani et al., 2022). These three processes are compatible with powder feedstock, which is fortunate since tungsten parts are already manufactured using

powder metallurgy, thus making high-quality tungsten powders readily available on the market.

The L-DED process consists of feeding the powdered material through a nozzle into the focus of a laser beam, thus fusing the sprayed powder particles to the substrate, whereas the L(EB)-PBF processes consist of spreading a powder layer on the previously-fused substrate, the new layer being then melted by the laser or electron beam. The L-DED process is mostly used for repairs but has demonstrated very limited success in the production of tungsten parts because of the difficulties involved in fully melting tungsten powders during the deposition. Regarding the two PBF processes, the EB-PBF process offers more powerful heat sources (5–10 kW) and greater build rates than its LPBF competitor (0.2–1 kW) with a lesser need for supports, which enables the stacking of parts during printing. Moreover, this process allows for the reduction in cooling rates and residual stresses, thus limiting the risk of distortion and cracking. On the other hand, the LPBF process provides a higher resolution and better surface finish, and LPBF printers are less expensive for buying and operating than their EB-PBF competitors (Colomo, Wood, Martina, & Williams, 2020; Dzogbewu & De Beer, 2023). As examples of the current use of LPBF printers to manufacture tungsten parts, one can mention collimators, radiation shields (Wolfmet 3D, M&I Materials Ltd., (Manchester, UK) (M&I Materials Ltd, 2023)) and anti-scatter grids (M 100, EOS GmbH (Munich, Germany) (« Tungsten for Industrial 3D Printing|EOS », 2023).

In more detail, LPBF relies on fusion by a laser of a 20–60 μm thick layer of metallic powder deposited on a baseplate that can sometimes be preheated to up to 800 °C. Once the layer is melted, the baseplate descends with a controlled increment (one layer thickness), and the operation is then repeated until the final part is obtained. To limit the risk of oxidation, this process takes place under a pressurized and inert atmosphere (often argon, with a typical residual oxygen content of around 800 ppmv) (Braun et al., 2019; Müller et al., 2019). Although promising for the shaping of tungsten, LPBF also presents its share of challenges and limitations. Actually, porosity (voids ranging from 5 to 500 μm in size), cracks and oxidation at the grain boundaries or inside the pores are among the most frequent defects

induced during the process (Colomo et al., 2020; Talignani et al., 2022). To date, pure tungsten parts have been produced with the highest claimed density of 99.6% but generally contain cracks and voids (Rebesan, Ballan, et al., 2021). Despite the presence of process-induced defects, the mechanical properties of printed tungsten parts could be comparable or even competitive to those from conventional forming processes (Tan et al., 2018). The difficulties of forming this metal by LPBF are attributable to the multitude of process parameters involved: more than a hundred of them directly or indirectly influence the quality of parts produced, and they can be grouped by category, depending on whether they are related to scanning strategy or to the laser, powder bed or printing chamber characteristics.

Numerous studies have been conducted to understand the effects of process parameters on the properties of printed parts and thus to optimize the process and facilitate the implementation of new printable materials. To reach these objectives, different experiment and computer-based approaches have mainly been used, the first leading to phenomenological models of the process and the second to numerical or analytical models of the physical phenomena involved. The design of experiment (DOE) approach is the most frequently used to optimize the LPBF process. For example, in (D. Wang et al., 2017), the DOE approach was initially used to assess the effects of powder morphology on the characteristics of pure tungsten parts. The authors compared the surface morphology and absorptivity of molten tracks formed by polyhedral and spherical powders and concluded that spherical powders having higher laser absorptivity than their polyhedral counterparts allowed for the formation of continuous tracks. Next, they used the same experimental approach to optimize the LPBF printing conditions (laser power and exposure time) for spherical powders and succeeded to print 96% density parts (measured according to Archimedes' principle).

Note that for the sake of process optimization, LPBF printing parameters are frequently compounded via the use of a single agglomerated metric, such as the volumetric energy density:

$$VED\ [J/mm^3] = \frac{P}{vht} \tag{2.1}$$

where P [W] is the laser power, v [mm/s] is the scanning speed, t [mm] is the layer thickness and h [mm] is the hatching space. Some authors (Tan et al., 2018; Xiong et al., 2020) studied the impact of this metric on the density and mechanical properties of printed parts by successively varying the laser power and scanning speed while maintaining the layer thickness and hatching space fixed, while others (Rebesan, Ballan, et al., 2021; Sidambe et al., 2019) focused on varying the scanning speed and hatching space by maintaining the laser power and layer thickness fixed. The problem in using VED as a single process-related metric is that for the same value of VED, the outcomes may differ significantly (M. Guo et al., 2019; Li, Wu, Zhou, & Wei, 2020). This notwithstanding, the advantages of experimental methods lie in their relative simplicity and in the possibility to carry out in situ or post-mortem control of printed parts. Because of these benefits, experimental approaches continue to be extensively used and can now benefit from the modern trends in experimental techniques, such as the use of deep learning algorithms that easily convert large amounts of data into phenomenological models also known as numerical twins (Gor et al., 2022; Marrey, Malekipour, El-Mounayri, & Faierson, 2019). However, these approaches are costly in terms of materials and time, and the results obtained are difficult to transfer from one piece of equipment to another and from one feedstock material to another.

To decrease the resources needed to implement a new material in the LPBF portfolio, different physical phenomena involved in the LPBF process, such as powder spreading or interactions between the laser and the powder bed, can be simulated using finite element-based models of different complexity (H. Chen et al., 2022; Chowdhury et al., 2022; S. Sharma et al., 2023; Todo et al., 2022; Vrancken et al., 2022), or analytical models based on exact resolutions of known mathematical equations (Bajaj et al., 2019; Letenneur et al., 2019; Promoppatum et al., 2017; Y. Wang et al., 2023; Wolfer et al., 2019). For example, a finite element-based model was used in (Todo et al., 2022) to simulate laser–powder bed interactions for pure tungsten powders. This model allowed for the printing of high-density tungsten parts, but these parts contained multiple cracks caused by thermal stresses. This cracking phenomenon was investigated in (S. Sharma et al., 2023; Vrancken et al., 2022) using different FEM approaches and in (Y. Wang et al., 2023) using a more complex thermomechanical coupled dislocation-

based crystal plasticity simulations. Despite the models' complexity and a deep understanding of the different phenomena involved, none of these works allowed for the production of crack-free tungsten parts. On the other hand, simplified analytical models of the process were used in (Bajaj et al., 2019; Letenneur et al., 2019) to optimize the LPBF process parameters for various metallic materials, such as pure molybdenum, nickel, titanium, iron and aluminum alloys, but, to the best of the authors' knowledge, the potential of these models has never been explored for LPBF of tungsten parts.

This study was devised to bridge this knowledge gap while trying to propose a cost-effective way of producing LPBF tungsten parts with good structural and mechanical properties. To reach this objective, analytical melt pool simulations and DOE are combined to study the effect of process parameters on the physical, structural and mechanical properties of printed specimens and to suggest some future directions for process improvement.

2.5 Materials and Methods

The following workflow was established for this study (Figure 2-1): first, a selected powder feedstock was characterized in terms of powder granulometry, morphology, flowability and physical properties. Then, an analytical model of the melt pool formed in the powder bed by a moving laser beam was used to define the plan of printing experiments. Next, printed specimens were characterized in terms of their density, structure and mechanical properties. Results of the process simulations were compared with their experimental equivalents, and the LPBF processing parameters were linked to the physical and mechanical properties of the printed specimens. Finally, using the optimized set of printing parameters, selected design artifacts were printed and analyzed to characterize the printability limits.

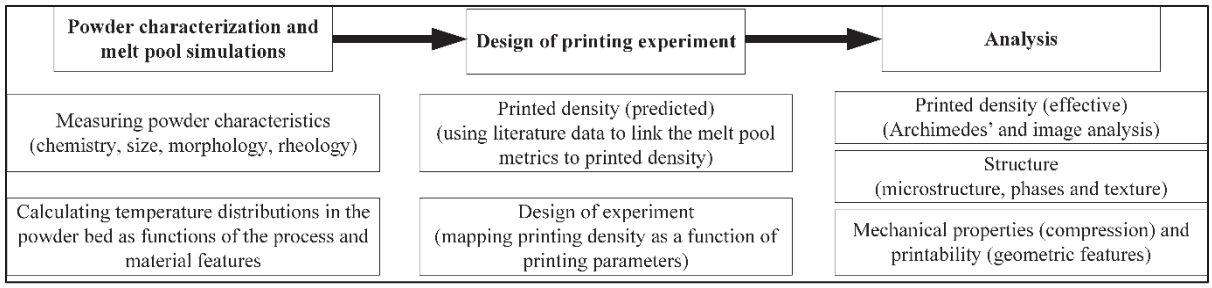

Figure 2-1 : Summary diagram of the methodology followed in this study

2.5.1 Powder Characterization

Plasma-spheroidized pure tungsten powders (W > 99.9%, O < 250 ppm, tap density > 10 g/cm^3 and Hall flow < 8 s/50 g) used in this work were produced by Tekna Co., Ltd. (Sherbrooke, QC, Canada). The particle size distribution (µm) was measured using a Beckman Coulter (Brea, CA, USA) LS13 320 XR particle size analyzer (D10 = 16, D50 = 27 and D90 = 41) (Figure 2-2), and the particle morphology was observed using a Hitachi (Tokyo, Japan) 3600 scanning electron microscope (Figure 2-2). The rheological properties of dry powders were obtained using an FT4 powder rheometer (Freeman Technology, Tewkesbury, UK). The results are shown in Figure 2-2 and collected in Tableau 2-1.

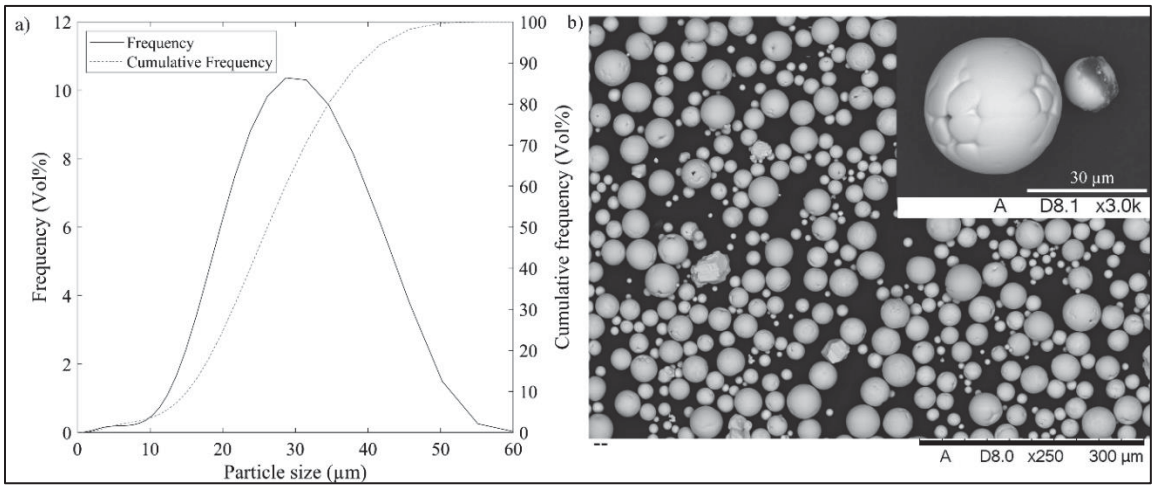

Figure 2-2 : Geometric characteristics of the tungsten powder: a) particle size distribution and b) particle morphology

Tableau 2-1 : Rheological properties of the −41 + 20 µm tungsten powder (indexes adopted from Brika et al. (2020)): BD (bulk density), CI (compressibility Index), PD (pressure drop), SE (specific energy), AE_{10} (aeration energy at 10 mm/s air velocity), BFE (basic flow energy), CC (Cohesion coefficient)

		FT4 Rheometer						
Carr Index	Hausner Ratio	BD (g/cm^3)	CI (%) at 15 kPa	PD (mBar) at 15kPa	SE (mJ/g)	AE_{10} (mJ)	BFE (mJ)	CC (kPa)
0.00	1.00	12.1 (±0.375%)	1.82 (±5.08%)	14.6 (±3.88%)	1.62 (±0.523%)	23.0 (±1.7%)	1182 (±2.09%)	0.38

2.5.2 Building the Printed Density Processing Map

2.5.2.1 Theoretical Considerations

The temperature field created by a moving Gaussian heat source in a semi-infinite solid (« Handbook of the EuroLaser Academy. 2 », 1998) can be expressed using Equations (2.2)-(2.4):

$$T(x,y,z) = T_0 + \frac{AP}{kr_f\pi^{\frac{3}{2}}}\int_{+\infty}^{0}\frac{1}{1+\tau^2}exp(C)\,d\tau \tag{2.2}$$

with

$$C = -\left(\frac{\tau^2}{1+\tau^2}\right)\left(\left(\xi - \frac{Pe}{2\tau^2}\right)^2 + \eta^2\right) - \tau^2\zeta^2 \tag{2.3}$$

$$\xi = \sqrt{2}\frac{x}{r_f}\,;\eta = \sqrt{2}\frac{y}{r_f}\,;\zeta = \sqrt{2}\frac{z}{r_f}\,;Pe = \frac{r_f v}{2\sqrt{2}\alpha}\,;\tau = \frac{r_f}{2\sqrt{2\alpha dt}}\,;\alpha = \frac{k}{\rho c_p} \tag{2.4}$$

where T_0 is the baseplate temperature (K); A, the absorptivity; P, the laser power (W); k, the thermal conductivity (W/(m.K)); r_f, the laser beam radius (m); Pe, the Peclet number; v, the scanning speed (m/s); α, the thermal diffusivity (m^2/s); ρ, the density (kg/m^3); c_p, the mass heat capacity (J/(kg.K)); and dt, the time (s).

This equation involves four material-specific parameters: density, absorptivity, thermal conductivity and specific heat capacity. To keep the model simple, these material-related properties are considered constant throughout the melting process. Since the material used in the LPBF process is not in its bulk form but rather forms a powder bed, three of the four material properties (specific heat capacity is already mass- and, therefore, density-independent) must be corrected, considering an effective powder bed density and interactions between powder particles.

Powder bed density

The fractional porosity ϕ was calculated using the relative powder bed density (ρ_{powder}), as in Equation (2.5):

$$\phi = 1 - \rho_{powder};\ \rho_{powder} = \frac{BD}{\rho_s} \tag{2.5}$$

where ϕ is the fractional porosity, ρ_s is the material density (kg/m^3) and BD (kg/m^3) is the bulk density measured using an FT4 powder rheometer (Tableau 2-1).

Powder bed absorptivity

The powder bed absorptivity was calculated according to (Sumin Sih & Barlow, 2004), where the powder bed was assumed as a porous surface composed of spherical bodies and holes, all at the same temperature. Considering the bodies as "gray" without transmission of radiation, absorptivity is then equal to emissivity ($A = \epsilon$). Thus, the powder bed absorptivity can be calculated using Equation (2.6):

$$\epsilon_{powder} = S_h\epsilon_h + (1 - S_h)\epsilon_s \tag{2.6}$$

where ϵ_{powder} is the powder emissivity; S_h, the surface fraction occupied by pores; ϵ_h, the pores emissivity; and ϵ_s, the emissivity of a bulk material. The emissivity (absorptivity) of the

bulk material (ϵ_s) can be calculated using the Hagen–Rubens model (« Handbook of the EuroLaser Academy. 2 », 1998):

$$\epsilon_s = A = 0.365 \left(\frac{R_s}{\lambda}\right)^{0.5} \tag{2.7}$$

where R_s is the electrical resistivity of the material (Ω.m) and λ is the laser wavelength (m). This model tends to be more accurate at higher temperatures (close to the melting point) and longer wavelengths (above 1 µm).

Next, S_h and ϵ_h can be linked to the fractional porosity of a powder bed and the bulk material emissivity using Equation (2.8), where these values are considered independent of the size of powder particles. This approach was validated for stainless-steel, titanium, aluminum and cobalt–chromium alloy powders in (Y. Zhao, Koizumi, Aoyagi, Yamanaka, & Chiba, 2021; Zhou, Zhang, et al., 2019).

$$S_h = \frac{0.908\phi^2}{1.908\phi^2 - 2\phi + 1} \; ; \; \epsilon_h = \frac{\epsilon_s\left(2 + 3.082\left(\frac{1-\phi}{\phi}\right)^2\right)}{\epsilon_s\left(1 + 3.082\left(\frac{1-\phi}{\phi}\right)^2\right) + 1} \tag{2.8}$$

Powder bed thermal conductivity

Thermal conductivity calculations assume that the powder bed represents a system composed of spherical bodies and holes (Bala, Pradhan, Saxena, & Saksena, 1989). The probability of two particles occurring face to face in two successive sections is considered using Equation (2.9):

$$k_{powder} = k_s(1 - \phi)^{\frac{4}{3}} \tag{2.9}$$

where k_{powder} and k_s are the thermal conductivities (W/(m.K)) of a powder bed and a bulk material, respectively. Here again, the relation is independent of the particle size; it is

dependent exclusively on the fractional porosity of the powder, and was validated for copper powders of different particle sizes and fractional porosities in (Bala et al., 1989).

Simplifications related to the temperature dependence of tungsten properties

To simplify calculations, the material properties in the analytical model in Equations (2.2)-(2.4) are deliberately considered temperature independent, in spite of their effective variations in the room temperature (RT) to melting temperature (TM) range (Figure 2-1). To implement such an approach, a series of melt pool simulations was carried out by varying the material properties from their RT to TM values (Tableau 2-2) and comparing the calculated melt pool dimensions with their experimental equivalents with the objective of selecting material properties that would result in the smallest discrepancies between the calculated and measured melt pool values.

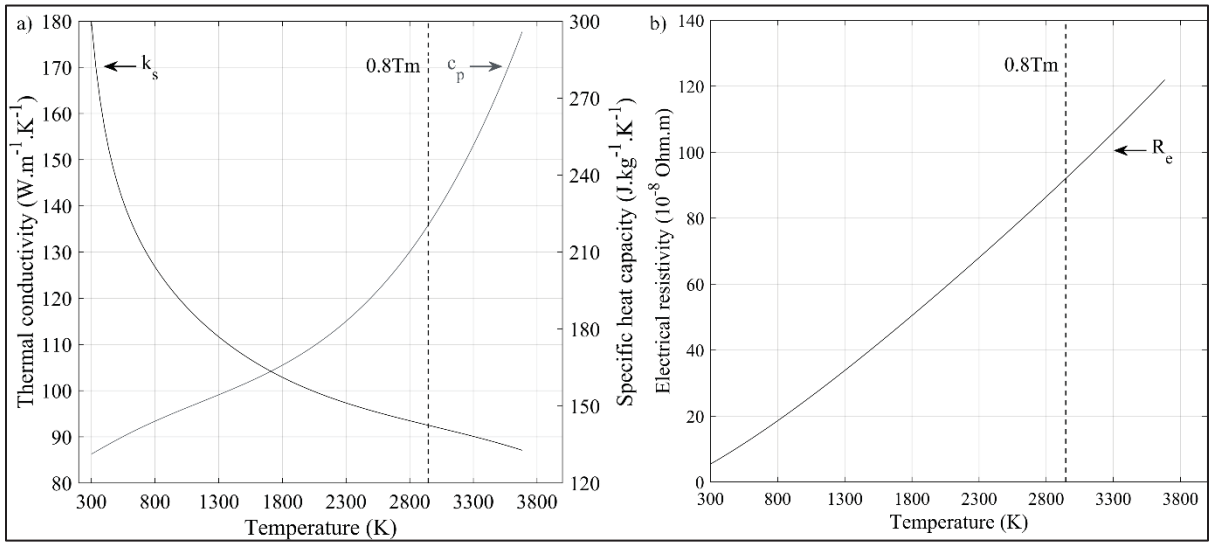

Figure 2-3 : Temperature evolutions of the pure tungsten properties adapted from Tolias (2017): a) specific heat capacity and thermal conductivity; b) electrical resistivity

Tableau 2-2 : Property variation ranges considered as model inputs; material density is taken from J. R. Davis & ASM International (1998, p. 115), and bulk density is extracted from the rheometer test (BD, Tableau 2-1); calculated properties are obtained using equations (in brackets); remaining properties are taken from Tolias (2017)

Temperature of Application (K)	Material Density (kg/m^3)	Bulk Density (kg/m^3)	Specific Heat Capacity (J/(kg.K))	Thermal Conductivity (W/(m.K))	Electrical Resistivity (nΩ.m)	Absorptivity (%)
293 (RT)–3683 (TM)	19,254	12,100	131–296	47–74 Equation (2.9)	53–1219	18–51 Equations (2.6)–(2.8)

To carry out this analysis, the volume surrounding the melt pool was modeled as a parallelepiped domain (dimensions are in mm): X = [−0.1; 1], Y = [−0.45; +0.45] and Z = [−0.3; 0], with N = 100 divisions for each axis) in the MATLAB software (R2022b, MathWorks, Natick, MA, USA) environment. Next, temperatures calculated in each cell of this domain using Equations (2.2)–(2.9) were compared to the melting temperature to extract the melt pool dimensions, and the calculated melt pool values (Figure 2-4a) were compared to the experimentally measured laser track equivalents. It was found that the smallest discrepancies between the calculated and measured values corresponded to the material properties taken at 0.8TM As an example, the calculated melt pool width for a specific case of P = 300 W, v = 400 mm/s and r_f = 50 μm with material properties taken at 0.8TM is presented in Figure 2-4b and compared to its measured laser track equivalent in Figure 2-4c from (Xiong et al., 2020). Note also that the calculated melt pool depths were also compared to their experimentally measured equivalents, whenever provided, and showed a decent correspondence. The results of a regression analysis confronting multiple measured laser track widths (Rebesan, Ballan, et al., 2021; S. Sharma et al., 2023; Vrancken et al., 2022; Xiong et al., 2020) with their calculated melt pool equivalents (0.8TM) are presented in Figure 2-4d with a directive coefficient of unity, the negligible constant term, R^2_{adj} = 0.90, RMSE = 3 and without any pattern in the residuals. Based on these results, the tungsten properties are selected at 0.8TM. The corresponding powder bed input parameters are therefore as follows: density, 12,100 kg/m^3; specific heat capacity, 221 J/(kg.K); thermal conductivity, 49 W/(m.K); electrical resistivity, 921 nΩ.m; absorptivity, 46%.

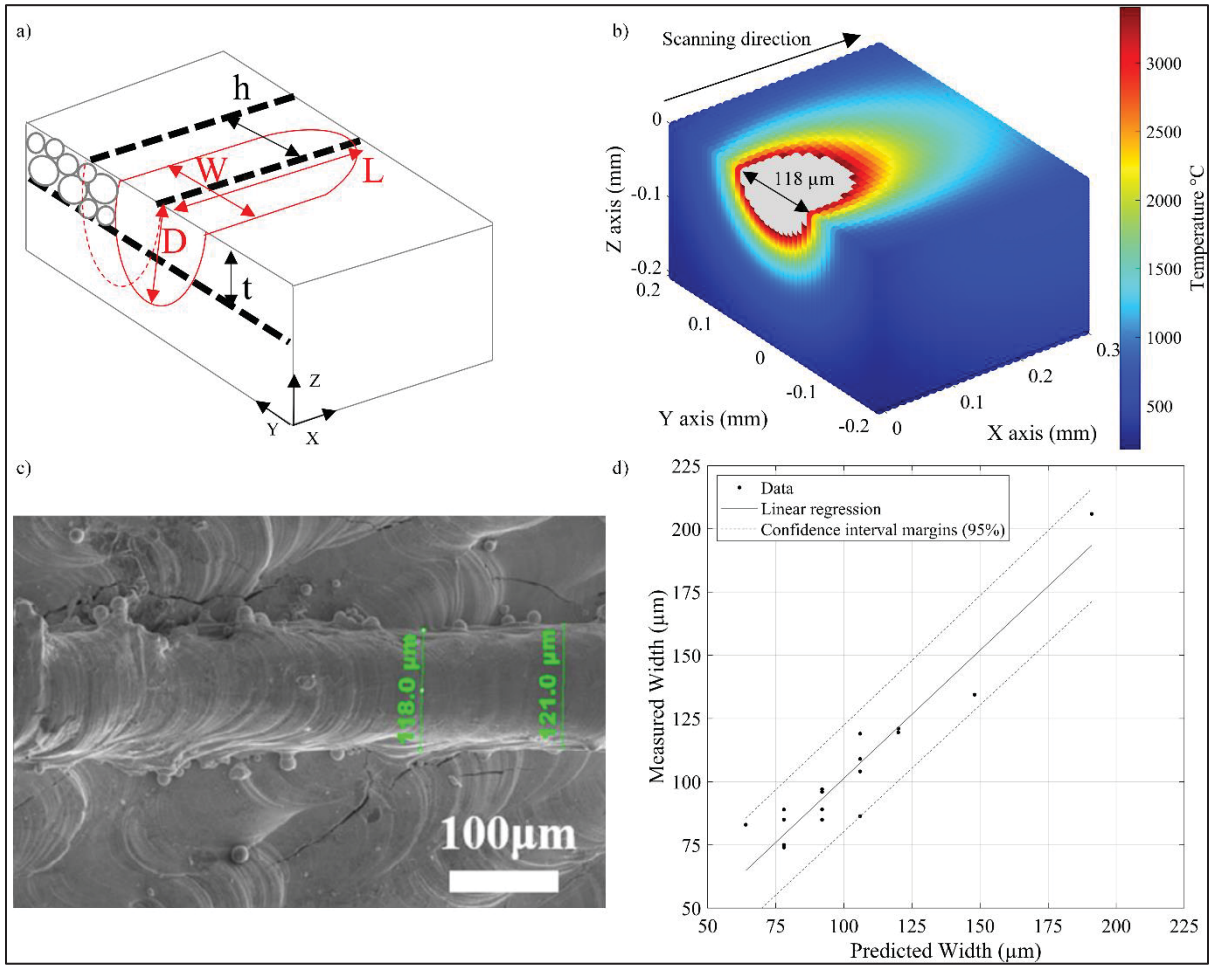

Figure 2-4 : a) Schematic representation of the melt pool, melt pool dimensions (depth D, width W and length L) and process variables (layer thickness t and hatching space h); b) calculated (0.8TM) melt pool for pure tungsten (P = 300 W, v = 400 mm/s et rf= 50 µm) and c) photo of a single laser track for the same process parameters from Xiong et al. (2020); d) comparison between the measured Rebesan, Ballan, et al. (2021); S. Sharma et al. 2023; Vrancken et al. (2022); Xiong et al. (2020) and calculated (0.8TM) melt pool widths for pure tungsten with 95% confidence margins.

2.5.2.2 Relating the Melt Pool Dimensions to Printed Density

Three dimensionless melt pool metrics (i.e., melt pool depth-to-layer thickness ratio (D/t), melt pool width-to-hatching space ratio (W/h) and melt pool length-to-width ratio (L/W)) were introduced based on the previously described melt pool calculations and process

parameters and then related to the relative density of printed parts using experimentally measured density values. The main idea of such an approach can be formulated as follows: to transform a powdered matter into a consolidated body, tracks of molten metal generated by a heat source must overlap in both the horizontal (XY) and vertical (XZ) directions, such as W/h and $D/t \in [1.5–2.5]$. Additionally, to avoid balling resulting from the melt pool instability, the L/W ratio must not exceed 4–4.5 (Letenneur et al., 2019).

To link the dimensionless melt pool metrics (D/t, W/h and L/W) to the printed density, 340 results taken from 19 studies on eight dissimilar materials (W, Mo, In625, Ti64, Ti2225, Fe, AlSi10Mg, AISI 1008) processed using 14 different printers (J. Chen et al., 2020; Enneti et al., 2020; Faidel et al., 2015; Guan et al., 2023; M. Guo et al., 2019; Letenneur et al., 2019; Li et al., 2020; Y. Liu et al., 2023; Mao et al., 2025; Müller et al., 2019; Rebesan, Ballan, et al., 2021, 2021; S. Sharma et al., 2023; Shi et al., 2023; Xiong et al., 2020; Xiuxuan Yang et al., 2021; Zhou, Li, et al., 2019; Zhou, Zhang, et al., 2019; Zhou et al., 2020) were used to establish a calibration function. As a result of this exercise, a polynomial function presented by Equation (2.10) relates the calculated dimensional melt pool metrics with the experimentally measured printed densities (coefficients are provided in Tableau 2-3, all of them having a significant impact according to their corresponding p-values). This function is valid for the laser powder ranging from 70 to 1000 W, the scanning speed from 10 to 2800 mm/s and the baseplate temperature from 20 to 1000 °C. The curve fitting was carried out using the “fit” function in MATLAB, choosing the nonlinear least-squares method and the least absolute residuals (LAR) error option. The $R^2_{adj} = 0.96$, the RMSE = 2.0 and the absence of any pattern in the residuals validated the fitting function (Thacker & Paez, 2014). The response surface is shown in Figure 2-5a and its projection on the W/h-D/t plan in Figure 2-5b, with the maximum printed density area encircled. Projections of the maximum densities on the W/h-D/t plan indicate that this response surface meets the established material consolidation criteria, i.e., that a density higher than 95% is obtained when W/h et $D/t \in [1.5–3.5]$.

$$\rho_{predicted} = a_{00} + a_{10}\left(\frac{D}{t}\right) + a_{01}\left(\frac{W}{h}\right) + a_{20}\left(\frac{D}{t}\right)^2 + a_{11}\left(\frac{D}{t}\right)\left(\frac{W}{h}\right) + a_{02}\left(\frac{W}{h}\right)^2 + a_{30}\left(\frac{D}{t}\right)^3 + a_{12}\left(\frac{D}{t}\right)\left(\frac{W}{h}\right)^2 + a_{03}\left(\frac{W}{h}\right)^3 + a_{40}\left(\frac{D}{t}\right)^4 + a_{31}\left(\frac{D}{t}\right)^3\left(\frac{W}{h}\right) + a_{22}\left(\frac{D}{t}\right)^2\left(\frac{W}{h}\right)^2 + a_{04}\left(\frac{W}{h}\right)^4 \quad (2.10)$$

Tableau 2-3 : Coefficients of the polynomial function linking dimensionless melt pool metrics to printed density.

$a_{00} = 16.8$	$a_{10} = 94.6$	$a_{01} = 40.1$	$a_{20} = -53.6$	$a_{11} = -7.5$
$a_{02} = -24.0$	$a_{30} = 14.4$	$a_{12} = 3.7$	$a_{03} = 6.0$	$a_{40} = -1.5$
$a_{31} = 0.5$	$a_{22} = -0.8$	$a_{04} = -0.6$		

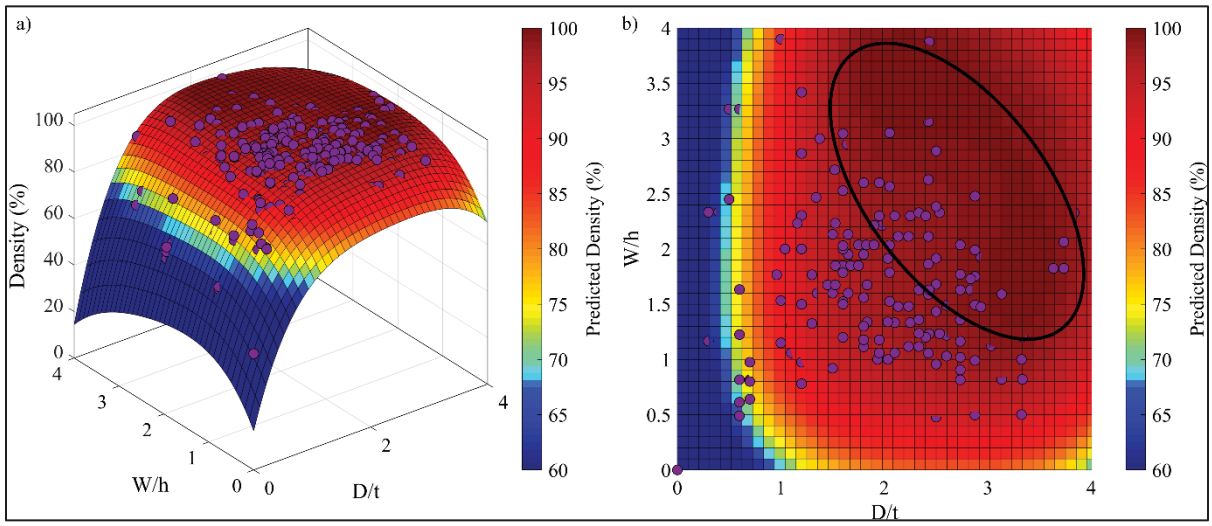

Figure 2-5 : Response surface of the polynomial function relating printed density to dimensionless melt pool metrics (experimental points in purple dots): a) 3-dimensional view and b) $D/t - W/h$ plane view highlighting a maximum density area defined from the experiment

2.5.2.3 Processing Map in the VED-BR Coordinates

Once defined, the analytical model was used to build the "printed density processing map" (Figure 2-6) in the volumetric energy density (VED, J/mm^3) build rate (BR, cm^3/h) coordinates where VED was calculated using Equation (2.1), whereas BR was calculated using

Equation (2.11), and their product corresponded to the maximum power of a laser source (P). Note that this representation allows for avoiding the previously mentioned shortcomings stemming from the use of VED as a single agglomerated metric of the LPBF process.

$$BR\ [\frac{\mathrm{cm}^3}{\mathrm{h}}] = \ vht \tag{2.11}$$

Each point on this density map corresponds to a specific set of printing parameters and represents the results of thousands of melt pool calculations carried out within the given process parameter ranges. In fact, Figure 2-6 shows a process map for pure tungsten corresponding to the capacities of a TruPrint 1000 system (TRUMPF GmbH, (Ditzingen, Germany), r_f = 27.5 µm, λ = 1.06 µm), where the laser power P can be varied from 20 to 200 W and the scanning speed v from 20 to 7000 mm/s. To build this map, the layer thickness t was set at 30 µm, and the hatching space h was set at 80 µm. On this map, the highest densities correspond to W/h et $D/t \in$ [1.5–3.5].

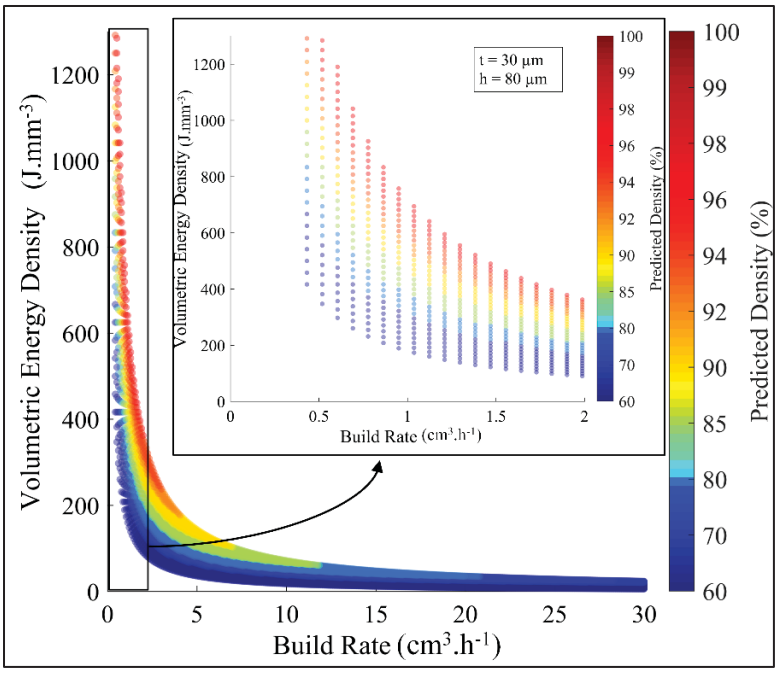

Figure 2-6 : Example of the tungsten density processing map for a TruPrint 1000 (t = 30 µm, h = 80 µm); insert contains the region with the highest predicted density

2.5.3 Experiments and Equipment

To validate the model predictions and study the impact of process parameters on the physical, structural and mechanical properties of printed specimens, the design of experiments (DOE) approach was applied. The DOE was intended to cover the entire high-printed-density region on the calculated map while being sufficiently large to cross the boundaries of this region by varying the expected printed density from 70 to 95%. To this end, a series of density maps was built for a constant layer thickness of t = 30 µm and a variable hatch distance h (20, 30, 40, 60, 80 and 100 µm), and on each of the maps, five identical $VED - BR$ printing sets, A, B, C, D and E, were defined (Tableau 2-4). Examples of such maps are given in Figure 2-7a,b for the cases of h = 20 µm and h = 80 µm. Each letter corresponds to a given $VED - BR$ set: A, B, C, D, E, and a number corresponds to the hatching space. For example, Specimen A-20 corresponds to a $VED - BR$ set of VED = 1170 J/mm^3 and BR = 0.43 cm^3/h and a hatching space of h = 20 µm. The detailed DOE plan of this study can be found in APPENDICE A Tableau-A A-1. On the basis of these assumptions, thirty 10 mm diameter, 20 mm high

cylindrical specimens (Figure 2-7c,d) were printed on a stainless-steel baseplate without preheating. After the printing, specimens were cut from the substrate, supports were removed, and the specimens were cut into different samples for subsequent analysis (Figure 2-7c).

Tableau 2-4 : DOE: Parameters sets definition

	A	B	C	D	E
VED, J/mm^3	1170	750	750	417	417
BR, cm^3/h	0.43	0.43	0.86	0.86	1.62

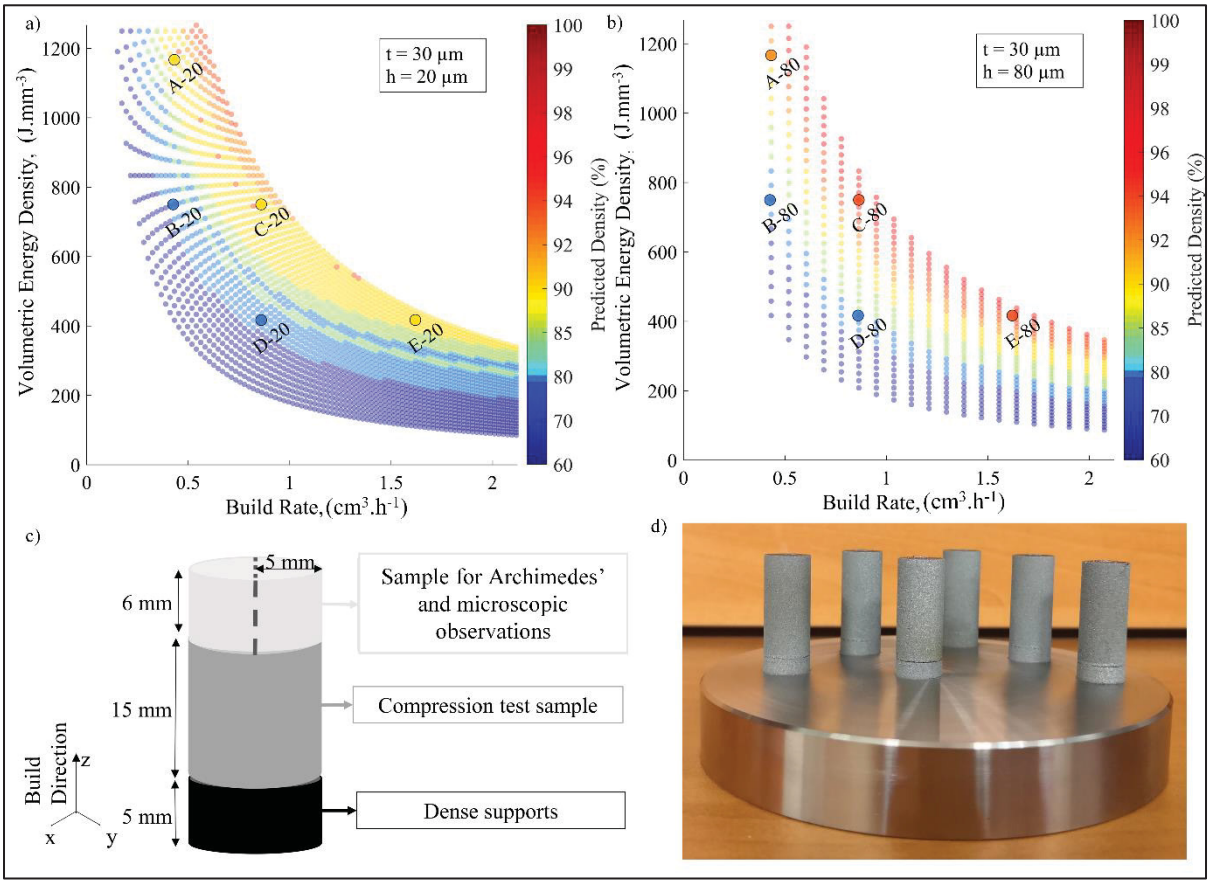

Figure 2-7 : Density maps for tungsten powders with a) h = 20 µm and b) h = 80 µm and selected $VED - BR$ sets for a TruPrint 1000; c) schematic representation of the printed specimens with different cuts; d) photo of a baseplate with printed specimens

The density of the LPBF-processed specimens was measured using the Archimedes' oil impregnation technique [49]. To this end, cylindrical specimens were weighed in air (m_{air}), then again after the oil impregnation (m_{oil}) and then in distilled water ($m_{oil+water}$) using a density kit (Sartorius (Sartorius Lab Instruments GmbH & Co. KG, Goettingen, Germany) VF4601) and an analytical balance (Sartorius SECURA324-1S with 0.1 mg readability). The specimens' densities were calculated using Equation (2.12):

$$\rho_{Arch} = \frac{m_{air}}{m_{oil} - m_{oil+water}} \rho_{water} \tag{2.12}$$

where the water density (ρ_{water}) was taken at room temperature (22 °C).

Next, the specimens were mounted in Bakelite, mirror polished and observed with a LEXT OLS4100 (Lext Olympus Corporation, Tokyo, Japan) laser confocal microscope. The density, as well as the number of pores, their sizes and shapes, were extracted using a proprietary routine developed in the MATLAB environment. The following metrics were considered in this study:

- Image analysis material density (ρ_{IM}), calculated as a white-to-black pixel ratio in the binarized image; the binarization procedure was applied using the "im2gray" function and a threshold specific to each image. Additionally, the "imfill" function was used to fill the holes and ensure that each pore was entirely black, with no embedded white pixels (Figure 2-8a,b);
- Pores density (Number of pores per mm^2, p/mm^2), which represents the sum of all the detected pores divided by the image area;
- The 10, 50 and 90% quotients of an entire pore population in terms of their equivalent diameter ($DE10p$, $DE50p$ and $DE90p$, μm), obtained by plotting the surface-based distribution of the equivalent pore diameters (Figure 2-8c). The equivalent diameter of a pore corresponds to the diameter of a circle having the same surface area as the pore, calculated using Equation (2.13);
- The 10, 50 and 90% quotients of an entire pore population in terms of their circularity ($C10p$, $C50p$, $C90p$, without unit) obtained by plotting the surface-based distribution

of the pore circularity (Figure 2-8d). The circularity of a pore was calculated using Equation (2.14):

$$Equivalent\ Diameter\ (DE) = \sqrt{\frac{4Area}{\pi}} \tag{2.13}$$

$$Circularity\ (C) = \frac{4\pi Area}{Perimeter^2} \tag{2.14}$$

In order to focus the study on pores that are the most impactful from the mechanical property viewpoint, those smaller than DE = 20 μm were removed from consideration, which corresponds to removing 75% of the entire pore population in terms of their number, but to only ~5% in terms of their cumulative surface area.

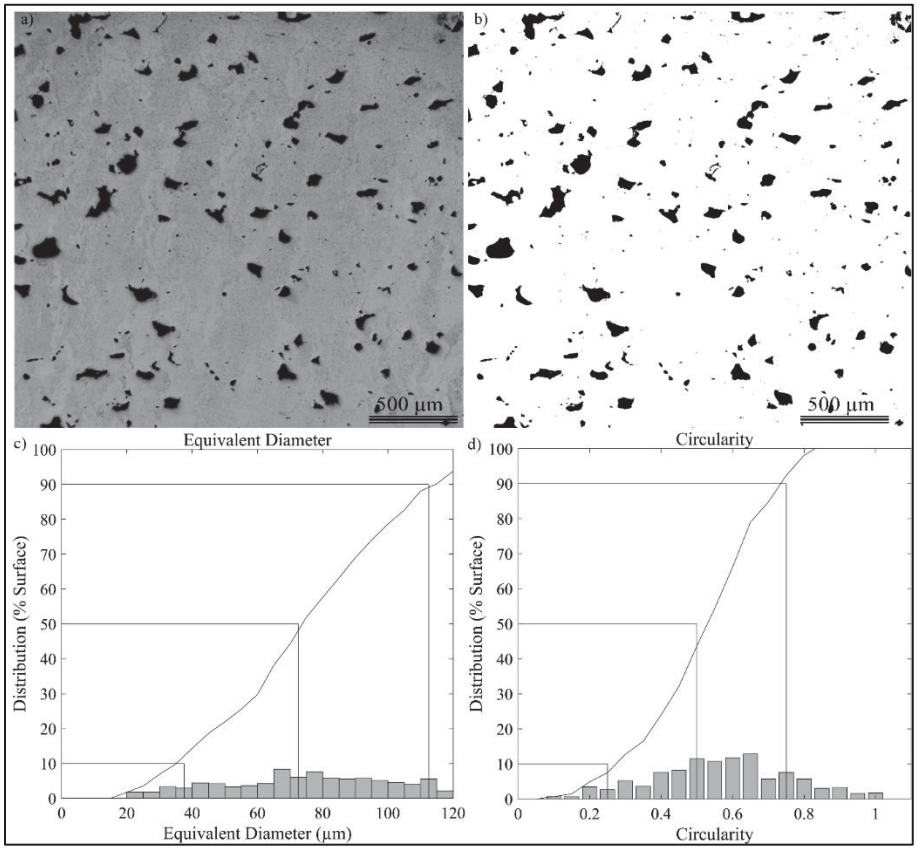

Figure 2-8 : a) LEXT and b) binarized images, c) pore size diagram and d) pore shape diagram for Specimen E-80

To carry out crystallographic analyses using the electron backscatter diffraction technique (EBSD), specimens were subjected to ion milling using a Hitachi EM 4000 plus (5 kV, 25 rpm, 15 min). The EBSD maps were built using a Hitachi SU-8230 Field Emission-STEM. These maps were then post-treated using the MTEX library (MATLAB software) to assess the grain size, shape, orientation and distribution following the procedure defined in the E2627 ASTM standard (E04 Committee, 2019). Only the z–y sections along the building direction were analyzed, and the misorientation angle threshold was set to 10°. Since the standard only defines procedures to obtain a number of grains and an average grain size of the entire EBSD map, the grain size and shape metrics were processed by analogy with those of pores and will be referred to as the grain density, i.e., the number of grains per mm^2 (g/mm^2); the grain size $DE10g$, $DE50g$ and $DE90g$ (µm); and the grain circularity, $C10g$, $C50g$ and $C90g$ without unit). Given that for both the pores and grains, their size and shape distributions are sometimes strongly asymmetrical, their median value (corresponding to 50% of the population) will be considered for future study.

Finally, compression tests were performed using an Alliance RF/200 electromechanical testing machine (MTS, Eden Prairie, MN, USA) according to the E9-09 ASTM standard (E28 Committee, 2019). The compression rate was set at 0.01 mm/s, and two high-resolution cameras were placed in front of the specimens during the tests to monitor the fracture mode. The force was measured using an MTS 4501036 load cell, while the displacement was measured by the machine LVDT (since no extensometer was used during testing, the elastic modulus values were not measured). Based on these measurements, strain–stress diagrams were plotted to obtain the following metrics (Figure 2-9):

- Ultimate compression strength (UCS, MPa), defined as the maximum stress reached during the test;
- Yield strength at 0.2% offset (YS, MPa), calculated by moving the slope at the origin (slope O) to 0.2% on the strain axis, according to the methodology described in the standard;

- Strain under maximum load (δ, %), representing the difference between the total compression strain and the elastic strain to failure, calculated by moving the slope at origin (slope O) to reach the UCS.

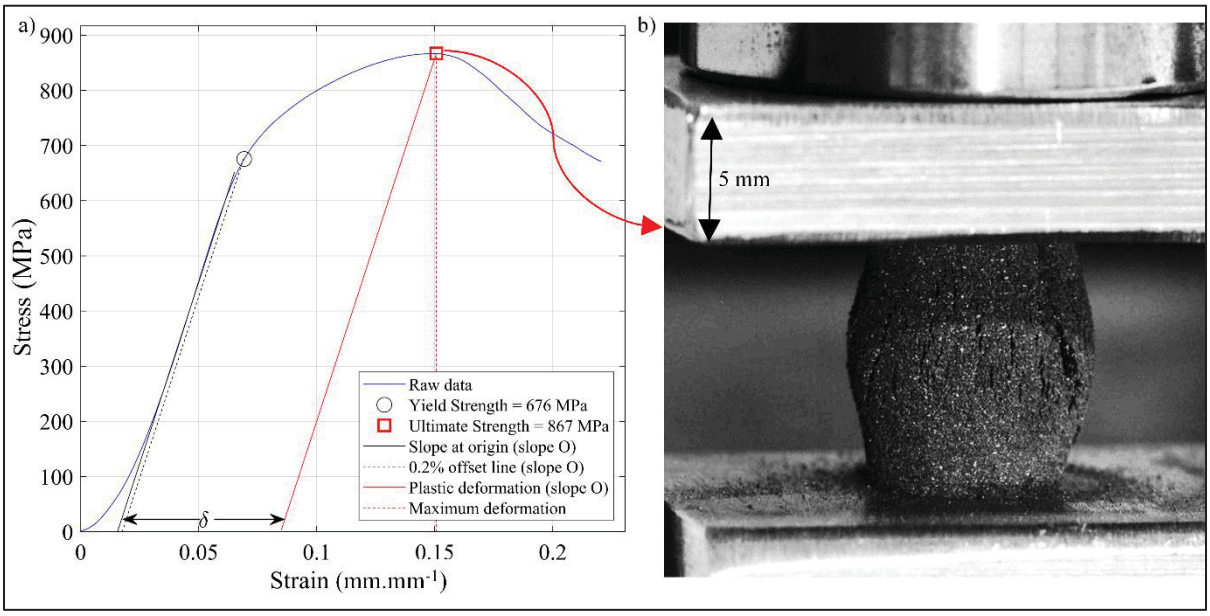

Figure 2-9 : a) Compression stress–strain diagram with the obtained metrics and b) photo of Specimen E-80 during the compression test at a total compression strain of 0.1

Five specimens (A-80, B-80, C-80, D-80 and E-80), all corresponding to $h/t = 2.7$, were selected for the phase and chemical analyses. First, the XRD analyses were performed using an X'Pert^3 Panalytical system (Malvern Panalytical Ltd, Malvern, UK) equipped with a cobalt source. Then, in order to detect a possible presence of oxides on fracture surfaces, similarly to (Braun et al., 2019), the fracture surfaces of 2 of 5 specimens (A-80 and E-80), corresponding to the best and the worst compression properties of this series of specimens, were studied using the XPS X-ray photoelectron spectroscopy technique (Escalab 250Xi (Thermo Fisher Scientific, Waltham, MA, USA) with a monochromatic Al Kα source at a power of 218.8W (14.7 kV, 14.9 mA)) and EDS (Hitachi SU-8230 Field Emission-STEM equipped with an X-flash energy-dispersive X-ray spectroscopy quad detector).

Finally, considering the results of mechanical testing, three types of geometric artifacts (Figure 2-10) -10 mm diameter, 20 mm high gyroid lattice structures two different porosities (50 and 60%) and the gap and wall printable design features in the 0.1 to 2 mm range (adapted from (Moylan, Cooke, Jurrens, Slotwinski, & Donmez, 2012))- were printed using one parameter set leading to the best mechanical properties (E-80). No beam offset or any contour adjustment was made during these prints. The gyroids were characterized in terms of their density through Archimedes' measurements. No further investigations were conducted on these features because of the high X-ray impermeability of tungsten. The walls and the gaps were measured using a LEXT OLS4100 confocal microscope. All the measurements of the minimum printable structures were repeated 20 times and statistically processed.

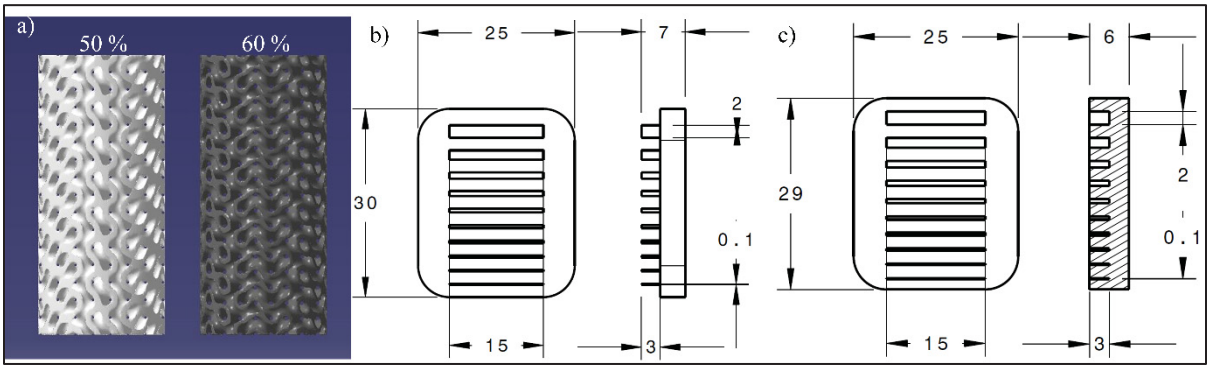

Figure 2-10 : Nominal structure of the printed specimens: a) 50% and 60% porosity gyroid lattice structures, b) minimum wall artifact and c) minimum gap artifact. Dimensions are given in mm.

2.6 Results

2.6.1 Archimedes- and Image-Measured Printed Densities

In Figure 2-11a, the results of the Archimedes' oil impregnation measurements (Archimedes' density) were compared with those obtained by image analysis (image density). A linear regression analysis between the two groups of results indicates that the difference between them is statistically significant with a confidence interval of 95%. Moreover, the image analysis revealed that pores in the higher-porosity specimens contained unfused powder

particles (Figure 2-11b), thus leading to systematically higher Archimedes' densities. Since these unfused particles do not contribute to the mechanical resistance of printed parts, relying upon the Archimedes' measurements may be misleading, and the use of image-based density measurements appears to be more relevant for this study. Furthermore, microscopic observations also highlighted that only two specimens contained microcracks, with an average size of 112 µm ± 3 µm (95%). Since these specimens were printed using $h \leq 60$ µm ($h/t \leq 2$) and they belong to the A $VED - BR$ set with the highest volumetric energy density values and the lowest build rate values, it can be hypothesized that they resulted from high temperature gradients generated during printing. Also, it is possible that these cracks came from the cold work occurring during the metallographic preparation and not from the process parameters, since they were very few and localized (Figure 2-11c). To validate the second hypothesis, polishing steps were repeated without a definitive conclusion, leaving the hypothesis of excessive temperature gradients as the most probable.

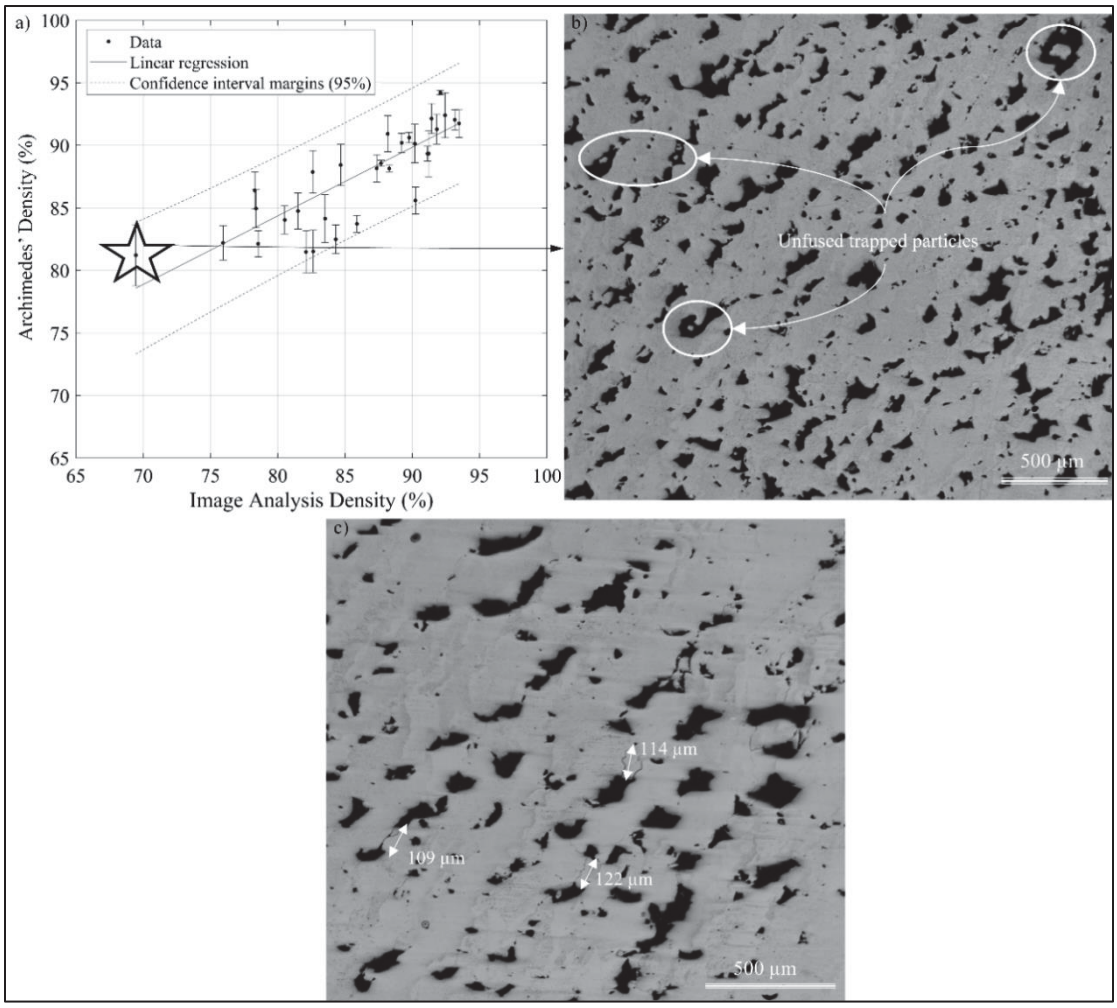

Figure 2-11 : a) Printed densities measured using the Archimedes' and image analysis techniques, where dotted lines correspond to the 95% confidence interval margins; b) SEM micrograph of Specimen D-20 containing unfused particles inside pores; c) microcracks in Specimen A-40

2.6.2 Predicted versus Measured Printed Density

The image-measured and predicted printed densities are compared in Figure 2-12 and subjected to a linear regression analysis to assess the model relevance, with the following results: the direction coefficient is close to 1 with a p-value < 0.05; the constant is not statistically significant according to its p-value (p-value > 0.05); $R2adj$= 0.8; and $RMSE$= 5.2, with no pattern in the residuals. The numerical values of discrepancies between the model and the experiments are presented in APPENDICE A Tableau-A A-1. It is hypothesized that the

observed discrepancies are due not only to the model-related limitations but also to the fact that the literature data used to relate the melt pool metrics to the printed density were obtained using the Archimedes' technique and could be misleading, as previously discussed.

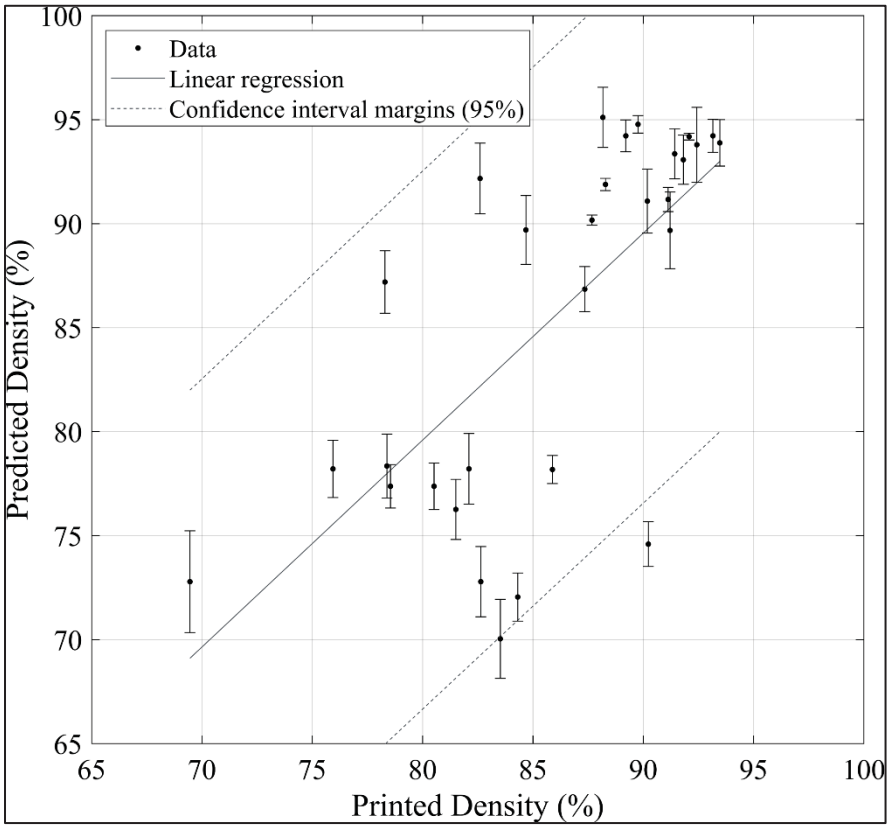

Figure 2-12 : Comparison between the measured and predicted printed densities with the confidence interval margins

Next, Figure 2-13a,b presents, respectively, the predicted and measured printed densities for different $VED - BR$ sets as functions of the h/t ratio. It can be seen that for each $VED - BR$ set, the predicted and measured densities follow similar trends: they first increase to reach a maximum at h/t = 2.5…2.7and then decrease. Moreover, for any h/t ratio, the E (417 J/mm^3; 1.62 cm^3/h) and C (750 J/mm^3; 0.86 cm^3/h) $VED - BR$ sets result in the highest printed densities, while the B (750 J/mm^3; 0.43 cm^3/h) and D (417 J/mm^3; 0.86 cm^3/h) $VED - BR$ sets result in the lowest printed densities. These results confirm the capacity of the model to relate process parameters and printed densities, both in terms of the trends and absolute values. It can

also be asserted, based on these observations, that the processing conditions leading to the highest printed densities, and therefore to potentially higher mechanical properties, correspond to the E-80 (417 J/mm^3; 1.62 cm^3/h) $VED - BR$ set with h/t = 2.7, which gives the following printing parameters: P = 188 W, v = 188 mm/s, h = 80 µm and t = 30 µm.

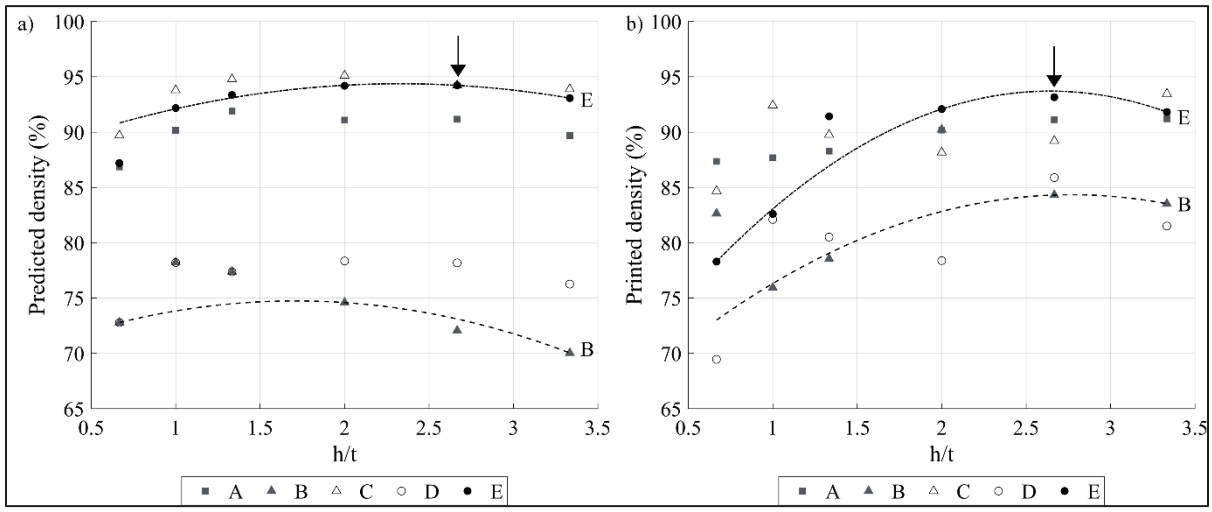

Figure 2-13 : a) Predicted and b) measured printed densities as functions of the h/t ratio for five $VED - BR$ sets (arrows indicate maxima, trend lines are added for visualization purposes)

2.6.3 Structural Studies

2.6.3.1 Porosity

No clear correlation can be established between the pore size and the printed density. For example, as shown in Figure 2-14a,b, for the same printed density of 92%, Specimen E-60 contains larger pores than Specimen E-100 (90 versus 75 µm), but their number per surface area is fewer (106 versus 158 p/mm^2). Some trends, however, become visible when plotting the pore number, size and circularity as functions of the h/t ratio for different $VED - BR$ sets (Figure 2-15). For $h/t > 1.5$ (under this value, no trend can be observed), pore number and size follow a trend opposite to that of pore circularity: for each $VED - BR$ set, the pore number and size first decrease to reach a minimum at h/t = 2.7and then increase, while the pore

circularity first increases to reach a maximum at h/t = 2.7 and then decreases. As a result, the E set results in the smallest number of pores and their highest circularity, while the B set results in the highest number of pores and their lowest circularity. These two $VED - BR$ sets were already established as the best and the worst in terms of the predicted and measured printed densities.

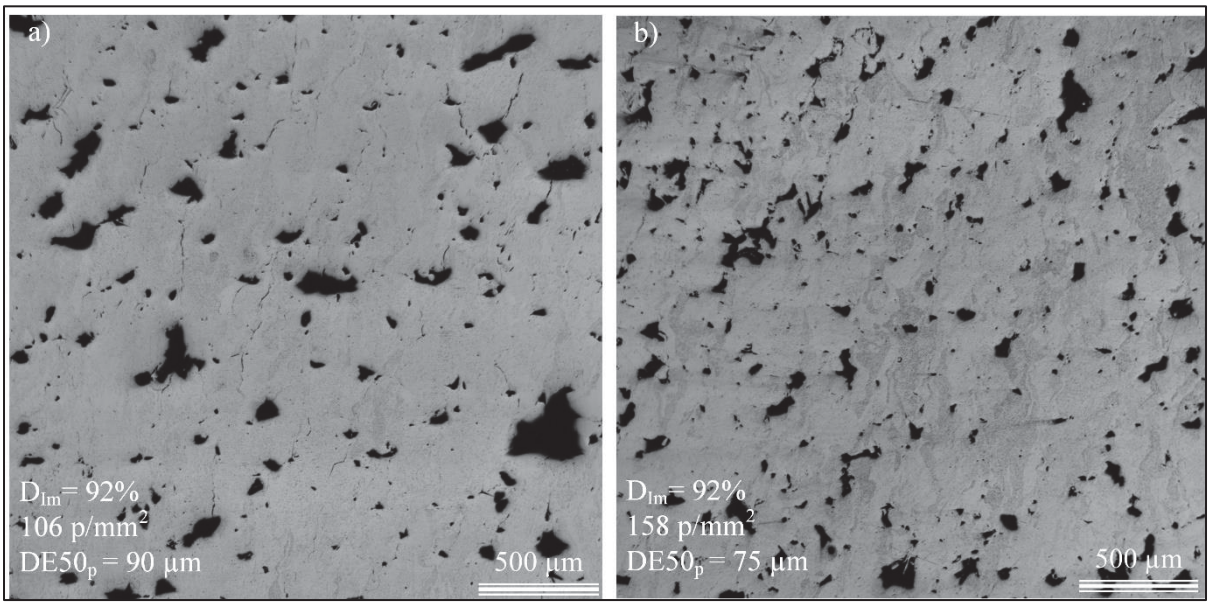

Figure 2-14 : Microscopic observations of a) Specimen E-60 and b) Specimen E-100 having the same printed density of 92% but different pore sizes and pore densities

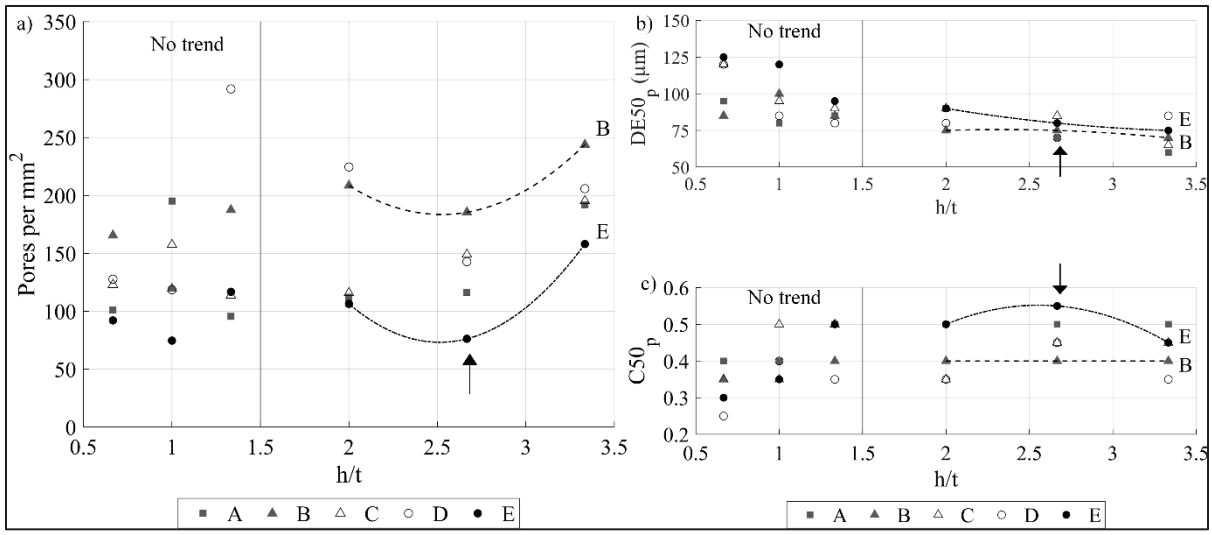

Figure 2-15 : a) Pore density, b) pore size and c) pore circularity as functions of the h/t ratio for five $VED - BR$ sets (arrows indicate extrema, trend lines are added for visualization purposes)

2.6.3.2 Grain Structure

Regarding the microstructure, no correlation could be established with either density or number of pores. As illustrated in Figure 2-16a,b, some specimens with the same printed density manifest different pore and grain structures ($D50_g$ ϵ [40; 220] µm). Also, the grains are quite elongated ($C50_g$ ϵ [0.2; 0.6]) and tend to follow the build direction. Finally, the crystallographic texture of all the specimens was analyzed, and, as can be seen on the pole figures for Specimen E-80 (Figure 2-16c), no preferential crystallographic orientation was found.

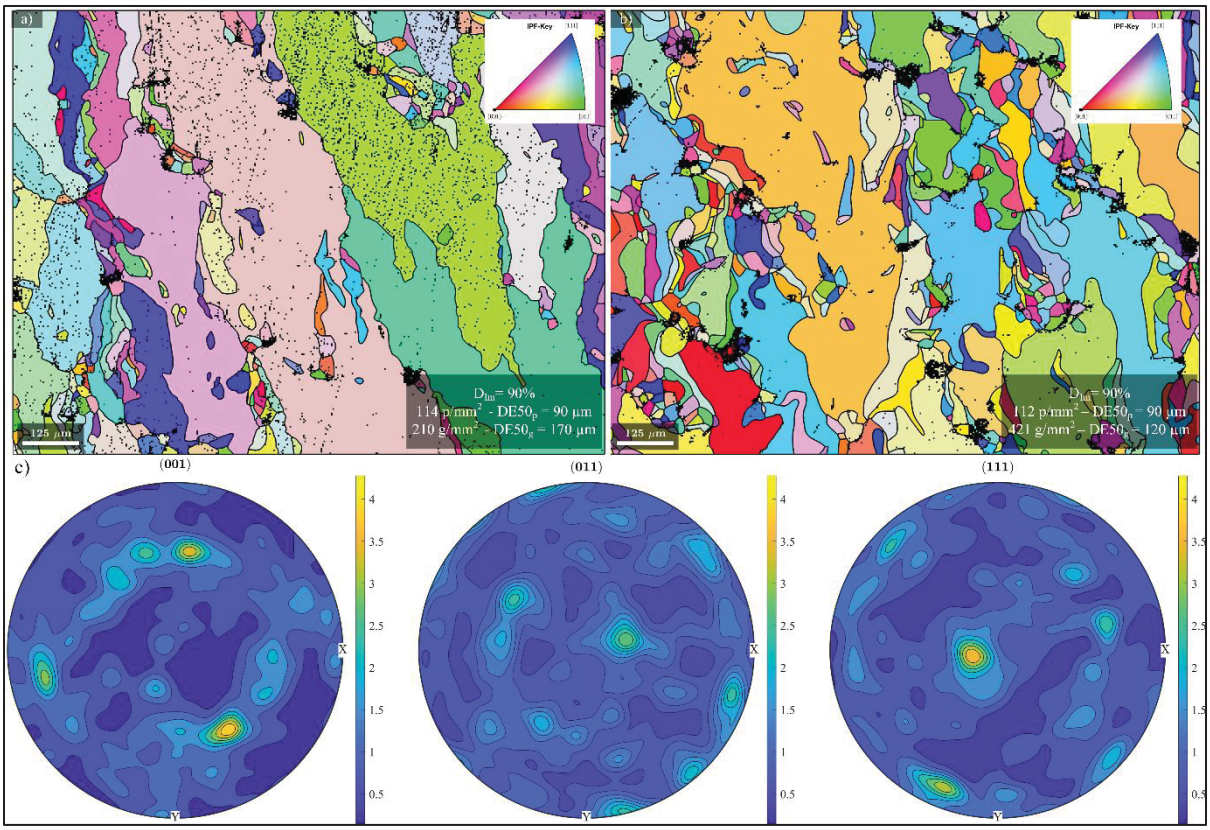

Figure 2-16 : EBSD maps (IPF Y) for specimens a) C-40 and b) A-60 with the same printed density of 92% but different pore and grain structures, and c) example of the pole figures corresponding to Specimen E-80

2.6.4 Compression Testing

In Figure 2-17, the UCS values are plotted as functions of the h/t ratio for all five $VED - BR$ sets, and it can be observed that, similarly to the printed density (Figure 2-13b), the UCS first increases to reach the maximum at h/t = 2.7 and then decreases. Also, for any h/t ratio, the E specimens show the highest strength, while the B specimens demonstrate the lowest. Thus, an initial selection of the best process parameters based on the printed density is justified, this combination being VED = 417 J/mm^3 and BR = 1.62 cm^3/h, with h/t = 2.7 (P = 188 W, v = 188 mm/s, h = 80 µm and t =30 µm).

Moreover, even though no quantitative relationships can be established between the compression strength and the pore and grain structures, some worthwhile qualitative

observations can be made. Figure 2-17a shows that the maximum strength is reached at h/t = 2.7with print set E, when the number of pores is the smallest and their circularity is the highest (see Figure 2-15a,b). On the other hand, maximum compression strain in Figure 2-17b was obtained with print set B at the expense of its lower mechanical resistance, which is a logical outcome.

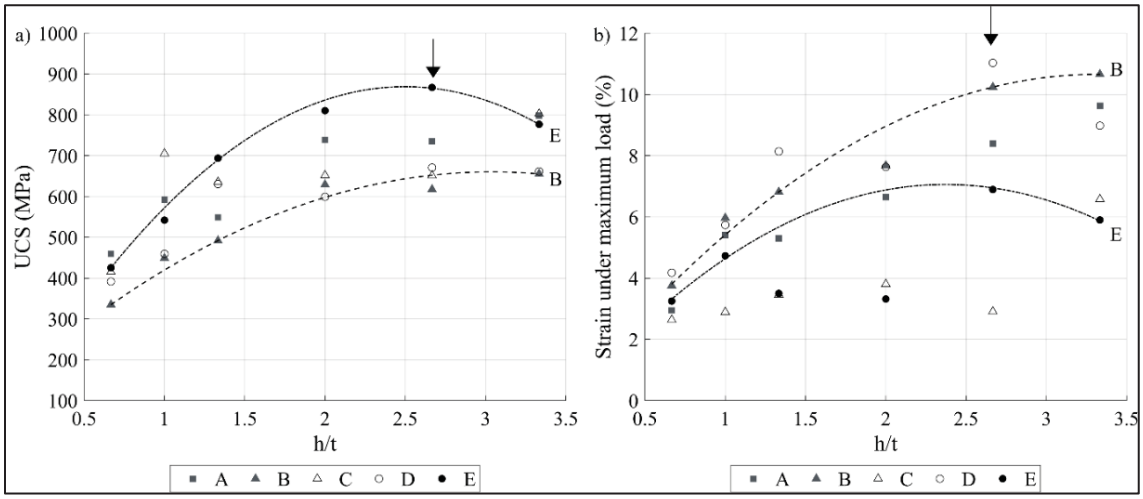

Figure 2-17 : a) UCS and b) compression strain under maximum load
as functions of the h/t ratio for five $VED - BR$ sets
(arrows indicate maxima, trend lines are added for visualization purposes)

In Figure 2-18, the ultimate compression strength values are plotted as functions of the strain under maximum load. Each dot represents one specimen and is colored according to its measured printed density. Overall, the higher the density, the higher the strength and the lower the strain under maximum load. During compression testing, two rupture modes were observed: in some specimens, a net fracture was observed, oriented at 45° to the compression direction without the crushing typical of the brittle material behavior, and in others, a complete crushing of the specimens was seen with many crack initiations, reflecting a more ductile behavior. These two failure modes could be linked to the measured maximum compression strain as follows: specimens with ductile compression failure manifest a maximum compression strain >6%, whereas specimens with brittle compression failure correspond to a maximum compression strain <6%.

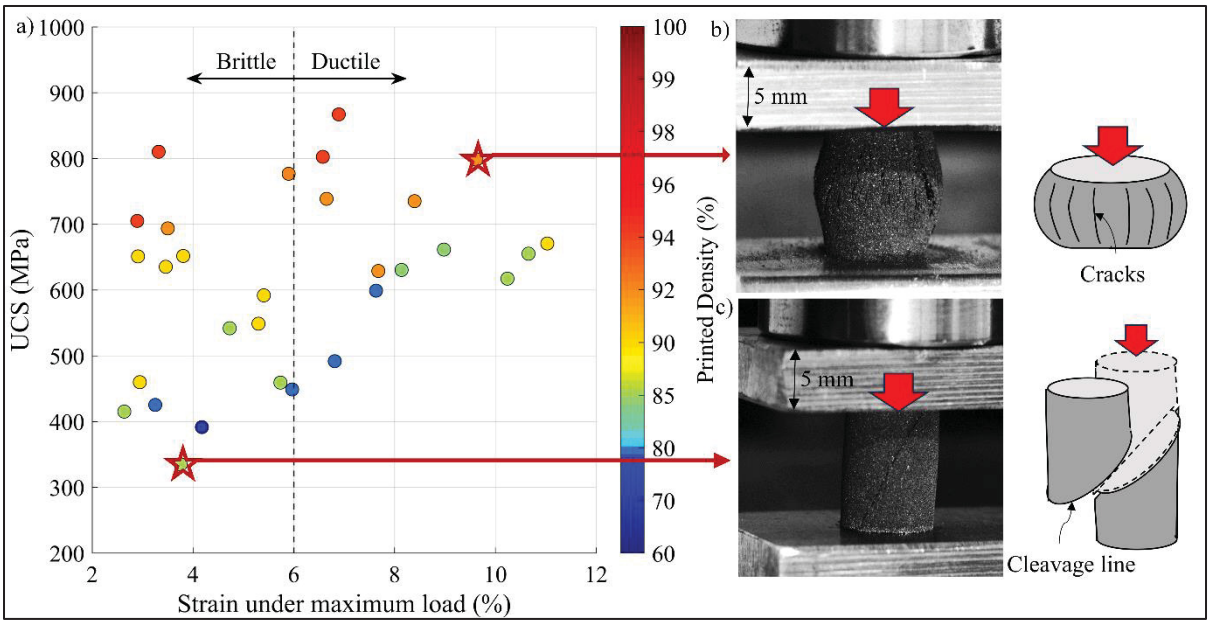

Figure 2-18 : a) UCS versus strain under maximum load (printed density is presented in color) showing a brittle-to-ductile failure separation line at 6%; photo and schematic representation of the b) ductile and c) brittle rupture modes

Furthermore, mechanical properties were related to printed densities and the number of pores. A multivariate analysis of variance (MANOVA) showed that a relation between the material strength, printed density and number of pores (APPENDICE A

Name	Hatch-ing Space (µm)	Power (W)	Speed (mm/s)	Volumetric Energy Density (J/mm3)	Built Rate (cm3/h)	Predicted Density (%)	Image Analysis Density (%)	Absolute Error between Densities (%)
A-100	100	140	40	1167	0.43	89.7	91.2	1.5
B-100		90	40	750	0.43	70.0	83.5	13.5
C-100		179	80	750	0.86	93.9	93.5	0.4
D-100		188	150	417	0.86	76.3	81.5	5.2
E-100		100	80	417	1.62	93.1	91.8	1.3

Tableau-A A-2) cannot be denied with a 95% confidence interval: the higher the printed density and the smaller the number of pores, the higher the UCS values. However, to decouple the impact on the material resistance of printed density from that of structural features (pore and grain sizes), statistics provided by the present study are not large enough. Finally, in the framework of this study, no relation could be established between the pore and grain structures and the strain at maximum load.

2.6.5 Analyses of the Crystalline Phases and Oxides

It was established that the h/t ratio of 2.7 led to the best physical and mechanical properties overall. Thus, the five corresponding specimens (A-80, B-80, C-80, D-80 and E-80) were selected for the XRD analysis (Figure 2-19a). The same results were found for all of them: four diffraction peaks could be indexed to the cubic structure of tungsten (ICDD 00-004-0806), but no signs of any oxide could be found. Knowing the limitations of this technique, if there were any oxides, their presence would be less than 5%. To further investigate potential signs of oxidation, the EDS and XPS analyses were conducted on the fracture surfaces of the best (E-80) and the worst (A-80) specimens in terms of their physical and mechanical properties. At first glance, the EDS analysis did not detect any trace of oxygen (Figure 2-19c). Then, after analyzing the interior of selected regions, some traces of oxygen were revealed (Figure 2-19d). In these locations, irregularities of the fracture surface were observed, highlighting the potential presence of oxides. This hypothesis was then confirmed by the XPS analyses (Figure 2-19b), which revealed the presence of WO_3 (binding energy BE between 35.8-36.1 eV), as well as traces of WO_2 (BE between 31.8–31.9 eV). Since no quantitative analysis was possible, oxidation can be considered to not have a dominant effect on the causes of rupture of these specimens.

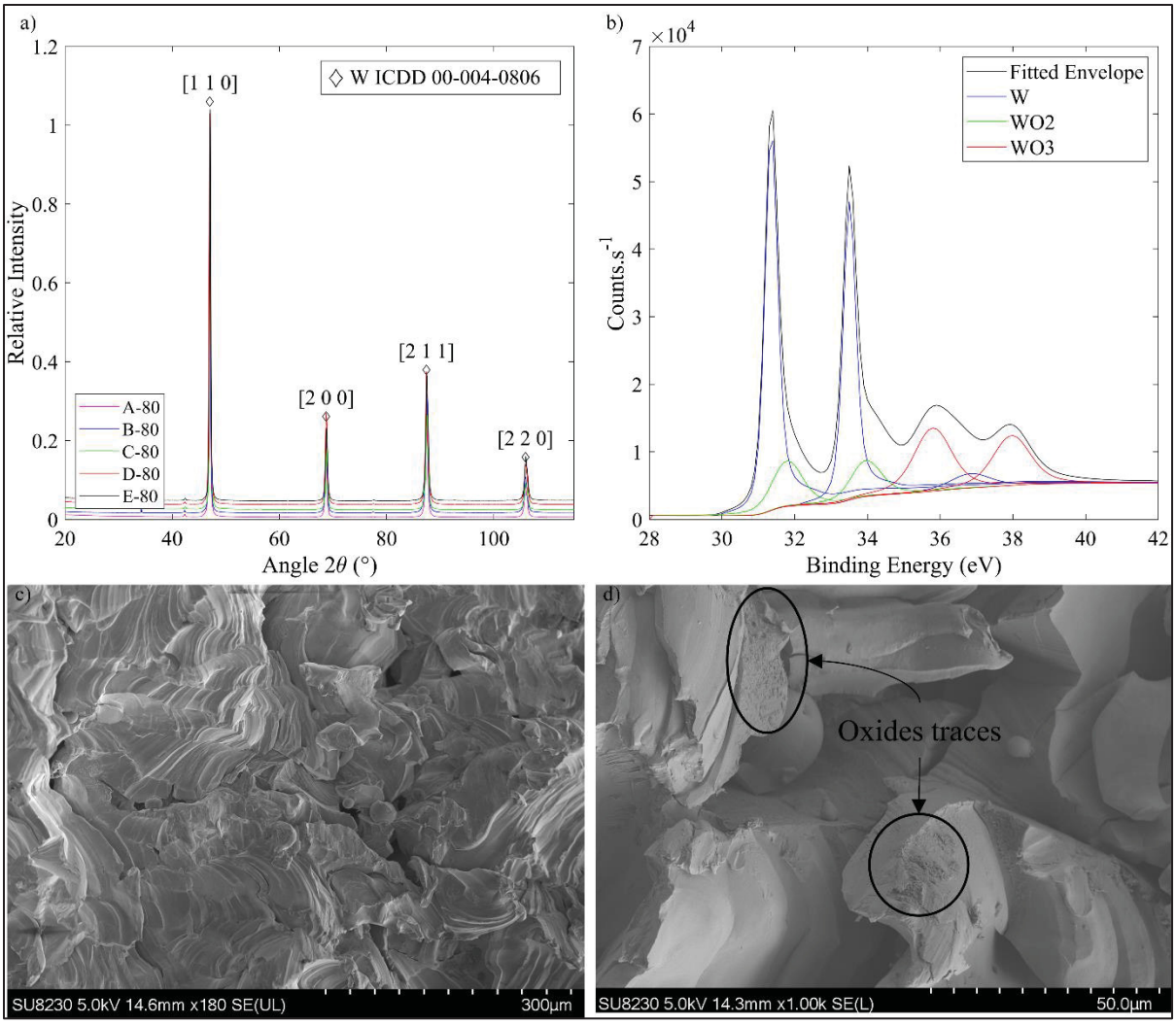

Figure 2-19 : a) XRD analyses of the selected specimens (A-80, B-80, C-80, D-80 and E-80), with four detected crystallographic orientations indicated by a diamond sign; b) XPS analysis of the specimen E-80; c) EDS observation of the fracture surface of Specimen E-80; d) EDS observation with a closer look at some traces of oxides

2.6.6 Printable Geometric Features

Geometric artifacts presented in Figure 2-20 were printed with the optimized E-80 parameters set and contain design attributes of interest, i.e., gyroid lattice structures and gap and wall thickness artifacts. The measured relative densities of the lattice structures were 41.2 and 44.2% as compared to the nominal values of 40 and 50%, respectively. Thus, lower porosity gyroid structures manifested a better conformity between the printed and nominal density

values. The minimum printable gap corresponded to 0.1 mm, whereas the minimum printed wall corresponded to 0.2 mm. To assess the printing resolution, the measured and nominal dimensions of both the gaps and the walls were compared and subjected to a linear regression analysis (Figure 2-21). For the walls and the gaps, the direction coefficients were close to 1 (0.99 and 0.89, respectively, with a p-value < 0.05), as well as the $R2adj$ (0.99 and 0.94, respectively), and the $RMSE$ values were 0.04 and 0.14, respectively, with no patterns in the residuals. The constant was not statistically significant for the gaps (p-value > 0.05) but amounted to 0.24 mm for the walls, meaning that they were ~0.2 mm thicker than their nominal values. A beam offset adjustment must be considered to rectify this systematic error.

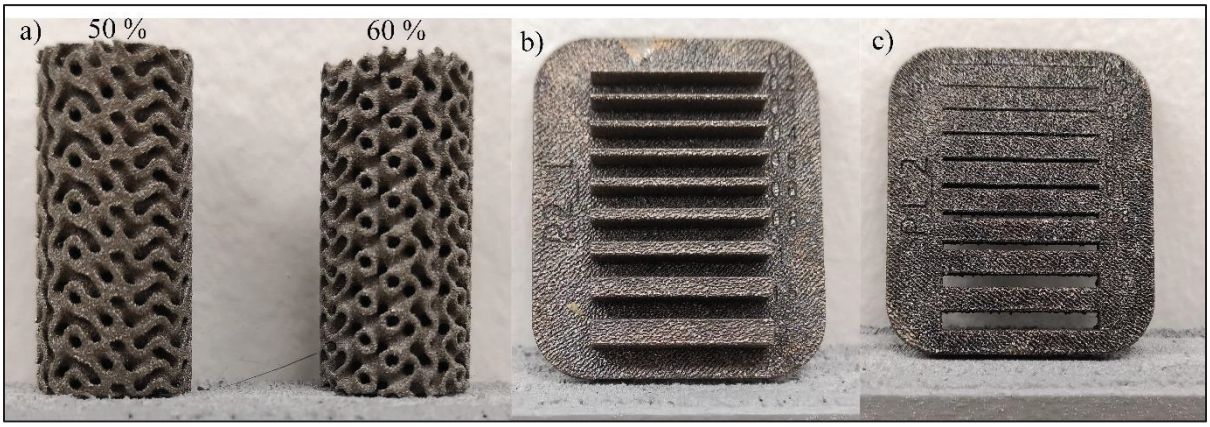

Figure 2-20 : Printed design artifacts: a) gyroids (numbers correspond to nominal printed densities), b) wall and c) gap artifacts

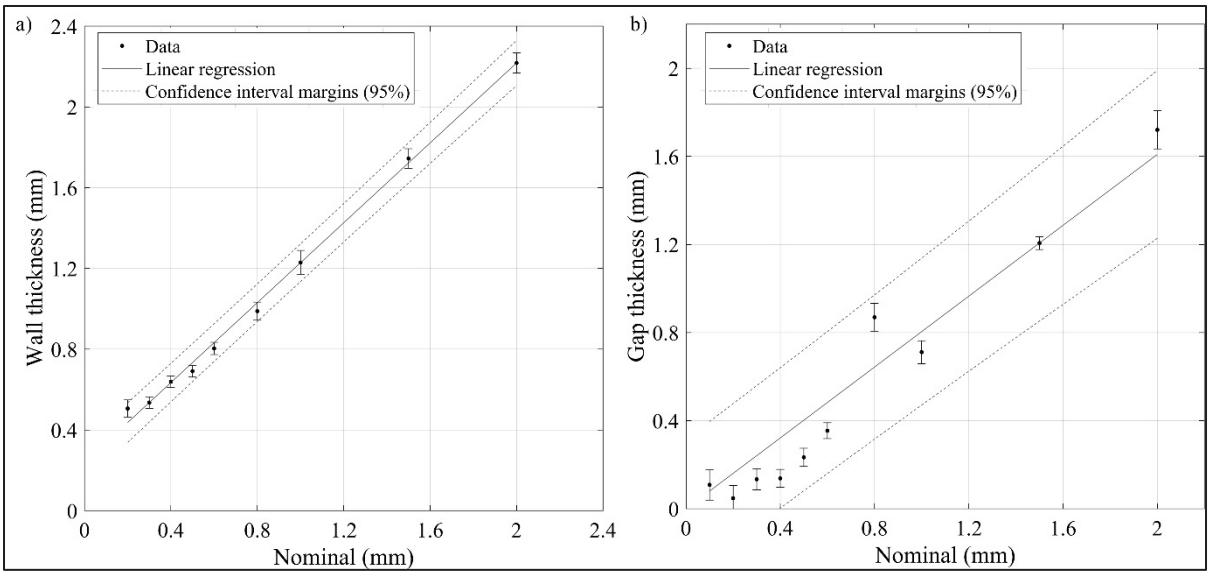

Figure 2-21 : Linear regression between the nominal and the microscope-measured thicknesses of a) walls and b) gaps

2.7 Discussion

The present study allowed for the maximization of the printed density and mechanical properties of pure tungsten specimens produced from a specific powder feedstock (µm) (D10 = 16, D50 = 27 and D90 = 41) on a given LPBF printer (TruPrint 1000 from Trumpf). To determine the relevance of our results, comparisons were made first with an industrial standard for tungsten parts produced by powder metallurgy B777-15 (B10 Committee, 2013) and then with the literature. This standard for "machinable, high-density tungsten base metal produced by consolidating metal powder mixtures, the composition of which is mainly tungsten" contains requirements for the mechanical properties and chemical composition of generic tungsten-based parts for their use at room temperature. The first comparison reveals that some specimens printed in this study reached classes 1 and 2, which correspond to the most stringent requirements for tungsten parts. However, this comparison must be interpreted with caution since the standard stipulates the tensile resistance of tungsten parts, while in present study, compression properties were measured and no requirements for these properties were found in the literature. Furthermore, the mechanical properties of specimens obtained in this study were compared with the best published data on pure tungsten LPBF parts (Tan et al.,

2018), as well as with the reference data resulting from other tungsten forming processes (Figure 2-22a). It can be seen that results of the present study are relatively close to those from LPBF and spark plasma sintering (SPS) (Tan et al., 2018) but sufficiently far apart from those of other processes, such as hot isostatic pressing (HIP) and powder metallurgy (PM).

Figure 2-22b presents a more detailed comparison between the UCS values of this study and those from the LPBF literature (M. Guo et al., 2019; Shi et al., 2023; Tan et al., 2018). It appears that for an equivalent relative density, specimens with thinner layers manifest a higher mechanical resistance. Moreover, in most studies, specimens are printed using more powerful LPBF printers, more specifically 400 W laser printers, versus the 200 W laser TruPrint 1000 unit used in the present study. Two main avenues for improvement of the mechanical properties of printed tungsten parts can therefore be contemplated: a) through the use of finer powders, and therefore thinner layers, and b) through the use of more powerful LPBF systems.

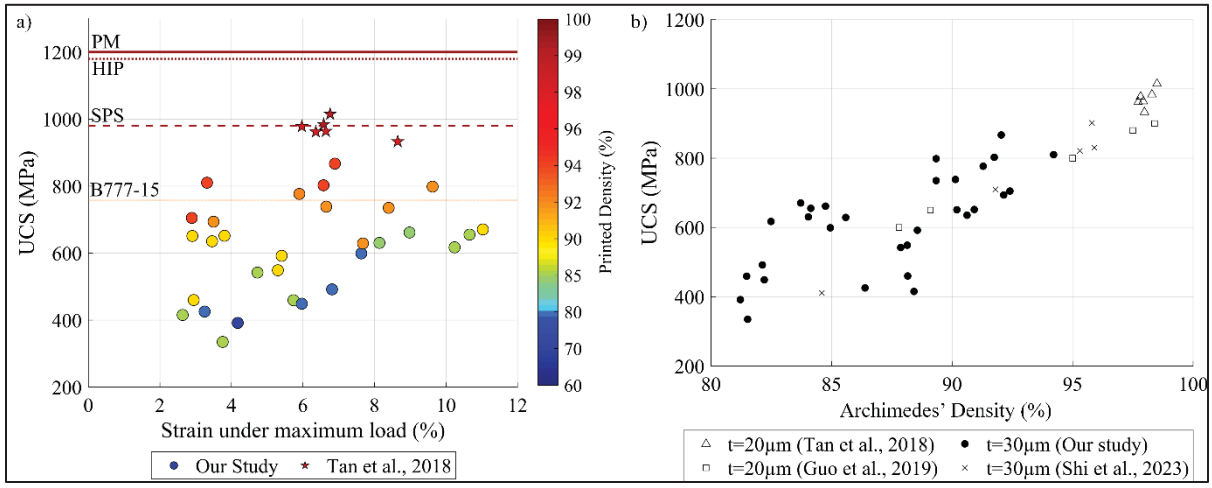

Figure 2-22 : a) Comparison of the mechanical properties of pure tungsten LPBF specimens (our study and Tan et al. (2018)) and tungsten parts formed by other processes Tan et al. (2018); b) UCS vs printed density of LPBF tungsten specimens for different layer thicknesses (data from M. Guo et al. (2019); Shi et al. (2023); Tan et al. (2018))

To investigate the potential impact of using a more powerful laser, such as 400 W (example M290 of EOS) as compared to 200 W (example TruPrint 1000 of Trumpf), and a thinner layer,

such as 20 µm as compared to 30 µm, two numerical studies were carried out using the model developed in this study.

For the first study, two different lasers (200 W) and (400 W) and two different layer thicknesses (t = 20 and 30 µm) were considered. The process parameters used for both lasers were the same and corresponded to the E $VED-BR$ set identified as having the best processing conditions from the results of previous experiments with a 200 W laser (417 J/mm^3; 1.62 cm^3/h). Moreover, the powder feedstock properties were also kept unchanged, and that despite the fact that this enabled the use of thinner layers, finer powder feedstocks than that used in this study must be considered. From this first study, the following observations can be made (see Figure 2-23a):

- For both layer thicknesses and both lasers, the predicted printed density evolves similarly: it increases as a function of the h/t to reach a maximum and then decreases. Globally, the thinner the layer thickness, the larger the recommended h/t ratio, irrespective of the laser power. In more detail, for the 200 W laser, when the layer thickness decreases from 30 to 20 µm, the recommended h/t value increases from 2.5 to 3, (stars, Figure 2-23a), and for the 400 W laser, when the layer thickness decreases from 30 to 20 µm, the recommended h/t value increases from 3 to 3.5 (triangles, Figure 2-23a);
- Printing with both devices using the same $VED-BR$ set leads to the following conclusion: the thinner the layers, the higher the predicted density, where the maximum predicted density for a 200 W laser is 97%, while for a 400 W laser, this density is 95 %.

The last observation is surprising, given the higher available laser power of the 400 W printer. The explanation for this discrepancy is, however, simple: it is the use with the 400 W printer of the printing parameters optimized for the 200 W printer. Knowing that the two systems have different beam spot diameters (55 µm for the 200 W laser and 100 µm for the 400 W laser) and different maximum laser powers, it is not surprising that the optimal parameters for the two systems are different. Thus, a second numerical study has been carried out to estimate a

possible increase in the printed density when using the 400 W printer with its specific optimized process parameters (444 J/mm^3; 3.24 cm^3/h) but different layer thicknesses (30 and 20 µm) (Figure 2-23b). From this study, the following observations can be made:

- Trends of the predicted density according to the h/t ratio are the same as in the previous numerical study. Also, for the 400 W printer, h/t leading to the maximum predicted density is 3, irrespective of the layer thickness, meaning that no improvements can be made to 400 W printers using thinner layers;
- Considering the optimal printing parameters for each of the printers, the 400 W printer leads to a higher maximum predicted density than the 200 W printer: 99 as compared to 97%.

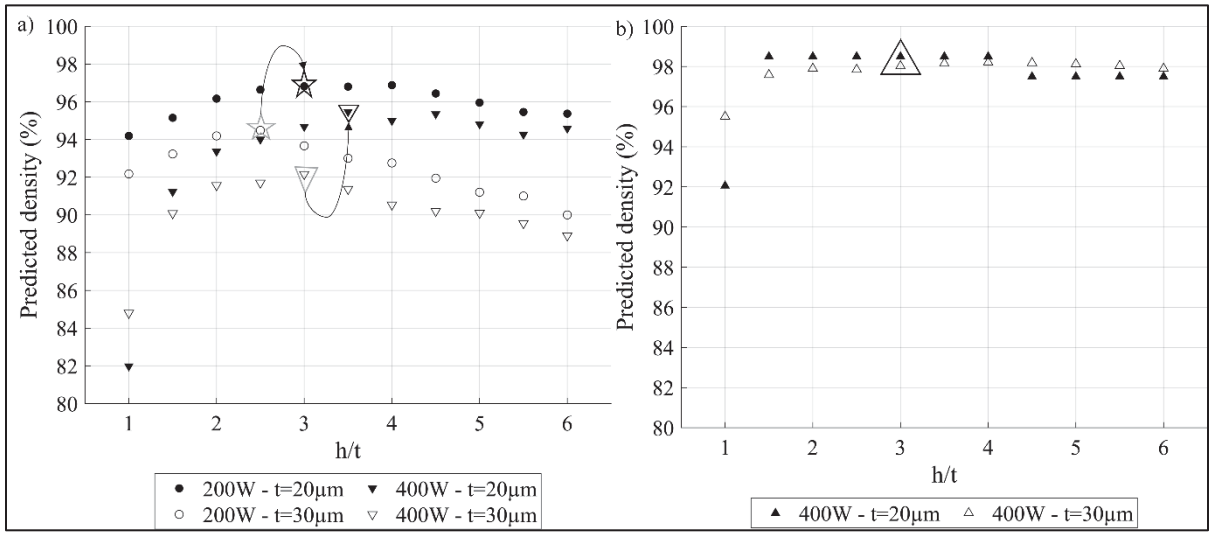

Figure 2-23 : Predicted density for two layer thicknesses (20 and 30 µm) as a function of the h/t ratio: a) using the $VED - BR$ set E (417 J/mm^3; 1.62 cm^3/h) optimized for the 200 W laser and b) using the $VED - BR$ set (444 J/mm^3; 3.24 cm^3/h) specifically optimized for the 400 W laser

Based on the preceding, it can be assumed that the density of printed parts, and therefore their mechanical strength, can be increased by reducing the layer thickness and increasing the laser power (to be experimentally verified in a future study). Moreover, reducing layer thickness would also improve the print resolution, as reported in (Brika et al., 2020). Using the results

of these two studies, the optimized sets of printing parameters leading to the maximum predicted densities potentially reachable on both devices are shown in Tableau 2-5.

Tableau 2-5 : Optimized sets of printing parameters and corresponding printed densities for 200 and 400 W LPBF printers (numerical predictions)

Layer Thickness (µm)	Device	Power (W)	Speed (mm/s)	Hatching Space (µm)	$VED - BR$ (J/mm^3; cm^3/h)	Predicted Density (%)
20	200 W	188	375	60	(417; 1.62)	96.9
	400 W	400	750	60	(444; 3.24)	98.7
30	200 W	188	200	75	(417; 1.62)	93.7
	400 W	400	333	90	(444; 3.24)	98.6

Reducing the number of structural defects and controlling the microstructures are other ways to improve the physical and mechanical characteristics of printed tungsten parts. According to the Hall–Petch relationship, the smaller the grain size, the higher the mechanical strength (B10 Committee, 2013). However, since refractory metals are mainly used for high-temperature applications, it is more reasonable to decrease the number of grain boundaries, thus moving towards single crystal-like textures (Durand-Charre, 2017; Jiao et al., 2023; Kassner, 2015; Koizumi et al., 2004; Milne, Ritchie, & Karihaloo, 2003; Reiser & Hartmaier, 2020; Taylor, 1965; Whang, 2011). Furthermore, the mean measured grain size range of this study is ~100 µm, which leads to a ductile–brittle transition temperature (DBTT) ranging between 500 and 700 K, which for its part corresponds to the maximum reported DBTT temperature (Koizumi et al., 2004; G. Yang & Park, 2019). To decrease the DBTT temperature, either ultrafine or single crystal-like grain structures are both legitimate targets. For the same reasons as previously mentioned with respect to the strength, a single crystal-like microstructure should be privileged. Therefore, HIP treatment is potentially well-suited to coarsen the microstructure of LPBF tungsten specimens while simultaneously reducing process-induced porosity. Even if there are only few studies on the impact of HIP on the LPBF tungsten parts, some of them already showed the beneficial effects of HIP on the density, microstructure and thus the mechanical properties. For example, (J. Chen et al., 2020) reported that the use of HIP allowed for an increase in the printed tungsten part density, a reduction in voids and cracks, improvements of the microstructure (more equiaxed structure, larger grain size) and an

increase in the thermal conductivity. Furthermore, (Shi et al., 2023) also reported an increase in the UCS and a decrease in microhardness after the HIP treatments.

Finally, (Vrancken et al., 2022) highlighted that cracks occur at temperatures of the same order of magnitude as the tungsten DBTT (around 570 K), regardless of the laser energy density. To reduce the DBTT and therefore improve the LPBF manufacturability of tungsten parts, adding rhenium could be suggested (Okamoto, 1998; Ren et al., 2018; Yih & Wang, 1979). This approach was implemented in (Stephens, J. R., 1972) for three different alloy compositions (W-10%Re, W-3%Re and W-1%Re) and compared to pure tungsten. This study particularly highlights a reduction in the size of cracks with an increase in the rhenium percentage. In addition to this advantage, it has been shown that combining tungsten with rhenium can also improve the material hardness and strength (Lakshmi Prasad & Raja Annamalai, 2021; Ren et al., 2018; Yamamoto, Hara, & Hatano, 2021). It was also reported that the beneficial effect of rhenium addition occurs when its concentration is either low (5 at%) or close to the maximum solubility of rhenium in tungsten (25 at%) (Ren et al., 2018).

2.8 Conclusions

- A numerical model based on simple analytical considerations of the LPBF process was developed to calculate the melt pool dimensions and predict the part density. The melt pool calculations have been validated using experimental data taken from the literature, and the density predictions were validated through experiments;
- Structural analyses revealed that the specimens are crack-free, but some of them possess unfused powder particles inside the pores, which means that the Archimedes' measurements overestimate the part density;
- A strong link between the physical and mechanical properties of the printed specimens and the process parameters was established, namely that:
    a. Density and strength first increase and then decrease according to the h/t ratio, whatever the selected $VED - BR$ set;
    b. A ratio of h/t = 2.7 was established as the best for all the $VED - BR$ sets;

c. A VED = 417 J/mm^3 - BR= 1.62 cm^3/h parameters set was found to lead to the best properties irrespective of the h/t value.

Thus, the best properties (density = 93.2%, $UCS = 867$ MPa and $\delta = 6.9$ %) were obtained for P = 188 W, v = 188 mm/s, h= 80 µm and t = 30 µm.

The above trends were also predicted by the model, meaning that the latter is relevant to predict the printed density as a function of the process parameters, at least in the framework of this study. If a more extensive validation of the model is carried out (different printers and powder feedstocks), this model could be generalized for use with other materials and other LPBF printers.

- Using the defined optimal set of parameters, gyroid lattice structures and wall and gap artifacts were printed. The comparisons between the nominal and the measured characteristics enable the conclusion that this set of parameters also leads to good printability and small printable limits;
- Comparisons with the literature followed by numerical studies using the developed model revealed that the printed density can be improved when considering thinner layers, more powerful LPBF devices, post-treatments and alloying. Also, the processing parameters must be specifically optimized for each individual printer and powder feedstock when such changes are made.

2.9 Future Work

The results of this study offer several avenues for future development. First, the numerical model needs to be tested and validated on different printers, powder feedstocks and materials in order to attest its robustness. Once this validation completed, it could become a powerful tool for the implementation of new LPBF-ready materials. Moreover, post-treatment and/or alloying studies should be carried out to improve the mechanical properties of tungsten-based parts produced by LPBF. Other mechanical testing routines (elevated temperature testing,

fatigue, etc.) could also be envisaged to complete the mechanical characterization of printed tungsten parts. Finally, other geometries could be printed to enrich the printability study of this material.

2.10 Author Contributions

Conceptualization, A.L. and V.B.; methodology, A.L. and V.B.; software, A.L.; validation, V.B.; formal analysis, A.L.; investigation, A.L.; resources, V.B.; data curation, A.L.; writing—original draft preparation, A.L.; writing—review and editing, V.B.; visualization, A.L. and V.B.; supervision, V.B.; project administration, V.B.; funding acquisition, V.B. All authors have read and agreed to the published version of the manuscript.

2.11 Funding

The authors also acknowledge the financial support provided by PRIMA Québec (Pôle de recherche et d'innovation en matériaux avancés) in the framework of the M-ERA.NET program, NSERC (Natural Sciences and Engineering Research Council of Canada) and PyroGenesis Canada inc.

2.12 Institutional Review Board Statement

Not applicable.

2.13 Informed Consent Statement

Not applicable.

2.14 Data Availability Statement

Data are contained within the article.

2.15 Acknowledgments

The authors acknowledge the contributions of Salah Eddine Brika in the pow-der analysis, Anatolie Timercan in the printing and Atefeh Tafti, Antoine Tahan and Thibault Mouret in specimen preparation and analyses using experimental techniques and statistical analyses.

2.16 Conflicts of Interest

The authors declare no conflicts of interest. The funders had no role in the design of the study; in the collection, analyses or interpretation of data; in the writing of the manuscript; or in the decision to publish the results.

CHAPITRE 3

LASER POWDER BED FUSION OF MOLYBDENUM: DENSITY, STRUCTURE AND MECHANICAL PROPERTIES AT ROOM AND ELEVATED TEMPERATURE

Aurore Leclercq[a], Thibault Mouret[b] and Vladimir Brailovski[c]

[a,b,c]Département de Génie mécanique, École de Technologie Supérieure,
1100 Notre-Dame Ouest, Montréal, Québec, Canada H3C 1K3

Article publié dans « Materials Science & Engineering A », février 2025

3.1 Avant-propos

En raison de son excellent rapport résistance mécanique (haute température)/densité et de sa meilleure capacité à former des revêtements de protection contre l'oxydation, le molybdène a été considéré plutôt que le tungstène pour la fabrication de l'injecteur de la turbine. Dans ce deuxième article, la méthodologie précédemment développée pour l'introduction du tungstène par le procédé de fusion laser sur lit de poudre est appliquée à du molybdène pur. Après avoir obtenu un ensemble de paramètres de fabrication menant à des échantillons non fissurés à haute densité, des essais mécaniques ont été réalisés jusqu'à 1000 °C, température pour laquelle les métaux réfractaires commencent à montrer leur intérêt. Ces tests ont permis de mettre en avant la sévérité des phénomènes d'oxydation sur ce matériau mais ont démontrés que les paramètres retenus permettaient l'obtention de pièces aux propriétés mécaniques comparables à celles obtenus par des procédés conventionnels de métallurgie des poudres, et ce sur une large plage de températures. Enfin, la production de différentes géométries a révélé le potentiel de cette technologie pour la production de pièces complexes.

3.2 Résumé

Le molybdène est un matériau d'un grand intérêt industriel en raison de ses propriétés spécifiques, notamment à des températures élevées. Les technologies de fabrication additive

ont récemment été proposées comme alternative aux procédés conventionnels de métallurgie des poudres en raison de leur flexibilité dans la production de géométries complexes. Dans cette étude, les interrelations entre les paramètres du procédé de fusion laser sur lit de poudre et les propriétés structurales et mécaniques des échantillons de molybdène imprimés sont étudiées afin de proposer un ensemble optimal de paramètres de fabrication. Pour soutenir cette approche, un plan d'expériences a été construit en utilisant une simulation numérique simplifiée du champ de température entourant le bain de fusion. Cette approche a conduit à la production de spécimens sans fissures avec une densité imprimée de 97 %, une contrainte ultime de 510 MPa, une limite d'élasticité de 340 MPa et une déformation maximale à rupture de 11 % (tout en compression à température ambiante) en utilisant un ensemble optimisé de paramètres d'impression $P = 179$ W, $v = 133$ mm/s, $h = 60$ µm et $t = 30$ µm. Les essais de compression dans la plage de température de 20-1000°C ont révélé que les propriétés mécaniques du molybdène imprimé (contrainte ultime de 260 et 150 MPa à 800 et 1000°C, respectivement) sont comparables à leurs homologues fabriqués par métallurgie des poudres conventionnelle. L'impression d'une série d'artefacts géométriques, tels que des murs (jusqu'à 0,1 mm d'épaisseur), des gorges (jusqu'à 0,3 mm de largeur) et des structures lattices (gyroïdes à 50 et 60 % de porosité), a prouvé le potentiel de la fusion laser sur lit de poudre pour produire des pièces complexes en molybdène pour des applications sur une large plage de température.

3.3 Abstract

Molybdenum is a material of great industrial interest due to its specific properties, particularly at elevated temperatures. Additive manufacturing technologies have recently been proposed as an alternative to conventional powder metallurgy processes because of their flexibility in producing complex geometries. In this study, interrelations between the laser powder bed fusion process parameters and structural and mechanical properties of printed molybdenum specimens are investigated with a bid to propose an optimal set of process parameters. To support this approach, a plan of experiments was built using a simplified numerical simulation of the temperature field surrounding the melt pool. This approach led to the production of crack-free specimens with a printed density of 97%, an ultimate strength of 510 MPa, a yield

strength of 340 MPa, and a maximum strain of 11% (all in compression at room temperature) using an optimized set of printing parameters $P = 179$ W, $v = 133$ mm/s, $h = 60$ µm and $t = 30$ µm. Compression testing in the 20-1000 °C temperature range revealed that the mechanical properties of printed molybdenum (ultimate strengths of 260 and 150 MPa at 800 and 1000 °C, respectively) are comparable to their conventional powder metallurgy manufactured counterparts. Printing of a series of geometric artifacts, such as walls (down to 0.1 mm in thickness), gaps (down to 0.3 mm in width) and lattice structures (50 and 60% porosity gyroids), has proven the potential of laser powder bed fusion to produce complex molybdenum parts for applications over a wide temperature range.

Keywords:

Laser powder bed fusion, Molybdenum, Numerical predictions, Mechanical testing, Elevated temperature, Crack-free specimens, Geometric analysis

3.4 Introduction

Molybdenum (Mo) is a transition metal belonging to the group of refractory metals with a high melting temperature (T = 2896 K / 2623 °C). Its low thermal expansion coefficient ($\alpha_{(25\text{-}500\ °C)}$ = 4.7–5.8 10^{-6}/K) (Hidnert & Gero, 1924), high thermal conductivity (130-140 W/(m.K) (Allen, Glasier, & Jordan, 1960; Rebesan, Ballan, et al., 2021), high mechanical properties (Baker, 1998; « Climax Molybdenum », 1950) and excellent wear and corrosion resistance (Badawy & Al-Kharafi, 1998; Cairang et al., 2021; Hampel, 1958; Shree Meenakshi & Ananda Kumar, 2022; H. Zhao et al., 2023) make this metal and its alloys particularly interesting for industrial applications. Thanks to its high biocompatibility, corrosion resistance and strength and a reduced weight, as compared to some alternatives (tungsten and tantalum), molybdenum is also used in medical applications (Fernandes & Taurino, 2022; Toschka et al., 2022). In the petrochemical industry (Aboul-Gheit, Awadallah, Abdel-Hamid, Aboul-Enein, & El-Desouki, 2012; Mota et al., 2016), like other refractory metals, molybdenum is mainly used as a metal catalyst for selective reactions, but it is also

employed within equipment parts exposed to severe corrosive environments. The mechanical properties of molybdenum at elevated temperatures (ultimate tensile strength ~210 MPa (Baker, 1998) and Young's modulus ~280 GPa at 800 °C (Plansee, 2023)) are exceeded only by those of tungsten, but for almost twice the density (10.2 g/cm^3 for Mo versus 19.2 g/cm^3 for W (J. R. Davis & ASM International, 1998)), making molybdenum appealing for the aerospace, defense and energy applications (Iqbal, Afzal, Khan, Khan, & Qurashi, 2021; L.B. Luntlberg, 1981; Moody, Smith, Haddock, & Dunn, 1976; Santagata et al., 2022; Wadsworth, Nieh, & Stephens, 1988). Finally, molybdenum and its alloys are noteworthy materials in the nuclear safety field. Their ability to absorb neutrons and their high thermochemical compatibility allow to improve the corrosion resistance of parts such as fuel claddings of light water reactors (LWRs) and fast neutron reactors (FNRs)(Cheng, Kim, & Chou, 2016; Duan et al., 2017; Shmelev & Kozhahmet, 2017).

Nowadays, conventional processes, such as those associated with powder metallurgy, followed by additional steps (forging, machining, etc.), remain the most common way to produce semi-finished refractory products such as sheets, rods, wires and tubes. To produce more complex geometries, joining and subtractive processes are used, but their application is hindered by technical issues: during welding, the molybdenum affinity to oxygen risks severe degrading the heat affected zone (Tabernig & Reheis, 2010), and during material removal, the elevated hardness of molybdenum significantly increases machining costs (Schneider, Šimůnková, Michaelis, & Hoogsteen, 2021). To produce complex geometries, additive manufacturing (AM) technologies help overcoming these limitations, thereby offering a promising solution. Furthermore, the recycling of unmelted powders allows to significantly decrease overall processing costs associated with such expensive materials. During the last decades, different AM technologies were used to produce parts from refractory metals and alloys (B. Liu et al., 2024; Talignani et al., 2022). One such technology is the layer-by-layer laser powder bed fusion (LPBF), which applies a laser heat source to sequentially melt one powder layer at a time following a selected pattern corresponding to a sliced 3D-CAD volume of the part to be fabricated. As compared to its principal competitor, electron-beam powder bed fusion (EB-PBF), LPBF stands out due to its higher resolution, printing flexibility and a relatively

lower cost (Colomo et al., 2020; Gradl et al., 2022). Multiple recent publications have covered the use of the LPBF process to produce 3D printed parts from different refractory metals, including tungsten, molybdenum, niobium and tantalum (Leclercq & Brailovski, 2024; Y. Liu et al., 2023; Rebesan, Ballan, et al., 2021; Song et al., 2022). While the printing of any refractory metal poses significant challenges related to their extremely high melting points, the present work focuses on the printability of pure molybdenum.

To overcome the issues reported for molybdenum LPBF printing, strategies are commonly established to mitigate the high sensitivity of molybdenum to hot and cold cracking. As well as the former is concerned, a study (Braun et al., 2019) have highlighted the fundamental role of impurities on the cracking susceptibility of refractory metals. Despite the inert atmosphere in the printing chamber, some residual oxygen enables molybdenum to form oxide MoO_2 which segregates at grain boundaries (GB) during the solidification step due to the low oxygen solubility of body-centered cubic molybdenum. The remaining liquid phase becomes enriched in oxygen and cannot withstand the thermal stresses and strains induced by the process (L. Yang et al., 2023). Since these impurities segregate at GB, the cohesion of the latter decreases, thus leading to their embrittlement. This phenomenon, combined with high temperature gradients and cooling rates accompanying the process, also increases the risk of cold cracking (Braun et al., 2019; Xing et al., 2022).

The above issues inherent to molybdenum highly complicates its 3D printing process. According to the current state of the art, fully dense and crack-free parts are extremely difficult to obtain on printers with power-limited laser sources ($Pmax \leq 200$ W). Only a few authors have claimed to have achieved printed densities greater than 98% with small printers (EOS M100 and SLM-50) (Alinejadian et al., 2023; Rebesan, Ballan, et al., 2021). Apart these cases, printed density reported for small printers is often quite low (between 50 and 90%) (Ellsworth et al., 2022; Faidel et al., 2015), and that despite the use of extremely high volumetric energy densities (VED (3.1) up to 1000 J/mm^3) and low building rates (BR (3.2) down to 0.35 cm^3/h). Note that these last two metrics conveniently aggregate the following process parameters: laser power P (W), scanning speed v (mm/s), hatching space h (mm) and layer thickness t (mm).

$$VED\ [J/mm^3] = \frac{P}{vht} \quad (3.1)$$

$$\text{BR}\ [cm^3/h] = vht \quad (3.2)$$

The use of more powerful printers ($P = 400$ W) appeared to be the solution to increase printed density to up to 99.9%. However, this increase in printed density was frequently achieved at the cost of persisting microcracks (Guan et al., 2023; Higashi & Ozaki, 2020). In addition to the tight control of the printing atmosphere, two technical solutions have been identified and tested in an attempt to prevent the microcrack formation. The first and the more evident solution is to preheat either the build plate or the powder bed to reduce thermal stresses. While direct preheating of the build plate has been reported to be highly ineffective, regardless of the preheating temperature (400 °C in (Iveković et al., 2018) and 1000 °C in (Müller et al., 2019)), laser preheating of the powder bed has shown its efficiency to reduce the microcrack formation. Another technical solution focuses on the optimization of printing parameters or the scanning strategy to control the microstructure and accommodate the thermal stresses generated by the process. An extensive study (Higashi & Ozaki, 2020) using a wide range of parameters highlighted the evolution of the crystallographic texture as a function of process parameters, but did not report any beneficial effect on the cracking occurrence, regardless of the microstructure orientation obtained. Other studies have reported some improvements achieved by modifying the rotational angle between layers (D. Wang et al., 2017) and by optimizing the design of support structures (Müller et al., 2019). However, all these solutions have apparently been insufficient to produce parts that are both dense and crack-free.

To better understand and optimize the process, different numerical tools of various complexity have been developed. To account for the majority of physical phenomena accompanying the LPBF process (solidification, evaporation, condensation, etc.) and determine the optimum powder characteristics and process parameters, some authors proposed 3D coupled thermo-fluid dynamical simulation models (Leitz et al., 2017, 2018). More recently, to simulate the printing of pure molybdenum, a coupled discrete elements model (DEM) and computational fluid dynamics (CFD) model was developed (Y. Wu et al., 2022). The simulation results were

then used with a machine learning algorithm to generate a process map considering both the powder bed and the molten track quality. However, such complex models are time- and computer resource-intensive, and their calibration is extremely delicate. While these simulation tools are useful for detailed studies of physical phenomena underlying the process, they are not well-suited for the process optimization purposes, in which case simpler models are preferred. As an example, (Bajaj et al., 2019) used an analytical heat transfer model to estimate the melt pool dimensions formed by a pulsed laser in high thermal conductivity alloys, including molybdenum. Following correlations with the experimental results, the authors were able to identify the processing window allowing to print high-density crack-free parts (~97%) using a reduced layer thickness of 20 μm.

The present study follows the same cost-effective path of process optimization via the application of a simplified model of the thermal field created by a moving laser source. The melt pool calculations are used to design the experiment and study the effects of process parameters on the structure and mechanical properties of printed parts, with an ultimate goal of optimizing the process parameters. In anticipation of high temperature applications of printed parts, the optimized process parameters are then used to print specimens for testing in the 20 to 1000 °C temperature range. The same optimized process parameters are also applied to print a series of geometric artifacts, such as walls, gaps and lattice structures, in order to demonstrate the ability of the process to produce complex geometries of potential industrial interest.

3.5 Materials and methods

The developed workflow aims to cover different process development phases, including powder characterization, process simulation and the establishment of an experimental setting. These phases are followed by a study of interrelations between the process parameters, the density, the microstructure and the mechanical properties of printed specimens. The final phase of the workflow involves the selection of an optimized set of process parameters, compression

testing over a large temperature range, and the printing of a series of geometric artifacts representative of some potential applications.

3.5.1 Powder characterization

Plasma-spheroidized molybdenum powder (Mo > 99.9%, O ≤ 500 ppm, Hall flow ≤ 15sec./50g) used in this study was produced by Tekna Co. Ltd. (Sherbrooke, Canada). The particle size distribution of D10 = 12.6, D50 = 20.6 and D90 = 32.0 (µm) was measured using a Beckman Coulter LS13 320 XR (Brea, CA, USA) particle size analyzer equipped with a water module, and the particle morphology was observed using a Hitachi TM3000 (Tokyo, Japan) scanning electron microscope (Figure 3-1). The rheological properties of the powder were measured using an FT4 powder rheometer (Freeman Technology, UK) and collected in Tableau 3-1. Based on these measurements, it can be asserted that the selected powder presents good flowability and is suitable for laser powder bed fusion additive manufacturing (Brika et al., 2020).

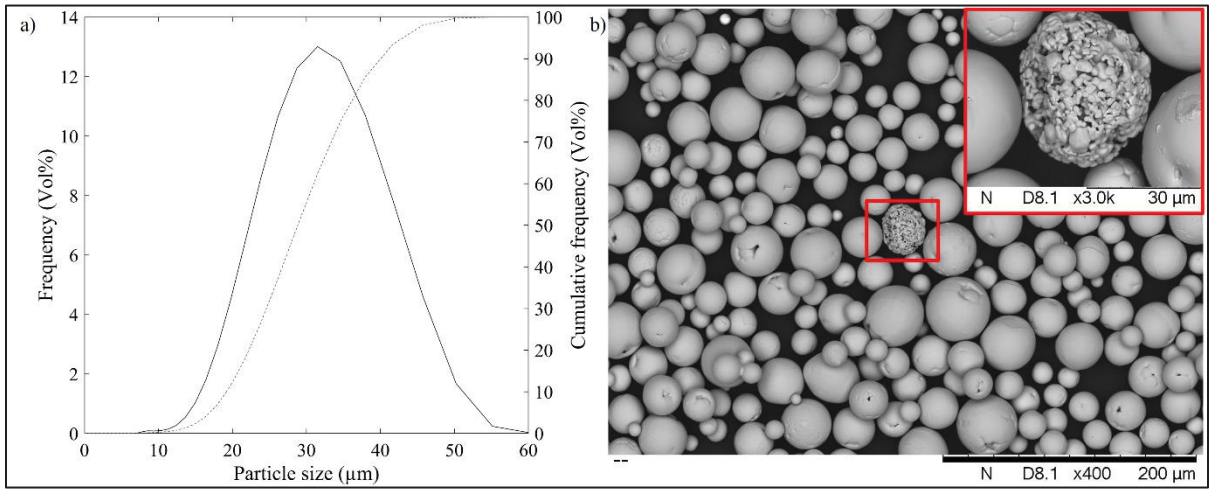

Figure 3-1: Geometry characteristics of molybdenum powder: a) particle size distribution and b) particle morphology

Tableau 3-1: Rheological properties of molybdenum powder (indexes adopted from Brika et al. (2020)): BD (Bulk Density), CI (Compressibility Index), PD (Pressure Drop), SE (Specific Energy), AE_{10} (Aeration Energy at 10 mm/s air velocity) BFE (Basic Flow Energy), CC (Cohesion Coefficient)

BD (g/cm³)	CI (%) at 15kPa	PD (mBar) at 15kPa	SE (mJ/g)	AE_{10} (mJ)	BFE (mJ)	CC (kPa)
6.04 (± 0.47%)	7.65 (± 6.57%)	8.31 (± 8.51%)	2.53 (± 2.65%)	10.60 (± 6.21%)	1084 (± 1.23%)	0.33

3.5.2 Experiments and equipment

To limit the number of specimens needed to study the effects of process parameters on the density, structure and mechanical properties of printed molybdenum, a plan of experiments was built with the help of a melt pool model successfully tested with tungsten powders in (Leclercq & Brailovski, 2024).

3.5.2.1 Numerical model of the melt pool

The numerical model (Leclercq & Brailovski, 2024) used in this work was developed in the MATLAB software (R2022b, MathWorks, USA) environment. This model calculates the melt pool dimensions on the basis of analytical calculations of the temperature field generated by a moving Gaussian heat source in a semi-infinite solid ((3.3)-(3.5)):

$$T(x,y,z) = T_0 + \frac{AP}{kr_f\pi^{\frac{3}{2}}}\int_{+\infty}^{0}\frac{1}{1+\tau^2}exp(C)\,d\tau \tag{3.3}$$

with

$$C = -\left(\frac{\tau^2}{1+\tau^2}\right)\left(\left(\xi - \frac{Pe}{2\tau^2}\right)^2 + \eta^2\right) - \tau^2\zeta^2 \tag{3.4}$$

$$\xi = \sqrt{2}\frac{x}{r_f}\ ;\eta = \sqrt{2}\frac{y}{r_f}\ ;\zeta = \sqrt{2}\frac{z}{r_f}\ ;Pe = \frac{r_f v}{2\sqrt{2}\alpha}\ ;\tau = \frac{r_f}{2\sqrt{2\alpha dt}}\ ;\alpha = \frac{k}{\rho c_p} \tag{3.5}$$

where T_0 is the baseplate temperature (K); A, the absorptivity; P, the laser power (W); k, the thermal conductivity (W/(m.K)); r_f, the laser beam radius (m); Pe, the Peclet number; v, the scanning speed (m/s); α, the thermal diffusivity (m^2/s); ρ, the density (kg/m^3); c_p, the mass heat capacity (J/(kg.K)); and dt, the time (s).

Knowing that during the LPBF process, the feedstock material is not solid, but forms a powder bed, some variables need to be corrected, namely:

- The density, using (3.6):

$$\phi = 1 - CBD; CBD = \frac{BD}{\rho_s} \tag{3.6}$$

where ϕ is the fractional porosity; CBD, the coefficient of bulk density (without unit); ρ_s, the material density (kg/m^3) and BD (kg/m^3), the bulk density measured using an FT4 powder rheometer Tableau 3-1.

- The absorptivity ((3.7)-(3.9)) (Sumin Sih & Barlow, 2004) is calculated using the Hagen-Rubens model approximating the material absorptivity using its electrical resistivity value:

$$\epsilon_{powder} = S_h \epsilon_h + (1 - S_h)\epsilon_s \tag{3.7}$$

with

$$\epsilon_s = A = 0.365 \left(\frac{R_s}{\lambda}\right)^{0,5} \tag{3.8}$$

and

$$S_h = \frac{0.908\phi^2}{1.908\phi^2 - 2\phi + 1} \; ; \; \epsilon_h = \frac{\epsilon_s\left(2 + 3.082\left(\frac{1-\phi}{\phi}\right)^2\right)}{\epsilon_s\left(1 + 3.082\left(\frac{1-\phi}{\phi}\right)^2\right) + 1} \tag{3.9}$$

where ϵ_{powder} is the powder emissivity (absorptivity); S_h, the surface fraction occupied by pores; ϵ_h, the pores emissivity; ϵ_s, the emissivity of a bulk material, R_s; the electrical resistivity of the material (Ω.m) and λ, the laser wavelength (m).

- The thermal conductivity (3.10), following the work of (Bala et al., 1989):

$$k_{powder} = k_s(1 - \phi)^{\frac{4}{3}} \tag{3.10}$$

where k_{powder} and k_s are the thermal conductivities (W/(m.K)) of a powder bed and a bulk material, respectively.

It is clear that during LPBF, the thermal conductivity, the specific heat capacity and the laser absorptivity vary from their values at room temperature to those near the melting point. Since in this model, the material properties are considered constant, it is necessary to find which values must be used to obtain relevant results. To find these values, the model was tested with different sets of the temperature-dependant properties. This study consisted of a series of melt pool simulations, with the material properties varying from their room temperature (RT) to their melting temperature (TM) values (Tableau 3-2).

Tableau 3-2: Properties variation ranges considered as model inputs: Material density is taken from Baker (1998); powder bed density is extracted from the rheometer test (BD, Tableau 3-1); Dense material: Specific heat capacity, thermal conductivity and electrical resistivity extrapolated from Plansee (2023) and absorptivity calculated using equation (3.8); Powder bed: Thermal conductivity and absorptivity are calculated using equations (3.7)-(3.10)

Temperature of Application (K)	State of Matter	Density (kg/m^3)	Specific Heat Capacity (J/(kg.K)		Thermal Conductivity (W/(m.K))		Electrical Resistivity (nΩ.m)		Absorptivity (%)	
Sensitivity study 293 (RT) – 2883 (TM)			RT	TM	RT	TM	RT	TM	RT	TM
	Dense	10220	255	411	141	56	52	744	8	31
	Powder	6040			70	28			19	45
Selected values 0.8 (TM) or 2306	Powder	6040	376		37		590		42	

Results of the melt pool calculations were then compared with their experimental equivalents (Gan et al., 2024; Rebesan, Ballan, et al., 2021) to select the temperature at which these material properties provide the smallest discrepancies between the calculated and measured melt pool sizes. It was found that if the material properties were taken at 0.8TM, the modeled and experimental melt pool sizes were the closest (the same result was obtained for pure tungsten in the reference work). As an illustration, results of the regression analysis between the calculated and experimentally-measured melt pool widths are presented in Figure 3-2a with a directive coefficient of unity, the negligible constant term, $R^2_{adj} = 0.83$, $RMSE = 5$, and without any pattern in the residuals. Also, it can be observed that the more continuous the experimentally measured melt tracks, the closer the model predictions were to the experiment. A visual example of the comparison between the calculated and experimentally-measured melt pool widths is given in Figure 3-2b,c for a specific case of $P = 130$ W, $v = 500$ mm/s and $r_f = 20$ µm, with an initial temperature of 80 °C, and the model properties taken at 0.8TM.

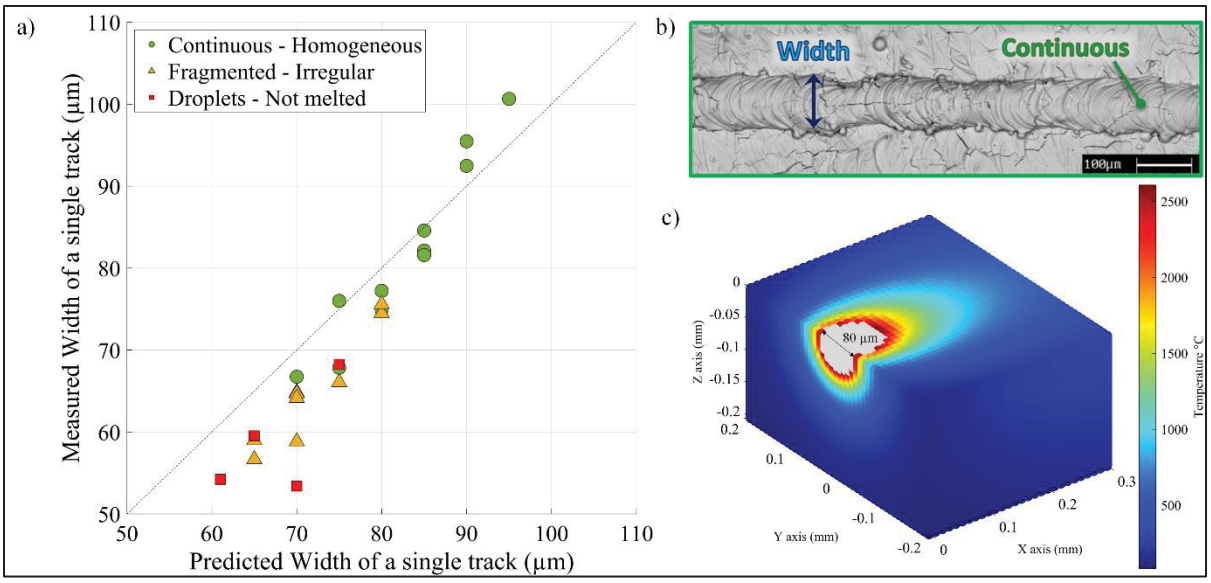

Figure 3-2: a) Comparison between the measured Gan et al. (2024); Rebesan, Ballan, et al. (2021) and calculated melt pool widths for pure molybdenum with 95 % confidence margins; b) photo of a single laser track extracted from Rebesan, Ballan, et al. (2021) ($P = 130$ W, $v = 500$ mm/s, $r_f = 20$ µm) and c) calculated temperature field of the melt pool with properties taken at 0.8TM (Tableau 3-2)

Finally, melt pool dimensions are linked to process parameters through the dimensionless metrics illustrated in Figure 3-3a,b (*i.e.*, melt pool depth-to-layer thickness ratio (D/t) and melt pool width-to-hatching space ratio (W/h), and the latter are used to predict the printed density using a calibrated polynomial function taken from (Leclercq & Brailovski, 2024) (Figure 3-3c). These density predictions are presented in the form of "printed density process map" in the volumetric energy density (VED, J/mm^3)-build rate (BR, cm^3/h) coordinates. Each map is built for one specific layer thickness and one specific hatching space, by varying the laser power and the scanning speed within the printer capacity limits. An example of such a map is given in Figure 3-3d for a TruPrint 1000 system (TRUMPF GmbH, Ditzingen, Germany), with the laser power varying from 20 to 200 W and the scanning speed varying from 20 to 2000 mm/s. In this case, the layer thickness and hatching space are set at 30 and 80 µm, respectively. These density maps are used to build the plan of experiments presented in the following section.

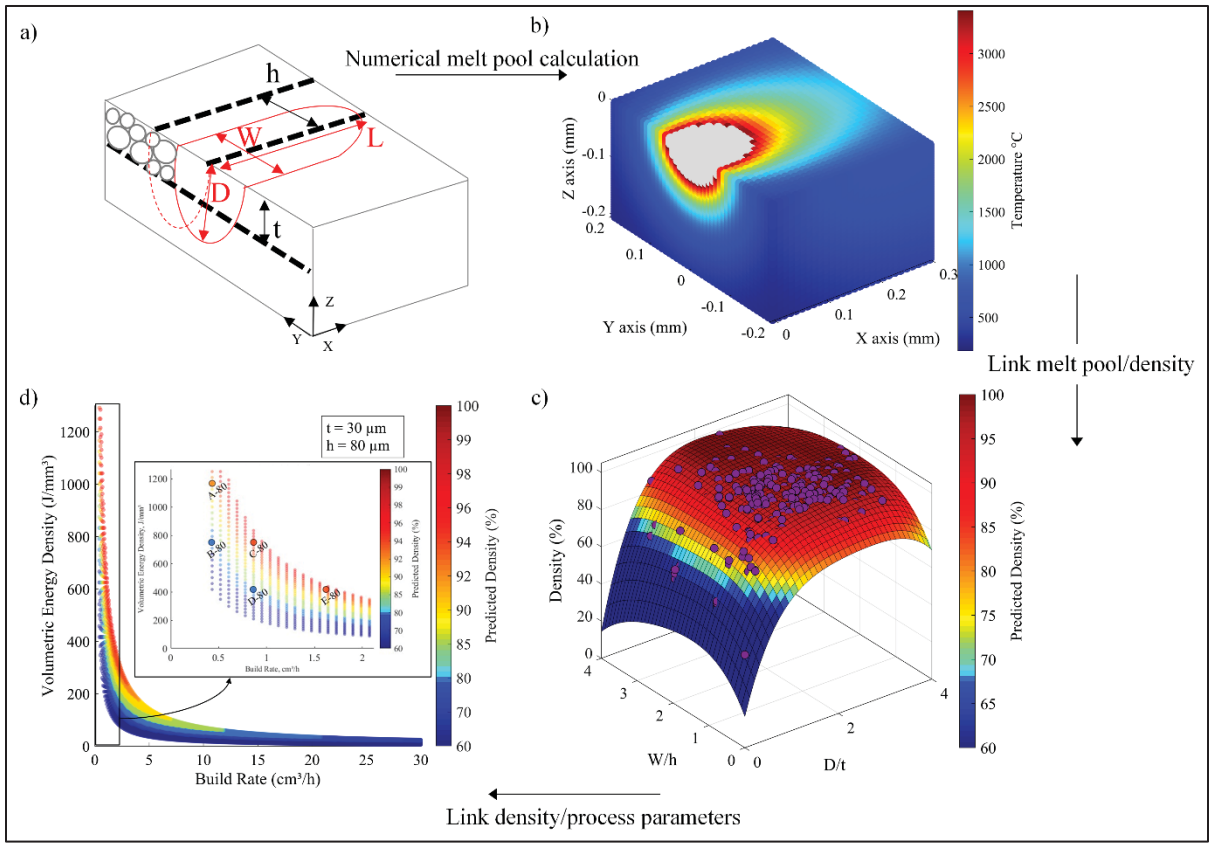

Figure 3-3: a) Schematic representation of the melt pool, melt pool dimensions (depth D, width W and length L) and process variables (layer thickness t and hatching space h); b) example of the calculated (0.8TM) melt pool for pure molybdenum, c) response surface of the polynomial function relating printed density to dimensionless melt pool metrics (experimental points in purple dots) Leclercq & Brailovski (2024) and d) example of the density map for molybdenum ($t = 30$ µm, $h = 80$ µm) with the selected five $VED - BR$ experimental sets for a TruPrint 1000

3.5.2.2 Impact of process parameters on the density, structure and properties of printed specimens

To study the impact of process parameters on the density, structure and mechanical properties of printed specimens, five identical $VED - BR$ sets (A, B, C, D and E (Tableau 3-3)) were selected on five different process maps with a fixed layer thickness of 30 µm and an incrementally increasing hatching space, namely h = 40, 60, 80, 100 and 120 µm. These five process parameter sets were selected to cover the 70 to 99% printed density range. The specimens were named according to the $VED - BR$ sets and hatching spaces selected. For

example, specimen A-40 corresponds to the specimen obtained with a $VED - BR$ set of 1170 J/mm^3 & 0.43 cm^3/h and a hatching space of h = 40 µm. (APPENDICE B Tableau-A B-1 provides the detailed plan of experiments, as well as the predicted densities.)

Tableau 3-3: Parameter sets definition

	A	B	C	D	E
VED, J/mm^3	1170	750	750	400	400
BR, cm^3/h	0.43	0.43	0.86	0.86	1.62

To conduct this experiment, twenty-five 10 mm-diameter, 21 mm-high cylindrical specimens with 5 mm dense supports were printed on a stainless-steel baseplate without preheating (Figure 3-4a). The printed specimens were removed by hand from the baseplate using a hammer and chisel, their supports were cut off, and the remaining parts partitioned to obtain samples for structural analyses and compression testing at room temperature (Figure 3-4b). Therefore, one specimen per each set of process parameters was produced and analyzed. Based on the results of this analysis (described in Section 3.6.3.1), one of the parameters sets of Tableau 3-3 was selected as being the best, and was then used to produce ten 10 mm-diameter, 21 mm-high cylindrical specimens for compression testing at elevated temperatures (600, 800 and 1000 °C).

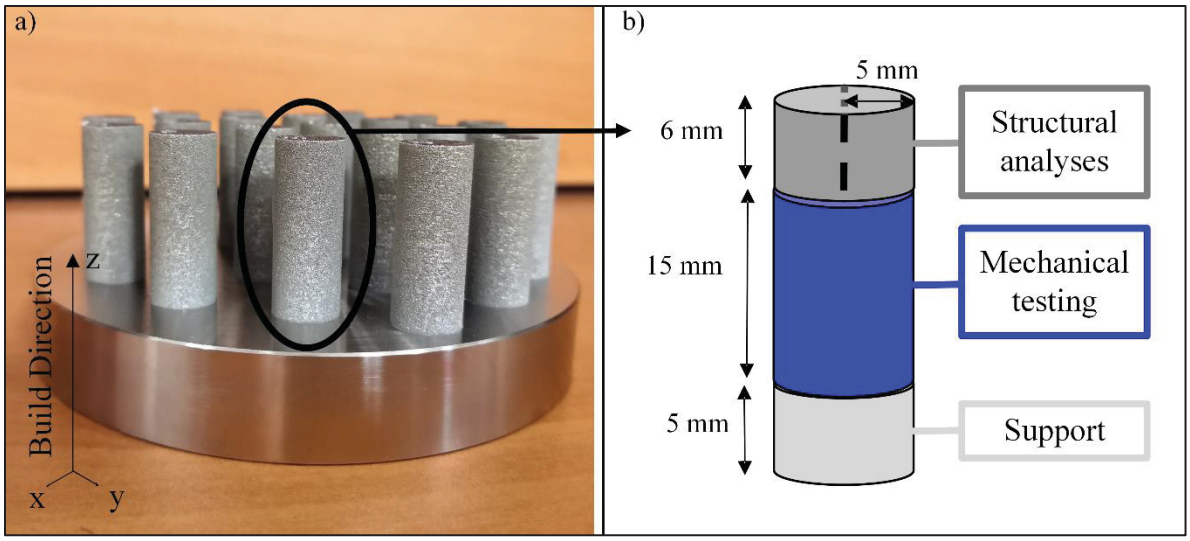

Figure 3-4: a) Photo of a baseplate with printed specimens; b) schematic representation of a printed specimen with samples for structural analyses and mechanical testing

3.5.2.3 Density measurements

Previous studies (Leclercq & Brailovski, 2024; Tan et al., 2018) highlighted that Archimedes measurements are not always suitable for LPBF-processed parts because of the possible presence of unmelted particles inside the pores, giving the false impression of a highly dense and therefore potentially highly resistant material. Moreover, the high density of molybdenum (10.22 g/cm³) limits the use of X-ray tomography for the porosity detection in parts printed with it. Because of these considerations, the density of printed samples was measured using images of their z-y cross-sections (Figure 3-5). To this end, samples were mounted in carbon-doped resin, mirror-polished, and observed with a LEXT OLS4100 (Lext Olympus Corporation, Tokyo, Japan) laser confocal microscope. These observations enabled the detection of defects (pores and cracks) larger than 3 µm in size (if no such defects were observed, samples are called crack-free). The obtained raw images (Figure 3-5ac) were binarized (Figure 3-5bd) in the MATLAB environment (R2022b, MathWorks, USA) using the grey level threshold which was locally adjusted considering the mean intensity (first-order statistics) in the vicinity of each pixel. Finally, the ratio of white-to-black pixels, i.e., the ratio of solid matter to void, was calculated. The density value retained for each sample

corresponded to a mean value obtained from 3 observations and this measurement routine was validated by comparison with the results of manual segmentations in the ImageJ software environment.

In addition to the printed density, the image observations were used to characterize pore populations in terms of pore density (pores/mm^2), size (equivalent diameter (3.11) in µm) and shape (circularity C (3.12), without unit). According to the microscope resolution (1 px = 2.5 µm), segmented defects with $DE < 20$ µm, which represented ~5% in terms of the cumulative pore surface area, were removed from the analysis. It enabled focusing the study on pores having the greatest impact on the mechanical properties.

$$Equivalent\ Diameter\ (DE) = \sqrt{\frac{4Area}{\pi}} \tag{3.11}$$

$$Circularity\ (C) = \frac{4\pi Area}{Perimeter^2} \tag{3.12}$$

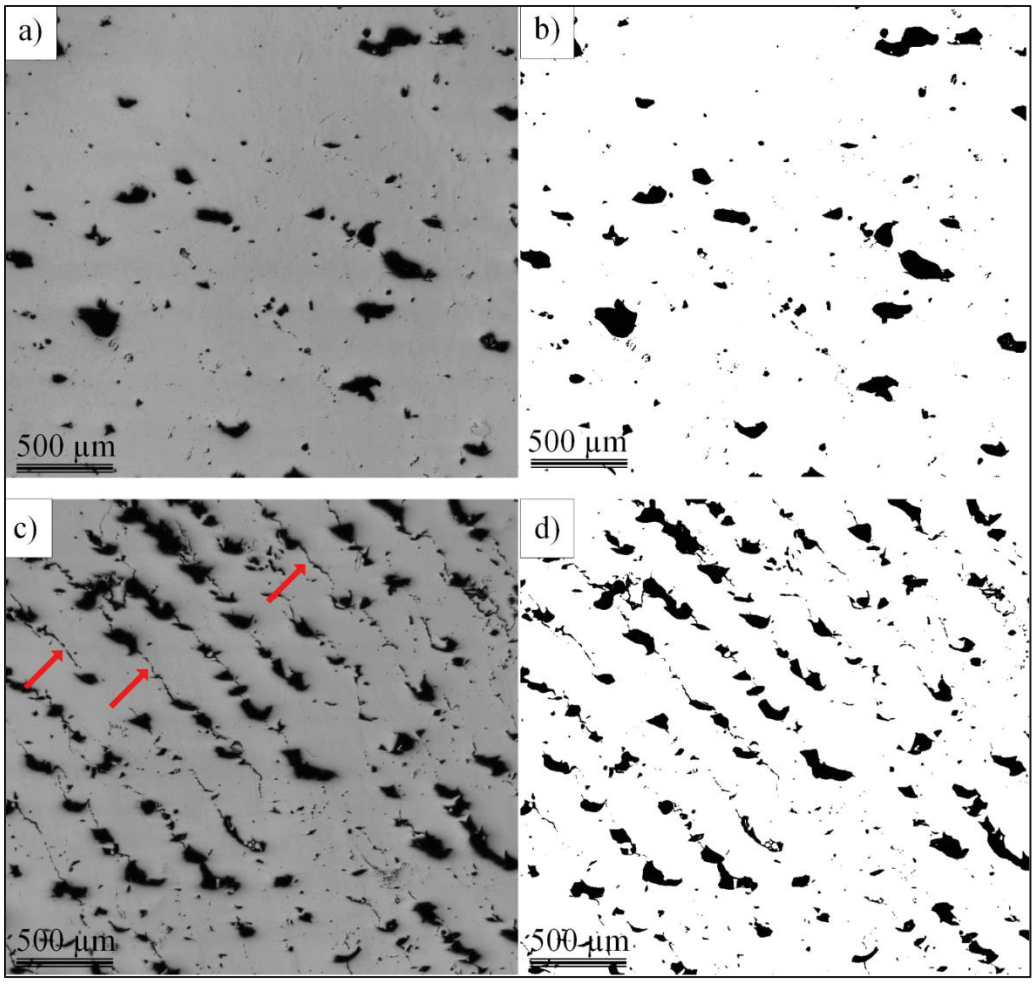

Figure 3-5: C-60 specimen (z-y cross-section): a) microscopic image;
b) binarized image (density d = 97%, pore population 40 p/mm^2,
$DE50_p = 82$ µm and $C50_p = 0.55$; C-40 specimen: c) microscopic image
(z-y cross-section, cracks are shown by red arrows);
d) binarized images (density d = 89%, pore population 100 p/mm^2,
$DE50_p = 100$ µm and $C50_p = 0.30$

3.5.2.4 Microstructure and phase analyses

Microstructure analyses of the as-built specimens were carried out using electron backscatter diffraction (EBSD) inspection of their z-y cross-sections. To this end, mounted samples were first subjected to ion milling using a Hitachi EM 4000 plus (5 kV, 25 rpm, 15 min). The EBSD maps were built using a Hitachi SU-8230 Field Emission-STEM and then post-treated using the MATLAB software MTEX library. First, the Band Contrast (BC) metric was used to

qualify the EBSD pattern quality. This metric is derived from the average intensity of Kikuchi bands with respect to the overall intensity within an EBSD pattern. It is evaluated by different levels of brightness going from 0 (bad EBSD pattern quality, black color) to 255 (good quality, white color). Unstrained materials would show higher-quality EBSD patterns, i.e., light-colored maps, while the presence of defects would obscure the maps. The quality of the samples can therefore be compared by plotting the BC statistical distributions (Kang et al., 2013).

Next, the MacKenzie distributions were plotted to address the texture and the presence of substructures (F. J. Humphreys & Hatherly, 2012). In this context, two groups of structural elements were identified as Low Angle Grain Boundary (LAGB) elements, having misorientation angles between 2 and 10°, and High Angle Grain Boundary (HAGB) elements, with misorientation angles larger than 10°. The LAGB and HAGB quantifications were carried out using their respective densities (μm^{-1}), which correspond to the boundary length divided by the indexed area (Wheeler et al., 2003; Yvell, Grehk, Hedström, Borgenstam, & Engberg, 2018). Structures corresponding to the HAGB elements were then used to assess the grain size, shape, orientation and distribution, following the procedure defined in the E2627-13 ASTM standard (E04 Committee, 2019). The grain size and shape metrics were obtained by analogy with those of pores and are referred herein to as the grain density, i.e., the number of grains per mm^2 (grains/mm^2); the grain size $DE10_g$, $DE50_g$ and $DE90_g$ (μm), and the grain circularity, $C10_g$, $C50_g$ and $C90_g$.

Finally, the extent of oxidation occurring during printing and high temperature mechanical testing was assessed by X-ray diffraction (XRD) analysis (X'Pert^3 system equipped with a cobalt source, Malvern Panalytical Ltd, Malvern, UK), and the energy dispersive spectroscopy (EDS) technique (Hitachi SU-8230).

3.5.2.5 Mechanical testing at room and elevated temperatures

All printed specimens were subjected to room-temperature compression testing using an Alliance RF/200 testing machine (MTS, Eden Prairie, MN, USA) according to the E9-09 ASTM standard (E28 Committee, 2019). The compression rate was set at 0.01 mm/s and two high-resolution cameras were placed in front of the specimens to monitor the fracture mode during the tests. The force was measured using a 200 kN MTS load cell, while the displacement was measured using an LVDT. Based on these measurements, strain-stress diagrams were plotted to obtain the following metrics: Ultimate Compression Strength (UCS, MPa), defined as the maximum stress reached during the test, Yield Strength (YS, MPa), calculated by moving the slope from origin to 0.2% on the strain axis and Strain under maximum load (δ, %), representing the difference between the total compression strain at UCS and the elastic strain to failure.

High temperature compression testing of the selected specimens was carried out on an MTS 810 (MTS, Eden Prairie, MN, USA) load frame under an argon flow of 27.5 ft^3/h, with the force measured by a 100 kN MTS load cell and the displacement measured by an LVDT. The compression rate was set to 0.075 mm/min as per the ASTM E209-18 standard (E28 Committee, 2018) and the temperature in the testing chamber was controlled using an infrared (IR) furnace. To ensure that the temperature in the core of the tested samples corresponded to that in the thermal chamber, one of the samples was instrumented with a K-type thermocouple and subjected to a controlled temperature rise up to 800 °C with a heating rate of 10 °C/min without applying stress. This enabled the validation of the temperature ramp and the establishment of a 3 min prior-to-testing dwell time. Three samples were compressed for each testing temperature and stress-strain diagrams were plotted and analyzed using the same procedure as that for the room-temperature testing.

3.5.2.6 Printability of complex structures

The optimized set of printing parameters was used to produce three geometric artefacts, namely the wall and gap artifacts with a thickness varying from 0.1 to 2 mm (adapted from (Moylan

et al., 2012), Figure 3-6a,b,d) and 10 mm-diameter, 20 mm-high, 50 and 60% porosity gyroid lattice structures (strut size respectively 345 and 240 µm) (Figure 3-6c,d). For all of them, the contours were printed using the same parameters as the body, and the laser offset was kept to zero during the print. The gap and wall artifacts were subjected to optical measurements using a Keyence VHX7000, while the density of the gyroid lattice structures was measured using the Archimedes technique.

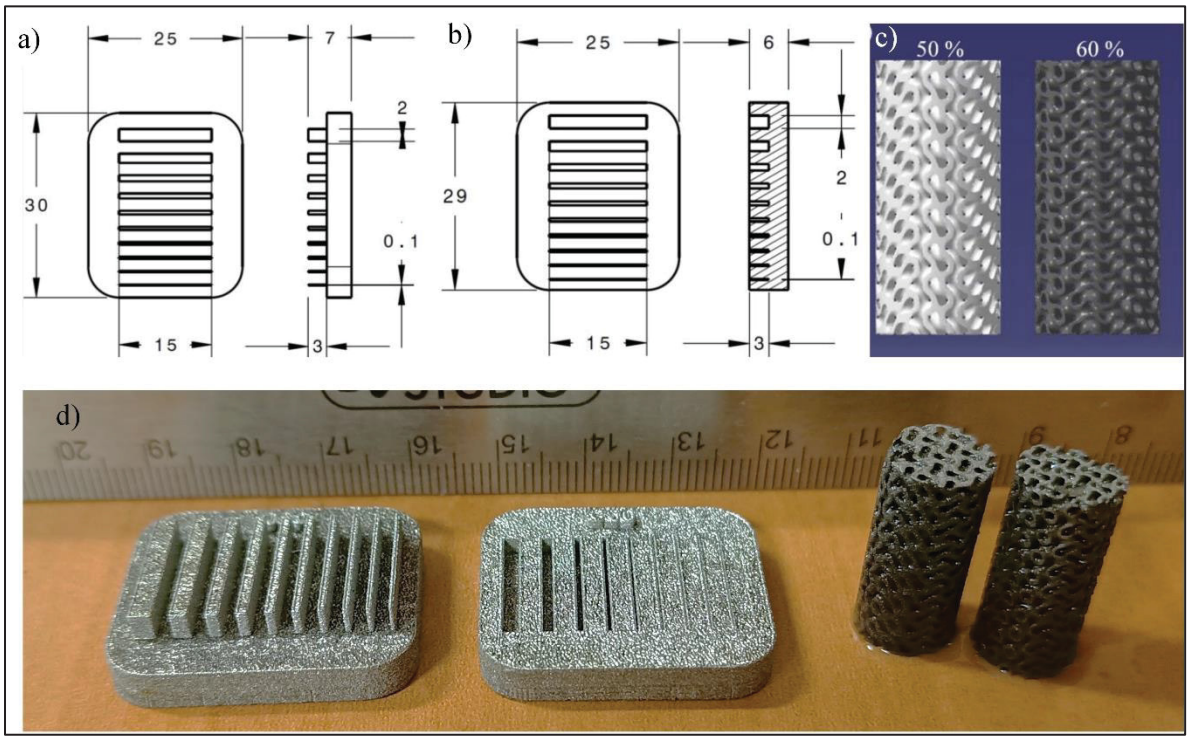

Figure 3-6: Drawings of the printed geometric artifacts: a) walls, b) gaps, c) 50 and 60% porosity gyroid lattice structures; d) printed artifacts. Dimensions are given in mm.

3.6 Results

3.6.1 Printed densities and pore structures

The predicted printed densities are plotted as functions of the process parameters in Figure 3-7a. For all printing sets, the predicted density monotonously increases to reach a maximum value at $h/t = 2.5$ and then decreases. The highest densities (98-99%) are predicted for the

C (750 J/mm^3; 0.86 cm^3/h) and E (400 J/mm^3; 1.62 cm^3/h) $VED-BR$ sets, while the lowest densities (91-93%), are predicted for the B (750 J/mm^3; 0.43 cm^3/h) and D (400 J/mm^3; 0.86 cm^3/h) $VED-BR$ sets, with the $VED-BR$ set A (1170 J/mm^3; 0.43 cm^3/h) occupying the intermediate position.

For comparison, the effective (image-measured) printed densities are plotted in Figure 3-7b. It can be observed that for any h/t ratio, with the exception of $h/t = 1.3$, the C and E $VED-BR$ sets also lead to the highest printed densities (up to 96%), while the B and D $VED-BR$ sets lead to the lowest printed densities (down to 87%). As for the A VED-BR set, it leads to intermediate density values, oscillating between 92 and 94%.

While the overall trends for the predicted and effectively measured printed densities are coinciding, two major discrepancies can be noted. The first is related to the printed density ranges, which are 91-99% (simulations) versus 87-96% (experiment), meaning that the model significantly overestimates the printed density. The second, more significant discrepancy is that for the two best VED-BR sets (C and E), when h/t increases, the density first increases to reach a maximum at h/t = 2-2.7 and then decreases to reach a minimum at h/t = 3.3, and finally, increases again to h/t = 4. The reasons why the model is not capable of predicting such a complicated density evolution are discussed in Section 3.7.1.

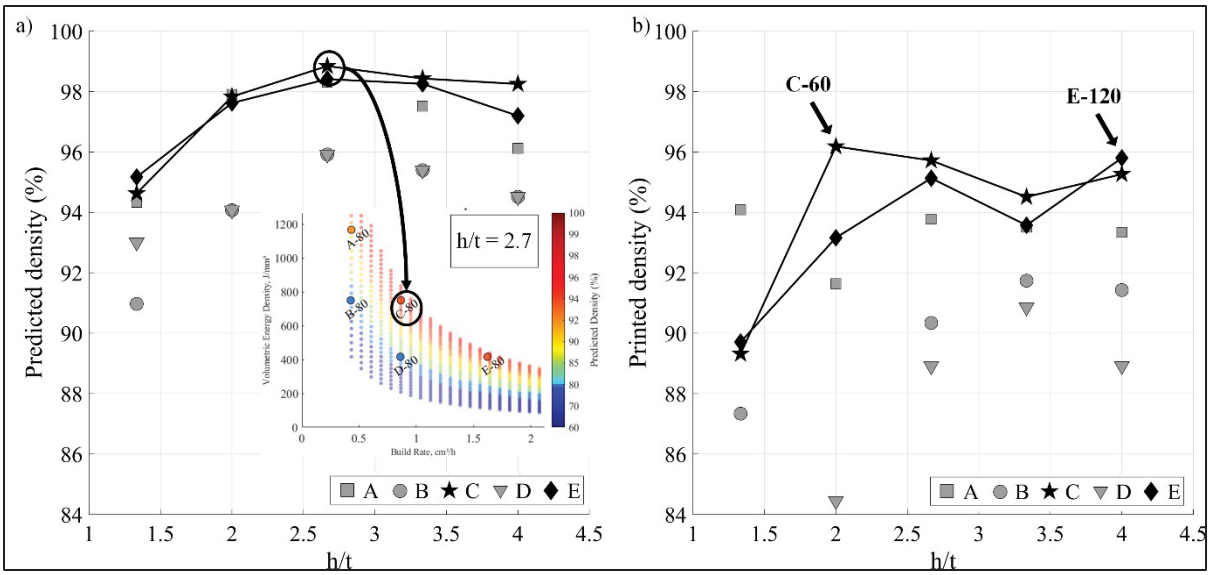

Figure 3-7: a) Predicted and b) measured printed densities for different process parameters sets (arrows point to the C-60 and E-120 sets leading to the highest measured printed densities).

Based on the experimentally obtained data, it can be stated that the processing conditions leading to the highest printed densities (~97%), and therefore to potentially higher mechanical properties, correspond to the following printing parameters $P = 179$ W, $v = 133$ mm/s, $h = 60$ µm and $t = 30$ µm (C-60 set with $h/t = 2$). Further, the printing parameters $P = 180$ W, $v = 125$ mm/s, $h = 120$ µm and $t = 30$ µm (E-120 with $h/t = 4$) leading to a printed density of ~96% should not be removed from consideration.

The porosity study revealed the pores population in the [30;121] p/mm^2 range, with a median circularity $C50_p$ = [0.30;0.55] and a median pore size $DE50_p$ = [65;100] µm. No clear trends can be observed with any of the porosity metrics in respect to the process parameters. Concerning the parameter sets C-60 and E-120 leading to the best measured densities (Figure 3-8), the C-60 samples contain slightly larger pores than their E-120 counterparts: [$DE50_p$; $DE90_p$] = [82; 120] µm for the former versus [$DE50_p$; $DE90_p$] = [70; 110] µm for the latter. However, the density (40 pores per mm^2) and circularity ($C50_p$ = 0.55) of pores are similar in both cases.

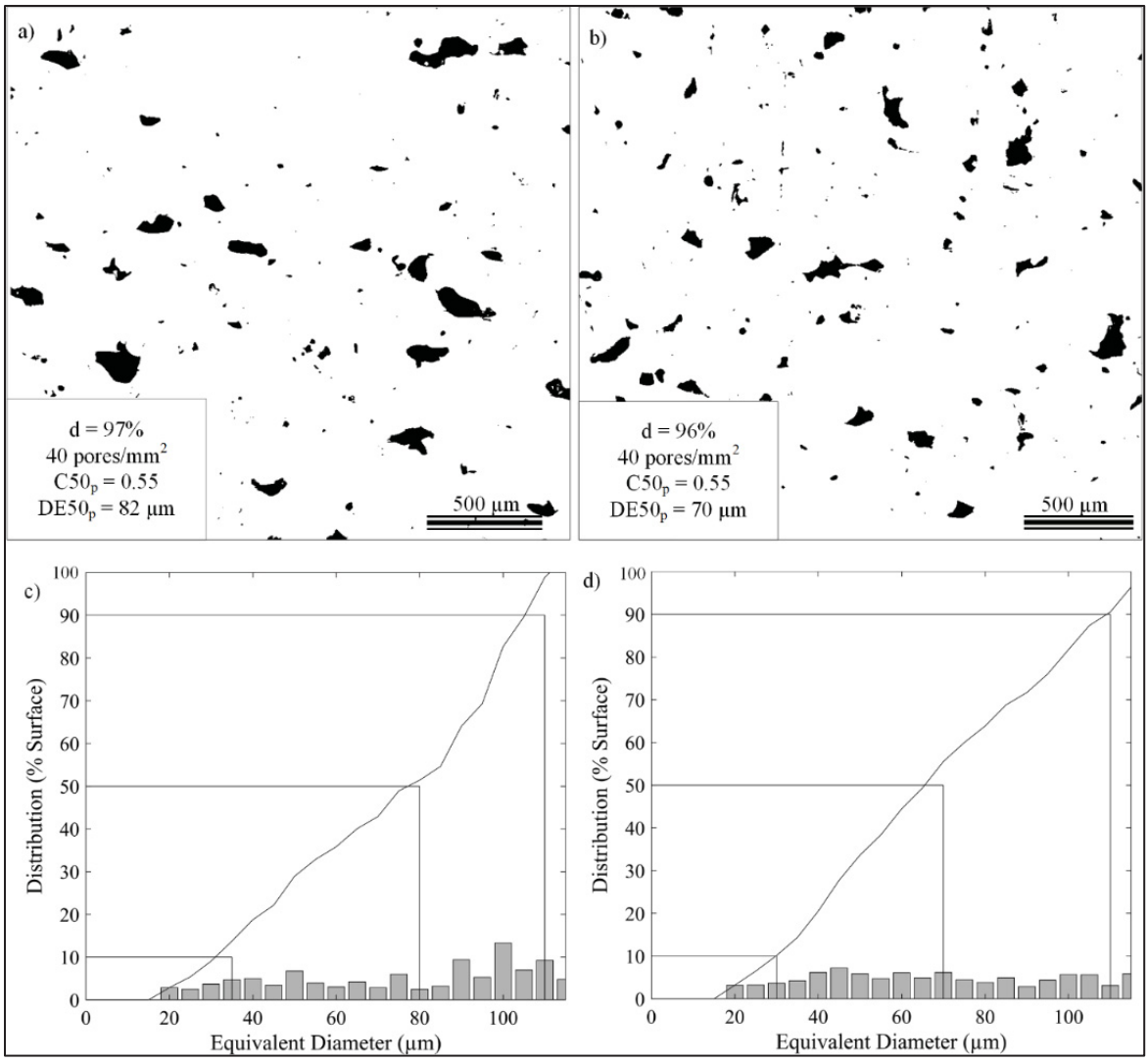

Figure 3-8: Binarized surfaces of the samples a) C-60 and b) E-120
with segmented pores and their pore distributions: c) C-60 and d) E-120

3.6.2 Crystalline phases and microstructures

Immediately following the printing, selected specimens were subjected to XRD analyses to detect traces of oxidation that may have occurred during the process. The XRD measurements conducted on samples C-60 and E-120 revealed only the bcc structure of pure molybdenum. To compensate for the detection limits of this technique, some additional investigations were conducted on the cross-polished sections and compression fracture surfaces, using the SEM and EDX techniques (Figure 3-9). For all the parameter sets, these analyses detected some

minor oxidation traces. Furthermore, observations made on the polished cross-sections demonstrated a higher concentration of oxygen at the grain boundaries. This is consistent with the related literature (Xing et al., 2022; Braun et al., 2019), which describes the tendency of molybdenum to have impurities segregating at these interfaces. However, such visual observations do not allow comparing the overall oxidation levels between the two different sets of parameters (C-60 and E-120).

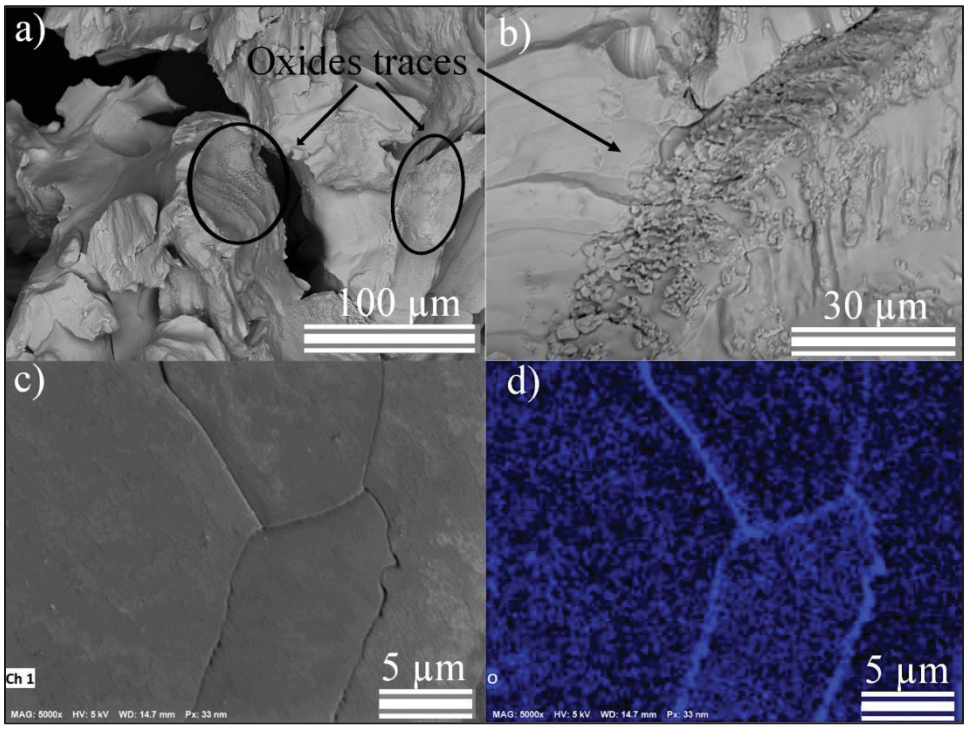

Figure 3-9: C-60 parameter set: (a and b) SEM images of oxidation traces observed on the compressive fracture surface; (c) SEM image on the polished cross-section and (d) corresponding EDS map.

The EBSD analyses were carried out on samples C-60 and E-120 with the highest printed densities. For both samples, the BC maps were relatively light-colored and showed no clear difference between them, as highlighted in Figure 3-10a,b. The statistical distributions obtained show one peak at BC = 160 (Figure 3-10c), which reflects the presence of only one phase in both samples. It should be noted that an increase in the h/t ratio leads to a slight shift of this peak to the left, meaning a small decrease in the pattern quality, and thus, a higher

presence of defects or internal stresses. Then, the MacKenzie plots of misorientation angles (Figure 3-10d) are similar to those of conventional polycrystalline cubic materials with random texture (Frederick John Humphreys & Hatherly, 1995). This absence of preferential orientation was also confirmed by the pole figures presented in Figure 3-10e. Also, these diagrams revealed a significant population of structural elements with small misorientation angles (LAGB, $< 10°$), thus revealing the presence of substructures accommodated by arrays of dislocations.

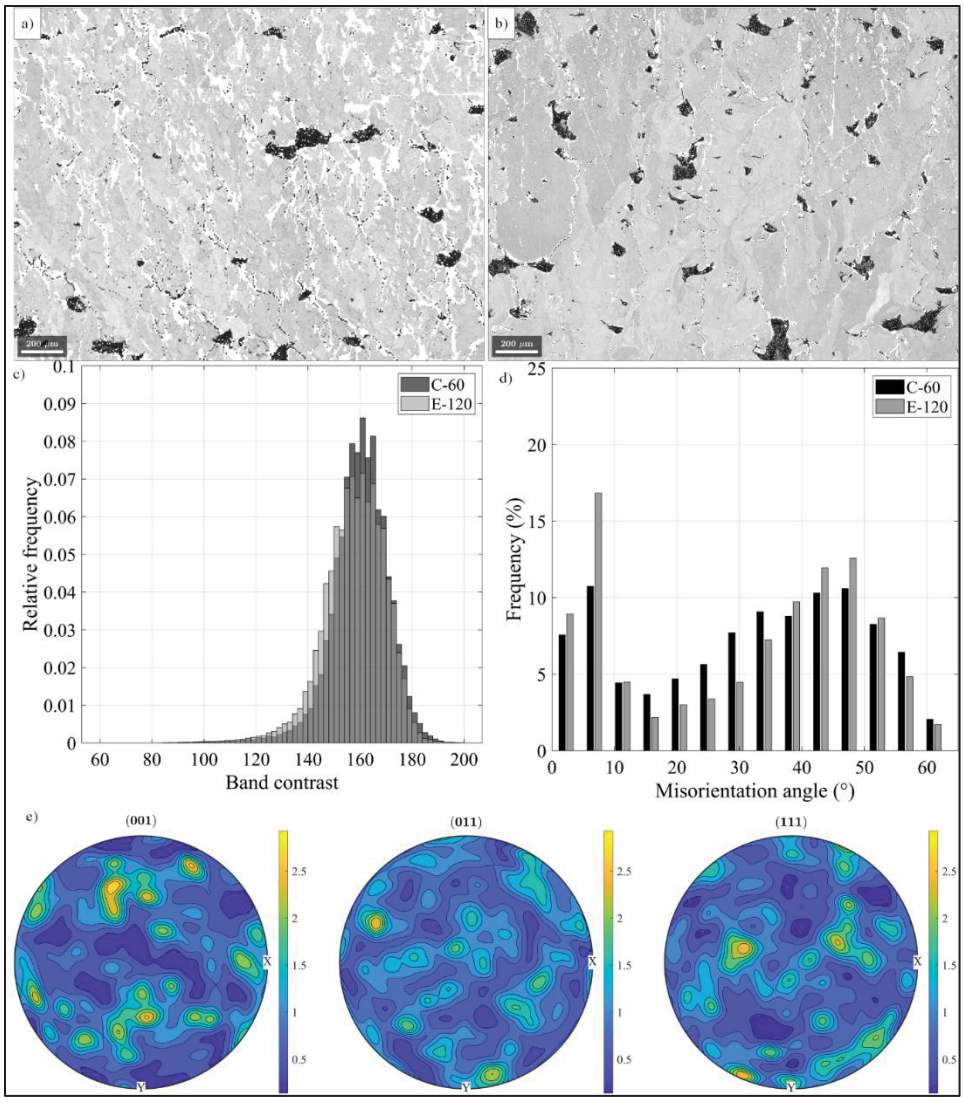

Figure 3-10: Band contrast (BC) diagrams of samples a) C-60 and b) E-120; c) BC cumulative histograms and d) MacKenzie plots of samples C-60 and E-120; e) pole figures of sample C-60

The boundary density values of the LAGB and HAGB structural elements are plotted as functions of the h/t ratio in Figure 3-11a,b. These evolutions can be compared to those of the grain size in the same figure. For a constant layer thickness, an increase in the h/t ratio means an increase in the hatching space and a smaller overlap of two subsequent laser tracks, and a lower inclination to trigger primary recrystallisation. A smaller overlap will therefore correspond to a higher density of the LAGB substructure elements at the expense of a lower

density of the HAGB structural elements (grains). To verify this point, a comparison was made between samples E-120 and C-60 having the same predicted melt pool widths ($W \approx 135$ µm), but for which the overlap ratio (W/h) goes from 1.1 (E-120) to 2.3 (C-60). As presented in Figure 3-11c,d,e,f, sample E-120 with a smaller overlap manifests a higher LAGB density, a lower HAGB density and larger grains than sample C-60 with a greater overlap. Finally, for all the studied samples, grains are elongated ($C50_g$ = [0.4; 0.55], $C90_g$ = [0.65; 0.75]) and oriented in the build direction, which is common for this process (Braun et al., 2019; Higashi & Ozaki, 2020).

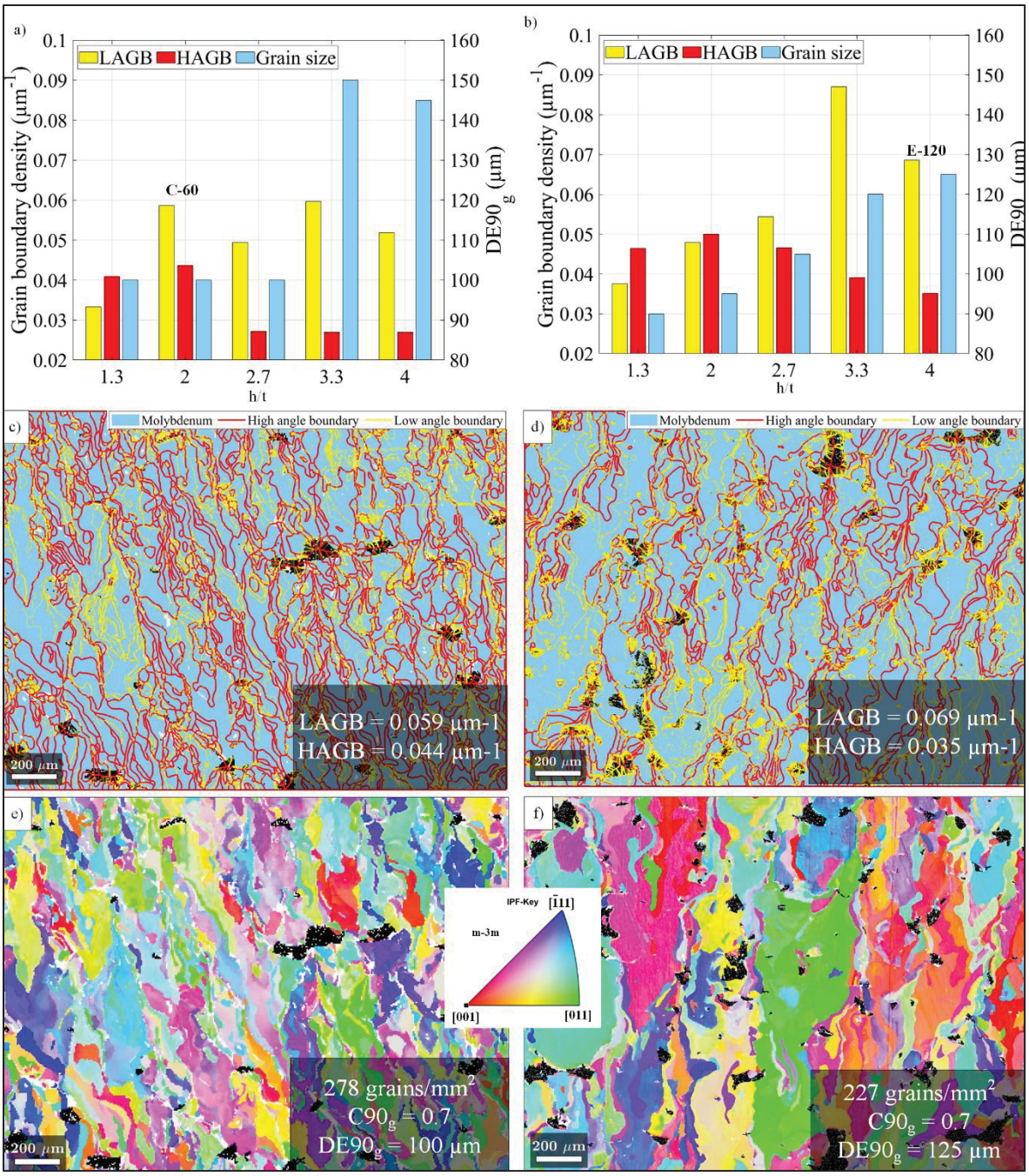

Figure 3-11: LAGB, HAGB densities and grain size (DE90g) as functions of the h/t ratio for the $VED - BR$ set C a) and E b); phase maps highlighting LAGB (yellow) and HAGB (red) for the specimens C-60 c) and E-120 d); orientation maps (IPF Y) for the specimens C-60 e) and E-120 (f)

3.6.3 Mechanical testing

3.6.3.1 Room temperature testing

The mechanical properties (YS, UCS and d) of all the tested samples are summarized in APPENDICE B Tableau-A B-2. It must be noted that two types of mechanical behavior were observed during compression testing (Figure 3-12a). Some of the samples broke under the maximum load, presenting "short" stress-strain diagrams with monotonically increasing stresses akin to conventional stress-strain diagrams for ductile materials. The associated fracture surface observed using SEM (Figure 3-12b) is relatively clean, without impurities, and shows standard ductile convection fracture marks. The others, "long" stress-strain diagrams, demonstrate two inflection points, the first accompanied by audible cracking far before reaching the second inflection point, corresponding to the maximum stress before failure. These last samples ($VED\text{-}BR$ sets A, B and D) can be distinguished by their lower values of printed densities ($\leq 92\%$) and yield strengths (≤ 250 MPa). This two-stage behavior is attributed to the presence of unmelted particles inside the pores which are crushed and deformed along the compression test, as seen in the SEM image of the fracture surface of sample B-60 (Figure 3-12c). Since this behavior is related to the presence in the specimens of a significant number of process-induced flaws (pores, unmelted particles inside the pores and micro-cracks), the A, B and D parameter sets are excluded from further analyses.

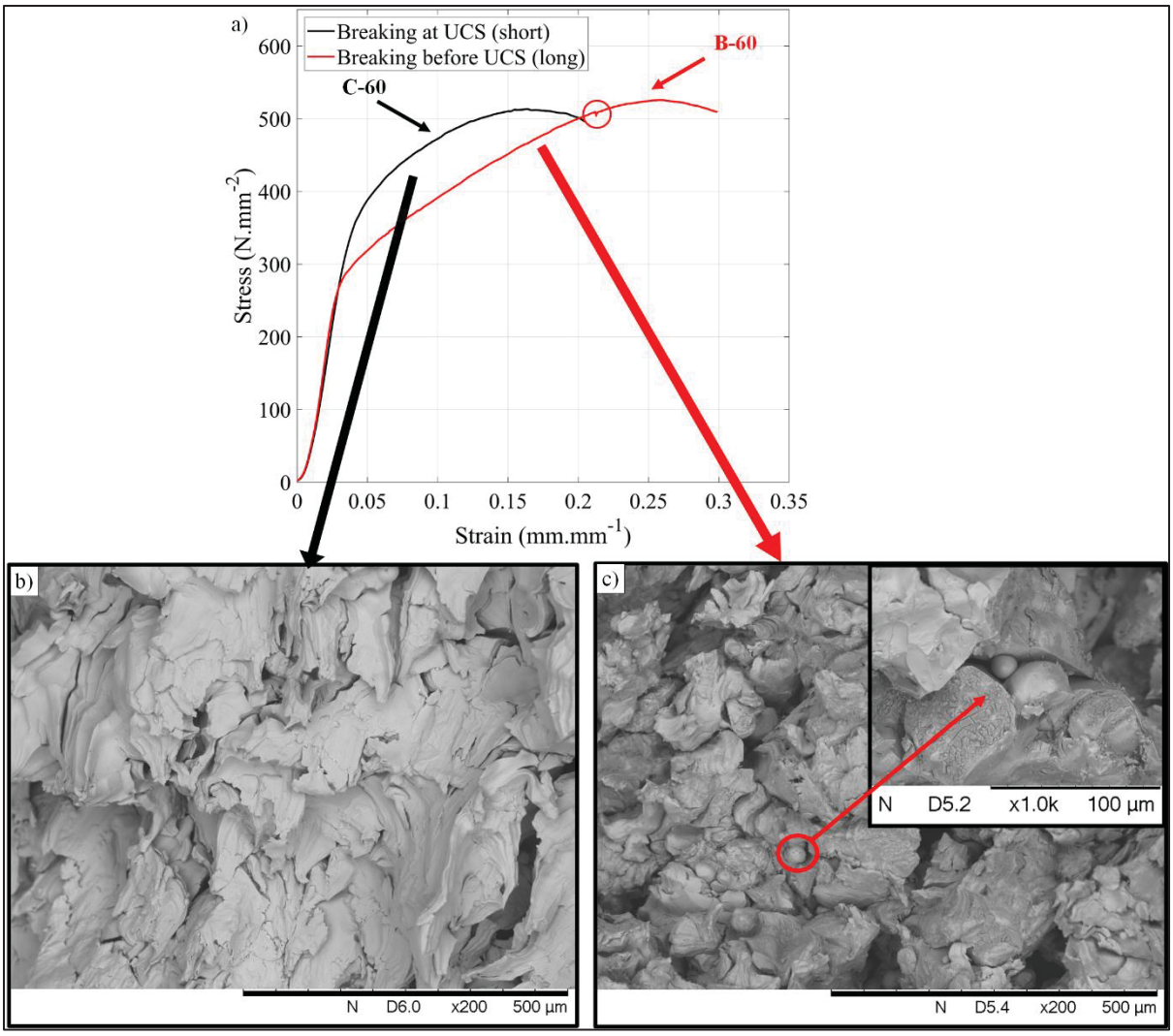

Figure 3-12: a) Stress-strain diagrams of the C-60 and B-60 samples highlighting two distinct behaviors observed during the compression tests; SEM images of the fracture surfaces of samples b) C-60 and c) B-60

Note furthermore that the mechanical properties of the remaining C and E sets follow the same trend as the printed densities (Figure 3-13 vs Figure 3-7b). Indeed, with the increase of h/t, the strength first increases to reach a maximum at $h/t = 2$, then decreases to $h/t = 3.3$ and finally increases again. When comparing the room-temperature mechanical properties of samples with the highest measured densities, C-60 and E-120, the mechanical properties of the former appear to be significantly higher than those of the latter: + 21% for UCS, +1 2% for YS and + 35% for strain under maximum load (not shown in Figure 3-13). This is consistent with a finer grain

structure of the C-60 samples as compared to their E-120 counterparts (~100 vs ~125 µm) (Figure 3-11c). The C-60 parameter set (P = 179 W, v = 133 mm/s, h = 60 µm) is therefore considered as an optimized set of printing parameters and retained for subsequent study.

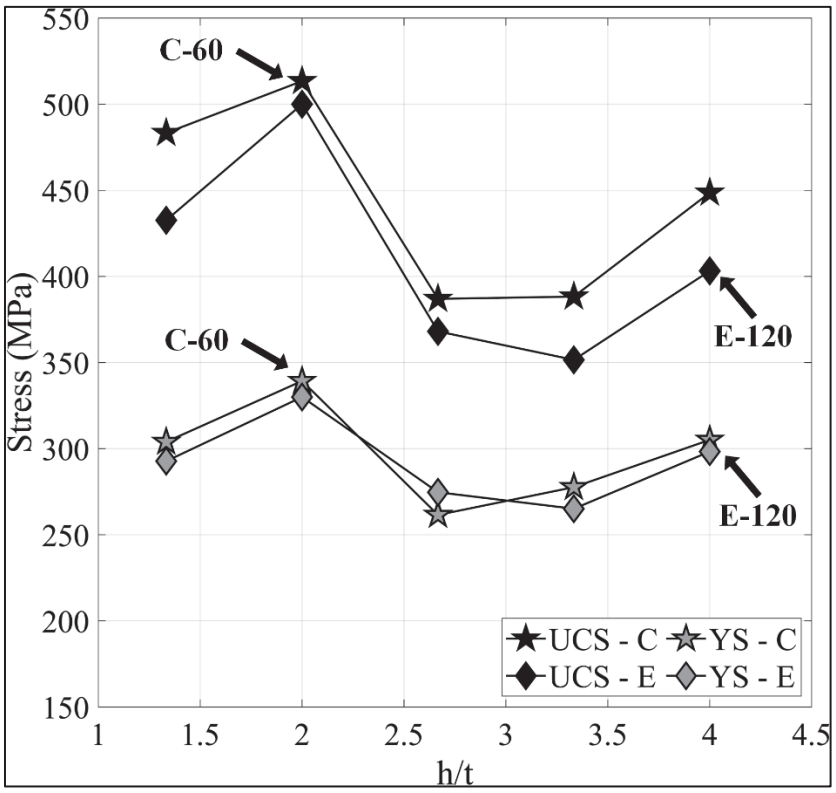

Figure 3-13: YS and UCS for C and E process parameter sets;
arrows point to the C-60 and E-120 specimens
with the highest printed densities

3.6.3.2 Elevated temperature testing

Using the C-60 set of printing parameters, selected using density measurements and mechanical testing at room temperature, new specimens were printed and tested at 600, 800 and 1000 °C. It must be noted that while the argon-filled atmosphere was sufficient to prevent oxidation at 600 °C, specimens suffered non-negligible oxidation during testing at 800 and 1000 °C. A thick white smoke was observed outside the compression chamber and samples were found covered with a shiny white lamina (Figure 3-14a) at the end of testing. The

estimated mass loss corresponded to 8.6 ± 2.7% at 800 °C and 9.4 ± 0.8% at 1000 °C. XRD analyses of the thermocouple-instrumented specimen (Figure 3-14b) before and after the thermal cycling revealed that this phenomenon corresponds to the formation and vaporization of MoO_3 oxides, which were not initially present in the sample. (Note that the reported values of YS, UCS and δ obtained at 800 and 1000 °C were not adjusted to compensate for this mass loss.)

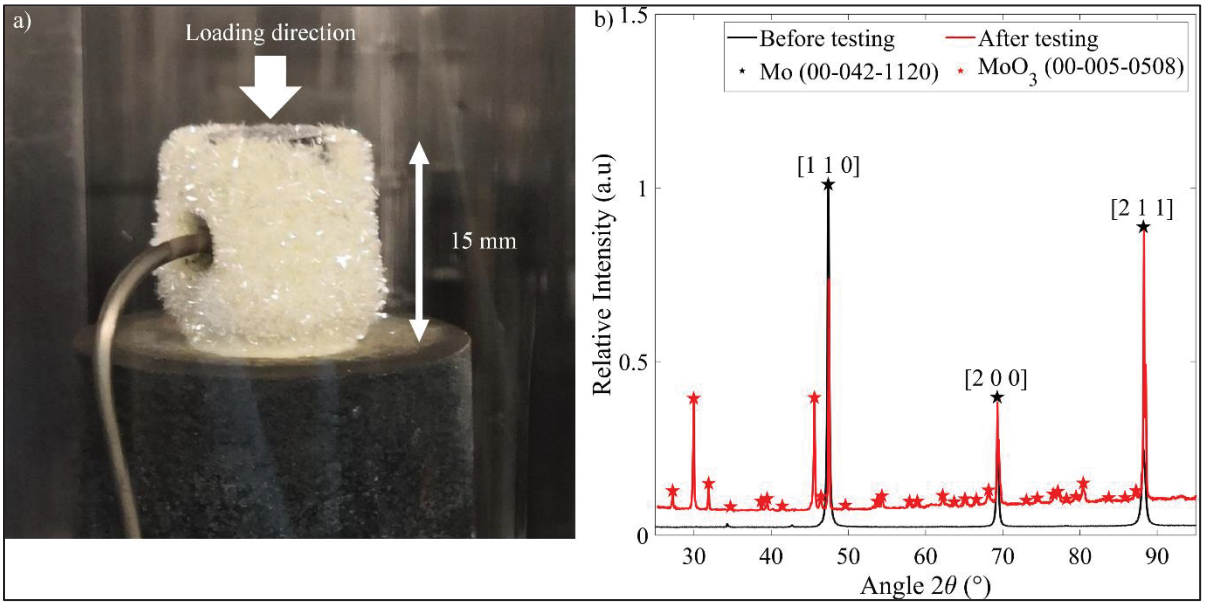

Figure 3-14: Thermocouple-instrumented sample: a) Photo with the oxide layer; b) XRD before and after the temperature cycling (without load)

Figure 3-15 presents the stress-strain diagrams obtained at 20, 600, 800 and 1000 °C. Globally, the higher the testing temperature, the lower the strength characteristics (YS, UCS), and the higher the strain under maximum load, but this evolution is not monotonic (Tableau 3-4).

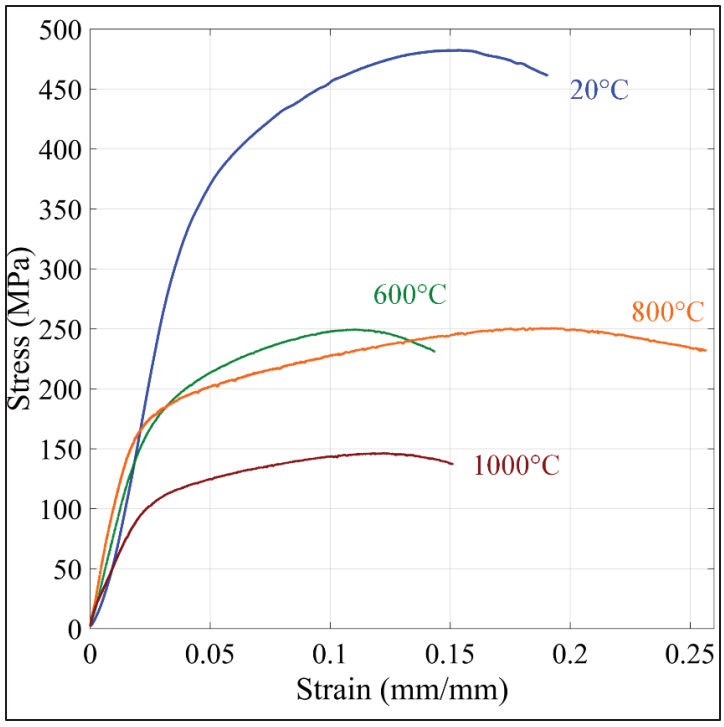

Figure 3-15: Representative stress-strain compression diagrams (C-60) at 20, 600, 800 and 1000 °C

Tableau 3-4: Mechanical properties in compression at room and elevated temperatures

Testing temp., °C	YS, MPa	UCS, MPa	δ, %
20	340 ± 20	500 ± 15	11 ± 1
600	150 ± 20	240 ± 30	8 ± 1
800	160 ± 5	260 ± 8	14 ± 1
1000	90 ± 10	150 ± 18	9 ± 4

3.6.4 Printability

To assess the printability limits of the parameter set selected (C-60), geometric attributes of some selected geometric features were measured. A stitched image of the wall artifact is presented in Figure 3-16a along with the methodology used to measure the wall thickness on top of the parts (Figure 3-16b). Regarding the wall features, all the thicknesses were successfully printed. Their measured dimensions were compared to the nominal values and

subjected to a linear regression analysis in Figure 3-16c. The direction coefficient was close to 1 (1.08), R^2_{adj} = 0.99 and RMSE = 0.063, with no pattern in the residuals.

For the gaps, the narrowest of them (0.1 and 0.2 mm) were not printed. For the 0.1 mm gap, since no offset was applied, two neighboring melt tracks overlapped (considering the melt pool width predicted with the model of ~ 140 μm). For the nominal sizes of 0.1 and 0.2 mm, the empty space between two neighboring tracks was commensurate with the diameter of powder particles. For wider gaps, the linear regression analysis (Figure 3-16d) gave a direction coefficient close to 1 (1.02), R^2_{adj} = 0.99 and RMSE = 0.041, with no pattern in the residuals. Note that particles attached to the surface induced significant deviations from the nominal values (Figure 3-16d). Regarding the gyroids structures, they were subjected to ultrasonic cleaning, and their porosity estimated using the Archimedes method provided an excellent correspondence with the nominal values, 50 and 59% versus 50 and 60%, respectively.

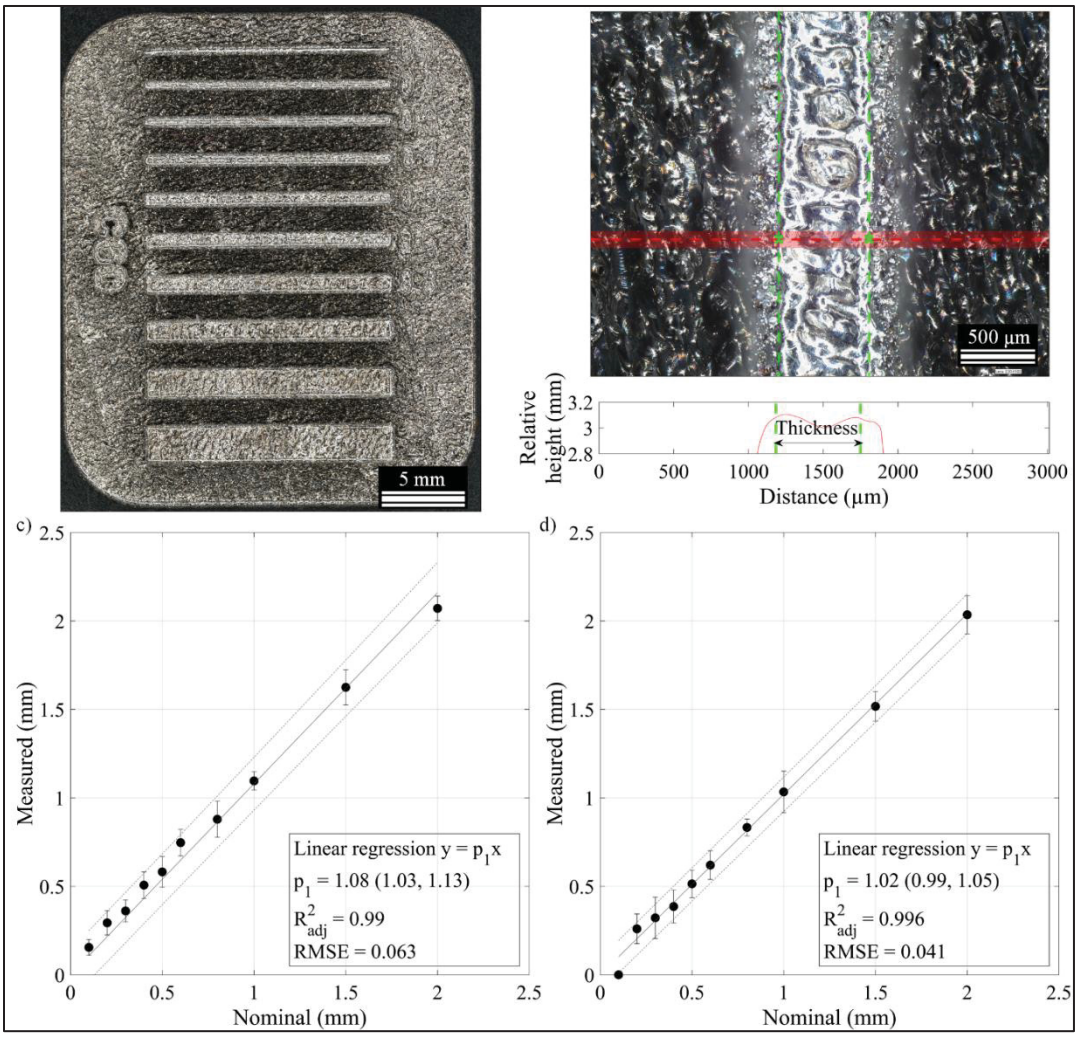

Figure 3-16: a) Optical microscopy observations of walls; b) measurement of its top thickness using the height profile line represented in red; c) linear regressions between the nominal and the microscope-measured thickness of (c) walls and (d) gaps, with the confidence interval at 95% margins

3.7 Discussion

3.7.1 Printed density: prediction versus experiment

This study showed the complexity of interactions between the process parameters and printed density. Indeed, if it is commonly accepted that VED is a reliable metric to quantify the LPBF process conditions, this study demonstrated that VED alone is not sufficient and must rather

be used in combination with the BR and h/t indicators to find the absolute values of printing parameters P, v, h and t. This highlights the usefulness of using numerical models for the rough assessment of printed density as a function of process parameters, thus reducing the often too costly and time-consuming plans of experiments. However, this work revealed a significant discrepancy between the predicted printed densities and their experimentally measured equivalents. While the predicted values show a clear optimum at h/t = 2.5 (Figure 3-7a), the experimentally observed trends are much more complicated and indicate two optimal regions at h/t = 2 and h/t = 4 (Figure 3-7b).

Such an irregular evolution of printed density as a function of the process parameters was also observed by (Higashi & Ozaki, 2020) in their study on pure molybdenum fabricated by LPBF. While the authors did not provide explanations for such discontinuities, it appears that a non-monotonic decrease in printed porosity observed in their study was accompanied by drastic changes in both the nature of process-induced flaws (small spherical gas-filled pores replaced the elongated lack-of-fusion defects) and the crystallographic texture (<110> replaced <001>). In our study, no significant texture modifications were observed, but the highest printed density cases C-60 and E-120 also presented the largest fractions of small spherical gas-filled pores (DE < 50 µm and C > 0.7) as compared to the other printing regimes.

It can be asserted that the printed density prediction model used in this study, which is merely a correlation between the calculated melt pool dimensions and the density calibration function (Figure 3-3c), was not meant to consider the complex physical phenomena impacting the final density of printed parts. It was used to establish a sound experimental plan of this work, thus avoiding the trial-and-error approach.

Since the objective of this study was to maximize the printed density and mechanical properties of as-built molybdenum specimens, Figure 3-17 compares the results obtained herein for h/t = 2 with those from the literature (Faidel et al., 2015; Guan et al., 2023; Higashi & Ozaki, 2020; Iveković et al., 2018). Only authors who measured their density using the image analysis were retained. According to this representation, the highest printed densities were obtained in

the 200-400 J/mm³ VED range and in the 2-5 cm³/h BR range. However, with the parameter sets corresponding to these conditions, all the authors reported the presence of microcracks. Conversely, the VED values used in this study were higher (>400 J/mm^3), while the BR values were lower (<1.63 cm^{3}h) than those in the literature, thus resulting in lower cooling rates. It can therefore be hypothesized that the appearance of microcracks in the previously cited works can be explained by excessively high cooling rates occurring during the process.

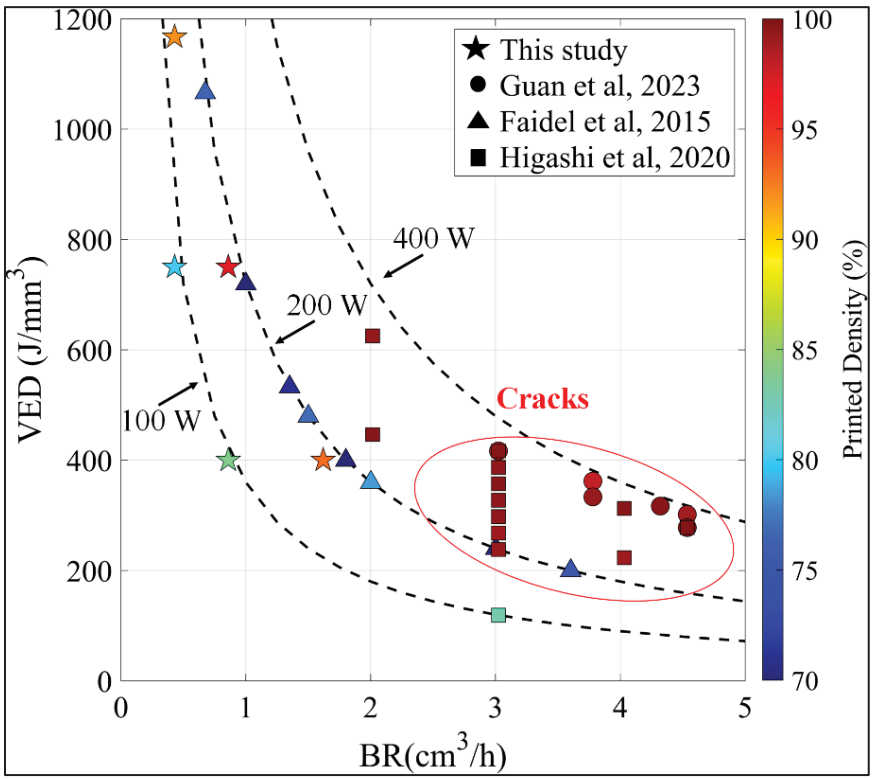

Figure 3-17: a) Image-measured printed density in the $VED - BR$ plan for this study ($h/t = 2$) and the current literature Bajaj et al. (2019); Faidel et al. (2015); Guan et al. (2023); Higashi et Ozaki (2020); red ellipse indicates zone corresponding to microcracks. Dashed lines delimit the frontier of 100, 200 and 400W printers' boundaries

(Faidel et al., 2015) performed experiments in the $VED - BR$ range which is the closest to the one used in this study and with a similar printer (P_{max} = 200 W). They reported printed densities ranging between 49-78% (Figure 3-17), which is are much lower than those obtained in this study. Such a significant decrease in printed density can be explained by the use of a

suboptimal $h/t \leq 1$. In fact, to be in the similar BR range, while using such a narrow hatching space, the authors of the refenced study were obliged to switch to higher scanning speeds (up to 4000 mm/s), thus generating smaller melt pools and potentially unstable melting conditions, resulting in highly porous parts. According to the observations above, the $VED - BR$ range leading to high-density crack-free printing of molybdenum corresponds to a combination of high VED (400-1200 J/mm^3), reduced BR (0.5-2 cm^3/h), and optimized $h/t \approx 2$.

3.7.2 Microstructure evolution

Considering printing with the C $VED - BR$ set (see Table A.1 in the appendix), the laser power was fixed at 180 W, the hatching space increased from 40 to 120 µm and the scanning speed decreased from 199 to 66 mm/s. In the case of a single-track fusion, this decrease in the scanning speed must correspond to an increase in the linear laser energy density ($LED = P/v$) from 0.9 to 2.7 J/mm, an increase in the melt pool size, decrease in the cooling rate and increase in the crystallized grains size, according to the welding analogy in (Kou, 2002). In the case of a multi-track fusion however, when the hatching space increased from 40 to 120 µm, the distance between two neighboring tracks and therefore the heat affected zone, become larger, thus additionally contributing to the microstructure coarsening (see an increase in the grain size from 100 to 150 µm, Figure 3-11a). For the lower h/t ratios (h decreases), a second competitive phenomenon associated with an increase in the melt pool overlapping ratio (W/h) occurs, and triggers complex crystallization/recrystallization phenomena leading to the small grain formation (LAGB density decreases and HAGB density increases (Figure 3-11a)). The formation of such small grains was also reported in the study using double laser exposure (Alinejadian et al., 2023).

Similar conclusions can be made for the specimens printed using the $VED - BR$ set E. The C-60 and E-120 parameters sets resulting in the highest printed density of this study (~97%) provide the same linear energy densities of 1.35 J/mm. However, the former case implies a greater overlapping of two neighboring tracks and consequently, a narrower heat affected zone

and potentially a greater recrystallization potential, leading at the end, to an overall finer microstructure (100 µm for C-60 as compared to 125 µm for E-120, Figure 3-11a,b).

Although the columnar aspect of a grain structure in LPBF molybdenum is sufficiently addressed in the literature (Braun et al., 2019; Higashi & Ozaki, 2020; D. Wang et al., 2017), the printing strategy to obtain a refined and equiaxed microstructure is not clear-cut, and is highly dependent on the characteristics of a printer used. (D. Wang et al., 2017) highlighted changes in the grain morphology caused by different scanning strategies, while (Higashi & Ozaki, 2020), using a 400 W printer, observed significant variations in the crystallographic texture and grain size, depending on the process parameters. Their observations, coupled with the results of this study, demonstrate the complexity of the crystallization/recrystallisation phenomena occurring during LPBF of molybdenum. To circumvent this complexity while trying to refine the printed microstructure, some authors, such as (Kaserer et al., 2019), have put forth a completely different strategy, using alloying with other elements, such as carbon (C).

3.7.3 Mechanical properties

The room temperature mechanical properties obtained in this study were first compared to an industrial standard B387-18 (B10 Committee, 2018) for vacuum arc-cast and powder metallurgy molybdenum and molybdenum alloy bars, rods and wires (see Figure 3-18). This standard could be considered as a potential target for printed molybdenum. The mechanical properties at elevated temperatures obtained in this study were also compared with the literature (Carreker & Guard, 1956; « Climax Molybdenum », 1950; Fernandez-Zelaia et al., 2022; Rebesan, Ballan, et al., 2021) as shown in Figure 3-18 for the ultimate strength. Note that the referenced authors performed tension testing and reported significant oxidation during high temperature testing.

Regarding our experiments, they were carried out in compression and the measured weight variations are consistent with the expected oxidation kinetics for molybdenum (Nelson et al.,

2014). At 600 °C, samples are supposed to undergo linear oxidation with low kinetics ($k \approx 3.4.10^{-4}$ mg/(cm^2.s)). The overall duration of these tests was too short (< 2h) for such small weight gains to be detected. However, at higher temperatures, competitive oxidation and volatilization occurred, and at over 700 °C, the volatilization of MoO_3 became predominant, leading to linear weight loss kinetics ($k \approx -1.2.10^{-2}$ mg/(cm^2.s)). The theoretical kinetic rates are consistent with our observations (Figure 3-14a) and measurements.

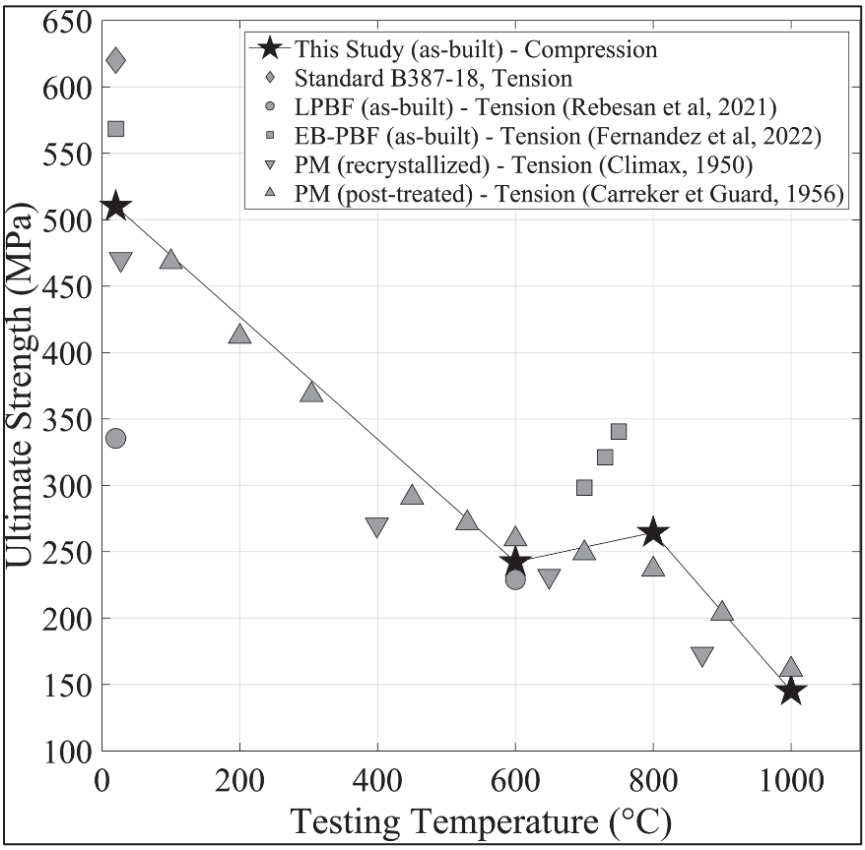

Figure 3-18: Evolution of the Ultimate Strength depending on the mechanical testing temperature. Comparison is made to the standard B387-18 B10 Committee (2018) and the literature Carreker & Guard (1956); « Climax Molybdenum » (1950); Fernandez-Zelaia et al. (2022); Rebesan, Ballan, et al. (2021)

Regarding the strength characteristics, compared to other LPBF-produced specimens (Rebesan, Ballan, et al., 2021), the values obtained in this study are either higher (room temperature) or comparable (600 °C), despite significantly lower printed densities: 97% in this

study as compared to 99.5% in the referenced work. One of the explanations for this discrepancy is the difference in testing modes (compression versus tension). Indeed, the presence of cracks is theoretically more critical in tension than in compression, which can explain higher mechanical resistance at room temperature of the specimens of this study. As far as the high temperature testing is concerned, this difference in testing modes becomes negligible compared to the degradation induced by the concomitant oxidation.

As compared to the EB-PBF molybdenum (Fernandez-Zelaia et al., 2022), the specimens of this study exhibit from 15 to 30% lower mechanical resistance at both room temperature and in the 700 - 750 °C temperature range: 570 MPa (RT) and 320 MPa (700-750 °C) for the former as compared to 500 MPa (RT) and 250 MPa (800 °C) for the latter. This discrepancy can be attributed to much higher printed densities of the EB-PBF specimens as compared to the specimens of this study: > 99.5% in the latter as compared to 96.5% in the former, and a more favorable as-printed texture (mixed (001)/(111)-fiber grains). Furthermore, with EB-PBF using a vacuum atmosphere, the final oxygen content measured in produced parts is generally much lower than within LPBF parts. With EB-PBF, the literature reports 100 ppm or even lower level of oxygen (Fernandez-Zelaia et al., 2021), while with the LPBF process, the values are rather in the 400-2000 ppm range (Braun et al., 2019; Ellsworth et al., 2022; Ramakrishnan, Kumar, Hudon, & Brochu, 2024). Consequently, oxygen segregation at the grain boundaries reported in the literature is more probable during LPBF, leading to a greater embrittlement and lower mechanical properties of the LPBF molybdenum as compared to its EB-PBF counterpart.

Finally, compared to the conventional PM processes, the results obtained in this study are very similar across the entire temperature range. The non-monotonic decrease of mechanical properties around 800 °C observed in this study was also encountered by (Carreker & Guard, 1956). They related this phenomenon to a manifestation of strain aging caused by the presence of impurities in body-centered cubic (BCC) metals. This theory was first proposed and well-studied by Cottrell (Cottrell & Bilby, 1949), who attributed discontinuous yielding in these metals to the pinning of dislocations by impurities or interstitial atoms. These observations are also in qualitative agreement with those of (Túry & Krausz, 1936) on molybdenum containing

nitrogen impurities. Of note, maximum values of strain to failure of pure molybdenum products found in the literature vary significantly: from < 2% for the LPBF Mo specimens in (Rebesan, Ballan, et al., 2021) to ~ 60% for the recrystallized press-sintered specimens in (« Climax Molybdenum », 1950), thus preventing any comparisons with the results of this study.
It is recommended that for high temperature applications, refractory metals, such as molybdenum, should be used in fully recrystallized condition (Cooper & Hoffman, 1984). If the mechanical properties of the as-built specimens of this study appear to be competitive compared to the traditional processes, at high temperatures and after long term exposure, the typical anisotropic microstructure associated with the LPBF process may evolve towards a coarser and equiaxed microstructure, thus negatively affecting the mechanical properties at room temperature. Consequently, depending on the objectives (targeting either room or high temperature applications), different post-treatments can be considered.

In the literature, basic post-treatments such as stress relief (980 °C for 2h) or annealing (1170 °C for 12h) are reported to be highly ineffective in modifying the microstructure and influence the mechanical properties of molybdenum (Rebesan, 2022). To transform the microstructure of LPBF tungsten parts, (Shi et al., 2023) tried to apply HIP treatments with at 1400 and 1600 °C (P = 150 MPa for 2h). According to them, only HIP at the highest temperature of their study (1600 °C) was sufficient to trigger the recrystallization process. Consequently, to improve the isotropy of mechanical properties of the LPBF refractory metals, they must be post-treated at extremely high temperatures, which represents an additional technological challenge. An alternative solution could be to add alloying elements in the feedstock material with the objective of improving its printing behavior, reducing oxidation and refining the microstructure during the process.

3.8 Conclusions

A numerical model previously developed for the melt pool predictions with tungsten powders was used to build a plan of experiments of this study. Structural analyses and mechanical testing at room temperature revealed a strong link between the physical and mechanical

properties of the printed specimens and the process parameters, leading to the selection of an optimal set of printing parameters (P = 179 W, v = 133 mm/s, h = 60 µm and t = 30 µm). This enables to produce crack-free specimens with a printed density of 97%, UCS = 510 MPa, YS = 340 MPa and δ = 11% at room temperature. This same set of parameters was then proven to be effective to obtain competitive mechanical properties at elevated temperatures and provide a sufficient resolution to build geometric artifacts, such as walls, gaps and lattice structures.

According to the results obtained, the possibilities to print high density molybdenum parts with low-power printers appear limited, since the optimal set of printing parameters obtained in the framework of this study are close to the technical limits of the equipment

3.9 CRediT authorship contribution statement

Conceptualization, A.L. and V.B.; methodology, A.L., T.M. and V.B.; software, A.L. and T.M.; validation, V.B.; formal analysis, A.L. and T.M.; investigation, A.L. and T.M.; resources, V.B.; data curation, A.L. and T.M.; writing—original draft preparation, A.L. and T.M.; writing—review and editing, V.B.; visualization, A.L., T.M. and V.B.; supervision, V.B.; project administration, V.B.; funding acquisition, V.B. All authors have read and agreed to the published version of the manuscript.

3.10 Declaration of competing interest

The authors declare no conflicts of interest. The funders had no role in the design of the study; in the collection, analyses or interpretation of data; in the writing of the manuscript; or in the decision to publish the results.

3.11 Acknowledgments

The authors acknowledge the financial support provided by PRIMA Québec (Pôle de recherche et d'innovation en matériaux avancés) in the framework of theM-ERA.NET program, NSERC (Natural Sciences and Engineering Research Council of Canada) and PyroGenesis Canada Inc.

3.12 Data availability

Data are contained within the article.

CHAPITRE 4

MOLYBDENUM 8WT% RHENIUM ALLOY PROCESSED BY LASER POWDER BED FUSION: FROM POWDER PRODUCTION TO MECHANICAL TESTING AT ELEVATED TEMPERATURES

Aurore Leclercq[a], Anna Czech[b], Thibault Mouret[c], Marcin Lis[d], Adriana Wrona[e] and Vladimir Brailovski[f]

[a,c,f] Mechanical Engineering Department, École de Technologie Supérieure, 1100 Notre-Dame Street West, Montreal, Québec, H3C 1K3, Canada

[b,d,e] Centre of Powder and Composite Materials, Łukasiewicz Research Network - Institute of Non-Ferrous Metals, 5 Sowińskiego Street, 44-100 Gliwice, Poland

Article publié dans « International Journal of Refractory Metals and Hard Materials», mai 2025

4.1 Avant-propos

Les premières publications au sujet du tungstène et du molybdène purs ont mis en avant la difficulté d'impression des métaux réfractaires, notamment en raison de leur tendance à la fissuration et ont soulevé de potentielles améliorations à l'aide d'éléments d'alliage comme le rhénium. Dans cet article, une poudre de haute sphéricité en alliage de molybdène-rhénium a été développée par les partenaires du projet et des paramètres d'impression ont été optimisés pour celle-ci. Des analyses physiques et des essais mécaniques à température ambiante et hautes températures ont su démontrer l'intérêt de l'ajout de cet élément d'alliage. Enfin, la fabrication de diverses géométries a permis de révéler le potentiel de cet alliage pour la production de pièces complexes par fusion laser sur lit de poudre.

4.2 Résumé

Le molybdène est très apprécié dans l'industrie en raison de ses propriétés uniques, en particulier à des températures élevées. Les technologies de fabrication additive, en particulier la fusion laser sur lit de poudre (LPBF), sont de plus en plus populaires pour produire des

formes complexes à un coût inférieur par rapport aux procédés de mise en forme conventionnels. Cependant, l'impression de molybdène par LPBF présente des défis, en particulier causés par sa susceptibilité à la fissuration à chaud. Plusieurs approches ont été explorées pour résoudre ce problème, y compris l'alliage de molybdène avec d'autres éléments, qui s'est avéré efficace pour améliorer l'imprimabilité et minimiser la présence de fissuration, en particulier avec l'ajout de rhénium. Dans cette étude, une combinaison de mélange mécanique de poudre de molybdène et d'un précurseur de rhénium, suivie de la réduction du précurseur et de la sphéroïdisation au plasma, a été utilisée pour produire une poudre sphérique d'alliage molybdenum-rhénium (8 % en poids, distribution 30-55 µm) aux propriétés rhéologiques adaptées au procédé LPBF. Par rapport au molybdène pur, l'utilisation de la poudre alliée a entraîné une augmentation de la densité imprimée sans fissure, de 97 à 98,5 %, et de la contrainte ultime en compression, de 240 à 340 MPa, à 600 °C et de 150 à 190 MPa à 1000 °C, au détriment d'une réduction de ~5 % de la déformation maximale à rupture. Pour démontrer le potentiel de l'impression de géométries complexes à l'aide des poudres développées, des artefacts géométriques complexes contenant des lettres de 0,25 mm de longueur, des sections denses larges et des structures lattices de type diamant à 50 % de densité de 0,7 mm de largeur ont été imprimés avec succès.

4.3 Abstract

Molybdenum is highly valued in industry because of its unique properties, especially at high temperatures. Additive manufacturing technologies, particularly laser powder bed fusion (LPBF), are becoming increasingly popular for producing complex shapes at a lower cost as compared to the conventional forming processes. However, printing molybdenum with LPBF presents challenges, especially caused by its hot cracking susceptibility. Several approaches have been explored to address this issue, including alloying molybdenum with other elements, which has proven effective in enhancing the printability and minimizing the occurrence of cracking, particularly with the addition of rhenium. In this study, a combination of mechanical blending of molybdenum powder and a rhenium precursor, followed by the reduction of the precursor and plasma spheroidization, was used to produce spherical 30-55 µm molybdenum-

rhenium (8 wt%) powders with rheological properties suitable for LPBF. Compared to pure molybdenum, the use of the alloyed powder led to an increase in the crack-free printed density, from 97 to 98.5%, and in the compressive strength, from 240 to 340 MPa, at 600 °C and from 150 to 190 MPa at 1000 °C, at the expense of a ~5% reduction in the compression strain. To demonstrate the potential of printing complex geometries using the developed powders, complex geometry artifacts containing 0.25 mm-thin letters, wide dense sections and auto-supported 50%-density 0.7 mm-thin strut diamond lattice structures were successfully printed.

Keywords: Laser powder bed fusion, Molybdenum-Rhenium alloys, Powder production, Mechanical testing, Elevated temperature tests; Crack-free specimens

4.4 Introduction

Molybdenum (Mo) belongs to the refractory metal group, coming in fourth in line after Tungsten, Rhenium and Tantalum in terms of melting temperature (T = 2896 K / 2623 °C). Like other refractory metals, molybdenum is distinguished by its excellent electrical (Holmwood & Glang, 1965) and thermal (Rebesan, Ballan, et al., 2021) conductivity, a low coefficient of thermal expansion (Hidnert & Gero, 1924), as well as a high mechanical (Baker, 1998), wear (Hwang, Kim, Park, Park, & Lee, 2024) and corrosion (H. Zhao et al., 2023) resistance. This element is regularly introduced in small concentrations into the compositions of advanced alloys (e.g., various INCONEL®, Hastelloy B or titanium alloys, such as Ti6246 for example) to improve their corrosion resistance. For elevated temperature applications, with UTS = 210 MPa (Baker, 1998) and E = 280 GPa (Plansee, 2023) at 800 °C, molybdenum manifests the highest strength- and stiffness-to-density ratios among all the refractory metals. Due to this unique combination of properties, molybdenum is a promising candidate for various applications in different fields, including the medical, petrochemical, aerospace and defense industries (Shields, 2013; Wadsworth et al., 1988).

The creation of semi-finished molybdenum products (e.g., sheets, rods and bars) is currently driven by conventional forming processes, mainly including powder metallurgy and plastic

deformation processes, such as forging, rolling, etc. To manufacture complex geometries, subtractive and joining processes are required, but these have their own limitations when applied to refractory metals, such as high machining costs and a strong oxygen affinity in the heat affected zone. In response, the recent and rapid development of additive manufacturing (AM) technologies offers a promising technical solution enabling the production of complex shapes at reduced processing cost. Over the years, numerous AM technologies have been tested to print refractory metals (Talignani et al., 2022; D. Wang et al., 2017), each with its own pros and cons. The layer-by-layer laser powder bed fusion (LPBF) is the most mature AM technology. The process uses a laser heat source to sequentially melt one layer of powder at a time according to a predefined pattern generated from a sliced 3D CAD model of the desired part. In contrast to its main competitor, electron beam powder bed fusion (EB-PBF), LPBF is distinguished by its higher resolution, greater printing flexibility, and lower processing costs (Colomo et al., 2020; Gradl et al., 2022).

Notwithstanding all the advancements in industrial LPBF application, the printability of molybdenum remains a significant challenge. The high energy input required to reach the melting temperature and the rapid solidification rate of the process result in substantial temperature gradients and residual stresses. Additionally, the high ductile to brittle transition temperature (DBTT) of molybdenum contributes to its susceptibility to cracking during printing. The DBTT of molybdenum is reported to be highly dependent on the segregation of impurities at the grain boundaries (GB) and on the material microstructure (E. Pink and R. W. Armstrong, 1970; Hiraoka, 1990; Hiraoka, Kurishita, Narui, & Kayano, 1995; Xing et al., 2022). Most researchers agree to consider molybdenum as a crack-prone material, and many of them tried to overcome this problem using different strategies including optimization of printing parameters (D. Wang et al., 2017), preheating of the baseplate (Braun et al., 2019; Iveković et al., 2018; Müller et al., 2019), and preheating of the powder bed using a multiple exposure approach. To date, the two first strategies have demonstrated low-to-zero efficiency, while the third approach has appeared to be more technologically promising but less economically efficient in this regard (Alinejadian et al., 2023).

In the literature, alloying molybdenum with different elements represents a common solution for improving its printability, increasing its density, and simultaneously, mitigating hot cracking (Ellsworth et al., 2022; Gan et al., 2024; Guan et al., 2023; Kaserer et al., 2019; Oehlerking et al., 2022). Various alloy compositions have been tested, and depending on the nature of the alloying elements involved, several types of microstructural modifications improving the cracking resistance of molybdenum have been reported. These modifications target the main factors responsible for cracking, including the propensity to form irregular microstructures or to segregate interstitial elements at grain boundaries (GB). In fact, alloying has been successfully used to transform coarse columnar microstructures into equiaxed grain structures or submicron cell structures (M. Guo, Liu, Sun, & Gu, 2022; Kaserer et al., 2019; D. Wang et al., 2019). Alloying has been also successfully used to promote GB cohesion and to limit their oxidation (Ellsworth et al., 2022; Gan et al., 2024), as well as to decrease the DBTT (Hu et al., 2015; Takida et al., 2004). Thus, depending on the physical, mechanical and microstructural features expected, the selection of alloying elements is fundamental. Moreover, both the pre-alloyed powders and in-process alloyed powders can also be considered in this regard.

As an example, dispersion within the powder bed of oxygen-sensitive elements, such as carbon (C, 0.45 wt%, (Kaserer et al., 2019)) under its elemental form, or through the use of silicon carbide (SiC, 0.1 wt%, (Ellsworth et al., 2022)), appeared to be a promising solution to increase the printed density of molybdenum and to reduce its brittleness. In the atmospheric conditions of the LPBF process (O_2 low partial pressure), these species enable the reduction of the overall oxygen content, through the outgassing of a volatile carbon monoxide CO. Thus, segregation at the grain boundaries and the formation of detrimental molybdenum oxide MoO_3 is limited. Furthermore, elemental carbon powders modify the solidification behavior and lead to a refined cellular microstructure, with molybdenum surrounded by molybdenum carbide Mo_2C, while nanosized SiC particles apparently block dislocations and inhibit the propagation of cracks. Effectively, by combining the dispersion of elemental carbon powders with the baseplate preheating to up to 800 °C, the authors of the referenced studies were able to reduce cracking.

Alloying refractory metals with others transition metals was also found to be effective in inhibiting the cracks formation associated with the LBPF process by (Gan et al., 2024) who successfully used chromium (Cr) and titanium (Ti) additions into molybdenum. For their part, (M. Guo et al., 2022) dispersed nickel (Ni) and iron (Fe) nanoparticles within tungsten powders. In both cases, the authors reported cracks suppression. From their observations, using nanosized particles with a large surface area promote the formation of an equiaxed fine grain microstructure with sufficient ductility to prevent cracking. Conversely, with coarser particles (µm range), they attributed the resistance to cracking to the formation of solid solutions strengthening the parts and capturing oxidation traces (MoO_3) in the melt pool. Recently, some authors have also steered their attention to high-entropy refractory alloys (RHEA) (Ron et al., 2022; J. Xu et al., 2022).

One of the most common and commercially available Mo alloys is Titanium-Zirconium-Molybdenum (TZM). It contains small concentrations (<1 wt%) of titanium, zirconium and carbon enhancing its mechanical strength through the precipitation of Mo and Ti carbides. This mechanism is analogous to the process observed with the addition of elemental carbon powders. In fact, oxidation, carboreduction and outgassing inhibit segregation of impurities at the grain boundaries through the formation of gaseous carbon monoxide and titanium oxides (TiO bp = 3227 °C, TiO_2 bp = 2970 °C) (Kaserer et al., 2019). The same authors also reported oxygen bounding with zirconium (ZrO_2) and with $(Mo,Ti)_xC_y$ precipitates, which lead to LPBF parts with purified grain boundaries. They also demonstrated that a TZM-modified alloy with an increased carbon content (up to 2.3 at%) enables to create refined and isotropic cellular microstructures with improved elevated-temperature mechanical properties (YS = 450 MPa, UTS = 600 MPa at 800 °C) over what could be obtained using conventional processes [34]. In all cases, the authors of the above works reported the LPBF production of high density and crack-free TZM samples. The main drawback of the TZM alloy is its high price per weight ratio, which is at least three times higher than that of pure molybdenum. This is the reason why the most common alloying solution for refractory metals continues to be their combination in

dual alloys with reduced DBTT, enhanced ductility, and suppressed cracking (Leonhardt et al., 1999; Li, Wu, Xue, & Wei, 2023; Yamamoto et al., 2021).

In the above context, rhenium (Re) represents one of the most promising alloying elements for dual refractory alloys, notwithstanding a related increase in powder cost. For example, alloys such as Mo47.5Re or W25Re30Mo (wt%) have shown remarkable enhancements in their mechanical properties at room (Leonhardt et al., 1999) and high (R. H. Cooper Jr and E. E. Hoffman, 1984) temperatures, respectively. (Oehlerking et al., 2022) reported the successful LPBF printing of complex demo parts with Mo47.5Re powders and an almost 60% improvement in their room-temperature mechanical properties. However, the authors were not able to prevent cracking due to an excessive residual oxygen content.(Eckley et al., 2023) investigated the impact of adding 5, 10 and 25 wt% of rhenium on the room-temperature flexural strength of Mo-Re alloys. They reported a softening effect occurring for the low Re content, no changes for the intermediate Re content, and a slight hardening for the high Re content. These results are in agreement with the extensive study conducted by J. Stephens and (Stephens & Witzke, 1971), who identified a Re threshold separating the softening and the hardening behavior of Mo-Re compounds at Re ≈ 16 at% and/or at 0.16 T_m Mo (~420 °C).

Although the production catalogues of powder manufacturers have grown significantly over the years, the process of obtaining molybdenum-based powders with specific alloying compositions, such as those described previously, remains challenging and costly. The powder production step is crucial as the quality of LPBF parts is significantly influenced by the uniformity and density of the powder bed, which in turn depends on the morphology and size distributions of powder particles (Field et al., 2020; Philips et al., 2020). Traditional mechanical methods (*e.g.*, grinding, mechanical synthesis, etc.) or physicochemical methods (*e.g.*, reduction of compounds, condensation from the gas phase, synthesis from solutions, etc.) used to produce alloyed powders are unsuitable for this process. Powders produced with such methods are generally characterized by an irregular particle shape and a low bulk density, likely to negatively affect the density and mechanical properties of printed parts.

Spherical powders can be produced using different physical atomization methods. Wide applications of some of these methods, such as the plasma rotating electrode process (PREP) (Hao et al., 2019; X. Liu, Wang, Hu, Chen, & Volinsky, 2015; Qiu, Chen, & Xiang, 2020) or ultrasonic vibrations-assisted atomization (Bałasz, Bielecki, Gulbiński, & Słoboda, 2023; Hinrichs et al., 2021), are limited because of the accompanying low production rates. The use of other physical methods, such as water atomization, is much more cost-effective, but results in somewhat coarse and irregular-shape particles. Moreover, the high oxygen intake inherent to this process makes it incompatible with reactive metals such as titanium or aluminum (Fedina, Sundqvist, Powell, & Kaplan, 2020) and unsuitable for refractory metals which are also highly sensitive to oxygen content. The gas atomization method, while being largely used for the production of metal powders for 3D printing (Kassym & Perveen, 2020; Soong, Lai, & Kay Lup, 2023), has limited applicability for refractory metals because of their extremely high melting temperatures.

To overcome the above difficulties related to the production of refractory powders with a high degree of purity and sphericity, industry principally uses plasma-based techniques, such as plasma atomization and plasma spheroidization (Caliari et al., 2016; J. Tang et al., 2020). In the former case, the feedstock is generally a wire, while in the latter, it consists of crushed powder particles. The use of a wire feedstock requires several resource-intensive steps, involving rolling and drawing, which result in extremely expensive products and carries a significant environmental footprint. For its part, the use of plasma spheroidization is less restrictive, since the technique produces spherical powders from their irregular precursors, the latter obtained by various mechanical (crashing, milling), and therefore, less expensive and less polluting methods. In both cases, however, an ingot of a given alloy composition must be cast, making the production of powders of different target formulations economically challenging. To overcome this, alloyed powders suitable for 3D printing can be produced via chemical modifications of their elementary precursors (Majewski, 2013; Wrona et al., 2022) and then subjected to plasma spheroidization.

This study delineates the methodology employed to produce LPBF-ready molybdenum alloy powders containing a low amount of rhenium, Mo8wt%Re, abbreviated as Mo8Re. The alloyed powder is subsequently characterized in terms of its physical and rheological properties and used in a comprehensive printability study involving the physical and microstructural analyses of specimens produced using different combinations of printing parameters. Two optimized sets of printing parameters found during this study are then used to produce specimens for mechanical testing in a wide temperature range. Finally, the results obtained with Mo8Re powders are compared to those acquired with ≥ 99.9%Mo powders, to reveal the effect of a relatively limited rhenium addition on the LPBF printability and mechanical properties of molybdenum.

4.5 Materials and methods

4.5.1 Powder production

Two powder lots were concurrently used in the context of this study: the first is a commercial (Tekna Co. Ltd, Sherbrooke, Canada) plasma-atomized molybdenum powder (99.9% Mo) with the following powder size distribution: D10 = 12.6, D50 = 20.6 and D90 = 32.0 (µm). This powder was considered as a reference feedstock for the LPBF process. The second is an alloyed Mo8Re powder developed for this study.

The production of Mo8Re powders was divided in three successive steps and was entirely realized at the Institute of Non-Ferrous Metal (Łukasiewicz Research Network, Poland). First, the preparation of a feedstock started with the mechanical blending of the molybdenum powder and the rhenium precursor, followed by the latter being reduced to obtain a Mo-Re mixture. To this end, commercial high purity Mo powder (99.99%, KAMB Import Export) with a particle size range of 17-78 µm was selected. Regarding the rhenium, it was introduced as ammonium perrhenate (APR) NH_4ReO_4 (99.9%, Innovator Ltd). The mixture was made according to the stoichiometric Mo8Re proportions (88.87 %wt Mo + 11.52 %wt NH_4ReO_4). The reduction process that enables to obtain metallic rhenium was conducted at 800 °C in 100% hydrogen atmosphere for two hours. This specific temperature is associated with the

APR reduction temperature. During the thermal treatment, direct NH_4ReO_4 reduction (4.1) and/or indirect reduction from the oxides (mainly Re_2O_7, ReO_3 and ReO_2) occur, depending on the temperature of the reaction (J. Tang et al., 2020).

$$2NH_4ReO_{4(s)} + 7H_{2(g)} = 2Re_{(s)} + 8H_2O_{(g)} + 2NH_{3(g)} \quad (4.1)$$

Then, the Mo-Re mixture was introduced in a customized plasma spheroidization system. To generate Ar-H_2 plasma, a 7MB plasma torch was used (Sulzer Metco (Caliari et al., 2016)). The addition of hydrogen enables to increase the enthalpy and temperature of plasma flame, which is beneficial in the production of spherical high-melting powders. The powder was injected perpendicularly into the plasma flame area, melted inside and sprayed in the form of spherical droplets. After leaving the plasma zone, liquid particles were rapidly cooled down in an inert atmosphere to minimize their oxidation. The plasma spheroidization parameters used are summarized in Tableau 4-1. This spheroidization step is an essential stage of the whole powder production technology chain. It enables to improve the flowability of powder by changing the particle morphology from irregular to spheroidal, also enhancing the overall chemical composition homogeneity and bulk density.

Tableau 4-1: Plasma spheroidization process parameters

Current (A)	Plasma gas flow rate-argon (l/min)	Plasma gas flow rate-hydrogen (l/min)	Carrier gas flow rate-argon (l/min)	Powder feeder plate revolutions (rpm)
500	50	10	4	2

The literature demonstrated that the presence of oxygen in powders and printed parts made of molybdenum is one of the main factors leading to embrittlement and cracking during the LPBF process. Consequently, to minimize the oxygen content, a supplementary deoxidization process of the spheroidal powder was conducted at 1050 °C for one hour in a 100% hydrogen atmosphere. A final sieving step through a 90 µm sieve was realized before the powder was used for LPBF printing.

4.5.2 Powder characterization

4.5.2.1 Chemical and phase analyses

The element distribution within the powder was assessed using an electron probe microanalyzer (EPMA) (JEOL JXA-8230, JEOL Ltd., Japan) and its EDS detector. The oxygen content in the powder was obtained with an IR spectroscope (LECO ON836, LECO Corp., USA). The crystalline structure of the powder was determined by X-ray diffraction (XRD) (Seifert XRD7, Cu source, GE Inspection Technologies, USA). These observations and analyses were conducted at different stages of the process to evaluate the efficiency of the production steps.

4.5.2.2 Physical and rheological analyses

The particle size distribution (PSD) was measured using an Analysette 22 Nanotec powder size analyzer (Fritsch, Germany), while its pycnometric density was obtained using an Accupyc 1340 helium pycnometer (Micromeritics, USA). The efficiency of the spheroidization step was evaluated by measuring the specific surface area, using the BET method (Gemini 2360, Micromeritics, USA). The powder flowability was measured using a Hall flowmeter according to the ISO 4490-2018 standard (50 g). Additional rheological measurements were carried out using an FT4 powder rheometer (Freeman Technology, UK). This equipment possesses different testing modes for which detailed information and listed outputs can be found in the manufacturer's documentation and publications (R. Freeman & Fu, 2008; Reg Freeman, 2007). The rheological behavior of the produced Mo8Re powder was compared to that of a pure molybdenum powder used in the reference work (Leclercq, Mouret, & Brailovski, 2025). Five testing modes were applied, namely dynamic flow, aeration, permeability, compressibility and shear. Tableau 4-2 summarizes the metrics obtained from these tests.

Tableau 4-2: List of metrics extracted from the rheometer FT4 analysis and their subsequent influence on the powder flowability

Testing mode	Metrics	Interpretation
Dynamic flow	Basic Flow Energy (BFE, mJ)	Represents the resistance to flow in confined environment
	Specific Energy (SE, mJ/g)	Indicates how powder will flow in an unconfined environment and provides an indication about the shear forces acting between particles
	Bulk Density (BD, g/cm^3)	Represents the bulk density of the conditioned powder
	Flow Rate Index (FRI, w. u.)	Represents the sensitivity of the powder to flow rate change
Aeration	Aeration Energy at 10 mm/s air speed (AE_{10}, mJ)	Traduces the sensitivity to aeration
	Aeration Ratio (AR, w. u.)	
Compressibility	Compressibility Index (CI, %)	Measures the ability of the powder to become compacted when subjected to normal stresses (Packing ability)
Permeability	Pressure Drop (PD, mbar)	Measures the ease with which the powder will release air over a range of stress conditions
Shear	Cohesion coefficient (CC, kPa)	Represents the powder internal resistance to flow
	Flow Function (FF, w. u.)	Measures the shear stress required to initiate flow in a consolidated powder

Finally, the Additive Manufacturing Suitability (AMS) figure of merit (4.2) was used to express the overall suitability of two powder lots for LPBF. The figure was first defined in a work dedicated to the comparison of Ti-6Al-4V powders (Brika et al., 2020) and aims to compare different powder lots of the same material based of selected rheological characteristics representative of the LPBF process. The smaller the AMS value, the more suitable the selected powder for the LPBF process:

$$AMS = \frac{\frac{1}{\rho_{powder}} + CI + PD + SE + AE_{10} + BFE + CC}{7} \quad (4.2)$$

where ρ_{powder} is the relative powder bed density obtained from (4.3).

$$\rho_{powder} = \frac{BD}{\rho_s} \tag{4.3}$$

where ρ_s is the material density obtained by the pycnometer measurements of each powder lot.

4.5.2.3 LPBF process and plan of experiment

In the literature, various printing parameter sets have been tested in a bid to improve the printability of pure molybdenum, leading to very divergent results due to the impact of multiple phenomena occurring during printing (lack of fusion, cracking, etc.). However, a critical analysis of the results obtained in a previous study using a 200W-power LPBF printer (Leclercq, Mouret, et al., 2025) enabled to highlight general trends and formulate some potential solutions to solve the above problems. These solutions include the reduction of the scanning speed and the optimization of the hatching space for a given laser spot size. That was carried out using a series of printing parameter sets defined in the volumetric energy density (VED, (4.4)) - build rate (BR, (4.5)) coordinates:

$$VED\ [J/mm^3] = \frac{P}{vht} \tag{4.4}$$

$$\text{BR}\ [cm^3/h] = vht \tag{4.5}$$

where P (W) is the laser power; v (mm/s), the scanning speed; h (µm), the hatching space and t (µm), the layer thickness.

For pure molybdenum, two different $VED - BR$ sets provided superior results in terms of the printed density and the mechanical properties at room and elevated temperatures: 750 J/mm^3-0.86 cm^3/h and 400 J/mm^3-1.62 cm^3/h. Consequently, the same two $VED - BR$ sets, herein called Set I and Set II (analogous to the $VED - BR$ combinations C and in E in the reference study (Leclercq, Mouret, et al., 2025)), were considered in the present study for

Mo8Re printing. To optimize the printing parameters using these $VED - BR$ combinations, the hatching space value was incrementally increased (h = 40, 60, 80, 100 and 120 µm) to cover the 1.1 to 4 h/t ratio range. The printed samples were tagged with their respective $VED - BR$ set and hatching space denominations. For example, specimen I-80 stands for the one obtained with VED = 750 J/mm³, BR = 0.86 cm³/h, i.e., laser power P = 179 W, scanning speed v = 100 mm/s and hatching space h = 80 µm. Note that the layer thickness t was constant and equal to 30 µm in all the cases. Tableau 4-3 summarizes the printing conditions of the experimental plan.

Tableau 4-3: Variations of the two parameters sets (I and II) printed with a layer thickness of 30 µm

Set	Name	Hatching Space (µm)	Power (W)	Speed (mm/s)	Volumetric Energy Density (J/mm^3)	Build Rate (cm^3/h)
I	I-40	40	179	199	750	0.86
	I-60	60		133		
	I-80	80		100		
	I-100	100		80		
	I-120	120		66		
II	II-40	40	180	375	400	1.62
	II-60	60		250		
	II-80	80		188		
	II-100	100		150		
	II-120	120		125		

The Mo8Re powders were printed under argon atmosphere on a Trumpf Truprint1000 system with a 200 W dual laser source. The printing parameters described in the plan of experiments above were used to produce ten cylindrical specimens (h = 20 mm, Φ = 10 mm), with 5 mm-thickness dense supports (Figure 4-1a). All the specimens were printed on a stainless-steel baseplate without preheating. After removal from the baseplate, the specimens were cut and the samples obtained were used for structural analyses and compression testing at room temperature, RT (Figure 4-1a). Based on the printed density values measured and on the results

of the RT testing, one parameter set was selected as being the best, and it was then used to print specimens for compression testing at elevated temperatures (600, 800 and 1000 °C).

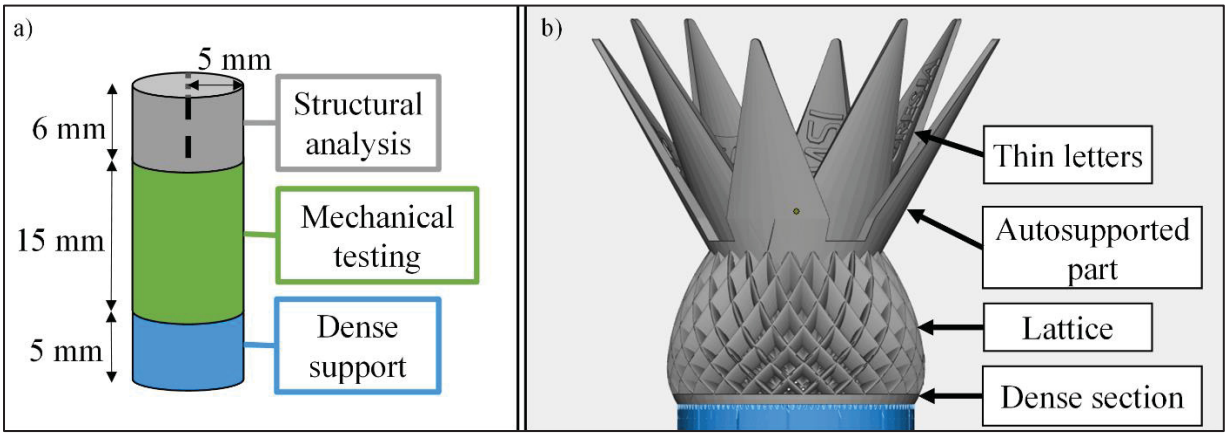

Figure 4-1: a) Schematic representation of a printed specimen with samples for structural analyses and mechanical testing; b) Pineapple artifact with design features

In addition to the cylindrical specimens used to optimize the printing parameters, lattice-containing artifacts in the shape of a pineapple were produced (Figure 4-1b). Apart from the aesthetic aspect, this complex geometry part contains some design features which are challenging to print with the LPBF process, such as thin walls, fine letters, wide dense sections and self-supported structures.

4.5.2.4 Density measurements

The densities of the printed samples reported in the study were evaluated using the image analysis method. Their z-y cross sections were mounted in carbon-doped resin and mirror-polished and subjected to microscopic observations using a LEXT OLS4100 (Lext Olympus Corp., Japan) laser confocal microscope. The raw images were binarized in the MATLAB environment (R2022b, MathWorks, USA), considering a local grey level threshold adjusted to the mean intensity of vicinity pixels. The overall level of porosity was quantified using the white-to-black pixels ratio. The image analysis was carried out on three different observation areas, representing a major part of the samples' cross-sections (~40 mm²). The same images

were also used to calculate the pore density (pore.mm^{-2}), size (equivalent diameter DE in µm, (4.6)) and shape (circularity C without unit, (4.7)). To focus on the most impactful pores (from a mechanical property viewpoint), while considering limitations related to the measurement resolution (1 px = 2.5 µm), all the pores smaller than DE = 20 µm were removed from the analysis. Of note, the contribution of these pores to the overall porosity was negligible, since they represented only ~ 5% in terms of the cumulative pore surface area.

$$Equivalent\ Diameter\ (DE) = \sqrt{\frac{4Area}{\pi}} \tag{4.6}$$

$$Circularity\ (C) = \frac{4\pi Area}{Perimeter^2} \tag{4.7}$$

The image-based density measurements were repeated on different cross-sections of the same sample and on different samples printed using identical parameters. These inter- and intra-part measurements demonstrated that the pore distributions in all the printed samples were relatively uniform, with only slight observable variations.

It should be noted that while the 2D image-based measurement technique used in this study provides only local information about process-induced porosity, it nevertheless represents a reasonable choice since no other porosity detection technique was found suitable for printed molybdenum. For example, the high density of molybdenum (ρ = 10.22 g.cm^{-3}) limits the use of X-ray micro-computed tomography with this material. Also, printed density values measured using the Archimedes technique are frequently compromised by the presence of unmelted particles trapped inside the pores (Leclercq & Brailovski, 2024; Tan et al., 2018).

4.5.2.5 Crystallographic and microstructural analyses

The crystallographic structure of printed samples and traces of their potential oxidation were assessed using X-ray diffraction analysis (X'Pert^3, Co source, Malvern Panalytical Ltd – UK). A deeper investigation of the oxidation of printed parts was realized using an IR spectroscope

(LECO ON836, LECO Corp., USA). A WDS analysis using an Electron Probe Microanalyzer (EPMA) (JEOL JXA-8230, JEOL Ltd., Japan) was used to evaluate the Mo/Re composition ratio inside the printed parts.

The microstructural analyses were carried out on the z-y cross-sections of printed samples using a field emission scanning electron microscope (Hitachi SU-8230, Hitachi Ltd., Japan) equipped with an electron backscattered diffraction detector (EBSD) (e^-Flash^{HR}, Bruker, USA). Prior to the inspection, the polished mounted surfaces were ion milled with a Hitachi EM 4000 plus system (5 kV, 25 rpm, 15 min). The post-treatment of EBSD maps was carried out using the MATLAB MTEX library. From these maps, the grain size, orientation and distribution were extracted according to the E2627-13 ASTM standard (E04 Committee, 2019). In the present work, these metrics are described by analogy to the pore description, as the grain density (grain/mm²), size DE_g (µm) and circularity C_g (without unit). Additional data, such as the band contrast (BC) diagrams and the MacKenzie distributions are also plotted to reveal the presence of substructures and defects. Two subgroups of structural elements are defined depending on the misorientation angle measured, the low angle grain boundaries (LAGB) structural elements, considering the angle range between 2 and 10°, and the high angle grain boundaries (HAGB) structural elements with angles greater than 10°. These substructural elements are quantified using their density values (μm^{-1}) calculated as a ratio of the LAGB and HAGB lengths to the total indexed area.

4.5.2.6 Mechanical properties

Room-temperature compression testing of the specimens in their as-built state was realized in conformity with E9-09 ASTM standard (E28 Committee, 2019) using an Alliance RF/200 testing machine (MTS, Eden Prairie, MN, USA) and 0.01 mm/s compression rate. The force applied during testing was measured by a 200 kN MTS load cell and the displacement monitored using an LVDT. From the strain-stress diagrams plotted, the following metrics were extracted: the maximum stress reached during the test (Ultimate Compression Strength, UCS, MPa), the yield stress (Yield Strength, YS, MPa), calculated at 0.2% on the strain axis, and the strain under maximum load (δ, %). For each testing temperature, three samples were

tested. The compression failure mode was monitored and recorded using a camera located in front of the sample.

High temperature compression testing (600, 800 and 1000 °C) was realized on an MTS 810 testing machine (MTS, Eden Prairie, MN, USA), under argon-controlled atmosphere (flow rate of 27.5 ft^3/h). The force applied was measured by a 100 kN MTS load cell and the displacement monitored by an LVDT. The compression rate was set to 0.075 mm/min according to the E209-18 ASTM standard (E28 Committee, 2018). An infrared furnace, regulated by a K-type thermocouple, was used to control the temperature during the test. Prior to testing, the sample was heated up (stress-free) to the test temperature with a 10 °C/min rate, while monitoring temperature in the core of the sample. This allowed to define a dwell time of 3 minutes to ensure that the temperature at the sample core corresponded to a preset value. For each testing temperature, three samples were tested. The mechanical properties obtained at room and elevated temperatures were then compared to their best equivalents reported in the previous study on LPBF of pure molybdenum powders (Leclercq, Mouret, et al., 2025).

4.6 Results

4.6.1 Elaboration and characterization of the Mo8Re powder

4.6.1.1 Morphological and chemical analyses

Figure 4-2 shows SEM images of the alloyed powder at different stages of its preparation. After mechanical blending and APR reduction (Figure 4-2a), the feedstock retains an irregular morphology (S_{BET} = 0.4 m²/g) of the raw molybdenum powder used. Adding rhenium slightly increases the powder density (ρ = 10.5 g/cm³). The local EDS analysis (Tableau 4-4) realized on the particle surface highlighted an excessive amount of rhenium as compared to the targeted composition, meaning that rhenium agglomerated on the Mo particle surfaces during the reduction process. This observation demonstrated that the temperature (800 °C) used was sufficient to reduce the rhenium precursor but too low to homogenize the chemical composition of the powder.

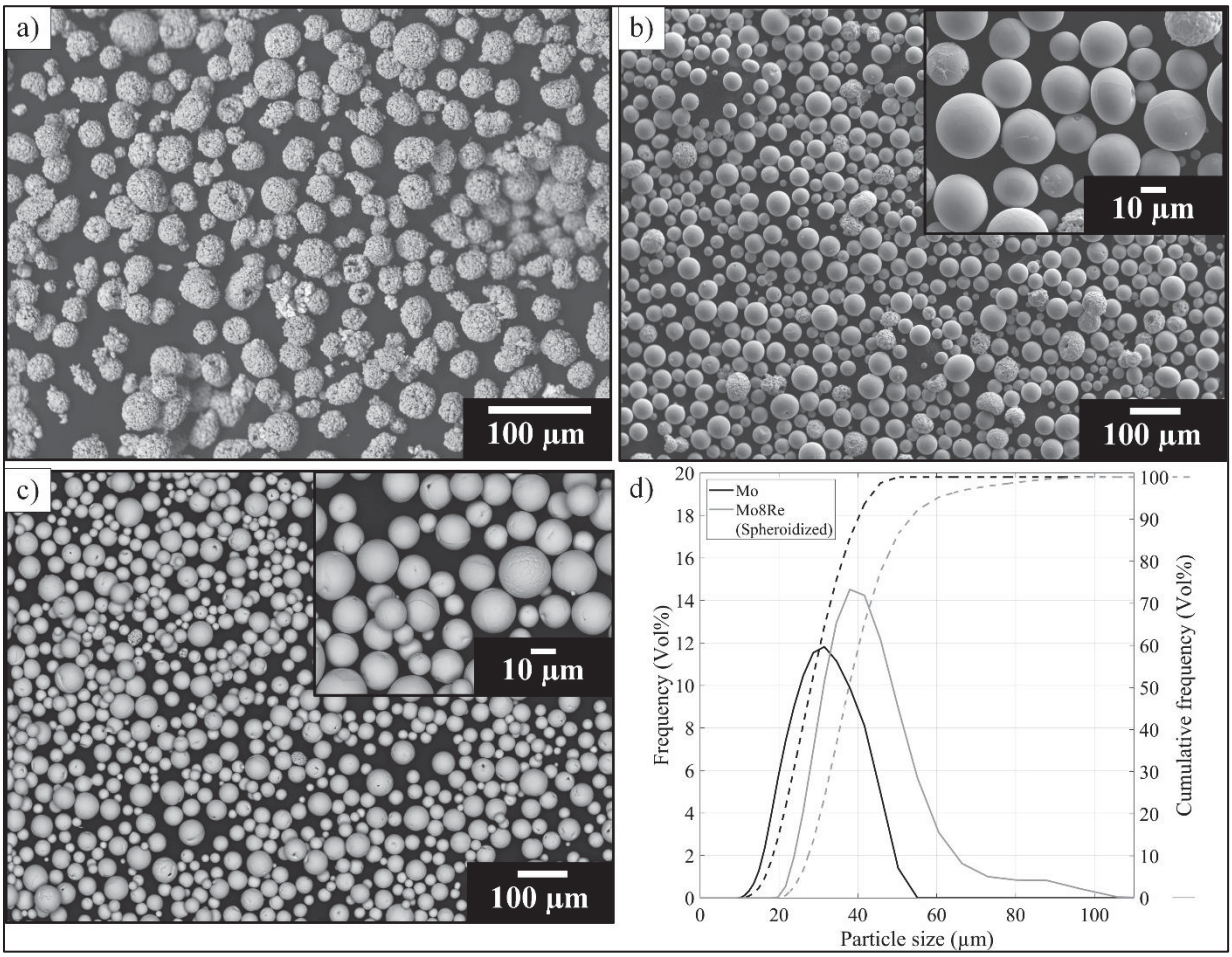

Figure 4-2: Scanning electron microscope images: a) Mo8Re powder after mechanical blending, b) Mo8Re after plasma spheroidization, c) Pure Mo used as reference, d) Particle size distributions of both spheroidized powders (Mo8Re and pure Mo)

Following the plasma spheroidization process (Figure 4-2b), the alloyed powder exhibits the typical spheroidal morphology expected for the LPBF process, resulting in a markedly reduced specific surface (S_{BET} = 0.08 m²/g). Observations revealed the presence of a limited number of satellite particles having irregular morphologies. However, the powder itself displayed a predominantly spheroidal morphology, much like that of the reference 99.9% Mo molybdenum powder (Figure 4-2c). According to the granulometry measurements (Figure 4-2d), the alloyed Mo8Re powder has a slightly larger particle size distribution as compared to its pure molybdenum counterpart.

Tableau 4-4: Chemical composition (Mo and Re: EDS, O: IR), morphology and physical properties of the pure and alloyed molybdenum powders

Powder	Chemical composition (%wt)			Morphology				Physical properties
	Mo	Re	O (ppm)	S_{BET} (m^2/g)	d_{10} (µm)	d_{50} (µm)	d_{90} (µm)	He pycno (g/cm^3)
Mo	99.9*	/	< 500*	/	19.5	29.7	42.1	10.2
Mo-Re Blend	67.1 ± 1.3	32.9 ± 1.3	198	0.4	/			10.5
Mo-Re Spheroidized (round)	92.4 ± 2.5	7.6 ± 2.5	84	0.08	28.7	39.4	55.5	10.5
Mo-Re Spheroidized (satellite)	71.6 ± 16.0	28.4 ± 16.0						

**Commercial data*

The EDS analyses realized on the Mo-Re spheroidized powder (Tableau 4-4) demonstrate the effectiveness of this step in enhancing the homogeneity of the chemical composition. The reported rhenium content is significantly lower and closer to the targeted proportion (~8 %wt), than in the Mo-Re blend, proving that rhenium which was initially concentrated on the surface is now distributed throughout the volume of the molybdenum particles. This observation is supported by the XRD diffractograms (Figure 4-3) and the crystalline patterns identified at each step. After blending, two crystalline structures (Mo, bcc, ICDD 00-042-1120); Re, hcp, ICDD 00-005-0702) are detected, while after the spheroidizing step, only the cubic structure of molybdenum is indexed. According to the Mo-Re phase diagram (Okamoto, 2010), such a reduced amount of rhenium can be accommodated inside the molybdenum crystalline lattice and form a solid solution. Note that introducing a larger element (such as rhenium) inside the molybdenum cubic structure reduces the interplanar distance and induces a slight shift towards larger angles, as observed in Figure 4-3. A simple comparison of this displacement was made with the only $Mo_{0.92}Re_{0.08}$ crystallographic reference available (ICDD 04-001-9280), and suggests a slightly reduced rhenium content compared to the expected composition (8 %wt).

No further qualitative estimation through the Rietveld refinement was performed. Moreover, irregular satellite particles retained an excessive amount of rhenium on their surface. The standard deviation obtained for the EDS measurements made on these particles is significant, highlighting the lack of homogeneity of these satellites. According to these observations, the satellite particles were probably not entirely melted by the flame, meaning that the plasma spheroidization process parameters described in Tableau 4-1 can still be optimized.

Regarding the final oxygen reduction step, the infrared spectroscopy measurements reaching below 100 ppm (Tableau 4-4), indicate a significant decrease in the residual oxygen content. This is beneficial for preventing the oxygen segregation issues at the GB, which are frequently reported for refractories.

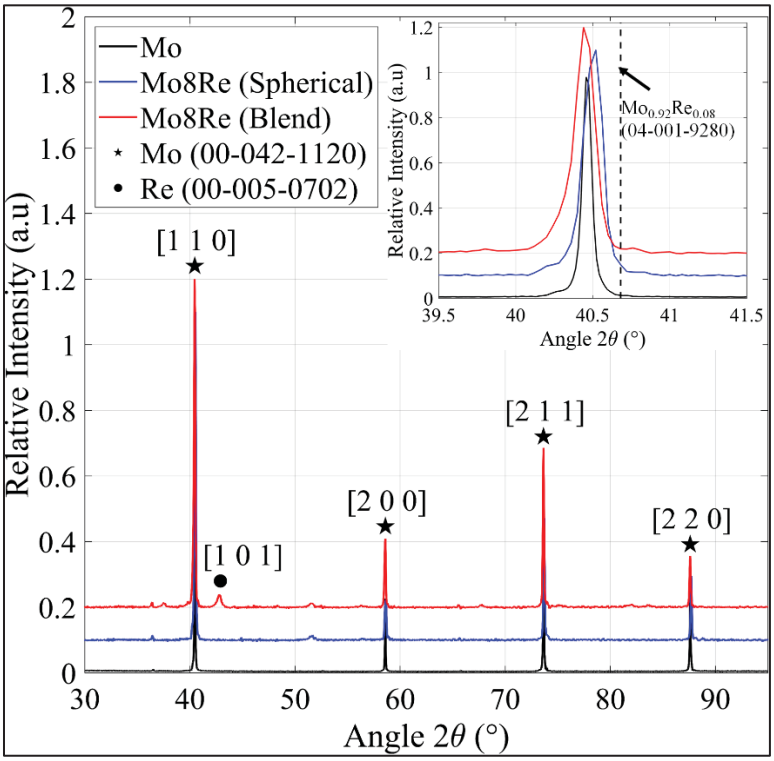

Figure 4-3: XRD diffractograms of the alloyed powder at different steps of the process and of pure molybdenum used for the reference study
Tiré de Leclercq, Mouret, et al. (2025)

4.6.1.2 Flowability and suitability for the LPBF process

The powder flowability measurements using a Hall flowmeter funnel demonstrate the benefits of the spheroidization process as it divides the required flow time (50 g) by two, between the blended and the spheroidized powders (Tableau 4-5). The Hall measurement results of both spheroidized powders, pure Mo and alloyed Mo8Re, are in the same order of magnitude.

The rheological testing made with a FT4 rheometer demonstrates that overall, the two powders are non-cohesive (Tableau 4-5). The aeration tests and the resulting elevated aeration ratio ($AR > 20$) show that air easily breaks the weak cohesive forces between the particles. This behavior is corroborated by the cohesive coefficient (CC) obtained with the shear tests, which is close to or less than 1. Note that the comparison of these metrics for the two powders highlights that the alloyed Mo8Re powder (AR = 45, CC = 1.3) is more cohesive than its Mo competitor (AR = 102, CC = 0.33). The flow function (FF) values measured during the shear tests, reinforce this conclusion, since this value is greater for pure Mo powder (FF = 12.5, i.e., the free-flowing powder category) than for the alloyed Mo8Re powder (FF = 5.4, i.e., the limited-to-easy powder flowing category).

The flow rate index (FRI) measured through the dynamic flow tests is close to unity for both powders (Mo 1.1 and Mo8Re 1.2), meaning that they are insensitive to flow rate variations. A low level of the aeration energy AE and the constant pressure drop lead to a similar conclusion about an excellent sphericity of particles of both powders. Slightly larger particles of the alloyed powder (Figure 4-2c) result in a lower pressure drop (PD) during permeability testing as compared to their pure Mo equivalents. Next, Figure 4-4a presents the results of the stability test obtained from the dynamic flow testing mode. Both powders exhibit unstable, but opposite behavior: a decrease in the total energy value observed with the pure Mo powder can be characteristic of deagglomeration, while an increase in this value in the Mo8Re powder can rather be linked to agglomeration, segregation moisture uptake or de-aeration.

Finally, the rheological properties measurements retained to calculate the AMS of the two powders are summarized in Tableau 4-5 and Figure 4-4b shows a radar graph representing all metrics used to calculate the AMS value. Since the AMS values of two powders show less than a 6% difference, they should not manifest any significant differences in terms of their spreading capacities and powder bed densities.

Tableau 4-5: Powder rheological characteristics (Hall flow and FT4 rheometer)

Powders	Hall flow	FT4 Rheometer							
	Flowability (s/50 g)	BD (g/cm³)	CI (%) at 15kPa	PD (mBar) at 15kPa	SE (mJ/g)	AE_{10} (mJ)	BFE (mJ)	CC (kPa)	AMS
Mo8Re (This study)	38.7 (Blend) 13 (Atom.)	5.16 (±0.99%)	3.48 (±12.30%)	2.51 (±14.10%)	3.35 (±4.24%)	24.50 (±12.10%)	1110 (±3.81%)	1.30	164
Mo (Leclercq, Mouret, et al., 2025)	< 15*	6.04 (±0.47%)	7.65 (±6.57%)	8.31 (±8.51%)	2.53 (±2.65%)	10.60 (±6.21%)	1084 (±1.23%)	0.33	159

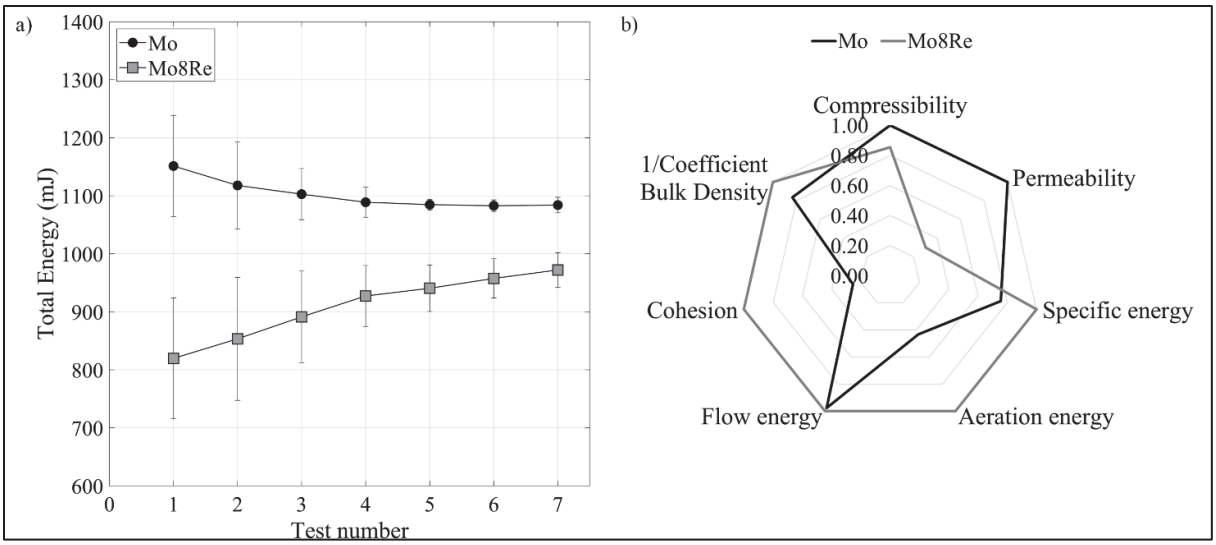

Figure 4-4: a) Stability test plots and b) Additive Manufacturing Suitability (AMS) radar chart for pure Mo and alloyed Mo8Re powders

4.6.2 Density and porosity analyses

Figure 4-5 presents the printed density as a function of the h/t ratio. All the process parameters tested led to a density higher than 95% with a maximum at 98%. No significant differences were observed between the two tested $VED - BR$ sets and a slight increase in density was noticed around h/t = 3.3. Based on these results, two parameter sets were retained, the first one leading to the best measured density of the alloyed powder (II-100) and the second set (II-80) having the same density as the highest-density pure molybdenum samples obtained in the previous study, i.e., ~97%. The latter comparison is intended to isolate the impact of 8% rhenium addition on the material microstructure from that on the printed density. The binarized images of these two samples are shown in Figure 4-5bc with the related information about pore populations. Note no clear tendency was observed with any of the pore-related metrics with respect to the process parameters. The pores population was evaluated in the [15;45] p/mm^2 range, with a median circularity $C50_p$ = [0.60;0.75] and a median pore size $DE50_p$ = [35;50] µm.

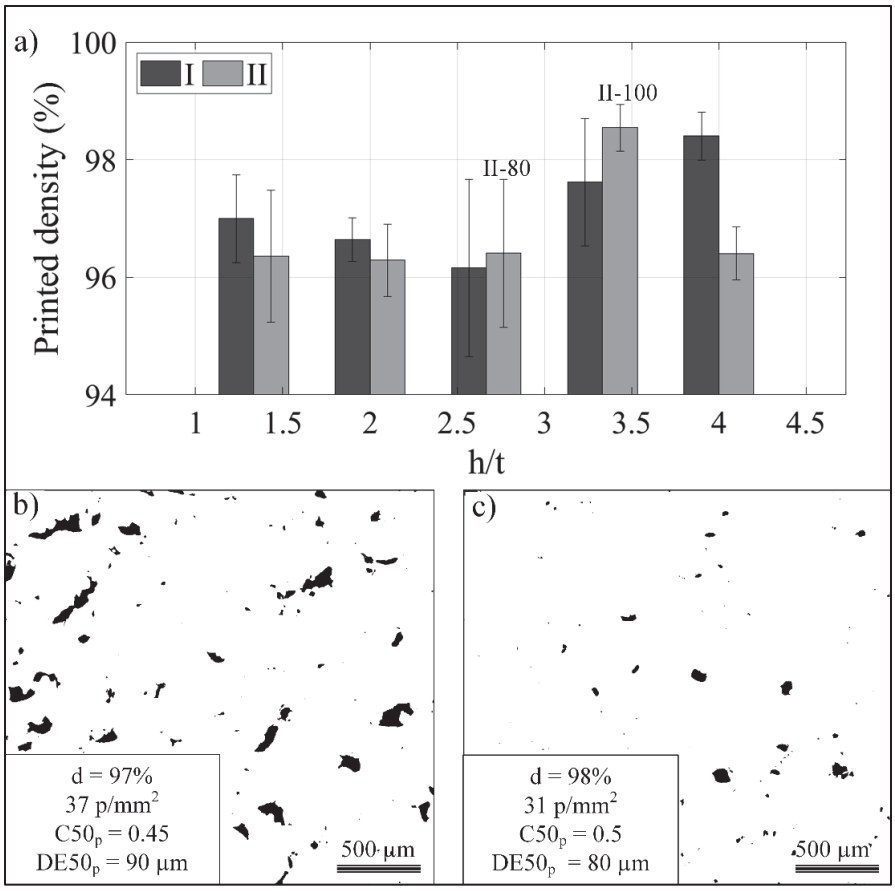

Figure 4-5: a) Measured printed densities as functions of the h/t ratio for the two $VED - BR$ sets; Examples of the binarized surfaces of the samples b) II-80 and c) II-100

4.6.3 Crystalline phases and microstructure

XRD analyses (no shown in this paper) were performed on samples just after their printing and only the bcc phase of pure molybdenum was revealed, with no traces of oxidation that may have occurred during the fabrication process. Further analyses were conducted on the polished surface using WDS to gauge the rhenium behavior in the molybdenum matrix and more precisely detect any oxidation signs. As presented in Figure 4-6abc, the samples are homogeneous, and rhenium did not segregate and was well diffused in the molybdenum matrix. The WDS analyses show an average rhenium content close to the nominal value regardless of the printing parameters used (II-80 Re wt% = 7.8 ± 0.3, II-100 Re wt% = 8.3 ± 0.4). Regarding the residual oxygen content after printing, the IR spectroscopy measurements made on the denser sample (II-100) highlight a significant increase in the oxygen content inside printed

parts (875 ± 210 ppm) as compared to the initial proportion inside the spheroidized powder (Tableau 4-4). The EBSD analyses were then carried out and the BC maps plotted, with the latter revealing no significant differences between the two samples. They were both relatively light-colored, which correspond to good quality patterns and indicate that no defects nor internal stresses were detected. Note that in Figure 4-6d, one of these maps is presented with a superposed bcc molybdenum phase map (uniformity of color proves a single-phase state of the material). These observations were confirmed by their corresponding statistical distributions (Figure 4-6e) which revealed only one peak at BC = 160, suggesting the presence of only one phase associated with molybdenum (Cubic, Im-3m, 229), which is consistent with the extracted phase map (Figure 4-6d), XRD and WDS analyses.

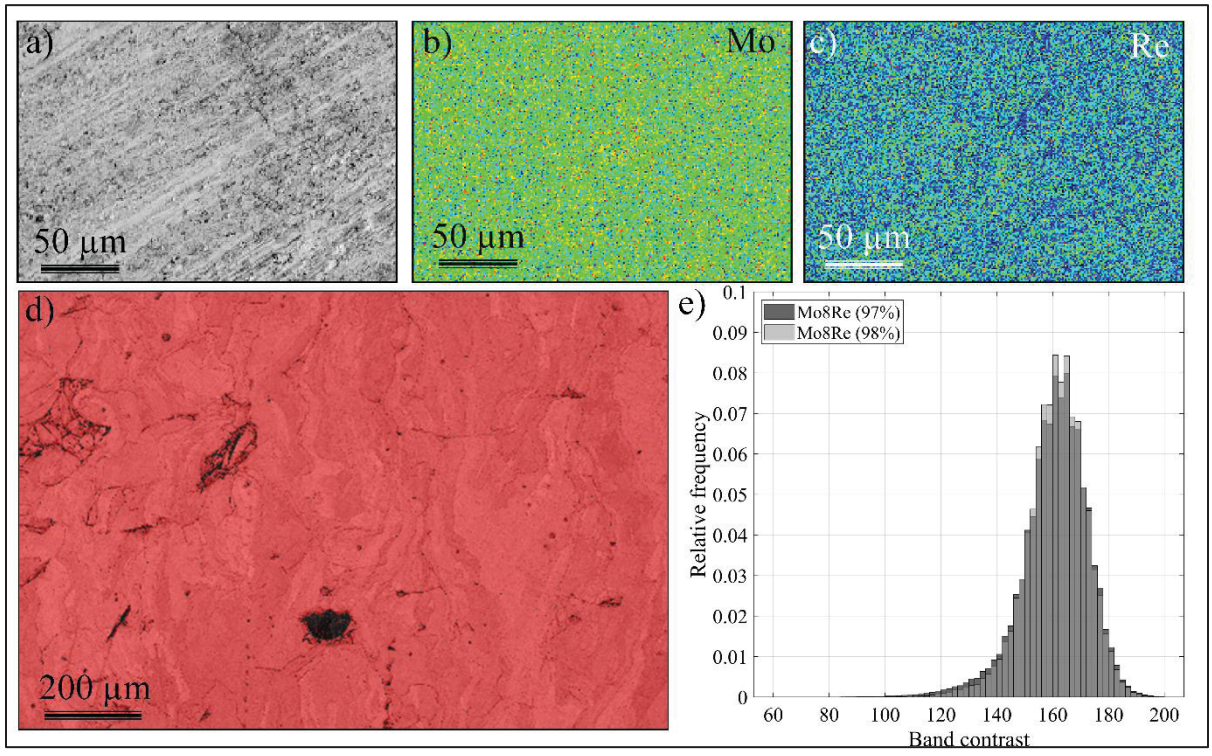

Figure 4-6: WDS mapping of the II-100 (98%) sample: a) polished surface, b) molybdenum and c) rhenium distributions; d) Superposition of the Band Contrast (BC) and bcc molybdenum phase maps of the II-100 (98%) sample; e) BC cumulative histograms of the two retained samples (II-80 (97%) and II-100 (98%))

Also from the EBSD analyses, the MacKenzie plots of the misorientation angles (Figure 4-7a) were analyzed and associated with those of a conventional polycrystalline cubic material having a random texture (Mason & Schuh, 2009), which was confirmed by the IPF maps (Figure 4-7b) and the pole figures (Figure 4-7c). These diagrams also revealed a significant population of structural elements with small misorientation angles (LAGB, < 10°), thus reflecting the presence of substructures accommodated by arrays of dislocations. Finally, no significant differences were found in the LAGB and HAGB densities of both Mo8Re samples (Tableau 4-6). However, the grain density of the Mo8Re 97%-density samples was found higher and coinciding with smaller grains and a greater porosity as compared to their Mo8Re 98%-density equivalents. However, compared to the pure molybdenum samples, the LAGB and HAGB densities of the Mo8Re samples were 1.5 to 2 times higher, and this increase in boundary densities was accompanied by a 15 to 20% decrease in the grain size.

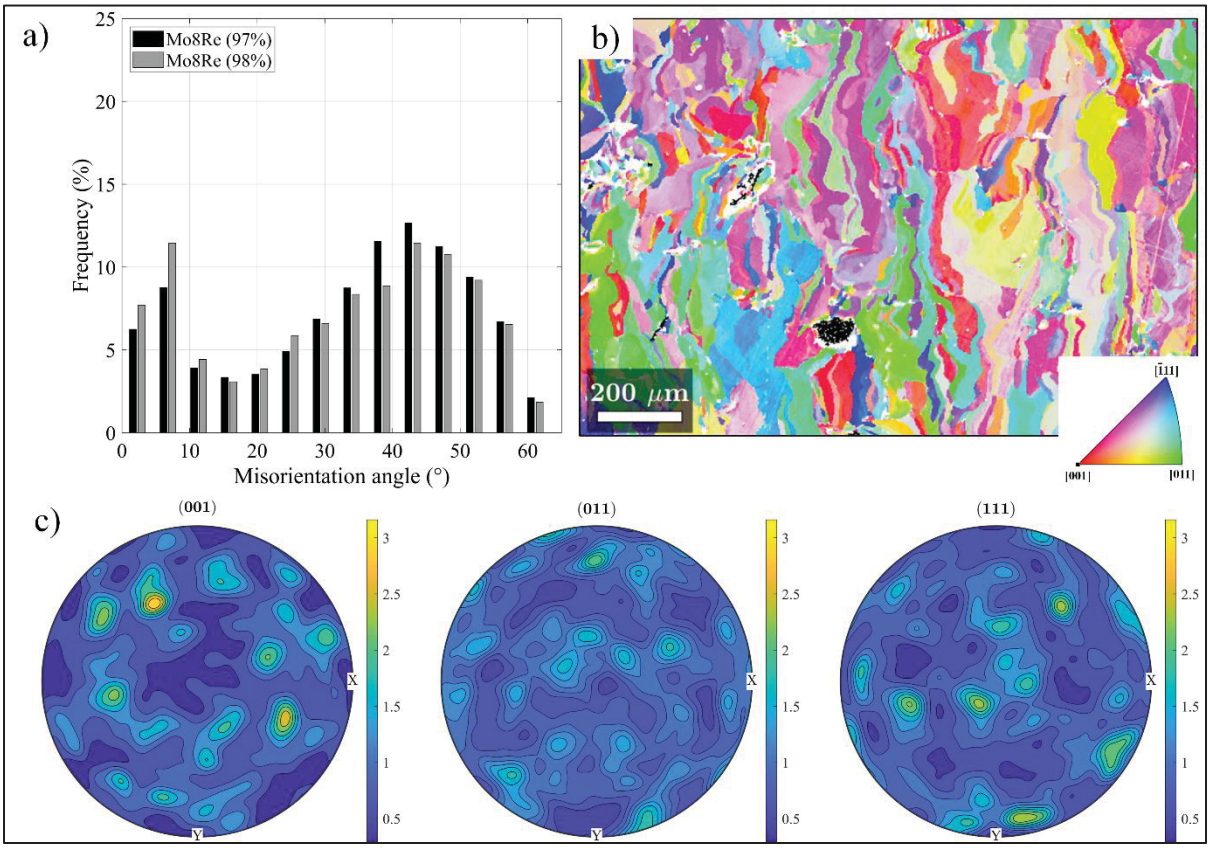

Figure 4-7: a) MacKenzie plots of Mo8Re (97%) and Mo8Re (98%) samples; b) orientation map (IPF Y) and c) pole figures of a Mo8Re (98%) sample

Tableau 4-6: Boundary densities, grain density, size and circularity of the two Mo8Re samples retained and the pure molybdenum from the reference work Tiré de Leclercq, Mouret, et al. (2025)

Sample	LAGB (μm^{-1})	HAGB (μm^{-1})	Grain density (g/mm^2)	$DE90_g$ (μm)	$C90_g$
Mo8Re (98%)	0.12	0.062	654	85	0.7
Mo8Re (97%)	0.10	0.067	804	80	0.65
Mo (97%)	0.06	0.044	278	100	0.7

4.6.4 Mechanical testing at room and elevated temperatures

Figure 4-8a presents the ultimate compressive strength as a function of the testing temperature for the 97% and 98% density Mo8Re samples and their reference 97%-density pure molybdenum counterparts. At room temperature, both Mo8Re samples show lower strength values than their molybdenum counterparts, and the higher the printed density, the higher the mechanical strength. However, at elevated temperatures, the strength values of two alloyed samples were higher than those of the molybdenum samples. It should be noted that the degree of oxidation of the alloyed and unalloyed samples during testing at elevated temperatures was equivalent, as witnessed by their mass loss (~ 4% at 800 °C and ~ 6% at 1000 °C). Of note, contrary to the 98%-density Mo8Re samples, 97%-density Mo8Re samples presented the same non-monotonic temperature evolution of strength as their pure molybdenum counterparts (aging-related increase in strength at around 800 °C (Carreker & Guard, 1956; Cottrell & Bilby, 1949)). This difference in the temperature-related behavior is illustrated by the stress-strain diagrams shown in Figure 4-8bc and comparing the highest-density (98%) Mo8Re samples with their highest-density (97%) pure Mo counterparts.

Regarding the strain under maximum load, no significant differences were observed for the alloyed samples when varying the testing temperature, nor between the 98%-density and the 97%-density Mo8Re samples. Indeed, as listed in Tableau 4-7, the strain under maximum load of the alloyed samples varied from 4 to 7%, following no particular trend, and representing half that of pure molybdenum. All the mechanical properties (YS, UCS and δ) extracted from these compressive tests, are summarized in Tableau 4-7.

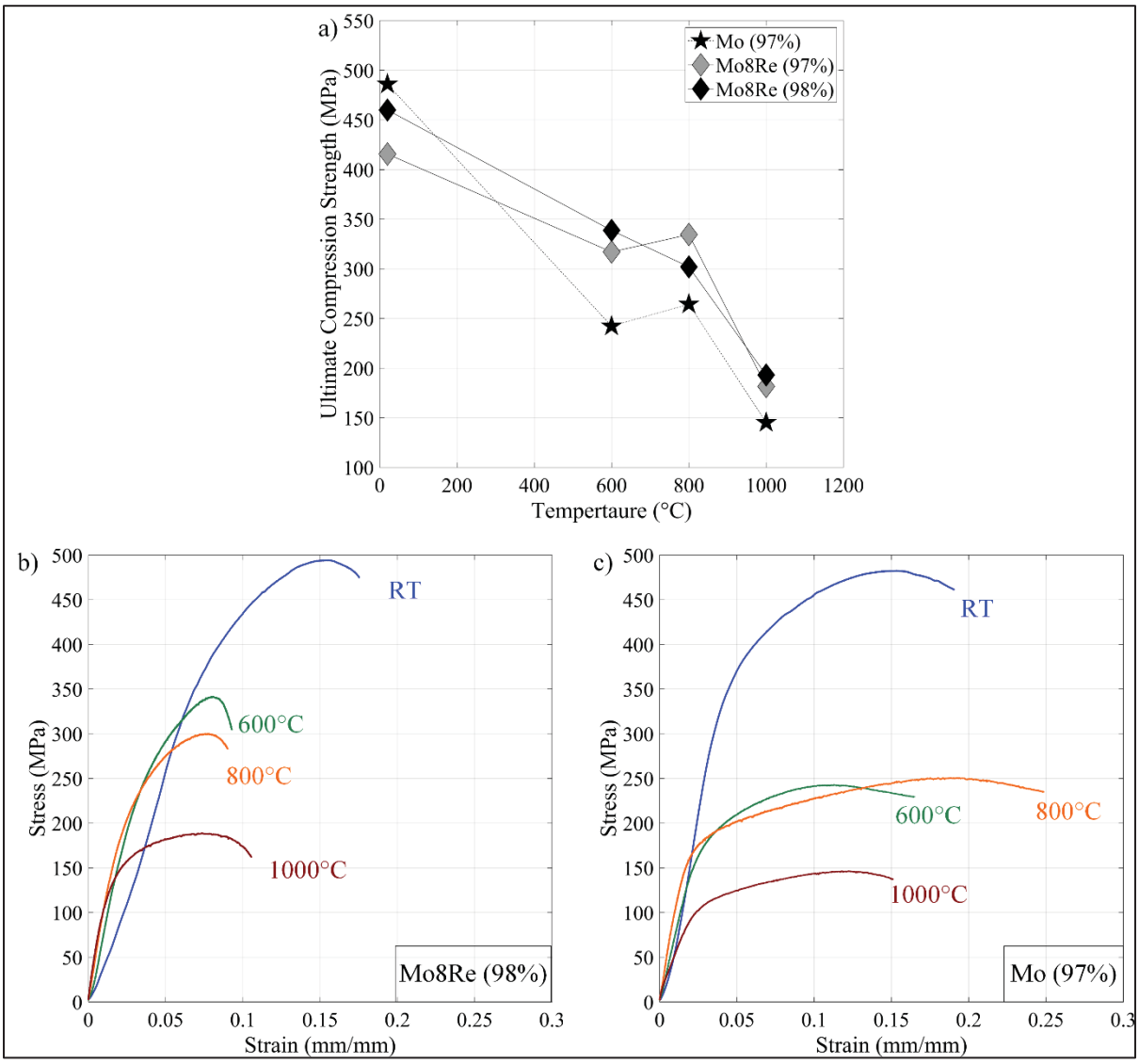

Figure 4-8: a) Evolution of the Ultimate Compression Strength as a function of the testing temperature; b) Typical stress-strain curves at all tested temperatures for b) Mo8Re (98%) and c) Mo (97%) samples

Tableau 4-7: Mechanical properties in compression at room and elevated temperatures

Sample	Temperature (°C)	YS (MPa)	UCS (MPa)	δ (%)
Mo8Re (98%)	20	303 ± 30	460 ± 31	7 ± 1.3
	600	206 ± 8	339 ± 1	4 ± 0.5
	800	186 ± 10	302 ± 20	4 ± 0.3
	1000	119 ± 28	193 ± 31	6 ± 0.6
Mo8Re (97%)	20	256 ± 2	416 ± 22	7 ± 0.8
	600	205 ± 28	317 ± 19	4 ± 1.2
	800	206 ± 8	335 ± 6	4 ± 0.6
	1000	119 ± 4	182 ± 11	6 ± 0.1
Mo (97%)	20	340 ± 20	500 ± 15	11 ± 1
	600	150 ± 20	240 ± 30	8 ± 1
	800	160 ± 5	260 ± 8	14 ± 1
	1000	90 ± 10	150 ± 18	9 ± 4

4.6.5 Artifacts

The complex pineapple-shaped structure was successfully printed in two different formats, measuring 4 and 2 cm in height, respectively. The smallest version is not a simple downsizing of the larger one, but rather, a geometric adaptation. Indeed, the leaves in the shorter one are of a shorter stature, with a restricted area allocated to fine letters. However, the lattice strut size of both formats remains almost identical (respectively 680 and 650 µm). No discontinuity was observed at the transition zone between the dense lower part and the lattice structure (Figure 4-9a). With regards to the self-supported leave structures (angle = 45 °), they were correctly printed throughout their height. On the smaller structure, the text was downsized to fit the available area, and distinguishable fine letters were printed with a minimal thickness going down to 250 µm (Figure 4-9b).

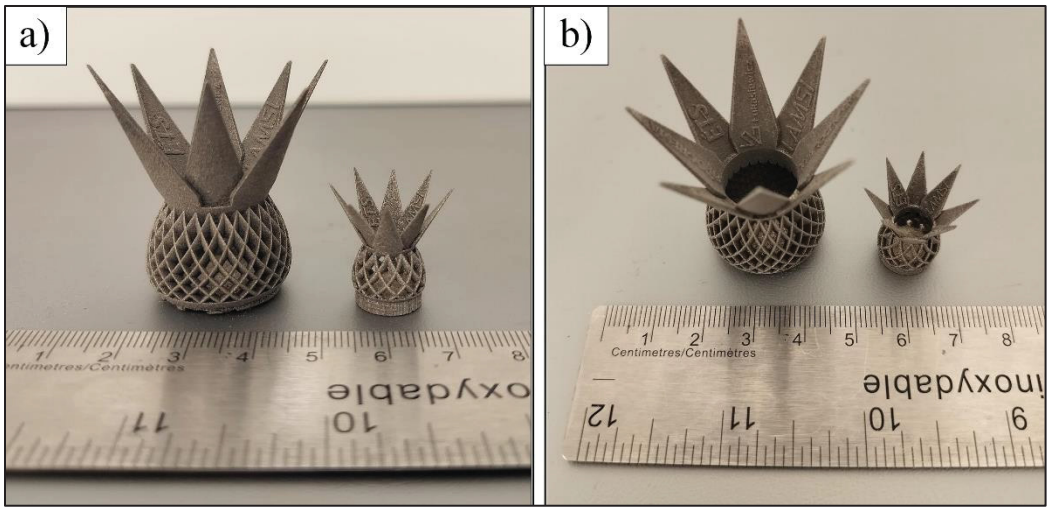

Figure 4-9: a) Side view and b) inclined view of the pineapple artifacts printed using Mo8Re powder

4.7 Discussions

4.7.1 Printability of the alloyed Mo8Re powder

Among the various prints realized with pure Mo and alloyed Mo8Re powders, a slight difference in terms of spreading behavior was observed. Both powders were found suitable for the LPBF process, exhibiting good flowability and spreading properties that enabled to obtain a highly dense powder bed. However, the alloyed Mo8Re powder appeared to be more sensitive to its environment and prone to agglomeration. Indeed, during printing preparation, it was observed that large agglomerates were formed inside the Mo8Re powder container. They were easily breakable during the powder loading by slight agitation inside the supply chamber and did not impact the quality of the powder spread over the baseplate (Figure 4-10a). The agglomerates were also clearly visible during the unloading of the printer (Figure 4-10b). Moreover, blue color traces were observed inside the unsealed containers not used for extended periods of time, evidencing the powder's sensitivity to humidity. This color is correlated with the water dissolution of traces of molybdenum oxide (MoO_3) (Figure 4-10c). This sensitivity to humidity and propensity to agglomeration were not observed for pure Mo powders. Overall,

the aforementioned printing behavior of the Mo8Re and Mo powders was in agreement with the conclusions of the rheological measurements (CC, AE) described in section 4.6.1.2.

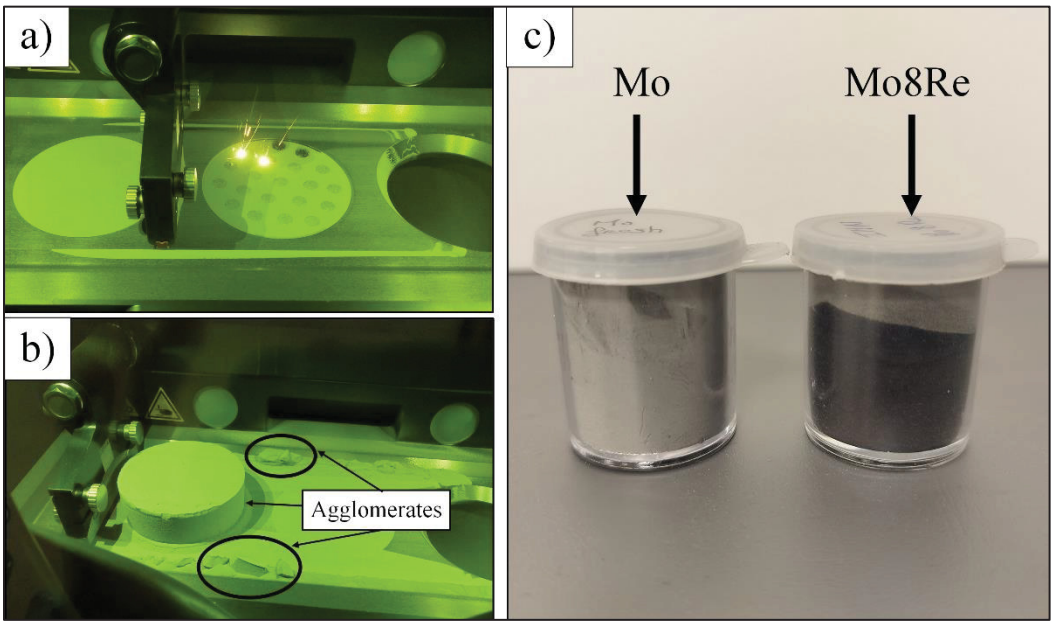

Figure 4-10: a) Powder bed of Mo8Re during printing.
b) Agglomerates of Mo8Re powders observed during the printer unloading.
c) Unsealed containers for storing samplings of pure Mo and alloyed

4.7.2 Impact of the 8wt% rhenium addition on the printed density and chemistry

It was observed in this work that adding 8wt% of rhenium increased the overall density of printed parts (Figure 4-5) as compared to those of pure molybdenum (Leclercq, Mouret, et al., 2025). Indeed, for the same combinations of process parameters, the printed density range of the Mo8Re parts (96-98%) is higher and narrower than that of the pure Mo parts (89-97%). Since it is a known fact that the rhenium addition (Klopp, 1968), even in small proportions (Klopp & Witzke, 1972), enables to decrease the DBTT, and therefore increase the ductility of refractory metals, it may be hypothesized that this phenomenon was one of the main contributing factors to the enhanced densification during printing.

As far as the Re content is concerned, the literature highlighted the metastability of brittle phases in Mo-Re alloys (σ (Carlen & Bryskin, 1994) or χ), especially for high rhenium contents and processes involving high cooling rates (Mannheim & Garin, 2003). Consequently, the production of high rhenium-containing powders and the use of these powders for 3D printing could be challenging as both processes, plasma atomization and LPBF, involve high cooling rates. In our study, a relatively small rhenium addition was homogeneously accommodated inside the bcc crystallographic structure of molybdenum, in agreement with the Mo-Re phase diagram (Okamoto, 2010). This excellent solid solubility of Re in Mo led to a final chemical composition close to the nominal value (≈ 8wt.%) regardless of the printing parameters (see section 4.6.3).

It is reasonable to assert that even higher printed densities can be obtained provided both the Re content and the LPBF conditions are optimized. However, the amount of data on the additive manufacturing of Mo-Re alloys actually available is insufficient to allow to propose an optimal rhenium content for these compounds. This is especially true because of the multitude of factors impacting the densification behavior and the cracking susceptibility of refractory alloys during their laser powder bed fusion.

4.7.3 Microstructure

In conventional powder metallurgy, it was observed that a rhenium addition contributes to a refinement of the microstructure and increases the recrystallization temperature of refractory alloys. In fact, a NASA technical report (Klopp & Witzke, 1972) showed that for the same manufacturing and post-treatment conditions, Mo-14Re (wt%) parts exhibited a finer microstructure than their pure molybdenum equivalents. Similar observations related to rhenium alloying have also been reported for LPBF Mo-Re alloys with respect to the grain refinement (Eckley et al., 2023) and texture evolution (Oehlerking et al., 2022). However, these effects have thus far only been reported for samples printed using rhenium contents greater than 25 wt%.

When comparing the microstructure of the Mo8Re (actual work) and Mo (Leclercq, Mouret, et al., 2025) samples printed using the same sets of printing parameters (II-80 or II-100 in Tableau 4-3, $P = 180$ W, $v = 188$ or 150 mm/s, $h = 80$ or 100 µm, $t = 30$ µm), it can be concluded that even a relatively small addition of rhenium, such as that in this study (8wt%), also results in microstructure refinement: (II-80: 105 µm (Mo) to 80 µm (Mo8Re) and II-100: 125 µm (Mo) to 85 µm (Mo8Re). For the other microstructural features, neither the columnar aspect nor the texture, seem to be affected by adding rhenium, regardless of the printing parameters used.

4.7.4 Mechanical properties

Alloying of Mo with Re has been proven efficient in strongly increasing the mechanical properties at room temperature, as demonstrated by compression testing of Mo-47.5wt%Re LPBF samples in (Oehlerking et al., 2022). An enhancement of the mechanical strength of alloyed LPBF parts as compared to their pure molybdenum equivalents has also been highlighted by flexural testing of MoRe samples with rhenium contents of 10 and 25 wt% (Eckley et al., 2023). In the latter study, parts with a lower rhenium concentration (5 wt%) were also tested, but showed lower mechanical properties at room temperature than their pure Mo counterparts. These findings align with the observations of the present study and can be attributed to the rhenium softening effect in MoRe alloys with lower Re contents described in (Stephens & Witzke, 1971). Note that this softening effect in Mo-low Re content alloy specimens processed by powder sintering and hot radial forging was observed in their as-worked conditions only (Leichtfried, Schneibel, & Heilmaier, 2006). Heat treatments, such as stress relief and recrystallization annealing, led to microstructural changes (dislocation density reduction, grain coarsening, etc.), which suppressed the softening effect. A dedicated study on the impact of heat treatments of LPBF-processed molybdenum-rhenium specimens with low rhenium content on their mechanical properties is yet to be conducted.

To the best of the authors' knowledge, the effect of rhenium addition on the mechanical properties of additively manufactured molybdenum parts at elevated temperatures is yet to be

addressed. However, the literature attests that the addition of rhenium, even in small proportions, improves the mechanical properties of conventionally-manufactured molybdenum parts. For example, (Klopp & Witzke, 1972), a progressive increase in rhenium content (from 7 to 14 at%) enabled to increase the ultimate strength of hot isostatic pressed (HIP-ed) tensile specimens in the 980 to 1650 °C temperature range (almost a twofold increase for 14at% Re addition). A more recent study on powder metallurgy processed Mo42.5 wt% Re parts (H. Huang et al., 2022) also showed a significant increase in the mechanical properties at temperatures of up to 1200 °C. These observations are in line with those of this study, indicating an increase in the elevated temperature properties of MoRe alloys as compared to their Mo equivalents.

4.8 Conclusions

In this study, the spheroidization process was used to change the shape of particles from agglomerated granules to a powder with good particles sphericity and rheological properties suitable for the LPBF process. It also reduced the specific surface area (BET) of the powders by 80%, but according to pycnometric measurements, had no effect on the powder density. The chemical composition within individual particles was homogenized to an average of 8% wt% of rhenium and was preserved and homogenously distributed in the molybdenum matrix after printing. The selected optimal set of printing parameters (P = 180 W, v = 188 mm/s, h = 100 µm and t = 30 µm) led to the printing of crack-free specimens with a density of 98%. Adding rhenium caused a decrease in both the compression strength and strain under maximum load at room temperature as compared to samples printed with pure Mo powders. However, it led to significantly higher mechanical properties in the 600-1000 °C temperature range (ultimate strength of 340 and 190 MPa at 600 and 1000 °C, respectively). Finally, fine letter- and lattice-containing complex structures were successfully printed to demonstrate the printability of these powders.

4.9 CRediT authorship contribution statement

Conceptualization, A.L. and V.B.; methodology, A.L., T.M., A.W. and V.B.; software, A.L. and T.M.; validation, V.B.; formal analysis, A.L. and T.M.; investigation, A.L., T.M.; A.C. and M.L.; resources, A.W. and V.B.; data curation, A.L., T.M., A.C., and M.L.; writing—original draft preparation, A.L., T.M., A.C. and M.L.; writing—review and editing, V.B.; visualization, A.L., T.M., A.C. and V.B.; supervision, A.W. and V.B.; project administration, V.B.; funding acquisition, V.B. All authors have read and agreed to the published version of the manuscript.

4.10 Declaration of competing interest

The authors declare no conflicts of interest. The funders had no role in the design of the study**;** in the collection, analyses or interpretation of data; in the writing of the manuscript; or in the decision to publish the results.

4.11 Acknowledgments

The authors acknowledge the financial support provided by PRIMA Québec (Pôle de recherche et d'innovation en matériaux avancés) in the framework of the M-ERA.NET program, NSERC (Natural Sciences and Engineering Research Council of Canada) and PyroGenesis Canada Inc.

4.12 Data availability

Data are contained within the article.

CHAPITRE 5

LPBF PRINTABILITY AND AS-PRINTED MECHANICAL PROPERTIES OF A TI6246 ALLOY AS FUNCTIONS OF PRINTING PARAMETERS AND MICROSTRUCTURE

Aurore Leclercq[a], Thibault Mouret[b] and Vladimir Brailovski[c]

[a,b,c]Département de Génie mécanique, École de Technologie Supérieure,
1100 Notre-Dame Ouest, Montréal, Québec, Canada H3C 1K3

Article publié dans « Materials Science & Engineering A », août 2025

5.1 Avant-propos

Dans l'optique d'améliorer les performances de l'anneau de refroidissement se trouvant dans l'assemblage du rotor de la turbine ICT, un nouvel alliage de titane plus performant sur une large gamme de températures, le Ti-6Al-2Sn-4Zr-6Mo (Ti6246), a été considéré pour remplacer l'actuel Ti-6Al-4V (Ti64). Dans cette première étude, un protocole expérimental reposant sur la mesure de la largeur de passes laser uniques avant de produire des échantillons d'analyses physiques et essais mécaniques de compression a été mis en place. Au travers de cette démarche, des seuils d'énergie linéique et volumique ont pu être définis, permettant de limiter l'apparition de défauts propres à ce procédé. Les analyses structurales et mécaniques ont révélé des propriétés prometteuses mais ont soulevé la nécessité de considérer des post-traitements avant de pouvoir être intégré dans un dispositif structurel.

La contribution majeure de ces travaux revient au Docteur Thibault Mouret, en charge de la conceptualisation, et nous partagions les travaux d'expérimentation et d'analyses.

5.2 Résumé

La fusion sur lit de poudre par laser (Laser Powder Bed Fusion, LPBF) des alliages de titane a été largement étudiée au cours des dernières décennies et introduite dans l'industrie par de concrètes applications. Récemment, la littérature a mis en évidence l'imprimabilité de divers alliages de titane présentant différentes compositions élémentaires. Parmi eux, un alliage très résilient, le Ti-6Al-2Sn-4Zr-6Mo (Ti6246), a été identifié comme un matériau prometteur pour les industries automobile et aérospatiale, et des résultats de réussite de son impression à l'aide de systèmes haute puissance (P_{max} = 400 W) ont déjà été rapportés. Dans le présent travail, l'alliage Ti6246 a été imprimé sur un système à puissance limitée (P_{max} = 200 W) en utilisant cinquante-trois jeux de paramètres d'impression, avec des variations de puissance laser, de vitesse de balayage et d'écart vecteur, tout en maintenant une épaisseur de couche constante de 50 µm. Les échantillons ainsi fabriqués ont ensuite été caractérisés afin d'établir une corrélation entre les paramètres d'impression, la microstructure, les phases présentes et les propriétés mécaniques. Les résultats ont révélé qu'une densité d'énergie volumique d'environ 100 J/mm³ combinée à un écart vecteur d'environ 150 µm étaient nécessaires pour produire des échantillons à haute densité (> 99,9 %) avec un nombre réduit de défauts liés au procédé (manque de fusion ou pores de surfusion) et une microstructure homogène. Ces échantillons ont montré une excellente résistance mécanique et une dureté élevée (UCS > 1000 MPa et HV > 450 HV0.3), mais une ductilité très limitée, indiquant ainsi la nécessité d'un post-traitement. L'utilisation de paramètres d'impression correspondant à l'apport énergétique le plus élevé (135 J/mm³) a conduit à une transformation de phase partielle in situ $\alpha'' \rightarrow \alpha + \beta$. Ce phénomène a été attribué à un chevauchement significatif entre deux bains de fusion consécutifs, réduisant ainsi la vitesse de refroidissement du matériau solidifié et favorisant la formation des phases stables α et β du titane. Cette dernière observation fournit des informations utiles pour l'impression de pièces Ti6246 à gradients de propriétés fonctionnelles.

5.3 Abstract

Laser Powder Bed Fusion (LPBF) of titanium alloys has been widely investigated in the last decades and introduced in industry with concrete applications. Recently, the literature has

highlighted the printability of various titanium alloys with different elemental compositions. Among them, a highly resilient Ti-6Al-2Sn-4Zr-6Mo alloy (Ti6246) was identified as a promising material for the automotive and aerospace industries, and the results of its successful printing using high-power systems (P_{max} = 400 W) have already been reported. In the present work, Ti6246 alloy was printed on a power-limited system (P_{max} = 200 W) using fifty-three printing parameter sets with variations in terms of laser power, scanning speed and hatching space, keeping the layer thickness constant at 50 µm. The as-built samples were then characterized to correlate the printing parameters to the microstructure, phases and mechanical properties. The results revealed that a volumetric energy density of ~100 J/mm^3 combined with a hatching space of ~150 µm was necessary to produce highly dense (> 99.9%) samples with a reduced number of processing-induced flaws (keyhole pores and lack-of-fusion defects) and with homogeneous microstructure. These samples manifested excellent mechanical resistance and hardness (UCS > 1000 MPa and HV > 450 HV0.3), but a very limited ductility, thus indicating the need for subsequent post-processing. Using printing parameters corresponding to the highest energy input (135 J/mm^3) resulted in a partial in-situ $\alpha'' \rightarrow \alpha + \beta$ phase transformation. This phenomenon was attributed to a significant overlap between two subsequently melted tracks, which reduced the cooling rate in the solidified material and promoted the formation of stable α and β phases of titanium. This latter observation provided useful insight into the printing of functionally graded Ti6246 parts.

Keywords:
Additive manufacturing; Laser Powder Bed Fusion; Titanium alloy; Microstructural evolution; Mechanical properties

5.4 Introduction

In the past decades, the aerospace, automotive and biomedical industries contributed significantly to the development of additive manufacturing (AM) processes, benefiting from their numerous advantages over conventional manufacturing techniques (Javaid, Haleem, Singh, Suman, & Rab, 2021; Tofail et al., 2018). These disruptive technologies are especially

interesting as they are versatile, agile and enable to print complex and intricate geometries with great accuracy, especially for small production lots that are not economically viable with conventional processes. AM processes are generally based on the sequential layer-by-layer build principle, and thus allow the near net shape manufacturing. As a result, the wastes generated during printing and the machining allowances needed to obtain final geometries are greatly reduced, thus decreasing the buy-to-fly ratio, and therefore, the cradle-to-gate environmental footprint. The well-known agility of AM processes facilitates their direct on-demand deployment, thus enhancing the efficiency of the supply chain and minimizing production downtime caused by the need for replacement of worn parts.

Among AM processes, laser powder bed fusion (LPBF) emerges as the best-suited for the production of small-to-medium size parts, since fine powdered feedstocks (20-50 μm) used in the process and narrow melt pools (50-200 μm) generated by the laser beam enable to print parts with resolutions as small as 0.1-0.2 mm at a lower cost than its principal competitors (electron beam powder bed fusion (EB-PBF) or directed energy deposition (DED)) (D. D. Gu, Meiners, Wissenbach, & Poprawe, 2012). During the last two decades, LPBF has been extensively implemented, and numerous printing parameter sets and varieties of printing equipment made available, covering almost all the families of metallic materials, including iron- (Hemmasian Ettefagh, Guo, & Raush, 2021), nickel- (Sanchez et al., 2021), aluminum- (S. K. Sharma et al., 2022) and even refractory (Leclercq & Brailovski, 2024) alloys. As far as the titanium alloys are concerned, LPBF has demonstrated its suitability to print most of them, providing the process parameters are adapted to the physical and chemical properties of the alloys. Among newer printable titanium alloys, titanium aluminide γ-TiAl (Schimbäck, Braun, Leichtfried, Clemens, & Mayer, 2021) and orthorhombic Ti_2AlNb alloy (Illarionov et al., 2023), deserve special mention since they offer an excellent combination of service properties. This notwithstanding, titanium alloys having only a small percent of elemental additions, and more specifically Ti-6Al-4V (hereafter referred as Ti64), are undoubtedly among the most studied LPBF-ready metallic materials (Bartolomeu et al., 2022; Cao, Zou, Lim, & Wu, 2021). Because of its exceptional strength-to-weight ratio (>180 MPa/(g.cm^{-3}) (Boyer, Welsch, & Collings, 2007; Xin Yang, Ma, Zhang, Liu, & Tang, 2022)), Ti64 was initially developed

primarily for aerospace applications (since the mid-1950s), but was ultimately also adopted as a biomedical implant material due to its excellent corrosion resistance and decent biocompatibility (Dias Corpa Tardelli, Bolfarini, & Cândido dos Reis, 2020; Khorasani, Goldberg, Doeven, & Littlefair, 2015).

The mechanical properties of conventional titanium alloys can be tailored to suit specific application requirements via the adjustment of their phase composition and microstructure. Depending on the chemical composition, at temperatures close to room temperature, α (hexagonal close-packed (HCP)), β (body centered cubic (BCC)) or a mixture of both crystallographic phases can generally be found (Destefani, 1990). The alloying elements play a fundamental role in the alloys' phase composition as they act as either α (*e.g.*, Al, N, O, Zr) or β (*e.g.*, Fe, V, Mo, Nb) stabilizers (Ezugwu & Wang, 1997). Alpha and near-α titanium alloys, such as Ti-3Al-2.5V (Grade 9) or Ti-5.5Al-3.5Sn-3Zr-1Nb (IMI 829), are especially interesting for the petrochemical industry because of their excellent weldability, high oxidation and corrosion resistance at elevated temperatures, and the highest strength in these conditions (Tabie, Li, Saifu, Li, & Xu, 2020). However, their modest room temperature mechanical properties, combined with poor workability, make them considerably less noteworthy. Furthermore, as single phase alloys, their mechanical properties cannot be improved by controlled heat treatment, but only using thermomechanical processing, which is significantly more expensive (Weiss & Semiatin, 1999). In this context, $\alpha + \beta$, near-β or β alloys with varying proportions of β stabilizers have been developed to improve both the strength and workability of these multiphase materials via the appropriate heat treatments (Jin et al., 2023; Yadav & Saxena, 2020). The ability of titanium alloys to retain a significantly high β content in the 20-900 °C temperature range is characterized by the beta-stability index (SI_β) (Cotton et al., 2015; Kolli & Devaraj, 2018; Soundararajan et al., 2020). This index is calculated using equation (5.1), where $[\mathrm{Mo}]_{\mathrm{EQ}}$ and $[\mathrm{Al}]_{\mathrm{EQ}}$ correspond respectively to the equivalent molybdenum (5.2) and aluminum (5.3) concentrations, and the higher the value of this index, the greater the alloy's propensity to retain β phase after quenching from the temperatures above the beta transus.

$$SI_\beta = [Mo]_{EQ} - [Al]_{EQ}\ (wt\%) \tag{5.1}$$

$$[Mo]_{EQ} = [Mo] + 0.67[V] + 0.44[W] + 0.28[Nb] + 0.22[Ta] + 2.9[Fe] + 1.6[Cr] + 1.25[Ni] + 1.7([Mn] + [Co]) \tag{5.2}$$

$$[Al]_{EQ} = [Al] + {}^1/_3\,[Sn] + {}^1/_6\,[Zr] + 10([C] + [O] + 2[N]) \tag{5.3}$$

Among duplex ($\alpha + \beta$) alloys, Ti-6Al-2Sn-4Zr-6Mo (hereafter called Ti6246) stands out and it is currently used to produce such parts as compressor disks and blades for turbine engines. Ti6246 provides excellent elevated temperature mechanical properties, such as YS = 935 MPa (Hucek, 1979), as compared to 755 MPa for Ti64 (Meier et al., 2023), both at 400 °C. Sometimes, Ti6246 is even considered a near-β titanium alloy as it is prone to retaining a greater fraction of β phase (SI_β = -1.33) compared to other $\alpha + \beta$ alloys, including Ti64 (SI_β = 3.33). In addition to its excellent strength, Ti6246 demonstrates a good oxidation resistance at moderate temperatures by forming a rutile TiO_2 layer on the surface (Evans & Ward, 2001; Vincent et al., 2021), as well as a great corrosion resistance in diverse environments thanks to its high molybdenum content (Hargrave, Gonzalez, Maskos, Skogsberg, & Grauman, 2010; F. F. Zhang, Feng, Zhu, & Song, 2021).

One of the specific and interesting features of Ti6246 alloys processed by LPBF is the formation of metastable martensite microstructures which differ from those obtained for the majority of titanium alloys. For example, in the majority of duplex ($\alpha + \beta$) alloys, such as Ti64, rapid cooling (~10^6-10^8 °C/s) inherent to the LPBF process induces the formation of hexagonal α' martensite (Motyka, 2021). On the contrary, for alloys with a higher β stabilizers content, such as Ti6246, the resulting martensite generally has an orthorhombic crystallographic structure (α'') (Bein & Béchet, 1996; Young, Levine, & Margolin, 1974). In both cases, however, the as-built LPBF titanium alloys need to be annealed to transform the metastable microstructures into their stable counterparts, thus improving the mechanical properties.

Although significantly less known than Ti64, Ti6246 has been recently studied to produce parts using the LPBF process. (Alessandro Carrozza et al., 2021) were the first to compare the LPBF

printability and post-processing of this alloy with those of the reference Ti64 alloy (Aversa et al., 2025; A. Carrozza, Bircher, Aversa, & Biamino, 2023; Alessandro Carrozza et al., 2021). The authors produced high density (≥ 99%) Ti6246 parts with significantly higher mechanical properties than those of their LPBF Ti64 counterparts, and even wrought Ti6246 alloys (Alessandro Carrozza et al., 2022). Their best compromise in terms of strength, hardness and ductility was achieved with a bi-lamellar α microstructure after annealing at 875 °C for 1h. Additional publications of this research group revealed the results of optimization of the solution and aging post-treatment treatments to further tailor the microstructure and obtain the best compromise in terms of tensile strength and ductility at room temperature (Pirro et al., 2025). Some other studies have demonstrated the possibility of achieving ultra-high hardness characteristics (≈ 600 HV) in this alloy (Cobbinah et al., 2024; Hassanin et al., 2021) via the formation of nano-sized α laths as a result of the application of specific process and post-process conditions (Peng et al., 2023). *Kan et al.* demonstrated that the nanocrystalline microstructure and the associated high hardness obtained for the heat-treated LPBF Ti6246 alloy enable to obtain samples which display remarkable wear resistance as compared to Ti64 (either conventionally manufactured or 3D-printed) (Kan et al., 2023). Recently, some publications were focused on the corrosion resistance of LPBF Ti6246 specimens to such corrosive species as H_2S, CO_2, NaCl, NaF, etc. (Han & Marya, 2025; Martucci, Iannucci, Lombardi, & Grassini, 2024). Nonetheless, to the best of the authors' knowledge, no comprehensive study comparing the microstructure and the as-built mechanical properties of a Ti6246 alloy for different LPBF parameter sets has yet been published.

To complement the existing body of knowledge, this study explores the basic printability of the Ti6246 alloy. To this end, a wide range of printing parameters was explored in a bid to correlate the printing conditions with the structural, physical and mechanical characteristics of printed Ti6246 parts and compare them with the literature data.

5.5 Material and methods

5.5.1 Powder characterization

The Ti-6Al-2Sn-4Zr-6Mo powder used in this study is a gas-atomized pre-alloyed powder provided by Eckart TLS GmbH. According to the supplier, the nominal composition of the powder fulfils the composition requirement of the AMS 4981 standard (AMS G Titanium and Refractory Metals Committee, n.d.), with low amounts of impurities (O, N, C, H < 0.15 %wt). The particle size distribution of D10 = 26, D50 = 43 and D90 = 64 (µm) was measured using the water module of an LS13 320 XR particle size analyzer (Beckman Coulter, Brea, CA, USA) (Figure 5-1a). The particle morphology was then observed using a TM3000 scanning electron microscope (SEM) (Hitachi, Tokyo, Japan), Figure 5-1b.

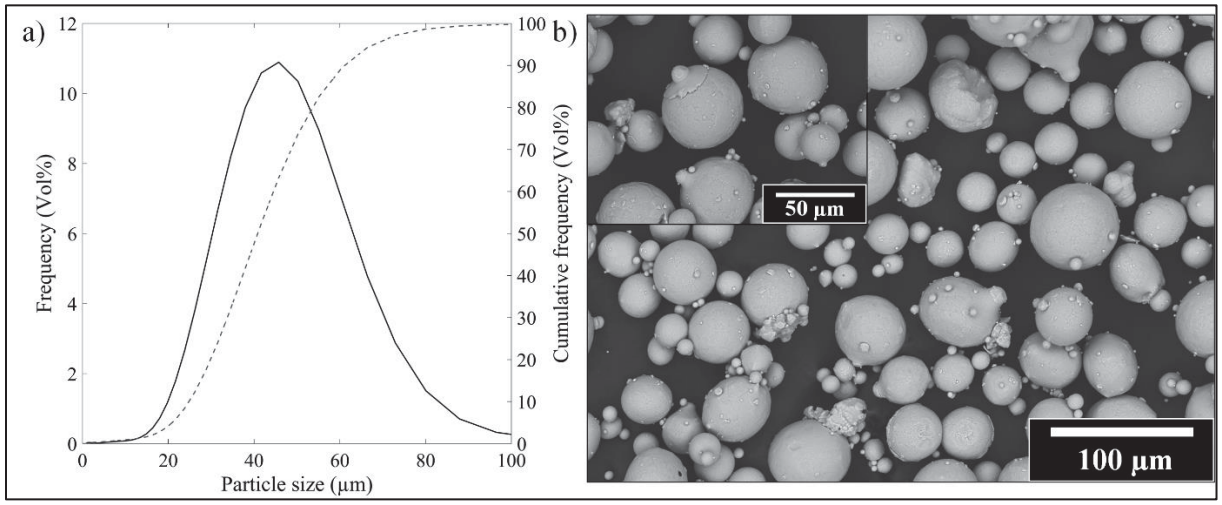

Figure 5-1: Ti6246 powder: a) Particle size distribution and b) SEM observations

5.5.2 Plan of experiments

The printer used in this study was a TruPrint 1000 system (TRUMPF GmbH, Ditzingen, Germany), with the laser power (P) varying from 20 to 200 W and the scanning speed (v) varying from 20 to 3000 mm/s. Based on the particle size distribution analysis, the layer thickness (t) was set at 50 µm (~0.8*D90) and kept constant over course of the study. Such

coarse layer thickness was considered according to the PSD of the powder (section 5.5.1) to limit mechanical sieving which could decrease the density of the powder bed. In order to study the impact of a wide range of process parameters on the density, structure and mechanical properties of printed specimens, 9 different sets of printing parameters (A, B, C, D, E, F, G, H, I) were selected in the VED (5.4) – BR (5.5) space (Figure 5-2):

$$VED\ [\mathrm{J/mm^3}] = \frac{P}{vht} \tag{5.4}$$

$$\mathrm{BR}\ [\mathrm{cm^3/h}] = vht \tag{5.5}$$

where VED (J/mm³) is the volumetric energy density; BR (cm³/h) is the build rate and h (µm) is the hatching space.

Each of the 9 sets of printing parameters corresponds to one of the 6 hatching space (h) values ranging incrementally as 50, 75, 100, 125, 150 and 175 µm. Each parameter set is named using the corresponding letter and hatching space value. For example, D-100 stands for parameter set D with hatching space h = 100 µm. Note that because of speed limitations (v < 3000 mm/s), it was not possible to use parameter set I with the smallest hatching space value of h = 50 µm. Overall, the plan of experiments represents a total of 9*6-1=53 different parameter combinations (Tableau 5-1).

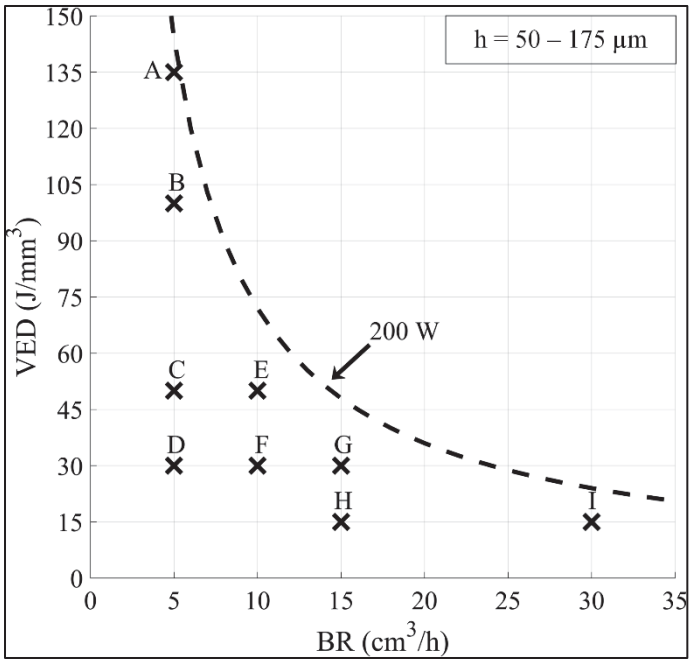

Figure 5-2: Representation of the nine $VED - BR$ experimentally printed parameter sets; the dashed line represents the $VED - BR$ limit corresponding to a maximal laser power of 200 W

Tableau 5-1: Plan of experiments in terms of the laser power (P), scanning speed (v) and hatching space (h) values used for each of the nine parameter sets

Set	VED (J/mm^3)	BR (cm^3/h)	P (W)	h (µm)					
				50	75	100	125	150	175
				v (mm/s)					
A	135	5	188	557	370	278	222	185	159
B	100		139						
C	50		69						
D	30		42						
E	50	10	139	1111	741	556	444	370	317
F	30		83						
G	30	15	125	1667	1111	833	667	556	476
H	15		63						
I	15	30	125	/	2222	1667	1333	1111	952

Using this plan of experiments, fifty-three 4.5 mm-long single tracks and 10 mm-diameter, 20 mm-high cylindrical specimens corresponding to each of the process parameter sets were printed on a Ti64 baseplate without preheating. The single tracks (Figure 5-3a), spaced at 1 mm intervals, were printed on the upper surface of three 10x15x15 (mm^3) rectangular specimens (Figure 5-3b). The cylindrical specimens were printed (Figure 5-3c) and then removed from the baseplate, their supports cut off, and remaining parts partitioned to obtain samples for structural analyses, microhardness measurements, micro-computed X-Ray tomography (μ-CT), and compression testing (Figure 5-3d).

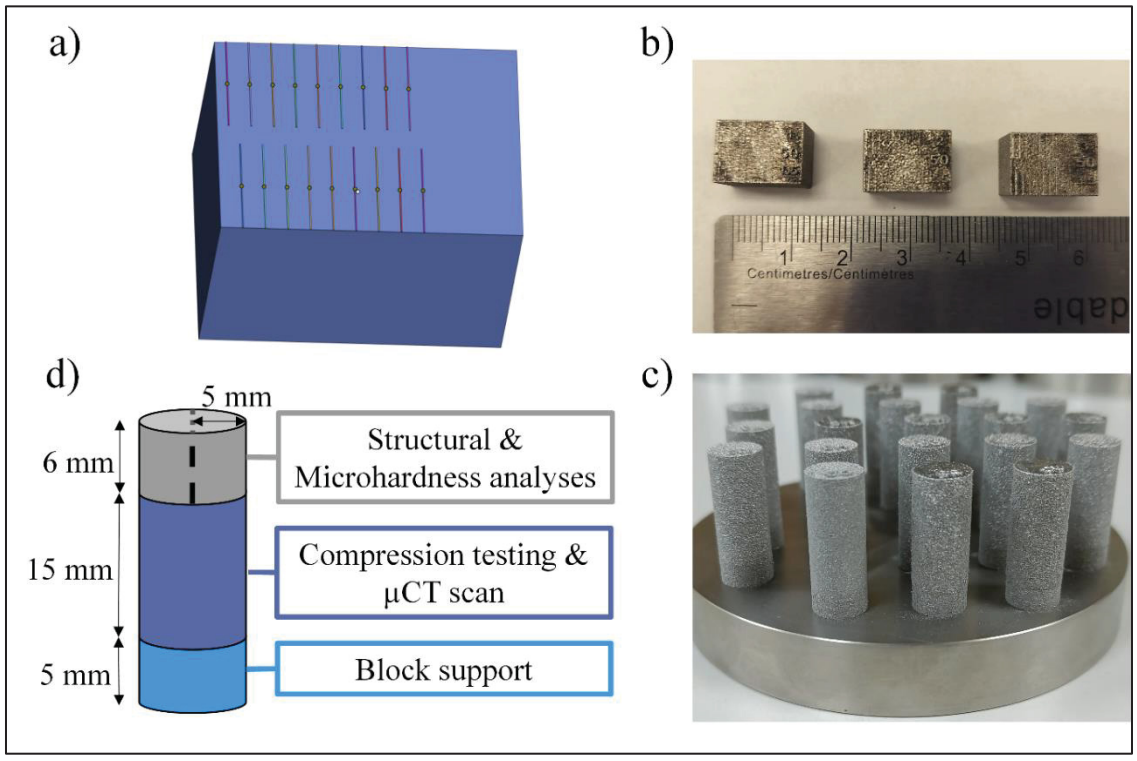

Figure 5-3: a) Drawing of one of the cubic samples with 18 single tracks; b) photo of three cubic samples with single tracks; c) photo of a baseplate with printed cylindrical specimens; d) schematic representation of the cylindrical specimen with samples used for various analyses

5.5.3 Physical and structural characterization

5.5.3.1 Single track measurements

The single tracks were analyzed using high magnification (x200) stitched images obtained with a Keyence VHX7000 optical microscope (Osaka, Japan). Ten profile lines were drawn perpendicular to each of the tracks to measure their average widths and corresponding standard deviations.

5.5.3.2 Density measurements

The level of porosity in the 53 printed samples (Tableau 5-1) was assessed using micro-computed tomography (μCT) scans of their 15 mm-long parts (analyzed volume ≈ 1000 mm^3) (Figure 5-3d). These parts were later used for compression testing. Multiple studies have highlighted the pertinence of using μCT as the density measurement technique for LPBF parts (Desrosiers et al., 2022). In comparison to alternative methods such as the Archimedes' technique and microscopy, μCT offers the distinct advantage of providing 3D information of the pore network (pore size, roundness, location, etc.)

The μ-CT analyses were performed using an FF35 CT system (Comet Yxlon, Germany). Given the large number of scans needed to inspect the 53 samples, a compromise between the acquisition time and scan quality was found, resulting in 1500 projections with an X-ray tube voltage of 140 kV, a tube current of 50 μA, and an exposure time of 475 ms over 3 frames integration. To limit the beam hardening effect, a 0.3 mm copper filter was used. The projection data were then corrected and reconstructed using the Siemens CERA software, with a resulting voxel size of 8 μm.

The porosity analyses were realized using the Dragonfly software (Comet Technologies, Canada). The pores were isolated through the manual adjustment of a grey-level threshold and the volume of a segmented region of interest was related to the overall volume of each individual sample to determine the printed density. To obtain statistical information regarding

the pore size and shape distributions, the connectivity of voxels corresponding to each individual pore was assessed considering 6-connected components (faces), and pores smaller than 3x3x3 voxels (< $1.4*10^{-5}$ µm³) in size were removed from the dataset. The pore volume (Vp) was computed considering the number of connected voxels in each isolated pore, while the pore sphericity (S) was calculated using equation (5.6).

$$S = \frac{\left(6\pi^{1/2}V_p\right)^{\frac{2}{3}}}{A_p} \tag{5.6}$$

where V_p is the pore volume and A_p the surface area of the pores estimated using Lindblad surface area method (Lindblad, 2005).

5.5.3.3 Microstructure and phase analyses

The microstructure and phase analyses were performed on Z-Y cross-sections of the distant parts of the printed samples (Figure 3d). The crystallographic phases were identified by X-Ray Diffraction (XRD), using an X'Pert^3 system (Malvern Panalytical Ltd, Malvern, UK) equipped with a cobalt source (Kα Co = 1.79026 Å). The acquisitions were made in the Bragg Brentano configuration, with a step size of 0.017° and a 2θ range between 38 and 50°. This reduced 2θ range encompasses the main reflections of all the expected phases (α'', α', α, β).

For in-depth microstructural observations, the Z-Y cross-sections of the samples for each parameter set were mounted in carbon-doped resin, mirror polished and etched (1 min) with a Kroll reagent (%vol: 2:5:93 HF/HNO_3/H_2O). Observations were performed at two distinct scales. A lower-resolution overview was carried out using a LEXT OLS4100 (Lext Olympus Corp., Japan) confocal microscope with the lowest magnification (x5). The columnar microstructure, some grain boundaries and especially crystallographic inhomogeneity were observed using this equipment. To observe finer microstructure features, including martensite laths formed in the as-built samples, higher magnification images were captured using a secondary electron detector (acceleration voltage 10 kV, magnification 30k) of an SU-8230 Field Emission STEM (Hitachi, Tokyo, Japan), and the average width of the lath structures

was measured using the ImageJ software. The homogeneity of the microstructure was asserted by repeating the measurements on ten images randomly acquired over each area of interest.

5.5.4 Mechanical characterization

5.5.4.1 Microhardness

Microhardness measurements were performed on the etched Y-Z cross-sections using a Duramin-40 M1 measurement system (Struers, Ballerup, Denmark). To prevent measurement variations caused by the presence of pores on planar cross-sections, only samples having a measured density higher than 95% were considered. For all of them, 10 measurements were performed in the middle of the samples with an applied force of 300 gF and a dwell time of 15 s. In addition, when phase inhomogeneities were revealed after etching, additional series of 10 microhardness measurements were carried out on these specific regions, using the same measurement conditions.

5.5.4.2 Compression testing

The middle part of each of the printed specimens (Figure 5-3d) was subjected to room-temperature compression testing using an Alliance RF/200 mechanical testing system (MTS, Eden Prairie, MN, USA) following the E9-09 ASTM standard (E28 Committee, 2019). The compression rate was set at 0.01 mm/s and a video camera coupled with a microphone was placed in front of the specimens. A 200 kN MTS load cell measured the force, while the displacement was measured using an LVDT. From these measurements, compression strain-stress diagrams were plotted and audio spectra recorded, to compare the onset of cracking with the inflexion points observed on the stress-strain diagrams. This step was necessary since the compression testing mode allowed to accommodate cracks and continue testing, especially when samples were porous or contained unmelted particles, resulting in significant overestimations of both the apparent material strength and ductility. The following metrics were extracted from the compression testing: the Ultimate Compression Strength (UCS, MPa), defined as the maximum stress reached during the test; the Yield Strength (YS, MPa),

calculated by moving the slope from origin to 0.2% on the strain axis, and the Strain to failure (δ, %).

5.6 Results

5.6.1 Single tracks

The optical measurements of single tracks allowed to assess their average widths (W) and classify them into three distinct groups, namely, continuous (Figure 5-4a), irregular (Figure 5-4b) and partially fused (Figure 5-4c). The width of the continuous tracks ranged from 85 to 400 µm and that of the irregular or partially fused tracks ranged from 65 to 150 µm (Tableau 5-2). A direct correlation was observed between the track quality and the linear energy density of the laser (LED, (5.7)) used to melt the powder bed (Figure 5-4d).

$$LED\ (J/mm) = \frac{P}{v} \tag{5.7}$$

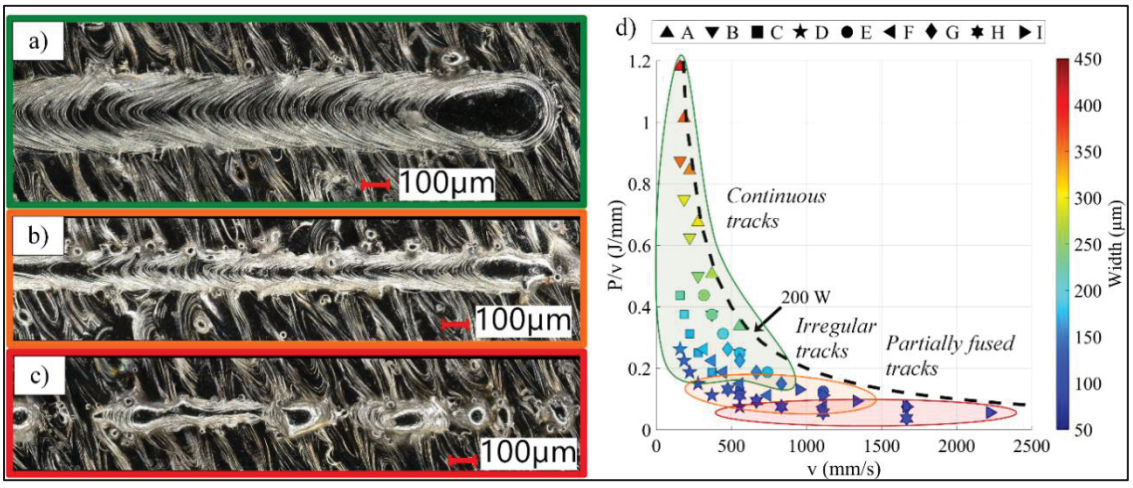

Figure 5-4: Optical observations of the a) continuous, b) irregular and c) partially fused single tracks; d) single track widths according to the scanning speed v and the linear energy density P/v

Tableau 5-2: Laser power (P), scanning speed (v) and single-track width (W) for each of the nine parameter sets

Set	P (W)	h (µm)											
		50		75		100		125		150		175	
		v (mm/s)	W (µm)	v (mm/s)	W (µm)	v (mm/s)	W (µm)	v (mm/s)	W (µm)	v (mm/s)	W (µm)	v (mm/s)	W (µm)
A	188	557	235 ± 19	370	266 ± 17	278	306 ± 25	222	348 ± 22	185	366 ± 15	159	404 ± 25
B	139		192 ± 16		222 ± 14		253 ± 21		284 ± 13		297 ± 11		360 ± 26
C	69		125 ± 11		165 ± 11		165 ± 11		171 ± 12		189 ± 9		220 ± 9
D	42		86 ± 19		120 ± 12		119 ± 15		123 ± 15		137 ± 7		150 ± 18
E	139	1111	134 ± 15	741	175 ± 24	556	175 ± 14	444	194 ± 16	370	231 ± 15	317	251 ± 28
F	83		99 ± 16		138 ± 16		137 ± 13		145 ± 7		154 ± 15		178 ± 12
G	125	1667	101 ± 14	1111	149 ± 13	833	139 ± 17	667	152 ± 18	556	164 ± 10	476	176 ± 6
H	63		113 ± 22		108 ± 23		91 ± 12		94 ± 14		104 ± 16		125 ± 16
I	125	/	/	2222	99 ± 11	1667	91 ± 12	1333	112 ± 14	1111	118 ± 16	952	121 ± 12

Based on these observations, two distinct process parameter-related threshold values were established. In the case of scanning speeds exceeding 550 mm/s, most of the single tracks were categorized as irregular or partially fused, and the higher the scanning speed, the greater the track non-uniformity, and the smaller the single track widths (Figure 5-4d). The appearance of the irregular and partially fused tracks may also be related to $LED \leq 0.2$ J/m. In both cases, the energy input delivered to the powder bed was insufficient, leading to the appearance of unmelted areas along the scanning tracks or to tracks with important discontinuities, and width and thickness variations. This behavior concerned mainly the parameter sets with low LED values, such as those using low laser powers (P) (e.g., sets D, F, H) or those with higher powers (P), but with much greater scanning speeds (v) (e.g., sets G, I). The formation of continuous and uniform single tracks corresponds to the A, B, C and E printing parameter sets with $v \leq 550$ mm/s and $LED \geq 0.2$ J/m.

5.6.2 Printed density

All the parameter sets mentioned in Tableau 5-1 allowed to successfully print cylindrical specimens, even if the associated single tracks were irregular or partially fused. The use of X-ray micro-computed tomography allowed to conclude that all the printed samples were crack-free, regardless of the printing parameters used. The as-printed densities obtained from the CT-scans of each of the printed specimens are summarized in the APPENDICE C Tableau-A C-1. To highlight the correlations between printed densities and printing parameters, the density values were plotted in the 3D $VED - BR - h$ space in Figure 5-5. Using this representation, it was determined that a minimum VED of 50 J/mm^3 was required to achieve a printed density greater than 95%; to reach a density greater than 99%, the VED had to be greater than 100 J/mm³.

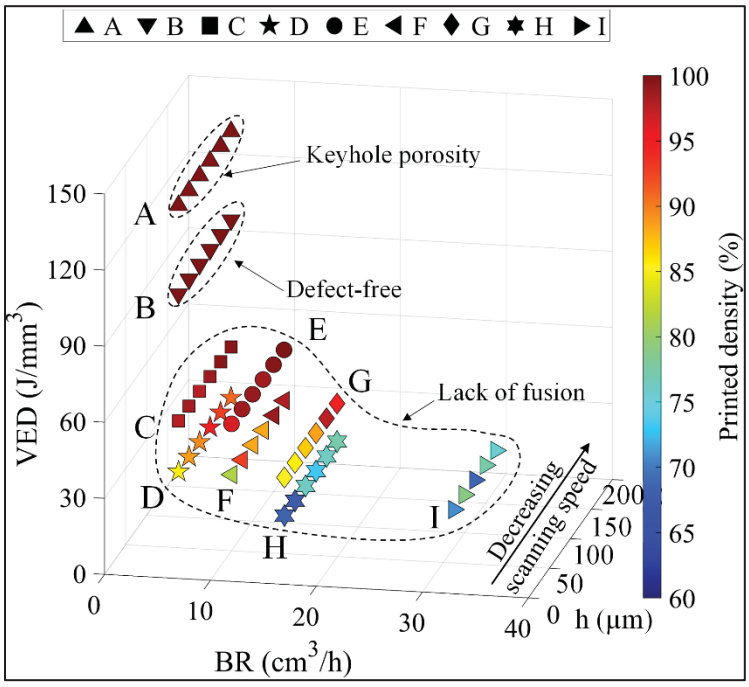

Figure 5-5: CT-scan measured density in the $VED - BR - h$ space, with different types of porosities encircled

In addition to higher VED, these results showed the benefits using greater hatching spaces h, *i.e.*, lower scanning speeds v, to improve the overall printed densities. This behavior was especially evident in sets exhibiting a broad range of densities (*e.g.,* D, F, G). These observations are consistent with the results of quality analysis of the corresponding single tracks. The parameter set B had the smallest number of defects (density systematically greater than 99.9%) and was found to be less sensitive to the hatching space (h) and scanning speed (v) variations.

To illustrate the influence of VED ranging from 50 to 135 J/mm^3 on the processing-induced porosity, Figure 5-6a,b,c summarizes the segmented pores inside the 15 mm high cylindrical samples (Figure 5-3d). Differences in terms of the porosity characteristics are visible above and below the optimized parameter set B (VED = 100 J/mm^3) (Figure 5-6b). For the highest energy input (set A, Figure 5-6a, VED = 135 J/mm^3), the segmented pores are mainly small and circular (Figure 5-6d), while for the lower energy inputs (set E, Figure 5-6c, VED = 50 J/mm^3), pores are larger and manifest non-uniform shapes (Figure 5-6e). In the highly porous samples ($VED \leq$ 30 J/mm^3, non-shown in the figure), pores of several dozens of mm^3 in size form an extended and interconnected pore network.

The pore volume and sphericity distributions for the VED ranging from 50 to 135 J/mm^3 are shown in Figure 5-6f,g. These statistical analyses confirm that samples printed with the highest VED (set A) contain a high proportion of small keyhole pores (V_p < 1e^{-5} µm^3) with a high sphericity (S close to 1). On the other hand, the B-set samples manifest a very limited number of larger pores with a comparably high sphericity as the A-set samples. Finally, the E-set samples contain numerous lower-sphericity defects (lack-of-fusion) with a broader volume distribution.

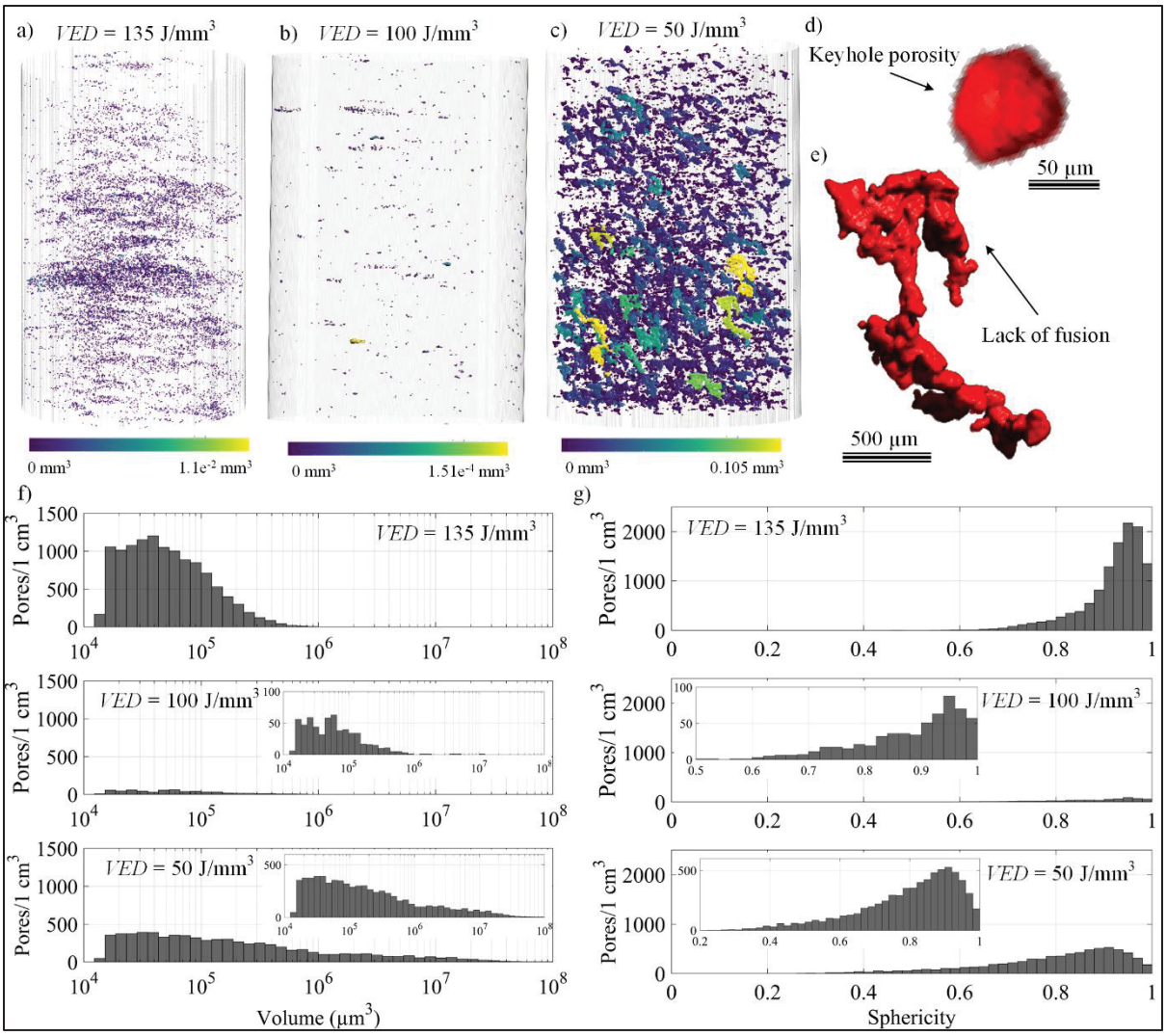

Figure 5-6: Examples of the porosity distributions inside the 15 mm-high cylindrical specimens printed at different VED: a) 135 J/mm^3 A-50; b) 100 J/mm^3 B-150; c) 50 J/mm^3 E-100; 3D segmented process-induced flaws: d) a keyhole pore (A-50) and e) a lack-of-fusion (E-50); Pore distributions for different VED: f) volume; g) sphericity

Optical observations made on the samples printed using the highest VED (set A, Figure 5-7a) attest the presence of small and circular keyhole pores. The round shape and position of these pores at the bottom of melt pools are typical for this kind of defects. Conversely, in highly porous samples, the porosities observed are wider and have highly irregular shapes (set E, Figure 5-7b), which is characteristic of lack-of-fusion defects.

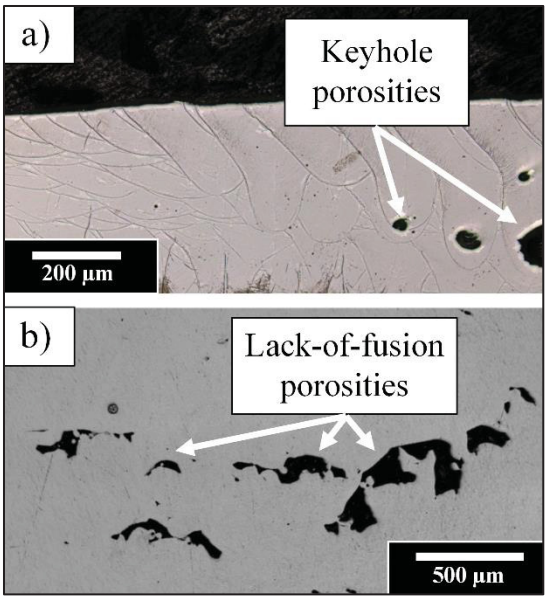

Figure 5-7: Optical images of the
a) keyhole porosities (A-75) and
b) lack-of-fusion porosities (E-100)

5.6.3 Phases and microstructure

The X-ray diffractograms for varying VED values (parameter sets A to H) with the smallest hatching space h (50 µm) are plotted in Figure 5-8a, whereas for the highest $VED - BR$ set A with the h values varying from 50 to 175 µm, they are plotted in Figure 5-8b. It can be observed that most of the samples (B-H with h = 50 µm) are indexed as containing orthorhombic martensite (α''), which was also detected in the powder feedstock. The orthorhombic martensite was expected in this titanium alloy, both in the powder and solid forms, given the significant level of β stabilizers and rapid cooling in both cases: up to 10^8 K/s during plasma atomization process and in the range of 10^4 – 10^6 K/s during LPBF. However, for some specific printing parameters, especially those with high VED (set A) and low hatching space h, and therefore, high scanning speeds, the X-ray diffractograms (Figure 5-8b) suggested the presence of mixed α / α' (HCP) – β (BCC) microstructures. These phases are distinguished by their distinct peaks in the 44 – 48° 2θ range which are shifted compared to those of the α'' orthorhombic martensite. Note that the XRD analysis does not allow to distinguish between α and α' phases as they both have the same hexagonal crystalline structure.

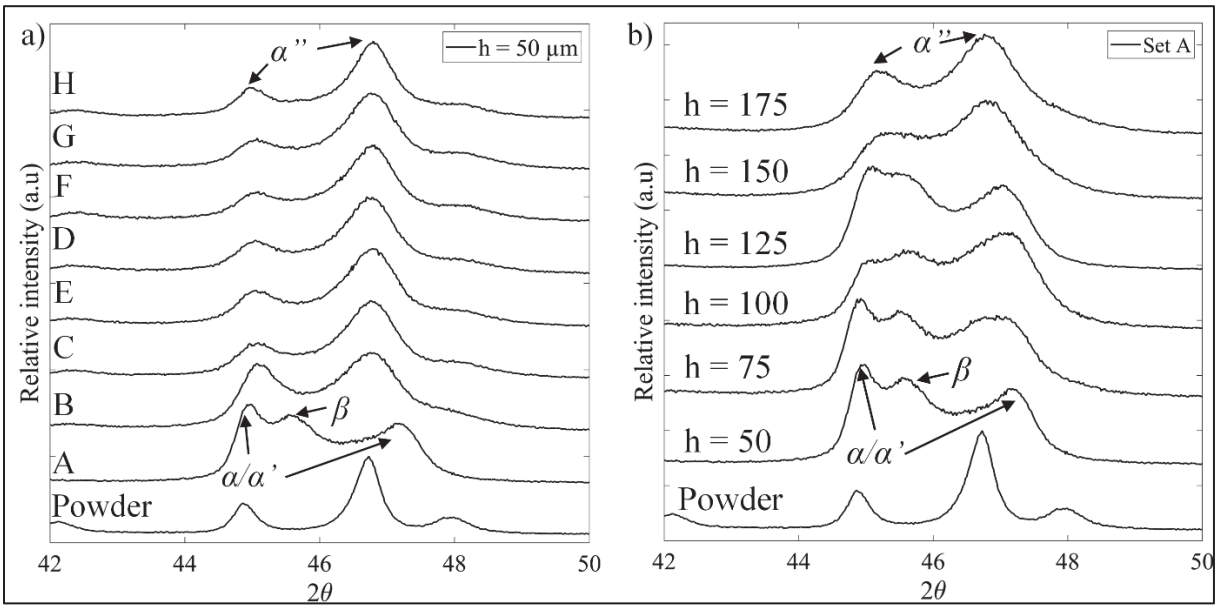

Figure 5-8: Microstructural evolution observed through XRD diffractograms depending on a) the parameter sets ($VED - BR$) with constant h value (h = 50 µm) and b) the h value at a constant $VED - BR$ parameter set (set A)

The observations of the etched surfaces made with a confocal microscope enabled to detect the feature characteristics of the various phases present in the material. Figure 5-9a corresponds to the completely α'' martensitic structure (B-150) which is a common reference phase in LPBF-processed titanium alloys with a high β stabilizers content. Conversely, a non-uniform microstructure was also observed in some samples (*e.g.*, A-50, Figure 5-9b). In the upper part of these samples, a wide bright martensite α'' layer that almost did not react with the Kroll reagent was systematically observed, while their remaining part was brown-colored due to the presence of β phase. Note that the B-set samples printed with small h values (*e.g.*, B-50), reveal slight traces of in situ transformation (brown areas) which cannot be found in the B-set samples with higher h values (e.g., B-150). Using such printing parameters enable to print samples with a homogeneous as-built microstructure.

The optical images taken at higher magnifications allowed to detect differences between the two competing microstructures. In fully martensitic samples (Figure 5-9a) or inside the bright

upper layers (Figure 5-9b) of the heterogenous samples, the melt pool borders and a few typical columnar prior-β grains were observed (Figure 5-9c). In the brown area of the heterogeneous samples (Figure 5-9d), wide columnar β grains and their borders were identified (Figure 5-9d). Thin elongated needles characteristic of the martensitic microstructure of titanium alloys could be observed using high magnification SEM images. Needles of orthorhombic α'' martensite were bright (Figure 5-9e), while those of hexagonal α' martensite were dark (see Figure 5-9f), but both types were arranged in a ± 90 fashion.

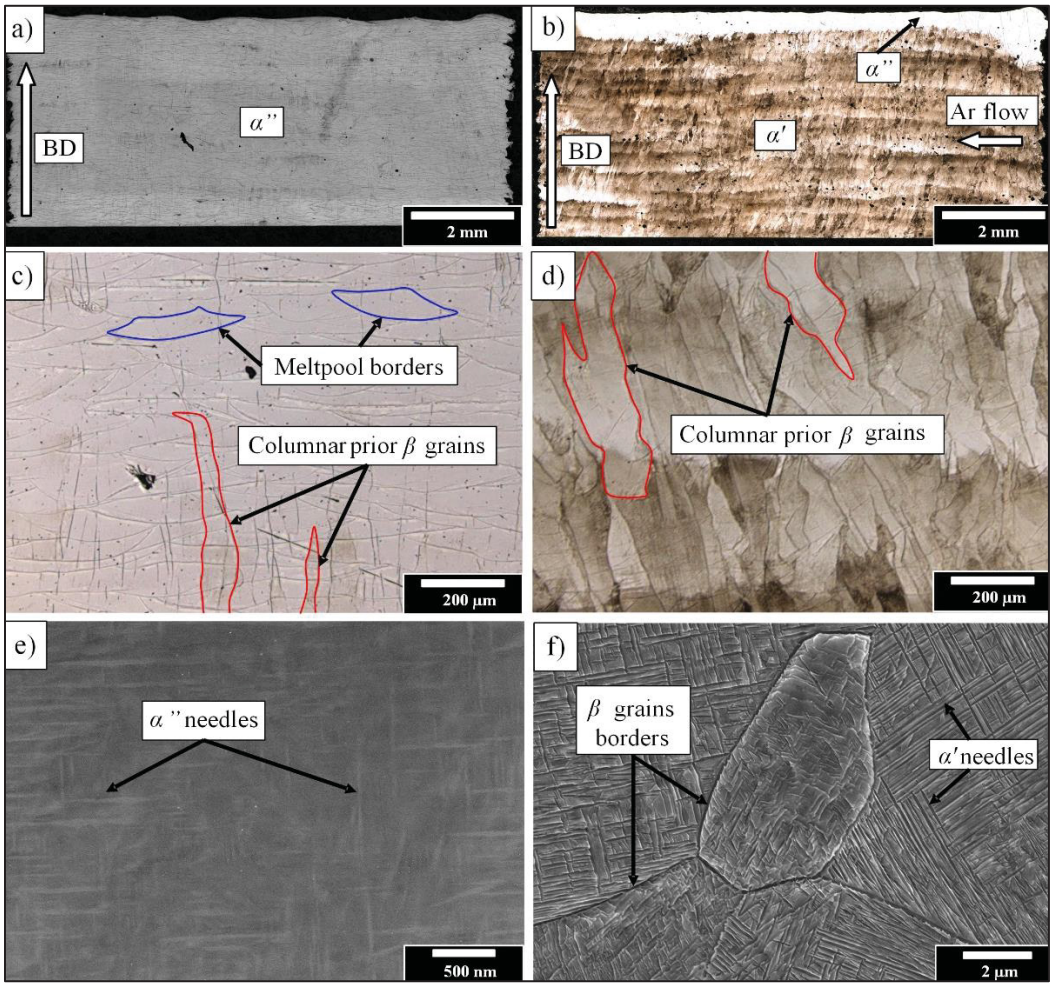

Figure 5-9: Observations with confocal microscope (a, b, c, d) and SEM (e, f) of (a, c, e) sample with the as-built α'' martensite microstructure (B-150) and (b, d, f) heterogeneous sample with α' and β phases (A-50)

Note that the thickness of the observed α'' layer increased with an increase in the hatching space h, *i.e.*, with a decrease in the scanning speed (Figure 5-10a). Next, according to the high-resolution SEM image measurements, the larger the hatching space h, i.e., the lower the scanning speed, the thinner the α' martensite needles (width decreases from ~50 to 20 nm) and the thicker the α'' needles (width increases from ~50 to 60 nm (Figure 5-10b). Note also that the same microstructure heterogeneity was observed on the lateral side of some cylindrical samples, especially those directly exposed to argon flow.

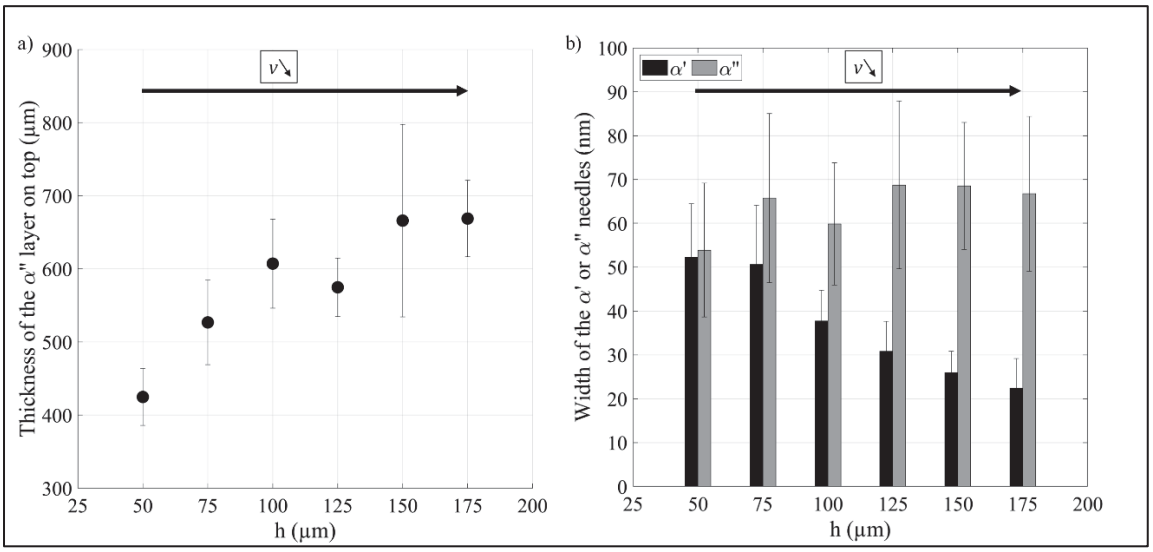

Figure 5-10: a) Thickness of the α'' layer on the top surface of heterogeneous samples (set A) depending on the h ratio. b) Needle widths of α' and α'' martensite as functions of the h value (set A)

5.6.4 Mechanical properties

5.6.4.1 Microhardness

The microhardness measurements were performed only on samples with densities exceeding 95% (A, B, C and E, $VED \geq 50$ J/mm^3, Figure 5-5). In Figure 5-11, a clear difference between the samples printed using higher (≥ 100 J/mm^3) and lower (≤ 50 J/mm^3) *VED* can be observed. Samples with a mixture of hexagonal α' martensite and β phase (set A) exhibited higher

microhardness ($HV > 450$) than their fully orthorhombic α''martensite counterparts (sets B, C, E). This is in agreement with the softening-hardening phenomenon related to the presence of orthorhombic α'' reported in (Y. Guo et al., 2013; Alessandro Carrozza et al., 2022). The additional measurements realized within the α'' martensite layers on the top of heterogeneous samples (Figure 5-9b) yielded similar hardness values as those measured in their fully α'' counterparts (Figure 5-9a). No clear trend was observed with respect to the hatching space h variations.

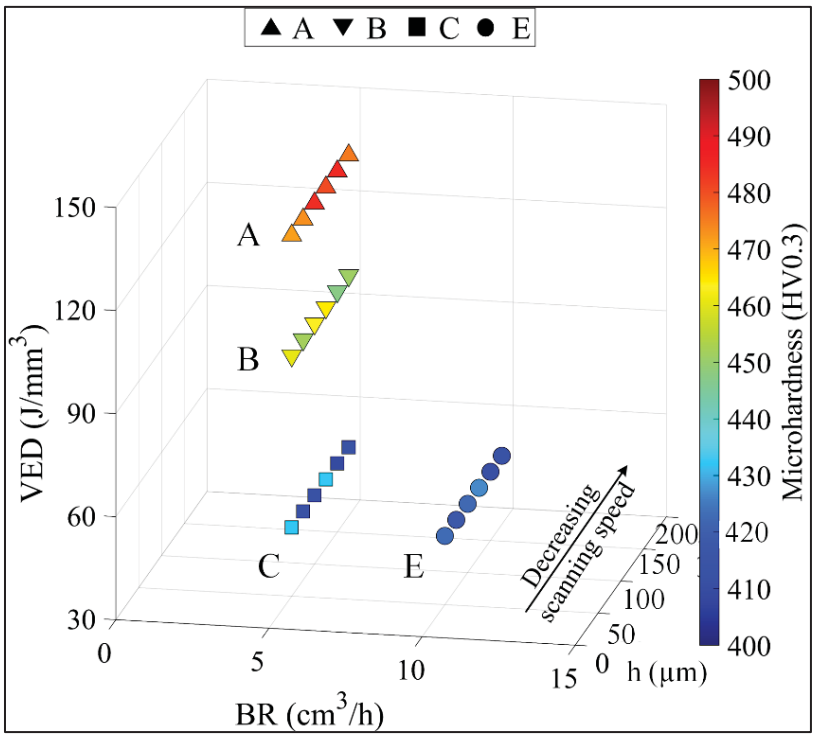

Figure 5-11: Evolution of the microhardness measured for the parameter sets A, B, C and E in the $VED - BR - h$ space

5.6.4.2 Compression testing

The printed samples were subjected to compression testing at room temperature, including those with the lowest measured density. Figure 5-12a presents typical stress-strain curves of the samples printed using each of the VED printing parameter sets. As mentioned in section 5.5.4.2, the curves were corrected according to audio spectra recorded to prevent the

overestimation of the material strength and ductility. The dashed lines in Figure 5-12a correspond to the data recorded during the compression tests after the onset of cracking (acoustic signal). Note that the material behavior depends significantly on the VED values, and the higher this value, the higher the stress, but the lower the strain to failure. Figure 5-12b and Figure 5-12c, correspond respectively to the photo recorded at the onset of cracking, of a "brittle" sample (A-50) and of a "ductile" sample (H-50).

Figure 5-12d represents the SEM fractography images of samples printed using a VED = 135 J/mm^3 (A-50). Although the flat surfaces and the presence of cleavage planes and ridges were observed and confirm the overall brittle behavior of the samples printed using a high $VED \geq 50$ J/mm^3, some local areas have dimples which are characteristics of a ductile fracture. Conversely, the fractography analysis of samples printed with a lower $VED \leq 30$ J/mm^3 (F-50) reveals uneven surfaces and a lot of dimples (Figure 5-12e) correlated with a ductile behavior. The SEM images allowed to observe unmelted particles trapped inside the pores, some of them being deformed during the compression tests (Figure 5-12e).

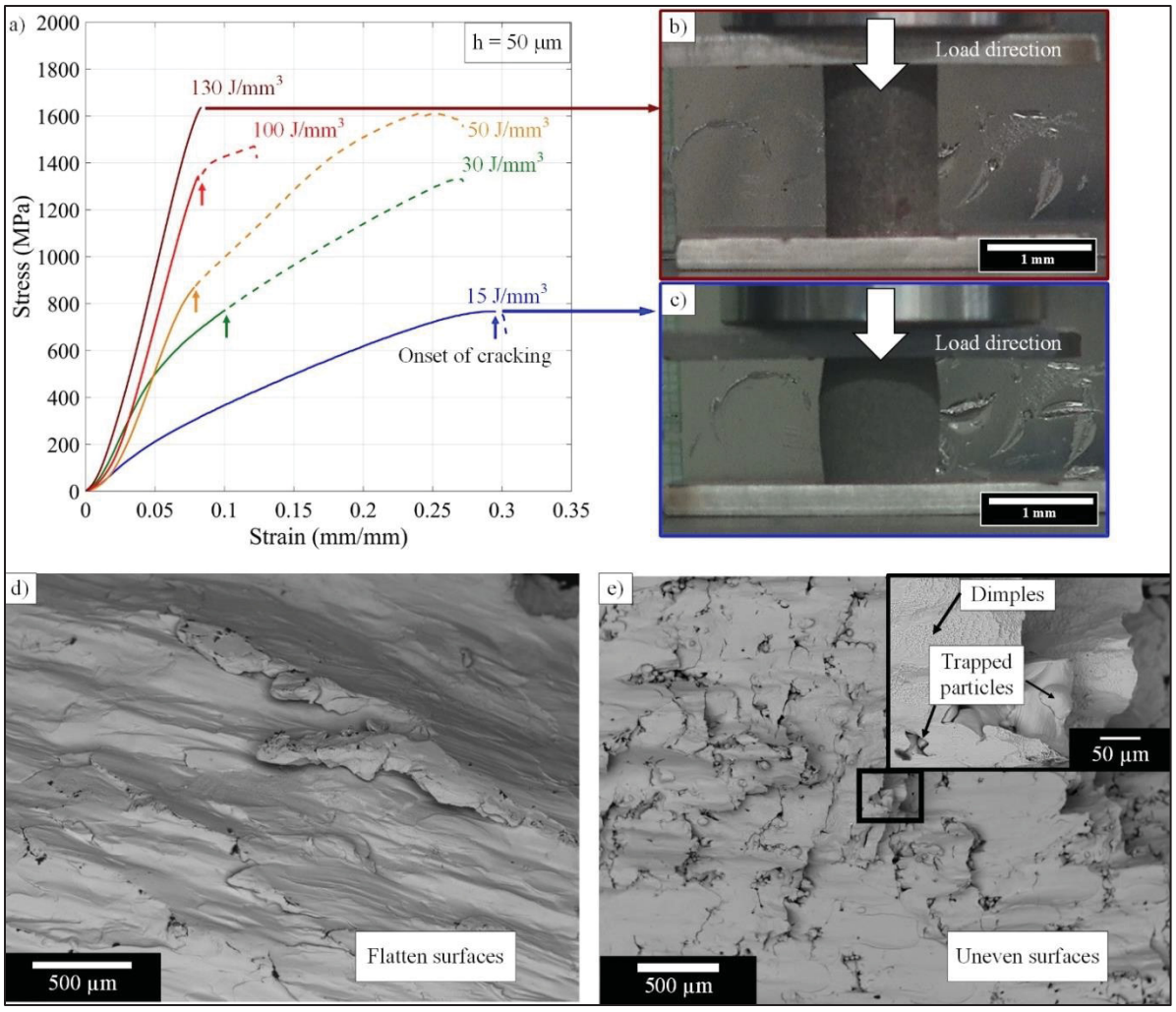

Figure 5-12: a) The representative compression stress-strain diagrams (A-50, B-50, E-50, D-50, H-50). The dashed lines correspond to data obtained after detecting an acoustic signal that indicates the onset of cracking identified by an arrow; Photo of the sample at the onset of cracking b) A-50, c) H-50, SEM fractographies: d) A-50 with "brittle" fracture, e) F-50 with "ductile" fracture

Figure 5-13a shows that the higher the VED, the higher the YS, the lower the strain to failure. Among all the samples, those printed with VED = 135 J/mm^3, i.e., with printed densities ≥ 99.8% and heterogeneous $\alpha' + \beta$ microstructures (Figure 5-8a and Figure 5-9b.d.f) had YS values ranging from 900 to 1570 MPa, with strains to failure approaching 6 - 8%. The B-set samples (VED = 100 J/mm^3) with fully α'' microstructures and even higher densities (> 99.9%) manifested a similar lack of ductility as their A-set counterparts, but YS

values systematically exceeding 1000 MPa. For these two high VED sets, the YS values decrease with an increase in hatching space (Figure 5-13b). For the remaining fully α'' martensite samples ($VED \leq 50$ J/mm^3), the YS values were systematically lower than 1000 MPa, but showed an inverse trend: they increase with an increase in hatching space (Figure 5-13b). To summarize, the microhardness measurements and compression tests revealed that overall, the higher the VED, the higher the hardness and strength of the material, and the lower its ductility.

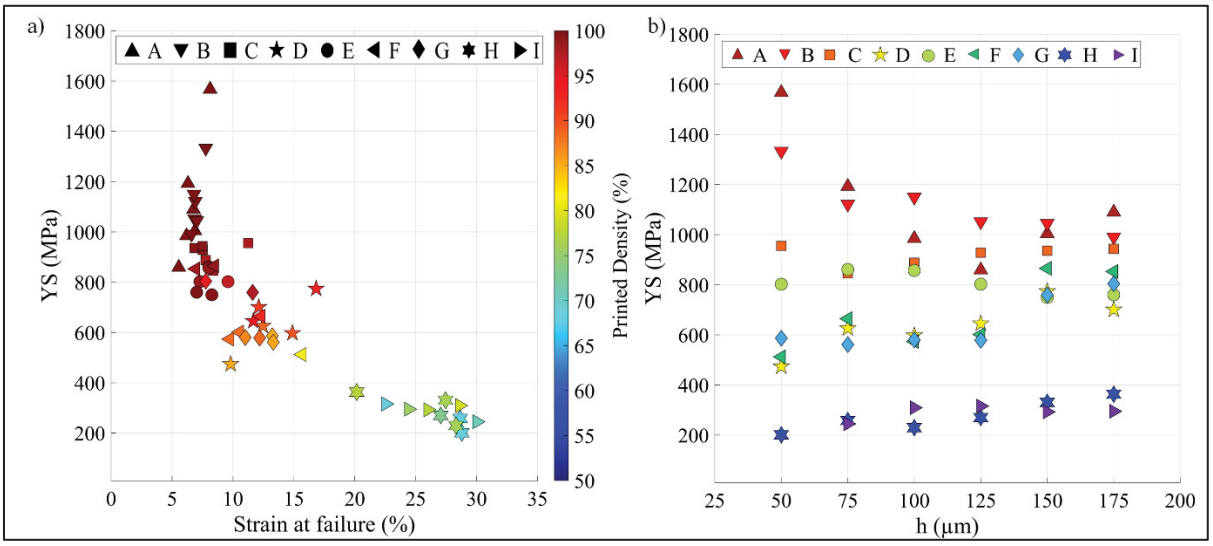

Figure 5-13: a) YS at 0.2% offset versus strain at failure. The relative printed density of the samples is presented in color; b) YS at 0.2% offset in function of the hatching space

5.7 Discussion

5.7.1 Influence of VED and hatching space on the as-built microstructure

This study established a correlation between the printing parameters and the as-built microstructure of the LPBF-processed Ti6246 alloy. A combination of high VED and small h values (high scanning speeds) promoted the formation of hexagonal α' martensite dispersed within the β phase matrix, while the use of opposite conditions (low VED, high h, and low scanning speeds) promoted the formation of orthorhombic α'' martensite, commonly observed

in the LPBF Ti6246 and other $\alpha + \beta$ titanium alloys with a high β stabilizers content (Figure 5-8). Both types of martensite were also reported in LPBF-processed titanium alloys where the α'' martensite is normally not expected, as in near-α Ti6242S (Fleißner-Rieger et al., 2022) or $\alpha + \beta$ Ti64 (Xie, Dai, Ou, Ni, & Song, 2020). The authors attributed such a microstructure evolution to the thermal history of samples and their respective cooling rates which are notably influenced by printing parameters. The highest cooling rates (~10^8 K/s) were associated with the formation of orthorhombic α'' martensite, while the lowest cooling rates (< 10^6 K/s) were associated with the formation of hexagonal α' martensite.

In the present study, the fused material thermal history was related to the overlapping ratio W/h, which corresponds to the width of an experimentally measured single track W (section 5.6.1), divided by the distance between two consecutive tracks (hatching space h). This value allows to estimate the number of times N (5.8) each solidified track is exposed to the laser energy input. Additionally, the relative width $R\%$ of a solidified track remelted by the next laser pass can be estimated using equation (5.9).

$$N = \frac{W}{h} - 1 \tag{5.8}$$

$$R\% = \frac{W-h}{W} * 100 \tag{5.9}$$

For example, for the parameter set A-125, the melt pool width corresponds to ~350 µm (Tableau 5-2), which, considering h = 125 µm, gives the overlapping ratio W/h = 2.8, indicating that during printing, the solidified track will be partially remelted during the next 2 laser passes (N = 1.8, Tableau 5-3). This parameter set has a remelting fraction of R = 64%, meaning that each laser pass generates a melt pool that remelts more than half of a previously solidified track (Figure 5-14).

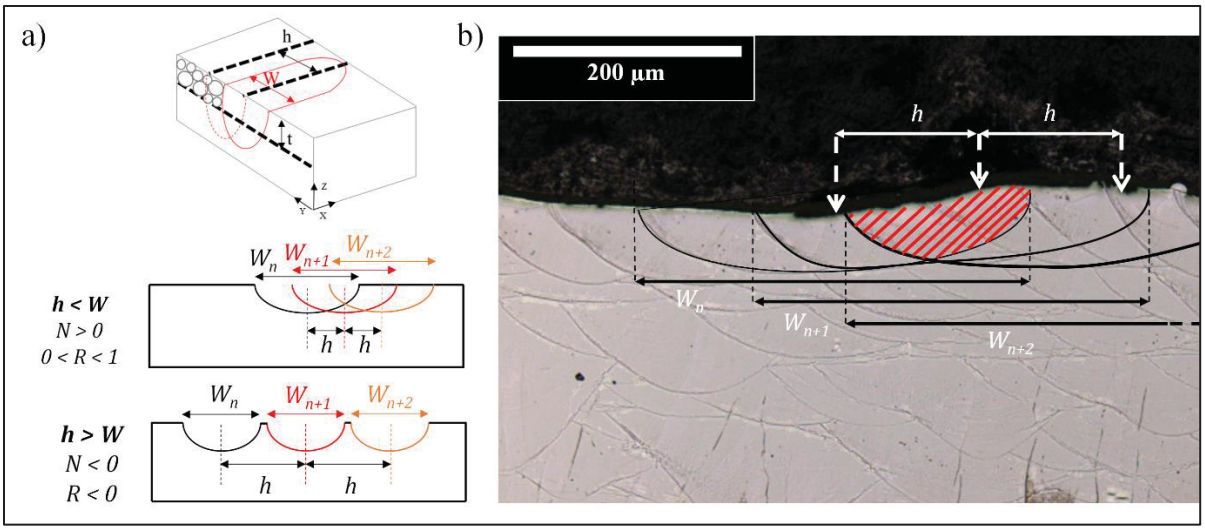

Figure 5-14: a) Schematic drawing of the melt pool and different associated metrics. Representation of the $h < W$ case with overlaps and of the $h > W$ case without overlaps, b) optical observations of the melt pools overlapping in sample A-125. The hatched zone is remelted two times (N = 1.8)

Tableau 5-3: Evolution of the calculated overlap value (N) as a function of the VED and h variations

Set	VED (J/m m^3)	h (µm)																		
		50			75			100			125			150			175		
		v (mm /s)	N	R%	v (mm /s)	N	R%	v (mm /s)	N	R%	v (mm /s)	N	R%	v (mm /s)	N	R%	v (mm /s)	N	R%
A	135	557	3.7	79	370	2.5	72	278	2.1	67	222	1.8	64	185	1.4	59	159	1.3	57
B	100		2.8	74		2.0	66		1.5	60		1.3	56		1.0	49		1.1	51
C	50		1.5	60		1.2	55		0.7	39		0.4	27		0.3	21		0.3	20
D	30		0.7	42		0.6	38		0.2	16		0.0	0		0	0		0	0
E	50	1111	1.7	63	741	1.3	57	556	0.8	43	444	0.6	36	370	0.5	35	317	0.4	30
F	30		0.9	49		0.8	46		0.4	27		0.2	14		0.0	3		0.0	2
G	30	1667	1.0	50	1111	1.0	50	833	0.4	28	667	0.2	18	556	0.1	9	476	0.0	1
H	15		1.3	56		0.4	31		0	0		0	0		0	0		0	0
I	15	/	/		2222	0.3	24	1667	0	0	1333	0	0	1111	0	0	952	0	0

It can be observed from Tableau 5-3 that increasing the VED value while keeping the h value constant increases the N value since a higher energy input generates a wider melt pool. This

trend is consistent with the results of the single tracks analysis (Figure 5-4d). Similarly, for a fixed VED, increasing h (*i.e.*, reducing speed) results in wider melt pools with lower overlaps N and therefore lower remelting proportion $R\%$. Overall, for the lowest VED (sets C-I), N varies from 0 to 1, while the two highest VED (A, B) generate the widest melt pools with N ranging from 1 to 3.7 and $R\%$, varying from ~50 to 80 %, thus minimizing the occurrence of lack-of-fusion defects but increasing the probability of keyhole pores formation.

Increasing the melt pool overlaps leads to the already solidified matter receiving an additional energy input, which partially remelts the previously solidified track, slows down the cooling rate of a repeatedly melted alloy, thermally affect (heat affected zone HAZ) the solidified alloy and thus potentially inducing transformation towards the stable phases ($\alpha + \beta$). The literature reports various mechanisms for the decomposition of α'' phase depending on the titanium alloy chemical composition and the decomposition temperature. For example, for alloys with high proportions of β stabilizers (*e.g.*, Ti-Mo, Ti-Nb, etc.), spinodal decomposition of the initial α'' phase into two rich and lean (in β elements) α'' phases, was reported in (Flower, Davis, & West, 1982). That study suggests the occurrence of path (5.10), which starts from the precipitation of metastable β_M phase from martensitic α'' phase, followed by the transformation of α''_{lean}phase into α' phase and finally, into α phase (Motyka, 2021).

$$\alpha'' \rightarrow \alpha''_{lean} + \beta_M \rightarrow \alpha' + \beta_M \rightarrow \alpha + \beta \qquad (5.10)$$

Note, however, that the large melt pool overlaps of the present study were not systematically correlated with the occurrence of in-situ solid state phase transformations. For example, despite their equivalent overlap values ($N \approx 1.5$, Tableau 5-3), C-50 and A-150 parameter sets have dissimilar microstructures, respectively α'' and $\alpha' + \beta$. This difference is mainly due to the level of laser energy (VED) used. The partially transformed microstructure was predominantly present in the samples printed with a high VED (> 100 J/mm^3) and a small hatching space h. In these samples, a combination of the high energy inputs with significant overlaps led to a reduction of the cooling rate, and finally, the formation of partially transformed ($\alpha' + \beta$) microstructures.

The presence of an orthorhombic α'' martensite layer (Figure 5-10a) in the upper part of the specimens printed with the highest VED (set A, 135 J/mm^3) can be justified by the thermal gradient evolution in the process. At the end of the printing of cylindrical samples, final layers contained letters used for sample identification. Therefore, the melted surface areas were significantly smaller than that of an entire cross-section of the cylinder, leading to higher cooling rates and inducing the formation of orthorhombic α'' martensite rather than hexagonal α' martensite. This assessment is consistent with the evolution of the α'' layer thickness on top of the samples printed with the parameter set A (Figure 5-10a). In these samples, when the hatching space h increases, N is reduced (Tableau 5-3) and the cooling rate increases, leading to thicker α'' layers. The validity of this attribution is reinforced by the presence of α''-martensite containing zones on lateral sides of the cylindrical samples (Figure 5-15a.b, *e.g.*, A-50 and B-50). These areas were directly exposed to argon flow (Figure 5-15c), and thus to higher thermal gradients. Therefore, the present study indicates that the as-built microstructure of printed samples depends on the thermal history of molten material and can be affected by any factor impacting the samples' temperature, including the number of simultaneously printed samples, the presence or absence of a preheated baseplate, etc.

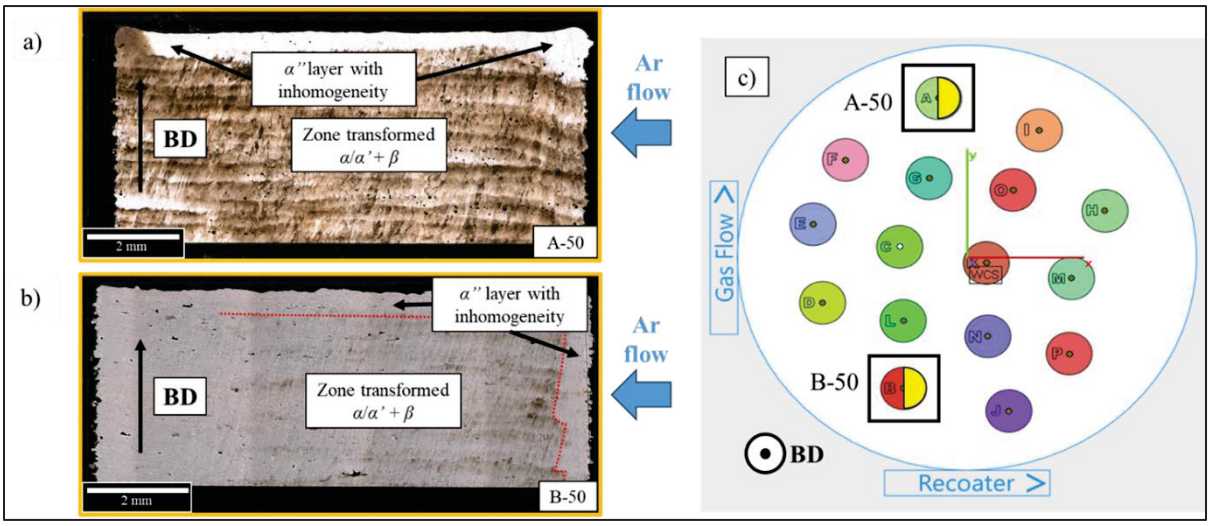

Figure 5-15: Cross-section of printed samples with partial transformation toward stable phase: a) A- 50 and b) B-50. c) Position of the samples printed using these two printing parameters on the baseplate

To the best of the authors' knowledge, among all the studies on LPBF processing of Ti6246 alloys, (Cobbinah et al., 2024) were the only ones to report the formation of $\alpha/\alpha' + \beta$ phase mixtures in the as-built material, and that, regardless of the printing parameters used. The authors did not provide explanations for the appearance of these mixtures instead of the commonly observed α'' martensite (Alessandro Carrozza et al., 2021; Hassanin et al., 2021). However, considering that powders used in (Cobbinah et al., 2024) study had a lower content of β-stabilizing molybdenum (5.14 wt.%) than reported in the majority of publications (5.5 < wt.% < 6.5), it can be hypothesized that this fact favorized the formation of the mixed microstructures.

Note also that very fine (≈ 50 nm) α'' needles observed in the present work have not been systematically reported. While Peng et al. described a similar nanostructure (Peng et al., 2023), (Alessandro Carrozza et al., 2021) observed much thicker α'' needles (≈ 550 – 700 nm). This discrepancy can be attributed to the use in the latter study of a preheated (T = 100 °C) baseplate which reduced the overall cooling rate, thus favoring the formation of coarser martensite needles.

5.7.2 Printability of the Ti6246 alloy: minimizing the risk of lack-of-fusion defects

The number of studies on the LPBF printability of Ti6246 alloys is limited as compared to the more common Ti64, and the results reported vary significantly. For example, (Hassanin et al., 2021) printed high-density (98.8-99.9%) Ti6246 samples using a wide range of volumetric energy densities (40 < VED < 160 J/mm^3), while (Alessandro Carrozza et al., 2021) succeeded in printing samples with comparable densities using relatively lower VED values of 40 - 60 J/mm^3. In the present study, such low VED (50 J/mm^3 of the parameter sets C and E) led to the printing of samples with a significant porosity (98 – 99%) and a high number of lack-of-fusion defects. Considering our printer configuration, only the use of $VED \geq 100$ J/mm^3 (parameter set B) allowed to print >99.9% density samples. Multiple reasons are susceptible to explain these discrepancies. In the aforementioned studies, the printers used had different

capacities (higher power, wider laser beam size). Additionally (Alessandro Carrozza et al., 2021) used a preheated baseplate, which reduced the level of laser energy needed to melt the material.

Using the LED and VED thresholds, respectively 0.2 J/mm and 100 J/mm^3, allows to establish another process condition in term of the hatching space h value. To print dense samples using a layer thickness t = 50 µm, h must be bigger than 40 µm (see equations (5.4) and (5.7)). Below this hatching space value, the resulting scanning speed v becomes too high (> 550 mm/s) to form continuous tracks according to the results of single-track analysis summarized in Figure 5-4d. Indeed, defects, such as irregular or partially melted tracks, were reported for most of the single tracks printed using a greater scanning speed.

5.7.3 Remelting phenomenon and keyhole formation

The multiple exposures caused by the previously described overlapping factor can be correlated with the keyhole porosity observed (Figure 5-6a.f and Figure 5-7a). Indeed, samples printed with the highest VED generated significant melt pool overlaps (set A, N = 1.3 to 3.7 and $R\%$ = 50 to 80 %) and were at risk of forming keyhole pores. These printing conditions combined high laser powers (P > 180 W), low scanning speeds (v < 550 mm/s) and therefore, high overlaps (N > 1.3). (Alessandro Carrozza et al., 2021) also reported a higher proportion of circular pores in the case of a very high laser power (P = 190 W), which is close to that of the A-set of this study (P = 188 W). The present study revealed that using higher hatching distances h reduces the overlaps and decreases the overall temperature in the vicinity of a melt pool, thus reducing the probability of keyhole formation and increasing the printed density from 99.84 (A-75) to 99.99% (A-175), APPENDICE C Tableau-A C-1.

5.7.4 Relationship between microstructure and mechanical properties

As observed in the present study, the higher the VED, the greater the hardness of as-printed Ti6246 samples. The same tendency can be observed elsewhere, as plotted in Figure 5-16a.

However, for equivalent VED values, the reported microhardness values differ. For example, for VED = 50 J/mm^3, some authors reported microhardness values close to 350 HV (Alessandro Carrozza et al., 2021; Hassanin et al., 2021) while for the same VED, (Cobbinah et al., 2024) and the authors of the present study obtained values closer to 435 HV. Such discrepancies can be explained by the differences in printing conditions in terms of powder composition, baseplate temperature, scanning strategy, etc., affecting the nature and morphology of phases present in the material.

Overall, the lowest microhardness values were reported for samples having an orthorhombic α'' martensite microstructure with relatively thick needles (Alessandro Carrozza et al., 2021), while the highest values were obtained for samples with a partial or complete transformation towards a stable $\alpha + \beta$ microstructure (Cobbinah et al., 2024). Orthorhombic α'' martensite is well known for its softening effect caused by its specific crystal structure and associated slip system, making it more sensitive to plastic deformation (Y. Guo et al., 2013). Conversely, the presence of hexagonal α' martensite strengthens the material and reduces its ductility (J. He et al., 2019). These statements are consistent with the generally recommended strategy of post-treating the LPBF-processed Ti6246 alloy to initiate $\alpha'' \rightarrow \alpha + \beta$ phase transformation and increase the material hardness (Hassanin et al., 2021; Alessandro Carrozza et al., 2022; Peng et al., 2023). For example, (Peng et al., 2023) in a bid to maximize the material hardness for tribological applications, varied the post-LPBF ageing time and temperature, and established a direct correlation between the hardness values and the width of α laths (5.11)

$$HV = HV_0 + Kd^{-0.5} \quad (5.11)$$

where HV is the Vickers hardness; HV_0, the intrinsic hardness of Ti6246 (424 HVN); K, the Hall-Petch constant (461 VHN.nm$^{-0.5}$), and d, the α laths width.

Note that the partially transformed A-set samples with a narrow hatching space h (Figure 5-9b.d.f) manifested an ultra-high hardness close to that of the above-referenced Peng *et al.* study with alternating thin α and β laths (respectively 35 and 5 nm in width). To support this

point, Figure 5-16b plots the microhardness values measured in the present study as a function of the $\alpha/\alpha'/\alpha''$ needle size and compares them to those reported in the literature, where it clearly appears that the thinner the needles, the higher the microhardness.

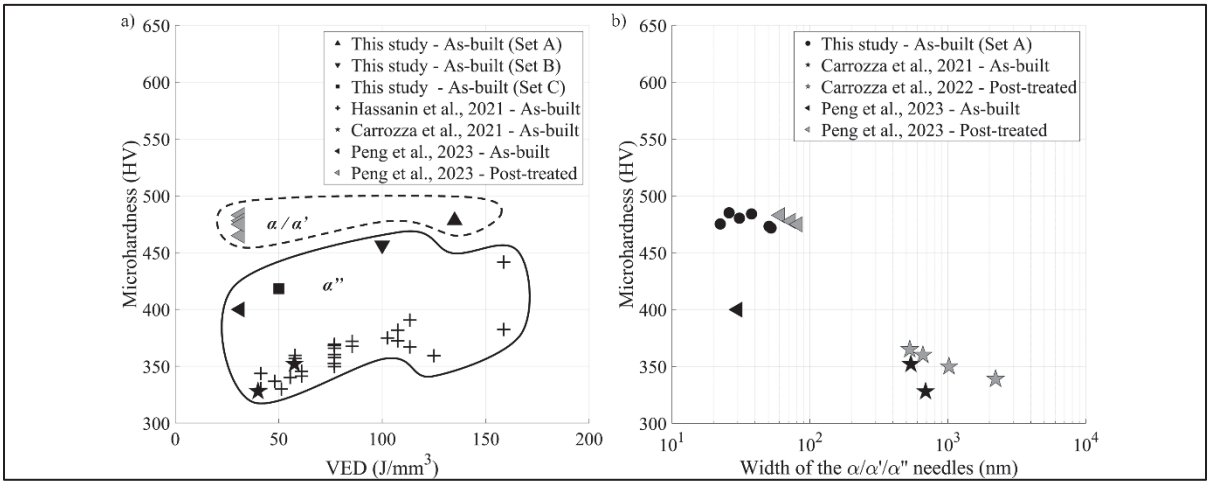

Figure 5-16: Evolution of the microhardness values reported in literature Alessandro Carrozza et al. (2021); Cobbinah et al. (2024); Hassanin et al. (2021); Peng et al. (2023) depending on a) the VED and b) the width of the α"/α' martensite needles or the α grains

As far as the others mechanical properties are concerned, this study showed that an increase in VED leads to an increase in strength at the expense of ductility. To support this observation, we must once again refer to (Alessandro Carrozza et al., 2021), the only authors to have carried out mechanical testing of this material in the as-built state. They obtained significantly lower strength ($YS \approx$ 450-600 MPa), but much higher ductility (> 25%) characteristics than those in the present study ($YS \approx$ 1000-1600 MPa and ≤ 8%). Note, however, that not only were the testing modes used in the reference and present studies different (tension versus compression), the microstructures of the samples tested were also significantly different: coarse 550-700 nm α'' martensite laths in the former case as compared to 50 – 70 nm α'' martensite laths in the latter case.

That notwithstanding, to provide a necessary balance between the strength and ductility characteristics of an LPBF Ti6246 alloy, the as-built alloy must be post-treated with the

objective of transforming the as-built α'' or mixed $\alpha' + \beta$ structure into an equilibrium $\alpha + \beta$ structure (Alessandro Carrozza et al., 2022).

5.8 Conclusion

In this study, a wide range of process parameters were applied to print Ti6246 alloy using a limited laser-power system (P_{max} = 200 W) without a preheated baseplate. During the printing of single tracks, a minimum linear energy density (LED) of 0.2 J/mm was necessary to guarantee their uniformity, while during full parts printing, an optimized volumetric energy density (VED) of ~100 J/mm^3 allowed to minimize defect formation and obtain highly dense parts (> 99.9%). Below this value, wide and irregular lack-of-fusion defects were systematically observed, while over it, the detected pores were small and circular, corresponding to keyhole pores. Overall, the printing parameter set B (volumetric energy density VED = 100 J/mm^3, build rate BR = 5 cm^3/h) led systematically to as-built samples with mainly an orthorhombic α'' martensite microstructure, manifesting high ultimate compressive strength (UCS > 1000 MPa) but a low strain to failure (δ ~ 6-8 %). Therefore, the printing parameter sets B with hatching space $h \geq 150$ µm (B-150 and B-175) was retained as the best to provide a combination of high mechanical properties and homogeneous initial as-built microstructures.

For the process parameters set A with the highest volumetric energy density (VED = 135 J/mm^3), partial in situ transformation from α'' martensite towards a mixture of stable $\alpha + \beta$ phases was reported. The transformed $\alpha / \alpha' + \beta$ microstructure induced a slight increase in the mechanical properties (microhardness $HV0.3$ and yield strength YS), without changing the material ductility. This phase transformation was attributed to a high level of laser power (P = 188 W) combined with a small hatching space h. This combination resulted in multiple laser overlaps (N) and to a large fraction of the remelted material ($R\%$) between each pass, decreasing the cooling rate of the solidified matter and affecting the as-built alloy microstructure.

An accurate control of the microstructure during the printing process is complicated by the fact that the cooling rate can be significantly affected by the baseplate configuration and how the printed part is exposed to gas flow. Furthermore, the identified transformed phases remain metastable, meaning that a subsequent heat treatment is mandatory to create the microstructure suitable for application. The occurrence of these in situ transformations can be beneficially used to tailor specific microstructures in printed parts by optimizing the printing parameters (especially using a double exposure system) and post-process conditions.

5.9 CRediT authorship contribution statement

Conceptualization, T.M. and V.B.; data curation, T.M. and A.L.; formal analysis, T.M. and A.L.; funding acquisition, V.B.; investigation, T.M. and A.L.; methodology, T.M., A.L. and V.B.; software, T.M. and A.L.; project administration, V.B.; resources, V.B.; supervision, V.B.; validation, V.B.; visualization, T.M., A.L. and V.B.; writing—original draft preparation, T.M. and A.L.; writing—review and editing, V.B.;

5.10 Declaration of competing interest

The authors declare no conflicts of interest. The funders had no role in the design of the study**;** in the collection, analyses, or interpretation of data; in the writing of the manuscript; or in the decision to publish the results.

5.11 Acknowledgments

The authors acknowledge the financial support provided by CRIAQ (Consortium de Recherche et d'Innovation en Aérospatiale au Québec) in the framework of the Exploring Innovation – INNOV-R program, NSERC (Natural Sciences and Engineering Research Council of Canada) and Exonetik Turbo inc.

5.12 Data availability

Data are contained within the article.

CHAPITRE 6

IMPRIMABILITÉ DE L'ALLIAGE DE TITANE TI-6AL-2SN-4ZR-6MO ET EFFETS DE POST-TRAITEMENTS EN VUE DE SON INTEGRATION POUR APPLICATION STRUCTURALE

Cette première étude au sujet de l'alliage de Ti-6Al-2Sn-4Zr-6Mo (Ti6246) a permis de démontrer la capacité à produire par fusion laser sur lit de poudre, sur une machine à puissance laser réduite et sans contrôle de la température de la chambre, des échantillons pour les analyses microstructurales et la caractérisation mécanique. Des paramètres de fabrication optimaux ont été définis pour une épaisseur de couche de 50 µm, permettant d'obtenir des pièces avec un minimum de défauts internes. Des géométries plus complexes et une étude sur la précision d'impression de cet alliage sont alors nécessaires avant d'envisager la production de l'anneau de la turbine ICT. En effet, celui-ci possède de faibles parois, mais également des centaines de petits canaux qui, en premier lieu, ne doivent pas être bouchés, et dont la qualité de l'aperture (en termes de taille et de rugosité notamment) impacte grandement ses performances. Ainsi, une deuxième étude a été menée, adressant cette notion d'imprimabilité au travers de la production et de la caractérisation de différentes géométries. Les paramètres optimisés lors de la première étude ont été déclinés selon deux épaisseurs de couches (25 et 50 µm), puisqu'il a largement été établi dans la littérature qu'une réduction de l'épaisseur de couche permet d'améliorer le fini de surface des pièces produites par LPBF. Après s'être assuré que ce changement d'épaisseur de couche n'avait pas d'impact sur les propriétés physiques et mécaniques des échantillons tels que fabriqués, l'analyse des différents artéfacts géométrique a mis en avant une nette amélioration de la précision d'impression compensé par une vitesse de production des pièces plus lente. Cependant, les analyses physiques ont révélé la présence de la phase martensitique α'', phase métastable conférant une grande résistance, mais une fragilité significative aux échantillons produits et testés mécaniquement, et ce, quelle que soit l'épaisseur de couche considérée. De fait, des post-traitements (thermiques ou thermomécaniques) doivent être ajoutés pour stabiliser la microstructure et améliorer les propriétés mécaniques avant de pouvoir considérer l'utilisation de cet alliage dans une application structurale. Une troisième étude a donc été envisagée pour explorer les effets de

deux protocoles de post-traitements thermiques sur les propriétés physiques, mais également mécaniques au travers de tests de traction à température ambiante et haute température. Il en ressort que, bien que les résultats soient prometteurs et aient permis d'améliorer la ductilité des pièces, des études supplémentaires sont nécessaires pour respecter les requis du cahier des charges et atteindre, voire surpasser, les performances mécaniques de l'alliage couroyé, notamment à température ambiante.

La contribution majeure des travaux sur les effets du changement d'épaisseur de couche (6.1) revient à M Thibault Mouret, PhD, responsable de la conceptualisation et des analyses par microtomographie à rayons X, et nous partagions les travaux d'expérimentation et d'analyses. En ce qui concerne les effets des post-traitements (6.2), si la conceptualisation été partagée, la majeure partie des expériences et analyses me revient.

6.1 Effect of layer thickness on the as-built density, microstructure, mechanical properties, surface roughness and printability of LPBF Ti6246 components

Aurore Leclercq[a], Thibault Mouret[b] and Vladimir Brailovski[c]

[a,b,c]Département de Génie mécanique, École de Technologie Supérieure,
1100 Notre-Dame Ouest, Montréal, Québec, Canada H3C 1K3

Article soumis pour publication, septembre 2025

6.1.1 Résumé

Un alliage relativement récent, le Ti-6Al-2Sn-4Zr-6Mo (Ti6246), connu pour sa haute résistance sur une large plage de températures, constitue un excellent candidat pour la fabrication de pièces aux formes géométriques complexes par fusion laser sur lit de poudre (LPBF). Étant donné que les paramètres d'impression en LPBF, en particulier l'épaisseur de couche, influencent fortement la conformité géométrique des pièces imprimées, ce travail est dédié à une analyse comparative de pièces en Ti6246 imprimées avec deux épaisseurs de

couche : 50 et 25 µm. Cette étude évalue l'influence de l'épaisseur de couche sur la densité, la microstructure et les propriétés mécaniques de ce matériau, ainsi que sur la conformité géométrique d'artéfacts en Ti6246 intégrant des parois, des interstices et des canaux. Les deux jeux de paramètres optimisés utilisés ici ont permis d'obtenir des échantillons très denses avec des microstructures similaires à l'état brut (aiguilles de martensite α'' nanométriques) et des propriétés mécaniques comparables (dureté et limite d'élasticité élevées, mais faible allongement à la rupture). Cependant, des différences significatives dans la taille des bains de fusion et leur continuité ont influencé la conformité géométrique des artéfacts imprimés avec les deux épaisseurs de couche, notamment pour les éléments de conception inférieurs à 1 mm pour lesquels l'impression avec des couches plus épaisses (50 µm) a conduit à des parois plus épaisses et à un bouchage partiel des interstices. À l'inverse, les couches plus fines (25 µm) ont permis d'imprimer des parois et des interstices aussi petits que 0,2 mm avec une excellente conformité géométrique (écart inférieur à 10 % par rapport au modèle CAO). Pour les artéfacts contenant des canaux, l'utilisation de couches plus fines a permis d'augmenter leur conformité géométrique de 10 % et d'éviter leur bouchage partiel, permettant un meilleur écoulement.

6.1.2 Abstract

A relatively new Ti-6Al-2Sn-4Zr-6Mo alloy (Ti6246), known for its high strength in a wide temperature range, is an excellent candidate for manufacturing parts with complex geometrical features using laser powder bed fusion (LPBF). Since LPBF printing parameters, especially the layer thickness, are known to significantly influence the geometric compliance of printed parts, this work is dedicated to a comparative analysis of Ti6246 parts printed using two layer thicknesses, namely, 50 and 25 µm. This study assesses the influence of the layer thickness on the density, the microstructure and the mechanical properties of this material, as well as the geometric compliance of wall-, gap- and channel-contained Ti6246 LPBF artefacts. The two optimized parameter sets used herein enabled to obtain highly dense samples having similar as-built microstructures (nanometric α'' martensite needles) and mechanical properties (high hardness and yield strength but low elongation to failure). However, significant differences in the melt pool size and its continuity influenced the geometric compliance of the artefacts

printed using the two different layer thicknesses. Notably, for design features smaller than 1 mm, printing with thicker layers (50 µm) led to thicker walls and partially clogged gaps. Conversely, thinner layers (25 µm), enabled to print wall and gap features as small as 0.2 mm with an excellent geometric conformity (less than 10% deviation from the CAD). For the channel-contained artefacts, using thinner layers allowed increasing their geometric compliance by 10% and preventing their partial clogging, resulting in a much better air flow through them.

Keywords: Additive manufacturing; Laser Powder Bed Fusion; Titanium alloy; Printability; Thin features; Internal channels

6.1.3 Introduction

Additive manufacturing (AM) technologies are currently on the rise as their high versatility and agility enable small series manufacturing which is economically unsustainable using conventional processes (Javaid et al., 2021; Tofail et al., 2018). Based on the sequential layer-by-layer shape forming principle, these technologies allow the manufacture of intricate and complex shapes with a significant reduction of overall material waste (Hegab, Khanna, Monib, & Salem, 2023). One of the best-known metal AM processes, laser powder bed fusion (LPBF), has been shown to be the most efficient technology for printing high density parts with small design features. The process uses fine powders (20-50 µm) and generates narrow melt pools, thus achieving relatively high resolutions (0.1-0.2 mm) and tight tolerances (± 50 µm). Additionally, it is less expensive than its principal competitors, namely, electron beam powder bed fusion (EB-PBF) and directed energy deposition (DED) (D. D. Gu et al., 2012).

In the last decades, LPBF has been extensively used to print almost all categories of metallic materials, ranging from nickel (Sanchez et al., 2021), aluminum (Rometsch, Zhu, Wu, & Huang, 2022), iron (Narasimharaju et al., 2022), and titanium (Colombo-Pulgarín et al., 2021) alloys, and going all the way to refractory metals. Most of the LPBF-related literature focuses on the optimization of printing parameters (*e.g.,* laser power, scanning speed, etc.) in a bid to

minimize the occurrence of process-induced volumetric imperfections (*e.g.,* pores, cracks, etc.) (Ayers et al., 2024; Sabzi et al., 2020; Stopyra, Gruber, Smolina, Kurzynowski, & Kuźnicka, 2020). These optimization routines are mainly realized using bulk simply-shaped specimens, such as cylindrical or prismatic coupons (B. Liu et al., 2024). However, to actually benefit from the outstanding potential of LPBF to manufacture complex and lightweight structures, another optimization target – the capacity to print high-precision small features in form of walls, gaps and channels – must be considered.

In the aftermath of the democratization of the LPBF process, a plethora of general printing recommendations have been advanced to improve the geometric compliance of printed parts (Kranz, Herzog, & Emmelmann, 2014) and to facilitate the removal of unmelted powder (Ceccanti, Giorgetti, Arcidiacono, & Citti, 2021), with the focus on the positioning and orientation of parts with respect to the building platform. Other studies have also targeted the printing of different design features, including channels, lattices and thin walls. The latter have demonstrated the possibility of minimizing distortions of thin-walled structures by adequately positioning them relative to the recoater blade (Calignano, Cattano, & Manfredi, 2018). They have also revealed that shear forces induced by powder spreading during recoating operations could induce the failure of thin (~0.1 mm) walls (Gaikwad, Imani, Yang, Reutzel, & Rao, 2019). Moreover, a lack of geometric compliance of thin-walled structures can be accompanied by local microstructure and therefore, mechanical properties variations, which also must be taken into consideration (Kushwaha, Subramaniyan, Bommanahalli Kenchappa, & Barad, 2022). Another technological challenge presents the manufacture of channels parallel or slightly inclined to the building platform, since such design features frequently demonstrate significant distortions, including the collapse of down-facing surfaces (Baier, Sinico, Witvrouw, Dewulf, & Carmignato, 2021; Charles et al., 2022).

Titanium alloys are of great interest in a variety of technological domains, including in the biomedical, petrochemical, automotive and aerospace industries, due to their excellent strength-to-weight ratio (> 180 MPa/(g.cm^{-3})) (Boyer et al., 2007; Xin Yang et al., 2022), corrosion resistance (Tabie et al., 2020; Jiayu Yang, Song, Dong, & Han, 2023) and

biocompatibility (Dias Corpa Tardelli et al., 2020; Khorasani et al., 2015). The near-net shape manufacturing of complex parts enabled by AM processes reduces buy-to-fly ratio of these expensive materials. While an $\alpha + \beta$ Ti-6Al-4V alloy (Ti64) is one of the commonly used titanium alloys (Luo, Yang, Li, & Zhang, 2024), LPBF of other similar alloys has also been explored with the objective of meeting ever increasing application requirements. Recently, another $\alpha + \beta$ titanium alloy, Ti-6Al-2Sn-4Zr-6Mo (hereafter referred to as Ti6246), has attracted significant interest because of its high mechanical properties, especially at elevated temperatures. These unique properties make Ti6246 particularly interesting for applications in gas turbines, where the geometrical complexity of parts improving the performance of such engines legitimates the use of LPBF as a manufacturing process.

The implementation of Ti6246 for the LPBF process started at the beginning of the present decade with the work of (Alessandro Carrozza et al., 2021) who were the first to report on the Ti6246 laser powder bed fusion printability. Other studies followed (Hassanin et al., 2021; Mouret, Leclercq, & Brailovski, 2025; Peng et al., 2023), highlighting the effects of process parameters, such as laser power, scanning speed and hatching space, on the structural and mechanical properties of as-built Ti6246 parts. The latter studies revealed the in-print formation of orthorhombic martensitic phase (α''), whose size and morphology varied as a function of process parameters. The studies aimed to understand the interaction between process parameters and structural and mechanical properties of printed materials, thus allowing the optimization of the process. The optimization was generally realized in two phases: a) maximizing the as-printed density while forming the most appropriate as-printed microstructure (Alessandro Carrozza et al., 2022) and b) finding a compromise between process productivity and precision of printed parts. To achieve the latter, (Alessandro Carrozza et al., 2022) compared the printability of thin features and hollow channels using Ti64 and Ti6246 alloys. Compared to Ti64, Ti6246 was found to provide a better precision with thin features, but less with hollow channels (A. Carrozza et al., 2023). In another study, the authors found that with its atypical α'' microstructure, Ti6246 provided a better accommodation of thermal stresses with a reduced risk of distortions than did Ti64 (Aversa et al., 2025).

To further improve the as-print precision of Ti6246 parts without compromising on their mechanical properties, the present work proposes to decrease the layer thickness during printing, while keeping the laser energy density, building rate and hatching distance-to-layer thickness ratio constant. Firstly, to ensure that layer thickness variations do not negatively impact the microstructure and mechanical properties of printed parts, bulk specimens were printed with two layer thicknesses, 50 and 25 μm, and subjected to microstructural analysis and mechanical testing. Next, to conclude on the impact of the layer thickness variation on the geometric fidelity of printed parts, a series of artefacts containing thin wall/gap features and narrow channels was also printed using both layer thicknesses and compared with their original CAD files.

6.1.4 Material and methods

6.1.4.1 Powder and printed specimens

It is common knowledge that an adequate powder bed density and uniformity are essential to obtain high quality LPBF parts, both in terms of the printed density and of the geometric accuracy, and these outcomes depend significantly on the powder particle characteristics (size, sphericity, uniformity (Brika et al., 2020)). The gas-atomized pre-alloyed Ti6246 powder produced by Eckart TLS Gmbh (Bitterfeld-Wolfen, Germany) used in this study is highly spherical (see image in Figure 6-1a obtained using a Hitachi TM300 (Tokyo, Japan) scanning electron microscope). The initial powder particle size distribution (PSD) was measured using a Beckam Coulter LS13 320 XR particle size analyzer (Brea, CA, USA). To ensure that the powder was not mechanically segregated during recoating using a thinner layer thickness (25 μm), the PSDs inside three printer compartments, namely in the dispensing and spreading platforms and the powder collector (Figure 6-1b), were measured for this layer thickness.

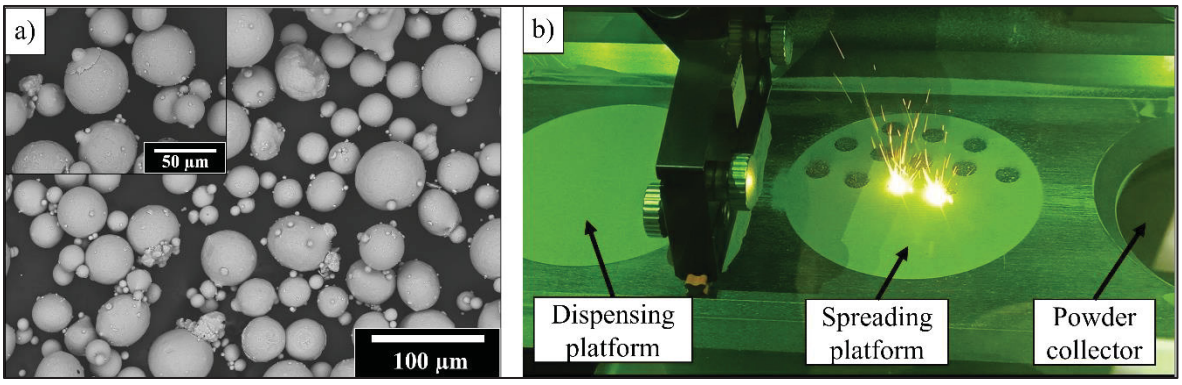

Figure 6-1: a) SEM observations of the Ti6246 powder; b) Photo of the printing chamber describing the different compartments

In the collector and dispensing platform, the PSDs were found almost identical (D10 = 26, D50 = 42 and D90 = 63 µm), while in the spreading platform, it was very slightly shifted towards finer particles (D10 = 21, D50 = 35 and D90 = 56 µm). Thus, decreasing the layer thickness from 50 to 25 µm has a negligible effect on the PSD and should not impact neither the quality of printed parts nor the powder reuse.

The powder was loaded into a Trumpf TruPrint 1000 LPBF system (TRUMPF GmbH, Ditzingen, Germany) (P = 200 W; laser spot size 55 µm). Based on the results of our previous study (Mouret, Leclercq, & Brailovski, 2025), the following sets of printing parameters were used in this study for a layer thickness t of 50 µm (referred to as Set I in Tableau 6-1): laser power P = 139 W, scanning speed v = 185 mm/s and hatching space h = 150 µm, resulting in a volumetric energy VED (6.1) = 100 J/mm^3, building rate BR (6.2) = 5 cm^3/h and h/t ratio = 3.

$$VED\ [\mathrm{J/mm^3}] = \frac{P}{vht} \tag{6.1}$$

$$BR\ [\mathrm{cm^3/h}] = vht \tag{6.2}$$

For a valid comparison, while reducing the layer thickness from t = 50 to 25 µm, the energy brought to the powder bed (VED), the process productivity (BR) and the hatching space-to-layer thickness ratio (h/t) were kept constant. To fulfill these conditions, dividing the layer

thickness in half was compensated by a four-fold increase in the scanning speed v, from 185 to 741 mm/s (Set II in Tableau 6-1).

Tableau 6-1: Printing parameter sets used to process the Ti6246 alloy with the two layer thicknesses (t) considered

Set	VED (J/mm^3)	BR (cm^3/h)	t (µm)	h (µm)	h/t	P (W)	v (mm/s)
I	100	5	50	150	3	139	185
II			25	75		139	741

Firstly, two types of bulk specimens were printed: dense cubic specimens with single laser tracks on their top surface (Figure 6-2a) and 10 mm-diameter, 21 mm-height cylindrical specimens (Figure 6-2b). The cubic specimens were removed from the baseplate and used for the single track width measurements with the second objective of evaluating the quality of single tracks and improving the printing accuracy via the adjustment of a laser beam offset. The cylindrical specimens were removed from the baseplate, their supports were cut off, and the remaining parts partitioned to obtain samples for porosity analyses, structural analyses and compression testing (Figure 6-2b). In addition, to assess the printability limits, wall (Figure 6-2c) and gap (Figure 6-2d) design artefacts with widths ranging from 0.1 to 2 mm were printed. Figure 6-2e and Figure 6-2f contains images of the printed artefacts.

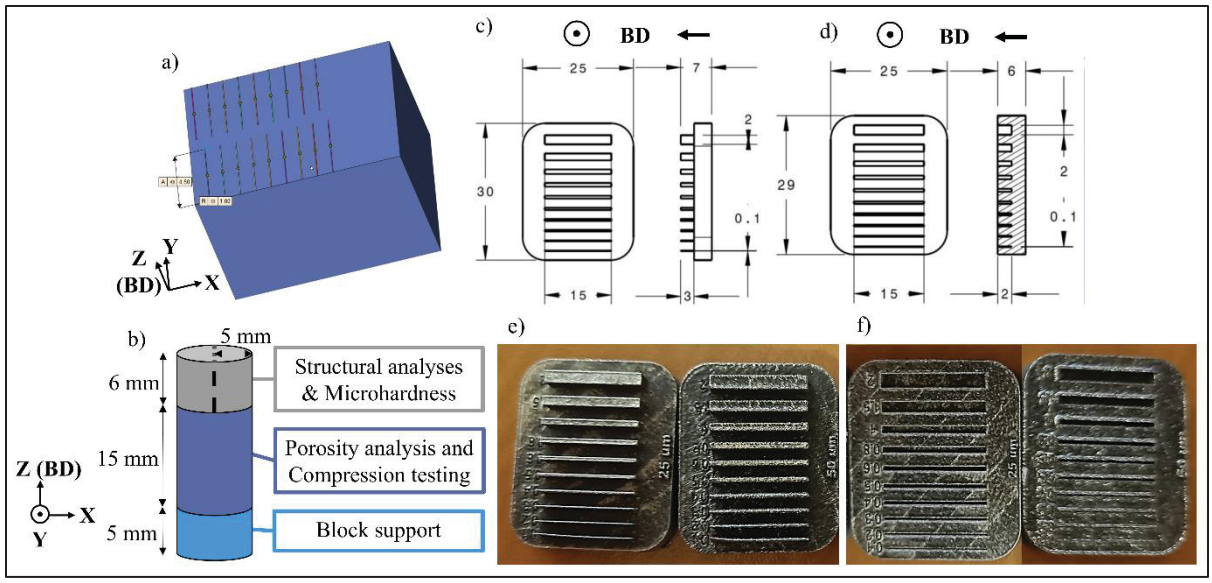

Figure 6-2: Schematic representation of the a) cubic specimen with single tracks printed on its upper surface; b) cylindrical specimen with samples used for various analyses. Drawings of the printed geometric artefacts: c) walls and d) gaps. Printed artefacts using 25 and 50 µm layer thicknesses: e) walls and f) gaps. All dimensions are in millimeters (mm)

To provide an example of a more complex part, the pressure drop measurement artefacts containing eight 60°-oriented hollow channels were also printed (Figure 6-3a). Channels 1 to 7 were identical (A = 0.86 mm^2) while Channel 8 was larger (A = 1.11 mm^2), but contained a narrower part (A = 0.13 mm^2) at one of the extremities (Figure 6-3b and Figure 6-3c). Images of the printed pressure drop artefacts are shown in Figure 6-3d.

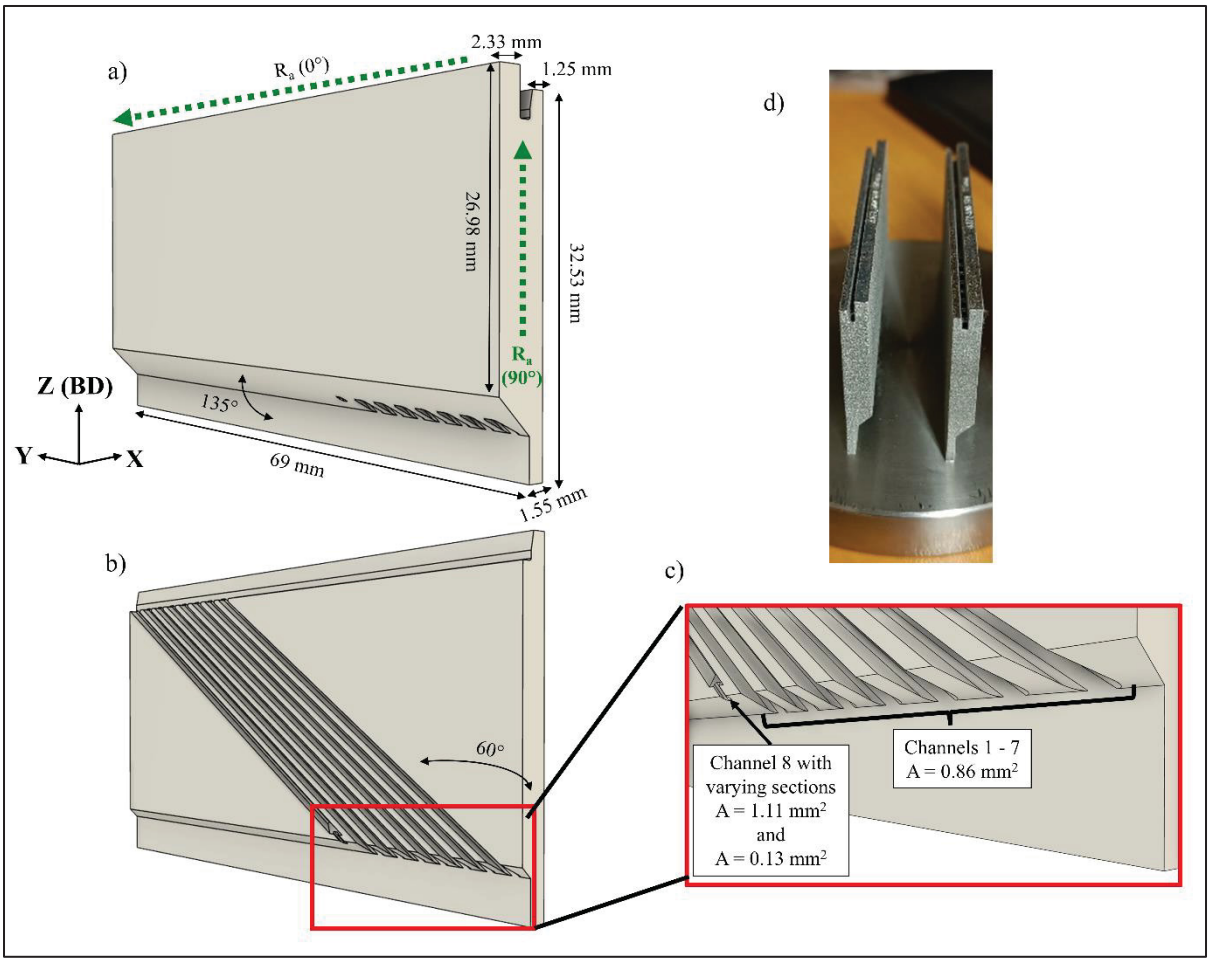

Figure 6-3: Schematic representation of the pressure drop artefacts: a) full view, b) cut view to observe the channels and c) zoomed view at the channels extremity; d) printed pressure drop artefacts. Green dotted lines on full view highlights the surfaces for roughness measurement

All the parts of the study were printed using both layer thicknesses. No specific printing strategy was used for cylindrical specimens, where the layers were melted using zigzag scan patterns with a ± 51° rotation between them. Conversely, to improve the geometric conformity of the wall, gap and pressure drop artefacts, they were contoured using the same printing parameters as for core printing with an offset obtained from the single-track measurements. No specific down-skin strategy was used to print channel-containing parts.

6.1.4.2 Specimen characterization

Single tracks and printed density

Single tracks produced on the dense cubic specimens (Figure 6-2a) were analyzed using a Keyence optical VHX7000 microscope (Osaka, Japan). Their average width was extracted from ten equally-distanced height profile lines traced perpendicular to the tracks. To obtain printed density information, micro computed tomography (μCT) scans were conducted on 15 mm long middle parts of the cylindrical specimens (volume analyzed ≈ 1000 mm^3). The scans were acquired using an FF35 CT system (Comet Yxlon, Germany), with the following acquisition parameters: a tube voltage of 140 kV, a tube current of 50 μA, 1500 projections, an exposure time of 475 ms over 3 frames integration and 0.3 mm thick copper filter for beam hardening correction. The projections were corrected and reconstructed using Siemens CERA software, resulting in a voxel size of 8 μm. Porosity analyses were carried out using Dragonfly software with manual thresholding for segmentation. A 6-connected component (faces) criterion was used to isolate each pore and pores smaller than 3x3x3 voxels (< $1.4*10^{-5}$ μm^3) were withdrawn from the dataset.

Microstructure

Upper 6 mm long parts of the cylindrical specimens (Figure 6-2b) were cut along the building direction, mounted in carbon-doped resin, grinded with SiC abrasive paper, polished using diamond suspensions and a colloidal silica + H_2O_2 suspension and subjected to microstructural analysis. An X'Pert^3 (Malvern Panalytical Ltd, Malvern, UK) diffractometer (XRD) was used to perform the phase identification. Acquisitions were made with a cobalt source (Kα Co = 1.79026 Å) operated at 45 kV and 40 mA, in the Bragg-Brentano configuration, with a step size of 0.017° and a 20°-90° 2θ range. The microstructural state was confirmed by metallographic analysis using chemical etching with a Kroll reagent (93% H_2O, 5% HNO_3, 2 HF) of the polished cross-sections. The prepared surfaces were then observed with a LEXT

OLS4100 (Lext Olympus Corp., Japan) confocal microscope and with a SU-8230 Field Emission STEM (Hitachi, Japan) scanning electron microscope.

Mechanical properties

Microhardness measurements were performed on the etched Y-Z cross-sections of the 6 mm long upper parts of the cylindrical specimens using a Struers Duramin-40 M1 microhardness tester. For each specimen, 10 measurements were carried out in the middle of the samples with an applied force of 300 gF and a dwell time of 15 s. After the as-printed density measurements, room-temperature compression tests were realized on 15 mm long middle parts of the cylindrical specimens using an Alliance RF/200 testing machine (MTS, Eden Prairie, MN, USA) according to the E9-09 ASTM standard (E28 Committee, 2018). The compression rate was set at 0.01 mm/s, and the force and the displacements were measured using a 200 kN MTS load cell and an LVDT, respectively. The following metrics were extracted from the measurements: the Ultimate Compression Strength (UCS, MPa), defined as the maximum stress reached during the test; the Yield Strength (YS, MPa), calculated by moving the slope from the origin to 0.2% on the strain axis, and the elongation to failure (δ, %).

Surface roughness measurements

The surface roughness measurements were performed using a Mitutoyo SJ410 profilometer (Mitutoyo, Japan), following the ISO 21920-2 (« Geometrical product specifications (GPS)—Surface texture : Profile—Part 2 : Terms, definitions and surface texture parameters », 2021) standard (R profile, λ_s = 8 µm, 5 repetitions with a cut-off at 2.5 mm and a Gauss filter) on the upper and lateral sides of the pressure drop artefacts, respectively at 0 and 90° (Figure 6-3a) with respect to the building direction.

Geometric analysis

To assess the geometric compliance of the printed parts relative to their CAD drawings, high quality µCT scans of each artefact were realized using the same equipment described in section Single tracks and printed density. Due to the difference in dimensions between the wall/gap and channeled artefacts, the acquisition parameters were adapted from one artefact to another. The voltage and the current of the X-ray tube were set to 175 kV and 140 µA and the copper filter used to harden the histogram was 0.5 mm thick. For each of the artefacts, 3000 projections were acquired. The walls and gaps were obtained with a 0.714 ms exposure time, while it was increased to 0.909 ms for the channeled parts due to their larger dimensions. Overall, each projection was integrated over 3 frames for noise reduction. Siemens CERA software was used to correct the beam hardening and reconstruct the 3D volumes, leading to a final voxel size of 15 µm and 30 µm for the wall/gap and channeled artefacts, respectively.

The Dragonfly software visualization tools (COMET technologies, Canada) and Python libraries (*e.g.,* scikit-image, OpenCV, etc.) were used for the artefacts' inspection and image processing. For the wall artefacts, the wall thickness was measured for each of the 200 15 µm-spaced 2D XY sections extracted from the 3D reconstructed volumes. For each section, the feature edges were segmented using a Sobel filter, Otsu thresholding and profile line averaging along the length of the artefact. For the gap artefacts, the gap width was calculated for each of the 133 15 µm-spaced 2D XY slices by dividing the surface of the gap by its length. Note that the surface of each gap corresponded to a sum of 15x15 (μm^2) pixels encompassed between its segmented edges. In addition, Dragonfly software was used to calculate the true volumes of each feature (walls and gaps) and to compare them with their nominal CAD values.

The channels conformity was analyzed by segmenting their 2D XZ cross-sections. Note that these 2D cross-sections were computed only in their middle part of the channels. Indeed, the channels are rectangular and oriented, therefore their areas in such 2D section vary at extremities. In the XZ 2D view, channels 1 to 7 have a nominal cross-section area equal to 0.99 mm^2, while the widest section of channel 8 has a nominal area value of 1.28 mm^2. The

variation of the thinnest section of channel 8 was not segmented for technical limitations. Indeed, with such poor resolution (voxel size = 30 µm), this narrow channel (width = 400 µm) corresponds to only 13 voxels, compromising the segmentation.

Next, the CT volumes of each of the artefacts (walls, gaps and channels) were segmented, converted into a mesh and registered with their nominal equivalents. The iterative closest point algorithm implemented in the software was used to register one mesh with another using the best fit approach. A signed deviation map was generated and the cumulative statistical deviation of each artefact was calculated.

6.1.5 Results and discussions

6.1.5.1 Printability and properties of printed part

Visual aspect of printing

For the two parameter sets of the study, the visual aspect of printing jobs differed. Set I with thicker layers generated much more sparkles during printing and much more residual spatters on the build chamber walls after printing. This is in agreement with the observations by (Pauzon et al., 2023) in their study on Ti64 LPBF printability, where increasing the layer thickness increased the quantity of spatters per scanned layer. In the present study, this effect was compounded by a four times slower scanning speed for Set I as compared to Set II: 185 mm/s for Set I versus 741 mm/s for Set II. Due to this slower scanning, the linear energy density $LED = P/v$ for Set I was four times higher than for Set II (0.75 J/mm versus 0.19 J/mm) theoretically making the vapor flume above the melt pool less stable, promoting the ejection of droplets (H. Zheng, Li, Lang, Gong, & Ge, 2018), and potentially influencing the final print quality.

Physical and mechanical properties of printed specimens

Both printing parameter sets led to overall continuous and homogeneous tracks (Figure 6-4). However, due to a decrease in the scanning speed, the single track (melt pool) width (W) generated by Set I (t = 50 µm) was almost twice that generated by Set II (t = 25 µm): 297 ± 11 µm versus 145 ± 12 µm (Figure 6-4a,b). The single-track width values are reported in Tableau 6-2. Note that regular rippled patterns were observed on the surface of single tracks printed with Set I, while Set II promoted the formation of some humps along the tracks. According to the literature (C. Tang, Le, & Wong, 2020; P. Tang et al., 2020), these features are consistent with the parameters used, where using lower linear energies with higher scanning speeds (Set II) promotes humps formation caused by the periodic separation of melt pools and solidification shrinking. Conversely, using higher linear energies with lower scanning speeds increases melt pool instability with strong recoil pressure pushing back the molten metal and inducing the formation of ripples. Overall, despite the above differences, both parameter sets enabled to print high-density parts, systematically denser than 99.98%, with only a limited number of small highly spherical pores observed (Figure 6-4c,d). Note also that in both cases, a certain number of partially-melted particles were stuck to the printed parts.

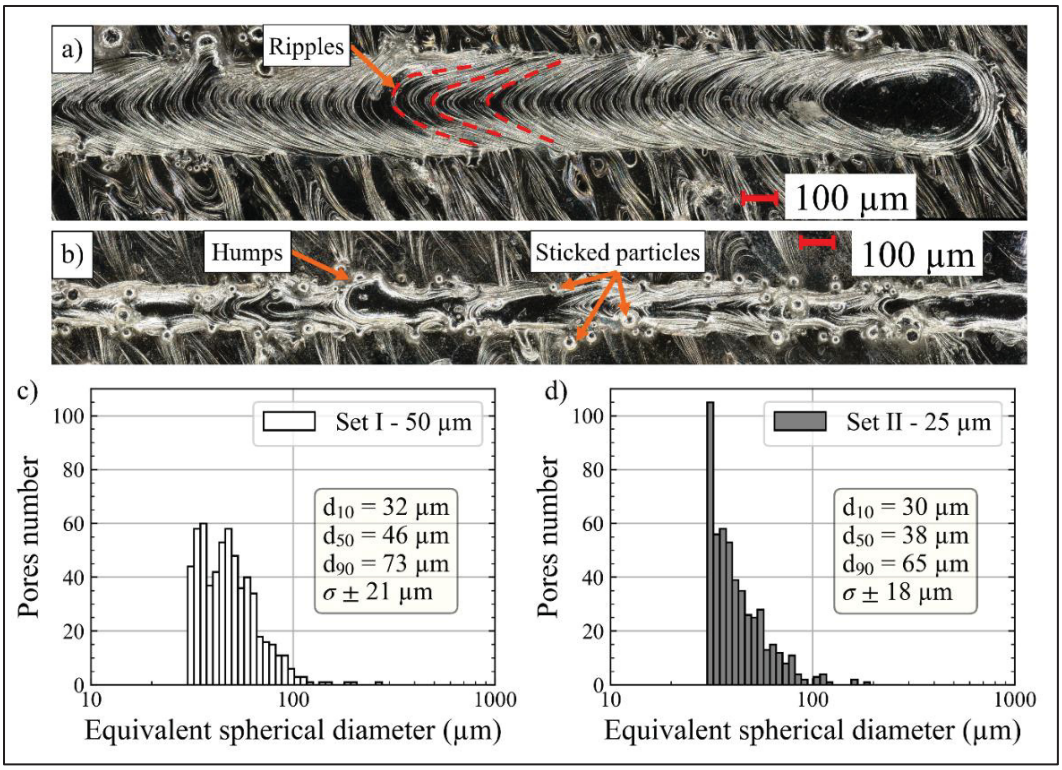

Figure 6-4: Optical observations of the continuous single tracks printed using a) Set I and b) Set II. Equivalent pore diameter distributions corresponding to a volume of 1 cm3: c) Set I – 50 µm, d) Set II – 25 µm; (cylindrical specimens)

Figure 6-5a shows the results of the XRD analysis and highlights the formation of orthorhombic α'' martensitic phase. For both cases, the confocal microscope observations (not shown here) revealed homogeneous microstructures with partially visible melt pool borders and typical columnar prior-β grains. Moreover, the higher magnification SEM observations shown in Figure 6-5b,c revealed a less than 2% difference in the size of martensite needles, arranged in a cross-hatch pattern for both sets of parameters used (Tableau 6-2). This microstructure similarity is caused by the almost identical W/h ratio for two cases, leading to the same relative overlap R% (6.3) of two neighboring tracks. Thus, even though the single track width for Set I was significantly larger that for Set II, this difference was compensated by a much larger hatching space for Set I than for Set II, thus enabling the formation of identical microstructures. The calculated R% values for the two sets of parameters are presented in Tableau 6-2.

$$R\% = \frac{W-h}{W} * 100 \quad (6.3)$$

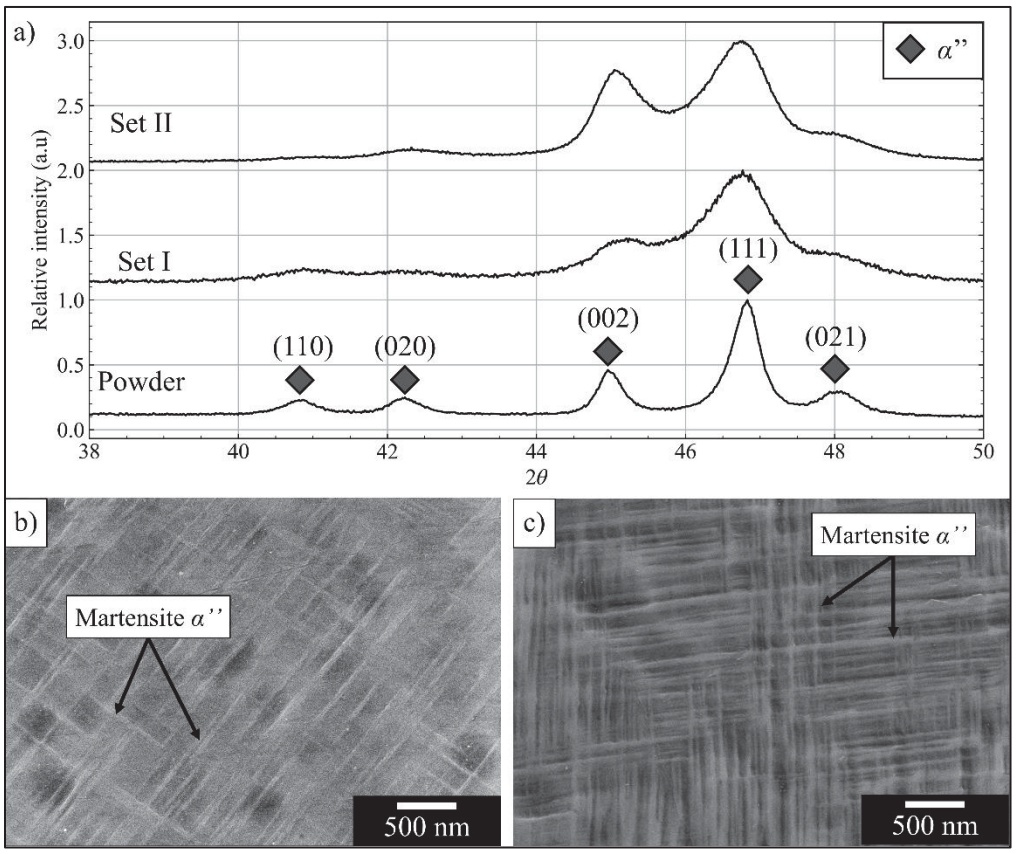

Figure 6-5: a) XRD diffractograms of the Ti6246 powder and of the as-built samples printed with both parameter sets; SEM images with the α'' martensite needles in samples printed with b) Set I and c) Set II

Finally, the two parameter sets led to the very close as-built mechanical properties summarized in Tableau 6-2, which is not surprising, given their structural similarities (α'' needle sizes and patterns). Regardless of the layer thickness used, the printed parts exhibited the same microhardness values, broke in a similar stress range (> 1000 MPa) and were relatively brittle ($d < 9\%$). It can therefore be certified that keeping constant the volumetric energy density VED, the process productivity BR and the hatching space-to-layer thickness ratio (h/t) allowed to maintain the as-built Ti6246 alloy's physical and mechanical properties almost identical, and that, despite the use of significantly different layer thicknesses.

Tableau 6-2: Physical and mechanical properties of the as-built samples printed using two different layer thicknesses t

Set	Single track width (W) (µm)	α'' needle width (nm)	W/h	R% (%)	Microhardness HV0.3	YS (MPa)	UCS (MPa)	δ (%)
I (50 µm)	297 ± 11	48 ± 11	2.0	49	447 ± 37	1075 ± 65	1115 ± 65	7 ± 0.4
II (25 µm)	145 ± 12	49 ± 17	1.9	48	471 ± 26	1045 ± 29	1120 ± 33	7 ± 1

6.1.5.2 Surface roughness and geometric compliance

Surface roughness

For each of the two layer thicknesses, the Ra values measured for the 0° (top) and 90° (lateral) oriented surfaces of the pressure drop artefacts, are summarized in Figure 6-6. As commonly observed (Hassanin et al., 2023; Masiagutova et al., 2021), the lateral surfaces were significantly rougher than the top surfaces. Moreover, for both surface orientations, the surface roughness of Set I artefacts (t = 50 µm) was significantly higher than that of their Set II counterparts (t = 25 µm), where thicker layers caused: a) a greater propensity to ripple formation on the top surfaces (see section Physical and mechanical properties of printed specimens for explanation) and b) a larger distance between layers on the lateral surfaces.

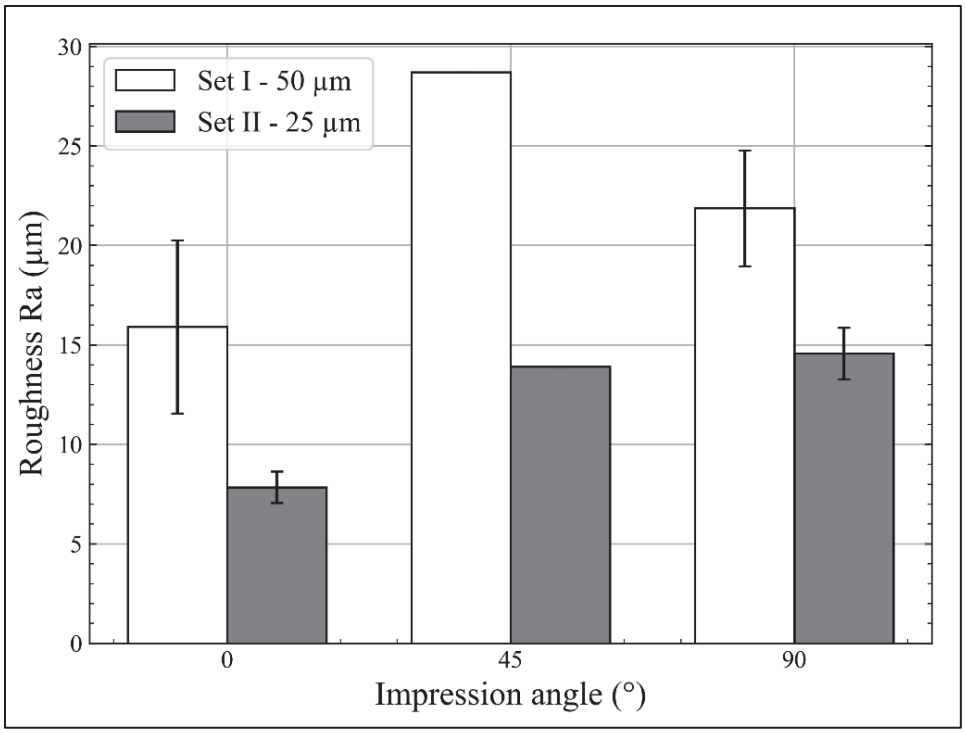

Figure 6-6: Surface roughness (Ra) measured on the pressure drop artefact as a function of the build angle for both parameter sets. 0° and 90° were obtained on the top and lateral surfaces of the artefact

Conformity of walls and gaps

The geometric compliance of the wall and gap artefacts was evaluated along the build direction and a summary of the average size of each feature is reported in Figure 6-7a**,** for wall thicknesses, and in Figure 6-7b, for gap widths. Note that for both cases, no significant variations of the wall thickness and gap width along the build direction were observed.

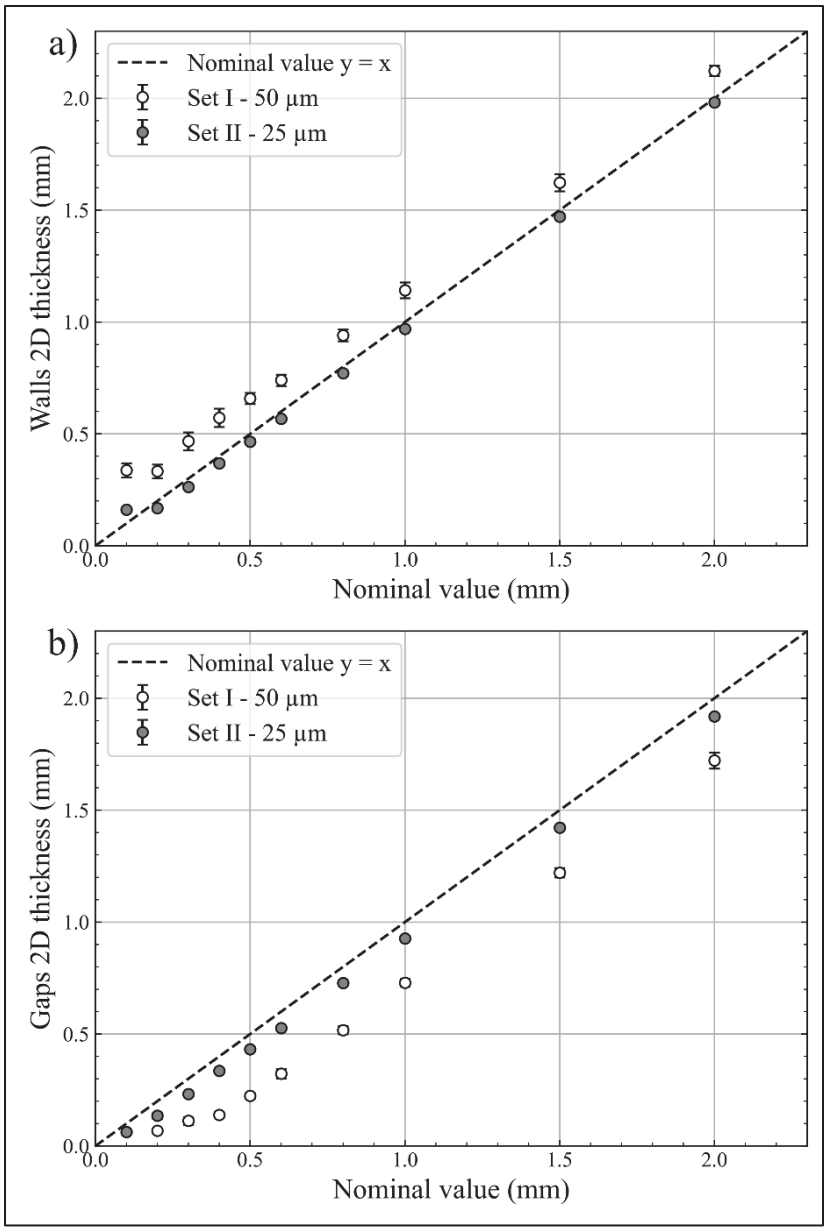

Figure 6-7: Average a) wall thickness and b) gap width for Sets I and II artefacts printing after segmentation of the µCT 2D XY sections; error bars are smaller than the markers

The 0.1 and 0.2 mm thick wall/gap features must be considered on their own merits, as they represent exceptional cases that fall within the range of single track widths, being formed by only one laser path (Tableau 6-2). In the case of wall artefacts, these two features had the same average thicknesses. However, the difference with the nominal values is greater for Set I than

for Set II because of wider melt pools (single tracks) in the former case (Figure 6-7a). Note that the wall thicknesses reported here are slightly larger than those reported for single tracks in section Physical and mechanical properties of printed specimens ($\Delta W \approx$ 20-30 μm) due to the thermal history of the powder bed, which can vary between the prints (*e.g.,* the number of parts on the build plate, the printing parameters used for surrounding parts, etc.). According to these observations, the thinnest printable wall thickness roughly corresponds to the single track width, i.e., 0.3 mm for Set I and 0.15 mm for Set II (Figure 6-7a). Given the substantial width of melt pools (single tracks) for Set I, gaps with a nominal width smaller than 0.2 mm were almost fully clogged, but they were printable with Set II (Figure 6-7b). For both layer thicknesses, the gaps were narrower than their nominal values, due to particles partially-melted to their edges, with these deviations being systematically greater for Set I artefacts as compared to their Set II equivalents. This behavior is consistent with the single track analyses (Figure 6-4a,b).

The 3D volume segmentation of each of the two features (Figure 6-8) allowed comparisons with the nominal volumes. Overall, the measurement performed on features printed using Set II (t = 25 μm) are in line with the nominal values, except for the thinnest features (0.1 mm) in which case deviations are observed, mainly because single tracks are wider that the desired feature. Conversely, a significant shift in the volume values is reported for features printed with Set I (t = 50 μm). For features with nominal values smaller than 1 mm, a rapid decline in the geometric compliance is observed. These observations are consistent with the melt pool (single track) measurements (see sections Visual aspect of printing and Physical and mechanical properties of printed specimens). Wider melt pools and more sparks associated with Set I promoted the sticking of particles to the outer contours of part printed. Therefore, using Set II with thinner layers allowed accurate (< 5% deviation) printing of features larger than 0.2 mm, while Set I induces notable deviations (> 20%) for features smaller than 1.0 mm.

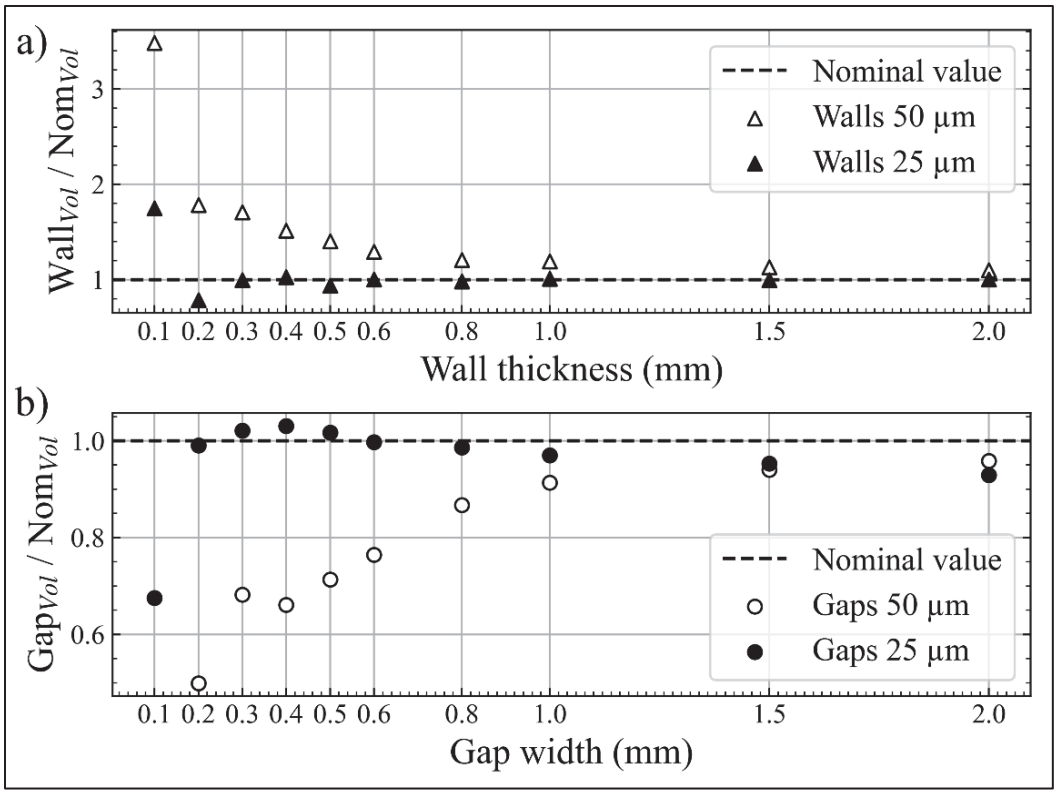

Figure 6-8: Evolution of the segmented 3D volume compared to
the nominal volume for both parameter sets for a) walls and b) gaps.
In each figure, black dashed lines correspond to the nominal thickness of features

The entire deviation analysis of the wall and gap artefacts was completed using the computation of signed distance maps (Figure 6-9). Note that the important deviations reported in both case for the 0.1 mm thick wall is related to its fragility and its maximal deformation at one edge, occurred during the sample removal from the baseplate. Overall, the colored deviation maps illustrate the major difference in printing accuracy between the two parameter sets. As mentioned in section Visual aspect of printing, Set I (Figure 6-9a), with the highest *LED,* was correlated with ripples and a large number of undesired spatters solidified on the top surface, generating some significant deviations. Conversely, the top surfaces which were printed with Set II (Figure 6-9b) had a much better geometric compliance, with deviations close to the particle size range (≈ 60 µm).

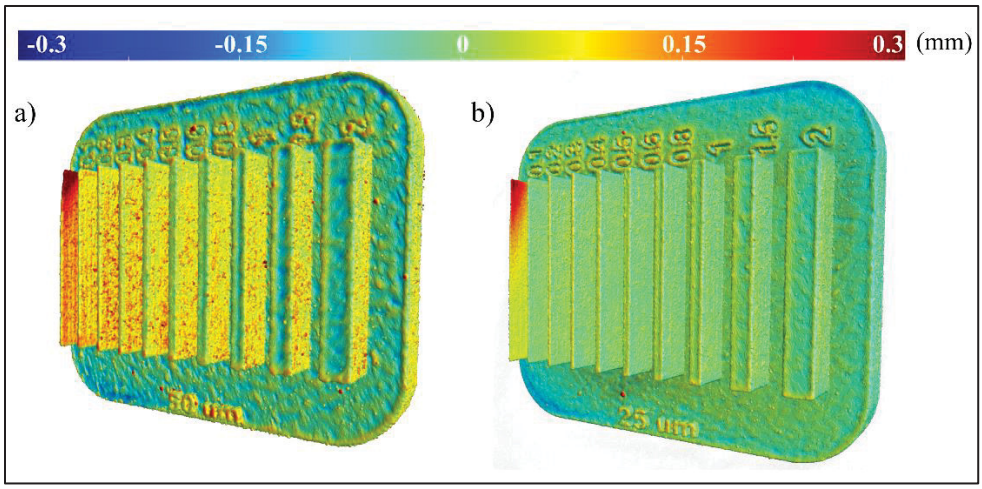

Figure 6-9: 3D visualization of the deviation map compared to the CAD for walls printed with: a) Set I (t = 50 µm), b) Set II (t = 25 µm)

Regarding the lateral faces (90°), significant deviations (> 100 µm) were systematically reported with Set I (Figure 6-9a), suggesting that these surfaces were more prone to attracting a lot of particles surrounding the melt pool. This behavior is attributed to the higher LED brought to the powder bed, which increases the melt pool size and average temperature (A. Wu et al., 2025), decreases the viscosity of molten metal and, finally, promotes the sticking of particles from the powder bed. The lateral faces of the 3D reconstructed volume of the wall artefacts printed using Set II were exempt of sticked particles and had smaller deviations (Figure 6-9b).

Figure 6-10 represent the statistical distribution of the deviations computed inside the map used for 3D rendering. Overall, the distributions obtained for walls and gaps printed with Set II were narrower, with lower standard deviations and a median value centered around 0 mm (Figure 6-10b,d). Conversely, due to the aforementioned reasons regarding the melt pool continuity, the specimens printed with Set I had larger standard deviations and shifted median values (Figure 6-10a,c).

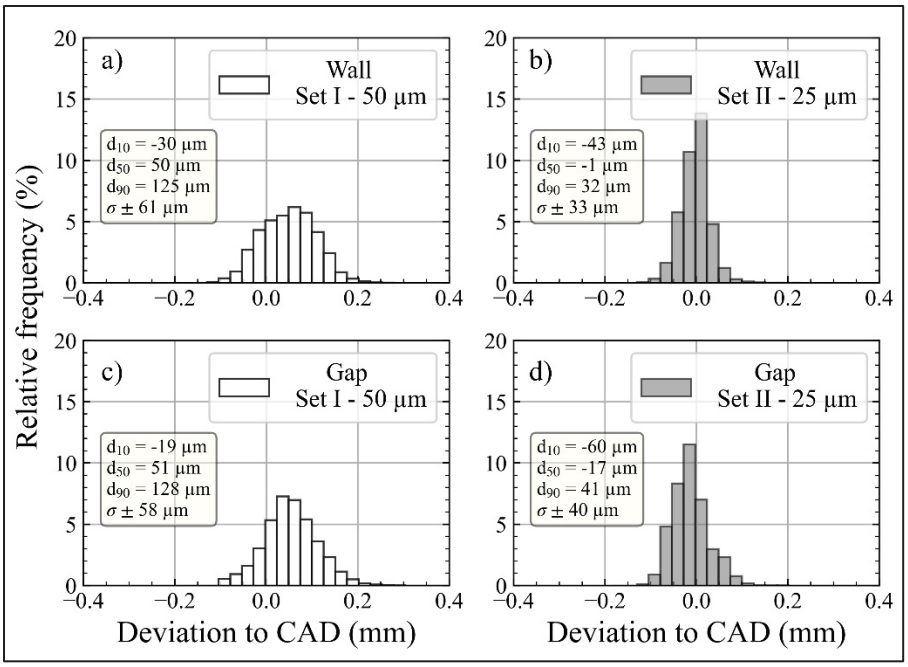

Figure 6-10: 3D Deviation distribution for the geometric artefacts:
a) walls Set I (t = 50 µm), b) walls Set II (t = 25 µm),
c) gaps Set I (t = 50 µm), d) gaps Set II (t = 25 µm)

Conformity of the internal channels

Similarly to the wall and gap artefacts, the pressure drop artefacts printed with both parameter sets were µCT-scanned to assess their geometrical compliance. Due to the channel orientation with respect to the building direction (60°), some stair and down-skin effects were expected. With the CAD registered on the µCT scan, these phenomena were observed in the 2D XZ sections (Figure 6-11a), with the partially collapsed upper edges. Each XZ slice along the length of the artefact (Y axis) was segmented (Figure 6-11b), and the cross-sectional areas of each channel were extracted for comparison with the nominal values.

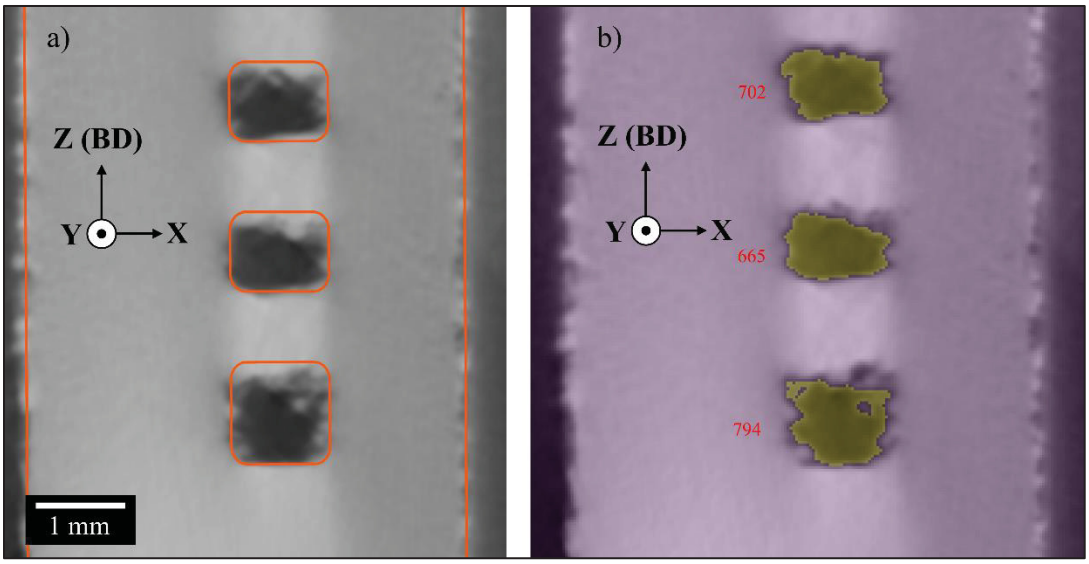

Figure 6-11: a) Overlapping of the µCT scan (Set I) and the CAD mesh (orange line) after registration in the 2D XZ section to highlight the down-skin effect on the upper surface of the channels. b) Segmented 2D XZ slice with the cross-sectional areas measured after segmentation

The results indicate that, regardless of the parameter sets used, the printed cross-sectional areas are much narrower than their CAD-specified values (Figure 6-12a,b). The following deviations were observed for the wider channel (8): $A = 0.77$ mm^2 ($\Delta A \approx 40\%$) for Set I and $A = 0.92$ mm^2 ($\Delta A \approx 29\%$) for Set II. For channels 1 to 7, the considered values correspond to the average of the values measured on each channel. Note that for the specimens printed with Set I, a significant variation was observed between the area values measured on each channel, while for the specimens printed with Set II, the channels were more uniform, and the area values were less dispersed ($\sigma_{A\ Set\ I} \approx 3\sigma_{A\ Set\ II}$). Overall, for Set I, the average area value was $A = 0.62$ mm^2 ($\Delta A \approx 37\%$) and for Set II $A = 0.71$ mm^2 ($\Delta A \approx 28\%$). The difference in dimensions between Channels 1-7 and Channel 8 does not impact the conformity of printed cross-section area values with their nominal equivalents. Indeed, the same shape factor (A_{Exp}/A_{Nom}) was obtained for all the channels: 0.6 for Set I (thicker layers) and 0.7 for Set II (thinner layers). Similarly to the wall/gap artefacts discussed in Section Conformity of walls and gaps, the distributions shown in Figure 6-12c (Set I) and Figure 6-12d (Set II) highlighted a significant difference in geometrical compliance between the parameter sets. Using thinner

layers (t) enabled to improve the geometric compliance, with reduced standard deviation values.

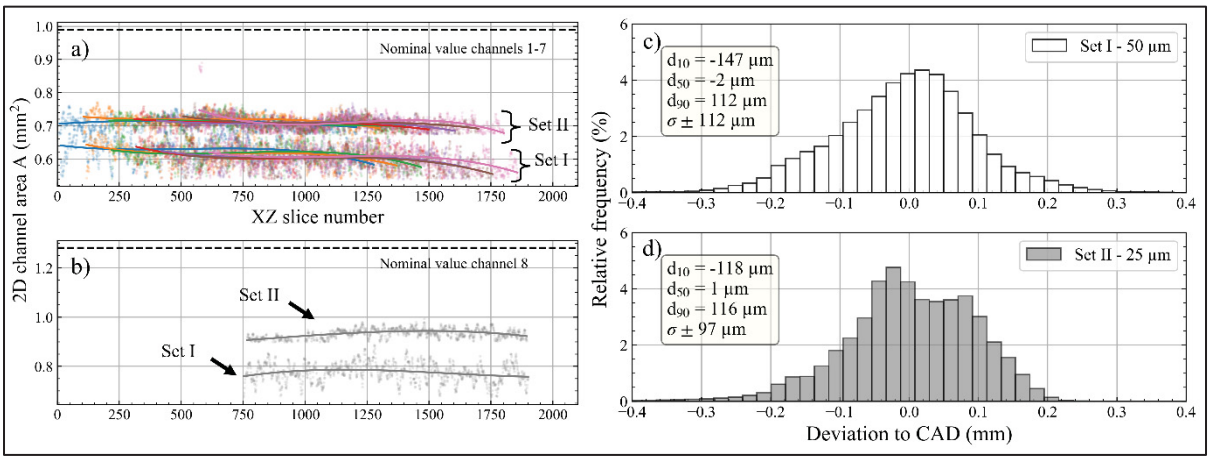

Figure 6-12: Evolution of the cross-section areas along the XZ direction of: a) channels 1 to 7, b) channel 8. Deviation distribution obtained for the pressure drop specimen printed with parameter sets: c) Set I, d) Set II

The geometric compliance analysis conducted on the pressure drop artefacts also highlighted that an excessive roughness obtained for the parameter set with thicker layers (Set I) (see Section Surface roughness) can be detrimental to the printability of such a complex channeled geometry. Indeed, it was observed that the reduced section of this specific channel (8) was partially clogged due to its internal roughness and the particles stuck to its surfaces (Figure 6-13a). In comparison, Figure 6-13b highlights that the same thin section has a greater geometrical compliance to CAD, when the artefact was printed with thinner layers (t = 25 µm, Set II). From the 3D views of the computed deviation maps, the flow passage in the artefact printed with Set I (Figure 6-13c) appears to be considerably more obstructed than for the case of Set II (Figure 6-13c). Overall, as expected, in printing the oriented channels, the largest deviations are systematically located at their upper partially collapsed surfaces.

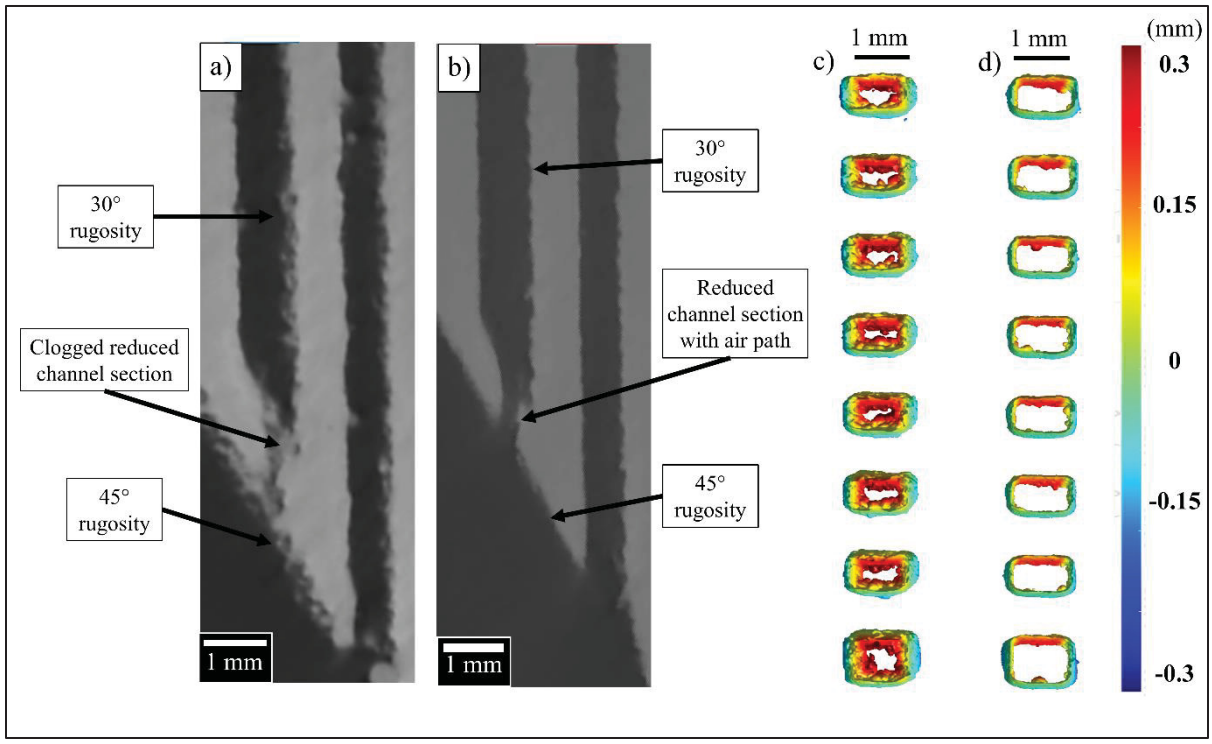

Figure 6-13: 2D slice of the reduced section of the widest channel (n°8) printed with a) Set I (t = 50 µm) and b) Set II (t = 25 µm). The section is partially clogged using the parameter with the higher layer thickness. c) 3D view of one extremity of the deviation map computed for the height channels: c) Set I (t = 50 µm), d) Set II (t = 25 µm)

It is thus evident that kind of internal roughness observed in Figure 6-13, combined with a lack of geometric compliance, must have a negative effect on the air flow inside the channel. The pressure drop tests realized with two channeled artefacts (description of the test conditions is omitted for brevity), manifested a ~30% difference in air flow between them, which is twice the difference in the corresponding cross-sectional areas. When printed with Set II, cross-sections of channel 1 to 7 were 13% wider than those printed with Set I, while the cross-section of channel 8 was 16% wider. Using the Set II enabled to print channels with cross-sections corresponding to ~70% of their nominal (CAD) values.

In can be stated that to obtain a better geometric compliance of such channel-contained parts, they should be printed with the smallest layer thickness t (Set II) available, albeit at the expense of process productivity. Several technical solutions can be considered to further improve the

geometric conformity of such complex parts. Some authors suggest to replace a circular shape of channels by the droplet shape to improve the channel roundness (Kasperovich et al., 2021). The other compensate deviations from the nominal values by adapting the CAD dimensions using the results of μCT analysis of printed parts (Solyaev, Rabinskiy, & Tokmakov, 2019; Baier, Sinico, Witvrouw, Dewulf, & Carmignato, 2023), or optimizing the printing strategy (T. Zhang et al., 2025).

6.1.6 Conclusions

In this study, two parameter sets (Set I and Set II) were applied to print Ti-6Al-2Sn-4Zr-6Mo alloy (Ti6246) specimens. These parameter sets used different layer thicknesses (t = 50 and 25 μm), but identical volumetric energy densities (VED), build rates (BR), and hatching distance/layer thickness ratios (h/t). The as-built characteristics of printed specimens showed that, regardless of the layer thickness, all the specimens were highly dense (> 99.9%), manifested a thin orthorhombic α'' martensite microstructure and close mechanical properties in terms of hardness, resistance and elongation to failure.

The same two parameter sets were then used to print design artefacts containing thin features (walls and gaps) and inclined channels (pressure drop artefacts). A critical difference was observed using the parameter set with thicker layers (Set I – t = 50 μm). This case corresponded to wider melt pools, significant amounts of spatters and partially melted particles stuck to the printed parts, creating a significant roughness and severe deviations from the nominal values (CAD). This parameter set was found unsuitable for printing features smaller than 1 mm in size, especially gaps or channels which were partially or entirely clogged.

Based on the analyses performed, it was concluded that while Set I (t = 50 μm) with thicker layers could reduce the production time, Set II (t = 25 μm) must be preferred for printing parts containing thin features with better geometric compliance and surface finish. Nonetheless, Set II does not provide a complete solution for the common issue of printing channel-contained

parts. To improve the geometric compliance of the latter, additional measures must be taken, including the optimization of these parts design and printing conditions.

6.1.7 Acknowledgments

The authors acknowledge the financial support provided by CRIAQ (Consortium de Recherche et d'Innovation en Aérospatiale au Québec) in the framework of the Exploring Innovation – INNOV-R program, NSERC (Natural Sciences and Engineering Research Council of Canada) and Exonetik Turbo inc.

6.1.8 Authors contributions

Conceptualization, T.M. and V.B.; data curation, T.M. and A.L.; formal analysis, T.M. and A.L.; funding acquisition, V.B.; investigation, T.M. and A.L.; methodology, T.M., A.L. and V.B.; software, T.M. and A.L.; project administration, V.B.; resources, V.B.; supervision, V.B.; validation, V.B.; visualization, T.M., A.L. and V.B.; writing—original draft preparation, T.M. and A.L.; writing—review and editing, V.B.;

6.1.9 Data availability

Data are contained within the article.

6.1.10 Declarations

Conflict of interest: The authors declare no conflicts of interest. The funders had no role in the design of the study**;** in the collection, analyses, or interpretation of data; in the writing of the manuscript; or in the decision to publish the results.

6.2 Effect of heat treatments on the structure and mechanical properties of a laser powder fused Ti-6Al-2Sn-4Zr-6Mo alloy at room and elevated temperatures

Aurore Leclercq[a], Thibault Mouret[b] and Vladimir Brailovski[c]

[a,b,c]Département de Génie mécanique, École de Technologie Supérieure,
1100 Notre-Dame Ouest, Montréal, Québec, Canada H3C 1K3

Article soumis pour publication, septembre 2025

6.2.1 Résumé

Le Ti-6Al-2Sn-4Zr-6Mo (Ti6246) est un alliage de titane de nouvelle génération conçu pour surpasser le très répandu Ti-6Al-4V (Ti64), notamment dans les applications à haute température. Associé aux technologies de fabrication additive (FA), telles que la fusion sur lit de poudre par laser (*Laser Powder Bed Fusion*, LPBF), le Ti6246 offre la possibilité de produire des géométries complexes et d'élargir son champ d'application. Cette étude examine l'influence de différents post-traitements thermiques sur la microstructure et les performances mécaniques de pièces de Ti6246 produites par LPBF. Il a été observé que les échantillons tels que fabriqués présentent une microstructure martensitique orthorhombique α'' ultrafine, conférant une résistance mécanique élevée (limite d'élasticité d'environ 1270 MPa) mais une faible ductilité (~5 % d'allongement). Deux protocoles de traitement thermique ont été appliqués à l'alliage imprimé pour améliorer sa performance : un recuit à basse température à 600 °C, suivi soit a) d'un recuit en dessous de la température de transus (875 °C), soit b) d'un recuit au-dessus de cette température (950 °C). Dans les deux cas, les analyses microstructurales de l'alliage post-traité ont révélé la transformation de la martensite α'' en une microstructure biphasée stable $\alpha + \beta$, avec un grossissement des lamelles α et une ségrégation chimique entre les phases α enrichie en Al et β enrichie en Mo. Les deux traitements ont permis d'améliorer significativement la ductilité à température ambiante (allongement jusqu'à ~14 %), mais au détriment de la résistance mécanique (limite d'élasticité réduite à environ 970 MPa), avec un adoucissement plus prononcé après le recuit supertransus.

À 480 °C, les échantillons post-traités ont conservés un bon compromis résistance-ductilité (567 - 577 MPa et 10 - 12%), mais les échantillons tels que fabriqués ont montrés les résultats les plus performants avec une force de ~958 MPa pour une ductilité de 13%. Les résultats mettent en évidence un compromis entre résistance et ductilité induit par les traitements thermiques, et soulignent la nécessité d'une optimisation supplémentaire pour égaler ou surpasser les performances du Ti6246 élaboré de manière conventionnelle pour les applications à haute température.

6.2.2 Abstract

Ti-6Al-2Sn-4Zr-6Mo (Ti6246) is a new generation titanium alloy designed to outperform the widely used Ti-6Al-4V (Ti64), particularly in high-temperature applications. Combined with additive manufacturing (AM) technologies, such as Laser Powder Bed Fusion (LPBF), Ti6246 offers the potential to produce complex geometries and expand their application range. This study investigates the influence of post-processing heat treatments on the microstructure and mechanical performance of LPBF-processed Ti6246. It is observed that as-built specimens exhibit an ultrafine orthorhombic α'' martensite microstructure, resulting in a high mechanical strength (yield strength ~1270 MPa) but poor ductility (~5% elongation). Two heat-treatment protocols were applied to the printed alloy to improve its applicability: low temperature annealing at 600 °C, followed by either a) subtransus (875 °C) or b) supertransus (950 °C) annealing. In both cases, structural analyses of the heat-treated alloy revealed the transformation of α'' martensite into a stable $\alpha + \beta$ duplex microstructure, with coarsening of α-laths and chemical partitioning between Al-rich α and Mo-rich β phases. Both treatments significantly enhanced the room temperature ductility (elongation up to ~14%) but reduced the strength (yield strength down to ~970 MPa), with more pronounced softening after the supertransus annealing. At 480 °C, the post-treated samples maintained a good strength-ductility balance (567-577 MPa and 10-12%), but the as-built samples showed the best performance, with a strength of ~958 MPa and a ductility of 13%. The results underscore a trade-off between strength and ductility induced by heat treatments and highlight the need for

further optimization to match or exceed the performance of conventionally processed Ti6246 for elevated temperature applications.

Keywords: Additive manufacturing; Laser Powder Bed Fusion; Post-processing Heat Treatment; Microstructure and Mechanical Properties; Elevated temperature testing

6.2.3 Introduction

Titanium alloys possess specific properties such has a high strength-to-weight ratio, excellent corrosion resistance and biocompatibility, which make them attractive for major industries (aerospace, automotive, biomedical, etc.). In solid state, titanium alloys can form α (hexagonal close-packed (HCP)), β (body centered cubic (BCC)) or duplex $\alpha + \beta$ crystallographic phases and are generally grouped according to these allotropic forms. Alloying elements in these alloys act as either α (e.g., Al, N, O, Zr) or β (e.g., Fe, V, Mo, Nb) stabilizers and their contents are generally adjusted to satisfy specific manufacturing and application requirements. The most used titanium alloy is $\alpha + \beta$ Ti-6Al-4V (Ti64), which was initially developed for the aerospace industry. The use of this alloy is however limited to applications where service temperatures do not exceed 315 °C, above which Ti64 starts to be outperformed by other titanium alloys, such as Ti-5.72Al-3.97Sn-3.82Zr-0.69Nb-0.57Mo-0.36Si (Ti834) and Ti-6Al-2Sn-4Zr-6Mo (Ti6246), among others. The latter normally retains its higher mechanical characteristics up to 540 °C, and this advantage, while being slightly offset by a higher mass density, makes Ti6246 promising for such applications as hot sections of gas turbines, for example (J. R. Davis & ASM International, 1998).

Gas turbine applications often require complex and customizable components produced in small series, the areas where additive manufacturing (AM) processes are particularly performant. These processes are generally based on the layer-by-layer forming principle and are preferred for small production lots of complex and multifunctional components with intricate geometries that must be reproduced with great accuracy. Among AM processes, laser powder bed fusion (LPBF), which uses fine powder feedstocks (20-50 μm), is considered

particularly suitable for producing small to medium-sized parts with print resolutions as fine as 0.1-0.2 mm. These results are generally achieved at a lower cost than in concurrent metal AM technologies, such as electron beam powder bed fusion (EB-PBF) or directed energy deposition (DED).

LPBF Ti6246 alloys have recently been widely studied (Aversa et al., 2025; Alessandro Carrozza et al., 2021; Cobbinah et al., 2024) and the dependence of their mechanical properties on as-printed microstructures was revealed. It has been observed that under the rapid cooling conditions inherent to the process, this alloy forms an orthorhombic α″ martensite phase (Alessandro Carrozza et al., 2021; Hassanin et al., 2023; Peng et al., 2023; Pirro et al., 2025). The presence of a metastable martensitic phase makes the as-built Ti6246 unsuitable for structural applications and requires the use of post-treatments. In contrast to LPBF Ti64, for which post-treatment strategies have been extensively developed through decades of research and application (Zou, Simonelli, Katrib, Dimitrakis, & Hague, 2021), only a limited number of studies have addressed the post-treatments of LPBF-produced Ti6246 alloys. To bridge this gap, (Alessandro Carrozza et al., 2022) focused their study on the effects of the annealing temperature on the microstructure, microhardness and tensile properties of this material. By applying subtransus (875 °C) and supertransus (950 °C) heat treatments, they found that the former leads to a bi-lamellar microstructure (columnar prior-β and primary α grains combined with secondary α needles in β grains), while the latter forms an equiaxed duplex $\alpha + \beta$ microstructure in the material. Both structures produce an excellent combination of room temperature mechanical properties: a yield strength of ~1000 MPa and an elongation to failure of 17-20%.

While the effects of these post-treatments on the room temperature mechanical properties of LPBF processed Ti6246 alloys have already been made public, their impacts on the mechanical properties of these alloys at elevated temperatures, where their application is the most appealing, are yet to be addressed in the literature. The present work aims to contribute to ongoing research efforts and to the understanding of the effects of post-treatments on the

structural characteristics and mechanical properties of Ti6246 at both room and elevated temperatures.

6.2.4 Material and methods

6.2.4.1 Plan of experiments

The Ti-6Al-2Sn4Zr-6Mo powder used in this study is a gas-atomized pre-alloyed powder provided by Eckart TLS GmbH (Bitterfeld-Wolfen, Germany). The D10 = 26, D50 = 43 and D90 = 64 (µm) particle size distribution (PSD) was measured using the water module of an LS13 320 XR (Beckman Coulter, Brea, CA, USA) particle size analyzer (Figure 6-14a). Then, the particle size and morphology distributions were attested using a TM3000 scanning electron microscope, SEM (Hitachi, Tokyo, Japan) (Figure 6-14b).

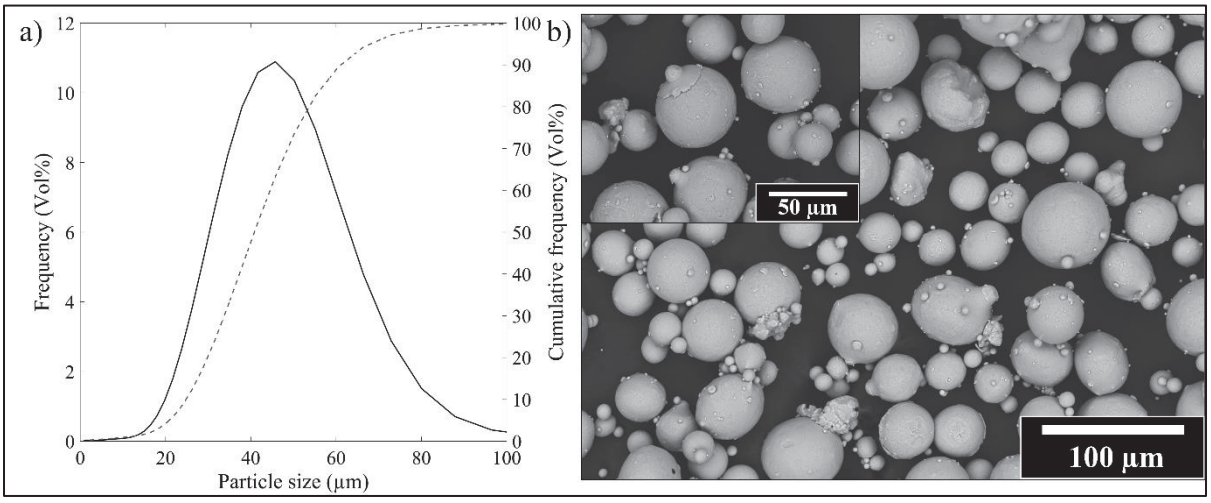

Figure 6-14: Ti6246 powder a) Particle size distribution and b) SEM observations

Ten cylindrical (10 mm diameter, 21 mm high) and eighteen prismatic (17 x 8 x 81 mm^3) specimens were printed using the following set of printing parameters: laser power P = 139 W, scanning speed v = 741 mm/s, hatching distance h = 75 µm and layer thickness t = 25 µm, obtained in a previous study on the LPBF printability of Ti6246 alloys (Mouret, Leclercq, Dubois, & Brailovski, 2025). The printing was carried out on a Ti-6Al-4V baseplate without

preheating using a TruPrint 1000 system (TRUMPF GmbH, Ditzingen, Germany). All the specimens were oriented along the build direction and contained 5 mm thick non-solid supports. They were removed from the plate using a chisel and divided into three groups, each containing three cylindrical and six prismatic specimens. The first group of specimens was kept in the as-built (AB) condition, while the two others were subjected to two heat treatment sequences under vacuum (10^{-6} hPa) atmosphere using a WEBB 120 furnace (R.D. WEBB COMPANY INC., Rhode Island, U.S.A).

These heat treatment sequences included a low-temperature annealing at 600 °C (S600) followed by either subtransus annealing at 875 °C (P875) or supertransus annealing at 950 °C (P950), as illustrated in Figure 6-15. For each of these treatments, the heating and cooling rates were respectively set to 5 and 2 °C/min, and the treatment duration, to 2h. S600 annealing allowed safe handling of the specimens. Preliminary experiments showed that the as-printed specimens were too fragile and prone to distortions, which complicated their removal from the building plate and subsequent machining. This phenomenon was attributed to an extreme finesse of the as-built microstructure (see the Results section), which contributed to a high level of residual stresses and significant fragility of printed specimens. This distinctive feature stemmed from the fact that, contrary to most studies covering LPBF of Ti6246 alloys, the building plate was not preheated in the present study, which increased both the thermal gradients and cooling speeds, thus significantly refining the as-built microstructure.

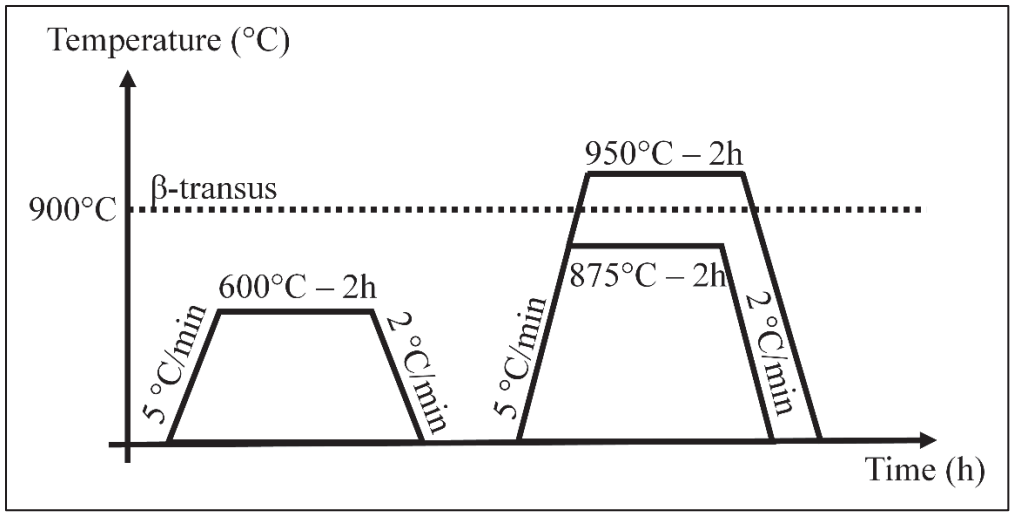

Figure 6-15: Two post-treatment sequences involving low-temperature annealing at 600 °C (S600) followed by two annealing conditions: subtransus 875 °C (P-875) and supertansus 950 °C (P-950); all heat treatments lasted 2h, with heating and cooling rates of 5 and 2 °C/min, respectively

To validate the selection of these heat treatment conditions, one as-built sample was subjected to a DSC analysis in the 25 to 1025 °C temperature range (heating rate of 5 K/min) using a NETZSCH DSC 404F3 (NETZSCH Gmbh, Germany). One clear exothermic peak can be distinguished in the 700-900 °C temperature range of the DSC graph (Figure 6-16), and can be attributed to stress-relaxation (Alessandro Carrozza et al., 2022). In fact, because of the high cooling speed inherent to the LPBF process, as-printed samples generally contain orthorhombic α″ martensite. Thus, before this exothermic peak, in the 200 - 700 °C temperature range, the transformation that occurs corresponds most likely to the decomposition of α'' martensite into a mixture of stable $\alpha + \beta$ phases. Therefore, low-temperature annealing (S600) corresponds to the advanced α'' phase decomposition. Finally, an absolute minimum on the DSC curve at 900 ± 15 °C corresponds to the β-transus temperature.

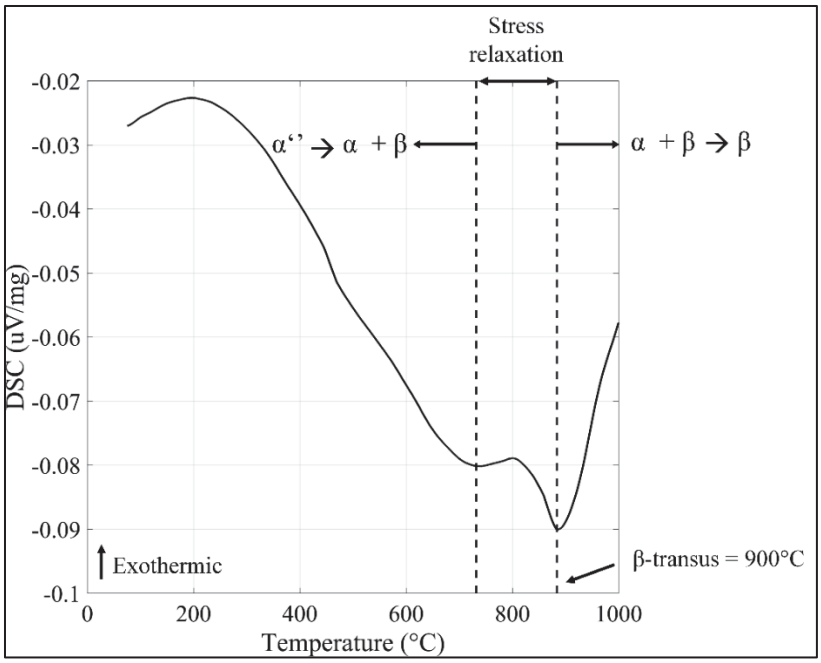

Figure 6-16: DSC graph of the as-built sample;
the dashed lines highlight the endothermic peaks

After the heat treatment, the cylindrical specimens were partitioned to obtain samples for structural analyses and microhardness measurements (Figure 6-17a), while the prismatic specimens were machined to obtain tensile testing samples (Figure 6-17b).

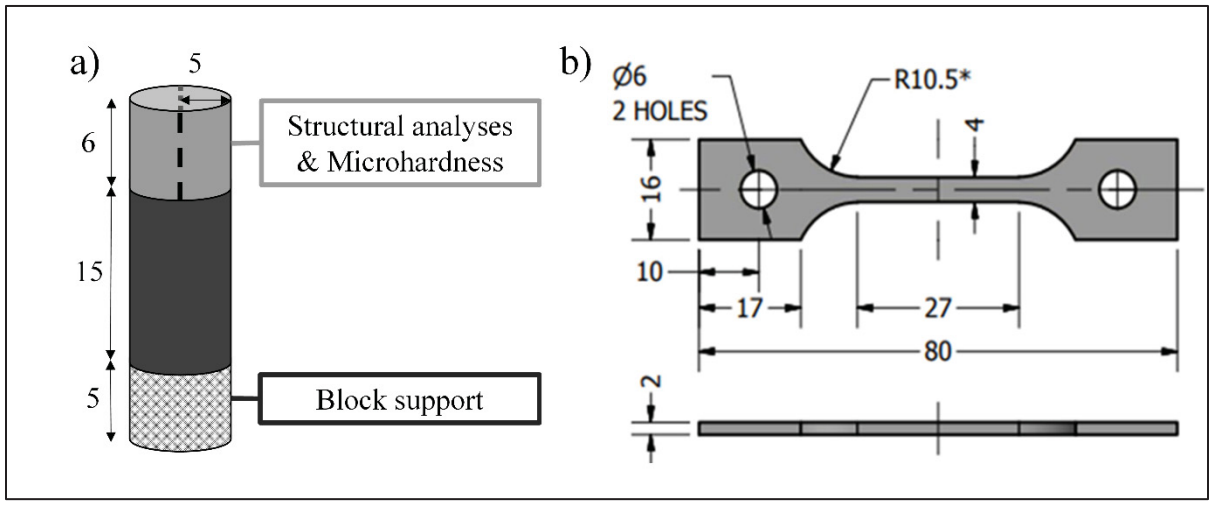

Figure 6-17: Schematic representation of the a) cylindrical specimen divided into samples used for various analyses and b) tensile testing sample; all dimensions are in mm

6.2.4.2 Microstructure and phase analyses

The Y-Z cross-sections of distant parts of the cylindrical specimens (Figure 6-17a) were analyzed using an X'Pert^3 X-Ray diffractometer (Malvern Panalytical Ltd, Malvern, UK), equipped with a cobalt source (K_α Co = 1.79026 Å). Acquisitions were made in the Bragg Brentano configuration, with a step size of 0.017° and an 2θ range between 38 and 50° (this reduced 2θ range encompasses the main reflections of each possible phase in this material, i.e., α'', α', α and β). Then, the samples were mounted in carbon-dopped resin, mirror-polished and etched (2 min) with Kroll reagent (%vol: 2:5:93 $HF/HNO_3/H_2O$). Firstly, low-resolution observations (x20) were carried out using a LEXT OLS4100 (Lext Olympus Corp., Japan) confocal microscope. Then, higher magnification (x1k, x5k and x30k) images were captured using a secondary electron detector (acceleration voltage 10 kV, magnification 30k) of an SU-8230 Field Emission STEM (Hitachi, Tokyo, Japan). Finally, energy dispersive spectroscopy (EDS) analyses were performed using the SU-8230 STEM to detect the potential occurrence of chemical segregation. A certified reference material for Ti-6Al-4V grade titanium alloy (BS T-5A, Brammer Standard Company, Inc., Houston, TX, USA) was used to quantify the elements.

6.2.4.3 Mechanical testing

Microhardness measurements were performed on the etched Y-Z cross-sections of all the cylindrical samples using a Struers Duramin-40 M1 (Struers, Ballerup, Denmark) microhardness tester. For each sample, 10 measurements were realized in the middle of the surface with an applied force of 300 gF and a dwell time of 15 s. Next, six coupons of each group were subjected to tensile testing using an MTS 810 load frame (MTS, Eden Prairie, MN, USA), with the force measured by a 100 kN MTS load cell and displacement measured by an LVDT: three tests at room temperature (RT) and three at 480 °C (ET, for elevated temperature testing). This testing temperature was situated between the upper limits of the Ti64 and Ti6246 temperature application ranges, i.e., between 315 and 540 °C, respectively. The strain rate was set to 0.405 mm/min (RT) and 0.135 mm/min (ET), as per ASTM E8-24 and ASTM E21 standards (E28 Committee, 2020, 2024). Elevated temperature testing was performed under a

constant argon flow of 27.5 ft^3/h in an infrared (IR) furnace. The heating rate was set to 10 °C/min and a 3-min prior-to-testing dwell time was applied after reaching the target temperature. Finally, strain-stress diagrams were plotted to obtain the following metrics of interest: the Ultimate Tensile Strength (UTS, MPa), defined as the maximum stress reached during the test, the Yield Strength (YS, MPa), calculated by moving the $\sigma - \varepsilon$ slope from the origin to 0.2% of strain, and the elongation to failure (δ, %).

6.2.5 Results and Discussion

6.2.5.1 Physical and structural analyses

The X-ray diffractograms obtained for each post-treated sample are plotted in Figure 6-18 alongside those of the powder feedstock and the as-built sample. It can be observed that while the powder and the as-built sample exhibit orthorhombic α'' martensite, low-temperature annealing (S600) and both high-temperature annealing conditions (P875 and P950) lead to its decomposition into stable α (hcp) and β (bcc) phases of titanium. These observations are in agreement with the rapid cooling conditions taking place during both the powder manufacturing and 3D printing stages, leading to the formation of martensite, and its subsequent decomposition into a stable $\alpha + \beta$ phase mixture during the heat treatments.

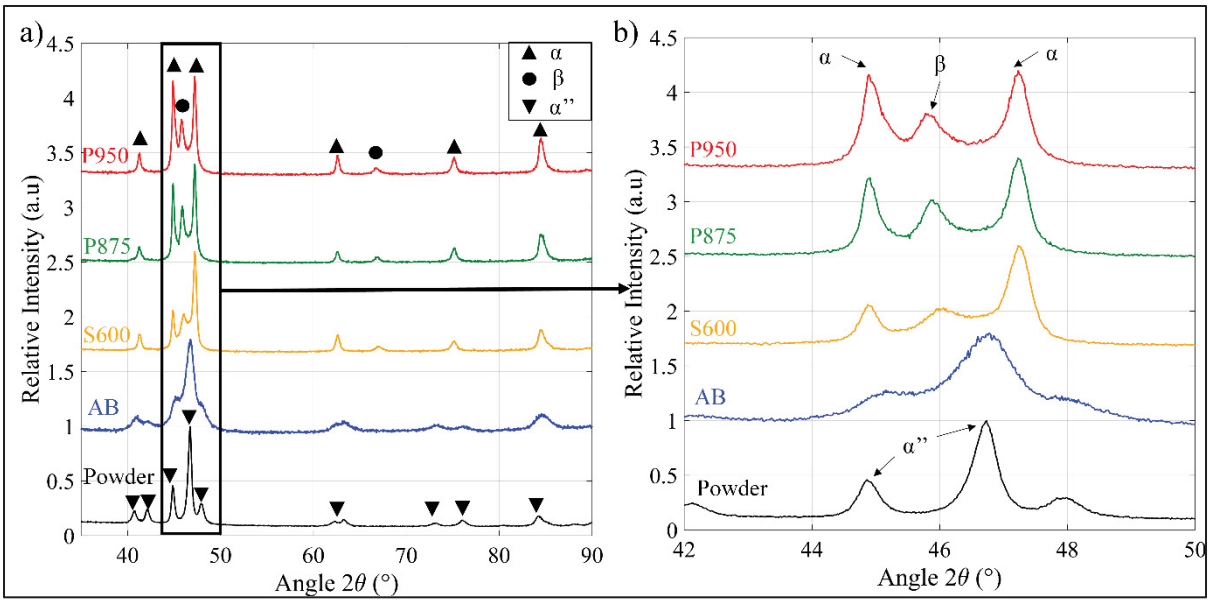

Figure 6-18: XRD diffractograms for different Ti6226 states including powder, as-built and heat-treated samples (S600, P875 and P950): a) 35-90° 2θ range and b) zoom in the 42-50° 2θ range

Figure 6-19 presents microstructures related to the as-built, S600, P875 and P950 post-treated states. As expected, the as-built microstructure contains very thin (49±17 nm) α'' needles within columnar prior-β grains (barely visible after etching) commonly observed after the LPBF process. The melt pool borders are also visible (Figure 6-19a). After low-temperature annealing (S600), samples turn brown when in contact with the etching solution, revealing columnar prior-β grains (Figure 6-19b) in which 57±26 nm-width α lamellae can be observed using higher resolution images (Figure 6-19j). After P875 annealing, coarser (828 ± 240 nm) α lamellae surrounded by a thin β-layer are encountered. The α lamellae mostly share the same crystallographic orientations, forming colonies within the columnar prior-β grains formed during printing. Following P950 annealing, the α lamellae and surrounding β-layer become even coarser (2495±1121 nm) than after P875 annealing. Although less pronounced, the columnar grain aspect persists, meaning that the formation of an $\alpha + \beta$ mixture with secondary β grains is not completed.

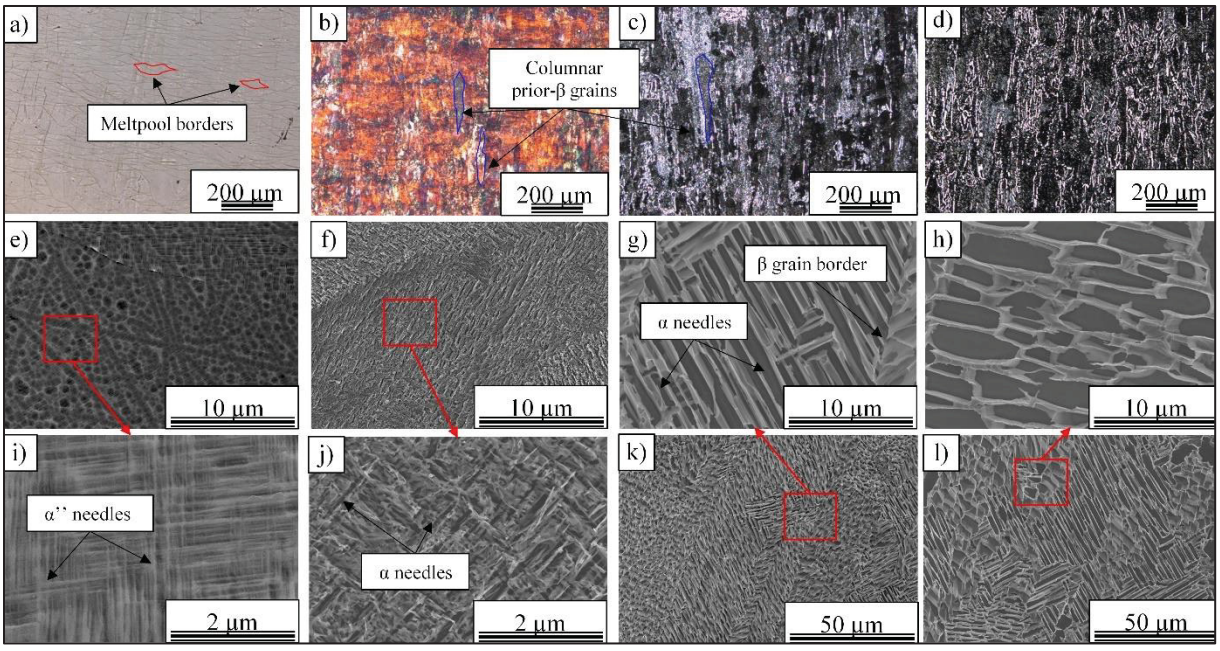

Figure 6-19: Observations with confocal microscope (a-d) and SEM (e-l) of: (a, e, i) as-built sample with orthorhombic α'' martensite; (b, f, j) samples after 600 °C annealing showing the beginning of $\alpha'' \rightarrow \alpha + \beta$ decomposition; (c, g, k) and (d, h, l) P875 and P950 annealed samples, respectively, with duplex $\alpha + \beta$ phase

Because of the very fine microstructure features, the as-built and S600 samples could not be subjected to EDS analysis, whereas it was possible with the P875 and P950 samples. In both latter samples, elemental maps revealed some Ti- and Al-rich zones in the dark areas, and Mo- and Zr-rich zones, in the light areas (Figure 6-20). Points measurements (Tableau 6-3) confirmed significant differences in the elemental concentrations between dark and light areas. Given that Ti and Al are α-stabilizers while Mo is β-stabilizer, light areas can be identified as belonging to β phase, while dark areas, where the opposite phenomenon is observed, can be identified as α phase (Alluaibi et al., 2024; Peng et al., 2023). Sn was homogeneously distributed in both phases and some very light features were randomly observed at the α/β grains boundaries as depicted in Figure 6-20d,h, which were associated with the Sn precipitates (Figure 6-21).

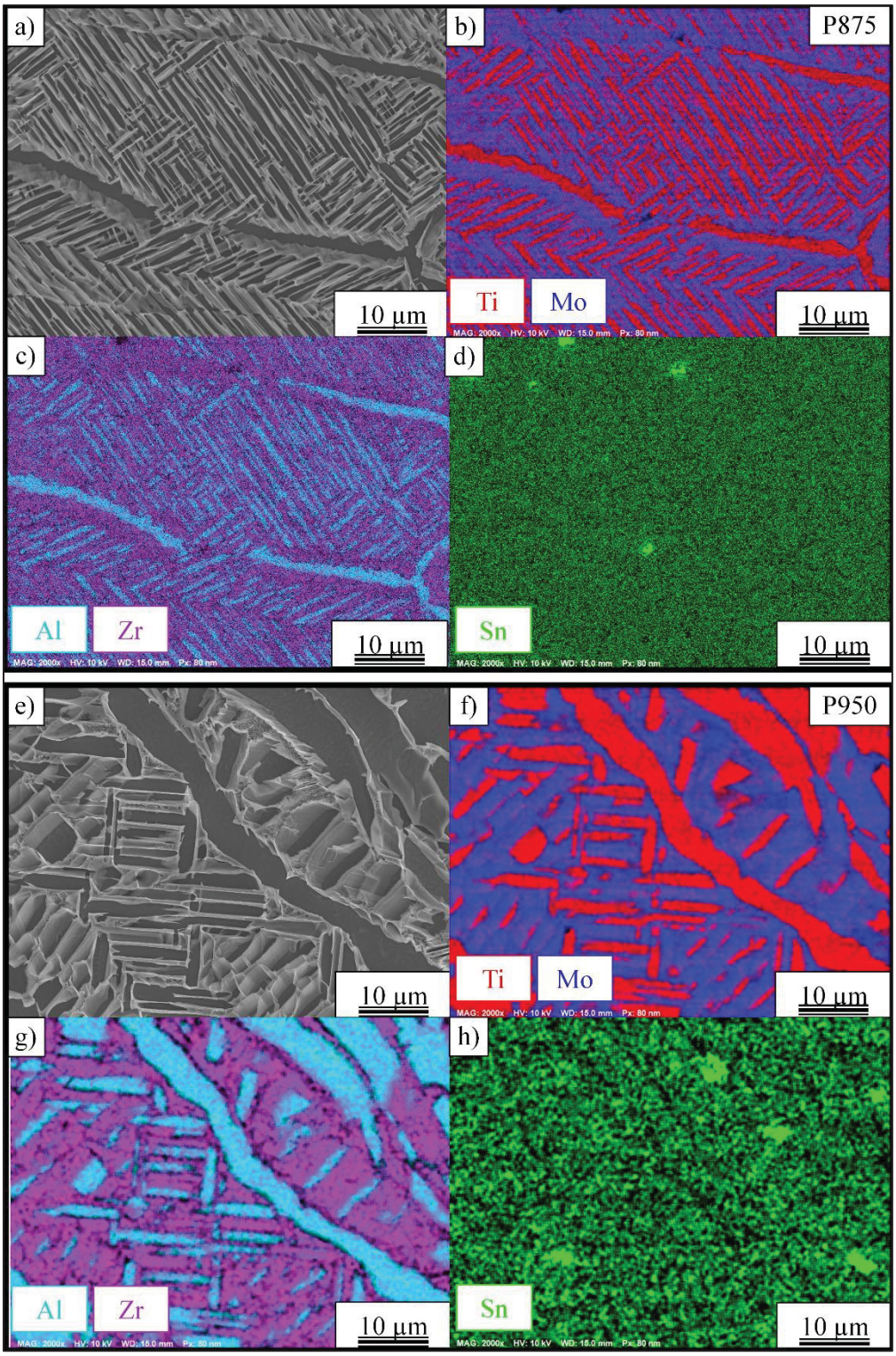

Figure 6-20: SEM observations and EDS maps:
(a,b,c,d) P875 sample and (e,f,g,h) P950 sample

Tableau 6-3: Elemental concentration (wt% normalized according to the certified reference material) obtained by the EDS points measurements in dark and light areas on samples after P875 and P950

Sample	Region	C (wt%)	O (wt%)	Al (wt%)	Ti (wt%)	Zr (wt%)	Mo (wt%)	Sn (wt%)
P875	Dark	0.0	0.7 ± 0.0	7.1 ± 0.0	91.0 ± 0.1	0.2 ± 0.0	0.1 ± 0.0	0.9 ± 0.1
	Light	0.0	1.0 ± 0.1	4.2 ± 0.3	91.6 ± 0.4	0.3 ± 0.0	1.9 ± 0.2	1.0 ± 0.3
P950	Dark	0.0	0.6 ± 0.1	6.8 ± 0.5	91.3 ± 0.5	0.2 ± 0.0	0.1 ± 0.0	0.9 ± 0.1
	Light	0.0	1.0 ± 0.1	4.2 ± 0.0	92.0 ± 0.4	0.3 ± 0.0	1.9 ± 0.0	0.5 ± 0.0

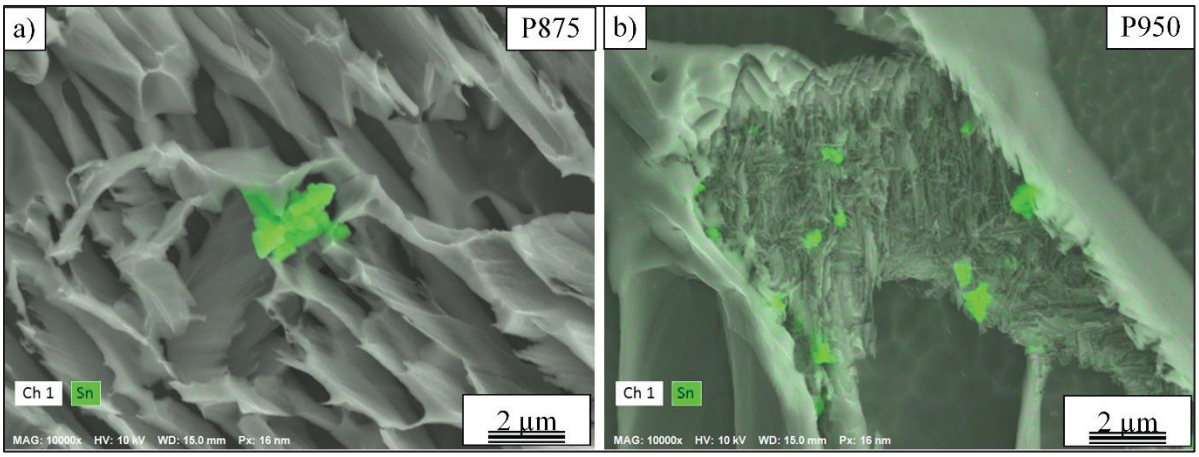

Figure 6-21: Superposition of the SEM observations and the EDS Sn map showing Sn precipitates in the a) P875 and b) P950 samples

6.2.5.2 Mechanical characterization

Microhardness measurements performed on the Y-Z sample cross-sections revealed that S600 led to a slight increase in hardness (528 ± 30 HV0.3 after S600 versus 514 ± 19 HV0.3 in the as-built state) while P875 and P950 caused a significant hardness decrease (down to 397 ± 32 HV0.3 for the former and 365 ± 20 HV0.3 for the latter). These microhardness variations can be related to the described microstructural changes, since it has been established

(Alessandro Carrozza et al., 2022; Peng et al., 2023; Pirro et al., 2025) that decomposing α'' martensite into duplex $\alpha + \beta$ phase increases the material hardness, whereas coarsening α-laths decreases it.

Typical tensile stress-strain curves of the as-built and post-treated samples are compared in Figure 6-22a (20 ºC) and in Figure 6-22b (480 ºC). At room temperature, the as-built samples manifested a relatively fragile behavior with an elongation to failure of ~5%, while the heat-treated samples showed much more ductile behavior, with a strain to failure reaching 13-14%, but this gain was obtained at the expense of a lower yield strength: 967 MPa (P875) and 972 MPa (P950) versus 1270 MPa (AB) (Tableau 6-4)).

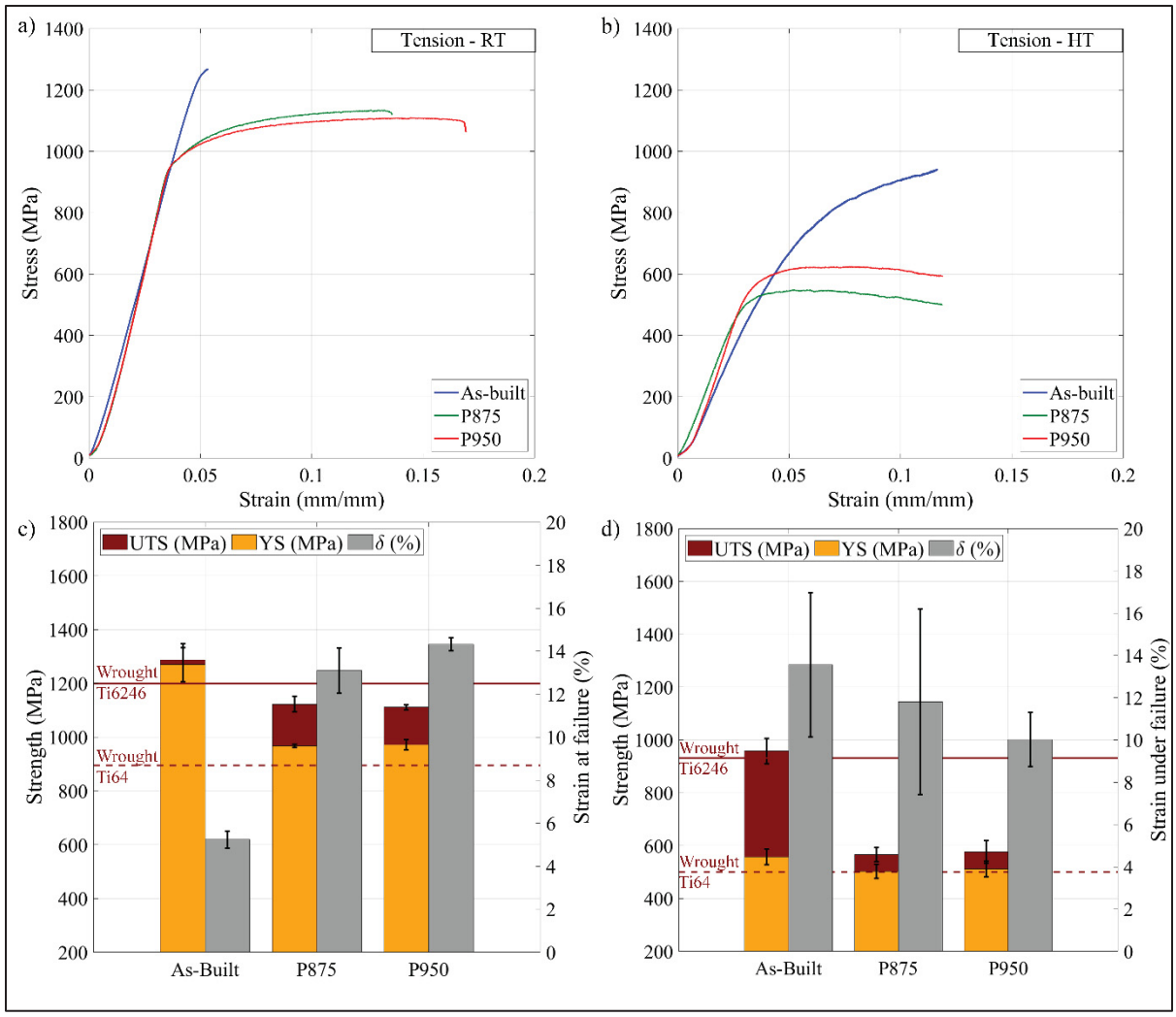

Figure 6-22: Representative tension stress-strain diagrams of the as-built and post-treated samples at: a) 20 °C and b) 480 °C; mechanical properties of the as-built and post-treated samples at c) room temperature and d) elevated temperature. The UTS values obtained for wrought Ti6246 and Ti64 alloys J. R. Davis & ASM International (1998, p. 587) are given as target values

Tableau 6-4: Mechanical properties of the as-built and post-treated samples at room and elevated temperatures

Protocol	Temperature	YS at offset = 0.2% (MPa)	UTS (MPa)	Elongation at failure (%)
As-built	20 °C	1270 ± 64	1287 ± 60	5.2 ± 0.4
	480 °C	558 ± 29	958 ± 48	13.6 ± 3.4
P875	20 °C	967 ± 6	1123 ± 29	13.1 ± 1.1
	480 °C	502 ± 27	567 ± 26	11.8 ± 4.4
P950	20 °C	972 ± 19	1111 ± 9	14.3 ± 0.3
	480 °C	512 ± 27	577 ± 26	10.0 ± 1.3

Note that the orthorhombic α'' martensite formed in the present study had a significantly higher yield strength (YS) than seen in a previous study (Alessandro Carrozza et al., 2021): 1270 MPa in the former as compared to 480 MPa in the latter. This difference is attributed to the one-order-of-magnitude finer α'' martensite microstructure in the present study as compared to the reference study (Alessandro Carrozza et al., 2021): 50-70 nm wide α'' laths in the former as compared to 550-700 nm wide α'' laths in the latter. Similar observations have been made for the LPBF-processed Ti64 alloys (Bartolomeu et al., 2022), where it was shown that the presence of very fine α' martensite needles formed in the as-built samples increased the room-temperature strength at the expense of a lower ductility.

Furthermore, the annealing post-treatment realized in the present work led to an increase in the room-temperature ductility and a decrease in strength, with YS ranging between 1000 and 1050 MPa and d ranging between 15 and 20%. Similar mechanical properties were observed previously by other authors after different post-treatment strategies, including annealing at 875 and 950 °C (Alessandro Carrozza et al., 2022). These changes were related to the decomposition of metastable α'' martensite into a stable duplex $\alpha + \beta$ phase and microstructure coarsening, where the higher the annealing temperature, the larger the α-lath and β-grain sizes.

The elevated-temperature testing carried out in the present study showed that, contrary to room temperature testing, P950 samples showed higher strength but lower ductility than their P875 counterparts, which can be attributed to microstructure coarsening (J. Zhao, Wang, Lv, & Liu, 2022). Note also that for RT applications, the heat-treated alloy of this study showed a more appealing strength-ductility combination than did its as-built counterpart (Figure 6-22c). For elevated temperature applications however, the as-built alloy largely outperformed its heat-treated counterparts (Figure 6-22d): it is similarly ductile (~14%), but significantly more resistant (~960 vs ~580 MPa). This observation leads to the conclusion that more work is needed to maximize the mechanical properties of LPBF Ti6246 alloys for both low and high temperature applications. Unfortunately, among the few studies that have examined the high-temperature mechanical properties of LPBF-processed titanium alloys, none has yet targeted Ti6246 alloys.

Finally, the LPBF Ti6246 alloy of the present study is more mechanically resistant in the 20 - 480°C temperature range than the wrought Ti64, but lower than the wrought Ti6246 (Figure 6-22c). To make this alloy competitive with its conventionally produced equivalents, new post-treatment strategies must be explored. Let us take for example the work of (Pirro et al., 2025), where a bi-lamellar structure composed of large primary α and ultrafine secondary α laths combined with Ti_3Al precipitates resulting from subtransus annealing at 825°C followed by ageing at 500 °C for 24h enabled to reach UTS = 1500 MPa and δ = 15% (room temperature testing). Pending verifications of whether these outstanding properties can be transposed to elevated temperatures, such a combined post-treatment appears to be a new avenue to explore.

6.2.6 Conclusion

In this study, two post-treatment protocols were applied to LPBF-processed Ti-6Al-2Sn-4Zr-6Mo alloy, and their effects on the structure and mechanical properties of the alloy were studied. Both protocols allowed the decomposition of α'' martensite initially present in the as-built samples, and α (enriched in Al) and β (enriched in Mo) grains were obtained.

Tin precipitates were also observed at the grain boundaries. Mechanical testing revealed that the increase in the α-lath width obtained after two post-treatments led to a significant decrease in microhardness and a significant increase in ductility at the expense of a lower mechanical strength at both room and elevated temperatures.

6.2.7 Acknowledgments

The authors acknowledge the financial support provided by CRIAQ (Consortium de Recherche et d'Innovation en Aérospatiale au Québec) in the framework of the Exploring Innovation – INNOVR program, NSERC (Natural Sciences and Engineering Research Council of Canada) and Exonetik Turbo inc. The authors also acknowledge the contributions of Emma Bisserié in preparing the samples used in the present work.

CHAPITRE 7

ÉTUDE PRÉLIMINAIRE SUR L'EFFET DES PARAMÈTRES D'IMPRESSION SUR L'IMPRIMABILITÉ DE L'INTERMÉTALLIQUE À BASE D'ALUMINURES DE TITANE TI-22AL-25NB PRODUIT PAR FUSION LASER SUR LIT DE POUDRE

Dans l'assemblage du rotor de l'ICT, le remplacement du superalliage à base de nickel utilisé pour le moyeu par un intermétallique à base d'aluminures de titane orthorhombique pourrait permettre un gain de masse significatif sans compromettre les performances, notamment à des températures élevées. À ce sujet, le Ti-22Al-25Nb (Ti2225) a été considéré pour ses propriétés physiques et mécaniques intéressantes, sa résistance à l'oxydation et sa compatibilité avec le procédé de fusion laser sur lit de poudre (Illarionov et al., 2023; Liao et al., 2025). Cependant, si des études ont révélé la capacité à produire des pièces saines, de haute densité et aux propriétés mécaniques prometteuses en utilisant des plateformes de fabrications préchauffée (170 à 1080 °C, (Q. Chen et al., 2023; Xiuxuan Yang et al., 2021)) ou des équipements à grande capacité (2 lasers de 400 et 1000 W (Polozov et al., 2019)), l'impression de cet alliage sans préchauffage et sur une machine à capacité réduite demeure inexplorée. Pour pallier ce manque d'information, cette étude propose d'appréhender les effets de différents paramètres du procédé sur les propriétés physiques de pièces imprimées en Ti2225 sans préchauffage et sur une machine disposant d'une puissance limitée à 200 W. Il s'agit de reprendre une démarche similaire à celle utilisée pour le développement de l'alliage de Ti6246, à commencer par la production et l'analyse de traces de passe unique de laser sur une large gamme de paramètres avant de passer à la production d'échantillons cylindriques pour des analyses structurales.

La matière première utilisée est une poudre sphérique pré-alliée atomisée au gaz de Ti-22Al-25Nb fournie par Guangzhou Sailong Additive Manufacturing Co., Ltd (Guangdong, Chine). D'après les données constructeur, la poudre ne contient qu'un faible taux d'impuretés (O = 0.08, H = 0.0007 et N < 0.003 wt%). Sa distribution granulométrique mesurée à l'aide du module à eau d'un analyseur de taille de particules LS13 320 XR (Beckman Coulter, Brea, CA, États-Unis) est D10 = 24 µm, D50 = 39 µm et D90 = 57 µm (Figure 7-1a). La taille et la

morphologie des particules ont été confirmées par microscope électronique à balayage (MEB) TM3000 (Hitachi, Tokyo, Japon) (Figure 7-1b).

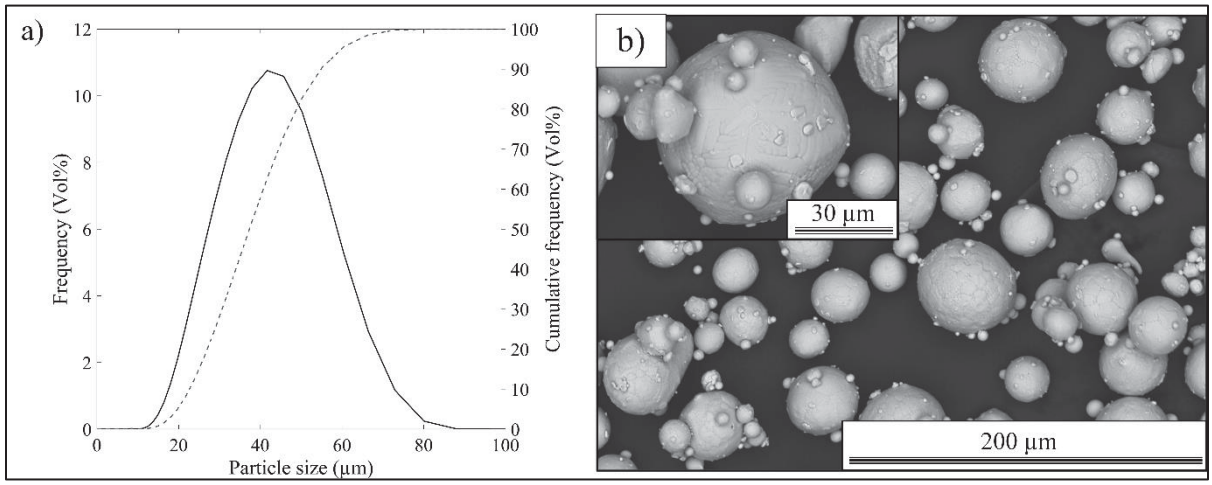

Figure 7-1 : Poudre de Ti2225 : a) Distribution de taille des particules et b) Observation au MEB

7.1 Traces de passe unique de laser

Dans un premier temps, 63 traces de laser de 4.5 mm de long espacées de 1 mm ont été produites sur des échantillons rectangulaires de 10x15x15 (mm^3) (Figure 7-2ab), à l'aide de la TruPrint 1000 (TRUMPF GmbH, Ditzingen, Germany), en utilisant une plaque de fabrication en alliage de titane Ti-6Al-4V sans préchauffage avec une épaisseur de couche fixée à $t = 25$ µm. Ces traces de passe unique de laser, ayant pour but d'apprécier la qualité de la fusion sur une large gamme de paramètres d'impression (Tableau 7-1). Ces derniers sont obtenus selon en utilisant 9 ensembles de paramètres d'impression (A, B, C, D, E, F, G, H, I), définis dans le plan VED (7.1)-BR (7.2) et déclinés selon 7 écarts vecteur h, augmentant graduellement entre $h = 25$ et 175 µm (Figure 7-2c). Pour faciliter la lecture, chaque échantillon sera nommé selon l'ensemble de paramètres auquel il appartient et la valeur de l'écart vecteur correspondant. Par exemple, l'échantillon E-150 correspond à l'échantillon produit avec l'ensemble de paramètres E et un écart vecteur de 150 µm.

$$VED\ [\mathrm{J/mm^3}] = \frac{P}{vht} \tag{7.1}$$

$$BR\ [\mathrm{cm^3/h}] = vht \tag{7.2}$$

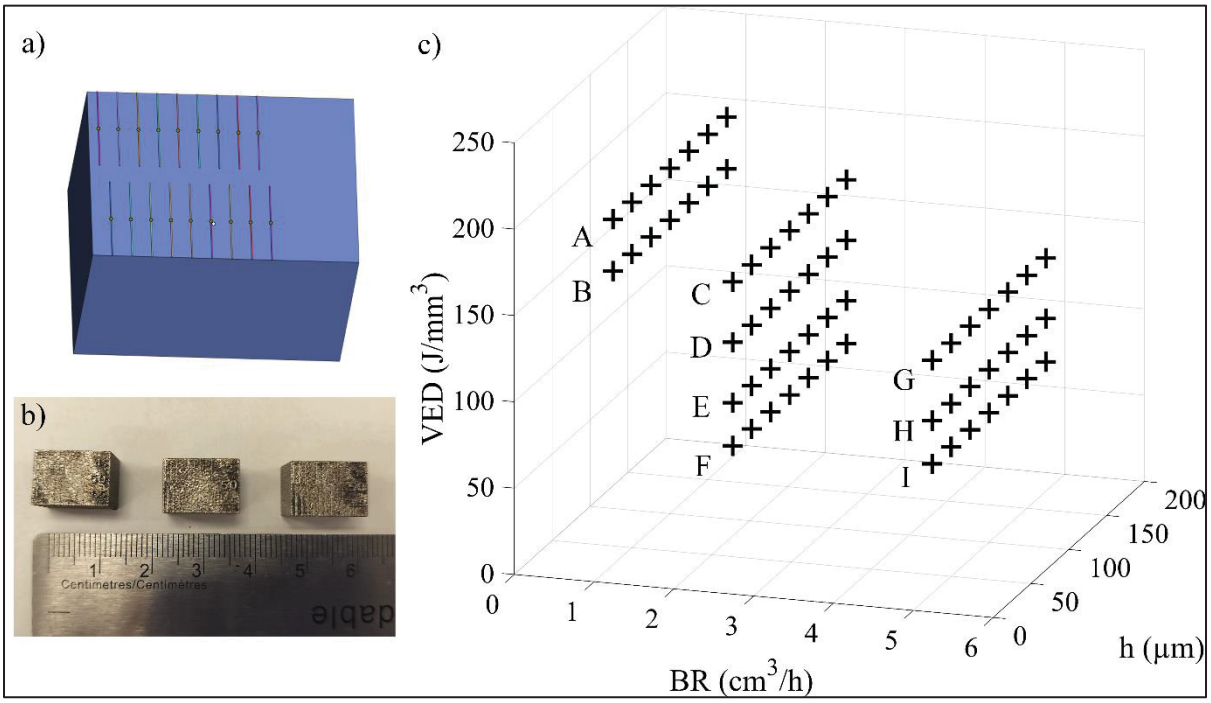

Figure 7-2 : a) schéma d'un échantillon cubique avec les traces de passe unique de laser; b) photo de trois échantillons cubiques avec les traces de passe unique de laser; c) représentation 3D dans le volume $VED - BR - h$ des 63 paramétries testées pour les traces de passe unique de laser

Tableau 7-1 : Plan d'expériences en termes de puissance laser (P), vitesse de balayage (v) et écart vecteur (h) retenus pour chacun des 9 ensembles de paramètres

Set	VED (J/mm^3)	BR (cm^3/h)	P (W)	h (µm)						
				25	50	75	100	125	150	175
				v (mm/s)						
A	200	1	56	444	222	148	111	89	74	63
B	170		47							
C	170	2.5	118	1111	556	370	278	222	185	159
D	135		94							
E	100		69							
F	75		52							
G	135	5	188	2222	1111	741	556	444	370	317
H	100		139							
I	75		104							

Les observations au microscope optique des traces d'un passage unique du laser ont permis de distinguer trois principaux groupes, à savoir les traces continues (Figure 7-3a), irrégulières (Figure 7-3b) et discontinues (Figure 7-3c) et de définir leur largeur moyenne (W). Celle-ci varie entre 140 et 260 µm pour les traces continues et entre 60 et 140 µm pour les traces irrégulières et discontinues (Tableau 7-3). Une corrélation a pu être établie entre la densité d'énergie linéique du laser (LED, (7.3)), la vitesse de balayage et la continuité de la trace de passe unique de laser. En effet, il est possible d'observer sur la Figure 7-3d que plus la LED diminue et plus la vitesse augmente, plus les traces se réduisent et deviennent irrégulières, voire discontinues. Ce phénomène apparaît pour chacun des 9 ensembles de paramètres dans des configurations où l'écart vecteur h est petit car en effet, en maintenant un taux de production BR constant, une réduction de l'écart vecteur h est compensé par une augmentation de la vitesse. De fait, un critère a pu être établi selon lequel la LED doit être supérieure à 0.18 J/mm afin d'obtenir une trace de qualité et de largeur suffisante pour permettre la production d'un échantillon.

$$LED\ [\mathrm{J/mm}] = \frac{P}{v} \tag{7.3}$$

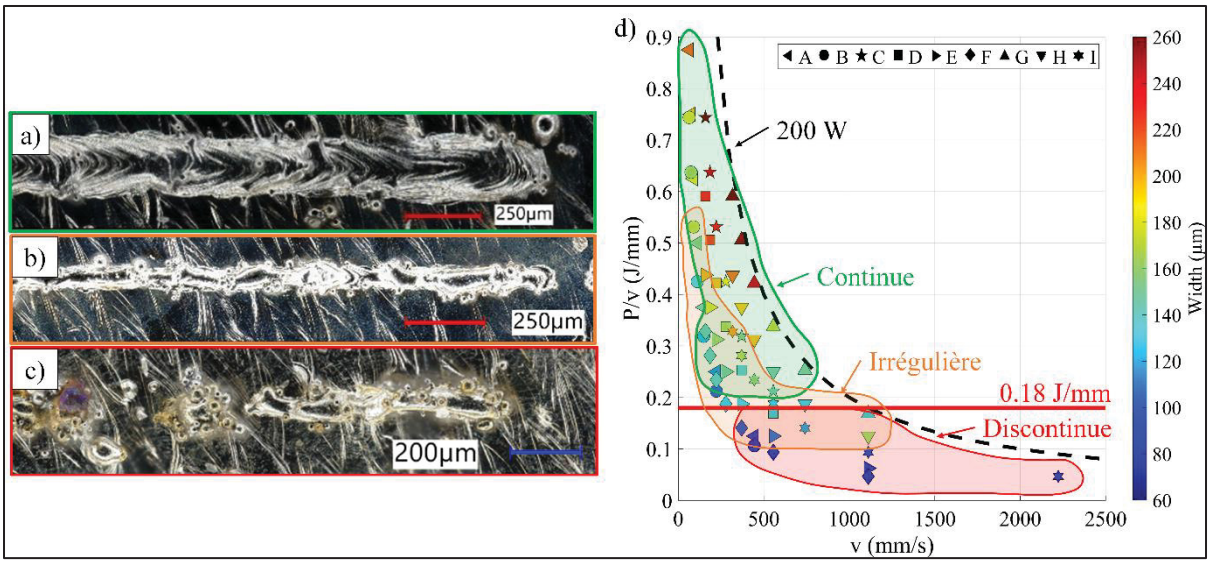

Figure 7-3 : Observations au microscope optique d'une trace de passe unique de laser a) continue, b) irrégulière et c) discontinue; d) largeur mesurée des traces de passe unique de laser en fonction de la vitesse de balayage v et de la densité d'énergie linéique P/v

Tableau 7-2 : Largeur des traces de passe unique de laser pour chaque ensemble de paramètres en fonction de l'écart vecteur h

Ensemble	h (µm)						
	25	50	75	100	125	150	175
	W (µm)						
A	90 ± 13	115 ± 15	147 ± 23	155 ± 17	181 ± 27	197 ± 28	215 ± 32
B	84 ± 17	104 ± 16	124 ± 12	132 ± 31	172 ± 30	165 ±15	178 ± 25
C	102 ± 13	145 ± 16	153 ± 16	186 ± 20	231 ± 18	241 ± 13	270 ± 24
D	80 ± 13	131 ± 14	136 ± 17	167 ± 23	197 ± 12	223 ± 12	229 ± 24
E	87 ± 23	109 ± 11	131 ± 12	148 ± 16	162 ± 18	179 ± 21	198 ± 26
F	82 ± 18	84 ± 12	103 ± 11	128 ± 21	137 ± 18	140 ± 13	142 ± 22
G	79 ± 5	131 ± 13	151 ± 21	172 ± 19	242 ± 28	252 ± 25	263 ± 23
H	67 ± 8	161 ± 13	128 ± 15	149 ± 9	197 ± 30	195 ± 16	212 ±14
I	84 ± 22	98 ± 14	121 ± 23	127 ± 18	157 ± 25	168 ± 13	202 ± 16

7.2 Phénomène de fissuration

A partir des observations faites sur les traces de passe unique de laser, seules les paramétries disposant d'une énergie linéique $LED > 0.18$ J/mm ont été retenues pour produire des cylindres de 10 mm de diamètre pour 21 cm de hauteur, réduisant ainsi le plan d'expérience à seulement

45 échantillons (Tableau 7-1). Bien que tous les échantillons aient pu être produits, aucune des paramétries testées n'a permis l'obtention d'un échantillon sain. En effet, certains échantillons présentaient des fissures importantes et visibles à l'œil nu avant même leur retrait de la plateforme de fabrication (Figure 7-4a) tandis que d'autres ont fissuré lors de leur retrait (Figure 7-4b). Enfin, certains échantillons ne présentaient pas de fissures visibles à l'œil nu même après leur retrait de la plateforme de fabrication mais des analyses par radiographie à rayons X ont révélées la présence de fissures internes (Figure 7-4c). Il est possible de supposer que la technique de retrait des échantillons, consistant au recours à un marteau, soit à l'origine de la formation de ces fissures. Enfin, un nombre important d'échantillons arboraient une coloration orangée ou bleuté (Figure 7-4d), associée à de l'oxydation. Ce phénomène a pu être corrélé à une densité volumique d'énergie trop importante (set A, B, C, D et G, $VED \geq 135$ J/mm^3).

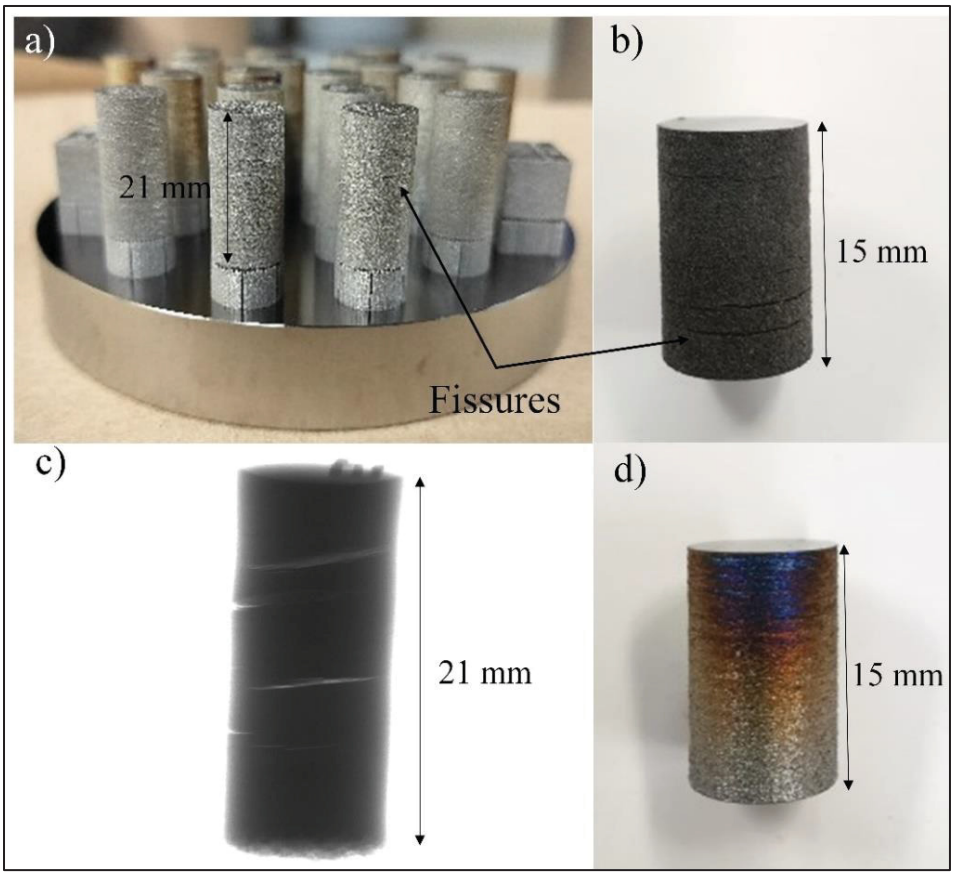

Figure 7-4 : Échantillons présentant des fissures visibles à l'œil nu
a) attachés à la plaque de fabrication et b) une fois retiré de la plaque;
c) radiographie au rayons X d'un échantillon fissuré
mettant en avant la présence de fissures internes
et d) échantillon retiré de la plaque d'impression
possédant une forte coloration de surface

Dans la littérature, les phénomènes de fissuration observés sur cet alliage lors de la fabrication par LPBF sont associés à la fois aux phases en présence (phase désordonnée β/β_0 instable, phase α_2 fragile, augmentation du volume lors du passage de phase β/β_0 vers O) ou à la présence d'un taux important de contraintes résiduelles (Gussone et al., 2023; Illarionov et al., 2023; Zhou, Li, et al., 2019). Des investigations ont donc été menées dans cette direction afin d'appréhender les effets des paramètres de fabrication sur les phases en présence.

7.2.1 Taux de recouvrement

Dans l'objectif de comprendre les effets des paramètres de fabrication et de déceler un éventuel lien avec les phases en présence sur les phénomènes de fissuration, des calculs du taux de recouvrement $R\%$ (7.4) ont été réalisés à partir des mesures faites sur les traces de passe unique de laser (Tableau 7-3). Il apparaît que pour chaque ensemble de paramètres, le taux de recouvrement $R\%$ augmente lorsque l'écart vecteur h diminue et que la vitesse augmente (Figure 7-5a). Cette tendance est cependant contraire à celle observée pour la largeur des traces laser (Figure 7-5b) et pourrait être expliquée par le fait que le pas de 25 µm choisi pour le passage d'un écart vecteur à l'autre est plus important que la variation de largeur provoquée par le changement des paramètres associé. Aussi, les échantillons produits avec les plus faibles niveaux d'énergie volumique (F et I, VED < 100 J/mm^3) possèdent des taux recouvrements inférieurs à 25% tandis que de plus hauts niveaux d'énergie permettent d'atteindre des taux de recouvrement allant jusqu'à 65%. Deux échantillons (F-150 et F-175) possèdent un recouvrement négatif, synonyme d'un écart vecteur trop large par rapport à la trace formée par le laser.

$$R\% = \frac{W-h}{W} * 100 \qquad (7.4)$$

Tableau 7-3 : Taux de recouvrement en fonction de l'écart vecteur pour chaque ensemble de paramètres; NP signifie échantillon Non Produit et les données en gras représentent les échantillons sélectionnés pour analyses structurales

Ensemble	h (µm)						
	25	50	75	100	125	150	175
	R (%)						
A	NP	**57**	49	35	31	24	**19**
B	NP	**52**	40	24	27	9	**2**
C	NP	**65**	51	46	46	38	**35**
D	NP	NP	**45**	40	37	33	**24**
E	NP	NP	**43**	32	23	16	**11**
F	NP	NP	NP	**22**	9	-7	-23
G	NP	NP	**50**	42	48	40	**33**
H	NP	NP	**41**	33	37	23	**17**
I	NP	NP	NP	21	20	10	**13**

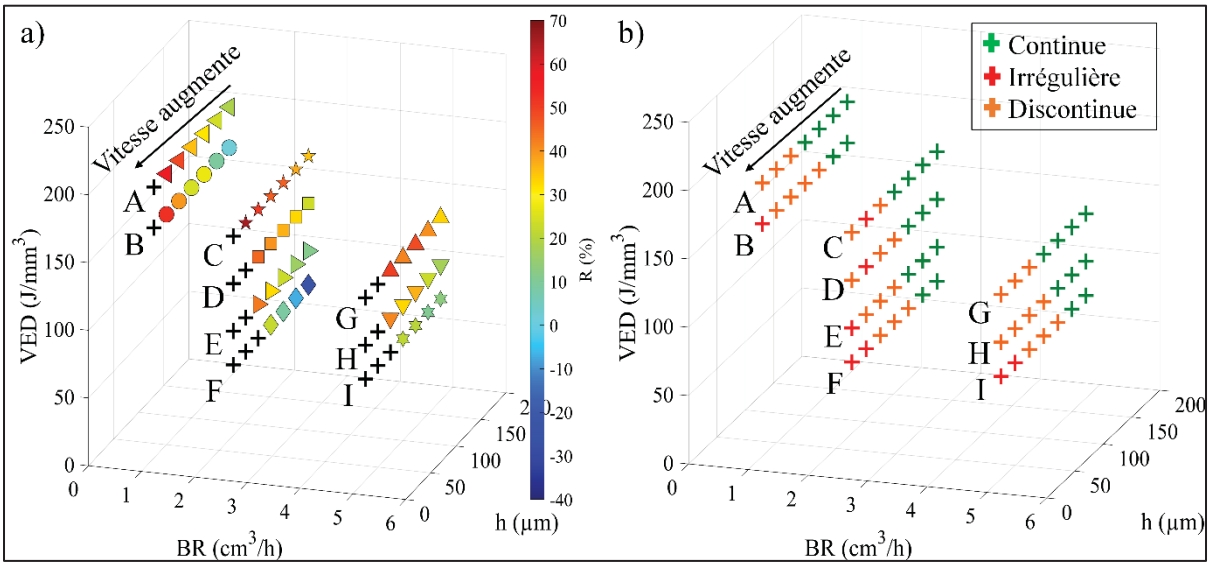

Figure 7-5 : a) Taux de recouvrement et b) continuité des traces de passe unique de laser en fonction de la densité d'énergie volumique VED, du taux de construction BR et de l'écart vecteur h pour chaque ensemble de paramètres

7.2.2 Analyses de phases par diffraction à rayons X

Puisque pour chaque set de paramètres, le taux de recouvrement augmente graduellement avec la diminution de l'écart vecteur, des analyses par diffraction à rayons X ont été menées sur

deux échantillons de chaque ensemble de paramètres, possédant les écarts vecteurs maximum et minimum de chacun (voir données en gras dans Tableau 7-3). En procédant ainsi, il est possible de découpler les effets des paramètres de ceux du taux de recouvrement sur la phase formée.

Il apparait que pour un taux de recouvrement plus petit que 10%, les échantillons présentent la phase désordonnée β/β_0 (ICDD 04-027-9533) uniquement au même titre que la poudre (Figure 7-6a). Lorsque le taux de recouvrement est compris entre 10 et 60%, la phase α_2 (ICDD 04-019-5158) s'établi et est progressivement remplacée par la phase O (ICDD 04-017-6136) lorsque le recouvrement dépasse 65% (Figure 7-6a). Ces changements de phase sont observés pour chaque ensemble de paramètres, signifiant que le taux de recouvrement seul est suffisant pour les expliquer. Des analyses complémentaires par microscopie à balayage pourraient être envisagées pour investiguer la morphologie des phases présentes. Aussi, une analyse du pic principale de la phase β/β_0 (2θ = 39.2°) permet de mettre en avant un décalage de ce pic vers les petits angles pour les échantillons possédant un taux de recouvrement compris entre 10 et 65% (Figure 7-6). Un décalage vers les petits angles est caractéristique d'un taux de contraintes résiduelles important d'après la loi de Bragg ((7.5), (Watkins, Schajer, & Lance, 2012)).

$$2d\,\sin\theta = n\lambda \qquad (7.5)$$

où d est la distance interréticulaire, c'est-à-dire la distance entre deux plans cristallographiques, θ l'angle de Bragg, soit le demi-angle de déviation (la moitié de l'angle entre le faisceau incident et la direction du détecteur), n l'ordre de diffraction (un nombre entier) et λ la longueur d'onde des rayons X.

Ainsi, la fissuration des échantillons semble principalement liée à un taux de contraintes internes trop important et des changements de phase vers une phase plus stable au moyen de changements des paramètres de fabrication ne semblent pas être une solution suffisante à l'obtention d'échantillons sains.

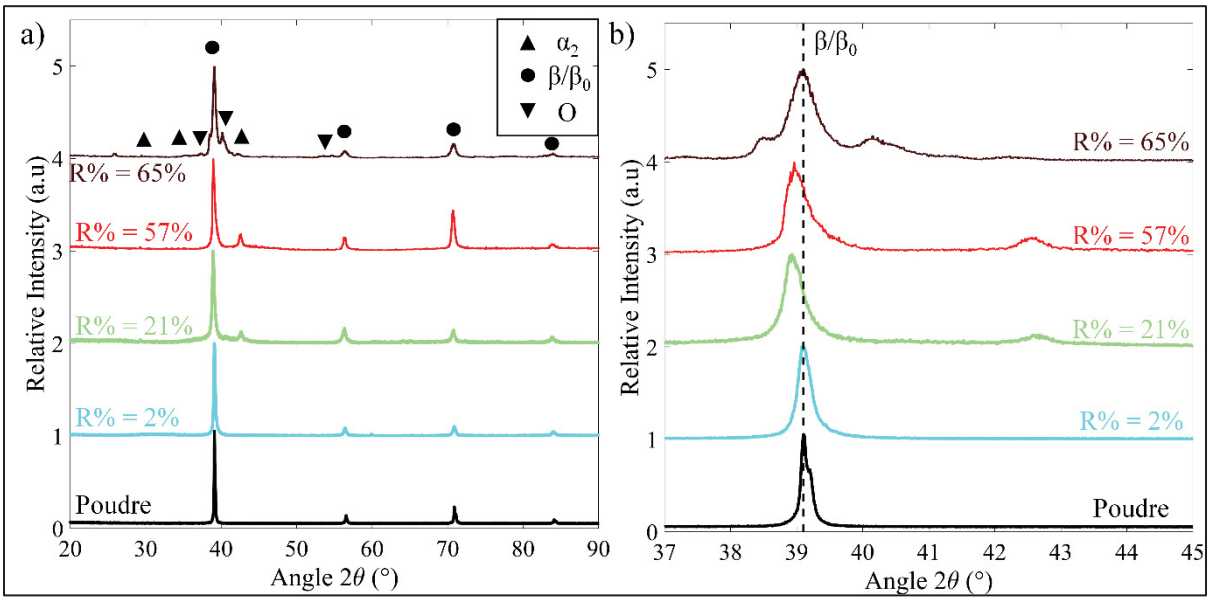

Figure 7-6 : Spectres de diffractions à rayon X de la poudre et des échantillons B-175 ($R\% = 2\%$), I-100 ($R\% = 21\%$), A-50 ($R\% = 57\%$) et C-50 ($R\% = 65\%$)

Dans la littérature, les auteurs parviennent à obtenir des échantillons sains en recourant à un préchauffage de la plateforme de fabrication, permettant de réduire les contraintes internes et menant également à des changements dans les phases présentes, leur proportion et leur morphologie Des post-traitements sont aussi envisagés dans l'objectif de stabiliser la phase β/β_0 en B2, de contrôler la formation de la phase O et de limiter la présence de la phase fragile α_2 (Illarionov et al., 2023; Zhou et al., 2021; Zhou, Li, et al., 2019).

7.3 Conclusion

Dans cette étude, les effets d'une large gamme de paramètres de fabrication sur l'imprimabilité de l'intermétallique à base d'aluminures de titane orthorhombique Ti-22Al-25Nb ont été investigués. Les observations faites sur les traces de passe unique de laser ont permis de mettre en avant les effets des paramètres de fabrication sur la qualité de celles-ci et de mettre en place un critère d'énergie linéique minimum pour la production d'échantillons. Des analyses par diffraction à rayons X réalisés sur des échantillons bruts ont permis de révéler des effets des

paramètres de fabrication sur la phase formée, corrélée à des taux de recouvrement d'une passe laser sur la suivante. Si des transformations de phase au moyen de changements des paramètres de fabrication ne semblent pas être suffisantes pour empêcher la fissuration dans les échantillons bruts, des post-traitements pourraient être envisagés pour à la fois stabiliser la microstructure mais également réduire le taux de contraintes internes.

CHAPITRE 8

DISCUSSION GÉNÉRALE

À travers ces études, différents degrés d'avancement ont été atteints pour les trois catégories de matériaux examinées. Concernant les métaux réfractaires, les résultats obtenus se sont révélés suffisamment encourageants pour envisager la réalisation d'un premier prototype (8.1). En revanche, pour l'alliage de titane Ti6246, une étude complémentaire a été envisagée afin d'évaluer la répétabilité des impressions sur une machine de capacité équivalente mais d'architecture différente (8.2). Enfin, les essais menés sur l'intermétallique à base d'aluminures de titane Ti2225 n'ayant pas été concluants, un post-traitement en sortie d'impression a été essayé dans le but d'obtenir des pièces exemptes de fissures (8.3).

Aussi, bien que le modèle numérique se soit avéré pertinent pour prédire les dimensions des bains de fusion de métaux réfractaires, certaines limites sont apparues lors de son applications aux alliages de titane et ont fait l'objet d'une dernière étude (8.4).

8.1 Fabrication d'un prototype d'injecteur micro-mélangé en molybdène pur par fusion laser sur lit de poudre et effets des post-traitements

Les trois études menées sur l'implémentation de divers matériaux réfractaires par le procédé de fusion laser sur lit de poudre ont permis de mettre en avant le potentiel de ces métaux pour la production de pièces complexes mais également les défis qu'ils restent à relever pour leur implémentation dans des systèmes fonctionnels. Des paramètres de fabrication ont été optimisés sur un équipement de fabrication à petite capacité (puissance maximale de 200 W) sans contrôle de la température dans la chambre d'impression, jusqu'à obtenir d'une part, des pièces aux propriétés physiques et mécaniques (Tableau 8-1) comparables à celles produites par des procédés conventionnels de métallurgie et atteignant les requis des normes sur ces métaux et d'autre part, des géométries avec différents niveaux de complexité et de précision.

Tableau 8-1 : Récapitulatif de la densité et des propriétés mécaniques à température ambiante obtenues avec les ensembles de paramètres optimisés pour chaque matériau réfractaire étudié

Matériau	Densité (%)	UCS (MPa)	YS (MPa)	δ (%)
W (19.3 g/cm³)	93	867	676	7
Mo (10.2 g/cm³)	97	500	340	11
Mo8Re (10.5 g/cm³)	98	460	303	7

A partir de ces résultats, le molybdène pur apparaît comme le meilleur compromis en termes de fabricabilité par le procédé de fusion laser sur lit de poudres, de poids et de prix et a de fait été retenu comme candidat pour la fabrication d'un prototype d'injecteur micro-mélangé. Avant de produire le prototype, des géométries supplémentaires ont été imprimées et contrôlées afin de s'assurer de la capacité à produire certaines composantes critiques de l'injecteur, à savoir les trous d'injection du carburant. En effet, des trous de petites dimensions permettent de réduire les émissions de gaz NOx. Ainsi, deux pièces de test ont été produites contenant des trous de dimensions variant de 0,15 à 0,5 mm, l'une possédant une épaisseur de 0,35 mm et l'autre, 0,5 mm (Figure 8-1a). Les mesures des aires ont permis de mettre en avant que les résultats aient été similaires aux performances obtenues avec la conception actuelle en superalliage de nickel Inconel 625. Une fois ces composants validés, une version réduite et une coupe de l'injecteur ont pu être imprimées avec succès, sans défauts géométriques (Figure 8-1b,c). En revanche, des tests de pression ont révélé la présence de fuites dans les parois, pouvant provenir d'un niveau de porosité encore trop élevé. Aussi, aucun test de combustion n'a pu être réalisé en raison du manque de maturité dans le développement de revêtements contre l'oxydation. Les détails de cette étude ont fait l'objet d'un article de conférence présenté par mon collègue sur ce projet et fourni en ANNEXE I. Ainsi, cette étude a pu démontrer le potentiel de fabriquer une pièce complexe en un métal réfractaire, mais a mis en avant la nécessité d'améliorer sa protection contre l'oxydation haute température avant de pouvoir envisager son implémentation dans un prototype fonctionnel.

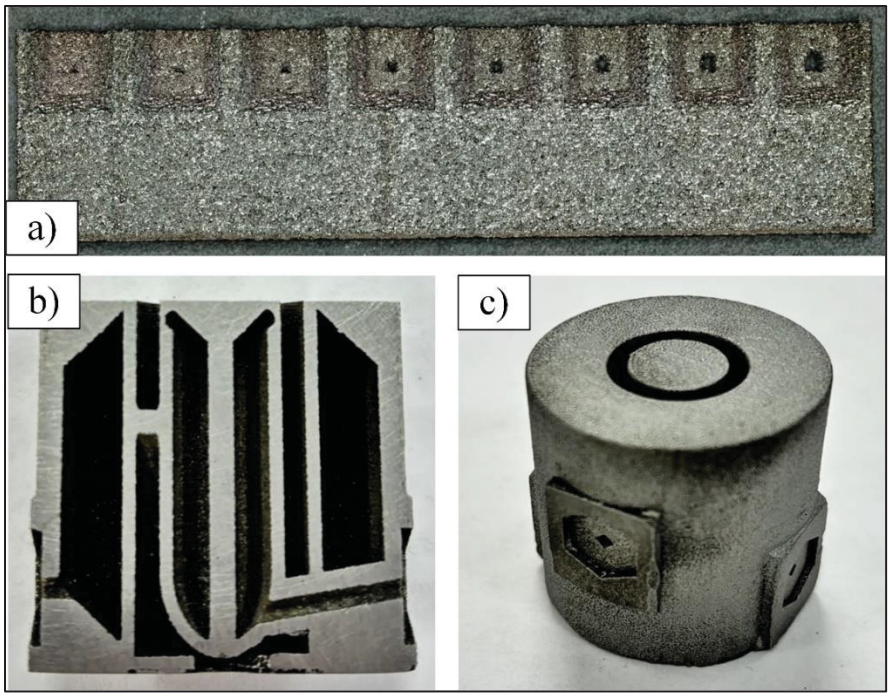

Figure 8-1 : a) Pièce de test d'impression de trous de différents diamètres; photo du b) demi-prototype et c) prototype complet d'injecteur micro-mélangé en molybdène pur

Avec en tête les problématiques liées au manque d'étanchéité des parois et en vue d'améliorer les propriétés physiques et mécaniques des pièces imprimées de manière plus large, différents post-traitements ont été envisagés sur, d'abord des échantillons en molybdène pur puis également sur des échantillons en alliage molybdène-8wt% rhénium. De ces deux études, il en résulte que, si le premier traitement HIP (1500 °C, 150 MPa, 3 h) a permis d'augmenter la densité des pièces (~1%) au détriment des propriétés mécaniques à température ambiante et haute température (~10%), le second à plus haute température (1800 °C, 150 MPa, 3 h) a permis une nette amélioration des propriétés mécaniques sur la plage de températures étudiée (jusqu'à presque 50% d'augmentation de la contrainte ultime et 70% de la déformation pour le Mo8Re par exemple) malgré une perte de densité s'élevant jusqu'à 3%. Ces études ont été présentées lors des conférences et les articles associés détaillant les démarches et les résultats sont fournis en ANNEXE II et ANNEXE III. Néanmoins, des études sur les effets des post-traitements sur des pièces en métaux réfractaires obtenues par fusion laser sur lit de poudre sont à poursuivre afin d'améliorer davantage leurs propriétés physiques et mécaniques.

8.2 Transfert de connaissances au sujet de l'impression de l'alliage Ti-6Al-2Sn-4Zr-6Mo

Au travers de trois différentes études, des paramètres de fabrication ont été développés et optimisés pour la production de pièces en alliage de titane Ti-6Al-2Sn-4Zr-6Mo par le procédé de fusion laser sur lit de poudre. Malgré l'absence de contrôle de température dans la chambre d'impression et l'utilisation d'une machine à puissance limitée (P_{max} = 200 W), des pièces de différents niveaux de complexité ont pu être produites sans fissures, avec un minimum de défauts caractéristiques de ce procédé (porosités induites par de la surfusion ou au contraire un manque de fusion) et un haut niveau de précision géométrique. Afin de discuter de la transférabilité de ces paramètres d'impression, une étude a été menée dans les locaux du 3IT de l'Université de Sherbrooke, un de nos partenaires lors de ce projet. En effet, ces derniers disposent d'une machine MLab cusing R (Colibrium Additive, GE Aerospace Company, États-Unis d'Amérique), aux capacités similaires (P_{max} = 200 W, diamètre du faisceau laser d = 50 µm, volume d'impression 10 x 10 x 10 cm^3) mais dont l'architecture et différente. L'étude suivante vise à appréhender les effets d'un changement des conditions d'impression pour des paramétries identiques. Aussi, puisque les pièces ne peuvent pas être utilisées telles que fabriquées, les deux protocoles de post-traitement précédemment étudiés ont également été appliqués.

Dans le cadre de cette étude, le même lot de poudre Ti-6Al-2Sn-4Zr-6Mo a été utilisé (CHAPITRE 5, CHAPITRE 6) pour produire neuf échantillons cylindriques (diamètre 10 mm, hauteur 21 mm) et neuf échantillons prismatiques (17 x 8 x 81 mm^3) en conservant les paramètres optimaux définis pour épaisseur de couche t = 25 µm (P = 139 W, vitesse de balayage v = 741 mm/s, écart vecteur h = 75 µm) sur une plaque de fabrication en Ti64 sans préchauffage. Trois groupes d'échantillons ont été formés, possédant chacun trois échantillons cylindriques et trois prismatiques : le premier groupe a été conservé dans l'état tel que fabriqués tandis que les deux autres ont subi les protocoles P875 et P950 tel que définis dans la section 6.2. La même procédure d'usinage et d'analyse que celle menée en 6.2 a ensuite été suivie pour caractériser les propriétés structurales et mécaniques des échantillons.

Pour simplifier la lecture, les échantillons produits dans le cadre de cette étude seront référencés sous l'appellation UDS et comparés à ceux fabriqués lors des trois premières études nommés ETS, en référence aux universités les ayant produits.

8.2.1 Analyses physiques et structurales

La densité d'un échantillon cylindrique UDS tel qu'imprimé a été mesurée à 99.87% contre une densité supérieure à 99,98% pour son homologue ETS (Mouret, Leclercq, Dubois, et al., 2025). L'analyse des distributions de porosités (Tableau 8-2, Figure 8-2) a révélé la présence d'une quantité plus élevée de pores plus volumineux et moins sphériques dans l'échantillon UDS en comparaison à celui de l'ETS.

Tableau 8-2 : D10, D50 et D90 extrait des distributions du volume et sphéricité des porosités observées par µCT dans les échantillons UDS et ETS

Échantillon	Volume (µm^3)			Sphéricité		
	D10	D50	D90	D10	D50	D90
UDS	2.3*10^4	8.9*10^4	1.2*10^6	0.58	0.79	0.92
ETS	1.5*10^4	3.1*10^4	1.5*10^6	0.66	0.89	0.97

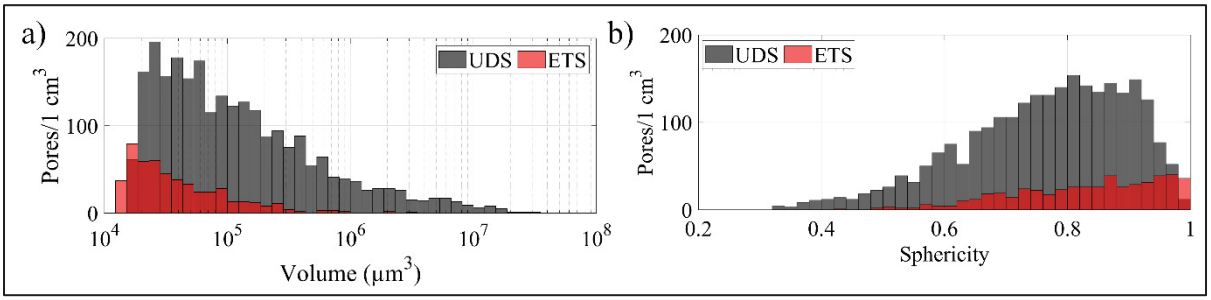

Figure 8-2 : Distributions a) du volume et b) de la sphéricité des porosités observées par µCT dans les échantillons UDS et ETS

Les analyses par diffraction à rayons X réalisés sur les échantillons bruts et après post-traitements dont les résultats sont présentés en Figure 8-3 et comparés avec ceux de la poudre comme référence. Il est possible d'observer que les échantillons bruts présentent, tout comme la poudre, la phase de martensite orthorhombique α'', tandis que les deux protocoles de post-

traitements (P875 et P950) entraînent sa décomposition en phases stables α (hcp) et β (bcc) du titane. Ces observations sont cohérentes avec les conditions de refroidissement rapide survenant à la fois lors de la fabrication de la poudre et pendant l'impression 3D, conduisant à la formation de la martensite, puis à sa décomposition en un mélange de phases stables $\alpha + \beta$ au cours des traitements thermiques.

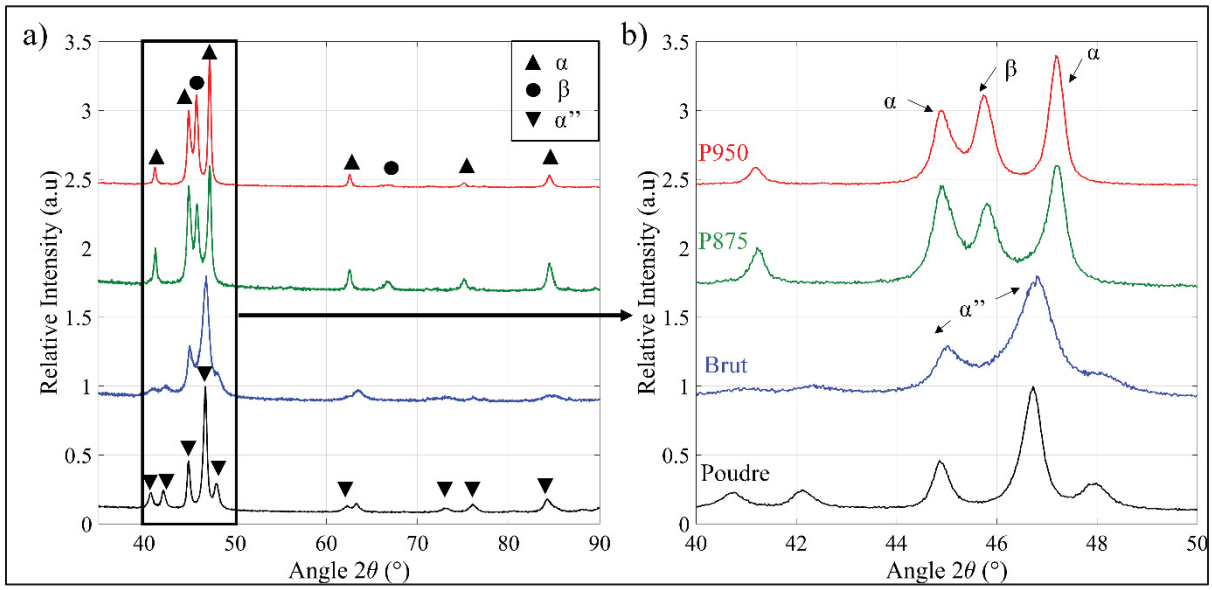

Figure 8-3 : Résultats d'analyses par diffraction à rayons X de la poudre de Ti6246, d'échantillon UDS brut et post-traités selon les protocoles P875 et P950

Bien qu'au niveau des phases en présence, les échantillons avant et après post-traitements correspondent à ce qui avait été obtenu pour les échantillons ETS (Figure 6-18), les observations au microscope confocal ont montré que les échantillons UDS après le protocole P950 (Figure 8-4c) semblent avoir des grains équiaxes, ce qui n'est pas le cas de leurs homologues de l'ETS (Figure 8-4f). En ce qui concerne les échantillons bruts et après le protocole P875, les analyses par microscope confocal n'ont pas permis de mettre en avant de différences significatives entre les échantillons UDS et ETS : sur les échantillons bruts (Figure 8-4a,d), la phase martensitique n'est pas visible mais les contours des bains de fusion sont apparents, tandis que pour les échantillons après le protocole subtransus (Figure 8-4b,e), les phases $\alpha + \beta$ sont clairement visibles et démontrent un aspect colonnaire selon la direction

de fabrication. Cet aspect colonnaire des grains est typique de ce procédé de fabrication et, si un traitement thermique subtransus ne permet pas de l'altérer, un traitement supertransus permet, la quant à lui, la transformation des grains de β primaires vers une structure plus équiaxe, lorsque le temps de recuit est suffisant par rapport à la microstructure initiale (Alessandro Carrozza et al., 2022).

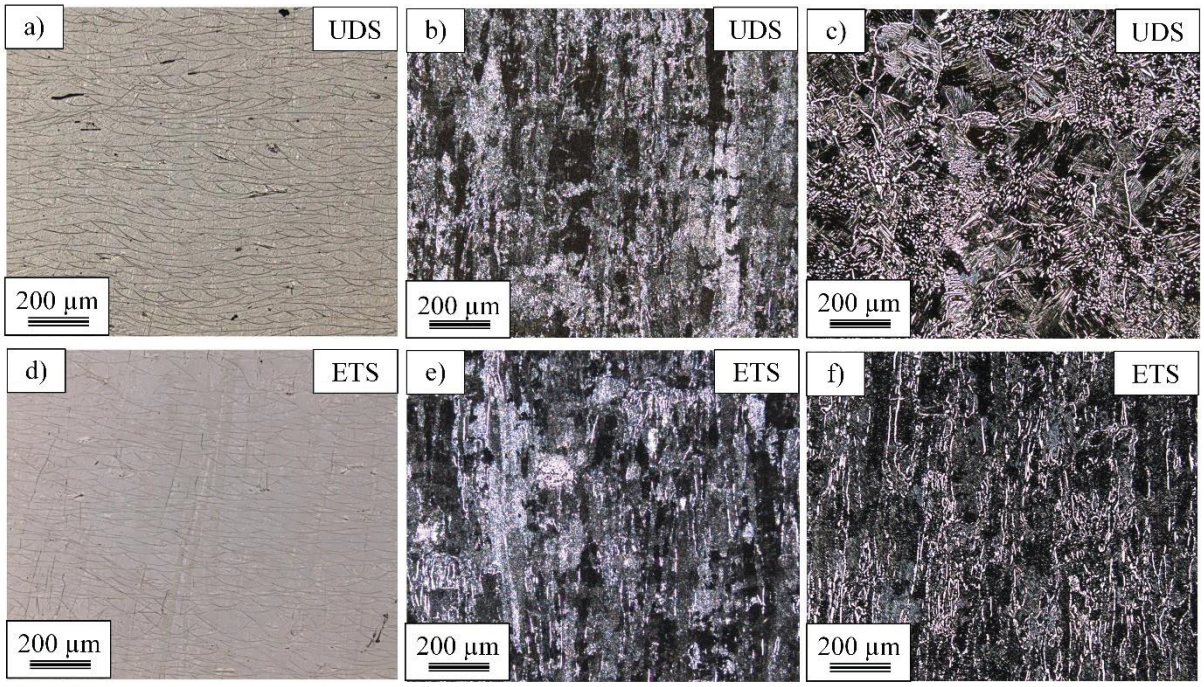

Figure 8-4 : Observations au microscope confocal des échantillons bruts (a,d) et post-traités selon les protocoles P875 (b,e) et P950 (c,f) de (a-c) UDS et (d-f) ETS

Les observations par MEB (Figure 8-5) ont permis de mesurer les aiguilles des phases α'' et α (Tableau 8-3). Pour les échantillons bruts (Figure 8-5a), la microstructure est composée d'aiguilles de martensite α'' environ 40% plus petites que celles mesurées dans les échantillons ETS (Tableau 8-3). Aussi, des petits précipités sont visibles et semblent être distribués de manière aléatoire; ils n'étaient pas présents chez leurs homologues de l'ETS. Il est important de noter que les analyses ont été répétées à plusieurs reprises, sur différents échantillons et après différentes stratégies de nettoyage de la surface afin de s'assurer qu'il ne s'agisse pas d'impuretés déposées en surface de l'échantillon. Après le traitement P875 (Figure 8-5b), des lamelles de α plus épaisses sont observées (Tableau 8-3), formant des colonies à l'intérieur des

grains de β primaires. Ces lamelles ont une taille semblable (< 5% de différence) à celles de leurs homologues de l'ETS, en dépit de la différence significative de microstructure avant traitement. Enfin, après le traitement P950, la microstructure obtenue est bi-lamellaire, composée de larges lamelles de α primaire (Figure 8-5c, Tableau 8-3) et de fines aiguilles de α secondaire contenues à l'intérieur de la phase β (Figure 8-5d). Cette microstructure particulière n'est en rien similaire à celle obtenue après le même traitement sur les échantillons de l'ETS, mais une microstructure semblable a déjà été observée par (Alessandro Carrozza et al., 2022; Pirro et al., 2025) après différents post-traitements.

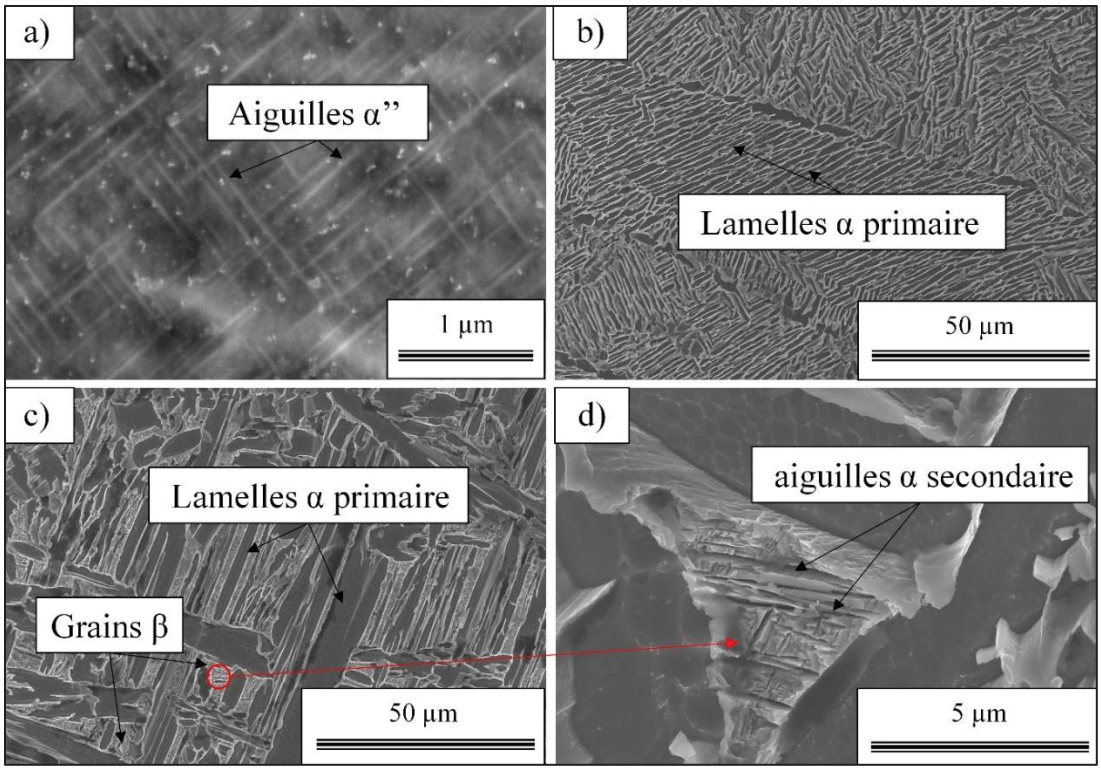

Figure 8-5 : Observation au MEB de : a) l'échantillon brut avec les aiguilles de α'', b) l'échantillon après protocole P875 avec la phase $\alpha + \beta$ et c) et d) l'échantillon après le protocole P950 montrant la microstructure bi-lamellaire composée de lamelles de α primaire et d'aiguilles de α secondaire contenues dans des grains β

Tableau 8-3 : Largeur mesurée des aiguilles de α'' et de lamelles de α pour les échantillons UDS et ETS

Échantillon	Brut	P875	P950
UDS	29 ± 7 nm	878 ± 217 nm	3830 ± 1852 nm
ETS	49 ± 17 nm	828 ± 240 nm	2495 ± 1121 nm

Compte tenu de la finesse de la microstructure, les échantillons bruts n'ont pas pu être soumis à des analyses de compositions chimiques par EDS. De fait, la nature des précipités demeure inconnue. Pour les échantillons post-traités, ces analyses ont révélé un enrichissement en Ti et Al dans les zones sombres et en Mo et Zr dans les zones claires, tandis que le Sn était distribué de manière homogène (Figure 8-6). Comme pour les échantillons ETS, les zones claires peuvent être identifiées comme appartenant à la phase β compte tenu de la présence du Mo (un stabilisateur de phase β), tandis que les zones sombres, où l'on observe la présence de Ti et Al (stabilisateurs de phase α), peuvent être identifiées comme appartenant à la phase α. En revanche, contrairement à leurs homologues ETS, aucun précipité de Sn n'a été trouvé dans les échantillons de UDS.

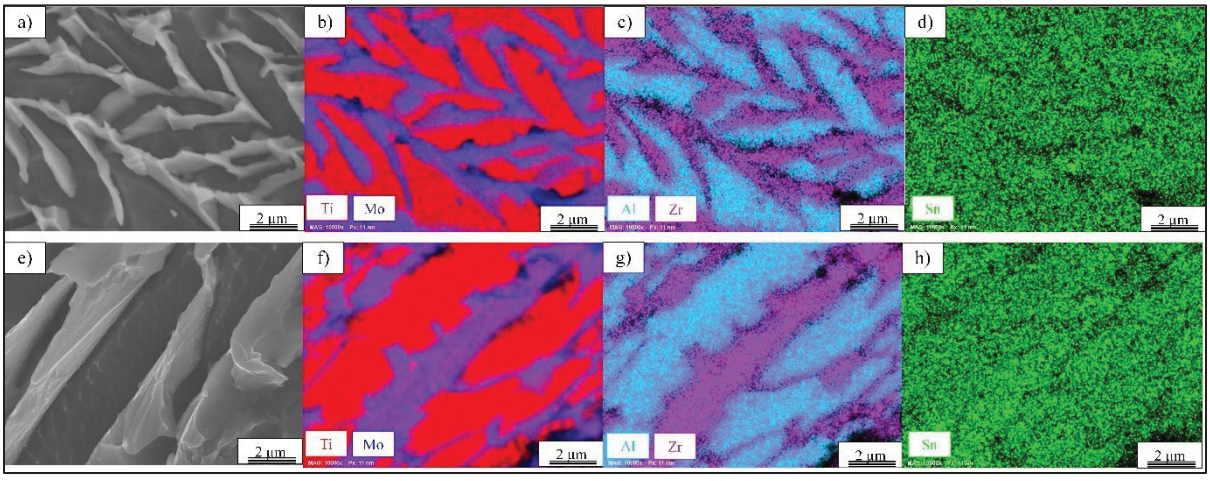

Figure 8-6 : Observations MEB et cartographies EDS des échantillons UDS après (a,b,c,d) protocole P875 et (e,f,g,h) protocole P950

8.2.2 Essais mécaniques

8.2.2.1 Microdureté

Les mesures de microdureté réalisées sur les surfaces préparées des échantillons ont révélé qu'après le protocole subtransus, la dureté mesurée est plus faible de 14% en comparaison avec les échantillons bruts tandis que le protocole supertransus permet quant à lui une augmentation de dureté d'environ 7% (Tableau 8-4). Ces variations de dureté s'expliquent par les différences significatives de microstructure observées et s'accordent avec ce qui est rencontré dans la littérature, à savoir qu'une augmentation de la taille des lamelles α mène à une diminution de la dureté tandis que la formation d'une structure bi-lamellaire l'augmente, malgré l'élargissement des lamelles α (Peng et al., 2023; Pirro et al., 2025).

En comparaison avec les échantillons ETS, la dureté des échantillons UDS bruts est 20% plus faible (Tableau 8-4) en dépit d'une taille d'aiguilles de martensite α'' plus fine. Cela pourrait être expliqué par le taux de porosité plus élevé de ces derniers (Hassanin et al., 2023). Après le protocole subtransus, les échantillons UDS ont une dureté légèrement inférieure (~10%) à leurs homologues ETS (Tableau 8-4), en adéquation avec des aiguille de α plus épaisses. Enfin, après le protocole supertransus, les échantillons UDS ont une dureté 20% plus élevée que ceux de l'ETS (Tableau 8-4), ce qui s'explique par la présence d'une microstructure bi-lamellaire qui n'a pas pu être formée dans ces derniers.

Tableau 8-4 : Mesures de dureté pour les échantillons brut et après post-traitements de UDS et ETS

Échantillon	Brut	P875	P950
UDS	406 ± 12 HV0.3	348 ± 12 HV0.3	433 ± 17 HV0.3
ETS	514 ± 19 HV0.3	397 ± 32 HV0.3	365 ± 20 HV0.3

8.2.2.2 Essais de traction

Les courbes contrainte-déformation obtenues pour les trois essais de traction sur les échantillons bruts sont présentés sur la Figure 8-7a tandis que des courbes représentatives des essais sur les échantillons post-traités sont fournies sur la Figure 8-7b. La variation significative de comportement observée dans les échantillons bruts pourrait provenir d'une part de la présence des précipités dans la microstructure et d'autre part d'un niveau de contraintes résiduelles différent dans chacun des échantillons. En effet, le chemin de solidification particulier du procédé LPBF génère des contraintes internes importantes dans le matériau pouvant aller jusqu'à des phénomènes de distorsion, de délamination ou même de fissuration (Aversa et al., 2025; Jamhari et al., 2023). Ces contraintes peuvent avoir un effet sur le réseau cristallin, entraînant un ralentissement du mouvement des dislocations qui permet à l'alliage de supporter des charges plus élevées avant de se déformer plastiquement lors de l'essai de traction. Cette augmentation de la limite d'écoulement s'associe à une réduction de la ductilité en raison de la diminution de la mobilité des dislocations (Alessandro Carrozza et al., 2022). Ici, la limite d'écoulement varie entre 836 et 991 MPa, la contrainte ultime, entre 875 et 1338 MPa et la ductilité, entre 13,4 et 4,3% (Tableau 8-5).

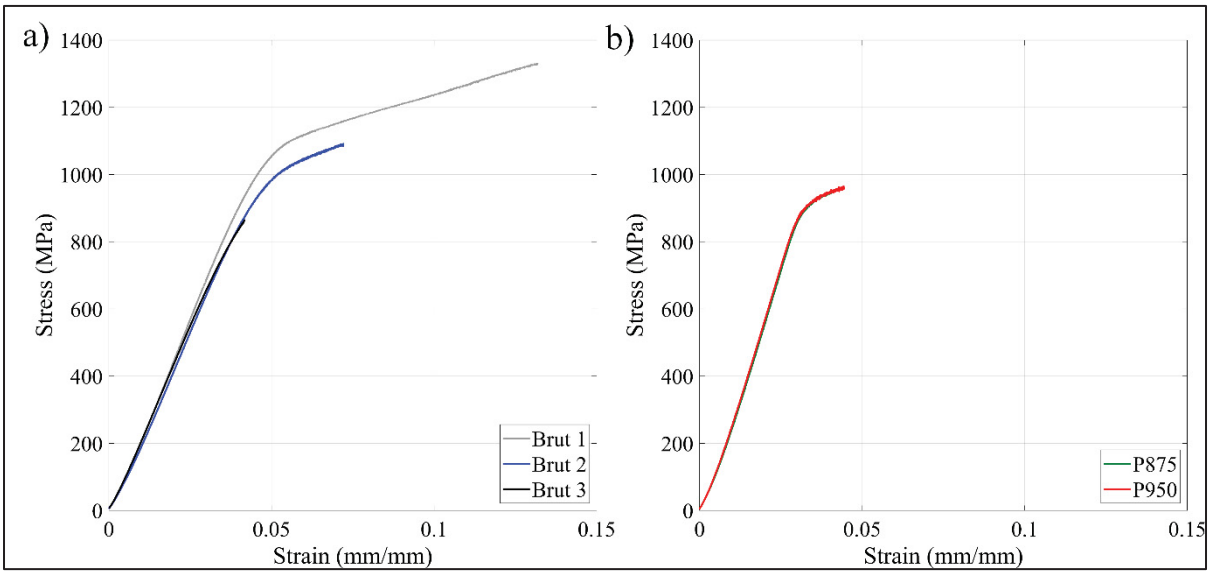

Figure 8-7 : Courbes contrainte-déformation obtenues pour a) les trois échantillons bruts UDS et b) représentatives des échantillons ayant subi les protocoles P875 et P950

Tableau 8-5 : Propriétés mécaniques extraites des tests de traction pour les échantillons brut et après post-traitements de UDS et ETS

Échantillon	Brut			P875			P950		
	UTS (MPa)	YS (MPa)	δ (%)	UTS (MPa)	YS (MPa)	δ (%)	UTS (MPa)	YS (MPa)	δ (%)
UDS	1101 ± 232	913 ± 77	8,3 ± 4,7	953 ± 35	895 ± 16	4,3 ± 0,6	966 ± 16	899 ± 1	4,6 ± 0.6
ETS	1287 ± 60	1270 ± 64	5,2 ± 0.4	1123 ± 29	967 ± 6	13.1 ± 1.1	1111 ± 9	972 ± 19	14,3 ± 0.3

Malgré des microstructures très différentes, les échantillons ayant subi les protocoles P875 et P950 démontrent des comportements très similaires avec une grande répétabilité, atteignant une limite d'écoulement d'environ 895 MPa, une limite ultime proche de 960 MPa pour seulement 4% de ductilité (Figure 8-7b, Tableau 8-5). Si une déformation similaire a été observée dans les travaux de (Pirro et al., 2025) sur des échantillons possédant également une microstructure bi-lamellaire, cette absence de ductilité est inhabituelle après le traitement subtransus (Alessandro Carrozza et al., 2022; Pirro et al., 2025). Aussi, l'allure des courbes tend à supposer une rupture prématurée et plutôt fragile des échantillons. Cela pourrait être la cause de contraintes résiduelles générées par le post-traitement et l'usinage. En effet, une augmentation du taux de contraintes résiduelles après post-traitement a été mesurée par (Aversa et al., 2025) et attribuée au changement de volume dû à la transformation de la phase martensitique α'' vers la phase $\alpha + \beta$, et une légère distorsion (de l'ordre de 1 mm environ) a été observée après traitement thermique aux extrémités des échantillons prismatiques avant usinage. Puisque les éprouvettes testées étaient planes, il est de fait possible de supposer que des contraintes internes ont été générées par l'usinage lors de la rectification du profil. Cette hypothèse est d'autant plus plausible que les échantillons ETS ayant subi le protocole P875 ne présentaient pas de phénomène de distorsions après post-traitement et montrent une élongation avant la rupture 68% plus importante (Tableau 8-5) bien qu'ils disposent d'une microstructure très similaire à ceux de l'UDS.

Ainsi, il est possible de penser que la différence significative des microstructures des échantillons bruts est à l'origine de changement du comportement vis-à-vis des différents post-

traitements et nécessite des études supplémentaires pour obtenir les propriétés mécaniques souhaitées.

8.2.3 Conclusion

Dans cette étude, les propriétés physiques et mécaniques d'échantillons en Ti6246 produits au moyen de deux équipements aux capacités d'impression similaires (diamètre du faisceau laser, paramètres d'impression, stratégie de balayage), mais aux architectures différentes ont étaient comparés avant et après avoir été soumis à deux protocoles de post-traitements. Bien que la poudre utilisée et les paramètres d'impression aient été identiques, la densité et les microstructures obtenues étaient sensiblement différentes, menant à des propriétés mécaniques également différentes. Au regard de ces résultats, il apparaît que la différence d'architecture ne permet pas d'obtenir des résultats semblables et, de fait, limite le transfert de connaissances. Cependant, les résultats de densité obtenus étant élevés et relativement proche de 99,9%, un plan d'expériences centré autour des paramètres optimisés pour l'ETS pourrait permettre d'obtenir rapidement et à moindre coût des paramètres optimisés pour ce nouvel équipement, sans avoir à refaire toutes les étapes sur les traces de passes uniques de laser et en considérant moins d'ensembles de paramètres pour la production d'échantillons pour analyses structurales et mécaniques.

Des études d'optimisation des paramètres d'impression d'un nouvel alliage doivent donc être réalisées pour chaque équipement, en dépit de capacités similaires, et des études supplémentaires sur les effets des post-traitements sur les propriétés physiques et mécaniques des pièces en alliage de Ti6246 obtenues par le procédé LPBF doivent être menées afin de mieux appréhender leurs effets et d'obtenir la combinaison de propriétés souhaitée pour une application donnée.

8.3 Poursuite du développement de l'alliage de Ti-22Al-25Nb

Les travaux d'implémentation de l'intermétallique à base d'aluminures de titane Ti-22Al-25Nb ont mis en avant la difficulté d'obtenir des échantillons sains en sortie d'impression sur une

machine de faible capacité (P_{max} = 200 W) et sans contrôle de la température de la chambre. Cependant, si une fois retirés de la plaque d'impression, les échantillons bruts possédaient tous des fissures, certains échantillons ne présentaient pas de fissures visibles à l'œil nu lorsqu'ils étaient encore soudés à la plaque. Le retrait de ces échantillons se faisant de manière mécanique à l'aide d'un marteau et d'un burin, il a été supposé que certaines fissures pussent être causées par de trop grandes contraintes générées lors de cette étape. Une étude supplémentaire a donc été envisagée, consistant à réaliser une étape de post-traitement avant le retrait des échantillons.

Pour cela, les 45 échantillons cylindriques de l'étude précédente (Tableau 7-1) ont été à nouveau produits puis simultanément soumis à un traitement de recuit à 950 °C pendant 2h (d'après les résultats d'une étude de (Zhou et al., 2021)), sous circulation d'argon à un débit constant de 20 l/min sans avoir été retiré des plaques de fabrication. A leur sortie de l'enceinte de traitement thermique, certains échantillons présentaient des signes d'oxydation assez prononcés (Figure 8-8), mettant en avant la nécessité d'un contrôle accru de l'étanchéité de celle-ci.

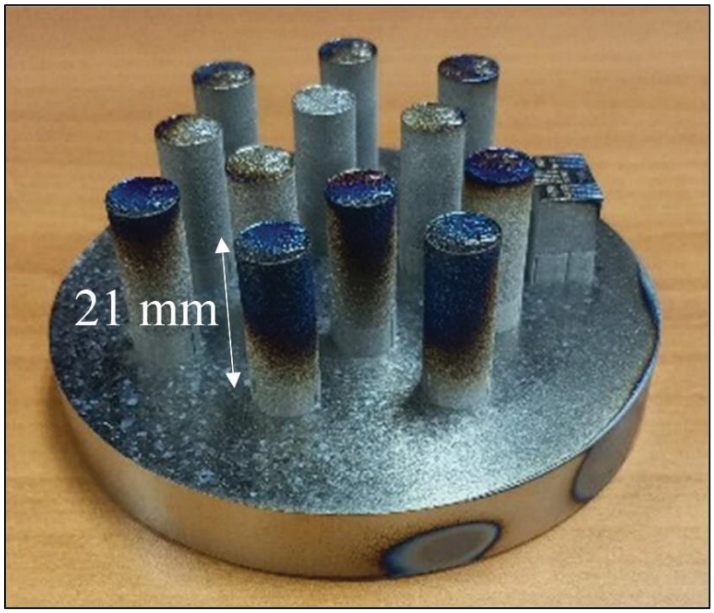

Figure 8-8 : Photo d'une plaque de fabrication après post-traitements montrant une coloration bleutée des échantillons signifiant le phénomène d'oxydation

8.3.1 Phénomène de fissuration

Après avoir été retirés des plaques de fabrication, seuls très peu d'échantillons présentaient des fissures visibles à l'œil nu. Des analyses de radiographies par rayons X ont donc été réalisés sur tous les cylindres et ont mis en avant une corrélation entre les phénomènes de fissuration et la densité d'énergie volumique du laser. En effet, comme illustré Figure 8-9a, seuls les 12 échantillons produits avec les sets de paramètres E, F et I, correspondant aux plus faibles niveaux d'énergie volumique du laser ($VED \leq 100 J/mm^3$) pour des taux de production de 2.5 et 5 cm^3/h, ne présentaient pas de fissure après post-traitement. Aussi, tous les échantillons possédant une énergie linéique $LED > 0.45$ J/mm possèdent des fissures (Figure 8-9b), permettant ainsi d'établir une limite supplémentaire lors du choix des paramètres de fabrication.

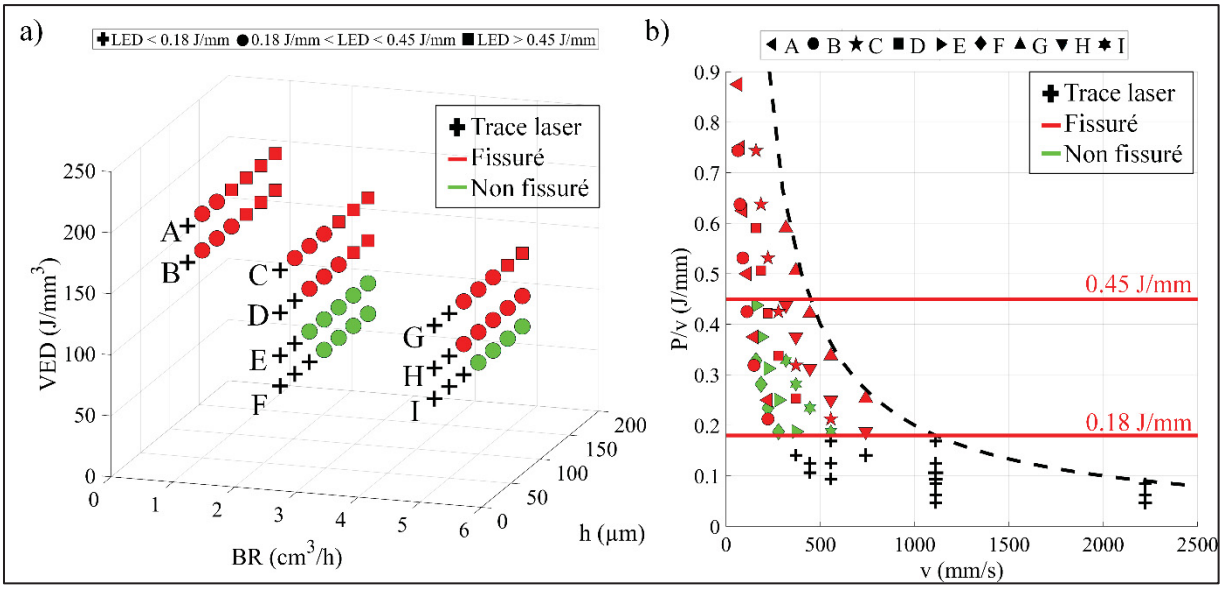

Figure 8-9 : Résultats d'analyses par radiographie à rayons X mettant en avant les phénomènes de fissuration pour chacun des ensembles de paramètres en fonction a) de la densité d'énergie volumique VED, du taux de production BR et de l'écart vecteur h et b) de la densité d'énergie linéique P/v et de la vitesse v

Des analyses supplémentaires de microtomographie à rayon X, diffraction à rayons X, observations microscopiques et des tests de microdureté ont alors été menés sur ces 12 échantillons sains afin d'analyser leur propriétés physiques et mécaniques.

8.3.2 Analyses structurales et mécaniques des échantillons sains

8.3.2.1 Densité

Une analyse de la porosité a été menée sur les scans 3D obtenue par microtomographie à rayons X à partir d'une approche d'apprentissage profond, compte tenu d'un effet de bord (*beam hardening* en anglais) trop important (Figure 8-10a). Cet effet se caractérise par une variation significative des niveaux de gris sur chaque image, jusqu'à un halo blanc en bordure d'échantillon, rendant la segmentation de la porosité difficile et peu précise. Le module d'apprentissage profond du logiciel DragonFly (Montréal, Canada) a été retenu pour segmenter la porosité de manière à s'affranchir de cet effet de bord (Figure 8-10b). Pour cela, trois à quatre images sont sélectionnées pour chaque échantillon et manuellement segmentées afin de servir de référence au modèle. L'entraînement se fait alors par itérations successives, jusqu'à atteindre une convergence. Une fois le modèle entrainé, il est appliqué à l'ensemble des images obtenues pour chaque échantillon. La densité de l'échantillon ainsi que le volume et la sphéricité de chaque pore sont extraits de cette analyse.

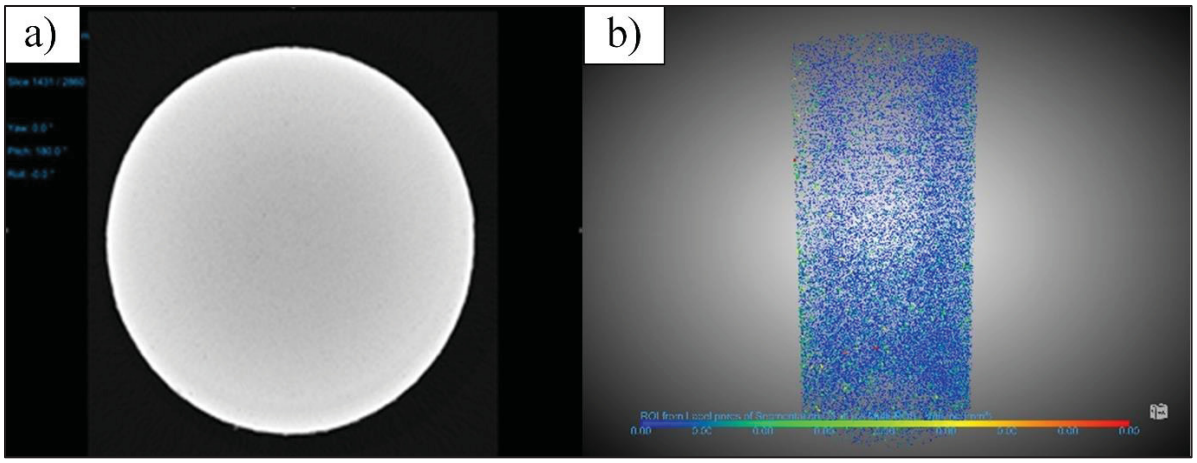

Figure 8-10 : Vue d'une tranche dans le plan XY normal à la direction de fabrication mettant en avant le phénomène de *beam hardening* et b) extraction de la porosité de l'échantillon E-175

La densité extraite pour chacun des 12 échantillons est présentée sur la Figure 8-11a dans l'espace 3D VED-BR-h. La plupart des échantillons disposent d'une densité supérieure à 99,5%, exceptés les échantillons Q 150, 175 et 200 pour lesquels la densité descend jusqu'à ~93%. Cela peut notamment s'expliquer par des taux de recouvrement très faibles, voire négatif, sur ces échantillons (de 9 à -40% Tableau 7-3), signifiant que la passe de laser suivante ne recouvre pas suffisamment la passe précédente. Les analyses des distributions de porosité ont mis en avant des pores relativement larges et de sphéricité de moyenne à élevée (Figure 8-11b), signe d'un manque de fusion. Il est ainsi possible de statuer qu'une absence de fissures se compense par une augmentation de la porosité. Il est donc nécessaire de trouver un compromis ou bien de recourir à d'autres types de post-traitements ayant fait leur preuve pour la réduction simultanée des fissures et des porosités comme la compression isostatique à chaud par exemple (Polozov et al., 2021, 2019).

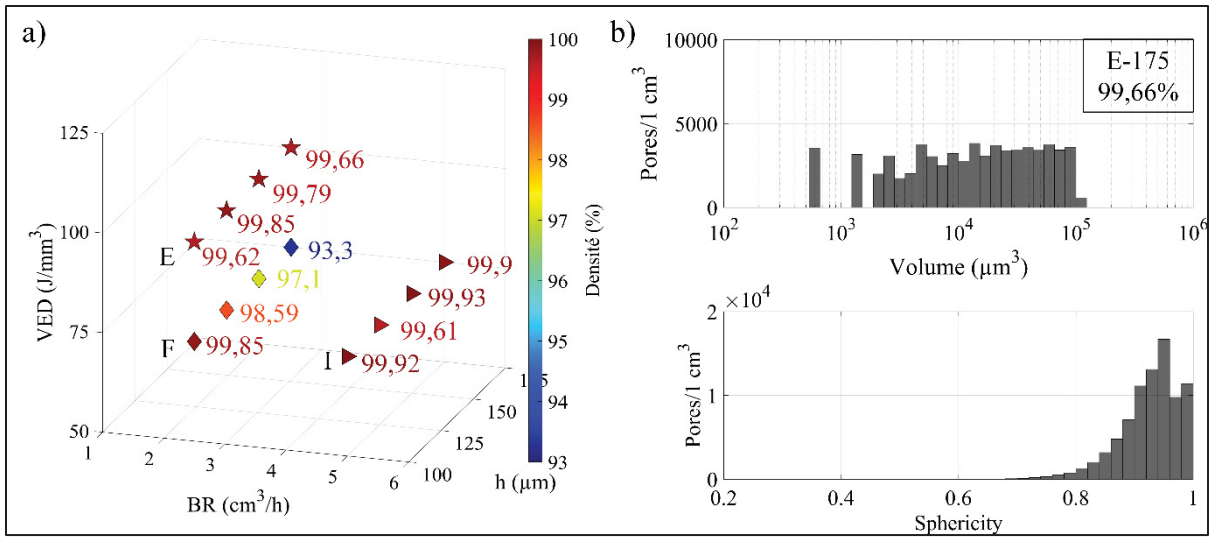

Figure 8-11 : a) Densité mesurée par µCT des échantillons imprimés sans fissures en fonction de la densité volumique d'énergie VED, du taux de production BR et de l'écart vecteur h et b) distributions du volume et de la sphéricité des pores contenus dans l'échantillon E-175

8.3.2.2 Microstructure et microdureté

Les analyses par diffraction à rayons X ont révélées la présence des phases B2, α_2 et O dans chacun des 12 échantillons (Figure 8-12a). Les observations au microscope optique et au microscope électronique à balayage ont permis de mettre en avant une microstructure semblable d'un échantillon à l'autre, constituée de grains colonnaires de B2/β (Figure 8-12b) dans lesquels se trouvent des aiguilles de α_2 et O et des concentrations de α_2 aux joints de grains (Figure 8-12c).

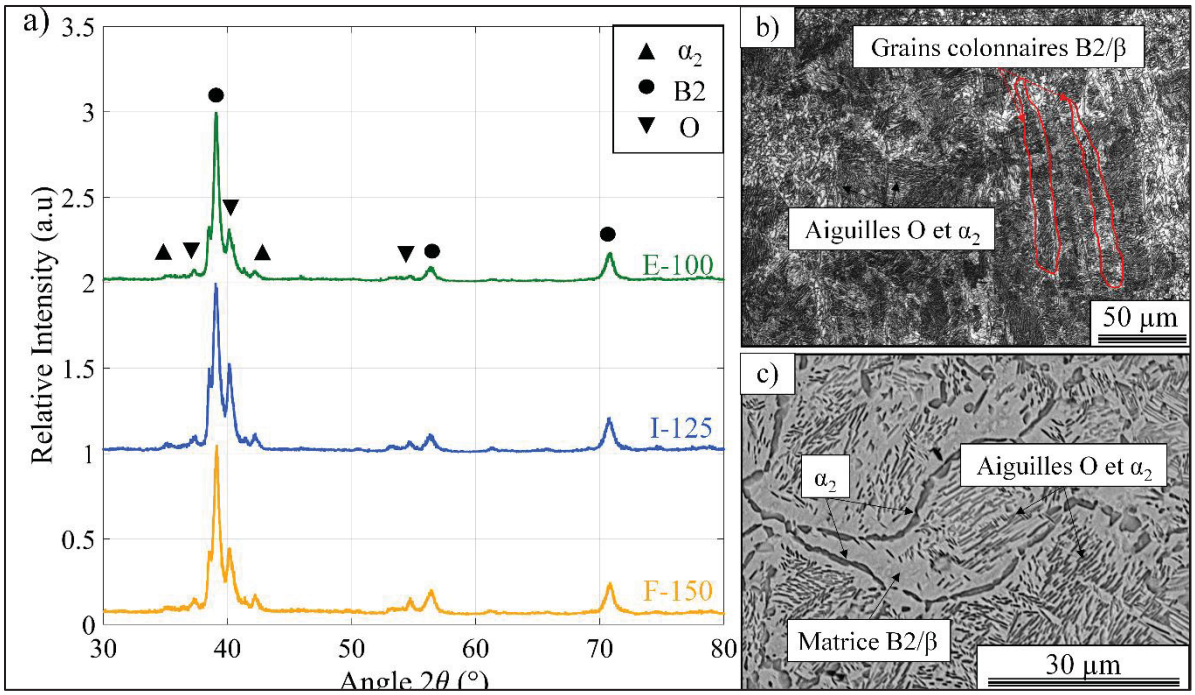

Figure 8-12 : a) Résultats d'analyse par diffraction à rayons X des échantillons E-100, I-125 et F-150; observations b) confocal et c) MEB de l'échantillon E-100 mettant en avant des grains colonnaires de β primaire et des aiguilles de O et de α_2 et de la phase α_2 concentrée aux joints de grains

Les tests de microdureté ont mis en avant des résultats semblables pour tous les échantillons sans que de corrélation puisse être formulée ni avec les paramètres de fabrication, ni la densité mesurée (Figure 8-13). Par ailleurs, ces résultats sont similaires (compris entre 300 et 425 HV0.3) à ceux obtenus par d'autres auteurs à l'issu de différents post-traitements permettant de former des microstructures comparables (Polozov et al., 2019).

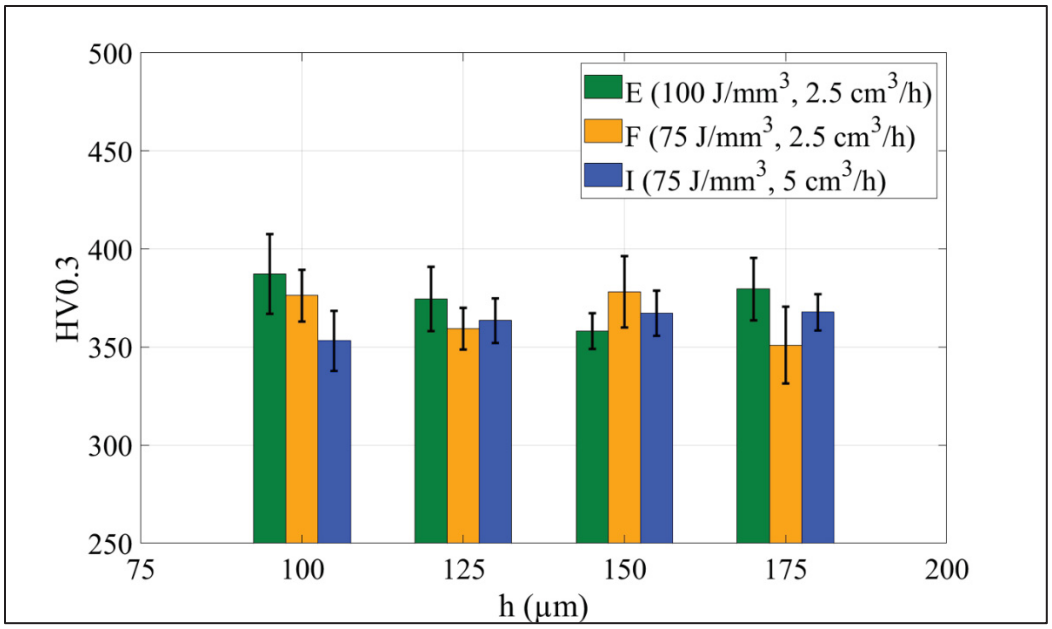

Figure 8-13 : Histogrammes des mesures de microdureté sur les échantillons sans fissures des ensemble E, F et I en fonction de l'écart vecteur *h*

8.3.3 Changement de géométrie

Compte tenu de ces résultats prometteurs sur les échantillons cylindriques, quatre de ces paramétries (E-100, F-100, I-125 et E-175) ont été sélectionnées pour produire des éprouvettes prismatiques (17 x 8 x 81 mm) en vue d'un usinage pour des tests de traction (Figure 6-17b) après post-traitements. Aussi, la paramétrie I-125 a arbitrairement été retenue pour la production d'artéfacts pour des mesures de parois et interstices (Figure 6-2). Cependant, tous les échantillons prismatiques présentaient de larges fissures visibles à l'œil nu (Figure 8-14a) en sortie d'impression et les artéfacts démontraient une forte distorsion et se sont partiellement arrachés de leurs supports de fabrication en cours de production (Figure 8-14c). Il est alors possible de conclure que les contraintes internes générées lors de la fabrication ne permettent pas d'envisager le passage à des géométries plus larges ou plus complexes dans de telles conditions.

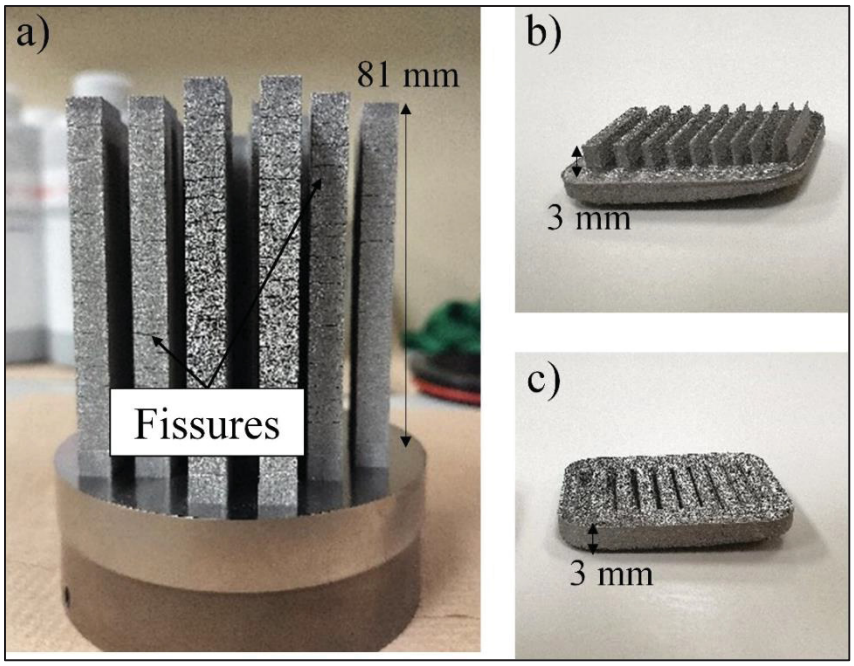

Figure 8-14 : a) Photo d'une plaque de fabrication d'éprouvettes prismatiques fissurées et photos des géométries de test d'épaisseur de b) parois et c) interstices mettant en avant le phénomène de distorsions

8.3.4 Conclusion

En conclusion, bien que l'application d'un post-traitement avant manipulation des échantillons ait permis d'obtenir des échantillons sains en Ti-22Al-25Nb produits sans contrôle de la température dans la chambre d'impression, les contraintes internes générées par le procédé ne permettent pas le passage à des géométries plus larges ou plus complexes. L'approche utilisée pour le développement des paramétries de fabrication ayant parcouru l'ensemble des paramètres disponibles avec cet équipement, il est possible d'affirmer qu'il n'est pas possible de poursuivre le développement de cet alliage dans de telles conditions. Des solutions seraient le passage à un équipement possédant une plus large gamme de paramètres ou un faisceau laser de diamètre plus large, ou bien le recourt à un préchauffage de la plateforme de fabrication.

8.4 Limitations du modèle numérique lors de la prédiction de bains de fusion d'alliages de titane

Le modèle numérique développé et utilisé pour prédire la densité des pièces imprimées en métaux réfractaires est basé sur l'analyse simplifiée d'un champ thermique généré dans le lit de poudre par une source de chaleur mobile. À partir de cette modélisation du champ thermique, les dimensions du bain de fusion (largeur W, profondeur D et longueur L) sont extraites comme étant les limites à partir desquelles ce champ thermique excède la température de fusion du matériau. Une fois ses dimensions extraites, des ratios de recouvrement sont calculés avec certains paramètres d'impression (écart-vecteur et épaisseur de couche) et sont ensuite associés à la densité mesurée des pièces afin de créer la fonction de prédiction de la densité. Ainsi, une première étape à la validation de ce modèle est de contrôler les prédictions des dimensions de bains de fusion. Pour cela, une approche expérimentale simple consiste à générer des traces de passe unique de laser et de comparer les mesures de largeur et de profondeur à celles générées par le modèle.

Avant son utilisation avec l'alliage de titane Ti-6Al-2Sn-4Zr-6Mo, une étude préliminaire a été réalisée sur l'alliage Ti-6Al-4V, plus étudié dans la littérature et pour lequel 155 mesures de largeur et 107 mesures de profondeur ont pu être recensées en provenance de 4 groupes de recherche possédant des équipements différents (Buffa et al., 2023; Gong et al., 2016; Vaglio et al., 2020; Jingjing Yang et al., 2016). Les modèles des équipements et les rayons du faisceau laser sont fournis en Tableau 8-6. Notez que dans tous les cas, la longueur d'onde du faisceau est égale à 1,07 µm et la température de la plateforme à 20°C (aucun préchauffage). Enfin, ne disposant pas des informations sur les densités du lit de poudre, cette dernière a été fixée à 0,6, la valeur moyenne obtenue pour les poudres de cette étude.

Tableau 8-6 : Groupes d'auteurs étudiés, leur modèle d'équipement et le rayon du faisceau laser associé

Auteurs	Modèle	Rayon du faisceau laser (µm)
(Vaglio et al., 2020)	Concept Laser M2 Cusing	25
(Buffa et al., 2023)	SLM 280HL	41
(Gong et al., 2016)	EOS M270	50
(Jingjing Yang et al., 2016)	LSNF-2	50

Les propriétés physiques de l'alliage constituant des données d'entrée du modèle (densité, température de fusion, conductivité thermique, capacité spécifique massique et résistivité électrique) ont été obtenue à partir du logiciel JMatPro (Tableau 8-7). Comme pour les réfractaires, une première étude a été menée pour statuer sur la température à laquelle ces propriétés devaient être considérées et encore une fois, 80% de la température de fusion (0,8Tm) a été retenue comme celle permettant de minimiser les écarts entre les mesures expérimentales et les prédictions du modèle.

Tableau 8-7 : Propriétés du Ti-6Al-4V à 0.8Tm retenues comme données d'entrée du modèle numérique

Densité du matériau dense (kg/m^3)	Température de fusion (K)	Température des propriétés (K)	Conductivité thermique (W/m.K)	Capacité spécifique massique (J/kg.K)	Résistivité électrique (Ohm.m)
4255	1963	1570 (0,8Tm)	27	700	$1,7*10^{-6}$
		298 (RT)	5	550	$1,8*10^{-6}$

Les comparaisons entre les prédictions du modèle et les dimensions des bains de fusion mesurées expérimentalement sont présentées en Figure 8-15a,c. En ce qui concerne les largeurs, plus les traces sont irrégulières ou discontinues et plus les prédictions du modèle s'éloignent des mesures. En revanche, lorsque les traces sont continues, les prédictions rejoignent les mesures (Figure 8-15b) et la régression linéaire associée permet de valider la pertinence des prédictions avec un coefficient directeur de 1,06, une constante négligeable, un R^2adj = 0,82 (proche de 1) et une erreur $RMSE$ = 28. Au sujet des profondeurs en revanche,

les prédictions s'éloignent des mesures, et ce, peu importe la continuité de la trace et de manière différente en fonction des auteurs (Figure 8-15d). Ainsi, le modèle ne peut être validé pour les profondeurs.

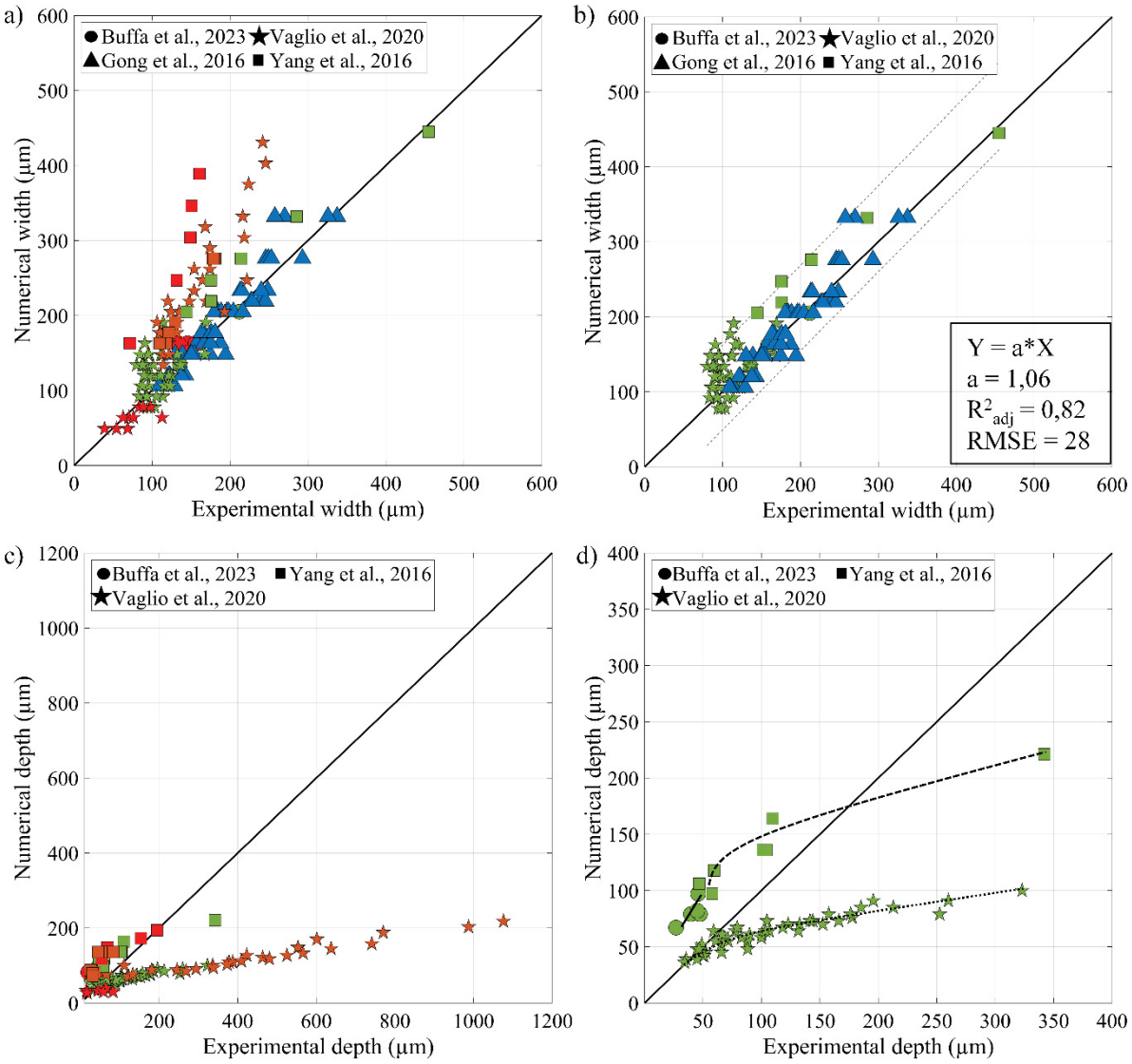

Figure 8-15 : Prédictions numériques face aux mesures expérimentales (vert pour trace continue, orange pour irrégulière, rouge pour discontinue et bleu pour non-indiquée); largeurs a) toutes les traces et b) traces continues ou non-indiquées uniquement; profondeurs : c) toutes les traces; d) traces régulières uniquement.

Les différences observées entre les mesures expérimentales et les prédictions ont différentes origines. D'abord, la précision des mesures expérimentales joue un rôle important puisque d'un auteur à l'autre, la méthode de mesures et les équipements diffèrent, de même qu'il est difficile de statuer sur la pertinence d'une mesure faite sur une passe unique de laser discontinue ou irrégulière. Ensuite, il est important de rappeler que le modèle numérique est basé sur une équation de transfert thermique fortement simplifié. D'abord, seuls quelques paramètres (10) servent d'entrées à ce modèle quand le procédé comporte à lui seul plus d'une centaine de paramètres pouvant avoir une influence de manière interdépendante ou corrélée (Centre technique des industries mécaniques, 2019). Ensuite, les propriétés du matériau sont considérées comme constantes et choisies à 0.8Tm alors qu'elles varient avec la température et lors de changements d'état. Enfin, une des hypothèses majeures de ce modèle est la considération des phénomènes de conduction uniquement (« Handbook of the EuroLaser Academy. 2 », 1998), négligeant ainsi les phénomènes de convection, de rayonnement ou tout autre phénomène irrégulier. Or, comme observé dans la littérature (CHAPITRE 1 section 1.4.2) ou dans nos travaux sur l'alliage de Ti-6Al-2Sn-2Zr-6Mo (CHAPITRE 5 section 5.5.3.3), les alliages de titane sont particulièrement sujets aux effets de fusion irrégulière comme l'effet « *keyhole* ». Cela explique notamment pourquoi les prédictions de profondeurs sont si éloignées des mesures expérimentales contrairement aux prédictions des largeurs qui s'alignent avec les expérimentations lorsque les traces obtenues sont continues.

Puisque les prédictions faites sur les bains de fusion générés ne sont pas en adéquation avec les expériences réalisées pour l'alliage de titane $\alpha + \beta$ Ti64, il n'est alors pas possible de passer à l'étape suivante liant les ratios de recouvrement avec la densité des pièces produites. Des études supplémentaires sur les limites du modèle sont à poursuivre, notamment au sujet d'autres métaux et alliages ou encore de la validation de la longueur des bains de fusion. En effet, cette dimension n'a pas su être vérifiée dans le cadre de ses travaux et nécessite le recours à des méthodes d'acquisition in-situ du champ thermique généré lors de la fabrication.

CONCLUSION

L'implémentation de nouveaux métaux et alliages par fusion laser sur lit de poudre pour des applications à haute température est complexe, en raison des phénomènes multiphysiques en jeu et du grand nombre de paramètres influents. Dans cette étude, une démarche basée sur l'analyse des bains de fusion de manière numérique ou expérimentale, vers des échantillons pour analyses structurales et mécaniques, jusqu'à des géométries plus complexes, a été employée sur différents groupes de métaux et alliages en utilisant un équipement à puissance limitée sans contrôle de la température dans la chambre d'impression.

Pour chaque matériau d'étude (métaux réfractaires, alliages de titane ou intermétalliques à base d'aluminures titane), des stratégies ont été mises en place pour réduire les plans d'expériences, soit par modélisation numérique ou par définition de critères expérimentaux. Dans tous les cas, la maîtrise des paramètres de fabrication s'est révélée cruciale pour éviter les fissurations, optimiser la densité, contrôler la microstructure et améliorer les propriétés mécaniques à température ambiante et jusqu'à haute température.

Si pour les métaux réfractaires, les paramètres optimisés ont permis d'obtenir des propriétés physiques et mécaniques compétitives avec les procédés conventionnels de métallurgie des poudres, les résultats obtenus sur l'alliage de titane nouvelle génération de type $\alpha + \beta$ Ti6Al-2Sn-4Zr-6Mo ne permettent pas d'atteindre les performances visées, et ce en dépit de l'application de post-traitements. Pour l'intermétallique à base d'aluminures de titane orthorhombique Ti-22Al-25Nb en revanche, aucun échantillon brut n'a pu être produit sans fissures.

Un prototype d'injecteur micro-prémélangé a été produit en molybdène pur, mais son implémentation dans le dispositif réel n'a pas pu être envisagée en raison de phénomènes d'oxydation importants révélés lors d'essais mécaniques à haute température. Suite à ces travaux, il apparaît que les métaux réfractaires pourraient être implémentés dans des dispositifs travaillant sous atmosphère contrôlée, mais des études sur les barrières de protection

environnementales doivent encore être menées pour leur implémentation dans une plus large gamme d'applications. Concernant les alliages de titane en revanche, d'autres travaux sur le développement de post-traitements doivent être menés avant d'envisager leur intégration dans des dispositifs.

Ainsi, cette démarche a permis d'optimiser rapidement et à faible coût les paramètres de production de différentes pièces, ou de définir les limites d'un équipement. Cependant, des recherches spécifiques restent nécessaires pour envisager l'intégration de ces matériaux dans un dispositif réel.

APPENDICE A

Tableau-A A-1: Printed specimens: nomenclature, plan of experiments, predicted density, measured density and error between the densities

Name	Hatching Space (µm)	Power (W)	Speed (mm/s)	Volumetric Energy Density (J/mm^3)	Built Rate (cm^3/h)	Predicted Density (%)	Image Analysis Density (%)	Absolute Error between Densities (%)
A-20	20	140	200	1167	0.43	86.9	87.4	0.5
B-20		89	197	750	0.43	72.8	82.6	9.9
C-20		179	398	750	0.86	89.7	84.7	5.0
D-20		100	398	417	0.86	72.8	69.5	3.3
E-20		188	750	417	1.62	87.2	78.3	8.9
A-30	30	140	133	1167	0.43	90.2	87.7	2.5
B-30		89	131	750	0.43	78.2	75.9	2.3
C-30		179	265	750	0.86	93.8	92.4	1.4
D-30		188	500	417	0.86	78.2	82.1	3.9
E-30		100	265	417	1.62	92.2	82.6	9.6
A-40	40	140	100	1167	0.43	91.9	88.3	3.6
B-40		90	100	750	0.43	77.4	78.5	1.2
C-40		179	199	750	0.86	94.8	89.8	5.0
D-40		188	375	417	0.86	77.4	80.5	3.1
E-40		100	200	417	1.62	93.4	91.4	1.9
A-60	60	140	67	1167	0.43	91.1	90.2	0.9
B-60		90	67	750	0.43	74.6	90.2	15.6
C-60		179	133	750	0.86	95.1	88.2	6.9
D-60		100	133	417	0.86	78.3	78.4	0.1
E-60		188	250	417	1.62	94.2	92.1	2.1
A-80	80	140	50	1167	0.43	91.2	91.2	0.0
B-80		180	100	750	0.43	72.1	84.3	12.3
C-80		89	49	750	0.86	94.2	89.2	5.0
D-80		188	188	417	0.86	78.2	85.9	7.7
E-80		100	100	417	1.62	94.2	93.2	1.1

Name	Hatching Space (μm)	Power (W)	Speed (mm/s)	Volumetric Energy Density (J/mm^3)	Built Rate (cm^3/h)	Predicted Density (%)	Image Analysis Density (%)	Absolute Error between Densities (%)
A-100	100	140	40	1167	0.43	89.7	91.2	1.5
B-100		90	40	750	0.43	70.0	83.5	13.5
C-100		179	80	750	0.86	93.9	93.5	0.4
D-100		188	150	417	0.86	76.3	81.5	5.2
E-100		100	80	417	1.62	93.1	91.8	1.3

Tableau-A A-2: Printed specimens: nomenclature, pore density, pore size, yield strength at 0.2% offset, ultimate compression strength, strain under maximum load and maximum compression strain

Name	Pore Density (p/mm^2)	Pore size $DE50_p$ (μm)	YS at 0.2% (MPa)	UCS (MPa)	Strain under Maximum Load (%)	Maximum Compression Strain (mm/mm)
A-20	101	95	357	460	2.9	0.10
B-20	166	85	222	335	3.8	0.08
C-20	123	120	315	415	2.6	0.07
D-20	128	120	274	392	4.2	0.11
E-20	92	125	320	425	3.3	0.09
A-30	195	80	418	592	5.4	0.13
B-30	120	100	258	449	6.0	0.11
C-30	157	95	537	705	2.9	0.07
D-30	119	85	288	459	5.7	0.11
E-30	75	120	376	542	4.7	0.10
A-40	96	85	323	549	5.3	0.12
B-40	187	85	275	492	6.8	0.12
C-40	114	90	547	635	3.5	0.11
D-40	292	80	376	631	8.1	0.14
E-40	117	95	544	694	3.5	0.09
A-60	112	90	513	739	6.7	0.13
B-60	209	75	396	629	7.7	0.14
C-60	116	90	526	652	3.8	0.09
D-60	225	80	394	599	7.6	0.13
E-60	106	90	669	810	3.3	0.09
A-80	116	70	458	735	8.4	0.14
B-80	185	75	347	617	10.2	0.16
C-80	149	85	540	651	2.9	0.08
D-80	143	70	396	671	11.0	0.18
E-80	76	80	676	867	6.9	0.15
A-100	192	60	521	799	9.6	0.16
B-100	244	70	368	655	10.7	0.17
C-100	195	65	584	803	6.6	0.12
D-100	206	85	449	662	9.0	0.17
E-100	158	75	591	777	5.9	0.11

APPENDICE B

Tableau-A B-1: Printed specimens: nomenclature, plan of experiments, predicted density, measured density, error between the densities

Name	Hatching Space (μm)	Power (W)	Speed (mm/s)	Volumetric Energy Density (J/mm^3)	Built Rate (cm^3/h)	Predicted Density (%)	Image Analysis Density (%)	Absolute Error between Densities (%)
A-40	40	140	100	1167	0.43	94	94	0
B-40		90	100	750	0.43	91	87	4
C-40		179	199	750	0.86	95	89	6
D-40		96	199	400	0.86	93	84	11
E-40		180	375	400	1.62	95	90	6
A-60	60	140	67	1167	0.43	98	92	7
B-60		90	66	750	0.43	94	80	18
C-60		179	133	750	0.86	98	96	2
D-60		96	133	400	0.86	94	84	11
E-60		180	250	400	1.62	98	93	5
A-80	80	140	50	1167	0.43	98	94	5
B-80		90	50	750	0.43	96	90	6
C-80		179	100	750	0.86	99	96	3
D-80		96	100	400	0.86	96	89	8
E-80		180	188	400	1.62	98	95	3
A-100	100	140	40	1167	0.43	98	94	4
B-100		90	40	750	0.43	95	92	4
C-100		179	80	750	0.86	98	95	4
D-100		96	80	400	0.86	95	91	5
E-100		180	150	400	1.62	98	94	5
A-120	120	140	33	1167	0.43	96	93	3
B-120		90	33	750	0.43	95	91	3
C-120		179	66	750	0.86	98	95	3
D-120		96	66	400	0.86	95	89	6
E-120		180	125	400	1.62	97	96	1

Tableau-A B-2: Printed specimens: nomenclature, plan of experiments, yield strength at 0.2% offset, ultimate compression strength and strain under maximum load

Name	Hatching Space (µm)	Power (W)	Speed (mm/s)	Volumetric Energy Density (J/mm^3)	Built Rate (cm^3/h)	YS at 0.2% (MPa)	UCS (MPa)	Strain under Maximum Load (%)
A-40	40	140	100	1167	0.43	230	380	11
B-40		90	100	750	0.43	220	510	21
C-40		179	199	750	0.86	300	480	11
D-40		96	199	400	0.86	250	490	19
E-40		180	375	400	1.62	290	430	9
A-60	60	140	67	1167	0.43	280	550	17
B-60		90	66	750	0.43	240	550	23
C-60		179	133	750	0.86	340	510	11
D-60		96	133	400	0.86	270	530	21
E-60		180	250	400	1.62	330	500	11
A-80	80	140	50	1167	0.43	240	430	14
B-80		90	50	750	0.43	200	430	20
C-80		179	100	750	0.86	260	390	9
D-80		96	100	400	0.86	190	360	15
E-80		180	188	400	1.62	280	370	7
A-100	100	140	40	1167	0.43	240	430	14
B-100		90	40	750	0.43	200	410	18
C-100		179	80	750	0.86	280	390	8
D-100		96	80	400	0.86	200	380	15
E-100		180	150	400	1.62	270	350	6
A-120	120	140	33	1167	0.43	240	430	14
B-120		90	33	750	0.43	180	400	19
C-120		179	66	750	0.86	300	450	11
D-120		96	66	400	0.86	220	390	11
E-120		180	125	400	1.62	300	400	7

APPENDICE C

Tableau-A C-1: Printed specimens nomenclature, plan of experiments, µCT density, yield strength at 0.2% offset, ultimate compression strength, stain to failure, microhardness

Name	Hatching space (µm)	Power (W)	Scanning speed (v)	Volumetric Energy Density (J/mm^3)	Build Rate (cm^3/h)	Density µCT (%)	YS at 0.2% (MPa)	UCS (MPa)	δ (%)	HV (HV0.3)
A-50	50	188	556	135	5	99.91	1567	1636	8	472 ± 11
B-50		139	556	100	5	99.96	1333	1343	8	461 ± 9
C-50		69	556	50	5	97.77	955	1242	11	432 ± 18
D-50		42	556	30	5	85.49	474	773	10	x
E-50		139	1111	50	10	96.51	802	1013	10	423 ± 12
F-50		83	1111	30	10	81.42	512	1029	16	x
G-50		125	1667	30	15	85.31	587	1016	13	x
H-50		63	1667	15	15	68.49	201	767	29	x
A-75	75	188	370	135	5	99.84	1193	1193	6	473 ± 10
B-75		139	370	100	5	99.99	1122	1122	7	452 ± 20
C-75		69	370	50	5	98.42	846	966	8	412 ± 21
D-75		42	370	30	5	88.67	626	901	12	x
E-75		139	741	50	10	98.66	861	1024	8	418 ± 13
F-75		83	741	30	10	92.68	665	1122	12	x
G-75		125	1111	30	15	85.54	561	1033	13	x
H-75		63	1111	15	15	67.81	258	997	29	x
I-75		125	2222	15	30	70.84	245	969	30	x

Name	Hatching space (µm)	Power (W)	Scanning speed (v)	Volumetric Energy Density (J/mm^3)	Build Rate (cm^3/h)	Density µCT (%)	YS at 0.2% (MPa)	UCS (MPa)	δ (%)	HV (HV0.3)
A-100	100	188	278	135	5	99.79	985	985	6	484 ± 14
B-100		139	278	100	5	99.99	1150	1150	7	464 ± 20
C-100		69	278	50	5	97.72	888	1048	8	412 ± 21
D-100		42	278	30	5	89.48	598	1085	15	x
E-100		139	556	50	10	98.94	857	979	8	423 ± 18
F-100		83	556	30	10	88.32	574	864	10	x
G-100		125	833	30	15	86.95	580	917	11	x
H-100		63	833	15	15	76.10	230	875	28	x
I-100		125	1667	15	30	79.00	309	1078	29	x
A-125	125	188	222	135	5	99.83	859	859	6	480 ± 12
B-125		139	222	100	5	100.00	1051	1051	7	464 ± 35
C-125		69	222	50	5	98.84	928	1056	8	433 ± 14
D-125		42	222	30	5	94.70	645	1054	12	x
E-125		139	444	50	10	98.49	802	870	7	427 ± 15
F-125		83	444	30	10	88.40	602	929	11	x
G-125		125	667	30	15	88.57	578	956	12	x
H-125		63	667	15	15	73.18	270	920	27	x
I-125		125	1333	15	30	68.61	316	920	23	x

Name	Hatching space (µm)	Power (W)	Scanning speed (v)	Volumetric Energy Density (J/mm^3)	Build Rate (cm^3/h)	Density µCT (%)	YS at 0.2% (MPa)	UCS (MPa)	δ (%)	HV (HV0.3)
A-150	150	188	185	135	5	99.96	1004	1004	7	485 ± 15
B-150		139	185	100	5	99.98	1045	1045	7	447 ± 37
C-150		69	185	50	5	99.58	936	1026	7	409 ± 30
D-150		42	185	30	5	92.77	774	1264	17	x
E-150		139	370	50	10	99.55	750	902	8	411 ± 8
F-150		83	370	30	10	98.89	865	1046	8	x
G-150		125	556	30	15	97.53	759	1194	12	x
H-150		63	556	15	15	76.20	330	972	27	x
I-150		125	1111	15	30	77.45	292	923	26	x
A-175	175	188	159	135	5	99.99	1090	1090	7	475 ± 14
B-175		139	159	100	5	99.99	991	991	7	451 ± 42
C-175		69	159	50	5	99.41	943	1094	8	412 ± 12
D-175		42	159	30	5	90.89	701	1084	12	x
E-175		139	317	50	10	99.95	760	840	7	413 ± 22
F-175		83	317	30	10	98.09	853	853	7	x
G-175		125	476	30	15	94.86	804	956	8	x
H-175		63	476	15	15	77.32	363	849	20	x
I-175		125	952	15	30	75.49	295	856	24	x

ANNEXE I

MICRO-MIXING INJECTOR MANUFACTURING IN REFRACTORY METAL USING LASER POWDER BED FUSION PROCESS

X. Bellavance[a], A. Leclercq[b], T. Mouret[c], A. Landry-Blais[d], M. Picard[e], V. Brailovski[f]

[a,d,e]Createk Design Lab, Université de Sherbrooke,
2500 Bd de l'Université, Sherbrooke, Québec, Canada J1N 3C6
[a,b,c,f]LAMSI, École de Technologie Supérieure,
1100 Notre-Dame Ouest, Montréal, Québec, Canada H3C 1K3

Article de conférence présenté à
« Turbomachinery Technical Conference and Exposition,
Proceedings of ASME Turbo Expo 2025», juin 2025

Résumé

La décarbonation et la réduction des émissions polluantes sont au cœur des recherches dans le domaine de la combustion des turbines à gaz. L'un des sujets majeurs dans ce contexte est l'intégration de l'hydrogène, qui pose des défis de conception et des limites en termes d'opérabilité des chambres de combustion, en raison de ses températures de flamme plus élevées et de sa tendance à former des flammes attachées aux injecteurs. Ces caractéristiques impliquent des exigences de température d'opération plus élevées pour les injecteurs alimentés à l'hydrogène afin d'en étendre les capacités opérationnelles. Les métaux réfractaires présentent un intérêt particulier car leur température de fusion est nettement supérieure à celle des gaz en sortie de chambre de combustion, ce qui ouvre de nouvelles possibilités de conception. Cependant, plusieurs défis apparaissent, notamment en matière d'oxydation et de fabrication. Le procédé de fusion sur lit de poudre par laser (LPBF) gagne en popularité dans la fabrication d'injecteurs micro-mélangé en raison de sa capacité à produire des pièces à géométrie complexe et peut être appliqué aux métaux réfractaires, ouvrant ainsi de nouvelles perspectives pour la conception de ces derniers. Dans cette étude, un injecteur micro-mélangé

à petite échelle en molybdène a été fabriqué à l'aide du procédé LPBF afin de démontrer la faisabilité d'impression de ce type de pièce en métal réfractaire. La précision géométrique obtenue était acceptable pour répondre aux exigences des systèmes de combustion micro-mélangé. Des orifices de petite taille, de 0,3 mm de diamètre nominal (représentant les buses d'injection), ainsi que des parois fines de 0,3 mm (démontrant la possibilité d'imprimer des géométries complexes), ont été fabriqués avec succès. Un revêtement de type barrière de protection environnementale (EBC) a été développé en parallèle afin d'explorer les défis liés à la protection des pièces complexes produites par LPBF dans un environnement oxydant à haute température.

Abstract

The decarbonization and reduction of pollutant emissions are at the core of research in the field of gas turbine combustion. One of the hot topics in this regard is the integration of hydrogen, which comes with design challenges and combustor operability limits due to its higher flame temperatures and its propensity to form nozzle-attached flames. These characteristics lead to higher operating temperature requirements for hydrogen fuel injectors to extend their operability. Refractory metals are interesting because their melting temperatures are significantly higher than the combustor outlet temperatures, which opens up new design possibilities. However, multiple challenges, such as oxidation and manufacturing issues, arise with refractory metals. The laser powder bed fusion (LPBF) process is gaining momentum in the manufacturing of micro-mixing injectors because of its suitability to produce complex geometry parts. This additive manufacturing process can be applied to refractory metals, opening up new perspectives for micro-mixing injector designs. In this paper, a small-scale micro-mixing injector in molybdenum was manufactured using the LPBF process to demonstrate the printability of such parts in refractory metals. The geometric precision achieved was acceptable for micro-mixing combustion requirements. Small holes with a nominal size of 0.3 mm, representing injection nozzles, and 0.3 mm-thin walls, demonstrating the possibility to print complex geometries, were successfully produced. An environmental

barrier coating (EBC) was developed in parallel to explore the challenges of protecting complex LPBF parts from high-temperature oxidizing environment.

Introduction

Gas turbine research is primarily focused, among others, on the reduction of NOx and carbon emissions. Improving fuel composition, gas turbine efficiency and combustion strategy are among the main options for reaching these goals (Graver & Mukhopadhaya, 2022; Guellouh, Szamosi, & Simenfalvi, 2019).

Hydrogen is a promising fuel, being carbon-free and thus exempt from CO and CO_2 products from combustion (Cecere, Giacomazzi, Di Nardo, & Calchetti, 2023; Park, Shin, Park, Lee, & Choi, 2025). However, hydrogen has its own challenges, including a predisposition to high NOx emissions (H.H.-W. Funke, Beckmann, & Abanteriba, 2019). To minimize the NOx emissions, while using hydrogen, the selection of an adequate combustion strategy is essential. Since premix combustion cannot be used with hydrogen because of higher flashback and autoignition risks, micro-mixing combustion has surfaced as a potential combustor concept (Haj Ayed et al., 2015). Micro-mixing combustion is characterized by the injection of fuel through an array of small injection holes, thus mixing fuel and air at the smallest scale possible. The smaller the injection holes, the faster the mixing of fuel with air, and the lower the NOx emissions (Landry-Blais et al., 2022). Micro-mixing injectors, because of their geometric complexity, are in some instances 3D-printed.

Another challenge associated with the high reactivity of hydrogen is its propensity to attached flame combustion regime, which is the attachment of flames to the injection nozzles and increases the level of thermal stress in the injectors, thus leading to combustor operability limitations caused by material integrity issues (Durocher et al., 2024). Moreover, the formation of a higher amount of H_2O during hydrogen combustion increases convective heat transfer, thus potentially amplifying the level of thermal stress in the injector (O'Connor et al., 2024).

Therefore, the combustor operability range could be improved with materials suited for higher temperature operations.

Gas turbine efficiency is a direct function of the turbine inlet temperature (TIT) and the pressure ratio. Current high efficiency gas turbines have TITs approaching 1600 °C (Hada, Takata, Iwasaki, Yuri, & Masada, 2015; Kwon et al., 2019). To allow higher TITs, injectors and liners with higher operating temperatures are consistently required.

Current injectors are usually manufactured from nickel-based superalloys because of their outstanding mechanical properties at high temperatures. Their melting temperatures are usually about 1320-1450 °C, while their maximum operating temperatures, considering the usual gas turbine constraints and requirements, are up to around 1100 °C (Pollock & Tin, 2006). A mismatch between the gas turbine TITs and the maximum material operating temperatures limits design possibilities, since the injector material needs to be protected from flames. Ceramic matrix composites (CMCs) are attractive materials for high-temperature applications, but their use is limited to simple parts such as liners (Binner et al., 2020; Zeng & Chen, 2023).

Molybdenum is a member of the refractory metal family (W, Mo, Re, Nb and Ta), which consists of metals with the highest melting temperatures. It melts at ~2620 °C, a temperature that greatly exceeds turbine inlet temperatures (Alan M. Russel & Kok Loong Lee, 2005). Molybdenum also displays excellent mechanical properties at high temperatures (yield stress up to ~200 MPa at 1600 ºC), a low thermal expansion coefficient (~$7.5*10^{-6}$/K at 1600 °C) and a high thermal conductivity (~100W/(m.K) at 1600 °C), making it desirable for high-temperature applications (Shabalin, 2014; Škoro, Bennett, Edgecock, & Booth, 2012). In addition, its density (10.2 g/cm^3) is much lower than that of tungsten (19.3 g/cm^3), the refractory metal with the highest melting temperature. However, manufacturing parts with molybdenum is challenging in many ways, thus limiting the geometric complexity of produced parts.

Additive manufacturing (AM) is well suited for the fabrication of complex parts, especially internal flow channels (Ahmed, 2019; Kirsch & Thole, 2017). Laser powder bed fusion (LPBF) and electron beam powder bed fusion (EB-PBF, or also named in some instance electron beam melting (EBM)) are among the main AM processes used with molybdenum (Fernandez-Zelaia et al., 2021, p. 202, 2022; G. Huang et al., 2024; Oehlerking et al., 2022; Rebesan, Ballan, et al., 2021).

With the LPBF process, molybdenum parts are not exempt of process-induced flaws, like porosities. While some studies report excellent printed relative density (>99%), cracks represent a serious issue in molybdenum printing (G. Huang et al., 2024; Rebesan, Ballan, et al., 2021). Alternatively, the EB-PBF process provides a better control of microstructures and allows printing crack-free parts with high relative density (Fernandez-Zelaia et al., 2021, 2022). Also, in general, this process induces lower levels of residual stresses (Sanchez et al., 2021; L. Wang et al., 2023).

However, because the LPBF process has a greater resolution, which is critical for the fabrication of micro-mixing injectors, it was selected for this study. Yet, few complex parts have been printed in molybdenum using the LPBF process. The printability of a pump impeller has been demonstrated (Oehlerking et al., 2022). However, to the best of the authors' knowledge, to date, the printability of molybdenum micro-mixing injectors has not been demonstrated.

Oxidation at temperatures over 400 °C is another major issue with molybdenum (Alan M. Russel & Kok Loong Lee, 2005). Therefore, molybdenum cannot be used in high-temperature oxidizing atmospheres, such as combustion environments, without protection. Silicide-based environmental barrier coatings (EBC) are simple and effective, and provide protection up to 1650 °C against dry oxidation (Cai et al., 2017). The simplest coating process consists in depositing a silicon layer over the molybdenum substrate and forming a $MoSi_2$ layer from the diffusion of silicon into molybdenum. At high temperatures, the so-formed $MoSi_2$ coating reacts with oxygen to form a protective SiO_2 layer. Mo_5Si_3 and Mo_3Si interlayers also form

between the $MoSi_2$ layer and the molybdenum substrate (Y. Zhang et al., 2019). Since the Mo_5Si_3 and Mo_3Si interface layers have a poorer oxidation resistance than does the $MoSi_2$ layer, their thickness must be minimized, while that of the $MoSi_2$ must be maximized. The major issue with this coating is the pest oxidation which occurs at intermediate temperatures, between 400 °C and 600 °C, temperatures that are too low to properly trigger the protective SiO_2 formation (Mitra, 2019). To improve their oxidation protection performance, silicide coatings can be doped with boron or YSZ, for example (Cai et al., 2018; Perepezko, 2018). However, the presence of H_2O in the combustion environment represents a serious issue for such coatings, since the protective SiO_2 layer formed is susceptible to recession caused by the reaction with steam: $SiO_2(s) + 2H_2O(g) \rightarrow Si(OH)_4(g)$ (Golden & Opila, 2016). To the best of the authors' knowledge, for refractory metals, no EBC composition has been found yet to be perfectly suitable for operation under a gas turbine combustion environment.

While the composition of an EBC is crucial, its application method is also critical. The application method impacts the quality of the coating in terms of surface roughness, homogeneity and integrity, which affect the coating durability (Y. Zhang et al., 2022). There are many methods for forming the coating on the substrate (molybdenum), including chemical vapor deposition (CVD), halide-activated pack cementation (HAPC), hot-dipped silicon plating (HDS), and slurry coating among others (Fu et al., 2021, 2022). Slurry dipping is one of the simplest methods for forming a silicide coating on molybdenum. To this end, the substrate is dipped in a slurry solution, and then thermally treated in a vacuum or inert atmosphere (Chakraborty, 2016).

The coating application is usually done on polished surfaces because of the inherent difficulty of applying good quality coatings on rough surfaces. Moreover, complex parts are difficult to coat uniformly. Thus, coating 3D printed injectors is considerably challenging.

This paper explores the possibility of manufacturing molybdenum micro-mixing injectors using the LPBF process. To demonstrate the feasibility of the process, a small-scale injector was printed in molybdenum. Then, preliminary experiments with silicide coating of as-printed

molybdenum parts revealed significant challenges with the oxidation protection of 3D-printed refractory metal injectors.

Molybdenum micro-mixing injector manufacturing using LPBF process

A considerable challenge in obtaining micro-mixing injectors in refractory metal is their manufacturing. In the present work, the key geometries of micro-mixing injectors were first identified. Then, these key features were printed to determine the limits of the LPBF process and find the best-suited printing strategy. Next, a small-scale injector prototype was printed using the optimized printing strategy.

Dimension tailoring of key features

Micro-mixing injectors have complex geometries which allow to maximize their performances, with the most crucial one being the small injection holes shown in Figure-A I-1. As stated in section Manufacturing of a small-scale micro-mixing injector, the smaller the injection holes, the lower the NOx emissions. Therefore, to be viable, the LPBF process using molybdenum must produce holes as small as those achievable with conventional materials. Additionally, micro-mixing injectors have complex internal channels. Thinner walls offer more design freedom for complex internal flows. Thus, a series of test samples containing small holes and thin walls was printed to assess the minimum achievable dimensions of injection holes and the potential to print complex internal channel networks.

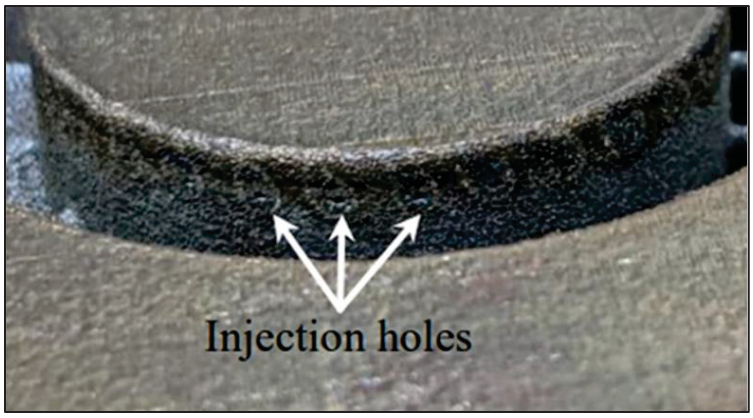

Figure-A I-1: Injection holes in an IN625 micro-mixing injector
Tiré de Landry-Blais et al. (2022)

Circular holes present poor printability because of the down-skin effect (Becker et al., 2024). In this study, in order to minimize this effect, printed holes had a pentagonal shape with a 90° interception at the top, as shown in Figure-A I-2 and Figure-A I-3. The nominal side dimensions of the holes ranged from 0.15 mm to 0.5 mm. The depth of holes has a direct impact on their printability. In fact, the smaller the injection hole side/depth ratio, the lower its printability. Therefore, two hole depths were tested: 0.35 mm (see Figure-A I-2) and 0.5 mm. Samples were printed using the printing parameters presented in Tableau-A I-1, with an initial border offset of 0.070 mm. These parameters are discussed in more detail in section Manufacturing of a small-scale micro-mixing injector. The plasma-spheroidized molybdenum powder used (Mo > 99.9%) was provided by Tekna Co. Ltd. (Sherbrooke, Canada). The particle size distribution (D_{10} = 12.6, D_{50} = 20.6 and D_{90} = 32.0 [μm]) was measured using a Beckman Coulter LS13 320 XR analyzer. The samples were printed under an argon atmosphere using a Truprint 1000 (TRUMPF GmbH, Ditzingen, Germany) 200 W printer. The areas of the printed holes were measured using an optical microscope (Keyence VR5000) and compared to their nominal (as-designed) values.

Figure-A I-2: Injection hole sample (0.35 mm depth)

Results obtained with the two sets of holes are presented in Figure-A I-3. The measured hole areas are compared to their nominal values (Y-axis). These values are presented as a function of the nominal side/depth ratio of the holes (X-axis). The minimum acceptable hole dimension is determined by a drop in the measured/designed values, which is equivalent to a drop in printability, highlighted by the dashed line in Figure-A I-3. For both hole depths (0.35 mm and 0.5 mm), the printability drops when the nominal side/depth ratio is around 0.825. The hole with a 0.15 mm nominal size and a 0.5 mm depth was even completely clogged. Thus, for a 0.5 mm hole depth, the printability drops when the nominal size of injection holes is smaller than 0.45 mm, while for a 0.35 mm hole depth, it drops when the nominal size of the injection hole is smaller than 0.30 mm. Therefore, for the molybdenum micro-mixing injector, the injection nozzle nominal size was set at 0.30 mm and the depth at 0.35 mm. These values are the same as those achieved with IN625 in (Landry-Blais et al., 2022).

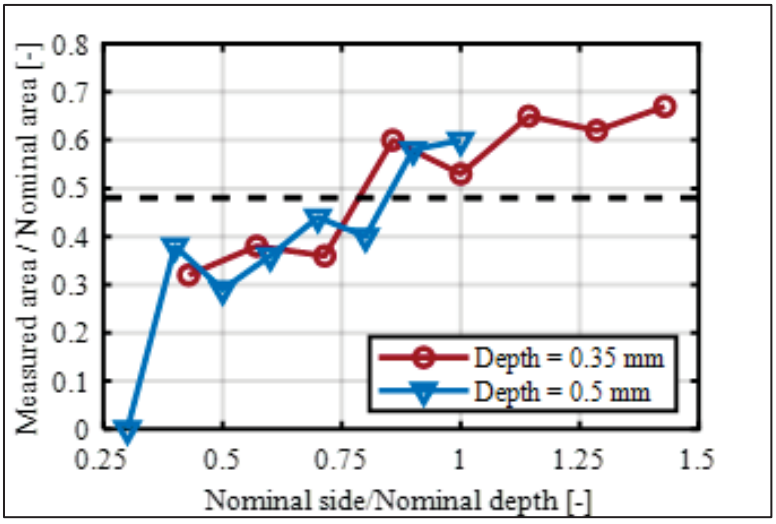

Figure-A I-3: Measurement of the injection hole samples

Next, the test sample shown in Figure-A I-4 was printed to determine the minimum printable wall thickness. The printed walls, height of 3 mm, had a thickness ranging from 0.2 mm to 2 mm. As shown in Figure-A I-4, the 0.2 mm thick wall had a defect caused by post-printing sample manipulations. Similarly to the injection hole samples, the wall thickness was measured using an optical microscope (Keyence VR5000). As shown in Figure-A I-4, the thicknesses of the printed walls were greater than their nominal values. A linear regression analysis (least-squares fit) with y-intercept was used to highlight deviations from the nominal thicknesses. The linear regression coefficient was equal to 0.995 with a y-intercept of 0.104 and the R^2_{adj} = 0.997. In addition, all the measured values, except for the wall with a 0.2 mm nominal thickness, were within a 5% error margin from the linear regression (see dashed lines in Figure-A I-5). All the offsets ($(Measured\ thickness - nominal\ thickness)/2$) of the walls were over 0.025 mm. Therefore, for the fabrication of the small-scale injector prototype, the laser border offset was increased from 0.070 mm to 0.095 mm. The minimum wall thickness of the injector prototype was taken at 0.3 mm, since the 0.2 mm-thick wall had an error margin exceeding 5% and was therefore considered less reliable.

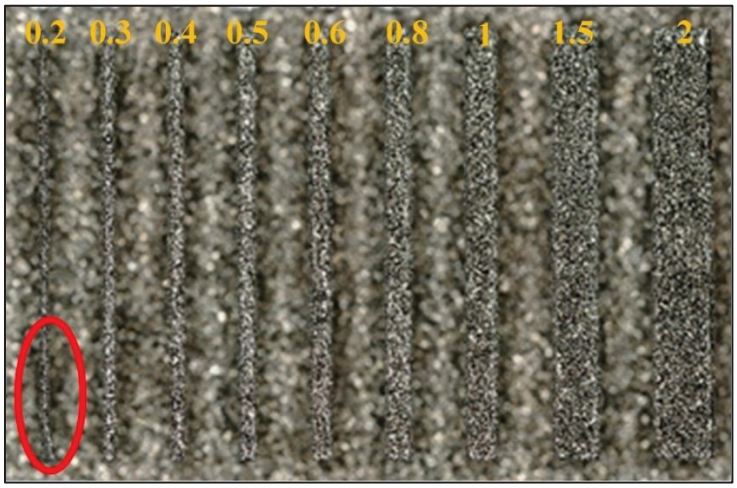

Figure-A I-4: Wall thickness sample [mm]

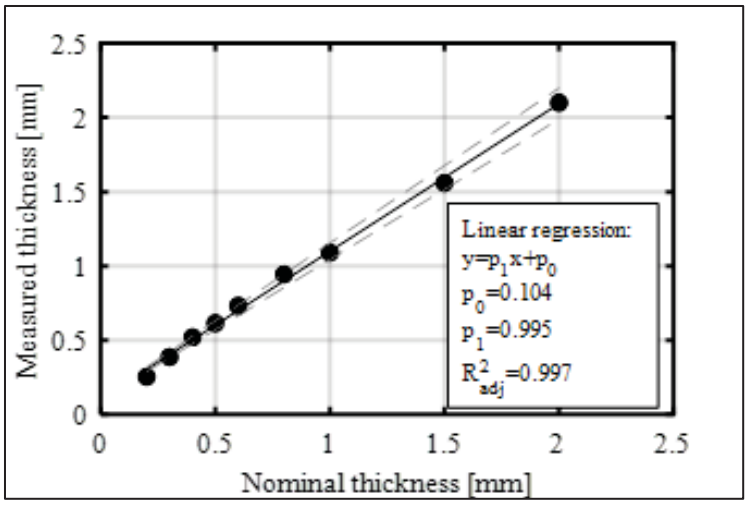

Figure-A I-5: Linear regression of the wall thicknesses

During printing of the samples, issues were observed with adhesion to the build plate. Spalling of the first layers occurred when printing large solid supports (2.5 cm x 3 cm). These issues were attributable to a mismatch between the molybdenum parts and the stainless steel build plate (Rebesan, Gennari, et al., 2021). On the other hand, printing thin supports (width ≤ 1 mm) caused neither adhesion nor printing issues. Therefore, for the fabrication of the small-scale injector prototype, thin supports (non-solid supports) were used.

Manufacturing of a small-scale micro-mixing injector

Based on the results of section Dimension tailoring of key features, a molybdenum small-scale injector prototype was manufactured. Tableau-A I-1 presents the printing parameters used. These parameters (laser power, laser speed, hatching space and layer thickness) allowed to print crack-free molybdenum parts with a relative density of ~96% and an ultimate compressive strength of 510 MPa at 20 °C, 260 MPa at 800 °C and 150 MPa at 1000 °C (details of the printing parameters selection will be presented in a soon-to-be-published paper).

Tableau-A I-1: Molybdenum small-scale injector printing parameters

Printing parameters	
Laser power	179 W
Laser speed	133 mm/s
Hatching space	0.060 mm
Layer thickness	0.030 mm
Contour	
Border offset	0.095 mm
Laser pattern strategy	
Pattern style	Stripes (ZigZag)
Stripe size	5 mm
Angle	45°
Incrementation	51°
Support	
Type	Non-solid: Block
Hatching	0.4 mm
Small-scale injector key dimensions	
Injection hole nominal diameter	0.3 mm
Smallest wall thickness	1 mm
Maximum overhang angle	45°
Outside diameter	30 mm
Height	32 mm

In addition to the small-scale injector prototype itself, its cut-view was also printed to allow easy visualization of its internal channels. The printed parts are shown in Figure-A I-6, and overall, they had no major defects. The 45° overhangs were well printed, no injection holes were clogged, and non-solid supports had no adhesion issues and manifested no spalling. No geometrical issues were thus observed with the printed small-scale injectors.

Figure-A I-6: Molybdenum small-scale injector cut-view (left)
and molybdenum small-scale injector (right)

However, when the inner and outer plenums of the injector were pressurized with air, leaks through the walls were observed. This could be explained by the fact that the printed molybdenum parts had pores (relative density ~ 96%) which had to be connected (open-cell porosities) to allow air to flow across the walls. Hot isostatic pressing (HIP) could be used as a potential solution to close pores, and ultimately to prevent leaks (Guan et al., 2023). Otherwise, a more powerful printer could be used to further optimize the printing parameters and obtain higher relative density (G. Huang et al., 2024). Alloying molybdenum (e.g., with rhenium) could also represent a suitable solution (Oehlerking et al., 2022).

On another note, the integration of a molybdenum injector into a combustor assembly also has its own challenges. Because of the extreme oxidation of molybdenum at high temperatures, connecting molybdenum injectors with other combustor parts using traditional welding techniques such as TIG (tungsten inert gas) or MIG (metal inert gas) is not possible. Thus, other bonding strategies must be sought. Fittings in combustors are in some instances made of stainless steel, and either diffusion or brazing can be used to bond molybdenum and stainless steel parts (Jia, Chen, Zhang, Huang, & Shen, 2022; Min, Mao, Deng, Wang, & Wang, 2020). Brazing was selected in this study because of its simplicity, since, compared to diffusion, it does not require the application of compressive pressure during the heat treatment. The brazing process described in (Min et al., 2020) was successfully applied in-house between

molybdenum samples and 316 stainless steel fittings, thus representing a potential solution for the implementation of a molybdenum injector into a combustor assembly. The brazing bond could be further improved using interlayers such as a copper sheet (Min et al., 2020).

The first steps to demonstrate the printability of molybdenum micro-mixing injectors were completed. The next step, in terms of manufacturing, should be to increase the printed relative density while avoiding crack-related issues.

EBC on AM molybdenum

As stated in section Introduction, molybdenum must be coated with an EBC to be viable in combustion environments. To explore the potential and discover the challenges associated with such coatings on LPBF molybdenum micro-mixing injectors, an EBC was applied to as-printed samples. The composition and structure of the EBC layers on these samples were then analyzed.

As a first step in the development of an acceptable EBC for combustion environments, a molybdenum disilicide coating ($MoSi_2$) was selected. This coating is known to be one of the most effective EBCs against dry oxidation of molybdenum.

Multiple factors must be considered in selecting the coating application method with the main criterion being its suitability for complex parts with internal channels. Micro-mixing injectors have complex internal channels and plenums, but above all, small injection holes. Therefore, the application method must also be able to coat all the surfaces, while avoiding hole clogging. Thus, processes such as slurry brushing and plasma spraying are unsuitable, and gaseous or liquid routes, such as slurry dipping, HAPC or CVD, must be preferred. The slurry dipping method was selected for this preliminary study, since it does not require highly specialized equipment, and the associated safety issues are less concerning. Moreover, slurry dipping is also suitable for multi-layer coatings. Therefore, this technology is suitable for potential

development of composite coatings for the protection of molybdenum against oxygen and steam in combustion environments.

Methodology

First, molybdenum 10 mm-diameter and 5 mm-height cylinder samples were printed. The top flat surfaces were polished with 80 grit SiC paper. Side surfaces were left as-printed (AM surfaces). The samples were cleaned with water in an ultrasonic bath for 30 minutes, after which they were cleaned with ethanol and left to dry for ~2 h.

Silicon powder (99.995% purity, D_{10} = 0.8, D_{50} = 3.9 and D_{90} = 8.1 [μm]) was used for the slurry. Polyvinyl butyral (PVB) was used as dispersant in the slurry and ethanol as the solvent. The ethanol was mixed with 20 vol% Si powder and PVB mixture. PVB represented 1 wt% of the Si and PVB mixture. The slurry was homogenized with a magnetic stirrer, at 1000 rpm for 1 h. The samples were dipped in the slurry solution at a speed of 50 mm/min using a semi-automatic custom-made system, immersed for 120 s in the slurry, withdrawn with the same speed of 50 mm/min, and left to dry for 24 h.

Next, the as-coated samples were heat treated at 1200 °C for 2 h with a heating rate of 5 °C/min and a cooling rate of 10 °C/min in a high-vacuum (< 10^{-5} mbar) oven (RD-Webb RD-G).

The composition of the coating was determined using X-Ray diffraction (XRD, PANalytical X'Pert PRO, K_α Co λ = 1.7902 Å). Afterward, the samples were cut in half and a scanning electron microscope (SEM, Hitachi TM3000) was used to analyze the structure of coating layers.

Results

First, an XRD analysis of the polished surfaces (see Figure-A I-7) showed that the coating contained mainly Mo_5Si_3 and $MoSi_2$ phases, which was expected from the diffusion of silicon into the Mo substrate. Next, Mo_3Si phase was detected as well, but with less intensity. This layer is generally formed between the substrate and the Mo_5Si_3 layer, or it can be dispersed in the Mo_5Si_3 layer. Traces of Mo, the substrate, and Si, which are the basis of the coating, were identified as well. However, at 45.7° (2θ), an unidentified peak was also observed, probably resulting from contamination during manipulations. In summary, the XRD analysis confirmed the formation of the expected silicide coating phases on the molybdenum substrate.

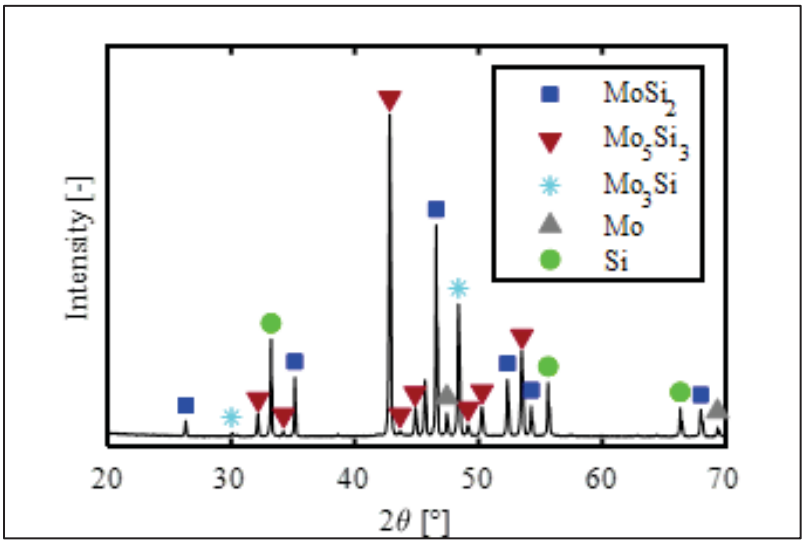

Figure-A I-7: XRD patterns of molybdenum silicide coating on polished surface of molybdenum sample (K_α Co)

Next, SEM was used to investigate the coating layers on the polished and as-printed surfaces. SEM imaging done on the polished surface showed a uniform $MoSi_2$ coating layer and a Mo_5Si_3 interlayer (see Figure-A I-8). However, the total coating thickness was only ~10 μm. Furthermore, the Mo_5Si_3 layer was almost as thick as the $MoSi_2$ layer, which is not desirable. Usually, silicide coatings are in the ~50-100 µm thickness range, with a $MoSi_2$:Mo_5Si_3 layer thickness proportion in the order of magnitude of ~20:1 (Fu et al., 2022). Therefore, the coating

process should be improved to obtain a better coating, both in terms of its thickness and layer distribution.

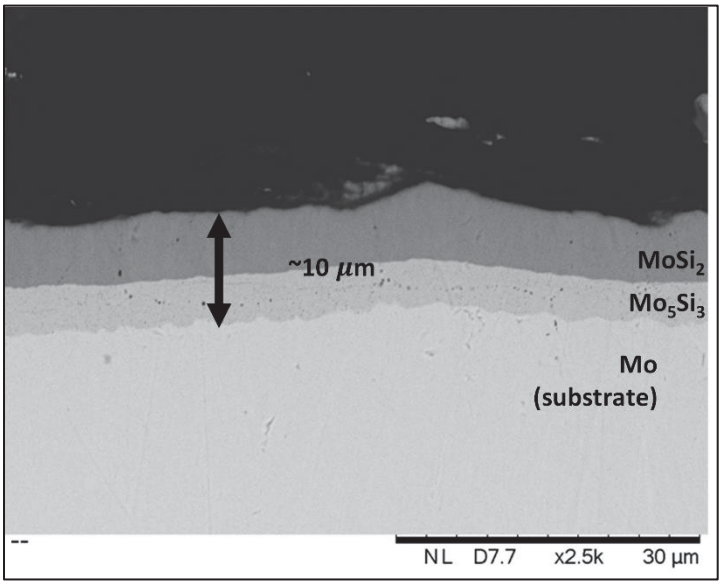

Figure-A I-8: Cross-sectional SEM image of the silicide coating on the polished surface

The surface roughness of LPBF parts is generally significantly higher than that of machined parts (Jiang, Tian, Zhu, & Huang, 2022). Usually, the average roughness (Ra) of LPBF parts is in the order of tens of microns, while that of machined parts is in the order of microns. Therefore, while a uniform coating was achieved on the polished surface, this would not guarantee the same outcome on the surfaces of micro-mixing injectors. Surface polishing is an option for LPBF parts, but in the case of micro-mixing injectors, this process is not appropriate. Polishing of the injection holes would enlarge their size, which would have a negative impact on the combustion performances. Therefore, whenever possible, molybdenum micro-mixing injectors should be coated with as-printed surfaces.

SEM imaging revealed some issues with the formation of silicide coatings on the as-printed LPBF surfaces using the slurry dipping method, as demonstrated in Figure-A I-9 and Figure-A I-10. First, while some protective layers were formed on the as-printed surfaces with the same thicknesses and layer distributions as on the smooth surfaces, uniformity was an issue.

The presence of crevasses created a non-uniform mixture deposition. Therefore, during the heat treatment, there was no diffusion of Si from the surface to the substrate on some spots. Because the Si diffusion depth was less than the size of the crevasses, some surfaces were left uncoated. This is problematic because in an oxidizing environment, the oxidation will consume the substrate, starting from the uncoated surfaces and moving to the substrate core and then from the core to the surface, leading to part failure. Cracks were also detected in the coating. These were not rooted in the substrate (Mo), and they were mostly perpendicular to the surface in the coating. This points to the mismatch between Mo, $MoSi_2$ and Mo_5Si_3 coefficients of thermal expansion and the presence of temperature gradients caused by heat treatment. The cracks could also lead to part failure because they would allow oxygen to reach the molybdenum substrate.

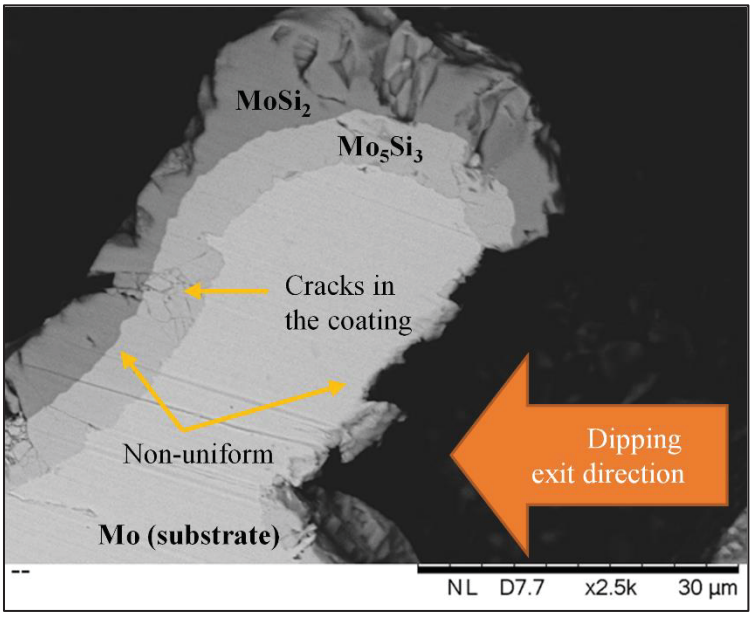

Figure-A I-9: Cross-sectional SEM image of the coating on as-printed LPBF surfaces

Next, looking at a larger scale in Figure-A I-10, one can note additional non-uniformities related to the EBC formation on the as-printed surfaces. While the thickness of the coating on surfaces parallel to the dipping direction was approximately the same as on the polished surfaces, surfaces perpendicular to this direction had thin to no coating. Note that silicon

powder is deposited on the surface by the meniscus formed when the part is removed from the slurry. For the meniscus to form properly, the surface to protect needs to be oriented perpendicular to the slurry surface (parallel to the dipping direction). The more it deviates from this orientation, the less effective the meniscus, and the smaller the amount of silicone to be deposited.

As shown in Figure-A I-10, coating spalling was observed on some surfaces. Moreover, agglomerated Si powder particles from the slurry that did not diffuse into the Mo substrate were also detected. Thus, dispersion of the Si particles in the slurry must be improved and the slurry viscosity optimized to prevent the formation of powder agglomerates.

To conclude, the use of slurry dipping technique on rough as-printed LPBF surfaces poses significant challenges for the formation of uniform and crack-free EBCs. Because of these challenges, the coating of molybdenum micro-mixing injectors is likely not an issue that can be fixed with a single solution. A combination of different surface polishes and coating technologies should therefore be explored. Surfaces that can be reworked (e.g., external faces) should be polished to ease the coating process, but without affecting the injection holes. Also, the question arises whether the protection of internal channels that are only filled with fuel and that are not in contact with oxygen is indeed mandatory. Finally, more shape-flexible coating technologies, such as CVD, should be considered for the manufacturing of EBCs on molybdenum micro-mixing injectors.

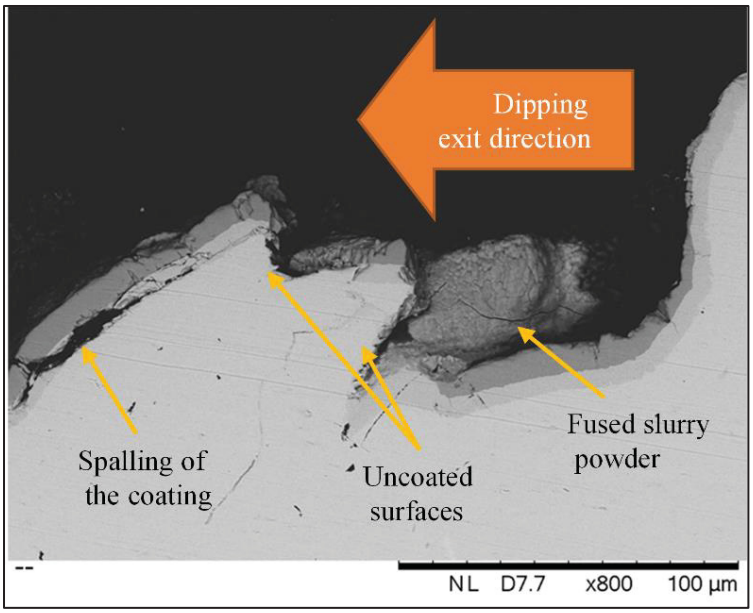

Figure-A I-10: Spalling and non-uniformity of the coating on as-printed LPBF surfaces

Conclusion

Laser powder bed fusion of micro-mixing injectors in molybdenum is explored in this paper. Refractory metals such as molybdenum are promising for the fabrication of high-temperature combustors because their melting temperatures are greater than turbine inlet temperatures (TIT). However, manufacturing and high-temperature oxidation of these metals poses significant challenges that must be addressed.

The LPBF process allows manufacturing parts with complex geometries. Using printing parameters determined in a previous study, experiments focusing on the key features of micro-mixing injectors were carried out to identify the smallest dimensions achievable. It was determined that 0.3 mm corresponds to both the minimum nominal dimensions of injection holes and the minimum wall thickness. Then, a small-scale micro-mixing injector in molybdenum was successfully manufactured. However, because of the porosity of printing parts, leaks through the walls of the injector were noticed.

Another major issue with molybdenum is its oxidation at high temperatures. Thus, to be viable in a combustion environment, an EBC must be applied to molybdenum micro-mixing injectors. To explore the potential and discover the challenges associated with protecting molybdenum micro-mixing injectors, a silicide-based coating was applied. Slurry dipping was used as a surface coating method because of its potential to coat complex internal channels. While smooth (polished) surfaces were uniformly coated, that was not the case for rough as-printed surfaces. Furthermore, cracks and spalling of the coating were observed on the as-printed LPBF surfaces. A combination of surface finishing with a more versatile coating technology such as CVD should be explored to produce required EBCs on LPBF molybdenum parts.

Acknowledgments

The authors would like to express their gratitude to the technical staff at École de technologie supérieure for their support throughout the project.

Funding

This work was funded by PRIMA Québec (Pôle de recherche et d'innovation en matériaux avancés) in the framework of the M-ERA.NET program, NSERC (Natural Sciences and Engineering Research Council of Canada) and PyroGenesis Canada Inc. Scholarship was provided by the Natural Sciences and Engineering Research Council of Canada (NSERC).

ANNEXE II

LASER POWDER BED FUSION AND HOT ISOSTATIC PRESSING OF PURE MOLYBDENUM: PHYSICAL AND MECHANICAL PROPERTIES AT ELEVATED TEMPERATURES

Aurore Leclercq[a], Thibault Mouret[b] and Vladimir Brailovski[c]

[a,b,c]Département de Génie mécanique, École de Technologie Supérieure,
1100 Notre-Dame Ouest, Montréal, Québec, Canada H3C 1K3

Article de conférence présenté à
« Euro Powder Metallurgy 2024 Congress & Exhibition», octobre 2024

Résumé

Le molybdène (Mo) est l'un des matériaux cibles pour les procédés de fabrication additive par fusion laser sur lit de poudre. En utilisant le jeu de paramètres d'impression suivant : P = 179 W ; v = 133 mm/s ; h = 60 µm ; t = 30 µm, des éprouvettes de Mo exemptes de fissures ont été imprimées, soumises à un traitement par pression isostatique à chaud (1300 °C et 150 MPa pendant 3 heures), puis caractérisées en termes de densité, de structure et de comportement en compression à température ambiante et à haute température. Les résultats obtenus avec les éprouvettes telles qu'imprimées, présentant une densité d'environ 97 % et une contrainte maximale en compression de 486, 242, 264 et 145 MPa à 20, 600, 800 et 1000 °C respectivement, sont comparables à ceux observés pour leurs homologues produits par des procédés conventionnels de métallurgie des poudres. Les conditions de HIP sélectionnées ont permis une augmentation d'environ 1 % de la densité des pièces, mais l'évolution simultanée de la porosité et le grossissement des grains ont conduit à une diminution d'environ 10 % des propriétés mécaniques à température ambiante et élevée des pièces imprimées.

Abstract

Molybdenum (Mo) is one of the target materials for laser powder bed fusion additive manufacturing processes. Using the following set of printing parameters: P = 179 W; v = 133 mm/s; h = 60 µm and t = 30 µm, crack-free Mo specimens were printed, subjected to hot isostatic pressing (1300 °C & 150 MPa for 3 hours), and characterized in terms of their density, structure, and compression behavior at room and elevated temperatures. The results obtained with as-built specimens with a printed density of ~97% and an ultimate compression stress of 486, 242, 264 and 145 MPa at 20, 600, 800 and 1000 °C respectively, are comparable to those shown by their counterparts produced by conventional powder metallurgy processes. The selected HIP conditions resulted in a ~1% increase in the part density, but simultaneous porosity evolution and grain coarsening led to a concurrent ~10% decrease in the room and elevated-temperature mechanical properties of printed parts.

Introduction

Molybdenum is a material of interest for high temperature applications due to its special properties, such as high melting point, high strength at elevated temperatures and low coefficient of thermal expansion. Like other refractory metals, it was highly explored for use in power applications in the sixties and eighties and was traditionally shaped using conventional powder metallurgy (PM) processes such as pressing and sintering (also called arc cast), often followed by forging, rolling, drawing and other plastic forming processes. The benefits of these forming processes were demonstrated in the fifties (« Climax Molybdenum », 1950) on hot-rolled specimens reaching an ultimate tensile strength (UTS) of 255 MPa at 871 °C, which was almost 5 times higher than that of their fully recrystallized equivalents at the same temperature. Also, more recent studies (Scapin, Peroni, & Carra, 2016; Xiao, Li, Xie, & Wang, 2012) highlighted that commercial pure molybdenum rods manufactured by powder metallurgy processes and subjected to thermomechanical post-treatments could reach UTS varying from 490 to 300 MPa in the 200-800 °C temperature range and UCS (ultimate compression strength) varying from 255 to 100 MPa in the 900-1450 °C temperature range.

However, due to a high ductile-to-brittle transition temperature of molybdenum (~400 K) and its extreme sensibility to oxidation at elevated temperatures, the use of plastic forming processes to increase the mechanical properties of PM molybdenum parts remains challenging, let aside the inherent limitations of these processes to produce parts with complex geometries (El-Genk & Tournier, 2005; Ham, 1951; Philips et al., 2020).

Fortunately, additive manufacturing (AM) processes, such as laser and electron beam powder bed fusion (LPBF and EB-PBF), offer promising avenues for the toolless production of molybdenum parts using the same powder feedstock as their PM equivalents, but with much greater process-related design flexibility. The LPBF and EB-PBF processes take place under inert atmosphere or vacuum and have already demonstrated their capabilities in processing difficult-to-cast materials (Fernandez-Zelaia et al., 2022; Philips et al., 2020). While the electron beam-based process limits the risk of distortion and cracking, its laser-based counterpart is less expensive to integrate in the process chain and has been already used to produce complex molybdenum parts (Oehlerking et al., 2022). However, the presence of process-induced defects, such as pores and microcracks, accentuates the need for further studies aimed at assessing the impact of these defects on the mechanical properties of printed molybdenum parts, especially at elevated temperatures.

A preliminary work aimed at studying the impact of LPBF parameters, such as laser power P (Watts), scanning speed (v, mm/s), hatching space (h, µm), and layer thickness (t, µm), on the physical, structural and mechanical properties of as-printed molybdenum parts allowed to optimize printing conditions and test printability limits, by producing a series of geometric artefacts. The objective of this work is to extend the temperature range of testing conditions up to 1000 °C and to assess the potential of hot isostatic pressing (HIP) to improve the mechanical properties of printed molybdenum parts at room and elevated temperatures.

Materials and Methods

Plasma-spheroidized molybdenum powder (Mo > 99.9%, O ≤ 500 ppm, Hall flow ≤ 15 sec./50g) used in this study was produced by Tekna Co. Ltd. (Sherbrooke, Canada). The particle size distribution of D10=12.6, D50=20.6 and D90=32.0 (µm) was measured using a Beckman Coulter LS13 320 XR (Brea, CA, USA) particle size analyzer equipped with a water module, and the particle morphology was observed using a Hitachi TM3000 (Tokyo, Japan) scanning electron microscope (Figure-A II-1).

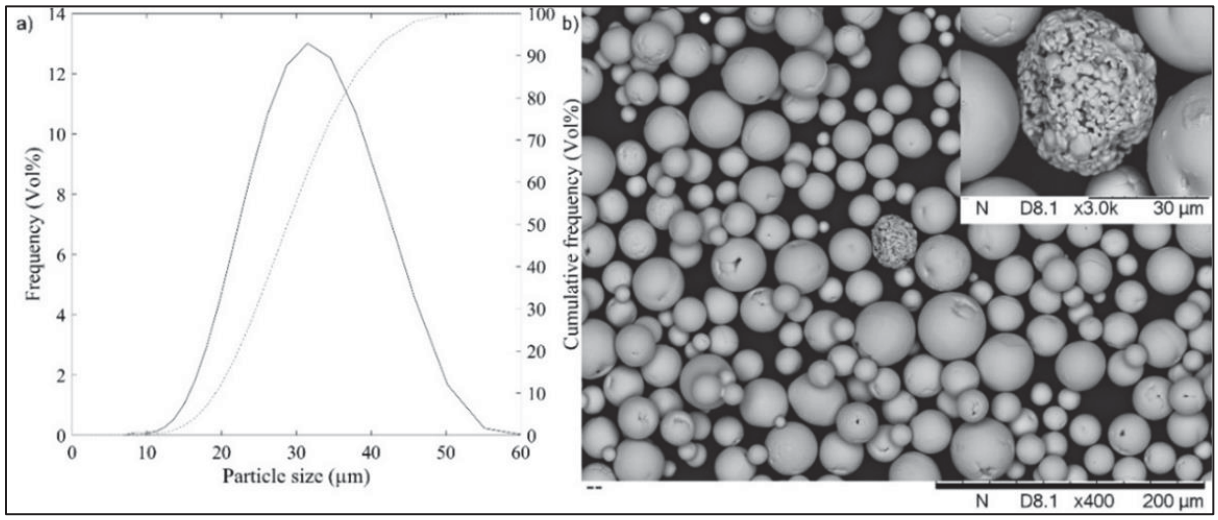

Figure-A II-1: Geometry characteristics of the molybdenum powder: a) particle size distribution and b) particle morphology

Based on the results of the preliminary study, the following printing parameters were used to produce eighteen 10 mm-diameter, 21 mm-high cylindrical specimens with 5 mm-thick supports (Figure-A II-2a): P = 179 W; v = 133 mm/s; h = 60 µm and t = 30 µm. The printing was carried out without preheating on a stainless-steel baseplate using a TruPrint 1000 LPBF system (TRUMPF GmbH, Ditzingen, Germany). Once removed from the baseplate, six specimens were subjected to a HIP treatment (1300 °C & 150 MPa for 3 hours) using a QIH3 Isostatic Press (Quintus Technologies, Västerås, Sweden); the HIP conditions being adopted from (Guan et al., 2023). Next, the as-built and HIP-ed specimens were cut to obtain samples for microscopic observations and mechanical testing as shown in Figure-A II-2a.

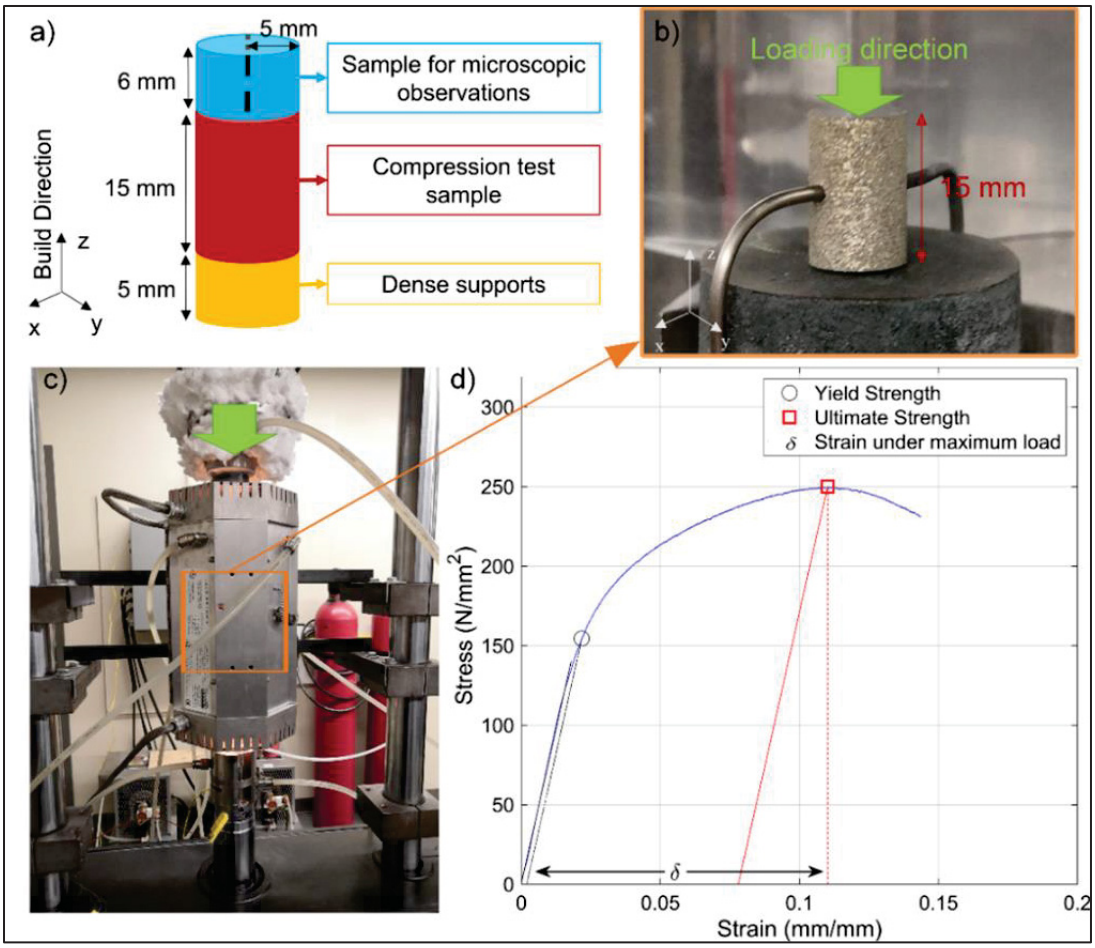

Figure-A II-2: a) Schematic representation of printed specimens with different cuts; b) photo of a compression testing sample instrumented with a thermocouple; c) thermal chamber; d) compression stress-strain diagram with metrics of interest

To measure the density of printed samples, they were mounted in a carbon-doped resin, and their Z-Y sections (see Figure-A II-2a for definition) were mirror-polished. Three image observations were made on each surface using a LEXT OLS4100 (Olympus Corporation, Tokyo, Japan) laser confocal microscope (x5). Next, raw images so obtained were binarized in the MATLAB environment (R2022b, MathWorks, USA) using an adaptative threshold, which was locally adjusted considering the mean intensity (first-order statistics) in the neighborhood of each pixel, and a ratio of the white-to-black pixels was calculated to assess the printed density. Note that the printed density for each sample corresponded to a mean value obtained from 3 observations and that the results obtained were validated by comparison with

manual segmentation in the ImageJ software environment. Complementarily, the following pore size and shape-related information was also retained: 50 and 90% quotients of the entire pore population in terms of their equivalent diameter ($DE50$ and $DE90$, µm) and circularity ($C50$ and $C90$, without unit). Given the resolution of the measurements, pores with an equivalent diameter smaller than 20 µm were removed from the study.

The as-built samples were subjected to compression testing at room temperature (RT), 600, 800 and 1000 °C, while the HIP-ed samples were tested at RT and 800 °C only. The compression rate was set to 0.075 mm/min as per the ASTM E209-18 standard (E28 Committee, 2018) (Figure-A II-2b,c), and all the elevated temperature tests were carried out under an argon flow of 27.5 ft^3/h. The tests were realized on an MTS 810 (MTS, Eden Prairie, MN, USA) load frame with force measured by a 100 kN MTS load cell and displacement measured by an LVDT located in the load frame's actuator. Temperature in the testing chamber was controlled using an IR furnace Eurotherm 3504 (Eurotherm US LLC, VA, USA) controller. To ensure that temperature in the heart of tested samples corresponded to that in the thermal chamber, one of the samples was instrumented with a K-type thermocouple and subjected to a controlled temperature rise up to 800 °C with a heating rate of 10 °C/min without applying stress. This enabled to validate the temperature ramp and establish a prior-to-testing dwell time of 3 min. Finally, three samples were compressed for each testing temperature and the stress-strain diagrams plotted in Figure-A II-2d were used to obtain the following metrics of interest:

- Ultimate Compression Strength (UCS, MPa), defined as the maximum stress reached during the test.
- Yield Strength at 0.2% offset (YS, MPa), calculated by moving the slope at the origin to 0.2% on the strain axis, according to the methodology described in the E9-19 standard (E28 Committee, 2019).
- Strain under maximum load (δ, %), representing the difference between a total compression strain to failure and an elastic strain, calculated by moving the slope at origin to reach the UCS.

To compare phase states of the as-built and HIP-ed samples, they were subjected to the X-Ray diffraction (XRD) analysis using an X'Pert³ Panalytical system (Malvern Panalytical Ltd, Malvern, UK) equipped with a cobalt source. The presence of potential oxidation traces induced by HIP was assessed using the energy dispersive X-ray spectroscopy (EDS) system of a Hitachi TM300 SEM. Next, these samples were polished using a Hitachi EM 4000 plus ion-milling system (5 kV, 25 rpm, 15 min) and subjected to the Electron Backscatter Diffraction (EBSD) analysis using a Hitachi SU-8230 Field Emission-STEM. The obtained EBSD maps were post-treated to assess the grains size, shape, orientation, and distribution following the procedure defined in the E2627 ASTM standard (« E2627-13; Standard Practice for Determining Average Grain Size Using Electron Backscatter Diffraction (EBSD) in Fully Recrystallized Polycrystalline Materials », n.d.) using the MTEX library (MATLAB software, R2022b). Only the Z–Y sections of the samples were analyzed with the misorientation angle threshold set to 10°. Finally, to study the oxides formation during the elevated-temperature testing, the thermocouple-instrumented sample was subjected to the XRD analysis before and after the thermal cycling, using the same X'Pert³ XRD system.

Results & Discussions

Structure

No cracks were detected in the as-built samples during the microscopic observations down to a 2 μm resolution. The density of printed samples was 97±1%, meaning that the selected printing parameters were adequate to produce high-density samples with good repeatability. After the HIP treatment, an increase in the printed density of ~1% was also observed (see Figure-A II-3a,b). Regarding the pore characteristics (equivalent diameter and circularity), HIP reduced the size of pores without affecting their circularity (Tableau-A II-1).

Of note, the results found in the literature on LPBF of pure molybdenum are quite scattered. For example, (Faidel et al., 2015) were also able to produce crack-free specimens, but the maximum printed density reached in their work did not exceed 82.5%. On the other hand, (Rebesan, Ballan, et al., 2021) produced specimens with an extremely high density of 99.5%,

but they were not able to avoid the appearance of 10-100 µm-long micro-cracks at the grain boundaries. The occurrence of these cracks was attributed to oxygen impurities in the powder feedstock, or the printing enclosure.

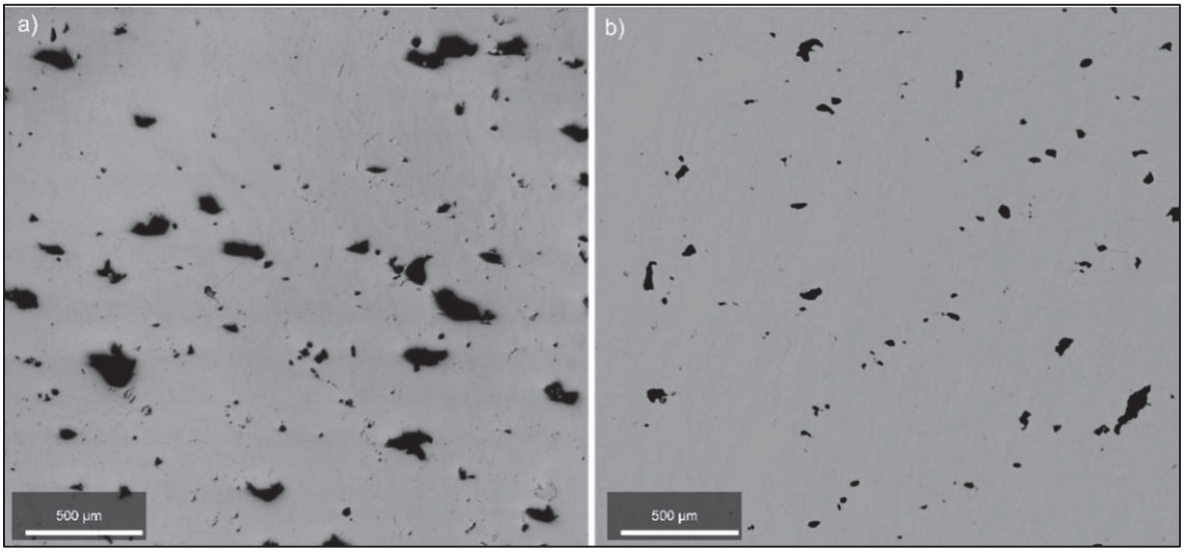

Figure-A II-3: Figure 3: LEXT observations of the a) as-built and b) HIP-ed samples

Tableau-A II-1: Pore characteristics of the as-built and HIP-ed samples

Treatment	$DE50$ (µm)	$DE90$ (µm)	$C50$	$C90$
As-built	80 ± 13	123 ± 15	0.55 ± 0.00	0.73 ± 0.03
HIP-ed	65 ± 15	102 ± 20	0.55 ± 0.05	0.77 ± 0.06

As far as the grain structure is concerned, the EBSD analysis (Figure-A II-4) revealed that while all the samples contained columnar grains (median measured circularity of 0.3), grains in the HIP-ed samples were 5-7% coarser than in the as-built samples: $D50(D90)$ = 135(295) µm, as compared to 125(275) µm. However, neither EBSD (grain/subgrain structure, texture), nor XRD (2θ shift, FWHM broadening) analyses were capable of detecting notable changes in the grain/subgrain structure, texture and dislocation density, which suggest that the HIP treatment did not induce noticeable microstructural changes.

Of note, (Shi et al., 2023) applied two HIP treatments to tungsten LPBF parts (T = 1400 and 1600 °C, P = 150 MPa for 2h) and reported the grain growth, the material densification and the relief of internal stresses for both treatments. The authors noted however that 1400 °C HIP did not affect the anisotropy of the as-printed structure (columnar grains along the build direction), while 1600 °C HIP triggered the recrystallization processes.

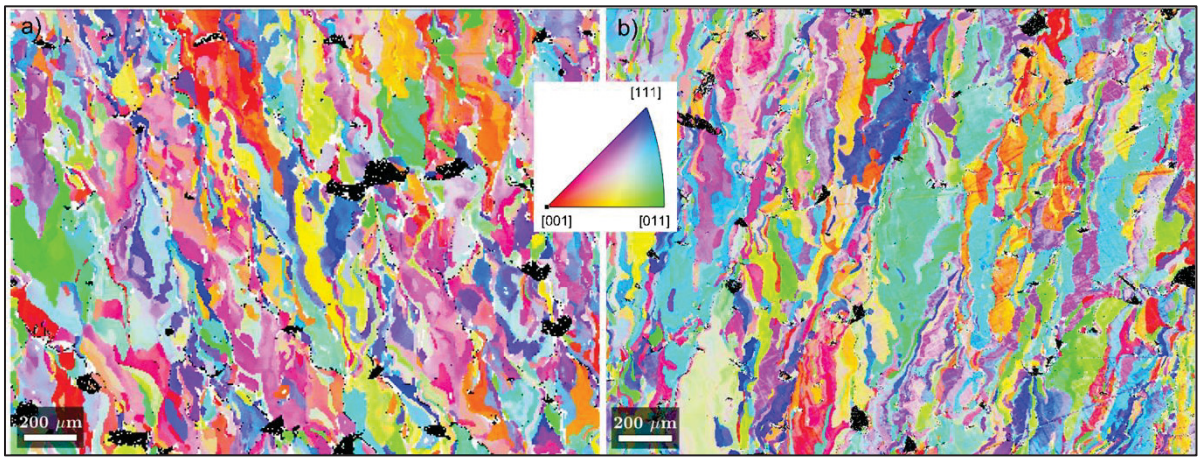

Figure-A II-4: EBSD maps (IPF X) of the a) as-built and b) HIP-ed samples

Oxidation

Chemical and structural analyses (EDS and XRD) of the HIP-ed samples did not detect significant oxidation traces in comparison to their as-built equivalents. Conversely, during testing at both 800 and 1000 °C, despite an argon-filled protective atmosphere, a thick white smoke was observed out of the compression chamber, and at the end of the testing, the samples were found covered with a shiny white lamina (Figure-A II-5a). The XRD analysis of the thermocouple-instrumented sample (Figure-A II-5b) before and after the thermal cycling revealed that this phenomenon corresponded to the formation and vaporization of MoO_3 oxides, the latter were not present initially in the sample. The estimated mass loss corresponded to 8.6 ± 2.7% at 800 °C and 9.4 ± 0.8% at 1000 °C (note that while this material loss was significant, the YS and UCS values presented in this paper were not consequently adjusted, for the sake of conservatism). The same phenomena were also reported by (Rebesan, Ballan, et

al., 2021), who were able to carry out tensile testing of Mo samples at 600 °C in air, but unable to pursue with the 800 °C testing because of the catastrophic sample oxidation.

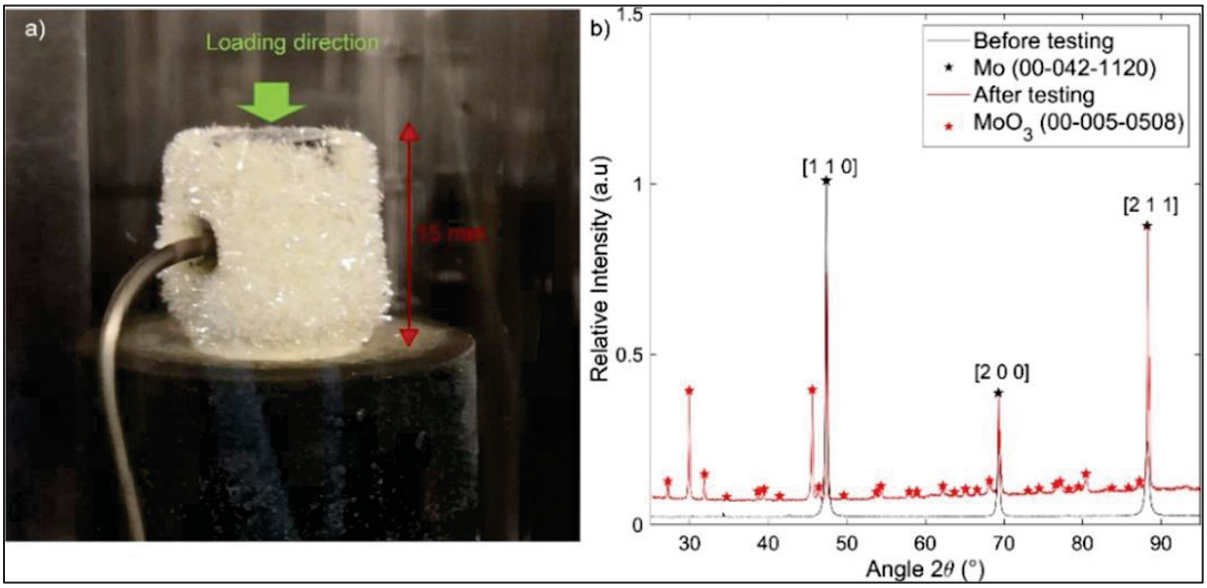

Figure-A II-5: Thermocouple-instrumented sample: a) Photo with the oxide layer; b) XRD before and after temperature cycling (without load)

Mechanical properties at elevated temperatures

Stress-strain diagrams of the as-built samples at room and elevated temperatures are plotted in Figure-A II-6a, while Figure-A II-6b compares stress-strain diagrams of the as-built and HIP-ed samples at RT and 800 °C (see extracted metrics in Tableau-A II-2). Globally, the higher the testing temperature, the lower the strength characteristics (YS, UCS), and the higher the strains corresponding to maximum stresses (d), but this evolution is not monotonic, since the highest stresses and strains were reached at 800 °C. Similar observations were also made by (Carreker & Guard, 1956) on tensile testing of pure molybdenum press and sintered parts. They attributed this effect to strain aging caused by the dislocation pinning by impurity atoms, the phenomenon studied by (Cottrell & Bilby, 1949) in the body-centered-cubic metals.

Moreover, at any testing temperature of this study, HIP reduced both the strength and strain characteristics and that, despite a ~1% increase in the material density. This can be related to the evolution of pore morphology (size and shape) and grain coarsening (Cordero, Knight, & Schuh, 2016), or some undetected changes in the oxides redistributions during the HIP treatment (the latter hypothesis requires additional study). Similar decrease in the elevated-temperature (up to 871 °C) strength and strain characteristics of the pressed-sintered and hot-rolled pure molybdenum samples was also observed after their stress-relief treatment (1 hour at 980 °C) (« Climax Molybdenum », 1950). The porosity was not addressed in this work, but the reported microstructure had essentially the same appearance as that of the "as-rolled" samples (columnar grains in the rolling direction), but the number of subgrain boundaries was reduced. In the same study, when submitted to the full recrystallisation process, molybdenum samples showed a significantly reduced strength but their strain to failure at the same testing temperatures almost tripled.

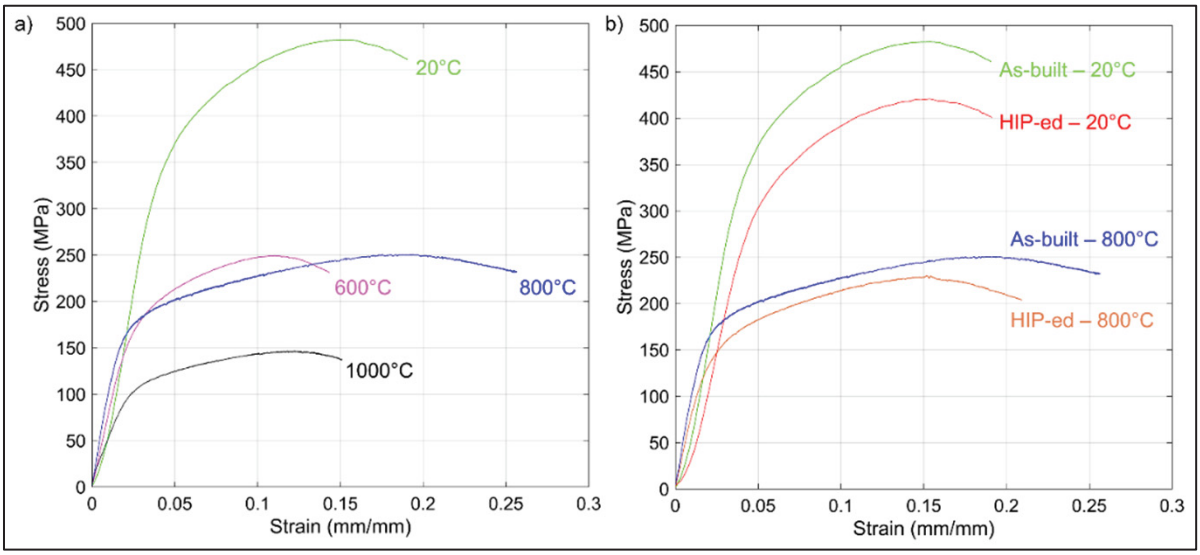

Figure-A II-6: Representative stress-strain compression diagrams: a) as-built samples at RT, 600, 800 and 1000 °C, b) as-built and HIP-ed samples at RT and 800 °C

Tableau-A II-2: Mechanical properties in compression at varying temperatures of the as-built and HIP-ed samples

Testing temp., °C	YS, MPa	UCS, MPa	δ, %
RT	315 ± 22 (as-built); 286 ± 2 (HIP-ed)	486 ± 15 (as-built); 438 ± 9 (HIP-ed)	10 ± 1 (as-built); 9 ± 0 (HIP-ed)
600	151 ± 20	242 ± 30	8 ± 1
800	160 ± 5 (as-built); 132 ± 3 (HIP-ed)	264 ± 8 (as-built); 228 ± 4 (HIP-ed)	14 ± 1 (as-built); 12 ± 1 (HIP-ed)
1000	92 ± 10	145 ± 18	9 ± 4

Figure-A II-7 compares the results of this study with the literature data. Note that only few authors performed mechanical testing of molybdenum at elevated temperatures, and most of the testing was done in tension (Carreker & Guard, 1956; « Climax Molybdenum », 1950; Fernandez-Zelaia et al., 2022; Rebesan, Ballan, et al., 2021):

- In the entire temperature range of this study, the results obtained are comparable to those obtained with conventional PM processes (Carreker & Guard, 1956; « Climax Molybdenum », 1950).
- At 600 °C, strength characteristics measured in this study are close to those reported for the LPBF-printed Mo specimens in (Rebesan, Ballan, et al., 2021), and this, despite significantly different printed densities: 97% in this study as compared to 99.5% in (Rebesan, Ballan, et al., 2021).
- In the 700 – 750 °C temperature range, the samples of this study demonstrated a significantly lower mechanical resistance than their EB-PBF counterparts (Fernandez-Zelaia et al., 2022): UTS of ~316 MPa in the latter as compared to UCS of ~250 MPa in the former. This discrepancy can be attributed to much higher printed densities of the EB-PBF specimens as compared to the samples of this study: >99.5% in the latter as compared to 97% in the former, and a more favorable as-printed texture (mixed (001)/(111)-fiber grains).

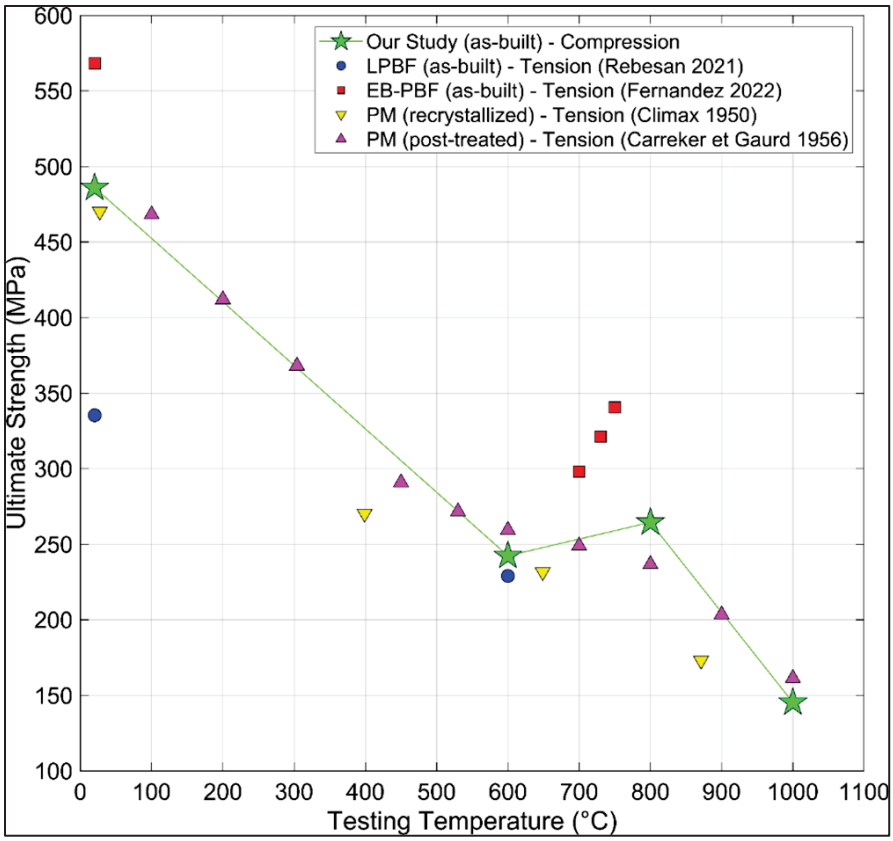

Figure-A II-7: Comparison of the ultimate strength at different temperature of pure molybdenum LPBF specimens (our study and Rebesan, Ballan, et al. (2021)) and molybdenum parts formed by other processes Carreker & Guard (1956); « Climax Molybdenum » (1950); Fernandez-Zelaia et al. (2022)

Of note, maximum strain values of pure molybdenum products found in the literature are significantly scattered: from <2% for the LPBF Mo specimens in (Rebesan, Ballan, et al., 2021) to ~60%, for the recrystallized press-and-sintered specimens in (« Climax Molybdenum », 1950), which make any comparison with the results of this study limited.

Conclusions

In this study, the as-built and HIP-ed LPBF pure molybdenum samples were compared in terms of their density, microstructure and mechanical properties under uniaxial compression at temperatures ranged from 20 to 1000 °C. While, the results obtained with the as-built samples

in the temperature range of this study are comparable to those found in the literature, the selected HIP conditions resulted in a ~10% decrease in the mechanical properties at all the testing temperatures. These results were not expected, since the HIP-ed samples showed a higher density, smaller pores and almost invariant grain structure and texture as compared to their as-built counterparts. The latter fundings require further studies.

Acknowledgments

The authors acknowledge the contributions of Salah Eddine Brika (powder analysis), Anatolie Timercan (printing), Simon Larivière and Serge Plamondon (specimen preparation and compression testing).

ANNEXE III

LASER POWDER BED FUSION AND HOT ISOSTATIC PRESSING OF MO AND MO8WT%RE PARTS: STRUCTURE AND MECHANICAL PROPERTIES AT ELEVATED TEMPERATURES

Aurore Leclercq[a], Thibault Mouret[b] and Vladimir Brailovski[c]

[a,b,c]Département de Génie mécanique, École de Technologie Supérieure,
1100 Notre-Dame Ouest, Montréal, Québec, Canada H3C 1K3

Article de conférence présenté à
« 21st Plansee Seminar», juin 2025

Résumé

Le molybdène appartient au groupe des métaux réfractaires et fait partie des matériaux cibles pour l'impression 3D par fusion sur lit de poudre laser. Cette étude vise à améliorer l'imprimabilité du molybdène en l'alliant avec du rhénium et à améliorer ses propriétés mécaniques grâce à un post-traitement par compression isostatique à chaud (HIP). À cette fin, une poudre de Mo commerciale et une poudre de Mo8Re (wt%) produites par une combinaison de techniques de réduction et de sphéroïdisation par plasma ont été utilisées pour imprimer des éprouvettes, lesquelles ont ensuite été traitées par HIP (1800 °C, 150 MPa, 3 h) et caractérisées en termes de densité, de structure et de comportement en compression dans la plage de température de 20 à 1000 °C. Pour les éprouvettes telles qu'imprimées, l'ajout de rhénium a permis d'augmenter la densité de 97 à 98 %, sans modifier les propriétés mécaniques dans la plage de température étudiée. Après le traitement HIP, les éprouvettes Mo8Re ont atteint une contrainte maximale en compression de 900 MPa à 20 °C (140 MPa à 1000 °C) et une déformation maximale en compression de 30 % à 20 °C (8 % à 1000 °C), ce qui représente une augmentation de la résistance par un facteur proche de deux et une augmentation d'environ

70 % de la déformation par rapport aux éprouvettes en molybdène pur soumises aux mêmes conditions de HIP.

Abstract

Molybdenum belongs to the refractory metals group and is one of the target materials for laser powder bed fusion 3D printing. This study aims at improving the printability of molybdenum by alloying it with rhenium and improving its mechanical properties using hot isostatic pressing (HIP) as a post-treatment. To this end, commercial Mo powder and Mo8Re (wt.%) powder produced using a combination of the reduction and plasma-spheroidization techniques were used to print specimens, which were then HIP-ed (1800°C, 150 MPa, 3 h) and characterized in terms of their density, structure and compression behavior in the 20-1000 °C temperature range. For the as-printed specimens, rhenium addition increased the printing density from 97 to 98% without modifying the mechanical properties in the studied temperature range. After the HIP treatment, the Mo8Re specimens reached a maximum compression stress of 900 MPa at 20 °C (140 MPa at 1000 °C) and a maximum compression strain of 30% at 20 °C (8% at 1000 °C), representing an almost twofold increase in strength and a ~70% increase in strain as compared to the pure molybdenum specimens subjected to the same HIP conditions.

Introduction

Being a part of the refractory metal group, molybdenum exhibits a low coefficient of thermal expansion and one of the highest strength- and stiffness-to-density ratios at elevated temperatures among all the refractory metals (Plansee, 2023). The production of semi-finished molybdenum products, such as sheets, rods, or bars, is mainly based on conventional methods including powder metallurgy (PM) pressing and sintering and plastic deformation processes. To create complex shapes, subtractive and joining processes are generally applied, but pose challenges when used with refractory metals because of their high machining costs and affinity to oxygen at elevated temperatures. Recently, additive manufacturing (AM) has emerged as a

promising solution, offering reduced processing costs and enabling the production of complex geometries using the same powder feedstock as their PM equivalents. The most common AM technique for metallic materials is laser powder bed fusion (LPBF), which offers a better resolution, greater flexibility, and lower costs than its main competitor, electron beam powder bed fusion (EB-PBF) (Garcia-Colomo, Wood, Martina, & Williams, 2020; Gradl et al., 2022). However, the LPBF printability of molybdenum remains a challenge due to the elevated ductile-to-brittle transition temperature of this metal and significant thermal gradients and cooling rates associated with the layer-by-layer melting, which make molybdenum parts prone to cracking. Alloying molybdenum powders with other elements has been a common approach to increase the density, reduce cracking, and improve the microstructure of molybdenum parts. Titanium-Zirconium-Molybdenum (TZM) alloys, containing small amounts of titanium, zirconium, and carbon, have shown promising results by enhancing the mechanical strength and suppressing cracking of LPBF parts (Kaserer et al., 2020, 2023). However, the price-per-weight ratio of TZM alloys is at least three times higher than that of pure molybdenum, which hinders their wider application. As an alternative, recent studies on high-entropy refractory alloys (RHEAs) and dual alloys, particularly those containing rhenium, have demonstrated a decrease in the hot cracking susceptibility of printed molybdenum-based parts and an increase in their mechanical properties (Eckley et al., 2023; Oehlerking et al., 2022).

Preliminary works (Leclercq, Czech, et al., 2025; Leclercq, Mouret, et al., 2025) have already been directed at studying the effects of LPBF process parameters on the physical, structural and mechanical properties of as-printed Mo and Mo8wt%Re parts. These works enabled the optimization of printing parameters for powders of both compositions, leading to crack-free parts with reduced porosity ($\leq$ 2%), and allowing to print complex geometry components, including 60%-density diamond and gyroid lattice structures with struts/walls as thin as 0.5 mm. To improve the mechanical properties of printed Mo parts, they were subjected to hot isostatic pressing (HIP) (Leclercq, Mouret, & Brailovski, 2024). However, the HIP conditions applied did not result in a better set of mechanical properties, notwithstanding a significant increase in the material density. This study was devised to apply a new set of the HIP conditions to both Mo and Mo8wt%Re LPBF parts with a twofold objective: a) to achieve notable

improvements in the mechanical properties of printed parts and b) to assess the printability of low-rhenium-alloy molybdenum powders.

Materials and Methods

Two powder lots were used as the feedstock for the LPBF process. The first was commercial (Tekna Co. Ltd), Sherbrooke, Canada) plasma-atomized molybdenum powder (99.9 wt% Mo, O < 500 ppm), and the second, molybdenum-rhenium alloyed powder (92.4 wt% Mo, 7.6 wt% Re, residual O = 84 ppm) developed by the Institute of Non-Ferrous Metal (Łukasiewicz Research Network, Poland) using reduction and plasma-spheroidization techniques (Majewski, 2013; Wrona et al., 2022). The particle size distributions (PSD, Tableau-A III-1) were measured using a Beckman Coulter LS13 320 XR (Brea, CA, USA) particle size analyzer equipped with a water module, and the particle morphology was observed using a Hitachi TM3000 (Tokyo, Japan) scanning electron microscope (Figure-A III-1).

Tableau-A III-1: Particle size distribution (PSD) of the two powder feedstocks

Powder/PSD (μm)	D10	D50	D90
Mo	19.5	29.7	42.1
Mo-8Re spheroidized	28.7	39.4	55.5

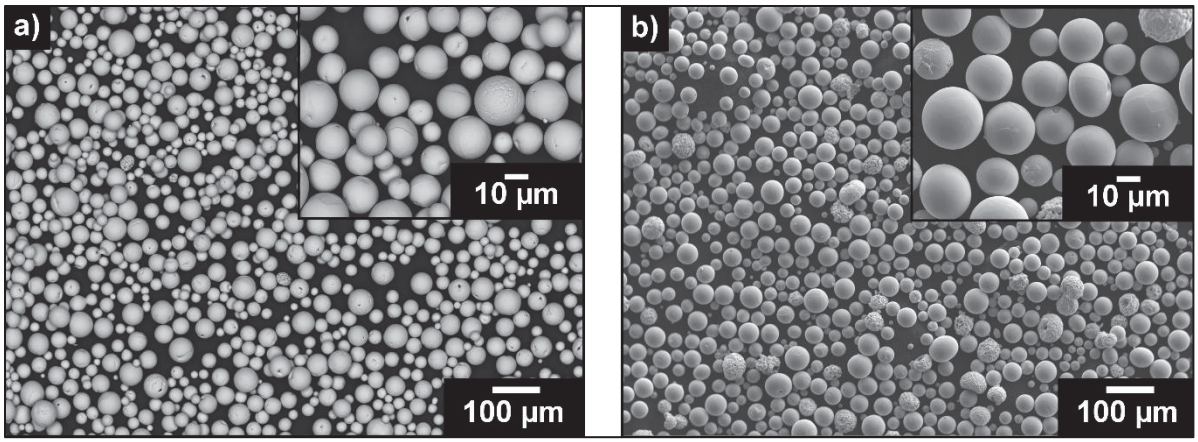

Figure-A III-1: Scanning electron microscope images of the a) pure Mo b) Mo8Re plasma spheroidized powders

Twenty-four cylindrical specimens (10 mm diameter, 21 mm high) were printed for each alloy using the optimized printing parameters obtained during preliminary studies (Tableau-A III-2) (Leclercq, Czech, et al., 2025; Leclercq, Mouret, et al., 2025). The printing was carried out without preheating on a stainless-steel baseplate using a TruPrint 1000 LPBF system (TRUMPF GmbH, Ditzingen, Germany) with 5 mm thickness dense supports. Once removed from the baseplate, twelve specimens of each alloy were kept in the as-built conditions, while the remaining twelve were subjected to an HIP treatment (1800 °C & 150 MPa for 3 hours) using a QIH3 Isostatic Press (Quintus Technologies, Västerås, Sweden).

The above HIP conditions were established on the base of a previous study (Leclercq et al., 2024) where the HIP post-treatment of printed Mo parts was conducted at 1300°C for 3 hours under an argon pressure of 150 MPa. This HIP resulted in a significant increase in printed density (97 to 98%) accompanied by an increase in the densities of low angle grain boundary (LAGB) and high angle grain boundary (HAGB) elements, with the grain size, texture and morphology remaining almost unchanged. All these indices correspond to the very beginning of the primary recrystallization “nucleation” phase (Frederick John Humphreys & Hatherly, 1995), the HIP temperature being too low. It was therefore decided to significantly increase this temperature trying to reach the developed recrystallization stage.

The printed Mo and Mo8Re specimens were weighed (Sartorius™ Entris™ Essential $\Delta m \pm 0.001$ g) before and after the HIP treatment and subjected to X-Ray diffraction (XRD) analyses using an X'Pert³ Panalytical system (Malvern Panalytical Ltd, Malvern, UK) equipped with a cobalt source. Finally, the specimens were cut into samples for microscopic observations and mechanical testing.

Tableau-A III-2: Selected process parameters
Extrait de Leclercq, Czech, et al. (2025); Leclercq, Mouret, et al. (2025)

Material	Power (W)	Speed (mm/s)	Hatching distance (µm)	Layer thickness (µm)
Mo	179	133	60	30
Mo8Re	180	150	100	30

To compare the density and structure of the HIP-ed samples and their as-built counterparts, they were mounted in a carbon-doped resin and their Z-Y sections were mirror-polished. First, to assess the printed density, three images for each surface were acquired using an OLS4100 (Olympus Corporation, Tokyo, Japan) laser confocal microscope (x5) and binarized in the MATLAB environment (R2022b, MathWorks, USA). Then, the same samples were polished using a Hitachi EM 4000 plus ion milling system (5 kV, 25 rpm, 15 min) and subjected to Electron Backscatter Diffraction (EBSD) analysis using a Hitachi SU-8230 Field Emission-STEM. The obtained EBSD maps were post-treated using the MATLAB software MTEX library. The Band Contrast (BC) metric was used to qualify the EBSD pattern quality (Kang et al., 2013, p. 213) and the MacKenzie distributions were plotted to analyze the texture and detect the presence of substructures (Frederick John Humphreys & Hatherly, 1995). Two groups of structural elements were identified as Low Angle Grain Boundary (LAGB) elements, having misorientation angles between 2 and 10°, and High Angle Grain Boundary (HAGB) elements, with misorientation angles greater than 10°. The LAGB and HAGB quantifications were carried out using their respective densities (μm^{-1}), which corresponded to the boundary length divided by the indexed area (Wheeler et al., 2003; Yvell et al., 2018). Structures

corresponding to the HAGB elements were then used to assess the grain size, shape, orientation and distribution, following the procedure defined in the E2627-13 ASTM standard (E04 Committee, 2019).

Finally, compression tests were performed at room temperature (RT), 600, 800 and 1000°C on an MTS 810 (MTS, Eden Prairie, MN, USA) load frame, with the force measured by a 100 kN MTS load cell, the displacement measured by an LVDT attached to the load frame actuator, and the temperature in the testing chamber controlled by an IR furnace Eurotherm 3504 (Eurotherm US LLC, VA, USA) controller. The compression rate was set to 0.075 mm/min as per the ASTM E209-18 standard (E28 Committee, 2018), the heating rate was set to 10°C/min, and a constant argon flow of 27.5 ft^3/h was used to limit oxidation. For each material, three samples were compressed for each testing temperature and stress-strain diagrams were plotted to obtain the following metrics of interest: Yield Strength (YS, MPa), calculated by moving the σ-ε slope from origin to 0.2% of strain; Ultimate Compression Strength (UCS, MPa), defined as the maximum stress reached during the test and strain under maximum load (δ, %), representing the difference between the total compression strain and the elastic strain at UCS.

Results & Discussion

Structure

After the HIP treatment, oxidation traces were observed on the samples and inside the furnace, notwithstanding the initial vacuum cycle (first down to 0.5 mbar then filled with argon before dropping down to 0.3 mbar and fill again with argon) and the constant argon flow. Indeed, the samples changed slightly in color and the surface of the crucible containing the samples was covered with bright flakes. A slight loss of mass was detected for each of the two studied materials: pure molybdenum lost 0.006% of its weight while Mo8Re suffered an almost 20-times greater loss of 0.1%. This difference is attributed to an enhanced oxidation kinetic caused by the rhenium addition. The effect of this addition on the oxidation kinetics of refractory metals is not well described in the literature. Some authors report that a low sublimation temperature of the rhenium oxide Re_2O_7 (T_s = 250 - 350 °C) can induce cracks and defects in

the protective refractory oxide layers generated at low temperatures ($T < 650°C$) (Ratschbacher & Luidold, 2015), while others consider that the sublimated rhenium oxide can act as a sintering agent and improve the oxidation resistance (Otsuka et al., 2020). Microscopic observations of the polished cross-sections of the Mo and Mo8Re specimens after their HIP treatments (Figure-A III-2d,j) enabled to assess their densities as 94 ± 1.1% for Mo and 94 ± 0.8% for Mo8Re, representing an overall density loss of about 3% for the former and 4% for the latter, as compared to their as-built counterparts (Figure-A III-2a,g). Since the refractory oxides were highly volatile under the HIP conditions, XRD analyses conducted on the HIP-ed samples did not detect any of the oxide phases.

The BC maps and associated frequency diagrams revealed no significant changes in pattern quality for either one of the two materials. Also, the post-treatment did not affect the crystallographic texture and columnar morphology of the grains (Figure-A III-2b,e), which remained oriented in the direction of fabrication. However, the HIP treatment decreased the density of both the LAGB (by 40% for pure Mo and almost 65% for Mo8Re) and HAGB (110% for Mo and 30% for Mo8Re), and increased the grain size (by 40% for Mo and 10% for Mo8Re) (Figure-A III-2b,c,e,f, Figure-A III-3), meaning that for both materials, the primary recrystallization phase (i.e., the “growth” phase, (Frederick John Humphreys & Hatherly, 1995)) was started but not completed. It is noteworthy that alloying molybdenum with rhenium increases the recrystallization temperature of the alloy (Lundberg, 1981; Leonhardt et al., 1999), thereby justifying the differences observed between the Mo and Mo8Re samples in terms of their grain size evolution caused by the HIP treatment.

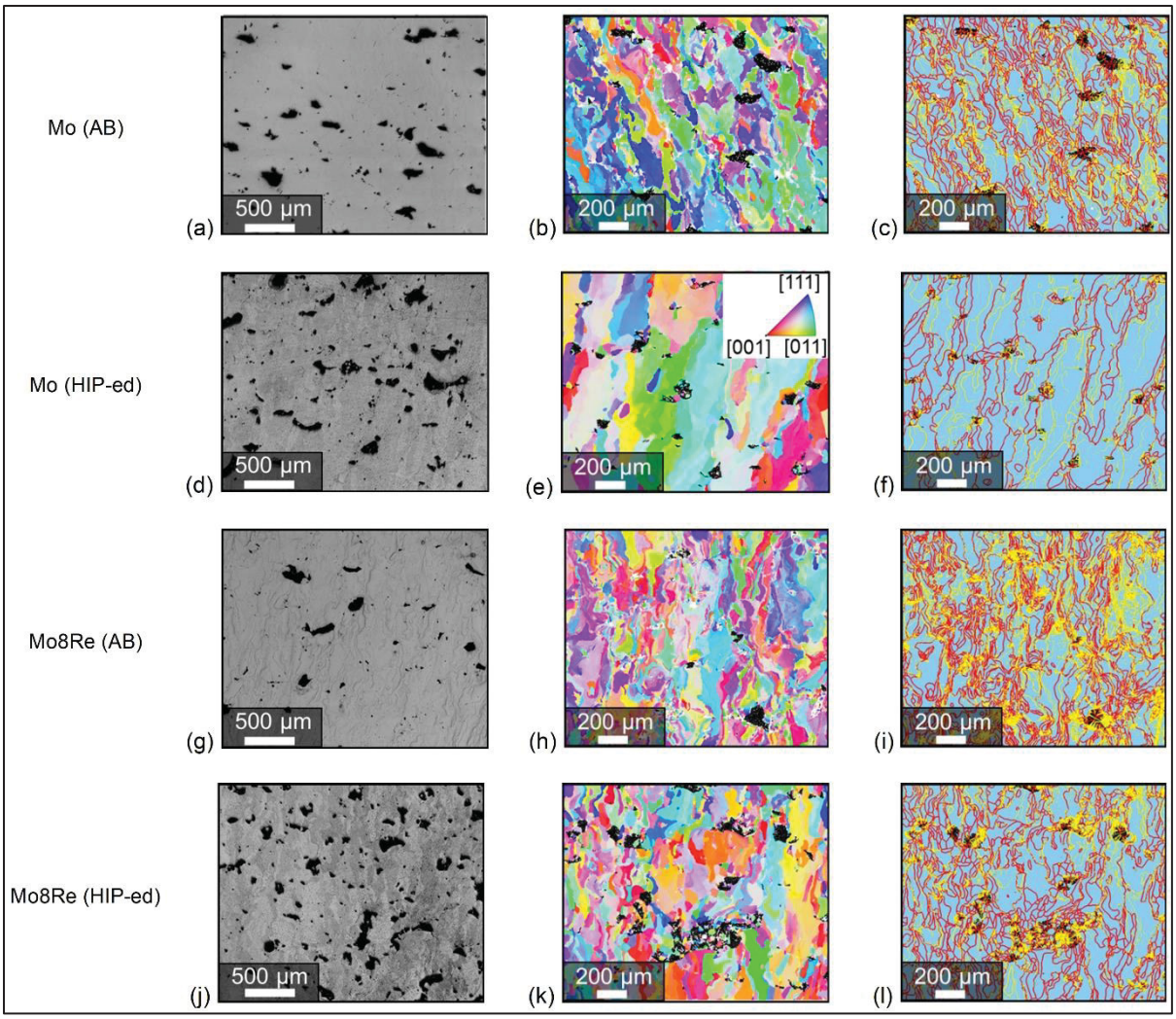

Figure-A III-2: LEXT observations of the Mo: a) as-built, d) HIP-ed and Mo8Re: g) as-built and j) HIP-ed specimens; Orientation maps (IPF Y) of the Mo: b) as-built, e) HIP-ed and Mo8Re: h) as-built and k) HIP-ed specimens, and Phase Maps of the Mo: c) as-built, f) HIP-ed and Mo8Re: j) as-built and l) HIP-ed specimens; LAGB (yellow) and HAGB (red)

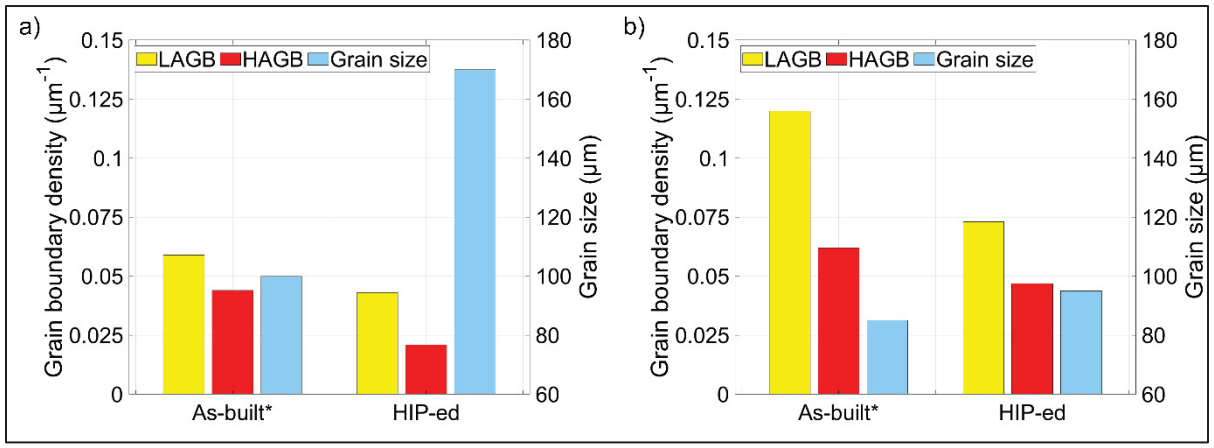

Figure-A III-3: Grain boundary densities and grain size of the a) Mo and b) Mo8Re samples before (Leclercq, Czech, et al. (2025); Leclercq, Mouret, et al. (2025)) and after the HIP treatment

Mechanical properties at room and elevated temperatures

During testing at elevated temperatures, both materials were subject to oxidation: at 600 °C, there was a 0.8% mass increase for pure Mo and a 0.3% increase for Mo8Re, while at 800 °C and 1000 °C, there was a 6% mass loss for both materials. These measurements are very close to the values obtained with their as-built counterparts in the reference works (Leclercq, Czech, et al., 2025; Leclercq, Mouret, et al., 2025), and mean that the applied HIP treatment did not affect the oxidation phenomena and kinetics during testing. At 600 °C, the oxidation kinetic was paralinear, with simultaneous protective oxidation and oxides volatilization, while above this temperature, the oxidation kinetic became linear, with direct oxide volatilization.

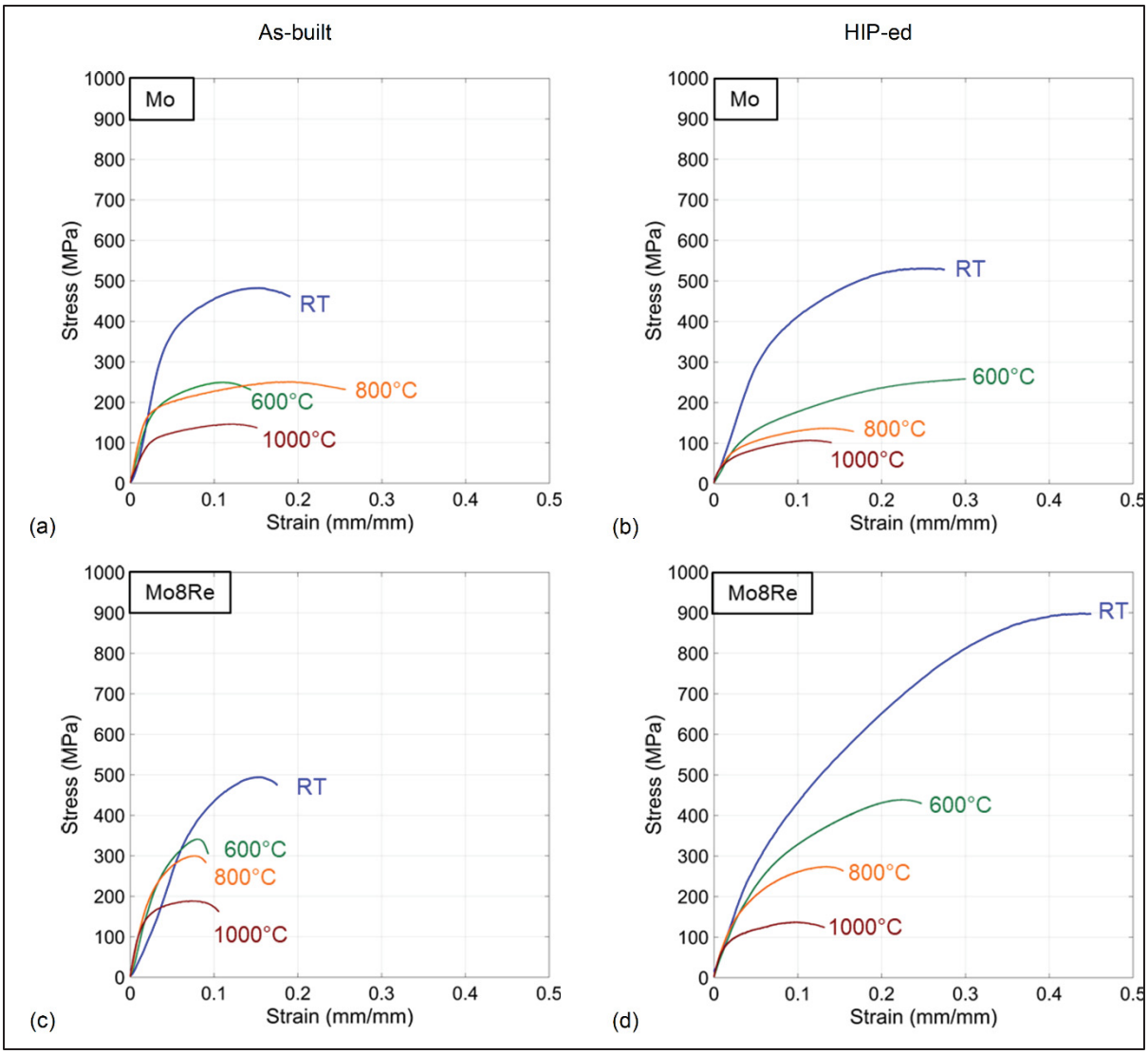

Figure-A III-4: Representative strain-stress diagrams at each tested temperature for the as-built and HIP-ed Mo (a,b) and Mo8Re (c,d) samples. The two materials exhibited a monotonic decrease in the ultimate compression stress, which was not observed for the as-built Mo Leclercq, Mouret, et al. (2025), but was encountered with the as-built Mo8Re Leclercq, Czech, et al. (2025) samples

At room temperature (RT), the HIP-ed Mo8Re samples reached a 900 MPa ultimate strength and a ~30% strain under maximum load, which represents an almost 70% increase in both stress and strain as compared to the Mo samples subjected to the same HIP conditions. Compared to their as-built equivalents (Figure-A III-5, Tableau-A III-3), the *YS* of the HIP-ed samples was reduced (10-150%) for the two materials in the entire temperature range

considered. However, for the ultimate compression strength (UCS) and strain under maximum load (δ), the selected HIP treatment impacted the materials differently. For the Mo samples, the HIP treatment led to a small increase in UCS (7-8%) and a more significant one in δ (43-66%) values in the 20-600 °C temperature range, with major losses in both the UCS (34-92%) and δ (9-26%) values in the 800-1000 °C temperature range. As far as the Mo8Re samples are concerned, the HIP resulted in significant gains in both the UCS (23-47%) and δ (~70%) values in the 20-600 °C temperature range, followed by a moderate decrease (10-39%) in the UCS values and a significant increase (27-53%) in the δ values, in the 800-1000 °C temperature range.

Tableau-A III-3: Mechanical properties in compression of the Mo and Mo8Re as-built and HIP-ed samples at varying temperatures

Material	Testing temperature (°C)	YS (MPa)		UCS (MPa)		δ (%)	
HIP	/	As-built	HIP-ed	As-built	HIP-ed	As-built	HIP-ed
Mo	RT	340 ± 20	289 ± 2	500 ± 15	531 ± 22	11 ± 1	17 ± 1
	600	150 ± 20	99 ± 8	240 ± 30	260 ± 6	8 ± 1	22 ± 1
	800	160 ± 5	65 ± 4	260 ± 8	137 ± 11	14 ± 1	11 ± 0
	1000	90 ± 10	46 ± 5	150 ± 18	108 ± 11	9 ± 4	9 ± 0
Mo8Re	RT	303 ± 30	250 ± 73	460 ± 31	899 ± 49	7 ± 1.3	29 ± 2
	600	206 ± 8	164 ± 8	339 ± 1	440 ± 8	4 ± 0.5	14 ± 0
	800	186 ± 10	113 ± 7	302 ± 20	275 ± 13	4 ± 0.3	9 ± 0
	1000	119 ± 28	71 ± 9	193 ± 31	139 ± 15	6 ± 0.6	8 ± 0

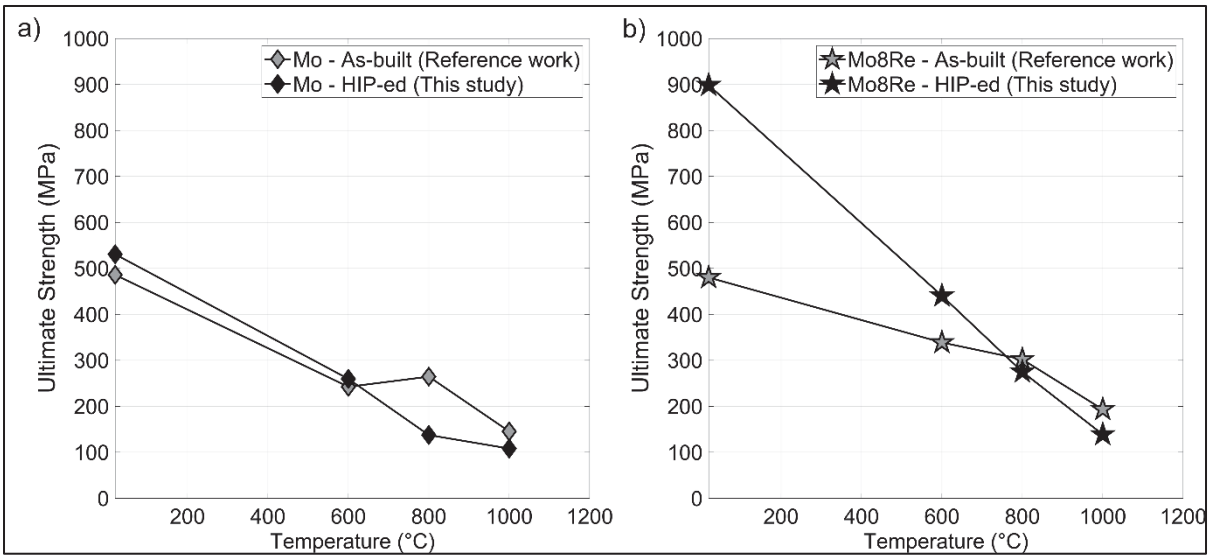

Figure-A III-5: Evolution of the ultimate compression strength as a function of testing temperature. Comparison is made with the as-built state from the two reference works Leclercq, Czech, et al. (2025); Leclercq, Mouret, et al. (2025)

To the best of authors' knowledge, the literature has this far not covered the room and elevated-temperature mechanical properties of LPBF-processed molybdenum or molybdenum-rhenium alloys subjected to HIP post-treatments. Further investigations should be carried out to obtain a deeper understanding of the effects of a HIP post-treatment on LPBF-processed molybdenum and molybdenum alloys parts.

Conclusions

In this study, a novel HIP treatment (1800 °C, 150 MPa, 3h) was applied to pure molybdenum and molybdenum-8wt%rhenium LPBF processed specimens. Density measurements and microstructure analyses revealed that such a treatment led to a decrease in the material density and to a beginning of the primary recrystallization process, but did not affect the grain morphology. Mechanical testing in the 20-1000 °C temperature range showed that despite a 3-4% loss in density, the selected post-treatment enabled to improve the ultimate strength and ductility of both materials in the 20-600 °C temperature range, this improvement being much more pronounced for Mo8Re specimens than for their pure Mo counterparts. In the

800-1000 °C temperature range, the Mo specimens suffered from a significant reduction in both strength and ductility, while their Mo8Re counterparts demonstrated a slight loss in strength compensated by a significant gain in ductility. Based on these observations, it is reasonable to consider the selected for this study HIP conditions (1800ºC, 150 MPa, 3 hours) only for LPBF Mo8Re parts designed for low-to-moderate temperature applications.

Acknowledgments

The authors acknowledge the contributions Anna Czech, Marcin Lis and Adriana Wrona for the powder production and the financial support provided by PRIMA Québec (Pôle de recherche et d'innovation en matériaux avancés) in the framework of theM-ERA.NET program, NSERC (Natural Sciences and Engineering Research Council of Canada) and PyroGenesis Canada Inc.

LISTE DE RÉFÉRENCES BIBLIOGRAPHIQUES

Aboul-Gheit, A. K., Awadallah, A. E., Abdel-Hamid, S. M., Aboul-Enein, A. A., & El-Desouki, D. S. (2012). Direct Conversion of Natural Gas to Petrochemicals Using Monofunctional Mo/SiO_2 and H-ZSM-5 Zeolite Catalysts and Bifunctional Mo/H-ZSM-5 Zeolite Catalyst. *Petroleum Science and Technology*, *30*(9), 893-903. https://doi.org/10.1080/10916466.2010.493912

Ahmed, N. (2019). Direct metal fabrication in rapid prototyping : A review. *Journal of Manufacturing Processes*, *42*, 167-191. https://doi.org/10.1016/j.jmapro.2019.05.001

Alan M. Russel & Kok Loong Lee. (2005). *Structure-Property Relations in Nonferrous Metals* (1re éd.). New Jersey: John Wiley & Sons, Ltd.

Alinejadian, N., Wang, P., Kollo, L., & Prashanth, K. G. (2023). Selective Laser Melting of Commercially Pure Molybdenum by Laser Rescanning. *3D Printing and Additive Manufacturing*, *10*(4), 785-791. https://doi.org/10.1089/3dp.2021.0265

Allen, R. D., Glasier, L. F., & Jordan, P. L. (1960). Spectral Emissivity, Total Emissivity, and Thermal Conductivity of Molybdenum, Tantalum, and Tungsten above 2300°K. *Journal of Applied Physics*, *31*(8), 1382-1387. https://doi.org/10.1063/1.1735847

Alluaibi, M. H. I., Balkan, I. V., Șerban, N., Cinca, I., Angelescu, M. L., Cojocaru, E. M., … Cojocaru, V. D. (2024). Optimizing Structural and Mechanical Properties of an Industrial Ti-6246 Alloy below β-Transus Transition Temperature through Thermomechanical Processing. *Materials*, *17*(5), 1145. https://doi.org/10.3390/ma17051145

AMS G Titanium and Refractory Metals Committee. (n.d.). Titanium Alloy Bars, Wire, and Forgings, 6Al—2Sn—4Zr—6Mo, Solution and Precipitation Heat Treated. SAE International. https://doi.org/10.4271/AMS4981

Aversa, A., Carrozza, A., Mercurio, V., Calignano, F., Sereda, O., Pejchal, V., & Lombardi, M. (2025). A Comparison Between the Residual Stresses of Ti6Al4V and Ti-6Al-2Sn-4Zr-6Mo Processed by Laser Powder Bed Fusion. *Materials*, *18*(3), 689. https://doi.org/10.3390/ma18030689

Ayers, N., Lucas, C., Mahmud, A., Kljestan, N., Knezevic, M., & Sohn, Y. (2024). Parameter Optimization and Flaw Type Dependent Tensile Properties of 15-5PH Stainless Steel Manufactured by Laser Powder Bed Fusion. *Advanced Engineering Materials*, *26*(23), 2401346. https://doi.org/10.1002/adem.202401346

B10 Committee. (2013). Specification for Tungsten Base, High-Density Metal. ASTM International. https://doi.org/10.1520/B0777-15

B10 Committee. (2018). Specification for Molybdenum and Molybdenum Alloy Bar, Rod, and Wire. ASTM International. https://doi.org/10.1520/B0387-18

Badawy, W. A., & Al-Kharafi, F. M. (1998). Corrosion and passivation behaviors of molybdenum in aqueous solutions of different pH. *Electrochimica Acta*, *44*(4), 693-702. https://doi.org/10.1016/S0013-4686(98)00180-7

Baier, M., Sinico, M., Witvrouw, A., Dewulf, W., & Carmignato, S. (2021). A novel tomographic characterisation approach for sag and dross defects in metal additively manufactured channels. *Additive Manufacturing*, *39*, 101892. https://doi.org/10.1016/j.addma.2021.101892

Baier, M., Sinico, M., Witvrouw, A., Dewulf, W., & Carmignato, S. (2023). Unravelling the dependency of dross formations in metal additively manufactured channels as a function of channel diameter and inclination angle. *CIRP Journal of Manufacturing Science and Technology*, *45*, 69-81. https://doi.org/10.1016/j.cirpj.2023.06.008

Bajaj, P., Wright, J., Todd, I., & Jägle, E. A. (2019). Predictive process parameter selection for Selective Laser Melting Manufacturing : Applications to high thermal conductivity alloys. *Additive Manufacturing*, *27*, 246-258. https://doi.org/10.1016/j.addma.2018.12.003

Baker, H. (1998). Properties of Metals. Dans Joseph R. Davis (Éd.), *Metals Handbook Desk Edition* (2e éd., pp. 114-121). (S.l.): ASM International. https://doi.org/10.31399/asm.hb.mhde2.a0003086

Bala, K., Pradhan, P. R., Saxena, N. S., & Saksena, M. P. (1989). Effective thermal conductivity of copper powders. *Journal of Physics D: Applied Physics*, *22*(8), 1068-1072. https://doi.org/10.1088/0022-3727/22/8/009

Bałasz, B., Bielecki, M., Gulbiński, W., & Słoboda, Ł. (2023). Comparison of ultrasonic and other atomization methods in metal powder production. *Journal of Achievements in Materials and Manufacturing Engineering*, *116*(1), 11-24. https://doi.org/10.5604/01.3001.0016.3393

Bartolomeu, F., Gasik, M., Silva, F. S., & Miranda, G. (2022). Mechanical Properties of Ti6Al4V Fabricated by Laser Powder Bed Fusion : A Review Focused on the Processing and Microstructural Parameters Influence on the Final Properties. *Metals*, *12*(6), 986. https://doi.org/10.3390/met12060986

Becker, R., Kasperovich, G., Tiessen, P., Haubrich, J., Behrendt, T., & Janus, B. (2024). Fuel Thermal Management and Injector Part Design for LPBF Manufacturing. Dans *Volume 9 : Manufacturing Materials and Metallurgy; Microturbines, Turbochargers, and Small Turbomachines; Oil & Gas Applications; Steam Turbine* (p. V009T17A021). London, United Kingdom: American Society of Mechanical Engineers. https://doi.org/10.1115/GT2024-128600

Bein, S., & Béchet, J. (1996). Phase Transformation Kinetics and Mechanisms in Titanium Alloys Ti-6.2.4.6,ß-CEZ and Ti-10.2.3. *Le Journal de Physique IV*, *06*(C1), C1-108. https://doi.org/10.1051/jp4:1996110

Bhat, B. N. (Éd.). (2018). *Aerospace Materials and Applications*. Reston ,VA: American Institute of Aeronautics and Astronautics, Inc. https://doi.org/10.2514/4.104893

Binner, J., Porter, M., Baker, B., Zou, J., Venkatachalam, V., Diaz, V. R., … Murthy, T. S. R. C. (2020). Selection, processing, properties and applications of ultra-high temperature ceramic matrix composites, UHTCMCs – a review. *International Materials Reviews*, *65*(7), 389-444. https://doi.org/10.1080/09506608.2019.1652006

Blouch, J., Li, H., Mueller, M., & Hook, R. (2012). Fuel Flexibility in LM2500 and LM6000 Dry Low Emission Engines. *Journal of Engineering for Gas Turbines and Power*, *134*(5), 051503. https://doi.org/10.1115/1.4004213

Blum Guillaume, De Blois, M., & Tadjine, N. (2017). *L'impression 3D : De l'émerveillement technique aux enjeux organisationnels, économiques et sociétaux*. Québec (Qc), Canada: École de design de l'Université Laval.

Boyer, R., Welsch, G., & Collings, E. W. (Éds). (2007). *Materials properties handbook : Titanium alloys* (4. printing). Materials Park, Ohio: ASM International.

Braun, J., Kaserer, L., Stajkovic, J., Leitz, K.-H., Tabernig, B., Singer, P., … Leichtfried, G. (2019). Molybdenum and tungsten manufactured by selective laser melting : Analysis of defect structure and solidification mechanisms. *International Journal of Refractory Metals and Hard Materials*, *84*, 104999. https://doi.org/10.1016/j.ijrmhm.2019.104999

Brika, S. E., Letenneur, M., Dion, C. A., & Brailovski, V. (2020). Influence of particle morphology and size distribution on the powder flowability and laser powder bed fusion manufacturability of Ti-6Al-4V alloy. *Additive Manufacturing*, *31*, 100929. https://doi.org/10.1016/j.addma.2019.100929

Buffa, G., Costa, A., Palmeri, D., Pollara, G., Barcellona, A., & Fratini, L. (2023). A new control parameter to predict micro-warping-induced job failure in LPBF of TI6AL4V titanium alloy. *The International Journal of Advanced Manufacturing Technology*, *126*(3-4), 1143-1157. https://doi.org/10.1007/s00170-023-11179-6

Cai, Z., Liu, S., Xiao, L., Fang, Z., Li, W., & Zhang, B. (2017). Oxidation behavior and microstructural evolution of a slurry sintered Si-Mo coating on Mo alloy at 1650 °C. *Surface and Coatings Technology*, *324*, 182-189. https://doi.org/10.1016/j.surfcoat.2017.05.054

Cai, Z., Wu, Y., Liu, H., Tian, G., Pu, R., Piao, S., … Xiao, L. (2018). Formation and oxidation resistance of a new YSZ modified silicide coating on Mo-based alloy. *Materials & Design*, *155*, 463-474. https://doi.org/10.1016/j.matdes.2018.06.011

Cairang, W., Li, T., Xue, D., Yang, H., Cheng, P., Chen, C., … Sun, J. (2021). Enhancement of the corrosion resistance of Molybdenum by La2O3 dispersion. *Corrosion Science*, *186*, 109469. https://doi.org/10.1016/j.corsci.2021.109469

Caliari, F. R., Miranda, F. S., Reis, D. A. P., Filho, G. P., Charakhovski, L. I., & Essiptchouk, A. (2016). Plasma torch for supersonic plasma spray at atmospheric pressure. *Journal of Materials Processing Technology*, *237*, 351-360. https://doi.org/10.1016/j.jmatprotec.2016.06.027

Calignano, F., Cattano, G., & Manfredi, D. (2018). Manufacturing of thin wall structures in AlSi10Mg alloy by laser powder bed fusion through process parameters. *Journal of Materials Processing Technology*, *255*, 773-783. https://doi.org/10.1016/j.jmatprotec.2018.01.029

Cao, S., Zou, Y., Lim, C. V. S., & Wu, X. (2021). Review of laser powder bed fusion (LPBF) fabricated Ti-6Al-4V : Process, post-process treatment, microstructure, and property. *Light : Advanced Manufacturing*, *2*(3), 313-332. https://doi.org/10.37188/lam.2021.020

Carlen, J.-C., & Bryskin, B. D. (1994). Concerning Sigma-Phase in Molybdenum-Rhenium Alloys. *Journal of Materials Engineering and Performance*, *3*(2), 282-291. https://doi.org/10.1007/BF02645854

Carreker, R. P., & Guard, R. W. (1956). Tensile Deformation of Molybdenum as a function of Temperature and Strain Rate. *JOM*, *8*(2), 178-184. https://doi.org/10.1007/BF03377669

Carrozza, A., Bircher, B. A., Aversa, A., & Biamino, S. (2023). Investigating Complex Geometrical Features in LPBF-Produced Parts : A Material-Based Comparison Between Different Titanium Alloys. *Metals and Materials International*, *29*(12), 3697-3714. https://doi.org/10.1007/s12540-023-01460-4

Carrozza, Alessandro, Aversa, A., Fino, P., & Lombardi, M. (2021). A study on the microstructure and mechanical properties of the Ti-6Al-2Sn-4Zr-6Mo alloy produced via Laser Powder Bed Fusion. *Journal of Alloys and Compounds*, *870*, 159329. https://doi.org/10.1016/j.jallcom.2021.159329

Carrozza, Alessandro, Aversa, A., Fino, P., & Lombardi, M. (2022). Towards customized heat treatments and mechanical properties in the LPBF-processed Ti-6Al-2Sn-4Zr-6Mo alloy. *Materials & Design*, *215*, 110512. https://doi.org/10.1016/j.matdes.2022.110512

Ceccanti, F., Giorgetti, A., Arcidiacono, G., & Citti, P. (2021). Laser Powder Bed Fusion : A Review on the Design Constraints. *IOP Conference Series : Materials Science and Engineering*, *1038*(1), 012065. https://doi.org/10.1088/1757-899X/1038/1/012065

Cecere, D., Giacomazzi, E., Di Nardo, A., & Calchetti, G. (2023). Gas Turbine Combustion Technologies for Hydrogen Blends. *Energies*, *16*(19), 6829. https://doi.org/10.3390/en16196829

Centre technique des industries mécaniques (Éd.). (2019). *Fabrication additive métallique : Les fondamentaux*. Senlis Saint-Denis: Centre technique des industries mécaniques Éditions Techniques de l'ingénieur.

Chakraborty, S. P. (2016). Development of Protective Coating of MoSi 2 over TZM Alloy Substrate by Slurry Coating Technique. *Materials Today : Proceedings*, *3*(9), 3071-3076. https://doi.org/10.1016/j.matpr.2016.09.022

Charles, A., Bayat, M., Elkaseer, A., Thijs, L., Hattel, J. H., & Scholz, S. (2022). Elucidation of dross formation in laser powder bed fusion at down-facing surfaces : Phenomenon-oriented multiphysics simulation and experimental validation. *Additive Manufacturing*, *50*, 102551. https://doi.org/10.1016/j.addma.2021.102551

Chen, H., Sun, Y., Yuan, W., Pang, S., Yan, W., & Shi, Y. (2022). A Review on Discrete Element Method Simulation in Laser Powder Bed Fusion Additive Manufacturing. *Chinese Journal of Mechanical Engineering : Additive Manufacturing Frontiers*, *1*(1), 100017. https://doi.org/10.1016/j.cjmeam.2022.100017

Chen, J., Li, K., Wang, Y., Xing, L., Yu, C., Liu, H., … Shen, Z. (2020). The effect of hot isostatic pressing on thermal conductivity of additively manufactured pure tungsten. *International Journal of Refractory Metals and Hard Materials*, *87*, 105135. https://doi.org/10.1016/j.ijrmhm.2019.105135

Chen, Q., Xu, L., Zhao, L., Hao, K., & Han, Y. (2023). Effect of scanning speed on microstructure and mechanical properties of as-printed Ti–22Al–25Nb intermetallic by laser powder bed fusion. *Materials Science and Engineering : A*, *885*, 145652. https://doi.org/10.1016/j.msea.2023.145652

Cheng, B., Kim, Y.-J., & Chou, P. (2016). Improving Accident Tolerance of Nuclear Fuel with Coated Mo-alloy Cladding. *Nuclear Engineering and Technology*, *48*(1), 16-25. https://doi.org/10.1016/j.net.2015.12.003

Chlebus, E., Kuźnicka, B., Dziedzic, R., & Kurzynowski, T. (2015). Titanium alloyed with rhenium by selective laser melting. *Materials Science and Engineering : A*, *620*, 155-163. https://doi.org/10.1016/j.msea.2014.10.021

Chowdhury, S., Yadaiah, N., Prakash, C., Ramakrishna, S., Dixit, S., Gupta, L. R., & Buddhi, D. (2022). Laser powder bed fusion : A state-of-the-art review of the technology, materials, properties & defects, and numerical modelling. *Journal of Materials Research and Technology*, *20*, 2109-2172. https://doi.org/10.1016/j.jmrt.2022.07.121

Clemens, H., & Mayer, S. (2013). Design, Processing, Microstructure, Properties, and Applications of Advanced Intermetallic TiAl Alloys. *Advanced Engineering Materials*, *15*(4), 191-215. https://doi.org/10.1002/adem.201200231

Climax Molybdenum. (1950). Climax Molybdenum Company of Michigan, Fourth Annual Report - Arc-Cast Molybdenum-Base Alloys.

Cobbinah, P. V., Matsunaga, S., Toda, Y., Ozasa, R., Okugawa, M., Ishimoto, T., … Yamabe-Mitarai, Y. (2024). Peculiar microstructural evolution and hardness variation depending on laser powder bed fusion-manufacturing condition in Ti–6Al–2Sn–4Zr–6Mo. *Smart Materials in Manufacturing*, *2*, 100050. https://doi.org/10.1016/j.smmf.2024.100050

Colombo-Pulgarín, J. C., Biffi, C. A., Vedani, M., Celentano, D., Sánchez-Egea, A., Boccardo, A. D., & Ponthot, J.-P. (2021). Beta Titanium Alloys Processed By Laser Powder Bed Fusion : A Review. *Journal of Materials Engineering and Performance*, *30*(9), 6365-6388. https://doi.org/10.1007/s11665-021-05800-6

Colomo, A. G., Wood, D., Martina, F., & Williams, S. W. (2020). A comparison framework to support the selection of the best additive manufacturing process for specific aerospace applications. *International Journal of Rapid Manufacturing*, *9*(2/3), 194. https://doi.org/10.1504/IJRAPIDM.2020.107736

Cooper, R. H., Jr, & Hoffman, E. E. (1984). *Refractory alloy technology for space nuclear power applications* (Rapport No. CONF-8308130; ON: DE84001745). Oak Ridge, Tennessee, USA: Oak Ridge National Laboratory and U.S Department of Energy Oak Ridge Operations.

Cordero, Z. C., Knight, B. E., & Schuh, C. A. (2016). Six decades of the Hall–Petch effect – a survey of grain-size strengthening studies on pure metals. *International Materials Reviews*, *61*(8), 495-512. https://doi.org/10.1080/09506608.2016.1191808

Cotton, J. D., Briggs, R. D., Boyer, R. R., Tamirisakandala, S., Russo, P., Shchetnikov, N., & Fanning, J. C. (2015). State of the Art in Beta Titanium Alloys for Airframe Applications. *JOM*, *67*(6), 1281-1303. https://doi.org/10.1007/s11837-015-1442-4

Cottrell, A. H., & Bilby, B. A. (1949). Dislocation Theory of Yielding and Strain Ageing of Iron. *Proceedings of the Physical Society. Section A*, *62*(1), 49-62. https://doi.org/10.1088/0370-1298/62/1/308

Dai, J., Zhu, J., Chen, C., & Weng, F. (2016). High temperature oxidation behavior and research status of modifications on improving high temperature oxidation resistance of titanium alloys and titanium aluminides : A review. *Journal of Alloys and Compounds*, *685*, 784-798. https://doi.org/10.1016/j.jallcom.2016.06.212

Dai, Z., Su, Y., Yang, T., Wang, Y., Liang, X., Wei, Z., & Zhang, X. (2022). Study on intermediate temperature brittleness mechanism of Inconel 625 deposited metal. *Journal of Materials Research and Technology*, *17*, 1812-1821. https://doi.org/10.1016/j.jmrt.2022.01.143

Das, J., Rao, G. A., Pabi, S. K., Sankaranarayana, M., & Nandy, T. K. (2014). Oxidation studies on W–Nb alloy. *International Journal of Refractory Metals and Hard Materials*, *47*, 25-37. https://doi.org/10.1016/j.ijrmhm.2014.06.016

Davis, J. R., & ASM International (Éds). (1998). *Metals handbook* (Desk ed., 2nd ed). Materials Park, Oh: ASM International.

Davis, Joseph R. & ASM International (Éds). (2010). *Metals handbook* (Desk ed., 2. ed., 5. print). Materials Park, Ohio: ASM International.

Desrosiers, C., Letenneur, M., Bernier, F., Cheriet, F., Brailovski, V., Piché, N., & Guibault, F. (2022). Correlative Laser Confocal Microscopy Study and Multimodal 2D/3D Registration as Ground Truth for X-ray Inspection of Internal Defects in LPBF Manufacturing. *E-Journal of Nondestructive Testing*, *27*(03). https://doi.org/10.58286/26642

Destefani, J. D. (1990). Introduction to Titanium and Titanium Alloys. Dans ASM Handbook Committee (Éd.), *Properties and Selection : Nonferrous Alloys and Special-Purpose Materials* (pp. 586-591). (S.l.): ASM International. https://doi.org/10.31399/asm.hb.v02.a0001080

Dias Corpa Tardelli, J., Bolfarini, C., & Cândido dos Reis, A. (2020). Comparative analysis of corrosion resistance between beta titanium and Ti-6Al-4V alloys : A systematic review. *Journal of Trace Elements in Medicine and Biology*, *62*, 126618. https://doi.org/10.1016/j.jtemb.2020.126618

Djanarthany, S., Viala, J.-C., & Bouix, J. (2001). An overview of monolithic titanium aluminides based on Ti3Al and TiAl. *Materials Chemistry and Physics*, *72*(3), 301-319. https://doi.org/10.1016/S0254-0584(01)00328-5

Duan, Z., Yang, H., Satoh, Y., Murakami, K., Kano, S., Zhao, Z., … Abe, H. (2017). Current status of materials development of nuclear fuel cladding tubes for light water reactors. *Nuclear Engineering and Design*, *316*, 131-150. https://doi.org/10.1016/j.nucengdes.2017.02.031

Dubois, P. K., Landry, C., Thibault, D., Plante, J.-S., Picard, M., & Picard, B. (2022). Benefits and Challenges of the Inside-Out Ceramic Turbine : An Experimental Assessment. *Journal of Propulsion and Power*, *38*(2), 221-228. https://doi.org/10.2514/1.B38004

Dubois, P. K., Landry-Blais, A., Gazzah, R., Sivić, S., Brailovski, V., & Picard, M. (2022). Cooling Performance of Additively Manufactured Pin Fins in Stacked Microchannels for the Inside-Out Ceramic Turbine Shroud-Cooling Ring. *Journal of Turbomachinery*, *144*(7), 071004. https://doi.org/10.1115/1.4053232

Durand-Charre, M. (2017). *The Microstructure of Superalloys* (First edition). London: Taylor and Francis.

Durocher, A., Fan, L., Füri, M., Bourque, G., Sirois, J., May, D., … Vena, P. (2024). Characterization of a 5-nozzle array using premix/micromix injection for hydrogen. *Applications in Energy and Combustion Science*, *18*, 100260. https://doi.org/10.1016/j.jaecs.2024.100260

Dzogbewu, T. C., & De Beer, D. (2023). Powder Bed Fusion of Multimaterials. *Journal of Manufacturing and Materials Processing*, *7*(1), 15. https://doi.org/10.3390/jmmp7010015

E. Pink and R. W. Armstrong. (1970). Total material variables influencing DBTT for molybdenum.

E04 Committee. (2019). Standard Practice for Determining Average Grain Size Using Electron Backscatter Diffraction (EBSD) in Fully Recrystallized Polycrystalline Materials. ASTM International. https://doi.org/10.1520/E2627–13R19

E28 Committee. (2018). Practice for Compression Tests of Metallic Materials at Elevated Temperatures with Conventional or Rapid Heating Rates and Strain Rates. ASTM International. https://doi.org/10.1520/E0209-18

E28 Committee. (2019). Test Methods of Compression Testing of Metallic Materials at Room Temperature. ASTM International. https://doi.org/10.1520/E0009-19

E28 Committee. (2020). Test Methods for Elevated Temperature Tension Tests of Metallic Materials. ASTM International. https://doi.org/10.1520/E0021-20

E28 Committee. (2024). Test Methods for Tension Testing of Metallic Materials. ASTM International. https://doi.org/10.1520/E0008_E0008M-24

E2627-13; Standard Practice for Determining Average Grain Size Using Electron Backscatter Diffraction (EBSD) in Fully Recrystallized Polycrystalline Materials. (n.d.). 100 Barr Harbor Drive, PO Box C700, West Conshohocken, PA 19428-2959. United States: ASTM International.

Eckley, C. C., Kinkade, R. X., Sexton, B. M., Shelton, T. E., Schubert-Kabban, C., Hartsfield, C. R., … Kemnitz, R. A. (2023). Evaluating Molybdenum-Rhenium Alloys Through Additive Manufacturing. *JOM*, *75*(6), 1928-1940. https://doi.org/10.1007/s11837-023-05813-7

El-Genk, M. S., & Tournier, J.-M. (2005). A review of refractory metal alloys and mechanically alloyed-oxide dispersion strengthened steels for space nuclear power systems. *Journal of Nuclear Materials*, *340*(1), 93-112. https://doi.org/10.1016/j.jnucmat.2004.10.118

Ellsworth, N. E., Kemnitz, R. A., Eckley, C. C., Sexton, B. M., Bowers, C. T., Machacek, J. R., & Burggraf, L. W. (2022). Influence of Nano-Sized SiC on the Laser Powder Bed Fusion of Molybdenum. *Crystals*, *12*(9), 1276. https://doi.org/10.3390/cryst12091276

Enneti, R. K., Trasorras, J. L., & Kestler, H. (2020). Additive Manufacturing of Tungsten, Molybdenum, and Cemented Carbides. Dans D. L. Bourell, W. Frazier, H. Kuhn, & M. Seifi (Éds), *Additive Manufacturing Processes* (pp. 380-387). (S.l.): ASM International. https://doi.org/10.31399/asm.hb.v24.a0006583

Evans, M., & Ward, A. R. (2001). Corrosion resistance of Ti-6246 for high power aeroengine compressor discs and blades. *Materials Science and Technology*, *17*(8), 945-953. https://doi.org/10.1179/026708301101510771

Ezugwu, E. O., & Wang, Z. M. (1997). Titanium alloys and their machinability—A review. *Journal of Materials Processing Technology*, *68*(3), 262-274. https://doi.org/10.1016/S0924-0136(96)00030-1

Faidel, D., Jonas, D., Natour, G., & Behr, W. (2015). Investigation of the selective laser melting process with molybdenum powder. *Additive Manufacturing*, *8*, 88-94. https://doi.org/10.1016/j.addma.2015.09.002

Fedina, T., Sundqvist, J., Powell, J., & Kaplan, A. F. H. (2020). A comparative study of water and gas atomized low alloy steel powders for additive manufacturing. *Additive Manufacturing*, *36*, 101675. https://doi.org/10.1016/j.addma.2020.101675

Feng, Y., Zhang, W., Cui, G., Chen, W., & Yu, Y. (2017). Room temperature tensile fracture characteristics of the oriented TiB whisker reinforced TA15 matrix composites fabricated by pre-sintering and canned extrusion. *Materials Science and Engineering : A*, *707*, 40-43. https://doi.org/10.1016/j.msea.2017.09.034

Fernandes, C., & Taurino, I. (2022). Biodegradable Molybdenum (Mo) and Tungsten (W) Devices : One Step Closer towards Fully-Transient Biomedical Implants. *Sensors*, *22*(8), 3062. https://doi.org/10.3390/s22083062

Fernandez-Zelaia, P., Ledford, C., Ellis, E. A. I., Campbell, Q., Rossy, A. M., Leonard, D. N., & Kirka, M. M. (2021). Crystallographic texture evolution in electron beam melting additive manufacturing of pure Molybdenum. *Materials & Design*, *207*, 109809. https://doi.org/10.1016/j.matdes.2021.109809

Fernandez-Zelaia, P., Ledford, C., Kim, S., Campbell, Q., Rojas, J. O., Rossy, A. M., & Kirka, M. (2022). Mechanical Behavior of Additively Manufactured Molybdenum and Fabrication of Microtextured Composites. *JOM*, *74*(9), 3316-3328. https://doi.org/10.1007/s11837-022-05379-w

Field, A. C., Carter, L. N., Adkins, N. J. E., Attallah, M. M., Gorley, M. J., & Strangwood, M. (2020). The Effect of Powder Characteristics on Build Quality of High-Purity Tungsten Produced via Laser Powder Bed Fusion (LPBF). *Metallurgical and Materials Transactions A*, *51*(3), 1367-1378. https://doi.org/10.1007/s11661-019-05601-6

Fleißner-Rieger, C., Tunes, M. A., Gammer, C., Jörg, T., Pfeifer, T., Musi, M., … Clemens, H. (2022). On the existence of orthorhombic martensite in a near-α titanium base alloy used for additive manufacturing. *Journal of Alloys and Compounds*, *897*, 163155. https://doi.org/10.1016/j.jallcom.2021.163155

Flower, H. M., Davis, R., & West, D. R. F. (1982). Martensite Formation and Decomposition in Alloys of Titanium Containing β-Stabilizing Elements. Dans J. C. Williams & A. F. Belov (Éds), *Titanium and Titanium Alloys : Scientific and Technological Aspects Volume 3* (pp. 1703-1715). Boston, MA: Springer US. https://doi.org/10.1007/978-1-4757-1758-7_8

Freeman, R., & Fu, X. (2008). Characterisation of powder bulk, dynamic flow and shear properties in relation to die filling. *Powder Metallurgy*, *51*(3), 196-201. https://doi.org/10.1179/174329008X324115

Freeman, Reg. (2007). Measuring the flow properties of consolidated, conditioned and aerated powders—A comparative study using a powder rheometer and a rotational shear cell. *Powder Technology*, *174*(1), 25-33. https://doi.org/10.1016/j.powtec.2006.10.016

Froes, F. H. (Éd.). (2015). *Titanium : Physical Metallurgy, Processing, and Applications*. (S.l.): ASM International. https://doi.org/10.31399/asm.tb.tpmpa.9781627083188

Fu, T., Cui, K., Zhang, Y., Wang, J., Zhang, X., Shen, F., … Mao, H. (2021). Microstructure and Oxidation Behavior of Anti-Oxidation Coatings on Mo-Based Alloys through HAPC Process : A Review. *Coatings*, *11*(8), 883. https://doi.org/10.3390/coatings11080883

Fu, T., Shen, F., Zhang, Y., Yu, L., Cui, K., Wang, J., & Zhang, X. (2022). Oxidation Protection of High-Temperature Coatings on the Surface of Mo-Based Alloys—A Review. *Coatings*, *12*(2), 141. https://doi.org/10.3390/coatings12020141

Funch, C. V., & Proust, G. (2024). Laser-based additive manufacturing of refractory metals and their alloys : A review. *Additive Manufacturing*, *94*, 104464. https://doi.org/10.1016/j.addma.2024.104464

Funke, Harald H.-W., Beckmann, N., Keinz, J., & Horikawa, A. (2021). 30 Years of Dry-Low-NOx Micromix Combustor Research for Hydrogen-Rich Fuels—An Overview of Past and Present Activities. *Journal of Engineering for Gas Turbines and Power*, *143*(7), 071002. https://doi.org/10.1115/1.4049764

Funke, H.H.-W., Beckmann, N., & Abanteriba, S. (2019). An overview on dry low NOx micromix combustor development for hydrogen-rich gas turbine applications. *International Journal of Hydrogen Energy*, *44*(13), 6978-6990. https://doi.org/10.1016/j.ijhydene.2019.01.161

Gaikwad, A., Imani, F., Yang, H., Reutzel, E., & Rao, P. (2019). In Situ Monitoring of Thin-Wall Build Quality in Laser Powder Bed Fusion Using Deep Learning. *Smart and Sustainable Manufacturing Systems*, *3*(1), 98-121. https://doi.org/10.1520/SSMS20190027

Gan, J., Du, K., Ji, X., Huang, Y., Li, K., Li, Y., … Gong, Q. (2024). Research about the microcrack mechanisms in molybdenum and corresponding suppression strategies during laser additive manufacturing process. *Materialia*, *36*, 102173. https://doi.org/10.1016/j.mtla.2024.102173

Garcia-Colomo, A., Wood, D., Martina, F., & Williams, S. W. (2020). A comparison framework to support the selection of the best additive manufacturing process for specific aerospace applications. *International Journal of Rapid Manufacturing*, *9*(2-3), 194-211. https://doi.org/10.1504/IJRAPIDM.2020.107736

Gatzen, C., Smokovych, I., Scheffler, M., & Krüger, M. (2021). Oxidation-Resistant Environmental Barrier Coatings for Mo-Based Alloys : A Review. *Advanced Engineering Materials*, *23*(4), 2001016. https://doi.org/10.1002/adem.202001016

Geometrical product specifications (GPS)—Surface texture : Profile—Part 2 : Terms, definitions and surface texture parameters. (2021, décembre).

Golden, R. A., & Opila, E. J. (2016). A method for assessing the volatility of oxides in high-temperature high-velocity water vapor. *Journal of the European Ceramic Society*, *36*(5), 1135-1147. https://doi.org/10.1016/j.jeurceramsoc.2015.11.016

Gong, H., Rafi, K., Starr, T., & Stucker, B. (2013). The Effects of Processing Parameters on Defect Regularity in Ti-6Al-4V Parts Fabricated By Selective Laser Melting and Electron Beam Melting. *24th International SFF Symposium—An Additive Manufacturing Conference*.

Gong, H., Teng, C., Zeng, K., Pal, D., Stucker, B., Dilip, J. J. S., … Lewandowski, J. J. (2016). Single Track of Selective Laser Melting Ti-6Al-4V Powder on Support Structure.

Gor, M., Dobriyal, A., Wankhede, V., Sahlot, P., Grzelak, K., Kluczyński, J., & Łuszczek, J. (2022). Density Prediction in Powder Bed Fusion Additive Manufacturing : Machine Learning-Based Techniques. *Applied Sciences*, *12*(14), 7271. https://doi.org/10.3390/app12147271

Gorr, B., Schellert, S., Müller, F., Christ, H.-J., Kauffmann, A., & Heilmaier, M. (2021). Current Status of Research on the Oxidation Behavior of Refractory High Entropy Alloys. *Advanced Engineering Materials*, *23*(5), 2001047. https://doi.org/10.1002/adem.202001047

Gradl, P., Tinker, D. C., Park, A., Mireles, O. R., Garcia, M., Wilkerson, R., & Mckinney, C. (2022). Robust Metal Additive Manufacturing Process Selection and Development for Aerospace Components. *Journal of Materials Engineering and Performance*, *31*(8), 6013-6044. https://doi.org/10.1007/s11665-022-06850-0

Graver, B., & Mukhopadhaya, J. (2022). ALIGNING AVIATION WITH THE PARIS AGREEMENT.

Gu, D. D., Meiners, W., Wissenbach, K., & Poprawe, R. (2012). Laser additive manufacturing of metallic components : Materials, processes and mechanisms. *International Materials Reviews*, *57*(3), 133-164. https://doi.org/10.1179/1743280411Y.0000000014

Gu, D., Guo, M., Zhang, H., Sun, Y., Wang, R., & Zhang, L. (2020). Effects of laser scanning strategies on selective laser melting of pure tungsten. *International Journal of Extreme Manufacturing*, *2*(2), 025001. https://doi.org/10.1088/2631-7990/ab7b00

Guan, B., Yang, X., Tang, J., Qin, L., Xu, M., Yan, Y., … Le, G. (2023). Strategies to reduce pores and cracks of molybdenum fabricated by selective laser melting. *International Journal of Refractory Metals and Hard Materials*, *112*, 106123. https://doi.org/10.1016/j.ijrmhm.2023.106123

Guellouh, N., Szamosi, Z., & Simenfalvi, Z. (2019). Combustors with Low Emission Levels for Aero Gas Turbine Engines. *International Journal of Engineering and Management Sciences*, *4*(1).

Guleryuz, H., & Cimenoglu, H. (2009). Oxidation of Ti–6Al–4V alloy. *Journal of Alloys and Compounds*, *472*(1-2), 241-246. https://doi.org/10.1016/j.jallcom.2008.04.024

Guo, M., Gu, D., Xi, L., Zhang, H., Zhang, J., Yang, J., & Wang, R. (2019). Selective laser melting additive manufacturing of pure tungsten : Role of volumetric energy density on densification, microstructure and mechanical properties. *International Journal of Refractory Metals and Hard Materials*, *84*, 105025. https://doi.org/10.1016/j.ijrmhm.2019.105025

Guo, M., Liu, K., Sun, J., & Gu, D. (2022). Laser powder bed fusion of a novel nano-modified tungsten alloy with refined microstructure and enhanced strength. *Materials Science and Engineering : A*, *843*, 143096. https://doi.org/10.1016/j.msea.2022.143096

Guo, Y., Jung, T., Chiu, Y. L., Li, H., Bray, S., & Bowen, P. (2013). Microstructure and microhardness of Ti6246 linear friction weld. *Materials Science and Engineering : A*, *562*, 17-24. https://doi.org/10.1016/j.msea.2012.10.089

Gussone, J., Rackel, M. W., Tumminello, S., Barriobero-Vila, P., Kreps, F., Kelm, K., … Requena, G. (2023). Microstructure formation during laser powder bed fusion of Ti-22Al-25Nb with low and high pre-heating temperatures. *Materials & Design*, *232*, 112154. https://doi.org/10.1016/j.matdes.2023.112154

Hada, S., Takata, K., Iwasaki, Y., Yuri, M., & Masada, J. (2015). *High-efficiency Gas Turbine Development applying 1600°C class « J » Technology* (Rapport No. Vol. 52, No. 2). Mitsubishi Heavy Industries.

Haj Ayed, A., Kusterer, K., Funke, H. H.-W., Keinz, J., Striegan, C., & Bohn, D. (2015). Experimental and numerical investigations of the dry-low-NOx hydrogen micromix combustion chamber of an industrial gas turbine. *Propulsion and Power Research*, *4*(3), 123-131. https://doi.org/10.1016/j.jppr.2015.07.005

Ham, J. L. (1951). An Introduction to Arc-Cast Molybdenum and Its Alloys. *ASTM-ASME Committee on Effect of Temperature on the Properties of Metals*, (50—A-70).

Hampel, C. A. (1958). Corrosion Properties of Tantalum, Columbium, Molybdenum and Tungsten. *Corrosion*, *14*(12), 29-32. https://doi.org/10.5006/0010-9312-14.12.29

Han, B., & Marya, M. (2025). An Evaluation of the Mechanical Properties and Sulfide Stress Cracking of Additively Manufactured Alloy Ti-6Al-2Sn-4Zr-6Mo for Sour Geothermal Use (pp. 1-15). Communication présentée au CONFERENCE 2025, Association for Materials Protection and Performance. https://doi.org/10.5006/C2025-00101

Handbook of the EuroLaser Academy. 2. (1998) (1. ed). London Weinheim: Chapman & Hall.

Hanzl, P., Zetek, M., Bakša, T., & Kroupa, T. (2015). The Influence of Processing Parameters on the Mechanical Properties of SLM Parts. *Procedia Engineering*, *100*, 1405-1413. https://doi.org/10.1016/j.proeng.2015.01.510

Hao, Z., Fu, Z., Liu, J., Zhu, X., Zhou, F., Shu, Y., … He, J. (2019). Spheroidization of a granulated molybdenum powder by radio frequency inductively coupled plasma. *International Journal of Refractory Metals and Hard Materials*, *82*, 15-22. https://doi.org/10.1016/j.ijrmhm.2019.03.023

Hargrave, B., Gonzalez, M., Maskos, K., Skogsberg, J., & Grauman, J. (2010). Titanium Alloy Tubing For Hpht Octg Applications. Communication présentée au CORROSION 2010, San Antonio.

Hassanin, H., El-Sayed, M. A., Ahmadein, M., Alsaleh, N. A., Ataya, S., Ahmed, M. M. Z., & Essa, K. (2023). Optimising Surface Roughness and Density in Titanium Fabrication via Laser Powder Bed Fusion. *Micromachines*, *14*(8), 1642. https://doi.org/10.3390/mi14081642

Hassanin, H., Zweiri, Y., Finet, L., Essa, K., Qiu, C., & Attallah, M. (2021). Laser Powder Bed Fusion of Ti-6Al-2Sn-4Zr-6Mo Alloy and Properties Prediction Using Deep Learning Approaches. *Materials*, *14*(8), 2056. https://doi.org/10.3390/ma14082056

He, J., Li, D., Jiang, W., Ke, L., Qin, G., Ye, Y., … Qiu, D. (2019). The Martensitic Transformation and Mechanical Properties of Ti6Al4V Prepared via Selective Laser Melting. *Materials*, *12*(2), 321. https://doi.org/10.3390/ma12020321

He, Y., Ma, Y., Zhang, W., & Wang, Z. (2022). Anisotropic tensile and fatigue properties of laser powder bed fusion Ti6Al4V under high temperature. *Engineering Fracture Mechanics*, *276*, 108948. https://doi.org/10.1016/j.engfracmech.2022.108948

Hegab, H., Khanna, N., Monib, N., & Salem, A. (2023). Design for sustainable additive manufacturing : A review. *Sustainable Materials and Technologies*, *35*, e00576. https://doi.org/10.1016/j.susmat.2023.e00576

Hemmasian Ettefagh, A., Guo, S., & Raush, J. (2021). Corrosion performance of additively manufactured stainless steel parts : A review. *Additive Manufacturing*, *37*, 101689. https://doi.org/10.1016/j.addma.2020.101689

Hidnert, P., & Gero, W. B. (1924). Thermal expansion of molybdenum. *Scientific Papers of the Bureau of Standards*, *19*, 429. https://doi.org/10.6028/nbsscipaper.171

Higashi, M., & Ozaki, T. (2020). Selective laser melting of pure molybdenum : Evolution of defect and crystallographic texture with process parameters. *Materials & Design*, *191*, 108588. https://doi.org/10.1016/j.matdes.2020.108588

Hinrichs, F., Kauffmann, A., Schliephake, D., Seils, S., Obert, S., Ratschbacher, K., … Heilmaier, M. (2021). Flexible Powder Production for Additive Manufacturing of Refractory Metal-Based Alloys. *Metals*, *11*(11), 1723. https://doi.org/10.3390/met11111723

Hiraoka, Y. (1990). Significant Effect of Carbon Content in the Low-Temperature Fracture Behavior of Molybdenum. *Materials Transactions, JIM*, *31*(10), 861-864. https://doi.org/10.2320/matertrans1989.31.861

Hiraoka, Y., Kurishita, H., Narui, M., & Kayano, H. (1995). Fracture and Ductile-to-Brittle Transition Characteristics of Molybdenum by Impact and Static Bend Tests. *Materials Transactions, JIM*, *36*(4), 504-510. https://doi.org/10.2320/matertrans1989.36.504

Holmwood, R. A., & Glang, R. (1965). Resistivity and Temperature Coefficient of Pure Molybdenum. *Journal of Chemical & Engineering Data*, *10*(2), 162-163. https://doi.org/10.1021/je60025a028

Hooper, P. A. (2018). Melt pool temperature and cooling rates in laser powder bed fusion. *Additive Manufacturing*, *22*, 548-559. https://doi.org/10.1016/j.addma.2018.05.032

Hu, P., Yang, F., Wang, K.-S., Yu, Z., Tan, J., Song, R., … Volinsky, A. A. (2015). Preparation and ductile-to-brittle transition temperature of the La-TZM alloy plates. *International Journal of Refractory Metals and Hard Materials*, *52*, 131-136. https://doi.org/10.1016/j.ijrmhm.2015.05.006

Huang, G., He, Y., Long, S., Duan, Q., Chen, H., Peng, X., … Huang, K. (2024). Microstructure, compressive performance and wear resistance of pure molybdenum additively manufactured via laser powder bed fusion. *International Journal of Refractory Metals and Hard Materials*, *123*, 106740. https://doi.org/10.1016/j.ijrmhm.2024.106740

Huang, H., Li, W., Liu, Y., Luo, B., Wang, W., Zheng, J., … Yin, C. (2022). Hot compression behaviors and microstructural evolution of Mo-42 wt%Re alloy. *Materials Letters*, *318*, 132252. https://doi.org/10.1016/j.matlet.2022.132252

Hucek, H. J. (1979). *Aerospace Structural Metals Handbook : 1989 Publication With 1988 Supplement XXI Incorporated.* (Vol. 4). Columbus, OH: (s.n.).

Humphreys, F. J., & Hatherly, M. (2012). *Recrystallization and Related Annealing Phenomena*. Jordan Hill: Elsevier Science.

Humphreys, Frederick John, & Hatherly, M. (1995). *Recrystallization and related annealing phenomena*. Oxford New York Tokyo: Pergamon.

Hwang, Y.-J., Kim, Y., Park, S.-H., Park, S.-C., & Lee, K.-A. (2024). Wear and Corrosion Properties of Pure Mo Coating Layer Manufactured by Atmospheric Plasma Spray Process. *Archives of Metallurgy and Materials*, 81-85. https://doi.org/10.24425/amm.2024.147790

Illarionov, A. G., Stepanov, S. I., Naschetnikova, I. A., Popov, A. A., Soundappan, P., Thulasi Raman, K. H., & Suwas, S. (2023). A Review—Additive Manufacturing of Intermetallic Alloys Based on Orthorhombic Titanium Aluminide Ti2AlNb. *Materials*, *16*(3), 991. https://doi.org/10.3390/ma16030991

Iqbal, N., Afzal, A., Khan, I., Khan, M. S., & Qurashi, A. (2021). Molybdenum impregnated g-C3N4 nanotubes as potentially active photocatalyst for renewable energy applications. *Scientific Reports*, *11*(1), 16886. https://doi.org/10.1038/s41598-021-96490-6

Iveković, A., Omidvari, N., Vrancken, B., Lietaert, K., Thijs, L., Vanmeensel, K., … Kruth, J.-P. (2018). Selective laser melting of tungsten and tungsten alloys. *International Journal of Refractory Metals and Hard Materials*, *72*, 27-32. https://doi.org/10.1016/j.ijrmhm.2017.12.005

Jamhari, F. I., Foudzi, F. M., Buhairi, M. A., Sulong, A. B., Mohd Radzuan, N. A., Muhamad, N., … Tan, K. S. (2023). Influence of heat treatment parameters on microstructure and mechanical performance of titanium alloy in LPBF : A brief review. *Journal of Materials Research and Technology*, *24*, 4091-4110. https://doi.org/10.1016/j.jmrt.2023.04.090

Javaid, M., Haleem, A., Singh, R. P., Suman, R., & Rab, S. (2021). Role of additive manufacturing applications towards environmental sustainability. *Advanced Industrial and Engineering Polymer Research*, *4*(4), 312-322. https://doi.org/10.1016/j.aiepr.2021.07.005

Jia, M., Chen, F., Zhang, L., Huang, Z., & Shen, Q. (2022). Interfacial microstructure and mechanical behavior of low-temperature diffusion bonded Mo/SS304 joints using NixCu1-x interlayers. *Journal of Materials Processing Technology*, *302*, 117513. https://doi.org/10.1016/j.jmatprotec.2022.117513

Jiang, D., Tian, Y., Zhu, Y., & Huang, A. (2022). Investigation of surface roughness post-processing of additively manufactured nickel-based superalloy Hastelloy X using electropolishing. *Surface and Coatings Technology*, *441*, 128529. https://doi.org/10.1016/j.surfcoat.2022.128529

Jiao, B., Zhao, Q., Zhao, Y., Zhang, W., Zhang, W., Li, Y., … Cui, C. (2023). Improving mechanical properties and achieving structural stability of large-size molybdenum single crystal during hot deformation by adding Nb element. *Journal of Alloys and Compounds*, *945*, 169369. https://doi.org/10.1016/j.jallcom.2023.169369

Jin, B., Wang, Q., Zhao, L., Pan, A., Ding, X., Gao, W., … Zhang, X. (2023). A Review of Additive Manufacturing Techniques and Post-Processing for High-Temperature Titanium Alloys. *Metals*, *13*(8), 1327. https://doi.org/10.3390/met13081327

Kan, W. H., Peng, H., Lim, S., Zhu, Y., Zhang, K., & Huang, A. (2023). The mechanisms behind the tribological behavior of titanium alloys processed by laser powder bed fusion sliding against steel. *Tribology International*, *180*, 108279. https://doi.org/10.1016/j.triboint.2023.108279

Kang, S. H., Jin, H.-H., Jang, J., Choi, Y. S., Oh, K. H., Foley, D. C., & Zhang, X. (2013). A Quantitative Evaluation of Microstructure by Electron Back-Scattered Diffraction Pattern Quality Variations. *Microscopy and Microanalysis*, *19*(S5), 83-88. https://doi.org/10.1017/S1431927613012397

Karhu, M., Kivikytö-Reponen, P., & Mroueh, U.-M. (2015). IMN: Katarzyna Bilewska, Adriana Wrona, Witold Kurylak (Mo, Re).

Kaserer, L., Braun, J., Stajkovic, J., Leitz, K.-H., Singer, P., Letofsky-Papst, I., … Leichtfried, G. (2020). Microstructure and mechanical properties of molybdenum-titanium-zirconium-carbon alloy TZM processed via laser powder-bed fusion. *International Journal of Refractory Metals and Hard Materials*, *93*, 105369. https://doi.org/10.1016/j.ijrmhm.2020.105369

Kaserer, L., Braun, J., Stajkovic, J., Leitz, K.-H., Singer, P., Letofsky-Papst, I., … Leichtfried, G. (2023). Molybdenum alloy Mo-Ti-Zr-C adapted for laser powder bed fusion with refined isotropic microstructure and excellent high temperature strength. *International Journal of Refractory Metals and Hard Materials*, *113*, 106174. https://doi.org/10.1016/j.ijrmhm.2023.106174

Kaserer, L., Braun, J., Stajkovic, J., Leitz, K.-H., Tabernig, B., Singer, P., … Leichtfried, G. (2019). Fully dense and crack free molybdenum manufactured by Selective Laser Melting through alloying with carbon. *International Journal of Refractory Metals and Hard Materials*, *84*, 105000. https://doi.org/10.1016/j.ijrmhm.2019.105000

Kasperovich, G., Becker, R., Artzt, K., Barriobero-Vila, P., Requena, G., & Haubrich, J. (2021). The effect of build direction and geometric optimization in laser powder bed fusion of Inconel 718 structures with internal channels. *Materials & Design*, *207*, 109858. https://doi.org/10.1016/j.matdes.2021.109858

Kassner, M. E. (2015). *Fundamentals of creep in metals and alloys* (3. ed). Amsterdam [u.a.]: Elsevier.

Kassym, K., & Perveen, A. (2020). Atomization processes of metal powders for 3D printing. *Materials Today : Proceedings*, *26*, 1727-1733. https://doi.org/10.1016/j.matpr.2020.02.364

Khaimovich, A., Balyakin, A., Oleynik, M., Meshkov, A., & Smelov, V. (2022). Optimization of Process Parameters for Powder Bed Fusion Additive Manufacturing Using a Linear Programming Method : A Conceptual Framework. *Metals*, *12*(11), 1976. https://doi.org/10.3390/met12111976

Khorasani, A. M., Goldberg, M., Doeven, E. H., & Littlefair, G. (2015). Titanium in Biomedical Applications—Properties and Fabrication : A Review. *Journal of Biomaterials and Tissue Engineering*, *5*(8), 593-619. https://doi.org/10.1166/jbt.2015.1361

Kim, Y.-W., & Kim, S.-L. (2018). Advances in Gammalloy Materials–Processes–Application Technology : Successes, Dilemmas, and Future. *JOM*, *70*(4), 553-560. https://doi.org/10.1007/s11837-018-2747-x

Kirsch, K. L., & Thole, K. A. (2017). Heat Transfer and Pressure Loss Measurements in Additively Manufactured Wavy Microchannels. *Journal of Turbomachinery*, *139*(1), 011007. https://doi.org/10.1115/1.4034342

Klopp, W. D. (1968). *Review of ductilizing of group via elements by rhenium and other solutes* (Rapport No. NASA-TN-D-4955). National Aeronautics and Space Administration, Cleveland, OH (USA). Lewis Research Center. Repéré à https://www.osti.gov/biblio/5785668

Klopp, W. D., & Witzke, W. R. (1972). *Mechanical properties of electron-beam-melted molybdenum and dilute molybdenum-rhenium alloys* (Rapport No. NASA-TM-X-2576). Cleveland, OH, USA: NASA Lewis Research Center. Repéré à https://ntrs.nasa.gov/citations/19720017873

Koizumi, Y., Kobayashi, T., Yokokawa, T., Zhang, J., Osawa, M., Harada, H., … Arai, M. (2004). Development of Next-Generation Ni-Base Single Crystal Superalloys. Dans *Superalloys 2004 (Tenth International Symposium)* (pp. 35-43). TMS. https://doi.org/10.7449/2004/Superalloys_2004_35_43

Kolli, R. P., & Devaraj, A. (2018). A Review of Metastable Beta Titanium Alloys. *Metals*, *8*(7), 506. https://doi.org/10.3390/met8070506

Kou, S. (2002). *Welding Metallurgy* (1re éd.). (S.l.): Wiley. https://doi.org/10.1002/0471434027

Kranz, J., Herzog, D., & Emmelmann, C. (2014). Design guidelines for laser additive manufacturing of lightweight structures in TiAl6V4. *Journal of Laser Applications*, *27*(S1), S14001. https://doi.org/10.2351/1.4885235

Kushwaha, A., Subramaniyan, A. K., Bommanahalli Kenchappa, N., & Barad, S. (2022). Microstructure, mechanical, and wear properties of thin-walled Ti6Al4V parts produced using laser powder bed fusion technique. *Materials Letters*, *308*, 131138. https://doi.org/10.1016/j.matlet.2021.131138

Kwon, H. M., Moon, S. W., Kim, T. S., Kang, D. W., Sohn, J. L., & Lee, J. (2019). A study on 65 % potential efficiency of the gas turbine combined cycle. *Journal of Mechanical Science and Technology*, *33*(9), 4535-4543. https://doi.org/10.1007/s12206-019-0850-8

Lakshmi Prasad, B. S., & Raja Annamalai, A. (2021). Effect of Rhenium addition on tungsten heavy alloys processed through spark plasma sintering. *Ain Shams Engineering Journal*, *12*(3), 2957-2963. https://doi.org/10.1016/j.asej.2021.02.022

Landry-Blais, A., Sivić, S., & Picard, M. (2022). Micro-Mixing Combustion for Highly Recuperated Gas Turbines : Effects of Inlet Temperature and Fuel Composition on Combustion Stability and NOx Emissions. *Journal of Engineering for Gas Turbines and Power*, *144*(9), 091014. https://doi.org/10.1115/1.4055190

Lavisse, L., Kanjer, A., Cheveau, K., Optasanu, V., Peyre, P., Gorny, C., … Marco De Lucas, M. C. (2020). Improving the high temperature oxidation resistance of Ti-β21S by mechanical surface treatment. *MATEC Web of Conferences*, *321*, 04001. https://doi.org/10.1051/matecconf/202032104001

L.B. Luntlberg. (1981). A Critical Evaluation of Molybdenum and its Alloys for Use in Space Reactor Core Heat Pipes. Los Alamos Scientific Laboratory.

Leclercq, A., & Brailovski, V. (2024). Improving Laser Powder Bed Fusion Printability of Tungsten Powders Using Simulation-Driven Process Optimization Algorithms. *Materials*, *17*(8), 1865. https://doi.org/10.3390/ma17081865

Leclercq, A., Czech, A., Mouret, T., Lis, M., Wrona, A., & Brailovski, V. (2025). Molybdenum 8wt% rhenium alloy processed by laser powder bed fusion : From powder production to mechanical testing at elevated temperatures. *International Journal of Refractory Metals and Hard Materials*, *132*, 107266. https://doi.org/10.1016/j.ijrmhm.2025.107266

Leclercq, A., Mouret, T., & Brailovski, V. (2024). Laser Powder Bed Fusion And Hot Isostatic Pressing Of Pure Molybdenum : Physical And Mechanical Properties At Elevated Temperatures. Dans *Euro PM2024 Proceedings*. EPMA. https://doi.org/10.59499/EP246281988

Leclercq, A., Mouret, T., & Brailovski, V. (2025). Laser powder bed fusion of molybdenum : Density, structure and mechanical properties at room and elevated temperatures. *Materials Science and Engineering : A*, *In Press*, 148004. https://doi.org/10.1016/j.msea.2025.148004

Leichtfried, G., Schneibel, J. H., & Heilmaier, M. (2006). Ductility and impact resistance of powder-metallurgical molybdenum-rhenium alloys. *Metallurgical and Materials Transactions A*, *37*(10), 2955-2961. https://doi.org/10.1007/s11661-006-0177-9

Leitz, K.-H., Grohs, C., Singer, P., Tabernig, B., Plankensteiner, A., Kestler, H., & Sigl, L. S. (2018). Fundamental analysis of the influence of powder characteristics in Selective Laser Melting of molybdenum based on a multi-physical simulation model. *International Journal of Refractory Metals and Hard Materials*, *72*, 1-8. https://doi.org/10.1016/j.ijrmhm.2017.11.034

Leitz, K.-H., Singer, P., Plankensteiner, A., Tabernig, B., Kestler, H., & Sigl, L. S. (2017). Multi-physical simulation of selective laser melting. *Metal Powder Report*, *72*(5), 331-338. https://doi.org/10.1016/j.mprp.2016.04.004

Leonard, G., & Stegmaier, J. (1994). Development of an Aeroderivative Gas Turbine Dry Low Emissions Combustion System. *Journal of Engineering for Gas Turbines and Power*, *116*(3), 542-546. https://doi.org/10.1115/1.2906853

Leonhardt, T., Carlén, J.-C., Buck, M., Brinkman, C. R., Ren, W., & Stevens, C. O. (1999). Investigation of mechanical properties and microstructure of various molybdenum-rhenium alloys. Dans *AIP Conference Proceedings* (pp. 685-690). Albuquerque, New Mexico (USA): AIP. https://doi.org/10.1063/1.57638

Letenneur, M., Kreitcberg, A., & Brailovski, V. (2019). Optimization of Laser Powder Bed Fusion Processing Using a Combination of Melt Pool Modeling and Design of Experiment Approaches : Density Control. *Journal of Manufacturing and Materials Processing*, *3*(1), 21. https://doi.org/10.3390/jmmp3010021

Leyens, C., & Peters, M. (2004). *Titanium and titanium alloys : Fundamentals and applications*. Weinheim: Wiley-VCH.

Li, J., Wu, Y., Xue, L., & Wei, Z. (2023). Laser powder bed fusion in-situ alloying of refractory WTa alloy and its microstructure and mechanical properties. *Additive Manufacturing*, *67*, 103493. https://doi.org/10.1016/j.addma.2023.103493

Li, J., Wu, Y., Zhou, B., & Wei, Z. (2020). Laser Powder Bed Fusion of Pure Tungsten : Effects of Process Parameters on Morphology, Densification, Microstructure. *Materials*, *14*(1), 165. https://doi.org/10.3390/ma14010165

Liao, J., Fan, A., Luo, H., & Du, Y. (2025). Research progress of laser powder bed fusion of Ti2AlNb-based alloys : Microstructure, defects and properties. *Journal of Materials Research and Technology*, *35*, 3393-3409. https://doi.org/10.1016/j.jmrt.2025.02.037

Lindblad, J. (2005). Surface area estimation of digitized 3D objects using weighted local configurations. *Image and Vision Computing*, *23*(2), 111-122. https://doi.org/10.1016/j.imavis.2004.06.012

Liu, B., Zhang, P., Yan, H., Lu, Q., Shi, H., Liu, Z., … Wang, Q. (2024). A Review on Manufacturing Pure Refractory Metals by Selective Laser Melting. *Journal of Materials Engineering and Performance*. https://doi.org/10.1007/s11665-024-09693-z

Liu, X., Wang, K., Hu, P., Chen, Q., & Volinsky, A. A. (2015). Spheroidization of molybdenum powder by radio frequency thermal plasma. *International Journal of Minerals, Metallurgy, and Materials*, *22*(11), 1212-1218. https://doi.org/10.1007/s12613-015-1187-7

Liu, Y., Shan, Z., Yang, X., Jiao, H., & Huang, W. (2023). Effect of Scanning Strategies on the Microstructure and Mechanical Properties of Ti-22Al-25Nb Alloy Fabricated through Selective Laser Melting. *Metals*, *13*(3), 634. https://doi.org/10.3390/met13030634

Lundberg, L. B. (1981). *A Critical Evaluation of molybdenum and its alloys for use in space reactor core heat pipes* (Rapport No. LA-8685-MS). Los Alamos, NM.

Luo, X., Yang, C., Li, D., & Zhang, L.-C. (2024). Laser Powder Bed Fusion of Beta-Type Titanium Alloys for Biomedical Application : A Review. *Acta Metallurgica Sinica (English Letters)*, *37*(1), 17-28. https://doi.org/10.1007/s40195-023-01654-0

Lütjering, G., & Williams, J. C. (2007). *Titanium* (2nd ed). Berlin ; New York: Springer.

Ma, C., Gui, Y., Wang, Y., Dong, X., Huang, Y., Fu, H., & Shu, G. (2025). Processing, Defect Formation, Microstructure, and Mechanical Properties of Additively Manufactured Refractory Metals : A Review. *Journal of Materials Engineering and Performance*, *34*(9), 7265-7287. https://doi.org/10.1007/s11665-024-10566-8

Majewski, T. (2013). Research of Spheroidization Processes of W-Re Powders. *Solid State Phenomena*, *199*, 490-495. https://doi.org/10.4028/www.scientific.net/SSP.199.490

Man, J., Huang, L., He, J., Yang, H., & Lin, X. (2024). Effect of heat treatment on microstructure and properties of Ti2AlNb alloy formed by selective laser melting. *Journal of Materials Research and Technology*, *33*, 2549-2559. https://doi.org/10.1016/j.jmrt.2024.09.243

Mannheim, R. L., & Garin, J. L. (2003). Structural identification of phases in Mo–Re alloys within the range from 5 to 95% Re. *Journal of Materials Processing Technology*, *143-144*, 533-538. https://doi.org/10.1016/S0924-0136(03)00342-X

Mao, J., Wu, Z., Ye, N., Wen, X., Zhang, F., Zhu, W., … Tang, J. (2025). Compressive performance and defects healing behavior of pure tungsten fabricated by LPBF coupled with subsequent hot isostatic pressing. *International Journal of Refractory Metals and Hard Materials*, *129*, 107100. https://doi.org/10.1016/j.ijrmhm.2025.107100

Marrey, M., Malekipour, E., El-Mounayri, H., & Faierson, E. J. (2019). A Framework for Optimizing Process Parameters in Powder Bed Fusion (PBF) Process Using Artificial Neural Network (ANN). *Procedia Manufacturing*, *34*, 505-515. https://doi.org/10.1016/j.promfg.2019.06.214

Martinz, H.-P., Nigg, B., Matej, J., Sulik, M., Larcher, H., & Hoffmann, A. (2006). Properties of the SIBOR® oxidation protective coating on refractory metal alloys. *International Journal of Refractory Metals and Hard Materials*, *24*(4), 283-291. https://doi.org/10.1016/j.ijrmhm.2005.10.013

Martucci, A., Iannucci, L., Lombardi, M., & Grassini, S. (2024). Effect of microstructural anisotropy and heat treatment on the corrosion behaviour of additively manufactured Ti-6Al-2Sn-4Zr-6Mo alloy. *Journal of Alloys and Compounds*, *1008*, 176746. https://doi.org/10.1016/j.jallcom.2024.176746

Masiagutova, E., Cabanettes, F., Sova, A., Cici, M., Bidron, G., & Bertrand, P. (2021). Side surface topography generation during laser powder bed fusion of AlSi10Mg. *Additive Manufacturing*, *47*, 102230. https://doi.org/10.1016/j.addma.2021.102230

Mason, J. K., & Schuh, C. A. (2009). The generalized Mackenzie distribution : Disorientation angle distributions for arbitrary textures. *Acta Materialia*, *57*(14), 4186-4197. https://doi.org/10.1016/j.actamat.2009.05.016

McDonald, C. F., & Rodgers, C. (2009). Heat-Exchanged Propulsion Gas Turbines : A Candidate for Future Lower SFC and Reduced-Emission Military and Civil Aeroengines. Dans *Volume 1 : Aircraft Engine; Ceramics; Coal, Biomass and Alternative Fuels; Controls, Diagnostics and Instrumentation; Education; Electric Power; Awards and Honors* (pp. 33-49). Orlando, Florida, USA: ASMEDC. https://doi.org/10.1115/GT2009-59156

Meier, B., Warchomicka, F., Petrusa, J., Kaindl, R., Waldhauser, W., & Sommitsch, C. (2023). High Temperature Tensile Strength of TI6AL4V Processed by L-PBF—Influence of Microstructure and Heat Treatment. *BHM Berg- und Hüttenmännische Monatshefte*, *168*(5), 247-253. https://doi.org/10.1007/s00501-023-01346-3

M&I Materials Ltd. (2023). Metal Additive Manufacturing—Tungsten 3D Printing. Repéré à https: //www.wolfmet.com/applications/slm/selective-laser-melting-tungsten/

Milne, I., Ritchie, R. O., & Karihaloo, B. L. (2003). *Comprehensive structural integrity* (1st ed). Amsterdam Boston: Elsevier/Pergamon.

Min, M., Mao, Y., Deng, Q., Wang, G., & Wang, S. (2020). Vacuum brazing of Mo to 316L stainless steel using BNi-2 paste and Cu interlayer. *Vacuum*, *175*, 109282. https://doi.org/10.1016/j.vacuum.2020.109282

Mitra, R. (2019). Oxidation Behavior of Silicides. *Diffusion Foundations*, *21*, 127-156. https://doi.org/10.4028/www.scientific.net/DF.21.127

Moody, H. L., Smith, D. H., Haddock, R. L., & Dunn, S. S. (1976). Tungsten and Molybdenum Ablation Modeling for Re-entry Applications. *Journal of Spacecraft and Rockets*, *13*(12), 746-753. https://doi.org/10.2514/3.57136

Mota, C. J. A., Gonçalves, Valter. L. C., Mellizo, J. E., Rocco, A. M., Fadigas, J. C., & Gambetta, R. (2016). Green propene through the selective hydrogenolysis of glycerol over supported iron-molybdenum catalyst : The original history. *Journal of Molecular Catalysis A: Chemical*, *422*, 158-164. https://doi.org/10.1016/j.molcata.2015.11.014

Motyka, M. (2021). Martensite Formation and Decomposition during Traditional and AM Processing of Two-Phase Titanium Alloys—An Overview. *Metals*, *11*(3), 481. https://doi.org/10.3390/met11030481

Mouret, T., Leclercq, A., & Brailovski, V. (2025). The LPBF printability and as-printed mechanical properties of a Ti6246 alloy as a function of printing parameters and microstructure. *Materials Science and Engineering : A*, 149061. https://doi.org/10.1016/j.msea.2025.149061

Mouret, T., Leclercq, A., Dubois, P., & Brailovski, V. (2025). Effect of layer thickness on the as-built density, microstructure, mechanical properties, surface roughness and printability of LPBF Ti6246 components. *Progress in Additive Manufacturing*.

Moylan, S., Cooke, A., Jurrens, K., Slotwinski, J., & Donmez, M. A. (2012). *A Review of Test Artifacts for Additive Manufacturing* (Rapport No. NIST IR 7858). National Institute of Standards and Technology. https://doi.org/10.6028/NIST.IR.7858

Müller, A. V., Schlick, G., Neu, R., Anstätt, C., Klimkait, T., Lee, J., … Seidel, C. (2019). Additive manufacturing of pure tungsten by means of selective laser beam melting with substrate preheating temperatures up to 1000 ∘C. *Nuclear Materials and Energy*, *19*, 184-188. https://doi.org/10.1016/j.nme.2019.02.034

Narasimharaju, S. R., Zeng, W., See, T. L., Zhu, Z., Scott, P., Jiang, X., & Lou, S. (2022). A comprehensive review on laser powder bed fusion of steels : Processing, microstructure, defects and control methods, mechanical properties, current challenges and future trends. *Journal of Manufacturing Processes*, *75*, 375-414. https://doi.org/10.1016/j.jmapro.2021.12.033

Nelson, A. T., Sooby, E. S., Kim, Y.-J., Cheng, B., & Maloy, S. A. (2014). High temperature oxidation of molybdenum in water vapor environments. *Journal of Nuclear Materials*, *448*(1-3), 441-447. https://doi.org/10.1016/j.jnucmat.2013.10.043

Ni, C., Zhu, J., Zhang, B., An, K., Wang, Y., Liu, D., … Liu, C. (2025). Recent advance in laser powder bed fusion of Ti–6Al–4V alloys : Microstructure, mechanical properties and machinability. *Virtual and Physical Prototyping*, *20*(1), e2446952. https://doi.org/10.1080/17452759.2024.2446952

O'Connor, J., Noble, D. R., Bridges, A., Shingledecker, J., Scheibel, J., & Gagliano, M. (2024). Review of the Impact of Hydrogen-Containing Fuels on Gas Turbine Hot-Section Materials. Dans *Volume 6 : Education; Electric Power; Energy Storage; Fans and Blowers* (p. V006T08A006). London, United Kingdom: American Society of Mechanical Engineers. https://doi.org/10.1115/GT2024-126005

Oehlerking, F., Stawovy, M. T., Ohm, S., & Imandoust, A. (2022). Microstructural characterization and mechanical properties of additively manufactured molybdenum and molybdenum alloys. *International Journal of Refractory Metals and Hard Materials*, *109*, 105971. https://doi.org/10.1016/j.ijrmhm.2022.105971

Okamoto, H. (1998). Section III : Supplemental Literature Review. *Journal of Phase Equilibria*, *19*(5), 486-486. https://doi.org/10.1007/BF02700865

Okamoto, H. (2010). Mo-Re (Molybdenum-Rhenium). *Journal of Phase Equilibria and Diffusion*, *31*(6), 580-581. https://doi.org/10.1007/s11669-010-9787-4

Otsuka, T., Sawano, N., Fujii, Y., Omura, T., Taylor, C., & Shimada, M. (2020). Effects of rhenium contents on oxidation behaviors of tungsten-rhenium alloys in the oxygen gas atmosphere at 873 K. *Nuclear Materials and Energy*, *25*, 100791. https://doi.org/10.1016/j.nme.2020.100791

Park, J., Shin, J., Park, S., Lee, S., & Choi, N. (2025). The Effect of Heterogeneous Natural Gas–Hydrogen Input Into F-Class Gas Turbine Combustor As a Combustion Optimization Method. *Journal of Engineering for Gas Turbines and Power*, *147*(3), 031017. https://doi.org/10.1115/1.4066471

Pauzon, C., Raza, A., Hanif, I., Dubiez-Le Goff, S., Moverare, J., & Hryha, E. (2023). Effect of layer thickness on spatter properties during laser powder bed fusion of Ti–6Al–4V. *Powder Metallurgy*, *66*(4), 333-342. https://doi.org/10.1080/00325899.2023.2192036

Peng, H., Wu, S., Kan, W. H., Lim, S. C. V., Zhu, Y., & Huang, A. (2023). Rapid hardening response of ultra-hard Ti-6Al-2Sn-4Zr-6Mo alloy produced by laser powder bed fusion. *Scripta Materialia*, *226*, 115209. https://doi.org/10.1016/j.scriptamat.2022.115209

Perepezko, J. H. (2018). High temperature environmental resistant Mo-Si-B based coatings. *International Journal of Refractory Metals and Hard Materials*, *71*, 246-254. https://doi.org/10.1016/j.ijrmhm.2017.11.033

Peters, M., Kumpfert, J., Ward, C. H., & Leyens, C. (2003). Titanium Alloys for Aerospace Applications. *Advanced Engineering Materials*, *5*(6), 419-427. https://doi.org/10.1002/adem.200310095

Philips, N. R., Carl, M., & Cunningham, N. J. (2020). New Opportunities in Refractory Alloys. *Metallurgical and Materials Transactions A*, *51*(7), 3299-3310. https://doi.org/10.1007/s11661-020-05803-3

Picard, B., Picard, M., Plante, J.-S., & Rancourt, D. (2020). Optimum sub-megawatt electric-hybrid power source selection. *Aircraft Engineering and Aerospace Technology*, *92*(5), 717-726. https://doi.org/10.1108/AEAT-06-2019-0119

Pirro, G., Martucci, A., Morri, A., Lombardi, M., & Ceschini, L. (2025). A novel solution treatment and aging for powder bed fusion-laser beam Ti-6Al-2Sn-4Zr-6Mo alloy : Microstructural and mechanical characterization. *International Journal of Minerals, Metallurgy and Materials*, *32*(2), 414-424. https://doi.org/10.1007/s12613-024-3006-5

Plansee. (2023). MOLYBDENUM material properties and alloys. Repéré à https://www.plansee.com/fr/materiaux/molybdene.html

Pollock, T. M., & Tin, S. (2006). Nickel-Based Superalloys for Advanced Turbine Engines : Chemistry, Microstructure and Properties. *Journal of Propulsion and Power*, *22*(2), 361-374. https://doi.org/10.2514/1.18239

Polozov, I., Starikov, K., Popovich, A., & Sufiiarov, V. (2021). Mitigating Inhomogeneity and Tailoring the Microstructure of Selective Laser Melted Titanium Orthorhombic Alloy by Heat Treatment, Hot Isostatic Pressing, and Multiple Laser Exposures. *Materials*, *14*(17), 4946. https://doi.org/10.3390/ma14174946

Polozov, I., Sufiiarov, V., Kantyukov, A., & Popovich, A. (2019). Selective Laser Melting of Ti2AlNb-based intermetallic alloy using elemental powders : Effect of process parameters and post-treatment on microstructure, composition, and properties. *Intermetallics*, *112*, 106554. https://doi.org/10.1016/j.intermet.2019.106554

Pragana, J. P. M., Sampaio, R. F. V., Bragança, I. M. F., Silva, C. M. A., & Martins, P. A. F. (2021). Hybrid metal additive manufacturing : A state–of–the-art review. *Advances in Industrial and Manufacturing Engineering*, *2*, 100032. https://doi.org/10.1016/j.aime.2021.100032

Promoppatum, P., Yao, S.-C., Pistorius, P. C., & Rollett, A. D. (2017). A Comprehensive Comparison of the Analytical and Numerical Prediction of the Thermal History and Solidification Microstructure of Inconel 718 Products Made by Laser Powder-Bed Fusion. *Engineering*, *3*(5), 685-694. https://doi.org/10.1016/J.ENG.2017.05.023

Qiu, S., Chen, B. K., & Xiang, C. S. (2020). Preparation and Properties of Spherical Mo Powders by Plasma Rotating Electrode Process for Additive Manufacturing. *Materials Science Forum*, *993*, 391-397. https://doi.org/10.4028/www.scientific.net/MSF.993.391

R. H. Cooper Jr and E. E. Hoffman. (1984). Refractory alloy technology for space nuclear power applications. Oak Ridge National Laboratory and U.S Department of Energy Oak Ridge Operations.

Ramakrishnan, T., Kumar, A., Hudon, P., & Brochu, M. (2024). Laser Powder Bed Fusion Additive Manufacturing of Mo and TZM Exoskeleton with Cu Infiltration for New Heat Sinks Configuration. *Advanced Engineering Materials*, *26*(3), 2301409. https://doi.org/10.1002/adem.202301409

Ratschbacher, K., & Luidold, S. (2015). Kinetics and Optimization of Refractory Metal Alloy Oxidation and Sublimation. *Chemie Ingenieur Technik*, *87*(11), 1558-1568. https://doi.org/10.1002/cite.201500059

Rebesan, P. (2022). *Characterization of Molybdenum Produced by Laser Powder Bed Fusion for the High-Temperature Ion Sources of the INFN SPES facility*. Politechnico di Milano.

Rebesan, P., Ballan, M., Bonesso, M., Campagnolo, A., Corradetti, S., Dima, R., … Vedani, M. (2021). Pure molybdenum manufactured by Laser Powder Bed Fusion : Thermal and mechanical characterization at room and high temperature. *Additive Manufacturing*, *47*, 102277. https://doi.org/10.1016/j.addma.2021.102277

Rebesan, P., Gennari, C., Zorzi, F., Bonesso, M., Calliari, I., Dima, R., … Vedani, M. (2021). Interface analysis of additively manufactured pure molybdenum and AISI 304 stainless steel building-plate. *Materials Letters*, *305*, 130763. https://doi.org/10.1016/j.matlet.2021.130763

Reiser, J., & Hartmaier, A. (2020). Elucidating the dual role of grain boundaries as dislocation sources and obstacles and its impact on toughness and brittle-to-ductile transition. *Scientific Reports*, *10*(1), 2739. https://doi.org/10.1038/s41598-020-59405-5

Ren, C., Fang, Z. Z., Koopman, M., Butler, B., Paramore, J., & Middlemas, S. (2018). Methods for improving ductility of tungsten—A review. *International Journal of Refractory Metals and Hard Materials*, *75*, 170-183. https://doi.org/10.1016/j.ijrmhm.2018.04.012

Rometsch, P. A., Zhu, Y., Wu, X., & Huang, A. (2022). Review of high-strength aluminium alloys for additive manufacturing by laser powder bed fusion. *Materials & Design*, *219*, 110779. https://doi.org/10.1016/j.matdes.2022.110779

Ron, T., Leon, A., Popov, V., Strokin, E., Eliezer, D., Shirizly, A., & Aghion, E. (2022). Synthesis of Refractory High-Entropy Alloy WTaMoNbV by Powder Bed Fusion Process Using Mixed Elemental Alloying Powder. *Materials*, *15*(12), 4043. https://doi.org/10.3390/ma15124043

Rowe, R. G. (1992). Advanced Ti_3Al-Base Alloy Property Comparison. *Key Engineering Materials*, *77-78*, 61-70. https://doi.org/10.4028/www.scientific.net/KEM.77-78.61

Sabzi, H. E., Maeng, S., Liang, X., Simonelli, M., Aboulkhair, N. T., & Rivera-Díaz-del-Castillo, P. E. J. (2020). Controlling crack formation and porosity in laser powder bed fusion : Alloy design and process optimisation. *Additive Manufacturing*, *34*, 101360. https://doi.org/10.1016/j.addma.2020.101360

Sanchez, S., Smith, P., Xu, Z., Gaspard, G., Hyde, C. J., Wits, W. W., … Clare, A. T. (2021). Powder Bed Fusion of nickel-based superalloys : A review. *International Journal of Machine Tools and Manufacture*, *165*, 103729. https://doi.org/10.1016/j.ijmachtools.2021.103729

Santagata, A., Pace, M. L., Bellucci, A., Mastellone, M., Bolli, E., Valentini, V., … Trucchi, D. M. (2022). Enhanced and Selective Absorption of Molybdenum Nanostructured Surfaces for Concentrated Solar Energy Applications. *Materials*, *15*(23), 8333. https://doi.org/10.3390/ma15238333

Scapin, M., Peroni, L., & Carra, F. (2016). Investigation and Mechanical Modelling of Pure Molybdenum at High Strain-Rate and Temperature. *Journal of Dynamic Behavior of Materials*, *2*(4), 460-475. https://doi.org/10.1007/s40870-016-0081-3

Schimbäck, D., Braun, J., Leichtfried, G., Clemens, H., & Mayer, S. (2021). Laser powder bed fusion of an engineering intermetallic TiAl alloy. *Materials & Design*, *201*, 109506. https://doi.org/10.1016/j.matdes.2021.109506

Schneider, M., Šimůnková, L., Michaelis, A., & Hoogsteen, W. (2021). Electrochemical machining of molybdenum. *International Journal of Refractory Metals and Hard Materials*, *101*, 105689. https://doi.org/10.1016/j.ijrmhm.2021.105689

Schuster, J. C., & Palm, M. (2006). Reassessment of the binary Aluminum-Titanium phase diagram. *Journal of Phase Equilibria and Diffusion*, *27*(3), 255-277. https://doi.org/10.1361/154770306X109809

Shabalin, I. L. (2014). *Ultra-High Temperature Materials I : Carbon (Graphene/Graphite) and Refractory Metals*. Dordrecht: Springer Netherlands.

Sharma, S. K., Grewal, H. S., Saxena, K. K., Mohammed, K. A., Prakash, C., Davim, J. P., … Tomków, J. (2022). Advancements in the Additive Manufacturing of Magnesium and Aluminum Alloys through Laser-Based Approach. *Materials*, *15*(22), 8122. https://doi.org/10.3390/ma15228122

Sharma, S., Krishna, K. V. M., Joshi, S. S., Radhakrishnan, M., Palaniappan, S., Dussa, S., … Dahotre, N. B. (2023). Laser based additive manufacturing of tungsten : Multi-scale thermo-kinetic and thermo-mechanical computational model and experiments. *Acta Materialia*, *259*, 119244. https://doi.org/10.1016/j.actamat.2023.119244

Shi, Q., Du, W., Qin, F., Tan, C., Khanlari, K., Xie, H., … Wu, A. (2023). Pure Tungsten Fabricated by Laser Powder Bed Fusion with Subsequent Hot Isostatic Pressing : Microstructural Evolution, Mechanical Properties, and Thermal Conductivity. *Journal of Materials Engineering and Performance*, *32*(23), 10910-10923. https://doi.org/10.1007/s11665-023-07891-9

Shields, J. A. (2013). Applications of Molybdenum Metal and Its Alloys.

Shmelev, A. N., & Kozhahmet, B. K. (2017). Use of molybdenum as a structural material of fuel elements for improving the safety of nuclear reactors. *Journal of Physics : Conference Series*, *781*, 012022. https://doi.org/10.1088/1742-6596/781/1/012022

Shree Meenakshi, K., & Ananda Kumar, S. (2022). Corrosion resistant behaviour of titanium – Molybdenum alloy in sulphuric acid environment. *Materials Today : Proceedings*, *65*, 3282-3287. https://doi.org/10.1016/j.matpr.2022.05.389

Sidambe, A. T., Tian, Y., Prangnell, P. B., & Fox, P. (2019). Effect of processing parameters on the densification, microstructure and crystallographic texture during the laser powder bed fusion of pure tungsten. *International Journal of Refractory Metals and Hard Materials*, *78*, 254-263. https://doi.org/10.1016/j.ijrmhm.2018.10.004

Singh, R., Gupta, A., Tripathi, O., Srivastava, S., Singh, B., Awasthi, A., … Saxena, K. K. (2020). Powder bed fusion process in additive manufacturing : An overview. *Materials Today : Proceedings*, *26*, 3058-3070. https://doi.org/10.1016/j.matpr.2020.02.635

Škoro, G. P., Bennett, J. R. J., Edgecock, T. R., & Booth, C. N. (2012). Yield strength of molybdenum, tantalum and tungsten at high strain rates and very high temperatures. *Journal of Nuclear Materials*, *426*(1-3), 45-51. https://doi.org/10.1016/j.jnucmat.2012.03.044

Smallman, R. E., & Ngan, A. H. W. (2014). *Modern physical metallurgy* (8th edition). Oxford Waltham, MA: Elsevier/Butterworth-Heinemann.

Solyaev, Y., Rabinskiy, L., & Tokmakov, D. (2019). Overmelting and closing of thin horizontal channels in AlSi10Mg samples obtained by selective laser melting. *Additive Manufacturing*, *30*, 100847. https://doi.org/10.1016/j.addma.2019.100847

Song, C., Deng, Z., Zou, Z., Liu, L., Xu, K., & Yang, Y. (2022). Pure tantalum manufactured by laser powder bed fusion : Influence of scanning speed on the evolution of microstructure and mechanical properties. *International Journal of Refractory Metals and Hard Materials*, *107*, 105882. https://doi.org/10.1016/j.ijrmhm.2022.105882

Soong, S. Z., Lai, W. L., & Kay Lup, A. N. (2023). Atomization of metal and alloy powders : Processes, parameters, and properties. *AIChE Journal*, *69*(11), e18217. https://doi.org/10.1002/aic.18217

Soundararajan, S. R., Vishnu, J., Manivasagam, G., Muktinutalapati, N. R., Soundararajan, S. R., Vishnu, J., … Muktinutalapati, N. R. (2020). Heat Treatment of Metastable Beta Titanium Alloys. Dans *Welding—Modern Topics*. (S.l.): IntechOpen. https://doi.org/10.5772/intechopen.92301

Stephens, J. R. (1972). Review of deformation behavior of tungsten at temperature less than 0.2 absolute melting temperature. NASA Lewis Research Center Cleveland, OH, United States.

Stephens, J. R., & Witzke, W. R. (1971). Alloy softening in group via metals alloyed with rhenium. *Journal of the Less Common Metals*, *23*(4), 325-342. https://doi.org/10.1016/0022-5088(71)90043-9

Stopyra, W., Gruber, K., Smolina, I., Kurzynowski, T., & Kuźnicka, B. (2020). Laser powder bed fusion of AA7075 alloy : Influence of process parameters on porosity and hot cracking. *Additive Manufacturing*, *35*, 101270. https://doi.org/10.1016/j.addma.2020.101270

Sumin Sih, S., & Barlow, J. W. (2004). The Prediction of the Emissivity and Thermal Conductivity of Powder Beds. *Particulate Science and Technology*, *22*(3), 291-304. https://doi.org/10.1080/02726350490501682a

Tabernig, B., & Reheis, N. (2010). Joining of molybdenum and its application. *International Journal of Refractory Metals and Hard Materials*, *28*(6), 728-733. https://doi.org/10.1016/j.ijrmhm.2010.06.008

Tabie, V. M., Li, C., Saifu, W., Li, J., & Xu, X. (2020). Mechanical properties of near alpha titanium alloys for high-temperature applications—A review. *Aircraft Engineering and Aerospace Technology*, *92*(4), 521-540. https://doi.org/10.1108/AEAT-04-2019-0086

Takida, T., Kurishita, H., Mabuchi, M., Igarashi, T., Doi, Y., & Nagae, T. (2004). Mechanical Properties of Fine-Grained, Sintered Molybdenum Alloys with Dispersed Particles Developed by Mechanical Alloying. *MATERIALS TRANSACTIONS*, *45*(1), 143-148. https://doi.org/10.2320/matertrans.45.143

Talignani, A., Seede, R., Whitt, A., Zheng, S., Ye, J., Karaman, I., … Wang, Y. M. (2022). A review on additive manufacturing of refractory tungsten and tungsten alloys. *Additive Manufacturing*, *58*, 103009. https://doi.org/10.1016/j.addma.2022.103009

Tan, C., Zhou, K., Ma, W., Attard, B., Zhang, P., & Kuang, T. (2018). Selective laser melting of high-performance pure tungsten : Parameter design, densification behavior and mechanical properties. *Science and Technology of Advanced Materials*, *19*(1), 370-380. https://doi.org/10.1080/14686996.2018.1455154

Tang, C., Le, K. Q., & Wong, C. H. (2020). Physics of humping formation in laser powder bed fusion. *International Journal of Heat and Mass Transfer*, *149*, 119172. https://doi.org/10.1016/j.ijheatmasstransfer.2019.119172

Tang, J., Sun, Y., Zhang, C., Wang, L., Zhou, Y., Fang, D., & Liu, Y. (2020). Reaction Mechanism and Process Control of Hydrogen Reduction of Ammonium Perrhenate. *Metals*, *10*(5), 640. https://doi.org/10.3390/met10050640

Tang, P., Wang, S., Duan, H., Long, M., Li, Y., Fan, S., & Chen, D. (2020). The Formation of Humps and Ripples During Selective Laser Melting of 316l Stainless Steel. *JOM*, *72*(3), 1128-1137. https://doi.org/10.1007/s11837-019-03987-7

Taylor, J. L. (1965). Tensile Behavior of Same-Lot Single-Crystal and Polycrystalline Tungsten from 2500 to 5000°F.

Thacker, B. H., & Paez, T. L. (2014). A Simple Probabilistic Validation Metric for the Comparison of Uncertain Model and Test Results. Dans *16th AIAA Non-Deterministic Approaches Conference*. National Harbor, Maryland: American Institute of Aeronautics and Astronautics. https://doi.org/10.2514/6.2014-0121

Thomas, M. (2020). Alliages intermétalliques à base de TiAl. *Étude et propriétés des métaux*. https://doi.org/10.51257/a-v2-m4782

Timetal 21S. (2000). Titanium Metals Corportaion. Repéré à https://www.timet.com/documents/datasheets/

Titanium alloys for aerospace structures and engines. (2012). Dans *Introduction to Aerospace Materials* (pp. 202-223). (S.l.): Elsevier. https://doi.org/10.1533/9780857095152.202

Todo, T., Ishimoto, T., Gokcekaya, O., Oh, J., & Nakano, T. (2022). Single crystalline-like crystallographic texture formation of pure tungsten through laser powder bed fusion. *Scripta Materialia*, *206*, 114252. https://doi.org/10.1016/j.scriptamat.2021.114252

Tofail, S. A. M., Koumoulos, E. P., Bandyopadhyay, A., Bose, S., O'Donoghue, L., & Charitidis, C. (2018). Additive manufacturing : Scientific and technological challenges, market uptake and opportunities. *Materials Today*, *21*(1), 22-37. https://doi.org/10.1016/j.mattod.2017.07.001

Tolias, P. (2017). Analytical expressions for thermophysical properties of solid and liquid tungsten relevant for fusion applications. *Nuclear Materials and Energy*, *13*, 42-57. https://doi.org/10.1016/j.nme.2017.08.002

Toschka, A., Pöhle, G., Quadbeck, P., Suschek, C. V., Strauß, A., Redlich, C., & Rana, M. (2022). Molybdenum as a Potential Biocompatible and Resorbable Material for Osteosynthesis in Craniomaxillofacial Surgery—An In Vitro Study. *International Journal of Molecular Sciences*, *23*(24), 15710. https://doi.org/10.3390/ijms232415710

Tungsten for Industrial 3D Printing|EOS. (2023). Repéré à https://www.eos.info/en/3d-printing-materials/metals/refractorymetals

Túry, P., & Krausz, S. (1936). Effect of Molecular Nitrogen on Molybdenum at High Temperatures. *Nature*, *138*(3486), 331-331. https://doi.org/10.1038/138331a0

Vaglio, E., De Monte, T., Lanzutti, A., Totis, G., Sortino, M., & Fedrizzi, L. (2020). Single tracks data obtained by selective laser melting of Ti6Al4V with a small laser spot diameter. *Data in Brief*, *33*, 106443. https://doi.org/10.1016/j.dib.2020.106443

Veeck, S., Lee, D., Boyer, R., & Briggs, R. (2004). The microstructure and properties of cast titanium alloy Ti-5553 were evaluated in a joint program by Howmet and Boeing.

Vincent, B., Optasanu, V., Herbst, F., Chevalier, S., Popa, I., Montesin, T., & Lavisse, L. (2021). Comparison Between the Oxidation Behaviors of Ti6242S, Ti6246, TiXT Alloys, and Pure Titanium. *Oxidation of Metals*, *96*(3-4), 283-294. https://doi.org/10.1007/s11085-021-10051-w

Vrancken, B., Ganeriwala, R., & Matthews, M. (2022). Local strain release due to microcracking in laser melted tungsten. *Procedia CIRP*, *111*, 148-152. https://doi.org/10.1016/j.procir.2022.08.139

Wadsworth, J., Nieh, T. G., & Stephens, J. J. (1988). Recent advances in aerospace refractory metal alloys. *International Materials Reviews*, *33*(1), 131-150. https://doi.org/10.1179/imr.1988.33.1.131

Wang, D., Wang, Z., Li, K., Ma, J., Liu, W., & Shen, Z. (2019). Cracking in laser additively manufactured W : Initiation mechanism and a suppression approach by alloying. *Materials & Design*, *162*, 384-393. https://doi.org/10.1016/j.matdes.2018.12.010

Wang, D., Yu, C., Zhou, X., Ma, J., Liu, W., & Shen, Z. (2017). Dense Pure Tungsten Fabricated by Selective Laser Melting. *Applied Sciences*, *7*(4), 430. https://doi.org/10.3390/app7040430

Wang, D.-Z., Li, K.-L., Yu, C.-F., Ma, J., Liu, W., & Shen, Z.-J. (2019). Cracking Behavior in Additively Manufactured Pure Tungsten. *Acta Metallurgica Sinica (English Letters)*, *32*(1), 127-135. https://doi.org/10.1007/s40195-018-0752-2

Wang, L., Li, Y., Zhou, L., Lou, Y., Liu, S., Zheng, D., & Yi, M. (2023). Progress in additive manufacturing, additive repair and fatigue evaluation of aviation titanium alloy blades. *Materials Research Letters*, *11*(12), 973-1012. https://doi.org/10.1080/21663831.2023.2275599

Wang, Y., Ji, X., & Liang, S. Y. (2023). Analytical modeling of temperature distribution in laser powder bed fusion with different scan strategies. *Optics & Laser Technology*, *157*, 108708. https://doi.org/10.1016/j.optlastec.2022.108708

Watkins, T. R., Schajer, G. S., & Lance, M. J. (2012). Residual Stress Measurements. Dans *Comprehensive Materials Processing* (pp. 113-134). (S.l.): Elsevier. https://doi.org/10.1016/B978-0-08-096532-1.00109-6

Weiss, I., & Semiatin, S. L. (1999). Thermomechanical processing of alpha titanium alloys—An overview. *Materials Science and Engineering : A*, *263*(2), 243-256. https://doi.org/10.1016/S0921-5093(98)01155-1

Wen, S., Wang, C., Zhou, Y., Duan, L., Wei, Q., Yang, S., & Shi, Y. (2019). High-density tungsten fabricated by selective laser melting : Densification, microstructure, mechanical and thermal performance. *Optics & Laser Technology*, *116*, 128-138. https://doi.org/10.1016/j.optlastec.2019.03.018

Whang, S.-H. (2011). *Nanostructured metals and alloys : Processing, microstructure, mechanical properties and applications*. Cambridge: Woodhead publishing.

Wheeler, J., Jiang, Z., Prior, D. J., Tullis, J., Drury, M. R., & Trimby, P. W. (2003). From geometry to dynamics of microstructure : Using boundary lengths to quantify boundary misorientations and anisotropy. *Tectonophysics*, *376*(1-2), 19-35. https://doi.org/10.1016/j.tecto.2003.08.007

Wohlers Associates (Éd.). (2016). *Wohlers report 2016 : 3D printing and additive manufacturing state of the industry annual worldwide progress report*. Fort Collins (Colo.): Wohlers Associates.

Wolfer, A. J., Aires, J., Wheeler, K., Delplanque, J.-P., Rubenchik, A., Anderson, A., & Khairallah, S. (2019). Fast solution strategy for transient heat conduction for arbitrary scan paths in additive manufacturing. *Additive Manufacturing*, *30*, 100898. https://doi.org/10.1016/j.addma.2019.100898

Wrona, A., Lis, M., Pęcak, K., Kalemba-Rec, I., Dymek, S., Wróbel, M., … Śliwiński, P. (2022). Ni–Cr Powders Modified with Rhenium as a Novel Coating Material—Physical Properties, Microstructure, and Behavior in Plasma Plume. *Materials*, *15*(11), 3844. https://doi.org/10.3390/ma15113844

Wu, A., Shi, Y., Jing, Y., Li, S., Li, W., & Su, X. (2025). Effects of linear energy density on melt pool and microstructure of selective laser melted AlSi10Mg : An experimental and numerical study. *Materials Today Communications*, *43*, 111703. https://doi.org/10.1016/j.mtcomm.2025.111703

Wu, Y., Li, M., Wang, J., Wang, Y., An, X., Fu, H., … Zou, Q. (2022). Powder-bed-fusion additive manufacturing of molybdenum : Process simulation, optimization, and property prediction. *Additive Manufacturing*, *58*, 103069. https://doi.org/10.1016/j.addma.2022.103069

Xiao, M., Li, F., Xie, H., & Wang, Y. (2012). Characterization of strengthening mechanism and hot deformation behavior of powder metallurgy molybdenum. *Materials & Design*, *34*, 112-119. https://doi.org/10.1016/j.matdes.2011.07.065

Xie, Z., Dai, Y., Ou, X., Ni, S., & Song, M. (2020). Effects of selective laser melting build orientations on the microstructure and tensile performance of Ti–6Al–4V alloy. *Materials Science and Engineering : A*, *776*, 139001. https://doi.org/10.1016/j.msea.2020.139001

Xing, H., Hu, P., Han, J., Li, S., Ge, S., Hua, X., … Feng, P. (2022). Effects of oxygen on microstructure and evolution mechanism of body-centred-cubic molybdenum. *International Journal of Refractory Metals and Hard Materials*, *103*, 105747. https://doi.org/10.1016/j.ijrmhm.2021.105747

Xiong, Z., Zhang, P., Tan, C., Dong, D., Ma, W., & Yu, K. (2020). Selective Laser Melting and Remelting of Pure Tungsten. *Advanced Engineering Materials*, *22*(3), 1901352. https://doi.org/10.1002/adem.201901352

Xu, C., Sikan, F., Atabay, S. E., Muñiz-Lerma, J. A., Sanchez-Mata, O., Wang, X., & Brochu, M. (2020). Microstructure and mechanical behavior of as-built and heat-treated Ti–6Al–7Nb produced by laser powder bed fusion. *Materials Science and Engineering : A*, *793*, 139978. https://doi.org/10.1016/j.msea.2020.139978

Xu, J., Duan, R., Feng, K., Zhang, C., Zhou, Q., Liu, P., & Li, Z. (2022). Enhanced strength and ductility of laser powder bed fused NbMoTaW refractory high-entropy alloy via carbon microalloying. *Additive Manufacturing Letters*, *3*, 100079. https://doi.org/10.1016/j.addlet.2022.100079

Yadav, P., & Saxena, K. K. (2020). Effect of heat-treatment on microstructure and mechanical properties of Ti alloys : An overview. *Materials Today : Proceedings*, *26*, 2546-2557. https://doi.org/10.1016/j.matpr.2020.02.541

Yamamoto, T., Hara, M., & Hatano, Y. (2021). Cracking behavior and microstructural, mechanical and thermal characteristics of tungsten–rhenium binary alloys fabricated by laser powder bed fusion. *International Journal of Refractory Metals and Hard Materials*, *100*, 105651. https://doi.org/10.1016/j.ijrmhm.2021.105651

Yang, G., & Park, S.-J. (2019). Deformation of Single Crystals, Polycrystalline Materials, and Thin Films : A Review. *Materials*, *12*(12), 2003. https://doi.org/10.3390/ma12122003

Yang, Jiayu, Song, Y., Dong, K., & Han, E.-H. (2023). Research progress on the corrosion behavior of titanium alloys. *Corrosion Reviews*, *41*(1), 5-20. https://doi.org/10.1515/corrrev-2022-0031

Yang, Jingjing, Han, J., Yu, H., Yin, J., Gao, M., Wang, Z., & Zeng, X. (2016). Role of molten pool mode on formability, microstructure and mechanical properties of selective laser melted Ti-6Al-4V alloy. *Materials & Design*, *110*, 558-570. https://doi.org/10.1016/j.matdes.2016.08.036

Yang, L., Yang, J., Han, F., Zhang, Z., Li, Q., Dong, Z., … Provatas, N. (2023). Hot cracking susceptibility prediction from quantitative multi-phase field simulations with grain boundary effects. *Acta Materialia*, *250*, 118821. https://doi.org/10.1016/j.actamat.2023.118821

Yang, Xin, Ma, W., Zhang, Z., Liu, S., & Tang, H. (2022). Ultra-high specific strength Ti6Al4V alloy lattice material manufactured via selective laser melting. *Materials Science and Engineering : A*, *840*, 142956. https://doi.org/10.1016/j.msea.2022.142956

Yang, Xiuxuan, Zhang, B., Bai, Q., & Xie, G. (2021). Correlation of microstructure and mechanical properties of Ti2AlNb manufactured by SLM and heat treatment. *Intermetallics*, *139*, 107367. https://doi.org/10.1016/j.intermet.2021.107367

Yih, S. W. H., & Wang, C. T. (1979). *Tungsten : Sources, metallurgy, properties, and applications*. New York: Plenum Press.

Young, M., Levine, E., & Margolin, H. (1974). The aging behavior of orthorhombic marten site in Ti-6-2-4-6. *Metallurgical transactions*, *5*(8), 1891-1898. https://doi.org/10.1007/BF02644157

Yvell, K., Grehk, T. M., Hedström, P., Borgenstam, A., & Engberg, G. (2018). EBSD analysis of surface and bulk microstructure evolution during interrupted tensile testing of a Fe-19Cr-12Ni alloy. *Materials Characterization*, *141*, 8-18. https://doi.org/10.1016/j.matchar.2018.04.035

Zeng, Q., & Chen, X. (2023). Combustor technology of high temperature rise for aero engine. *Progress in Aerospace Sciences*, *140*, 100927. https://doi.org/10.1016/j.paerosci.2023.100927

Zhang, F. F., Feng, C., Zhu, L. J., & Song, W. W. (2021). Research Progress on Corrosion Resistance of Titanium Alloy Oil Well Tubing. *Materials Science Forum*, *1035*, 528-533. https://doi.org/10.4028/www.scientific.net/MSF.1035.528

Zhang, K., Lei, Z., Chen, Y., Yang, K., & Bao, Y. (2019). Heat treatment of laser-additive welded Ti2AlNb joints : Microstructure and tensile properties. *Materials Science and Engineering : A*, *744*, 436-444. https://doi.org/10.1016/j.msea.2018.12.058

Zhang, K., Lei, Z., Ni, L., Zhou, H., & Chen, Y. (2021). Improvement in microstructure and high-temperature brittleness of laser-welded Ti-22Al-25Nb joints with the addition of TiB2 powder. *Journal of Materials Processing Technology*, *288*, 116848. https://doi.org/10.1016/j.jmatprotec.2020.116848

Zhang, T., zhou, X., Wang, D., An, Z., Ding, G., Gao, H., & Bian, D. (2025). Mechanism of double exposure strategy for improving down-skin roughness and dimensional accuracy in support-free printing. *Materials & Design*, *254*, 113990. https://doi.org/10.1016/j.matdes.2025.113990

Zhang, X.-Q., Liu, J.-Q., Zhu, X.-Y., & Wu, Y.-C. (2025). Effect of laser powder bed fusion process parameters on the microstructure and properties of pure tungsten. *Annals of Nuclear Energy*, *223*, 111691. https://doi.org/10.1016/j.anucene.2025.111691

Zhang, Y., Fu, T., Yu, L., Shen, F., Wang, J., & Cui, K. (2022). Improving oxidation resistance of TZM alloy by deposited Si–MoSi2 composite coating with high silicon concentration. *Ceramics International*, *48*(14), 20895-20904. https://doi.org/10.1016/j.ceramint.2022.04.080

Zhang, Y., Hussain, S., Cui, K., Fu, T., Wang, J., Javed, M. S., … Aslam, B. (2019). Microstructure and Mechanical Properties of MoSi $_2$ Coating Deposited on Mo Substrate by Hot Dipping Processes. *Journal of Nanoelectronics and Optoelectronics*, *14*(12), 1680-1685. https://doi.org/10.1166/jno.2019.2676

Zhang, Y. Z., Liu, Y. T., Zhao, X. H., & Tang, Y. J. (2016). The interface microstructure and tensile properties of direct energy deposited TC11/Ti2AlNb dual alloy. *Materials & Design*, *110*, 571-580. https://doi.org/10.1016/j.matdes.2016.08.012

Zhao, H., Xie, L., Xin, C., Li, N., Zhao, B., & Li, L. (2023). Effect of molybdenum content on corrosion resistance and corrosion behavior of Ti-Mo titanium alloy in hydrochloric acid. *Materials Today Communications*, *34*, 105032. https://doi.org/10.1016/j.mtcomm.2022.105032

Zhao, J., Wang, K., Lv, L., & Liu, G. (2022). Effect of grain size on the yield stress and microscopic mechanism of a near-α titanium alloy during non-superplastic hot deformation. *Materials Science and Engineering : A*, *840*, 142932. https://doi.org/10.1016/j.msea.2022.142932

Zhao, Y., Koizumi, Y., Aoyagi, K., Yamanaka, K., & Chiba, A. (2021). Thermal properties of powder beds in energy absorption and heat transfer during additive manufacturing with electron beam. *Powder Technology*, *381*, 44-54. https://doi.org/10.1016/j.powtec.2020.11.082

Zheng, H., Li, H., Lang, L., Gong, S., & Ge, Y. (2018). Effects of scan speed on vapor plume behavior and spatter generation in laser powder bed fusion additive manufacturing. *Journal of Manufacturing Processes*, *36*, 60-67. https://doi.org/10.1016/j.jmapro.2018.09.011

Zheng, Z., Balint, D. S., & Dunne, F. P. E. (2017). Mechanistic basis of temperature-dependent dwell fatigue in titanium alloys. *Journal of the Mechanics and Physics of Solids*, *107*, 185-203. https://doi.org/10.1016/j.jmps.2017.07.010

Zhou, Y. H., Li, W. P., Wang, D. W., Zhang, L., Ohara, K., Shen, J., … Yan, M. (2019). Selective laser melting enabled additive manufacturing of Ti–22Al–25Nb intermetallic : Excellent combination of strength and ductility, and unique microstructural features associated. *Acta Materialia*, *173*, 117-129. https://doi.org/10.1016/j.actamat.2019.05.008

Zhou, Y. H., Li, W. P., Zhang, L., Zhou, S. Y., Jia, X., Wang, D. W., & Yan, M. (2020). Selective laser melting of Ti–22Al–25Nb intermetallic : Significant effects of hatch distance on microstructural features and mechanical properties. *Journal of Materials Processing Technology*, *276*, 116398. https://doi.org/10.1016/j.jmatprotec.2019.116398

Zhou, Y. H., Wang, D. W., Song, L. J., Mukhtar, A., Huang, D. N., Yang, C., & Yan, M. (2021). Effect of heat treatments on the microstructure and mechanical properties of Ti2AlNb intermetallic fabricated by selective laser melting. *Materials Science and Engineering : A*, *817*, 141352. https://doi.org/10.1016/j.msea.2021.141352

Zhou, Y. H., Zhang, Z. H., Wang, Y. P., Liu, G., Zhou, S. Y., Li, Y. L., … Yan, M. (2019). Selective laser melting of typical metallic materials : An effective process prediction model developed by energy absorption and consumption analysis. *Additive Manufacturing*, *25*, 204-217. https://doi.org/10.1016/j.addma.2018.10.046

Zou, Z., Simonelli, M., Katrib, J., Dimitrakis, G., & Hague, R. (2021). Microstructure and tensile properties of additive manufactured Ti-6Al-4V with refined prior-β grain structure obtained by rapid heat treatment. *Materials Science and Engineering : A*, *814*, 141271. https://doi.org/10.1016/j.msea.2021.141271